The Dissertation Committee for Drew Richard Eddy Certifies that this is the approved version of the following dissertation:

Mesozoic rifting along the eastern seaboard of North America: insights from the seismic velocity structure of the Newfoundland margin and the northern Gulf of Mexico

Committee:

Harm Van Avendonk, Supervisor

Gail Christeson

Luc Lavier

Danny Stockli

Sean Gulick

Donna Shillington

Mesozoic rifting along the eastern seaboard of North America: insights from the seismic velocity structure of the Newfoundland margin and the northern Gulf of Mexico

by

Drew Richard Eddy, M.S.; A.B.

Dissertation

Presented to the Faculty of the Graduate School of

The University of Texas at Austin

in Partial Fulfillment

of the Requirements

for the Degree of

Doctor of Philosophy

The University of Texas at Austin

December 2014

Acknowledgements

I sincerely thank my dissertation committee and especially my supervisor, Harm van Avendonk, for taking the time to mentor, encourage, critique, and ultimately improve both this project and my understanding of geology and geophysics. I thank The University of Texas Institute for Geophysics for awarding me the Maurice Ewing and J. Lamar Worzel Graduate Student Fellowship. I thank the captain, crew, and scientific party of the R/V *Iron Cat* for their help with data acquisition and processing during the GUMBO Project. I thank FUGRO and ION/GXT for permissions to display MCS reflection profiles in the Gulf of Mexico. I thank the following co-authors for their contributions to published and in-review manuscripts: D. Shillington, G. Christeson, I. Norton, J. Snedden, G. Karner, and C. Johnson. I also thank D. Clark, L. Gahagan, L. Lawver, J. Sanford, and M. Duncan for manuscript comments and technical support. Last, but certainly not least, I thank Philip Guerrero for his endless assistance throughout my tenure as a graduate student in the Jackson School of Geosciences.

Mesozoic rifting along the eastern seaboard of North America: insights from the seismic velocity structure of the Newfoundland margin and the northern Gulf of Mexico

Drew Richard Eddy, Ph.D.
The University of Texas at Austin, 2014

Supervisor: Harm Van Avendonk

Passive margins along the eastern seaboard of North America formed during early Mesozoic continental rifting and seafloor spreading, tectonic processes that are not fully understood. Seismic refraction and reflection data at the northeastern and north-central Gulf of Mexico and the Grand Banks of Newfoundland, Canada, are used to interpret the deep seismic velocity structure of sediments, crust, and mantle. These interpretations allow for a better understanding of continental rifting, mantle upwelling, magmatism, and seafloor spreading. Magma-poor rifting of the Newfoundland-Iberian margin developed a wide continent-ocean transition zone (COT). I present an analysis of 2-D marine seismic refraction and reflection data from the SCREECH project, including a shear velocity model to constrain the composition of the Newfoundland COT. Comparing SCREECH Line 2 *Vp*/*Vs* ratios with depth to potential lithologies supports a COT comprised of hyperextended continental crust and serpentinized mantle. Reconstructions of the opening of the Gulf of Mexico basin are impeded by a lack of seafloor magnetic anomalies and an abundance of sediments that obscure acquisition of seismic refraction datasets. Accordingly, the roles of mantle upwelling, magmatism, and lithospheric extension in

this small ocean basin are poorly known. I present new 2-D marine seismic refraction data from the U.S. Gulf of Mexico collected during the 2010 GUMBO project. Rifting in the eastern Gulf of Mexico developed above a zone of anomalously high mantle potential temperatures that led to abundant magmatism. Syn-rift basins in continental crust, high velocity lower crust, a narrow zone of crustal thinning, and seaward-dipping reflectors support this interpretation. Oceanic crust here is thick despite slow seafloor-spreading rates, implying continuation of a thermal anomaly after rifting. In the north-central Gulf of Mexico, transitional crust is consistently thin (~10 km) across a wide zone. Velocity-depth comparisons, asymmetry of the north-central Gulf with the Yucatán margin, and dating of onshore xenoliths support either stretched and magmatically intruded continental crust or a multi-stage episode of seafloor spreading with ridge jumps. I contend that although tectonic inheritance may ultimately influence the location of a passive margin, the rifting process is largely controlled by mantle potential temperature and upwelling rate.

Table of Contents

Chapter 1: Introduction

1.1 Magma-poor and Volcanic Rift Margins

Tectonic and geologic processes that formed the passive margins along the eastern seaboard of North America are poorly understood, particularly with respect to how rifting initiated at these margins and how the expression of magmatism during continental breakup and seafloor spreading is controlled. Although tectonic inheritance plays an important role in determining the location of continental rifting, the effects of mantle upwelling and melting exert first-order controls on the evolution of rifted margins surrounding the Gulf of Mexico and Atlantic Ocean basins. During rifting at magma-poor margins, the impact of heat from the underlying mantle is minimal and melting is inhibited. Accordingly, magma-poor rifts lack extensive magmatic diking and melt production to weaken the lithosphere. Instead, continental crust is hyperextended ($\beta > 5$), and lower crust and mantle are often exhumed to the seafloor along shallow, asymmetric detachment faults [*Whitmarsh et al*., 2001; *Lavier and Manatschal*, 2006]. Compared to volcanic margins that often transition abruptly from thick continental crust to normal ocean crust, magma-poor margins exhibit a wide continent-ocean transition (COT; >100 km) separating stretched continental crust from the earliest oceanic basement (Figure 1.1) [*Whitmarsh et al.*, 2001]. Faulting of thinned and/or exhumed basement in the COT can lead to shallow hydrothermal circulation and serpentinization of mantle peridotites, which potentially lubricates detachment rift zones and causes to small increases in rock volume that further weaken the lithosphere [*Lavier and Manatschal*, 2006]. Weakening

and extension in the normally strong upper mantle eventually gives way to the initiation of melting from the heat of upwelling asthenospheric mantle, generating enough melt to begin production of mid-ocean ridge basalts [*Manatschal*, 2004; *Reston & McDermott*, 2011]. Upwelling of the mantle is a passive response at magma-poor rifts (*e.g.*, upwelling rate equals the half-spreading rate), filling the void created by far-field stresses pulling apart the thick upper lithosphere (Figure 1.2) [*Franke*, 2013].

Of all the Atlantic Ocean and Gulf of Mexico passive margins, ~75% are thought to be volcanic in nature [*Menzies et al.*, 2002]. At volcanic rifted margins, upwelling of the mantle may be a passive response to lithospheric stresses as with most magma-poor margins, or it may play a more active role in the onset of rifting with the upwelling rate several times greater than the half-spreading rate (Figures 1.1, 1.2). Early rift extension and thermal upwelling of the mantle thin and weaken the lithosphere, replacing it with hot, lower-density asthenospheric mantle and often leading to pre-rift doming of the crust [*Kelemen and Holbrook*, 1995; *Ziegler and Cloetingh*, 2004; *Armitage et al.*, 2009]. Adiabatic decompression melting in the upwelling mantle can create extensive diking and eruption of flood basalts in the form of large igneous provinces (LIPs) [*Menzies et al.*, 2002; *Geoffroy*, 2005; *Franke*, 2013]. Intrusive magmatism and underplating of mafic material at the developing volcanic rifted margin lead to ~10-25 km-thick zones of high seismic velocities (6.8-7.3 km/s) in the lowermost crust (HVLC) [*White and McKenzie*, 1989; *Holbrook and Kelemen*, 1993; *Holbrook et al.*, 2001]. A seaward-dipping series of reflections (SDRs) result from subaerial and submarine volcaniclastics, and these SDRs delimit the transition from continental to oceanic crust at volcanic rifted margins, known

as the landward limit of oceanic crust (LOC). At the LOC, the initial igneous crust is typically thicker than normal owing to the continued effects of an abnormally hot asthenosphere [*Smallwood and White*, 1998; *Korenaga et al.*, 2000]. Volcanic margins can also arise from passive mantle upwelling if mantle potential temperatures are high enough to generate sufficient syn-rift melting. In this case, mantle melting models predict a thinner HVLC (<10 km) with higher average seismic velocities (>7.0 km/s) [*Korenaga et al.*, 2000; *Holbrook et al.*, 2001].

1.2 A Brief Tectonic History of the Eastern Seaboard of North America

The Wilson Cycle, repeating episodes of continent-continent collision, lithospheric breakup, and seafloor spreading, helped shape the present-day eastern seaboard of North America, including the Gulf of Mexico. Aggregation of the supercontinent Rodinia in the Mesoproterozoic led to the Grenville orogen (~1.1 Ga), which created much of the oldest lithosphere along the southeastern margin of Laurentia (Figure 1.3) [*Karlstrom et al.*, 2001; *Stern et al.*, 2011]. Cambrian rifting (~530 Ma) broke apart Rodinia, with rifts following the trend of the Grenville orogeny [*Thomas*, 2011]. Thereafter, Paleozoic collision of Laurentia with Gondwana-derived terranes formed the supercontinent Pangaea and closed the Iapetus and Rheic oceans (~310 Ma). By the end of this collision in the Permian, a continuous Ouachita-Appalachian orogen extended nearly the entire length of the eastern and southern margins of Laurentia. The most recent stage in the Wilson Cycle involved the Triassic breakup of Pangaea and rifting throughout the Mesozoic, with rifts trending along-strike of inherited orogenic structures [*Tommasi and Vauchez*, 2001] (Figure 1.3).

Mesozoic rifting along the eastern seaboard of North America began in the Late Triassic (~230-240 Ma) with the formation of extensive rift basins that generally parallel the present-day Gulf of Mexico and Atlantic Ocean passive margins [*Salvador*, 1987; *Withjack et al.*, 1998; 2012]. Interbedded with non-marine sediments in Triassic-Jurassic rift grabens are remnants of the Central Atlantic Magmatic Province (CAMP), a massive, yet brief (<1 Myr) igneous event that emplaced tholeiitic basalts across three continents at the Triassic-Jurassic boundary ~200 Ma (Figure 1.3) [*Oyarzun et al.*, 1997; *McHone*, 2000; *Olsen et al.*, 2003]. Continental rifting first progressed to seafloor spreading in the Central Atlantic in the Early to Middle Jurassic (~190-170 Ma) [*Sahabi et al.*, 2004; *Withjack et al.*, 2012], and this transition migrated northward as the North American and African continents separated. Approximately coincident to opening of the early Atlantic Ocean, Triassic-Middle Jurassic rifting in the Gulf of Mexico basin led to Late Jurassic seafloor spreading as the Yucatán block separated from the southern U.S. Gulf margin. Complete lithospheric breakup between the Newfoundland and Iberian margins in the northern Atlantic Ocean progressed more slowly and may have been diachronous, with the onset of seafloor spreading in the Aptian [*Tucholke et al.*, 2007].

1.3 Bookends of the Central Atlantic: Rifting of the Newfoundland and Gulf of Mexico Margins

Offshore Nova Scotia, a transition is shown from volcanic margins and normal seafloor-spreading spreading rates in the central Atlantic Ocean to magma-poor, slow to ultraslow seafloor spreading to the northeast at the Newfoundland margin (Figure 1.4) [*Funck et al.*, 2004; *Müller et al*., 2008]. Far-field stresses associated with the breakup of

Pangaea initiated rifting at the Newfoundland margin in the Late Triassic. Lasting until the Early Jurassic, an initial rift episode distributed strain broadly, stretching the ~35-km thick continental crust to form deep grabens on both the Newfoundland and Iberian conjugate margins (*e.g.*, Jeanne d'Arc, Flemish Pass, Orphan, and Lusitanian basins). A hiatus in rift intensity lasted until the onset of a second episode of rifting in the Late Jurassic (~160 Ma), which concentrated strain at the distal ends of both margins and thinned the continental crust to less than 10 km [*Dean et al.*, 2000; *Lau et al.*, 2006; *Van Avendonk et al.*, 2006; 2009; *Tucholke et al.*, 2007]. During the Early Cretaceous, northward propagation of the widening Atlantic Ocean opened the Southern Newfoundland and Galicia Interior basins, and subsequently separated the Flemish Cap of Newfoundland from the Iberian Galicia Bank [*Van Avendonk et al.*, 2006].

At the Grand Banks of Newfoundland, complete separation of the crystalline crust led to the formation of a broad COT. Rifting models suggest concave downward detachment faults rooted beneath Newfoundland may be responsible for possible zones of of exhumed lower crust and upper mantle within the COT [*Whitmarsh et al.*, 2001; *Van Avendonk et al.*, 2006; *Eddy et al.*, 2013]. These faults may then further weaken the lithosphere through serpentinization of exhumed mantle peridotites via hydrothermal circulation [*Lavier et al.*, 2006; *Manatschal et al.*, 2007; *Robertson*, 2007; *Sibuet et al.*, 2007]. Slow seafloor spreading between Iberia and Newfoundland began by the end of the Aptian (ca. 115 Ma) [*Robertson*, 2007; *Tucholke et al.*, 2007]. Seafloor spreading was initially relatively amagmatic and formed incipient or 'embryonic' ocean crust [*Jagoutz et al.*, 2007]. Post-rift magmatism from the formation of nearby seamounts at the

southern end of the Grand Banks may also have sourced Albian-Cenomanian post-rift sills into sediments above the basement in the Newfoundland transition zone [*Tucholke et al.*, 1989; *Karner and Shillington*, 2005].

Although it is well-established that rifting in the Gulf of Mexico formed a small ocean basin as the Yucatán block separated from North America during the breakup of Pangaea, the role of pre-rift tectonic inheritance compared to processes of melting and mantle upwelling are not constrained for the Gulf of Mexico. A 'soft' Paleozoic arc-continent collision prevented extensive crustal thickening at the Ouachita orogen, and instead led to thick (~40 km), thermally unstable crust near present-day basement highs of the Sabine, Monroe, and Wiggins uplifts [*Huerta and Harry*, 2012]. Rifting likely began in the Late Triassic and continued slowly until the Middle Jurassic, stretching and thinning the thick continental crust beneath the U.S. Gulf coastal region. The timing and nature of Gulf rifting is not well known, owing to a lack of seafloor spreading magnetic anomalies in the basin and thick sediments impeding previous deep seismic studies of rifted margins [*Ewing et al.*, 1960; *Ibrahim et al.*, 1981; *Ebeniro et al.*, 1986; 1988]. Pre-rift doming and gravity and magnetic potential data support a volcanic rift margin beneath the Texas coastline [*Dickinson et al.*, 2010]. Geophysical data support a wide transitional zone in the central Gulf of Mexico between thick continental crust and oceanic crust in the central Gulf basin [*Marton and Buffler*, 1994; *Mickus et al.*, 2009], which may suggest decreasing syn-rift magmatism there [*Stern et al.*, 2011]. However, estimates for the LOC vary widely [*Ibrahim and Uchupi*, 1981; *Marton and Buffler*, 1994; *Schouten and Klitgord*, 1994; *Sawyer et al.*, 1991; *Pindell and Kennan*, 2009;

Hudec et al., 2013a]. In the eastern Gulf of Mexico, despite the lack of deep refraction data, SDRs are interpreted near the COT from MCS data [*Imbert and Philipe*, 2005; *Kneller and Johnson*, 2011; *Rowan*, 2014], and onshore syn-rift magmatism has been sampled by cores and imaged by MCS data the South Georgia Rift basin and in Florida [*McBride*, 1991; *Heatherington and Mueller*, 1991; 2003].

Kinematic models for the opening of the Gulf of Mexico basin vary with respect to the initial direction the Yucatán block rotation from North America, predicting either southeastern or southwestern movement [*Pindell*, 1985; *Dunbar and Sawyer*, 1987; *Hall and Najmuddin*, 1994; *Marton and Buffler*, 1994; *Schouten and Klitgord*, 1994; *Bird et al*., 2005; *Imbert and Philippe*, 2005; *Stern et al.*, 2010; *Godínez-Urban et al.*, 2011; *Hudec et al*., 2013a]. Both models agree, however, that Late Jurassic rotation of the Yucatán block took place about a pole in the southeastern Gulf of Mexico, leading extension and seafloor spreading rates in the western Gulf of Mexico (~30 mm/yr) that decrease to the east [*Marton and Buffler*, 1994; *Pindell and Kennan*, 2009]. Comparatively little extension of the crust took place at the conjugate northern Yucatán margin, suggesting a pronounced asymmetry that may be caused by the shape of the pre-rift orogenic belt and/or low-angle detachment faulting [*Marton and Buffler*, 1992; 1994; *Van Wijk*, 2005]. In a short period before seafloor spreading, intermittent flooding and desiccation of the shallow Gulf basin precipitated thick evaporites on the subsiding rifted basement from ~165-161 Ma. Dating and onlap of post-rift sediments, as well as kinematic models, suggest seafloor spreading began ~158 Ma, continued until the Early Cretaceous at ~140 Ma, and divided the extensive salt province into northern and

southern sections [*Salvador*, 1987; 1991; *Sawyer et al.*, 1991; *Hudec et al.*, 2013a]. Rotation of the Yucatán block ended once it docked with southern Mexico and set in place the present-day configuration of the Gulf of Mexico basin [*Guerrero et al.*, 1990; *Pindell and Kennan*, 2009].

1.4 SCREECH and GUMBO Marine Seismic Refraction Projects

Deep marine seismic refraction data are vital to better understanding the nature of rifted margins and the geological processes that led to their formation. The 2000 SCREECH Project (Studies of Continental Rifting on the Eastern Canadian Shelf) collected wide-angle seismic refraction and MCS reflection data along three transects across the eastern Grand Banks, Newfoundland. Chapter 2 shows an analysis of data from the 18 ocean-bottom seismometers (OBSs) from the seaward end of SCREECH Line 2 in the Newfoundland Basin. Previous analyses have focused on compressional waves to build *Vp* models of the Newfoundland rifted margin [*Van Avendonk et al*., 2006.] I present a new analysis that utilizes wide-angle seismic reflection and refraction phases in the shallow sediments, as well as coincident marine seismic reflection data [*Shillington et al.*, 2006], to build an updated seismic velocity model of *Vp*. The main focus of Chapter 2, however, deals with the integration of shear wave (Vs) arrivals, which help constrain the *Vp*/*Vs* ratio in the basement of the continent-ocean transition zone, an important quantity for interpretations of composition and evolution of rifted margin crust. A version of this chapter is available in *Geophysical Research Letters*, Vol. 40 [*Eddy et al.*, 2013].

In the fall of 2010, I helped collect wide-angle seismic refraction data along four transects in the northern U.S. Gulf of Mexico for the GUMBO Project (Gulf of Mexico Basin Opening). Chapter 3 deals with the deep crustal seismic velocity structure in the northeastern Gulf (GUMBO Line 3), which extends offshore Pensacola, Florida, across the De Soto Canyon and into the deep basin Gulf of Mexico. The four profiles of the GUMBO project targeted the northwestern, north-central, and eastern Gulf of Mexico, with dip lines across the margin from the coast to deep basin (Figure 1.3). I analyze compressional refraction data from 38 OBSs to image seismic velocities and key crustal boundaries along GUMBO Line 3 (*i.e.*, top of basement, Moho). I further interpret existing industry MCS reflection data (FUGRO 533) to better resolve the LOC, the nature of the basement surface, and overlying sediments. I make comparisons of velocity-depth profiles and compare GUMBO Line 3 to existing mantle melting models to help determine the impact of mantle upwelling on rifting in the northeastern Gulf of Mexico. A shorter version of Chapter 3 is published in *Journal of Geophysical Research – Solid Earth*.

In Chapter 4, I analyze the deep crustal structure of the north-central Gulf of Mexico, which extends offshore southwestern Louisiana across the Louisiana shelf and seaward of the Sigsbee escarpment. Velocity-depth comparisons are made with normal continental and oceanic crust, as well as type examples of magma-poor and volcanic rifted margins, to better understand the rifting processes and the influence of melting on the crust in the north-central Gulf of Mexico. Comparisons of GUMBO Line 2 to existing MCS data (GXT GulfSPAN Line 2000) helps delimit the LOC in the central Gulf basin.

Analysis of deep crustal structure is integrated with geologic data from mantle xenoliths in southern Louisiana and the present-day distribution of salt provinces to reconstruct a kinematic model for the opening of the Gulf of Mexico.

1.5 Figures

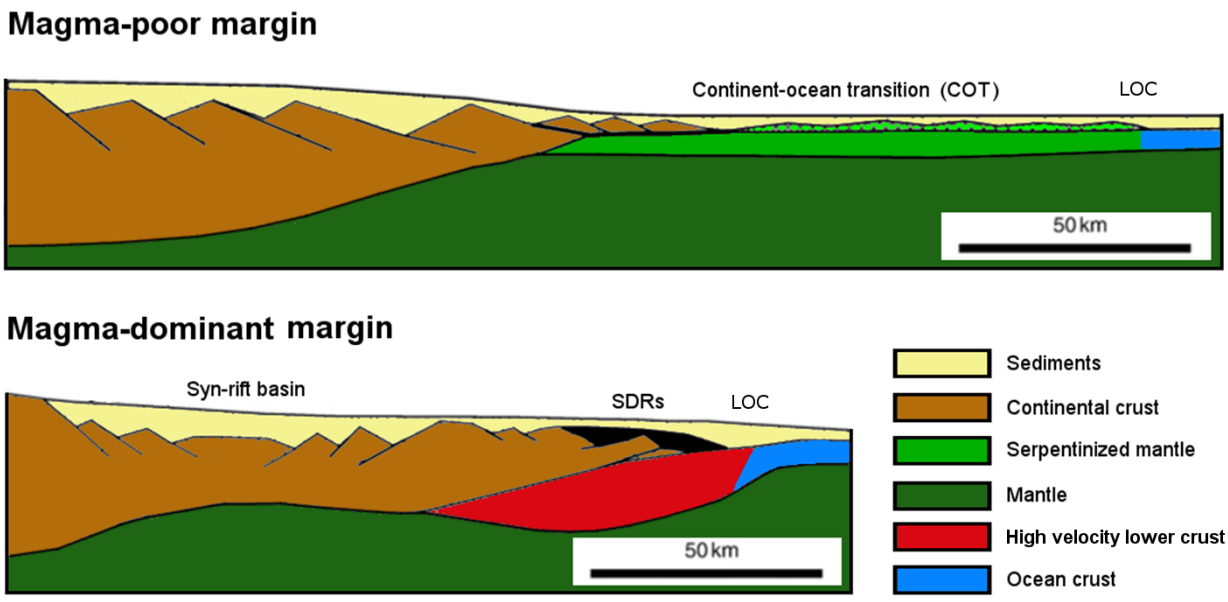

Figure 1.1 – Generalized models of magma-poor and magma-dominated margins, modified from *Reston* [2009].

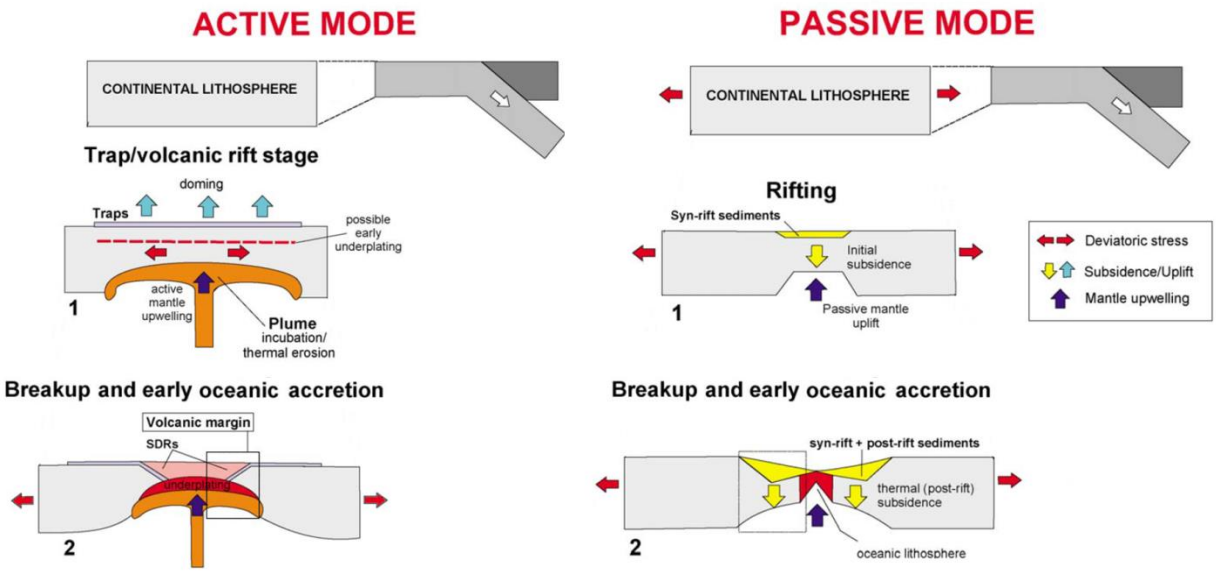

Figure 1.2 –Continental rifting with active and passive modes of mantle upwelling, modified from *Geoffrey* [2005].

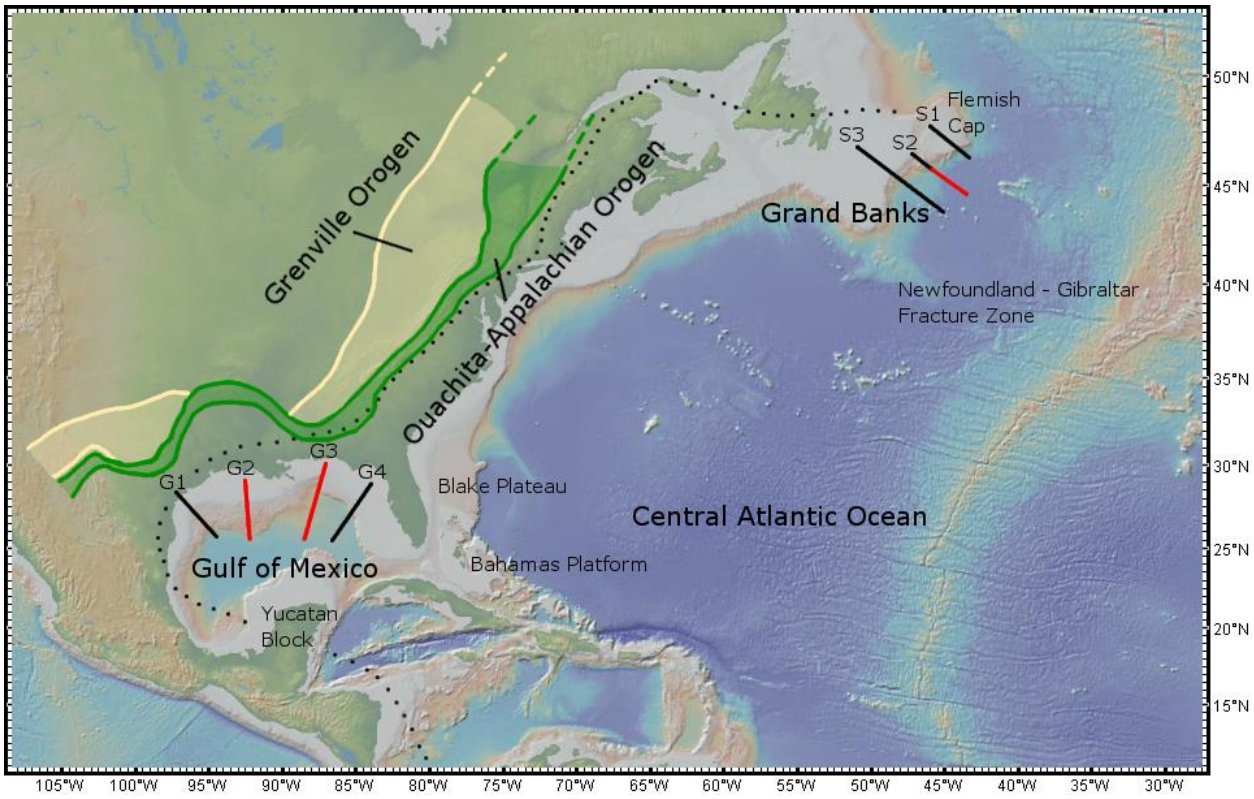

Figure 1.3 - Location of seismic lines and key geologic features. Marine seismic transects investigated by this dissertation shown in red. Dotted line approximates extent of CAMP basalts [*McHone*, 2000]. G1 – G4, GUMBO lines 1 – 4; S1 – S3, SCREECH lines 1 – 3.

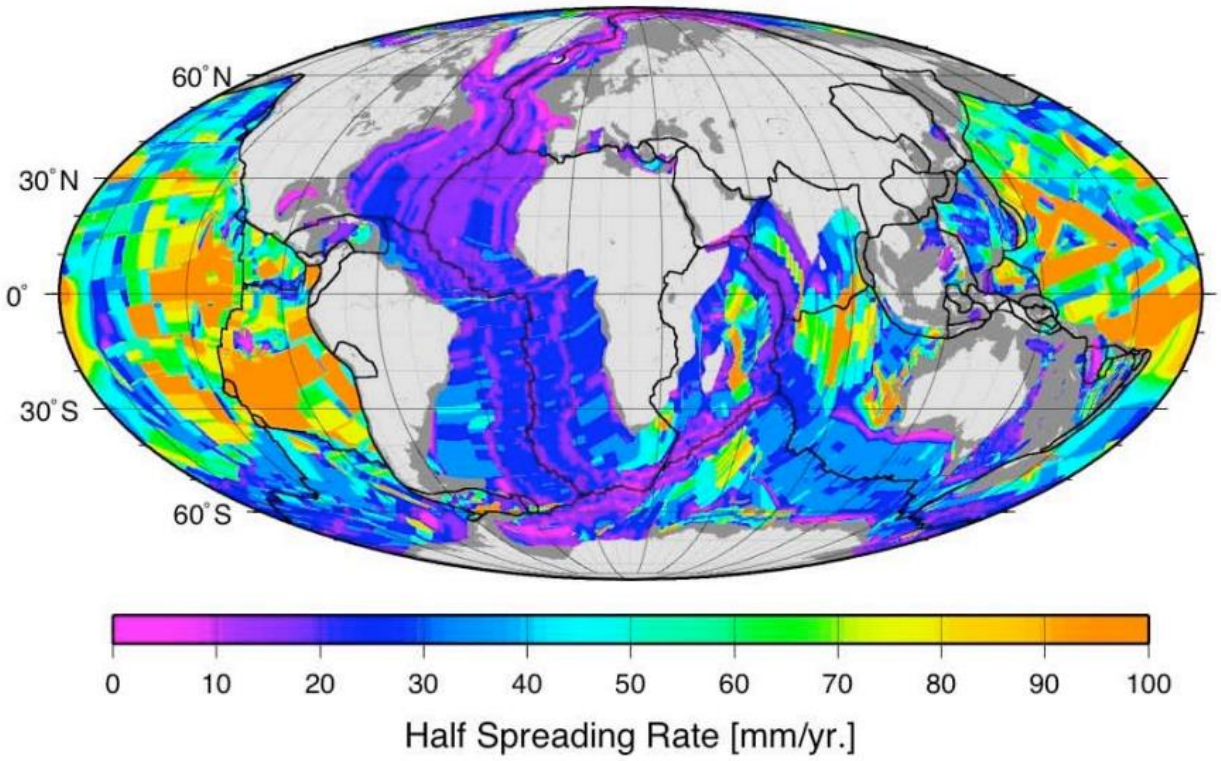

Figure 1.4 – Global half-spreading rates for oceanic crust [*Müller et al*., 2008].

Chapter 2: Compressional and shear-wave velocity structure of the continent-ocean transition zone at the eastern Grand Banks, Newfoundland[1]

Abstract

The seismic structure of the continent-ocean transition (COT) at magma-poor rifted margins can explain geological processes leading to continental breakup. At the Newfoundland-Iberia rift, compressional seismic velocity (V_p) is interpreted with multichannel seismic reflections (MCS) and drilling results to document continental crustal stretching and thinning, exhumation of the mantle, and incipient seafloor-spreading. However, V_p cannot uniquely constrain COT geology. We present an updated 2-D model for V_p and a new shear-wave velocity model (V_s) for SCREECH Line 2 on the Newfoundland margin using MCS and coincident ocean-bottom seismometer (OBS) refraction data. In shallow COT basement we find V_p / V_s ratios average 1.77, which is normally too high for upper continental crust and too low for serpentinized mantle. This observation can be explained by stretching of a mafic middle and/or lower continental crust into the COT. We further support the presence of hydrated mantle peridotites at depth during rifting.

2.1. Introduction

Slow rifting at magma-poor margins often occurs without the weakening effects of magmatic diking. Continental crust may be therefore stretched by a large factor ($\beta > 5$),

[1]**Eddy, D. R.**, H. J. A. Van Avendonk, and D. J. Shillington (2013), Compressional and shear-wave velocity structure of the continent-ocean transition zone at the eastern Grand Banks, Newfoundland, *Geophys. Res. Lett.*, *40*, 3014-3020, doi: 10/1002/grl.50511.

and rocks from the lower continental crust and mantle may be brought to shallow depths via detachment faults [*Whitmarsh et al*., 2001]. During the final phases of rifting, brittle faulting and hydrothermal circulation can lead to serpentinization of mantle peridotites, weakening the lithospheric mantle [*Manatschal*, 2004; *Reston and McDermott*, 2011]. Before complete breakup of the lithosphere and the onset of normal seafloor-spreading, a ~100-km-wide zone of continental mantle may thus be exhumed to the surface in continent-ocean transition zones (COT) [*Whitmarsh et al.*, 2001]. The polarity of lithospheric detachment faults with respect to the locus of breakup often results in asymmetry at conjugate magma-poor margins [*Manatschal*, 2004; *Lavier and Manatschal*, 2006]. In the footwall of a detachment, small amounts of lower crust and, more extensively, uppermost mantle rocks are exhumed to form the COT. At the conjugate rift flank, continental crust of the hanging wall is often highly thinned and stretched above the upper mantle. Strain localization in weakened mantle rocks eventually leads to complete lithospheric breakup and a gradual increase in melt supply from the upwelling asthenosphere [*Lavier and Manatschal*, 2006].

Continental rifting may be accompanied by small amounts of magmatism even if the lithospheric mantle is relatively cold or significantly depleted during rifting [*Müntener and Manatschal*, 2006]. Although rifting of thick continental lithosphere often produces ample magma by decompression melting, only limited amounts of extrusive volcanism may reach the surface if the extension rate is very low [*Lizarralde et al.*, 2004]. Syn-rift melts can therefore be trapped below thick COT lithosphere, so it is possible that not all magmatism is accounted for in an ocean-bottom seismometer (OBS)

refraction study of a rifted margin [*Bronner et al*., 2011]. A better understanding of the melting history of nominally magma-poor margins is important, because even a small amount of melt introduced in the lithosphere during rifting can alter the style of deformation [*Kaczmarek and Müntener*, 2010].

The Newfoundland-Iberia conjugate margins are a type example of mature magma-poor rift systems [*Tucholke et al.*, 2007]. A large wealth of data from drilling expeditions and marine geophysical studies here document brittle extension of continental crust, exhumation and serpentinization of continental mantle, and a slow onset of seafloor-spreading. The distal Iberian margin is interpreted as almost entirely exhumed continental mantle with a wide zone of compressional seismic velocities (V_p) between 7.0-7.5 km/s [*Whitmarsh et al.*, 2001]. This high velocity zone in the Iberian COT is capped by lower velocities (V_p = 4-5 km/s) interpreted as mantle rock that was pervasively serpentinized after exhumation [*Dean et al.*, 2000]. A similar evolution has been proposed for the conjugate margin in the Newfoundland Basin [*Sibuet et al.*, 2007], though seismic images from the SCREECH project (Studies of Continental Rifting and Extension on the Eastern Canadian Shelf; Figure 2.1) suggest that crust in the COT is significantly different. Multi-channel seismic (MCS) reflections [*Shillington et al.*, 2006] demonstrate that the Newfoundland Basin lacks the faulted allochthonous crustal blocks that have been imaged off the Iberian margin [*Krawczyk et al.*, 1996]. In addition, V_p in the shallow basement of the Newfoundland Basin is often lower than 6.0 km/s [*Lau et al.*, 2006; *Van Avendonk et al.*, 2006], which may indicate unroofed continental crust or exhumed, highly serpentinized mantle peridotites.

Interpretation of the structure and evolution of the COT is complicated by strong seismic reflections from a package of post-rift diabase sills just above the Newfoundland basement at SCREECH Line 2 [*Shillington et al.*, 2006; *Péron-Pinvidic et al.*, 2010]. A large injection of mafic material likely accompanied off-axis volcanism following the complete breakup of the Newfoundland-Iberia lithosphere and production of oceanic crust by the early Albian [*Karner and Shillington*, 2005; *Tucholke et al.*, 2007]. We present an integrated analysis of travel-time constraints from MCS reflection and compressional OBS refraction and reflection data to better characterize the post-rift sills and underlying basement on SCREECH Line 2. As a result, we are able to present a new analysis of shear waves that sample the Newfoundland COT basement, and we develop smooth seismic velocity models with regularized tomographic inversions of P- and S-wave travel times. We use both V_p and V_p / V_s ratio models in our geological interpretations of the rifted margin, assessing our interpretations by plotting seismic velocities with depth at key SCREECH Line 2 intervals. We also use shear-wave data to test simple bulk V_p / V_s models for the flat COT basement.

2.2. Travel-time Tomography

The travel times of reflected and refracted phases observed in marine seismic data can be inverted for a layered seismic velocity model with smoothly varying seismic velocities [*Van Avendonk et al.*, 2004, and references therein]. Observation of a series of distinct seismic reflections and refractions in OBS data (Figure 2.2) provides evidence for layering near the top of crystalline basement that must be included explicitly in the seismic velocity model if we want to correctly model the travel times of later arrivals. We

therefore express travel-time residuals for compressional seismic arrivals $\delta T_{p,i}$ as a sum of perturbations δV_p and perturbations in the depth of layer boundaries δz [*Thurber*, 1985; *Van Avendonk et al*., 2004]. If ray paths calculated in the reference model are good estimates of the true source-receiver paths, this relationship can be approximated with a linearization:

$$\delta T_{p,i} \approx \int_{path\ i} \frac{-1}{{V_p}^2} \delta V_p ds + \sum_{layer\ j} \Gamma_{i,j} \delta z_j \quad (1)$$

The first term of (1) accounts for the contribution to $\delta T_{p,i}$ of seismic velocity perturbations δV_p by integration over the ray path. The coefficient $\Gamma_{i,j}$ represents the partial derivatives of travel-time $\delta T_{p,i}$ with respect to the depth of velocity boundary z_j in the model [*Stork and Clayton*, 1991]. We use (1) to express the model constraints of wide-angle reflections and refractions in the OBS data of SCREECH Line 2 [*Van Avendonk et al.*, 2006], and to incorporate two-way travel times from coincident MCS data [*Shillington et al.*, 2006; *Péron-Pinvidic et al.*, 2010].

To find a smooth seismic velocity model we add spatial first- and second-derivative constraints on the structure of V_p and z to the system of equations (1), and solve them for a model perturbation in a least-squares inversion [*Van Avendonk et al.*, 2004]. This linear inversion step is followed by raytracing in the updated seismic velocity model to calculate new ray paths and travel times. We iterate the raytracing and linearized inversion procedures until we obtain a smooth seismic velocity model that fits the travel-time data within a specified tolerance level.

Once we have estimated V_p in a profile along SCREECH Line 2, we use a similar procedure to construct a V_s model from shear-wave travel times. However, unlike compressional wave arrivals, shear waves are not consistently observed in OBS records, and their travel times have relatively large uncertainties (100 ms) [*Mjelde* et al., 2003; *Eccles et al.,* 2009]. We therefore cannot constrain the V_s structure along our profile with the same accuracy as the V_p image. We must also assume that the two models have seismic velocity discontinuities at the same depths z_j. In most studies V_p and V_s appear well correlated [*Brocher et al.*, 2005] such that their ratio $R = V_p / V_s$ may be a more smoothly varying medium property than V_s itself. Accordingly, we express the shear-wave travel-time residual $\delta T_{s,i}$ in R, and we omit terms that assume a dependence on further perturbations of the model layer boundaries z_j:

$$\delta T_{s,i} = \int_{path\ i} \frac{1}{V_s} \delta R ds \qquad (2)$$

As in the case of the inversion of $\delta T_{p,i}$, we add smoothness constraints for R and solve (2) for this parameter in a least-squares inversion.

2.3. P-wave Modeling

We use wide-angle [*Van Avendonk et al.,* 2006] and near-vertical seismic travel-time constraints [*Shillington et al.,* 2006] on the sediments and shallow basement structure along SCREECH Line 2 in a joint inversion of these data with the methodology described in the previous section. The new V_p model, which has detailed information on

the sediment and basement interface structure, helps us understand the nature of P-S converted waves which we must interpret before we invert shear-wave travel times for a model of V_p / V_s along SCREECH Line 2.

The choice and geometry of the layers in our new V_p seismic velocity model is guided by MCS imaging of sediments, magmatic sills, and basement along SCREECH Line 2 [*Shillington et al.*, 2006; *Péron-Pinvidic et al.*, 2010] (Figures 2.3d, A1). *Shillington et al.* [2006] identified two distinct sediment layers above the crystalline basement in their MCS image that are divided by horizon A^U. At larger depth in the COT, *Péron-Pinvidic et al.* [2010] distinguished an interval of anomalously bright reflections topped by the so-called U reflection. This ~1200-m-thick sequence lies between the flat basement and overlying sediments, and is interpreted as a package of post-rift sills. This interpretation differs from that of *Van Avendonk et al.* [2006] and *Van Avendonk et al.* [2009] whose P-velocity model for SCREECH Line 2 assumed a negligible thickness for the post-rift sills in the COT. Basement beneath post-rift sills between 180 km and 240 km model distance is relatively flat when compared to the highly variable topography of faulted basement at the seaward end of SCREECH Line 2 (Figure A1).

In the OBS records of SCREECH Line 2 we interpret three pairs of reflected and refracted phases that appear to be consistent with the layering we describe in the MCS image. We assign four compressional refraction (P1-P4) and three reflection (R1-R3) arrivals in the wide-angle data. As the earliest-arriving phase present in all OBS records, P4 increases in apparent velocity from 5.0-6.0 km/s at 15-20 km offset to 6.0-8.5 km/s at

offsets up to 150 km (Figures 2.2, A2-A5). Local variations in P4 apparent velocity mimic MCS basement relief. Refraction P3 is a straight travel-time branch in x-t space and is typically observed at source-receiver offsets of 10-15 km. Apparent velocities for P3 are 2.2-3.2 km/s, with most being slightly higher than 3.0 km/s, on par with the average velocity reported for post-rift sill and sediments [*Péron-Pinvidic et al.*, 2010]. The slowest refracted arrivals P2 and P1 intersect the direct water wave with apparent velocities of 1.9-2.5 km/s and 1.7-2.2 km/s, respectively, and their amplitudes diminish at larger offsets. The x-t diagrams also show that at short source-receiver offsets the seismic refraction P4 is asymptotic to the wide-angle seismic reflection R3, and both arrivals are observed from each instrument. Limited to instruments above the post-rift sills, refraction P3 is asymptotic to reflection R2. Refraction P2 is asymptotic to reflection R1.

We picked 6647 arrival times of P-waves from air-gun shots recorded on 17 OBSs between the continental slope and the seaward end of SCREECH Line 2, and 1213 reflection travel times in the coincident MCS data. We assigned uncertainties to these travel times based on pick and data quality. After carrying out the inversion of these data using equation (1), we obtained a new P-velocity model that has a low root-mean-square misfit (RMS = 116 ms) and a χ^2 value of 1.0.

2.4. Shear-wave and V_p / V_s Modeling

We picked 863 arrival times from shear waves (S) turning beneath the basement surface to obtain different constraints on basement structure and composition. Not all of the SCREECH Line 2 instruments have observable S-waves (Figure 2.3a), so the ray

coverage in our S-wave inversion is more sparse compared to the P-wave inversion. S-waves have apparent velocities ranging from 3.2 to 4.5 km/s, much lower than phase P4, and often have a variable slope in x-t space due to basement depth variations, distinguishing them from compressional refractions with similar (P3) and slightly slower (P1 and P2) velocities.

A challenge with using shear-wave travel times is the fact that the depth of conversion from P- to S-wave energy in the downgoing raypath is not known. Such conversions may happen at the seafloor or on a deeper boundary with significant impedance contrasts [*Mjelde et al.*, 2003; *Eccles et al.*, 2009]. Based on inspection of the S-wave arrivals from SCREECH Line 2, we find that the majority of these observations must represent phases that converted at the top of basement (Figure A8). We use this assumption to calculate travel-time residuals for the S-wave picks and invert the data for a V_p / V_s ratio in the basement, applying equation (2) where we use the V_p model from the tomographic inversion of the previous section. After a few iterations of the raytracing and linearized inversion steps, we obtain a V_p / V_s ratio model (Figure 2.3c) with a low RMS misfit of 135 ms. It is difficult to quantify the uncertainty in our V_p / V_s model from a statistical standpoint given the paucity of shear-wave data. However, we understand our models to be reasonably well constrained with average V_p / V_s uncertainties between 0.1-0.2 based on comparisons of bulk V_p / V_s models (Figure A7).

In order to better estimate the lithology of the Newfoundland COT, we plot four depth profiles of V_p against V_p / V_s (Figure 2.4). Key model distances of 185, 210, 250,

and 315 km (Figure 2.3c) are plotted in an attempt to characterize the most outboard remnant of probable upper continental crust, the region beneath the flat COT basement, the onset of basement with variable topography near ODP 1277, and the seaward end of SCREECH Line 2, respectively. Velocities are plotted every 0.2 km depth for all model space that is constrained by shear waves. SCREECH Line 2 velocities are plotted above established ranges of V_p and V_p / V_s for common COT lithologies [Table A1]. For the middle and lower continental crust we plot the felsic rocks quartzite and granite and the mafic rocks gabbro and granulite [*Holbrook et al*., 1992]. We also plot seismic velocities of basalts found in older oceanic crust [*Hyndman*, 1979; Brocher, 2005] and mantle peroditites with 0-100% serpentinization [Christensen, 2004].

2.5. Discussion

Between 130 and 180 km model distance on SCREECH Line 2 (Figure 2.3), low V_p / V_s ratios (1.57-1.65) are consistent with previous interpretations that this region represents the last portion of upper continental crust on the Newfoundland margin, including a small package of pre-rift sediments at ~170 km model distance [*Shillington et al.,* 2006; *Van Avendonk et al.,* 2006]. The uppermost 3.5 km of basement at 185 km model distance (Figure 2.4, blue diamonds) plots V_p and V_p / V_s consistent with quartzite and granite [*Holbrook et al.,* 1992], supporting the interpretation that continental crust with a predominantly felsic composition typifies this inboard section of the Newfoundland margin (Figure 2.5).

The most enigmatic aspect of our seismic velocity models is the uppermost 3-5 km of flat COT basement between 180 and 240 km model distance where seismic

velocities are relatively homogeneous (V_p = 5.0-6.2 km/s; V_s = 3.0-3.3 km/s) compared to those in the shallow, rough basement immediately seaward. The V_p in the flat COT basement is low enough to be consistent with continental crust [*Holbrook et al.,* 1992], as is suggested by *Van Avendonk et al*. [2006]. Other workers contend that the COT in the Newfoundland Basin comprises slow-spreading oceanic crust [*Srivastava et al.,* 2000] or exhumed mantle [*Reid*, 1994; *Sibuet et al.*, 2007]. Our recovered V_p / V_s ratios alone cannot rule out the possibility proposed by *Srivastava et al.* [2000] that the Newfoundland basement is capped by thin ocean crust, although we note that V_p in the flat COT is lower than what we expect for ocean crust (5.0-7.5 km/s). In this case, weak magnetization in the COT used to support the presence of oceanic crust (e.g., M0 and older; Figure 2.3d) may be masked by post-rift sills above the flat basement [*Péron-Pinvidic et al.,* 2010]. Though zones of exhumed continental mantle often have V_p around 7.6 km/s [*Dean et al*., 2000; *Whitmarsh et al.*, 2001], mantle peridotites range in V_p from 4.8-8.0 km/s depending on the extent of serpentinization [*Christensen,* 2004]. Thus, serpentinized peridotite is a viable explanation for the 5.5 km/s shallow COT basement in the Newfoundland Basin if exhumed mantle rock here is 75% serpentinized. Such a large degree of serpentinization, however, would require S-wave velocities as low as 2.75 km/s (V_p / V_s = 2.0). We find that V_p / V_s ratios between 1.67-1.77 in the uppermost basement of the COT are too low to primarily represent serpentinized peridotite (Figure 2.3c). Plots of V_p versus V_p / V_s at 210 km model distance show the top ~2 km of the flat-lying basement approaching velocities of felsic continental crustal rocks (Figure 2.4, red squares). As V_p increases to >6.5 km/s at depths >5 km beneath the top of basement, the

210 km profile plots more closely to velocities of mafic rocks such as gabbro and/or 10-25% serpentinized mantle peridotite. These results are consistent with interpretations of the uppermost COT basement as unroofed and stretched continental lower crust overlying hydrated mantle peridotites (Figure 2.5) [*Van Avendonk et al*., 2006].

The shallow, rough basement at 250 km model distance between ODP Sites 1276 and 1277 exhibits seismic properties (V_p = 4.0-6.0 km/s; V_p / V_s = 1.72-1.83) that are inconsistent with serpentinized mantle as an average composition (Figure 2.4, green triangles), although such ultramafic rocks (along with minor amounts of basalt and gabbro) were drilled at Site 1277 [*Robertson*, 2007]. Our model instead plots velocities in the uppermost ~3 km of basement between oceanic basalt and granite, which could indicate the presence of continental rocks far seaward in the COT and/or increasing amounts of volcanics in the shallow basement emplaced during the gradual transition from rifting to seafloor-spreading (Figure 2.5). Poisson's ratios indicating shallow granodioritic crust (V_p / V_s = 1.78) were similarly found northeast of the Flemish Cap, and a seaward increase in Poisson's ratios (V_p / V_s = 1.86-1.89) near a ridge-like structure were interpreted as a combination of serpentinized mantle and volcanic material [*Gerlings et al*., 2011]. At depths >5 km below the top of SCREECH Line 2 basement, the 250 km depth profile exhibits velocities (V_p >7.7 km/s; V_p / V_s = 1.78-1.88) that match the seismic properties of hydrated mantle rocks and may indicate a decrease in peridotite serpentinization from 25% to 0% with increasing depth.

The most seaward section of SCREECH Line 2 is relatively poorly constrained by the S-wave data (Figure 2.3), and thus the dominant presence of either oceanic crust or

serpentinized mantle is equivocal. Furthermore, we cannot rule out gabbroic underplating and melt infiltration at the seaward end SCREECH Line 2 [*Bronner et al*., 2011], which would perhaps be consistent with a gradation from exhumed lithosphere to 'incipient' oceanic crust of intermediate composition. The seaward-most V_p versus V_p / V_s plot at 315 km exhibits seismic velocities between granite and oceanic basalt at shallow basement depths, and approaches velocities of minorly serpentinized (0-10%) mantle peroditites at depths of 5 km below basement (Figure 2.4, purple circles). We caution that plots of seismic properties here may be artifacts of insufficient shear-wave raypath coverage. In order to image the onset of 'true' oceanic crust with normal, 6-7 km thickness, additional seismic reflection and refraction data need to be acquired seaward of SCREECH Line 2.

2.6. Conclusions

Our analysis of V_p / V_s ratios from SCREECH Line 2 supports the hypothesis that highly stretched continental lower crust extends far into the Newfoundland Basin COT. Development of flat basement in the COT was likely shaped by low angle, landward-dipping detachment faults, although post-rift volcanic sills mask the observation of such large-scale faults in MCS data. Shear velocities support the presence of exhumed mantle deep beneath the flat COT basement and around ODP Site 1277, where extensive basement faulting led to partial serpentinization of peridotites that subsequently were infiltrated and overprinted by melt products from the upwelling asthenosphere. Mantle hydration is suggested to decrease with depth. Continued plate divergence between Newfoundland and Iberia led to increasing volcanism that eventually emplaced normal thickness oceanic crust in the Atlantic, but this transition is either not observed at

SCREECH Line 2 or is unable to be distinguished from available seismic velocity models.

2.7. Figures

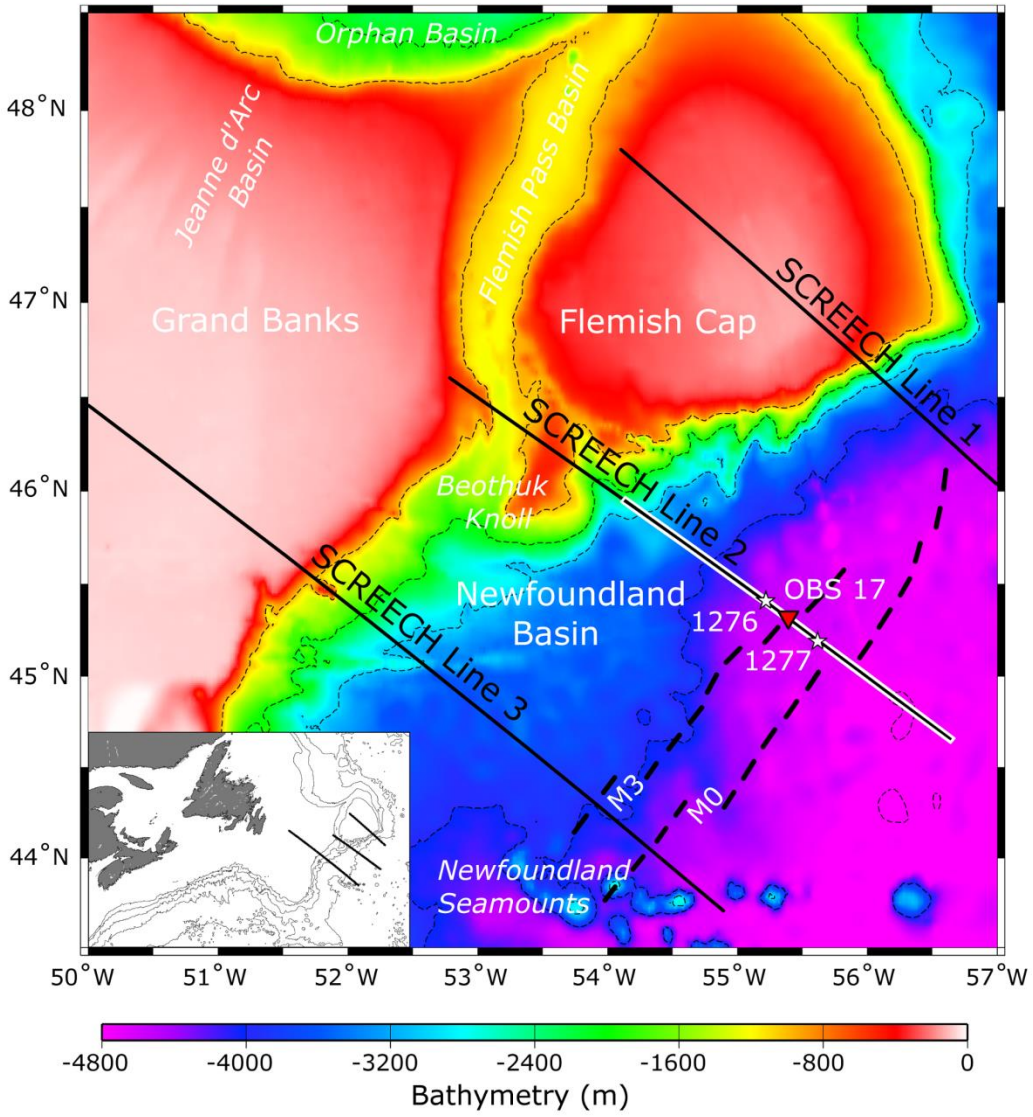

Figure 2.1 – Bathymetric map of the Grand Banks of Newfoundland overlain by 800-m contours, basin features, ODP sites 1276 and 1277 (stars), magnetic anomalies M0 and M3 (dashed lines) [*Srivastava et al*., 2000], and the location of SCREECH seismic lines (solid lines) and OBS 17 (inverted red triangle). The segment of SCREECH Line 2 analyzed herein is outlined in white. Left lower inset shows Grand Banks in relation to the northeastern seaboard of North America.

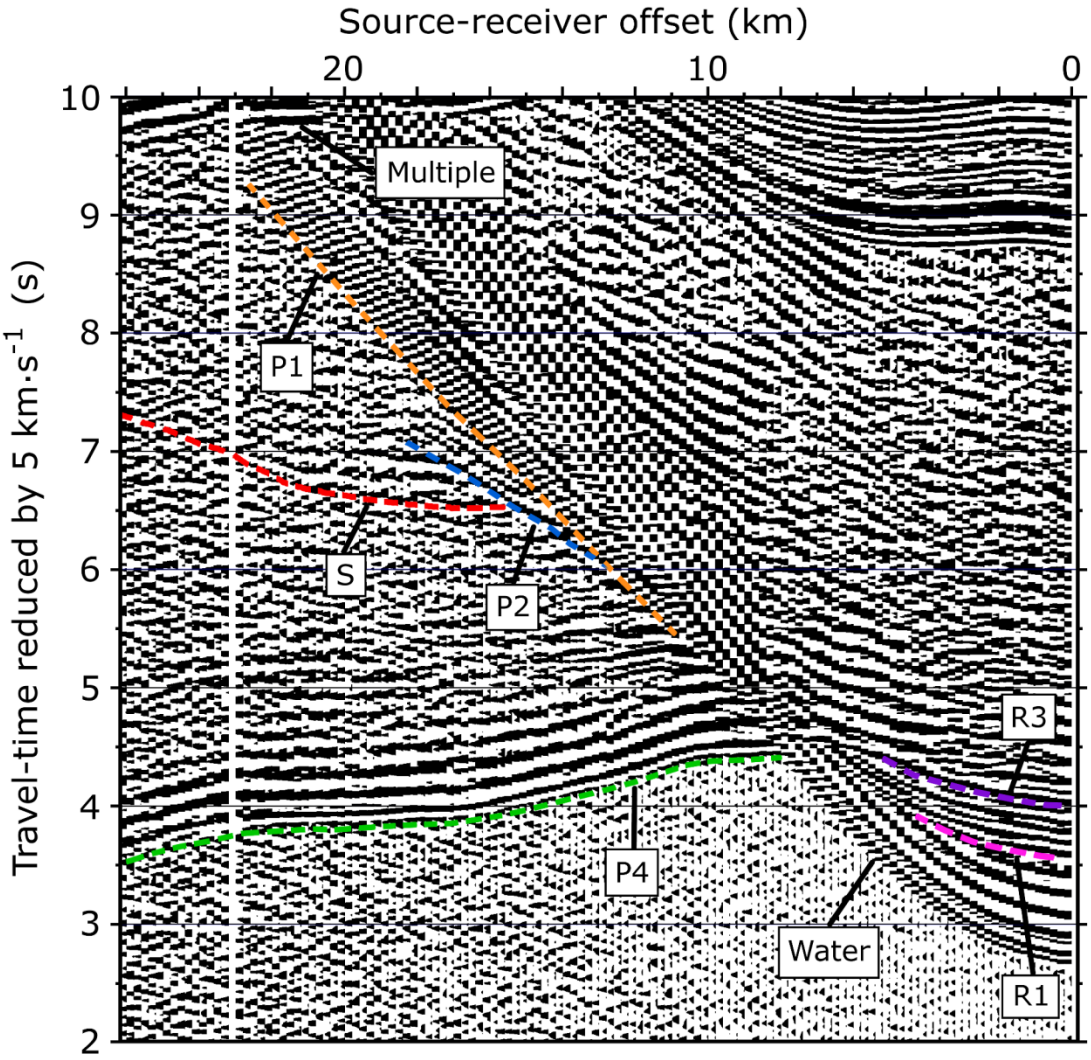

Figure 2.2 – A portion of the receiver gather for OBS 17. See text for descriptions of compressional refractions and reflections (P1-P4, R1-R3). Also labeled are arrivals of the direct wave in water (Water), P4 multiples (Multiple), and a shear-wave refraction (S). Additional receiver gathers are available in the Appendix.

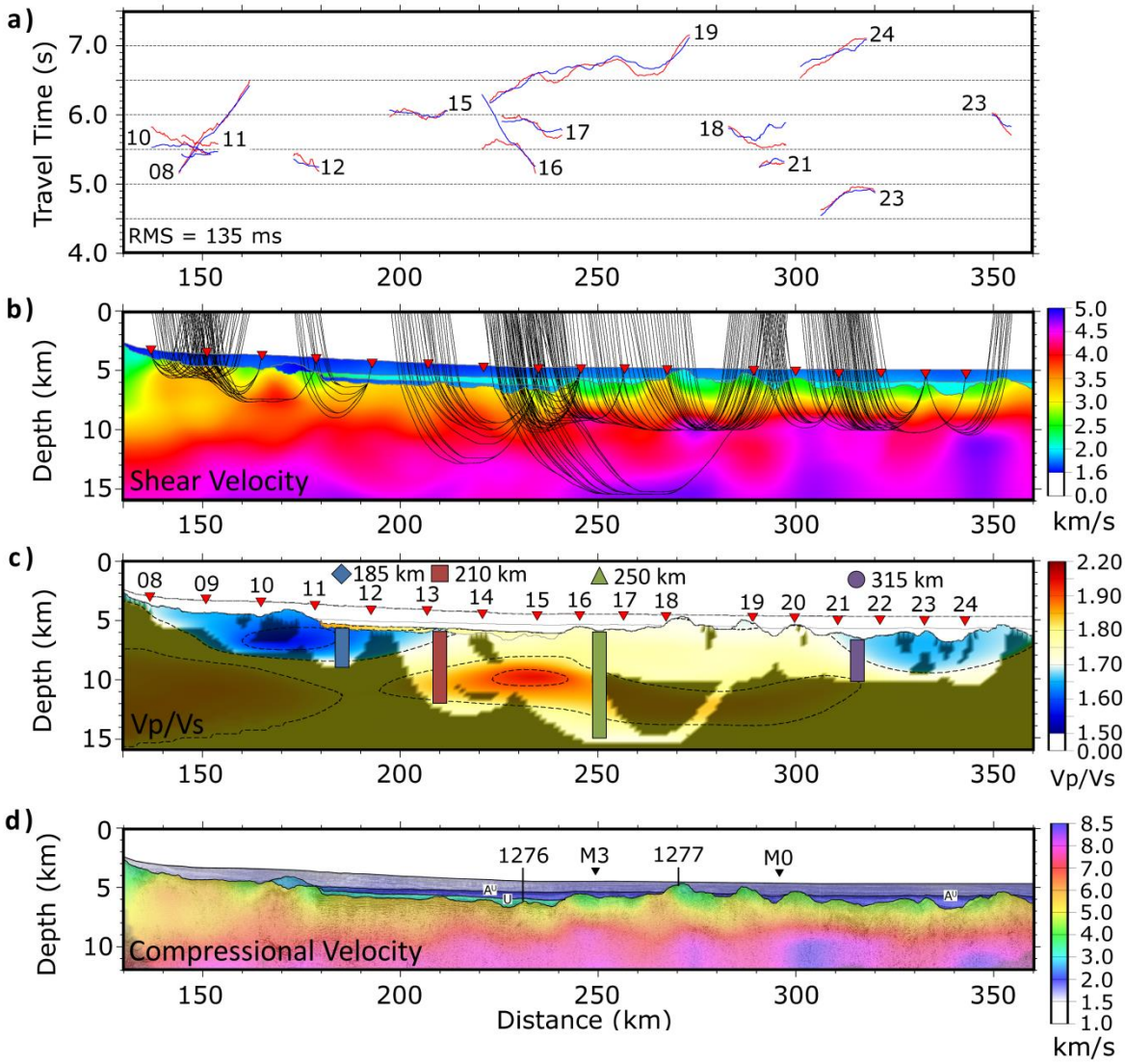

Figure 2.3 – P- and S-wave seismic velocity structure of SCREECH Line 2. Vertical exaggeration is ~ 6:1 for all diagrams. a) Picked (blue) and calculated (red) S-wave travel-time curves. RMS represents root-mean-squared misfit. Reduction velocity is 4.0 km/s. S-wave uncertainties are 100 ms; b) Shear velocity structure and calculated S-wave paths; c) V_p / V_s model with depth profiles plotted in Figure 2.4. Shaded material represents unconstrained model space. Red triangles are OBS locations; d) Compressional velocity structure overlain by coincident MCS data. M3 and M0 are magnetic anomalies. 1276 and 1277 - ODP drilling locations with approximate drill depths. A^U - Horizon A^U. U - U reflection.

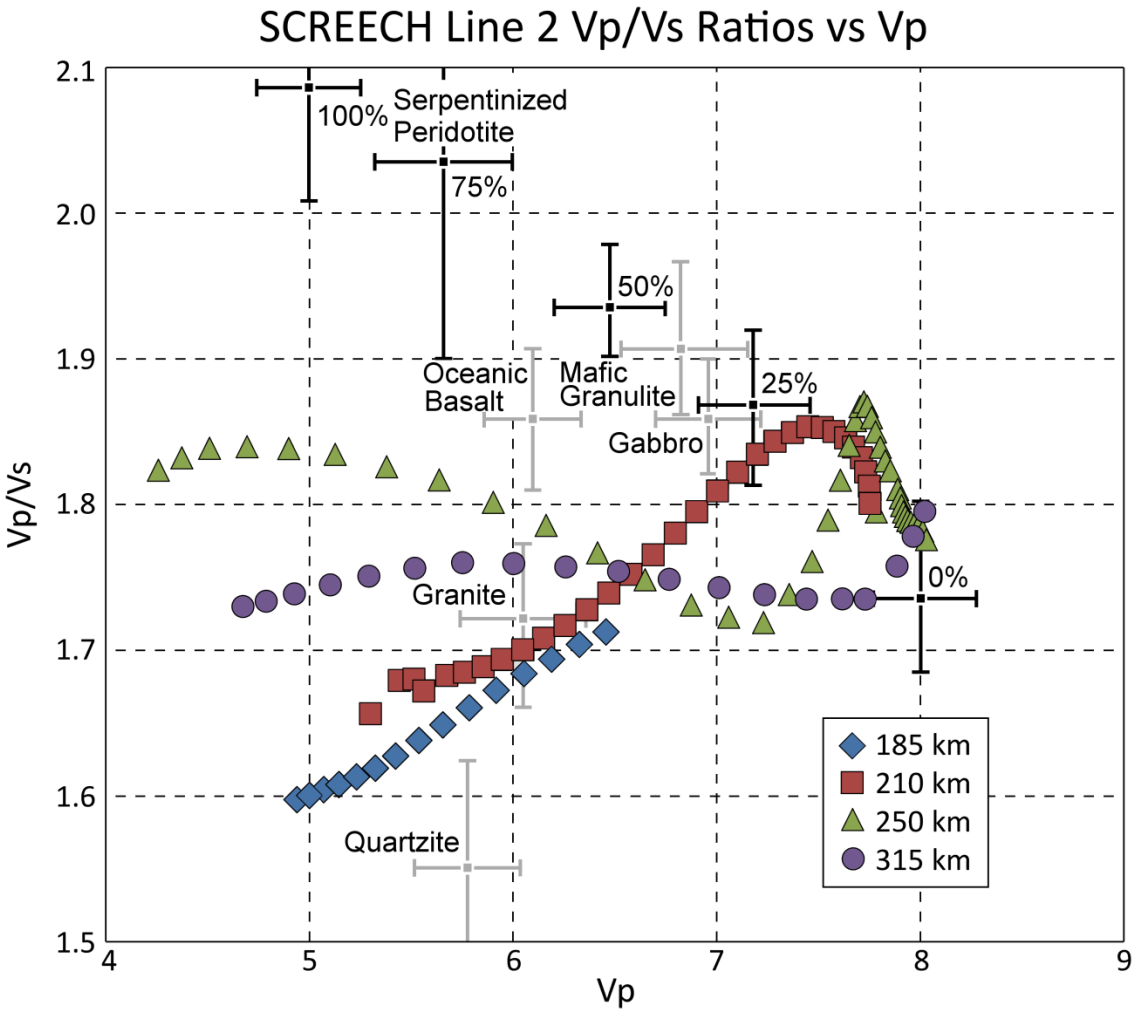

Figure 2.4 - Four depth profiles of *Vp* / *Vs* against *Vp* along SCREECH Line 2. Seismic velocities are plotted every 0.2 km depth for all model space that can be constrained by shear waves in the basement (Figure 2.3c). Common COT lithologies are also plotted, and values for their seismic velocities can be found in the Appendix.

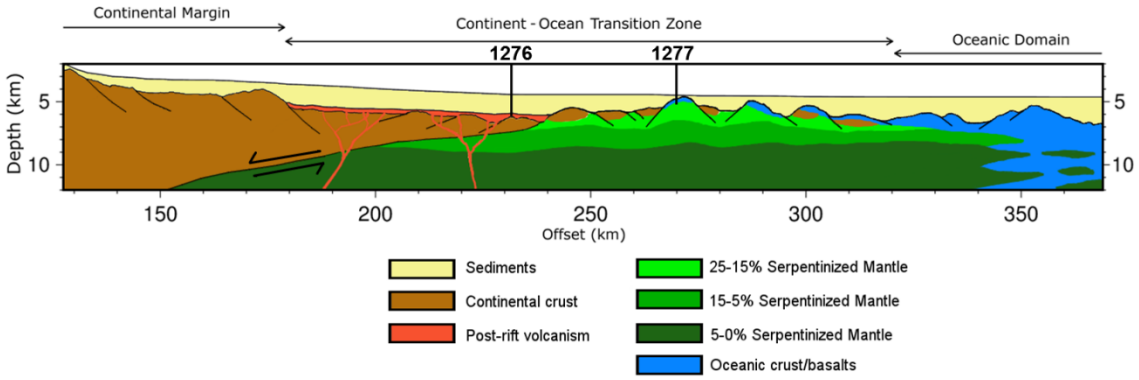

Figure 2.5 – Geologic interpretation of the Newfoundland margin at SCREECH Line 2.

Chapter 3: Deep crustal structure of the northeastern Gulf of Mexico: implications for rift evolution and seafloor spreading [2]

Abstract

We image deep crustal structure using marine seismic refraction data recorded by a linear array of ocean-bottom seismometers in the Gulf of Mexico Basin Opening project (GUMBO Line 3) in order to provide new constraints on the nature of continental and oceanic crust in the northeastern Gulf of Mexico. GUMBO Line 3 extends ~524 km from the continental shelf offshore Pensacola, Florida, across the De Soto Canyon and into the central Gulf basin. Travel times from long-offset, wide-angle reflections and refractions resolve compressional seismic velocities and layer boundaries for sediment, crystalline crust, and upper mantle. We compare our results with coincident multichannel seismic reflection data. Our velocity model recovers shallow seismic velocities (~2.0-4.5 km/s) that we interpret as evaporites and clastic sediments. A Cretaceous carbonate platform is interpreted beneath the De Soto Canyon with seismic velocities >5.0 km/s. Crystalline continental crust thins seaward along GUMBO Line 3 from 23-10 km across the De Soto Canyon. High seismic velocity lower crust (>7.2 km/s; HVLC) and outer wedge seaward-dipping reflectors are interpreted as extensive syn-rift magmatism and possibly mafic underplating, common features at volcanic rift margins with high mantle potential temperatures. In the central Gulf basin we interpret thick oceanic crust (>8 km)

[2] **Eddy, D. R.**, H. J. A. Van Avendonk, G. L. Christeson, I. O. Norton, J. W. Snedden, G. Karner, and E. Johnson (2014), Deep crustal structure of the northeastern Gulf of Mexico: implications for rift evolution and seafloor spreading, *J. Geophys. Res.*, *119*, doi: 10/1002/2014JB011311.

emplaced at a slow full-spreading rate (~24 mm/yr). We suggest a sustained thermal anomaly during slow seafloor-spreading conditions led to voluminous basalt flows from a spreading ridge that overprinted seafloor magnetic anomalies in the northeastern Gulf of Mexico.

3.1 Introduction

The Gulf of Mexico is a small ocean basin that began forming in the Late Triassic when the Yucatán (Maya) continental block rifted southward from the southern Laurentian margin [*Salvador*, 1987; *Sawyer et al*., 1991; *Pindell and Kennan*, 2009]. In the initial Triassic phase of continental rifting, deep, isolated rift basins developed in the continental lithosphere of the present-day Gulf margins and subsequently filled with volcanics and nonmarine sediments [*Salvador*, 1987]. Distribution of Jurassic evaporites, which are thin in the eastern Gulf of Mexico compared to the west [*Bird et al.*, 2005; *Imbert and Philippe*, 2005; *Rowan*, 2014], suggests that the western Gulf of Mexico experienced a more prolonged episode of continental rifting. Rifting transitioned to seafloor spreading in the Middle – Late Jurassic as the Yucatán rotated ~40˚ counterclockwise relative to North America around a pole in the present-day southeastern Gulf of Mexico [*Hall and Najmuddin*, 1994; *Marton and Buffler*, 1994; *Bird et al*., 2005]. The onset of seafloor spreading split the widespread Gulf of Mexico salt province into northern (U.S.) and southern (Mexican) sections [*Salvador*, 1991; *Sawyer et al.*, 1991; *Hudec et al*., 2013a]. The timing of Yucatán block rotation (~158 to 140 Ma) predicts a slow seafloor-spreading rate of 30 mm/yr in the western Gulf of Mexico with spreading rates, and therefore total width of opening, decreasing to the east [*Marton and Buffler*,

1994; *Pindell and Kennan*, 2009]. Rotation of the Yucatán ended once the block docked against southern Mexico in the Early Cretaceous (~140 Ma), finalizing the present-day configuration of the Gulf of Mexico basin [*Guerrero et al.*, 1990; *Pindell and Kennan*, 2009].

Although there is general agreement on the plate kinematic history of the Gulf of Mexico [*Bird et al.*, 2005, and references therein; *Galloway*, 2008], the paucity of seismic constraints on the deep crustal structure, as well as the absence of clear seafloor spreading magnetic anomalies, make it difficult to determine the extent to which opening of the basin was accompanied by lithospheric stretching, syn-rift volcanism, subcontinental mantle exhumation, and/or oceanic crust emplacement [e.g., *Pindell*, 1985; *Marton and Buffler*, 1994; *Bird et al*., 2005; *Stern and Dickinson*, 2010; *Hudec et al*., 2013a; *Rowan*, 2014]. Rifting in the Gulf of Mexico is often interpreted as a passive response to divergence between the North and South American plates [*Pindell*, 1985; *Ebeniro et al.*, 1988]. The postulation that thinned continental crust and/or exhumed mantle forms the basement of the northern Gulf of Mexico [*Ebeniro et al.*, 1988; *Marton and Buffler*, 1994; *Pindell and Kennan*, 2009; *Rowan*, 2014] would support the notion that this is a magma-poor margin. On the other hand, some studies show evidence for thermal uplift and magmatism in the early stages of Gulf rifting [*Bird et al.*, 2005; *Mickus et al.*, 2009; *Dickinson et al.*, 2010], suggesting active rifting and possibly abundant magmatism during continental breakup [*Ruppel*, 1995; *Geoffroy*, 2005]. Accordingly, *Mickus et al.* [2009] use potential magnetic field data to suggest magma-dominant rifting in the western Gulf of Mexico, with decreasing magmatic activity in the central Gulf. In

the eastern Gulf of Mexico, *McBride* [1991] and *Imbert* [2005] interpret rift-related volcanism from both onshore and offshore seismic reflection data, while *Heatherington and Mueller* [1991; 2003] describe abundant syn-rift Early Jurassic volcanic rocks from the Florida peninsula.

The proximity of the northeastern Gulf of Mexico to the U.S. Atlantic margins allows us to compare possible mechanisms of rift initiation in these two ocean basins. Since the Gulf of Mexico formed soon after the breakup of Pangaea and the widespread emplacement of basalts of the Central Atlantic Magmatic Province (CAMP) [*Oyarzun et al.*, 1997; *McHone*, 2000], we must evaluate the role of this major magmatic event in the process of continental breakup. Prior to the opening of the Gulf basin, the lithosphere of the southeastern U.S. amalgamated by suturing of the Suwannee terrane and Gondwana crustal blocks to Laurentia [*Heatherington and Mueller*, 2003; *Poole et al.*, 2005; *Thomas*, 2010]. Late Paleozoic collapse of the Ouachita-Appalachian orogeny and potential delamination of the lithosphere [*Nelson*, 1992; *Thomas*, 2011; *Huerta and Harry*, 2014] preceded rifting in the nearby South Georgia Rift and Gulf of Mexico basins. Geophysical constraints on the structure and composition of crystalline crust in the eastern Gulf of Mexico suggest that this region experienced a complete rift-to-drift transition from thinned continental crust near the Gulf coast to oceanic crust [*Ewing et al.*, 1960; *Ibrahim et al.*, 1981; *Ebeniro et al.*, 1986]. However, until recently marine seismic refraction studies on the Florida platform failed to map the Moho [*Ebeniro et al.*, 1986], so the nature of rifted crust in the eastern Gulf of Mexico has yet to be determined.

We provide new constraints on structure of the crust and upper mantle in the northeastern Gulf of Mexico, including the distribution of continental and oceanic crust, using the first marine seismic refraction study in this area in over thirty years. We present data and results from the 2010 Gulf of Mexico Basin Opening project (GUMBO), which collected four long-offset, wide-angle seismic refraction profiles in U.S. Gulf of Mexico waters. We describe the compressional seismic velocity structure of GUMBO Line 3 extending offshore Pensacola, Florida, across the De Soto Canyon and into the central Gulf basin (Figure 3.1). We discuss new interpretations of a volcanic rift margin with abundant syn-rift magmatism, thinning of continental crust, and formation of thick oceanic crust under slow seafloor-spreading conditions.

3.2 Data

3.2.1 GUMBO Marine Seismic Experiment

In the fall of 2010, wide-angle marine seismic refraction profiles were acquired aboard the R/V *Iron Cat* operated by Reservoir Geophysical. The four profiles of the GUMBO project targeted the northwestern (GUMBO Line 1), central (GUMBO Line 2), and eastern U.S. Gulf of Mexico (GUMBO Line 3, GUMBO Line 4), with dip lines across the margin from the coast to deep basin (Figure 3.1). Three arrays of 12 air-guns towed at a depth of 9-10 m provided an average 77.4 L source capacity. Source navigation provided by NCS SubSea ensured ~150 m shot spacing by initiating a trigger to the R/V *Iron Cat* gun controller; shot confirmation from the gun controller was sent to a Novatel GPS receiver to determine the exact time of each shot. Instruments were provided by Geopro and the University of Texas Institute for Geophysics (UTIG). Forty-

five short-period, four-component ocean bottom seismometers (OBSs) were deployed at 12 km spacing along the 540 km-long NNE to SSW GUMBO Line 3 transect (Figure 3.2), which is the focus of the present analysis. A total of 38 of the original 45 GUMBO Line 3 instruments provided high-quality, interpretable seismic data at offsets up to 200 km, with five OBSs from the Florida shelf (OBS 301-305), seven OBSs along the Florida escarpment (OBS 308-314), and twenty-six OBSs in the deep-water Gulf of Mexico basin (OBS 315-345).

3.2.2 OBS Wide-angle Refractions and Reflections

We differentiate three phases of long-offset compressional seismic refractions from our OBS receiver gathers (P1, P2, and P3; Figures 3.3-3.6) and two wide-angle seismic reflection phases (R1 and R2) using apparent velocity, source-receiver offset, and position in x-t space. Typical frequencies for all arrivals are between 8 and 15 Hz at all water depths. On the Florida shelf and across the De Soto Canyon, data from the OBS hydrophones and horizontal- and vertical-component geophones achieved similar signal/noise ratios; vertical-component geophones produced better quality data in deeper parts of the basin. We briefly describe the characteristics of these phases on the shallow Florida shelf, De Soto Canyon, and deep water Gulf of Mexico.

We observe the first-arriving seismic refraction phase P1 in all 38 instruments gathers. On the Florida shelf, arrivals of P1 are distinct from the direct wave in water at source-receiver offsets greater than 1.6 km and diminish in amplitude at offsets of 25-48 km (Figure 3.3). At near-offsets (2-7 km), Florida shelf instruments record P1 apparent velocities of 2.6-2.9 km/s with apparent velocity increasing gradually to 4.5-5.0 km/s at

larger offsets. Instruments in the De Soto Canyon similarly record a gradual increase in P1 apparent velocity from 3.0-4.5 km/s to 5.5-6.0 km/s, although some instruments on this slope record landward P1 arrivals with substantially faster apparent velocities than oceanward arrivals likely associated with the relative difference in water depth. Instruments in the deep basin Gulf of Mexico record P1 at offsets greater than 5.5 km (Figures 3.4-3.6) to a maximum of 20 km, far less than landward OBSs. The P1 arrivals of deep basin instruments display consistent initial apparent velocities of 2.0-2.2 km/s that sharply increase to 2.5-2.7 km/s at 10-15 km offsets and again at >15 km offsets to 3.3-4.5 km/s.

The second-arriving seismic refraction P2 is observed from all but one instrument. On the Florida shelf, P2 is distinct from P1 at offsets greater than 35 km and has an apparent velocity of ~6.0 km/s to offsets of 110 km (Figure 3.3). The transition from P1 to P2 appears to step back towards later arrival times, which could suggest small zones of lower velocity. For instruments in the De Soto Canyon, P2 is first observed at a range of minimum (25-60 km) and maximum offsets (40-90 km) with an apparent velocity of 6.2-7.2 km/s (Figure 3.4). Instruments in the deep basin Gulf of Mexico record P2 at much closer offsets (20-25 km) than shallower instruments (Figures 3.5, 3.6). Arrivals of P2 recorded by OBSs in the deep basin are observed over a short offset distance (~45 km) with high apparent velocities of 6.0-7.5 km/s (Figure 3.6).

Two instruments in the De Soto Canyon and 17 instruments in the deep basin Gulf of Mexico record the third- and last-arriving refraction phase P3. Apparent velocity of P3 is remarkably consistent across all instruments that record this phase (~7.6-8.4

km/s). The two landward OBSs that record P3 show initial arrivals at 70-100 km to maximum offsets of 110-200 km (Figures 3.3, 3.4). Instruments in the deep basin record P3 initially at 30-60 km and up to maximum offsets >100 km (Figures 3.5, 3.6).

Wide-angle seismic reflections of large amplitude can be recognized as retrograde travel-time branches behind the crossover point of two adjacent refraction arrivals (Figure 3.6). For example, seismic reflection R1 appears behind the P1/P2 crossover in x-t space at 15-20 km offsets (Figures 3.4-3.6) with apparent velocities of 5.5-6.0 km/s. Reflection R1 is recorded by most instruments, but is noticeably absent from OBSs across the De Soto Canyon. We record the later R2 phase behind the P2/P3 crossover on all but three OBSs. On the Florida shelf, we find R2 typically at 75-125 km offsets with apparent velocities from 7.9-8.0 km/s. Instruments in the De Soto Canyon recover landward R2 arrivals at offset ranges of 60-120 km (Figure 3.4). In the deep basin, R2 is found at much closer offsets of 30-80 km (Figures 3.5, 3.6).

3.2.3 Travel-time Picks and Reciprocity Testing

We densely sample P1, P2, and P3 refractions and R1 and R2 reflections by picking an average of every third shot (~500 m spacing) for all phases (Figures 3.3-3.6, B3-B36). This process generates a total of 22,219 travel-time picks, with 7505 picks for P1, 6062 picks for P2, and 2770 picks for P3 (Table 3.1). We make 1633 and 4249 travel-time picks for reflections R1 and R2, respectively. The reciprocity of picks of source-receiver pairs are plotted from surrounding instruments during our travel-time interpretations. We do not allow discrepancies larger than 250 ms between reciprocal source-receiver pairs. Uncertainties are assigned to travel times of all refraction and

reflection phases to account for user error and the effects of instrument noise on our travel-time picks (Table 3.1). At near-offsets, arrivals P1 and P2 often have amplitudes that are easily distinguished from the background signal and therefore are assigned low uncertainties of 50 and 75 ms, respectively. At larger offsets, reflection and refraction arrivals P3 and R2 are slightly noisier and thus assigned higher travel-time uncertainties of 100 ms. We also assign an uncertainty of 100 ms to the wide-angle reflection R1.

3.2.4 MCS Data

Coincident with GUMBO Line 3, the FUGRO 533 multi-channel seismic reflection (MCS) profile allows us to interpret the top of basement boundary layer and more detailed geologic features that cannot be resolved with wide-angle refraction data alone (Figures 3.2, 3.7). The FUGRO 533 profile uses a 10 km-long streamer to record shot-points at 37.5 m intervals with a source capacity of ~79 L. Standard industry algorithms convert the Kirchoff pre-stack time migration image to pre-stack depth migration. Although we cannot constrain the Moho boundary from the MCS image, layering of the basement allows us to be more confident in our interpretation of later-arriving seismic refraction phase P2 in the tomographic inversion.

The sedimentary section is 8-10 km thick and includes the Florida Platform from 0-150 km along the FUGRO 533 profile, with salt visible below the platform to 320 km model distance (Figure 3.7). The base of the sedimentary section is marked by a discontinuous basement reflection that separates layered sediments from more chaotic and less continuous reflections. The basement reflection deepens beneath the shelf edge from ~6.5 to 11.5 km before stepping up to ~8 km beneath the De Soto Canyon at 180

km model distance. Beneath this ~150 km-wide depression in the top of basement, seaward- and landward-dipping reflections are present at 50-90 km and 100-120 km model distance, respectively. The stronger, deeper seaward-dipping reflections dip at angles increasing with depth from 15° to 30° (Figure 3.7). At 100-120 km we observe reflections below the basement over a shorter horizontal and vertical distance and with a landward dip of ~25°. We interpret these reflections in combination with the large basement depression as representing a rift graben structure, likely the eastern portion of the Apalachicola Basin (*i.e.*, Apalachicola embayment of *Hudec et al.* [2013a]; Figure 3.2). A broad basement high is interpreted directly seaward of the De Soto Canyon from ~150-250 km and images the top of basement at a depth of ~8 km. We interpret this as the western margin of the Southern Platform, a continental arch that experienced less severe thinning during continental extension than the surrounding crystalline crust. Deeper reflections beneath the basement are scarce in the landward portion of the MCS image, although bright patches of reflectivity at ~33 km depth from 0-100 km model distance may represent the Moho.

Shallow, discontinuous reflections above the basement from ~170 to 310 km model distance are interpreted as sediments disrupted by salt structures (Figure 3.7). The basement reflection beneath these salt bodies is weak, but still bright enough to estimate its depth as increasing from ~9.0-10.5 km. We interpret a ~1 km step-up in basement height from ~270-290 km. Beneath the top of basement at ~220-290 km, additional reflectors are observed with seaward dips of ~25°-30° and interpreted as faults in crystalline crust. At 465 km model distance we observe a sharp step-down in the

basement reflector from ~15.5 to 17 km depth; the basement reflector steps-up again to 15 km at 480 km model distance. We interpret this feature as a half-graben, likely part of the axial valley of an extinct spreading ridge [*e.g.*, *Pindell and Kennan*, 2009] (Figures 3.1, 3.2, 3.7). Intra-basement reflections beneath the half-graben are likely too shallow to represent the Moho and instead likely represent oceanic crustal basement faults associated with seafloor spreading. Deep reflections beneath the top of seaward basement are weak and discontinuous, although a series of reflections from 300-400 km model distance at depths of ~17 km may represent the Moho.

3.3 Results

3.3.1 Tomographic Inversion

To obtain a first estimate of the seismic velocity structure along GUMBO Line 3, we use only first-arriving travel times in our OBS records since they are easily identified and do not require a phase interpretation. From these first-arriving phases we build a single-layer velocity model that does not explicitly define the top of basement or Moho (Figure B1). If ray paths associated with first-arriving travel times sufficiently sample the GUMBO 3 model space, we can interpret the basic lithology of this transect from the imaged seismic velocity structure [*Zelt et al.*, 2003; *Van Avendonk et al.*, 2004]. We pick 23,698 first-arriving phases for all 38 OBS record sections and assign 25-150 ms travel-time uncertainties, with higher uncertainties given to larger offsets and areas with high signal-to-noise ratios. On inspection we choose an appropriate starting seismic velocity to trace rays between all sources and receivers [*Van Avendonk et al*., 2001]. Subsequently, we reduce chi-squared in a stepwise, iterative tomographic inversion to 1.0, which

corresponds to an RMS travel-time misfit of 90 ms after 15 iterations. Since we apply smoothness constraints in each linear inversion step, we obtain a smooth seismic velocity model with velocities increasing from ~2.0 km/s near the seafloor to >8.0 km/s at larger depths (Figure B1). We use this preliminary inversion result as a starting model to build a new, layered velocity model where the different phases observed in the OBS refraction data provide information on the interfaces between the sediment, crust, and mantle.

We use all wide-angle refraction (P1-P3) and reflection phases (R1-R2) in a layered GUMBO Line 3 seismic velocity model (Figure 3.8), aided by our interpretations of model boundaries in the coincident MCS FUGRO 533 transect. Wide-angle reflections R1 and R2 are modeled as compressional waves that reflect off the top of basement (*PbP*) and Moho (*PmP*) boundaries, respectively. We model P1 as refractions turning in the sediment (*Psed*), P2 as crustal refractions (*Pg*), and P3 as mantle refractions (*Pn*). The joint inversion method of *Van Avendonk et al.* [2004] allows us to simultaneously constrain velocity and layer boundaries, with instantaneous velocity discontinuities at the boundaries between the layers. Within each seismic velocity layer, we parameterize velocity variations on a rectangular grid using 174 m horizontal and 65 m vertical grid spacing. The model parameters, which include seismic velocities and boundary interface depths, are estimated by using travel times of all picked reflection and refraction phases. To regularize the inversion, smoothness constraints are applied to both velocities and interface depths [*Van Avendonk et al.*, 2004]. After 22 iterations between raytracing and linear inversion we derive a compressional seismic velocity model with a chi-squared value of 1.0 that corresponds to an RMS travel-time misfit of 97 ms (Figure 3.8).

We calculate ray paths through the layered velocity model using the shortest path and ray-bending methods [*Moser*, 1991; *Moser et al.*, 1992; *Van Avendonk et al.*, 2001]. This process allows us to compare the picked and calculated travel times of wide-angle refractions and reflections. Figures 3.9-3.12 illustrate typical misfits between picked and calculated travel times, and the location of seismic sources and paths of downgoing rays for OBSs 305, 316, 326, and 340. Visual inspection of travel time misfits for the final velocity model, the time between picked and calculated travel times, shows that they are often low (0-100 ms). A scatter plot of travel-time misfits compared to source-receiver offsets for all GUMBO Line 3 instruments confirms a good data fit (Figure B2). The largest misfits (>100 ms) are associated with wide-angle refraction *Pn* and reflections *PbP* and *PmP*, phases that have also been assigned the largest uncertainties. Misfits for all other instruments and individual phases are shown in Appendix B (Figures B37-B75).

3.3.2 GUMBO Line 3 Seismic Velocity Structure

The seismic velocity structure of GUMBO Line 3 (Figure 3.8) is described in detail to allow comparisons of the eastern Gulf of Mexico with other rifted margins. Based on the outcome of our inversion, we can broadly divide the profile into three sections with distinct seismic velocity structures: the shallow Florida shelf north of the De Soto Canyon (0-150 km model distance), the continental rise south of the De Soto Canyon (150-250 km), and the deep basin Gulf of Mexico (250-524 km). Model distances are measured from a starting point at the landward limit of GUMBO Line 3, ~30 km southeast of Pensacola, Florida.

The shallow seafloor landward of the Florida shelf break (0-75 km model distance) is nearly flat and deepens from <0.2 km to 2.0 km across the De Soto Canyon (75-150 km). In the uppermost 3.5 km of sediment on the Florida shelf, seismic velocities increase sharply from 2.1 to 4.6 km/s. At greater depths, the velocity exceeds 5.0 km/s in a broad zone above the basement from ~50 to 140 km model distance. Sediment thickness increases substantially from 6.8 km at the landward limit of our model to 10.7 km beneath the Florida shelf break, at which point the seafloor depth increases southward across the De Soto Canyon from 2.0 km to 3.2 km. We find 20-23 km-thick crystalline crust beneath the Florida shelf and De Soto Canyon (0-150 km model distance). This zone displays a gradual increase in seismic velocity with depth from 5.5-7.2 km/s. Although our ray coverage does not directly constrain the crustal thickness at the landward limit of our profile (Figure 3.8), we show crystalline crust to be at least 23 km thick at 40 km model distance. Beneath the Florida Escarpment from ~90-150 km, the Moho shallows from ~34 km to 28 km whereas crystalline crust thickness decreases accordingly from 23 km to 16.5 km. A ~50 km-wide zone at the base of crystalline crust with seismic velocities greater than 7.4 km/s exceeds typical crustal velocities of the eastern North American continent [*Holbrook et al.,* 1992; *Thomas,* 2011]. Between 110 km and 150 km in our model, we find mantle seismic velocities of 7.7-8.0 km/s to depths of 35 km.

South of the continental rise of the De Soto Canyon, crystalline crust decreases in thickness from 16.4 km at 150 km model distance to 10.7 km at 250 km, comprising nearly half of the 12.5 km of total crustal thinning at GUMBO Line 3 (Figure 3.8).

Sediment thickness (~7.5 km) is nearly constant over this distance, with a steep seismic velocity gradient (1.6-4.0 km/s) in the uppermost 3.5 km of sediment that shallows (4.0-5.0 km/s) in the lowermost 4 km of sediment. A 20 km-wide velocity anomaly above the basement at 200 km model distance shows sediment seismic velocities >4.7 km/s. A disparity between the depth to top of basement in our seismic velocity model (~10 km) and the FUGRO 533 MCS reflection image (~8 km) suggests that this boundary may be obscured by the presence of salt above the basement (Figure 3.7), or the discrepancy is the result of industry time-to-depth migrations that use different sediment velocities than we observe at GUMBO Line 3. Crustal seismic velocities from 150-250 km model distance increase gradually from 5.9 km/s at the top of basement to 7.0-7.5 km/s above the Moho. Shallow mantle seismic velocities beneath this zone of intermediate crustal thickness are substantially lower (7.6-7.9 km/s) than elsewhere along GUMBO Line 3. From ~215-250 km model distance mantle velocities increase to >8.0 km/s and are constrained to ~1 km beneath the Moho.

Sediments in the deep-water Gulf of Mexico exhibit low seismic velocities (<1.8 km/s), with a much shallower sediment velocity gradient here than beneath the Florida shelf and De Soto Canyon. The thinnest crystalline crust (<10 km) in the GUMBO 3 velocity model is found in the deep-water basin between 250-524 km model distance (Figure 3.8) and shows laterally homogeneous seismic velocities. Similar to crust beneath the foot of the De Soto Canyon, the top of basement in the deep basin is relatively flat. Since the Moho depth is also nearly flat (~17-21 km deep), we find a consistent crustal thickness of 7.5-10.5 km. We observe a prominent, ~1.2 km basement high between 470-

500 km model distances that corresponds to the lowest crustal velocities found in the deep basin (<5.1 km/s). Elsewhere, crustal velocities near the top of basement are higher and display a moderately steep velocity gradient to the base of crystalline crust (5.8-7.3 km/s). We observe high seismic velocity zones (>7.5 km/s) in the lower crust directly above the Moho at 300 km and between 410 km and 470 km model distance. The uppermost 2-4 km of the mantle in the deep basin shows laterally homogeneous mantle velocities from 7.9-8.3 km/s.

3.3.3 Resolution Tests

One distinct advantage of the least-squares inversion method is that it provides insight into the spatial resolution of seismic velocities and boundary interfaces in seismic velocity models [*Menke*, 1984]. For the GUMBO Line 3 profile we constructed a resolution matrix for the linearized least-squares inversion that produced the final seismic velocity model (Figure 3.8) following the methodology of *Van Avendonk et al.* [2004]. The resolution matrix is square (N x N), where N is the number of model parameters that includes the amount of discretized seismic velocities and boundary depths in our model. The resolution matrix maps 'true Earth structure' into the imaged seismic velocity structure. In areas that do not have adequate ray coverage, smoothing of the inversion method will average the Earth's structure over a wider region. In order to show the degree of local averaging in our tomographic inversion, we determine how model features of a fixed size are resolved in different parts of the model. We conduct two resolution tests to investigate the resolving power of the data at two different scales (Figure 3.13). We define ellipses in model space that are 8 km wide by 3 km high and 16

km wide by 6 km high, dimensions that allow us to verify how well seismic velocity structures of different sizes are resolved in our model. If the tomographic image generated by the resolution test perfectly reproduces the original ellipse, the resolution matrix becomes an identity matrix and the local resolution is 1.0. If the test structure is partially resolved, the resolution will fall between 0 and 1.0, and we consider a resolution value of 0.5 to be sufficient for interpretation.

Our tests show excellent spatial resolution of the GUMBO 3 velocity model at both 16x6 km and 8x3 km scales (Figure 3.13). At the 16x6 km scale, resolution is high (>0.7) at model depths of up to 25 km, but the deepest parts of the model have moderate to low resolutions (0.6-0.1). Our interpreted model boundaries are also well constrained (0.8) at the 16 km scale, although the top of basement is more poorly constrained (0.2-0.4) between 60 and 100 km model distance. The uppermost 10 km of GUMBO Line 3 model space is well constrained at the 8 km scale, but resolution decreases below 0.4 at depths of 10-20 km. This decrease suggests that smaller velocity features in the lower portion of our seismic velocity model cannot be interpreted with much confidence. On the other hand, some of the basement and Moho model boundaries are well resolved (~0.8-0.6) at the 8 km length scale.

3.4 Discussion

We use deep seismic structure to interpret the geologic history of rifted margins. The amount and nature of magmatism and stretching (β) during rifting are two of the most basic observations that lend insight into the geologic processes that lead to

continental breakup [*Menzies et al.*, 2002; *Buck*, 2004; *Ziegler and Cloetingh*, 2004]. In the absence of a high geothermal gradient that could produce a volcanic rifted margin due to the expected abundance of syn-rift magmatism [*Korenaga et al.*, 2000], extreme lithospheric thinning can also lead to adiabatic decompression melting in the rising upper mantle. Thermal anomalies can lead to mantle convection that will enhance decompression melting and volcanism at rifted margins, but may require preexisting thinning of the lithosphere to advect into a rift zone and avoid conductive cooling beneath thicker lithosphere [*Armitage et al.*, 2009]. Conversely, if the mantle is cold and/or β is small, the resultant magma-poor rifted margin may be characterized by highly attenuated continental crust and exhumed mantle [*Whitmarsh et al.*, 2001].

3.4.1 Rifted Crust

To understand how rifting progressed in the northeastern Gulf of Mexico, we must make some assumptions regarding the structure of the continental crust before extension. Continental crust in the northeastern Gulf achieved its pre-rift configuration by the Late Pennsylvanian (~290-300 Ma), modified by the collision of Laurentia and Gondwana that formed the surrounding Ouachita and Appalachian orogenies [*Poole et al.*, 2005]. When the lithosphere in the eastern Gulf of Mexico experienced Late Triassic rifting (~210-230 Ma) it was likely still relatively warm and weak compared to the interior of Laurentia, and therefore rifting preferentially localized outboard of the orogenic belt [*Nelson*, 1992; *Huerta and Harry*, 2012]. The northern portion of GUMBO Line 3 (0-100 km) contains relatively thick crystalline basement interpreted as continental crust (Figure 3.14). Previous studies report 20-25 km thick transitional crust

beneath the northeastern U.S. Gulf coast [*Ibrahim et al.*, 1981; *Driskill et al.*, 1988; *Sawyer et al*., 1991; *Marton and Buffler*, 1994], and such estimates are in close agreement with the 23 km-thick continental crust we interpret for the landward end of GUMBO Line 3. From 0-100 km model distance, we calculate moderate stretching factors (β=1.7-1.9) given an estimated original crustal thickness of ~40 km for the nearby Wiggins Arch [*Huerta and Harry*, 2012]; our β-values (Figure 3.14) also agree with previous estimates for the northeastern Gulf of Mexico (β=1.65 to 1.85) [*Driskill et al.*, 1988]. Our model finds compressional seismic velocities for this section of continental crust (5.5-7.2 km/s) consistent with velocities reported for Paleozoic and other ancient orogenic belts [*Holbrook et al.*, 1992], which are substantially higher than velocity averages for continental crust at comparable depths (Figure 3.15) [*Christensen and Mooney*, 1995].

We observe landward and seaward-dipping reflectors (LDRs, SDRs) in the FUGRO 533 MCS profile at ~50-130 km model distance that extend ~ 10 km beneath basement (Figure 3.7). The geographic position of this zone of deep reflections is approximately coincident with the Apalachicola Basin [*Sawyer et al*. 1991; *Hudec et al.*, 2013a]. Although GUMBO Line 3 seismic velocities in this region are too high for an entirely sediment-filled basin, they are within the range for buried flood basalts (5.0-6.5 km/s) [*Christensen and Mooney*, 1995; *Planke et al.*, 2000]. We suggest these SDRs may be part of an 'inner wedge' system of syn-rift basins that were filled with basalts and volcaniclastic sediments during continental extension [*e.g.*, *Planke et al.*, 2000; *Menzies et al.*, 2009], and thus do not represent the 'outer wedge' SDRs that characterize the limit

of oceanic crust at volcanic rift margins [*Mutter*, 1985; *Planke and Eldholm*, 1994]. The LDRs likely indicate the presence of bounding faults that deepened the Apalachicola Basin in conjunction with a series of onshore Triassic grabens that comprise the South Georgia Rift basin (SGRB; Figures 3.2, 3.14). Alternatively, the SDRs and LDRs could represent structures inherited from earlier orogenic events in the northeastern Gulf region that are well preserved.

We interpret the western margin of the Southern Platform from ~160 to 200 km model distance as an isolated block of thicker rifted crust above unusually low mantle velocities (7.6-7.8 km/s; Figures 3.2, 3.7, 3.8, 3.14). Low mantle velocities in the Gulf of Mexico are also observed to the southwest at GUMBO Line 4 [*Christeson et al.*, 2014]. Mantle flow can lead to alignment of olivine crystals and anisotropic seismic velocities, with lower velocities perpendicular to the flow direction [*Hess*, 1964]. Low mantle velocities in the northeastern Gulf of Mexico may therefore be a result of transform or oblique motion of the Yucatán block during early Gulf rifting (Figure 3.17), which is consistent with most kinematic models for the Gulf of Mexico [*Klitgord et al.*, 1984; *Marton and Buffler*, 1994; *Pindell and Kennan*, 2009; *Hudec et al.*, 2013a].

We observe abnormally high velocity zones (>7.2 km/s) in the lowermost 5-10 km of crust between 70 km and 270 km model distance, as well as significant thinning of the crust (β>3.0) from >20 km to ~10 km (Figure 3.8). At volcanic rifted margins, lithospheric extension leads to decompression melting in the rising asthenospheric mantle that can create regions of high seismic velocities in the lowermost crust [*Menzies et al.*, 2002; *Ziegler and Cloetingh*, 2004; *Voss and Jokat*, 2007; *Franke*, 2013]. High-velocity

lower crust (HVLC) at GUMBO Line 3 could represent syn-rift magmatic underplating of a mafic, possibly gabbroic layer near the Moho, although absence of discernible wide-angle reflections from an underplated layer (Figures 3.3, 3.9) may instead suggest the HVLC represents substantial intrusions of melt into the lower continental crust during rifting [*White and McKenzie*, 1989; *Holbrook and Kelemen*, 1993]. We further interpret high seismic velocities (6.5-7.2 km/s) in the crust above GUMBO Line 3 HVLC as magmatic additions to the middle and/or upper continental crust during rifting. Relatively little HVLC >7.2 km/s is observed to the southeast at GUMBO Line 4, despite the interpretation of increased magmatic input during and after rifting [*Christeson et al.*, 2014]. Lower crustal velocity differences at GUMBO Line 3 and Line 4 may advocate an along-strike variation in mantle potential temperature and/or melt supply during rifting in the eastern Gulf of Mexico; a similar variation in syn-rift mantle potential temperature is inferred for adjacent transects at the Southeast Greenland margin near the Iceland hotspot [*Korenaga et al.*, 2000; *Holbrook et al.*, 2001].

We infer the presence of an abnormally high geothermal gradient during the Late Triassic – Early Jurassic onset of rifting in the northeastern Gulf of Mexico. Rifting occurred ~40-50 Ma after the Late Paleozoic collision of Suwannee terranes with Laurentia, and it likely reactivated this lithospheric boundary [*Harry and Londono*, 2004; *Thomas*, 2011]. CAMP-aged volcanics in the nearby SGRB and Suwannee terrane of Florida also indicate elevated mantle temperatures during the onset of Gulf rifting [*McBride*, 1991; *Heatherington and Mueller*, 2003; *Heffner et al.*, 2012]. Our observations of HVLC and probable volcanism in the Apalachicola Basin are consistent

with volcanic rifted margins offshore southwestern Morocco and at the Rockall Trough offshore Scotland [*Klingelhöefer et al.*, 2005; 2009] and support high mantle potential temperatures during rifting in the northeastern Gulf of Mexico.

Besides higher mantle potential temperatures, small-scale mantle convection may have instead led to adiabatic decompression melting along GUMBO Line 3, though the mantle melts would be generated at lower pressure and temperature in that case [*Korenaga et al.*, 2000; *Menzies et al.*, 2002]. Low-temperature mantle melting tends to result in less mafic magmatic additions and lower seismic velocities (<7.1 km/s) in the thick crust of volcanic rifted margins [*Korenaga et al*., 2000]. In contrast, we show that for GUMBO Line 3 smaller thickness crust with relatively high seismic velocities support a higher mantle potential temperature during rifting (>1350 °C; Figure 3.16). We find no evidence for enhanced mantle upwelling and small-scale convection, and instead suggest that passive mantle upwelling (*i.e.*, upwelling rate equals the half-spreading rate) characterizes the northeastern Gulf of Mexico. Similar conditions are inferred for the southern portion of the southeastern Greenland margin, where effects of the Iceland hotspot are not a controlling factor [*Holbrook et al.*, 2001].

3.4.2 Limit of Oceanic Crust and Evaporite Deposition

We provide a new estimate on the landward limit of oceanic crust (LOC) in the northeastern Gulf of Mexico. The LOC corresponds to both an increase in average crustal seismic velocity to >7.0 km/s and a stabilization in crustal thickness to ~8 km starting at ~270-290 km GUMBO Line 3 model distance (Figures 3.2, 3.8, 3.14). We place the LOC farther to the northeast than previous estimates that use gravity data, limited seismic

refraction and reflection data, or salt deposits to locate the boundary [*e.g.*, *Saywer et al.*, 1991; *Bird et al.*, 2005; *Pindell and Kennan*, 2009]. On the other hand, our new LOC is proximal to that of *Schouten and Klitgord* [1994] and southwest of *Hall and Najmuddin* [1994] who used magnetic anomaly grids to delimit the LOC (Figure 3.2).

Our estimation of the LOC at GUMBO Line 3 is supported by the fact that its location coincides with the Gulf Coast Magnetic Anomaly (GCMA) [*Hall*, 1990] and a trend of 'outer wedge' SDRs (Figures 3.2, 3.14, 3.17) [*Imbert and Philippe*, 2005*; Kneller and Johnson*, 2011]. The LOC coincides with the seaward margin of the GMCA [*Hall*, 1990], a basin-wide magnetic feature linked to continental breakup and a potential volcanic rift margin in the northwestern Gulf of Mexico [*Mickus et al.*, 2009]. The East Coast magnetic anomaly (ECMA) similarly overlies the LOC in the Atlantic Ocean [*Sahabi et al.*, 2004]. Magnetic anomalies along the west Yucatán escarpment also suggest rift-related volcanism near the LOC at the conjugate margin in the southern Gulf of Mexico [*Imbert and Philippe*, 2005]. Our LOC, the GCMA in the northeastern Gulf of Mexico, and the ECMA also coincide with 'outer wedge' SDRs (Figure 3.2) [*Withjack et al.*, 1998; *Imbert and Philippe*, 2005; *Jourdan et al.*, 2009; *Kneller and Johnson*, 2011], features that characterize the LOC at volcanic rift margins [*Menzies et al.*, 2002; *Franke*, 2013].

The location of both a landward-dipping basement ramp and the basinward edge of salt interpreted from coincident MCS data strengthen our choice of the LOC from 270-290 km GUMBO Line 3 model distance. Here we interpret a ~1 km step-up in the top of basement height in the coincident FUGRO 533 image, as well as a similar rise in

GUMBO Line 3 top of basement (Figures 3.7, 3.11). This 'inner ramp' is interpreted by *Hudec et al.* [2013a] to mark the LOC across much of the northern U.S. Gulf region. The ramp may have also initially acted as a barrier to block the basinward flow of salt [*Hudec et al.*, 2013a], and the proximity of the seaward edge of evaporites to the basement ramp supports this notion (Figures 3.7, 3.14). Intermittent influx and desiccation of seawater accumulated evaporites on subsiding crust in the early Gulf of Mexico basin prior to complete lithospheric breakup [*Salvador*, 1987; *Hudec et al.*, 2013a]. With the onset of seafloor spreading at the present-day LOC, the subsiding rift basin established deep seawater exchange with neighboring oceans, after which evaporite deposition ceased [*Sawyer et al.*, 1991; *Galloway*, 2008]. The overburden of prograding clastic sediments led to basinward migration of allochthonous salt [*Hudec et al.*, 2013a], which slightly overlaps ocean crust in the northeastern Gulf of Mexico (Figure 3.14).

3.4.3 Seafloor Spreading

Following a prolonged Middle-Late Triassic – Late Jurassic rifting episode (~240-158 Ma), lithospheric breakup led to a comparatively brief period (~20 Ma) of seafloor spreading in the Gulf of Mexico basin [*Marton and Buffler*, 1994; *Bird et al*., 2005, and references therein]. Regional plate tectonic models predict that the short-lived spreading center in the Gulf of Mexico was not connected to mid-ocean ridges in the Atlantic or Pacific realms (Figure 3.17) [*Marton and Buffler*, 1994; *Schouten and Klitgord*, 1994]. However, plate reorganizations that affected Middle – Late Jurassic seafloor spreading in the Atlantic Ocean [*Bird et al.*, 2007; *Labails et al.*, 2010; *Kneller et al.*, 2012] may be contemporaneous with changes in movement of the Yucatán block, and thus Gulf of

Mexico seafloor spreading events. To the west, the Yucatán block is interpreted to have translated along the Tamualipas-Golden Lane-Chiapas continental transform fault near the present-day Mexican Gulf margin [*Pindell*, 1985, *Dickinson and Lawton*, 2001; *Bird et al*., 2005], whereas in the east another strike-slip zone between the eastern margin of the Yucatán block and the Florida Platform may have isolated the Gulf of Mexico basin from mid-ocean ridges between North America and Africa [*Klitgord et al*., 1984; *Christenson*, 1990] (Figure 3.1). Amalgamation of present-day Mexico in the Early Cretaceous halted rotation of the Yucatán block and effectively set in place the shape of the present-day Gulf of Mexico [*Guerrero et al.*, 1990].

We calculate an upper and lower limit for seafloor-spreading rates in the northeastern Gulf using: (1) University of Texas Institute for Geophysics (UTIG) Plates Project plate tectonic constraints on the opening history of the Atlantic and estimated motion of surrounding continents, which estimate 158 Ma for the beginning and 140 Ma for the end of seafloor spreading [see also *Hudec et al.*, 2013a]; (2) UTIG Gulf Basin Depositional Synthesis ages of 154 Ma and 137 Ma for the beginning and end of seafloor spreading, respectively, as determined by stratigraphic mapping of Middle – Late Jurassic horizons in the northeastern Gulf of Mexico (J. W. Snedden *et al.*, Interaction of deep-water deposition and a mid-ocean spreading center, Eastern Gulf of Mexico Basin, USA, submitted to *Transactions of the Gulf Coast Association of Geological Societies*, herein referred to as *Snedden et al*., 2014); and (3) our interpretation of a ~210 km distance between the LOC and an extinct spreading ridge (Figures 3.7, 3.8, 3.14). Our estimate of a full-spreading rate of 23-25 mm/yr agrees with previous approximations (<30 mm/yr)

for the eastern Gulf of Mexico [*Marton and Buffler*, 1994]. The rate of opening at GUMBO Line 3 is only slightly higher than estimates for GUMBO Line 4 (22 mm/yr), suggesting that slow-spreading oceanic crust characterizes much of the eastern Gulf basin [*Christeson et al.*, 2014]. Spreading rates increase slightly to the northwest, as expected given a pole of rotation in the southeastern Gulf of Mexico [*Dunbar and Sawyer*, 1987; *Hall and Najmuddin*, 1994; *Marton and Buffler*, 1994].

Despite slow spreading rates, the nature of oceanic crust at GUMBO Line 3 is not typical for slow-spreading ridges. The ocean crust at the seaward end (270-524 km) of GUMBO Line 3 has an average thickness of 8.1 km with a maximum thickness >10 km, which is slightly thicker than expected for oceanic crust globally (7.1 +/- 0.8 km) [*Chen*, 1992; *White et al.*, 1992]. Thick oceanic crust in the northeastern Gulf of Mexico may indicate a higher rate of melt delivery due to post-rift persistence of elevated mantle potential temperatures (Figure 3.16) [*Bown and White*, 1994; *Smallwood and White*, 1998; *Korenaga et al.*, 2000], which is consistent with our interpretation of a volcanic margin and a long-lived mantle thermal anomaly at GUMBO Line 3. In comparison, ocean crust at GUMBO Line 4 is noticeably thinner (5.6-5.7 km) with abnormally high seismic velocities in the uppermost crust (6.0-6.7 km/s) [*Christeson et al.*, 2014]. Mantle seismic velocities beneath oceanic crust at GUMBO Line 3 (7.8-8.1 km/s) are consistent with either normal continental or oceanic lithosphere [*White et al.*, 1992; *Christenson and Mooney*, 1995]. We observe the lowest GUMBO Line 3 crustal seismic velocities (<5.0 km/s) at ~470 km model distance; the MCS image shows a half-graben here ~22 km wide and ~2 km deep (Figures 3.7, 3.8, 3.14). This feature matches the morphology of axial

valleys at other slow seafloor-spreading ocean ridges (*e.g.*, 8-20 km wide, 1-2 km deep) [*Sempéré et al*., 1993; *Perfit and Chadwick*, 1998; *Snedden et al*., 2014] and we interpret the half-graben as the extinct Gulf of Mexico spreading center. This paleo-ridge also corresponds to the location of an ocean ridge segment in the eastern Gulf of Mexico proposed by *Pindell and Kennan* [2009] and *Snedden et al.* [2014].

The absence of discernible magnetic anomalies CM29r-CM18r in the northeastern Gulf of Mexico [*Malinverno et al.*, 2012] can be explained by the combination of slow seafloor-spreading rates and a robust magma supply to the spreading axis. The high frequency of magnetic reversals (~250-500 kyr) under slow seafloor-spreading conditions during the Oxfordian to Berriasian (158-140 Ma) would result in seafloor magnetic anomalies of only a few kilometers in width (Figure 3.8). If these basalts flowed laterally from the spreading ridge by just a few kilometers, normal- and reversed-polarity magnetic signatures could easily overprint each other and mask the reversals [*Christeson et al.*, 2014]. Given that the seaward end of GUMBO Line 3 is characterized by a ~2 km-deep valley (Figures 3.7, 3.14), the lateral flow of basalts away from the ridge crest may have been limited to this axial valley. Abundant magmatism at this spreading center may have formed a topographic high during opening of the northeastern Gulf of Mexico, despite the slow spreading rates. Similar conditions exist at the present-day Reykjanes Ridge near the Iceland hotspot, where 10 km-thick crust is accreted at slow full spreading rates of ~20 mm/yr [*Smallwood and White*, 1998]. We suggest that the axial valley at GUMBO Line 3 merely characterizes the morphology of the spreading center just before it went extinct.

3.4.4 Post-rift Evolution

The landward end of GUMBO Line 3 provides a unique window into basin subsidence since it crosses the Cretaceous shelf edge. The sediment cover includes the Upper Jurassic (Oxfordian) Norphlet and Smackover formations [*Mancini et al*., 2004; *Galloway*, 2008; *Snedden et al.*, 2013] beneath predominantly Late Cretaceous and Cenozoic post-rift sediments. The Oxfordian units were the first deposits on the Callovian (~163-161 Ma) Louann salt, and their deposition likely directly preceded the initiation of seafloor spreading in the eastern Gulf basin [*Hudec et al*., 2013a; *Snedden et al.*, 2013]. Although our GUMBO Line 3 seismic velocity model does not constrain small-scale differences in stratigraphy, the near absence of sediment seismic velocities >4.5 km/s seaward of the LOC may indicate the seaward limit of Upper Jurassic Smackover-Norphlet sediments, or conversely the edge of evaporites. The highest sediment velocities from GUMBO Line 3 (5.0-5.6 km/s) are found landward of the De Soto Canyon at ~4-10 km depth and are consistent with a carbonate platform (Figure 3.14) [*Rafavich et al.*, 1984; *Dobson and Buffler*, 1997; *Wang*, 1997]. During post-rift subsidence, reef-building organisms kept this Cretaceous carbonate shelf edge in the photic zone, resulting in 2-3 km of carbonate growth near the Florida shelf [*Galloway*, 2008]. Sediment seismic velocities decrease landward of the carbonate shelf (4.8-5.1 km/s), indicating that the inner margin may not have subsided as much as the shelf edge. Seaward of the carbonate shelf, post-rift cooling and subsidence of the mantle (and therefore the crust) outpaced upward reef growth and allowed clastic influx from adjacent fluvial and deltaic systems to halt carbonate production [*Galloway*, 2008]. Accordingly,

the uppermost 2-5 km of GUMBO Line 3 sediments have lower seismic velocities (1.6-3.5 km/s) representing Late Cretaceous and Cenozoic clastics that infilled newly created accommodation space in the Gulf of Mexico [*Galloway*, 2008].

3.5 Conclusions

Compressional seismic velocities in the northeastern Gulf of Mexico indicate that the crust here is comprised of distinct domains shaped by rifting and seafloor spreading: (1) thinned continental crust with high seismic velocities, indicating that it is intruded and possibly under-plated by mantle-derived melts; and (2) thick oceanic crust emplaced at slow spreading rates. Landward of the LOC, the presence of high-velocity lower crust (>7.2 km/s) suggests high mantle potential temperatures during Late Triassic – Early Jurassic rifting, which are expected given the proximity of GUMBO Line 3 to Late Paleozoic suture zones and Late Triassic CAMP volcanism. Comparison of GUMBO Line 3 crust to mantle melting models supports passive mantle upwelling in the northeastern Gulf of Mexico. We show support for a two-stage kinematic model for the opening of the Gulf of Mexico, which includes: (1) Triassic – Middle Jurassic southwestern movement of the Yucatán block until 158-154 Ma, which may have resulted in strike-slip movement in the eastern Gulf of Mexico and (2) counter-clockwise rotation of the Yucatán block as it separated from Laurentia until ~140-137 Ma, accompanied by seafloor spreading in the eastern Gulf basin. We locate the LOC at ~270-290 km GUMBO Line 3 model distance given the following: (1) crustal seismic velocities and thicknesses seaward of the LOC are consistent with oceanic crust; (2) a landward-dipping step in basement height (i.e. ‘inner ramp’ of *Hudec et al.* [2013a]) is

interpreted in coincident MCS data; (3) a sharp decrease in magnetic intensity at the edge of the GCMA overlaps the LOC; and (4) the LOC coincides with the seaward limit of autochthonous salt. Location of the LOC and an extinct spreading center at ~470 km model distance help constrain the extent of ocean crust and support a slow rate of seafloor spreading (~24 mm/yr). A long-lived thermal anomaly may have enhanced melt production and emplaced thick oceanic crust in the northeastern Gulf of Mexico until the Early Cretaceous, when the Yucatán block docked against southern Mexico and seafloor spreading in the Gulf of Mexico stopped.

3.6 Tables

Table 3.1 – GUMBO Line 3 pick counts, travel time fits, and uncertainties

Phase	Number of Picks	RMS Misfit (ms)	Average assigned uncertainty (ms)
Psed (P1)	7505	67	50
PbP (R1)	1633	68	100
Pg (P2)	6062	88	75
PmP (R2)	4249	97	100
Pn (P3)	2770	145	100
Total	22219	97	89

3.7 Figures

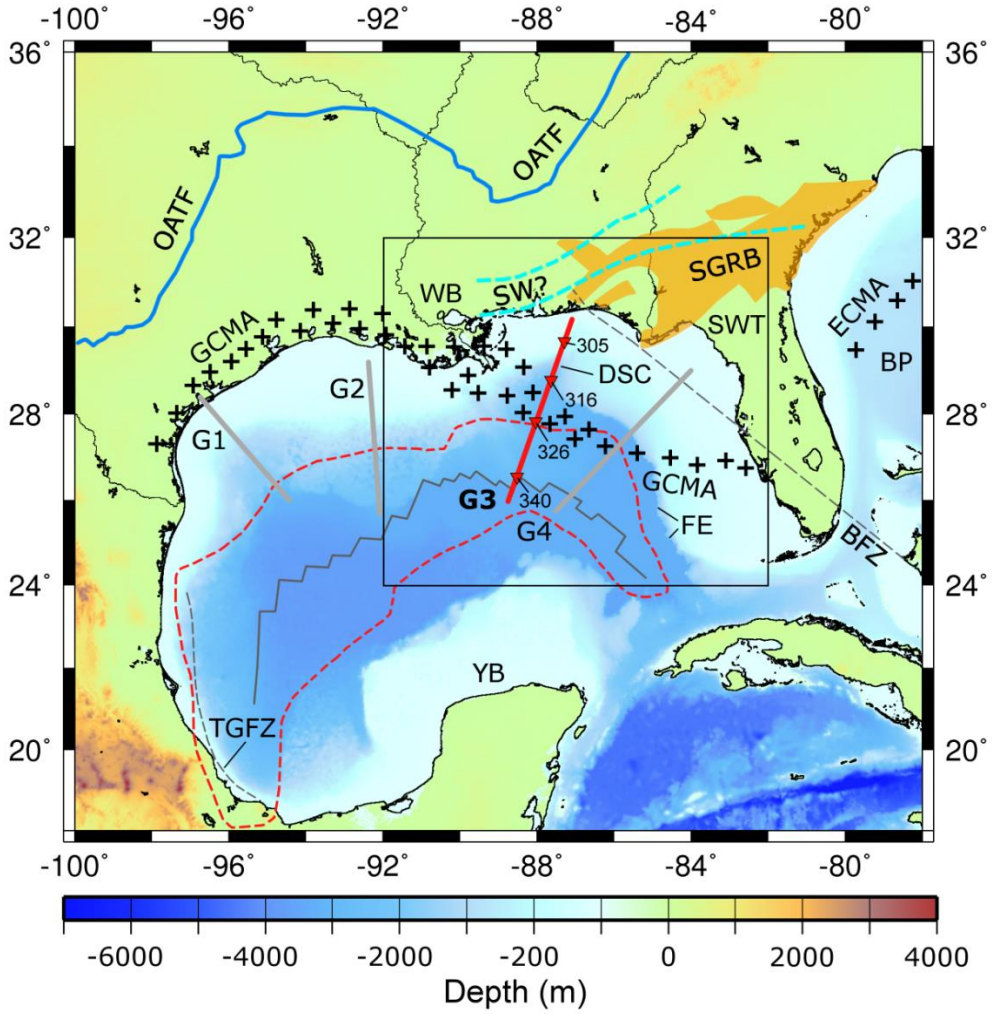

Figure 3.1 - Bathymetric map of the Gulf of Mexico region. Dashed red line and solid dark grey line indicate limit of oceanic crust and spreading ridge, respectively, as proposed by *Pindell and Kennan* [2009]. Red inverted triangles are locations for GUMBO Line 3 instruments 305, 316, 326, and 340. Box shows Figure 3.2 outline. **BFZ** – Bahamas Fracture Zone (dashed grey line) [*Klitgord et al.*,1984]; **BP** – Blake Plateau; **DSC** – De Soto Canyon; **ECMA**, East Coast magnetic anomaly (plus symbols) [*Nelson et al.*, 1985]; **FE** – Florida Escarpment; **G1-G4** – GUMBO transects (grey and red lines); **GCMA** – Gulf Coast magnetic anomaly (plus symbols) [*Hall*, 1990]; **OATF** – Ouachita-Appalachian thrust front (solid blue line) [*Thomas,* 2010]; **SGRB** – South Georgia Rift Basin (orange overlay) [*McBride and Nelson*,1988; *Clendenin*, 2013]; **SW** –Suwannee-Wiggins suture zone (dashed blue line) [*Thomas*, 2010]; **SWT** – Suwannee terrane; TGFZ – Tamaulipas-Golden Lane-Chiapas Fracture Zone [*Bird et al.*, 2005]; **WB** – Wiggins block/arch; **YB** – Yucatán block.

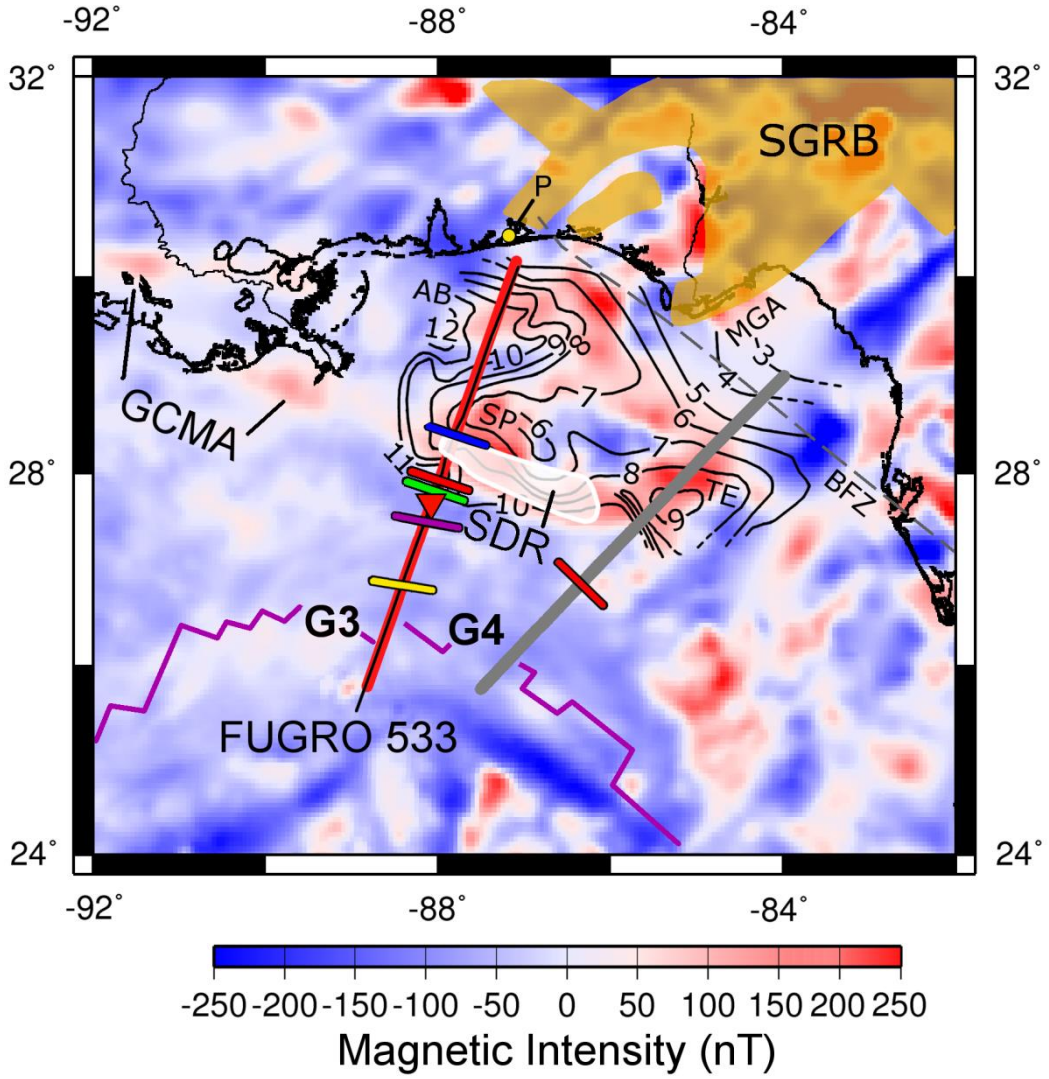

Figure 3.2 - Magnetic anomaly [*Maus et al.*, 2009] and depth to basement map for the northeastern Gulf of Mexico. Black lines offshore are basement depth contours (in km) from *Dobson and Buffler* [1991; 1997]. Locations of GUMBO Lines 3 and 4 (G3, thick red line; G4, thick grey line) and FUGRO 533 (thin black line) are shown. Short line segments indicate limit of oceanic crust (LOC) from the following studies: GUMBO project (red), *Hall and Najmuddin* [1994] (blue), *Schouten and Klitgord* [1994] (green), *Pindell and Kennan* [2009] and *Sawyer et al.* [1991] (purple), and *Bird et al.* [2005] (yellow). Purple line shows spreading ridge location proposed by *Pindell and Kennan* [2009]. **AB** – Apalachicola Basin; **BFZ** – Bahamas Fracture Zone (dashed grey line) [*Klitgord et al*., 1984]; **MGA** – Middle Ground arch; **P** – Pensacola, Florida (yellow dot); **SDR** – zone of seaward-dipping reflectors (white outline) [*Imbert and Philippe*, 2005; *Kneller and Johnson*, 2011]); **SGRB** – South Georgia Rift Basin (orange outline); **SP** – Southern Platform; **TE** – Tampa Embayment.

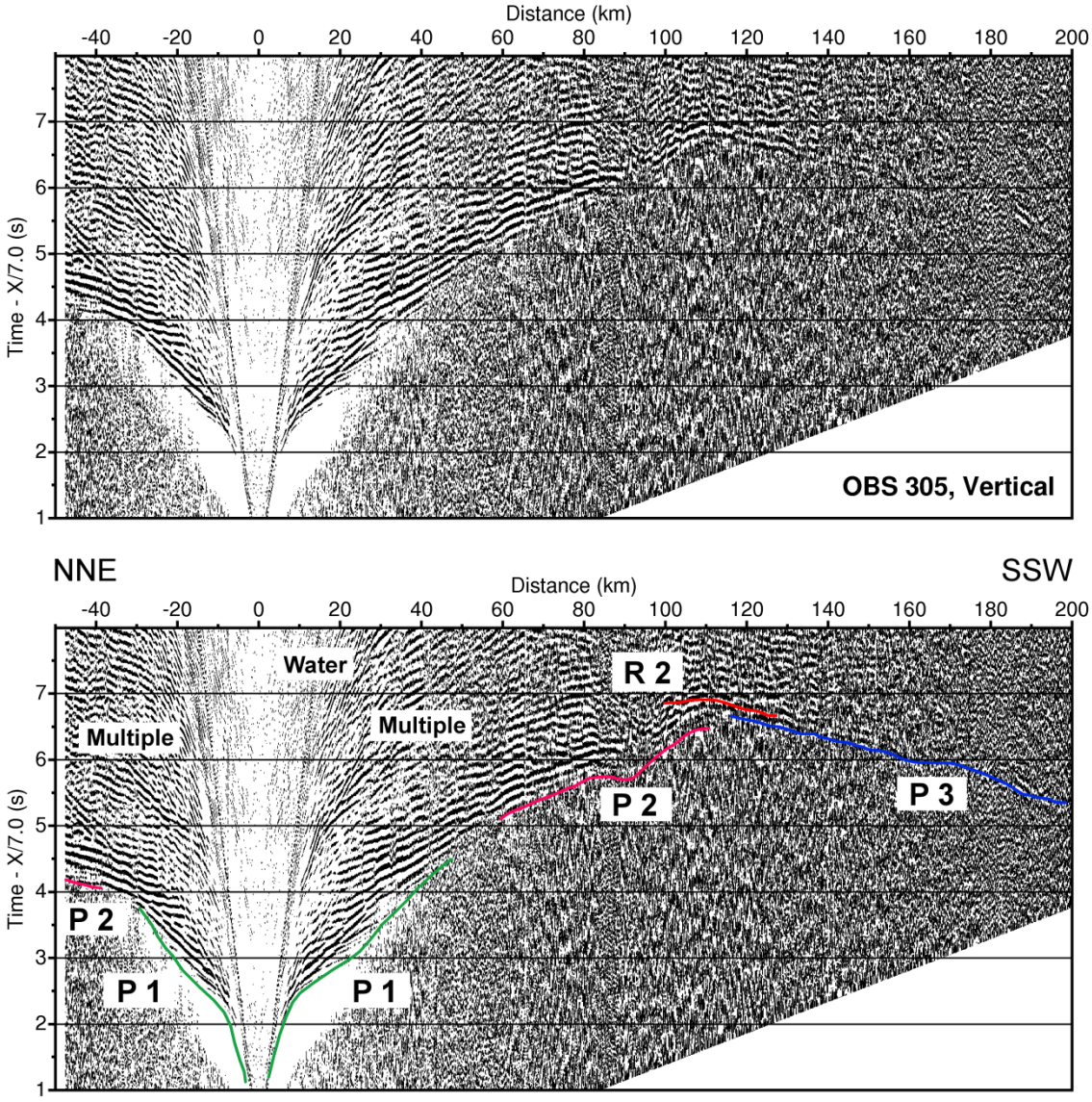

Figure 3.3 - Receiver gather from the vertical component of OBS 305 (top) with interpreted travel time arrivals (bottom). A reduction velocity of 7.0 km/s is applied. Bandpass filters are used with a frequency range of 6-14 Hz. Gain is set to 1.0 and increases linearly with offset. See text for descriptions of compressional refractions (P1-P3) and reflections (R1-R2). Also labeled are arrivals of the direct wave in water (Water) and multiples (Multiple). OBS location displayed on Figure 3.1.

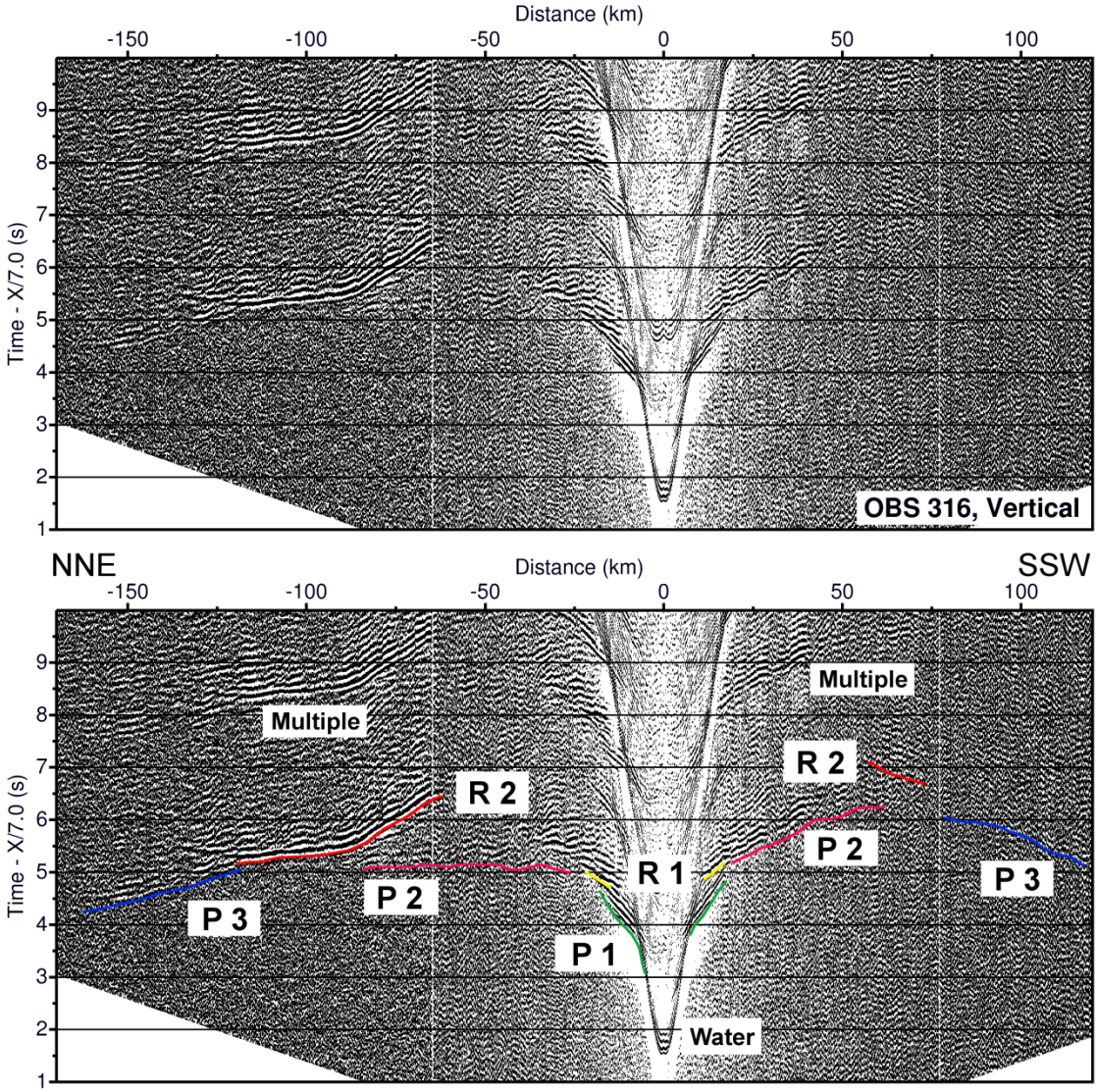

Figure 3.4 - Receiver gather from the vertical component of OBS 316 (top) with interpreted travel time arrivals (bottom). See Figure 3.3 for further details.

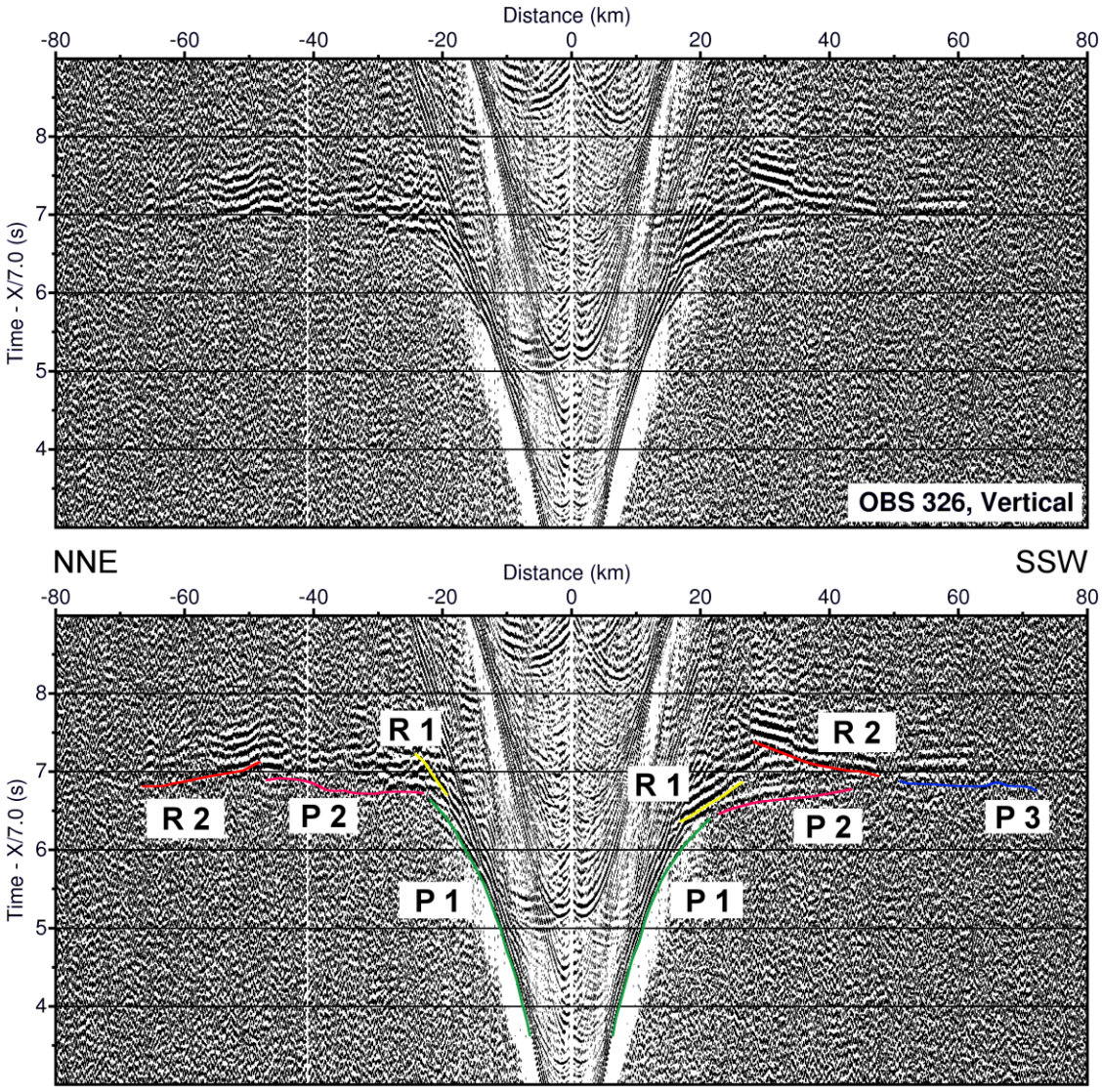

Figure 3.5 - Receiver gather from the vertical component of OBS 326 (top) with interpreted travel time arrivals (bottom). See Figure 3.3 for further details.

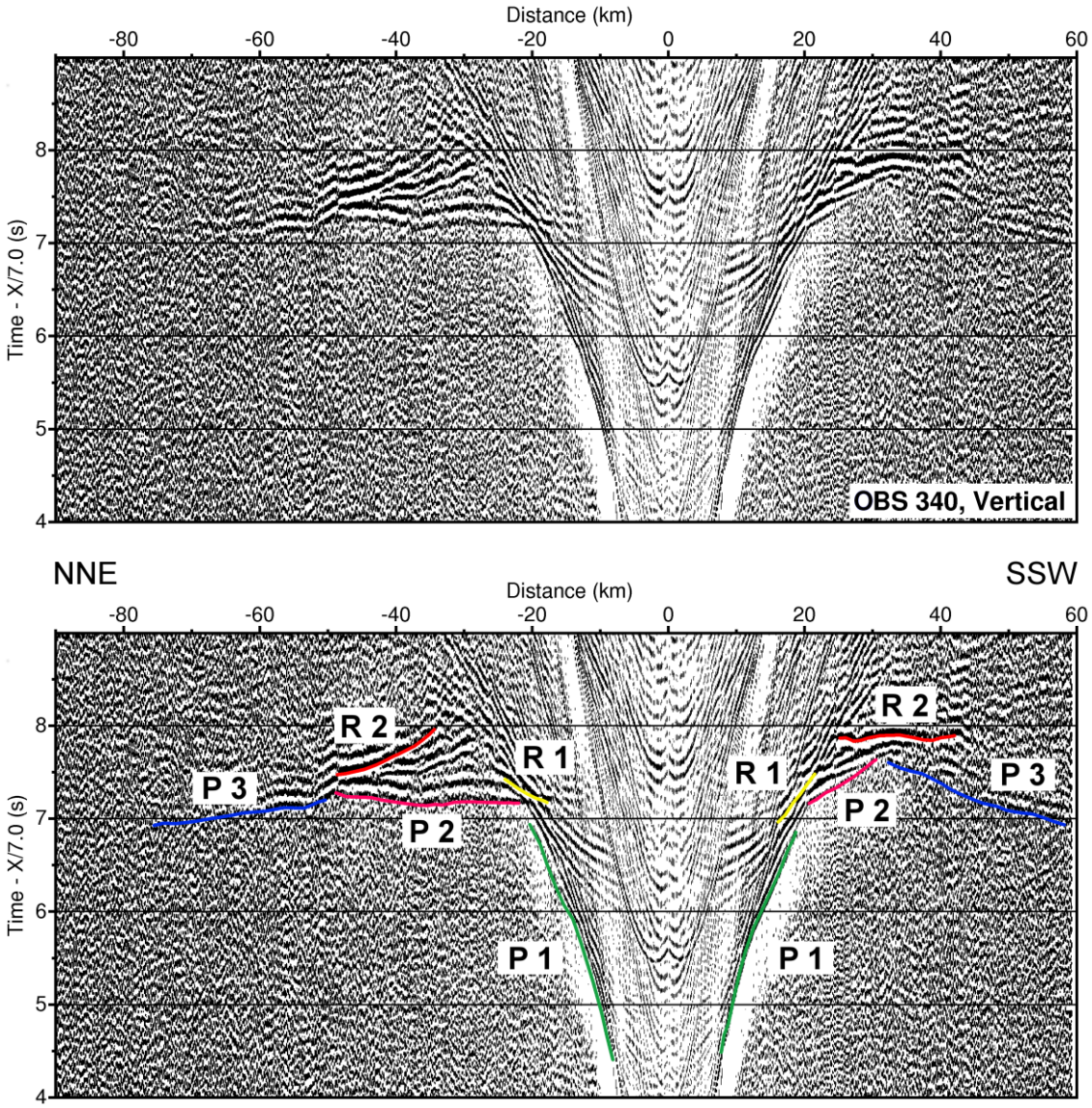

Figure 3.6 - Receiver gather from the vertical component of OBS 340 (top) with interpreted travel time arrivals (bottom). See Figure 3.3 for further details.

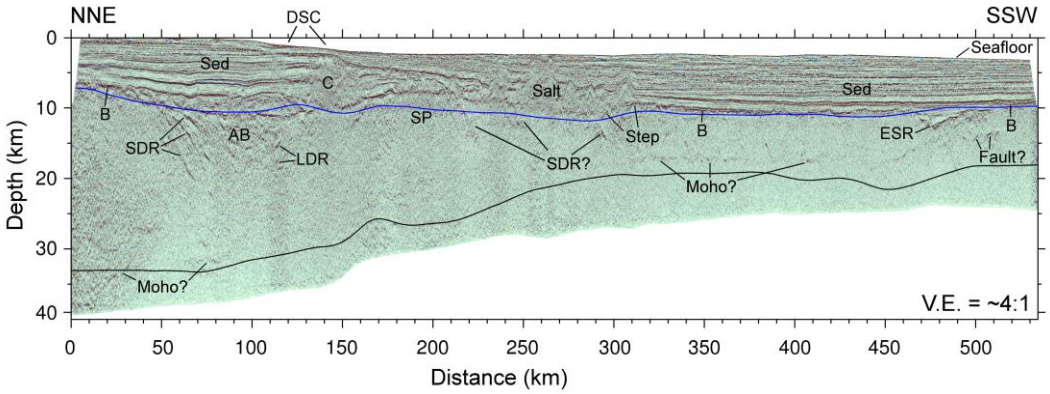

Figure 3.7 - FUGRO 533 multi-channel seismic reflection (MCS) image. Plotted boundaries constrained by coincident GUMBO 3 wide-angle data include top of basement (blue line) and Moho (black line). **AB** – Apalachicola Basin; **B** – MCS Basement; **C** – carbonate platform; **DSC** – De Soto Canyon; **ESR** – extinct spreading ridge; **LDR** – landward dipping reflector; **SDR** – seaward dipping reflector; **SP** – Southern Platform.

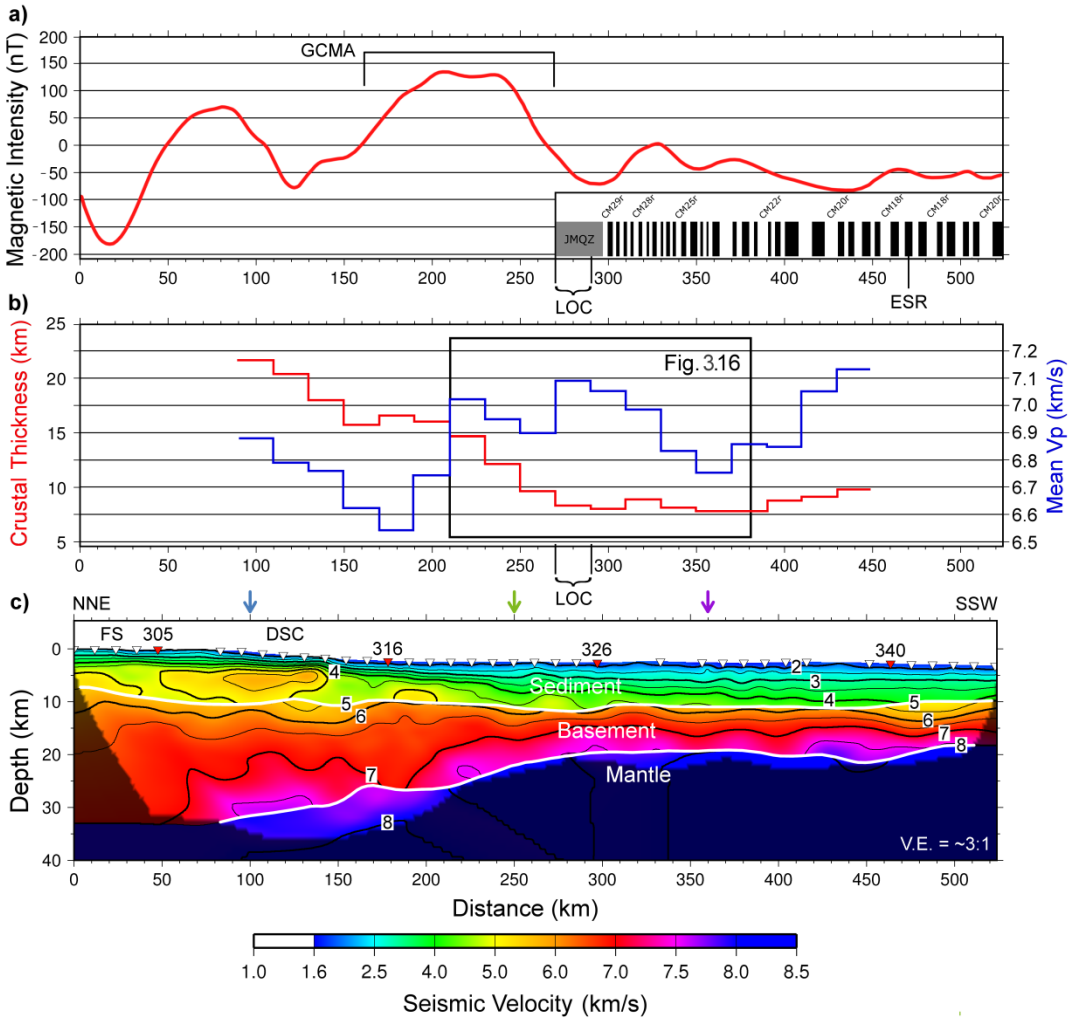

Figure 3.8 - Seismic velocity model and magnetic intensity plot for GUMBO Line 3. a) Magnetic anomaly plot [*Maus et al*., 2009] with M-series magnetic polarity chrons for GUMBO 3 ocean crust [*Malinverno et al*., 2012]. Chron thickness calculated using a full-spreading rate of 23 mm/yr, 158 Ma start of seafloor spreading, and locations shown for the LOC; b) Crustal thickness versus average crustal compressional velocities. Crustal thickness and mean *Vp* plots are calculated using a 20 km-wide averaging window; c) GUMBO 3 seismic velocity model. Upper and lower white lines on velocity model represent top of basement and Moho boundaries, respectively. Shading denotes model space not constrained by ray paths. Inverted triangles show OBS locations, with red symbols and numbers corresponding to record sections displayed in Figures 3.3-3.6. Colored arrows indicate locations of velocity versus depth profiles for Figure 3.15. **DSC** – De Soto Canyon; **ESR** – extinct spreading ridge; **FS** – Florida Shelf; **GCMA** – Gulf Coast magnetic anomaly; **JMQZ** – Jurassic Magnetic Quiet Zone; **LOC** – limit of oceanic crust.

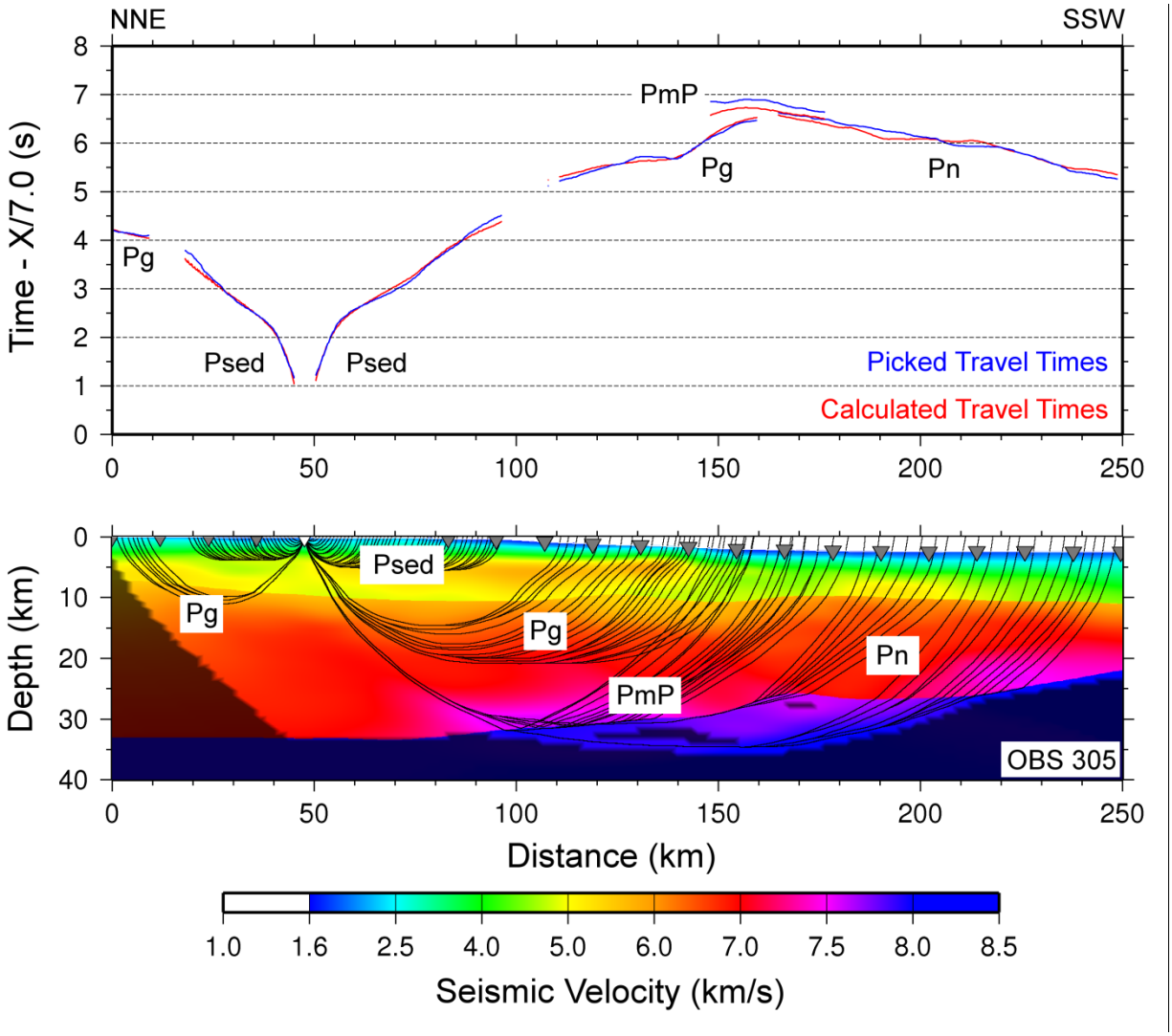

Figure 3.9 - Picked and calculated travel times for OBS 305 (top) and ray paths through final tomographic model (bottom). Rays plotted for every sixth pick. Shading denotes model space not constrained by ray paths. **PbP** – basement reflections; **Pg** – basement layer refractions; **PmP** – Moho reflections; **Pn** – mantle layer refractions; **Psed** – sediment layer refractions.

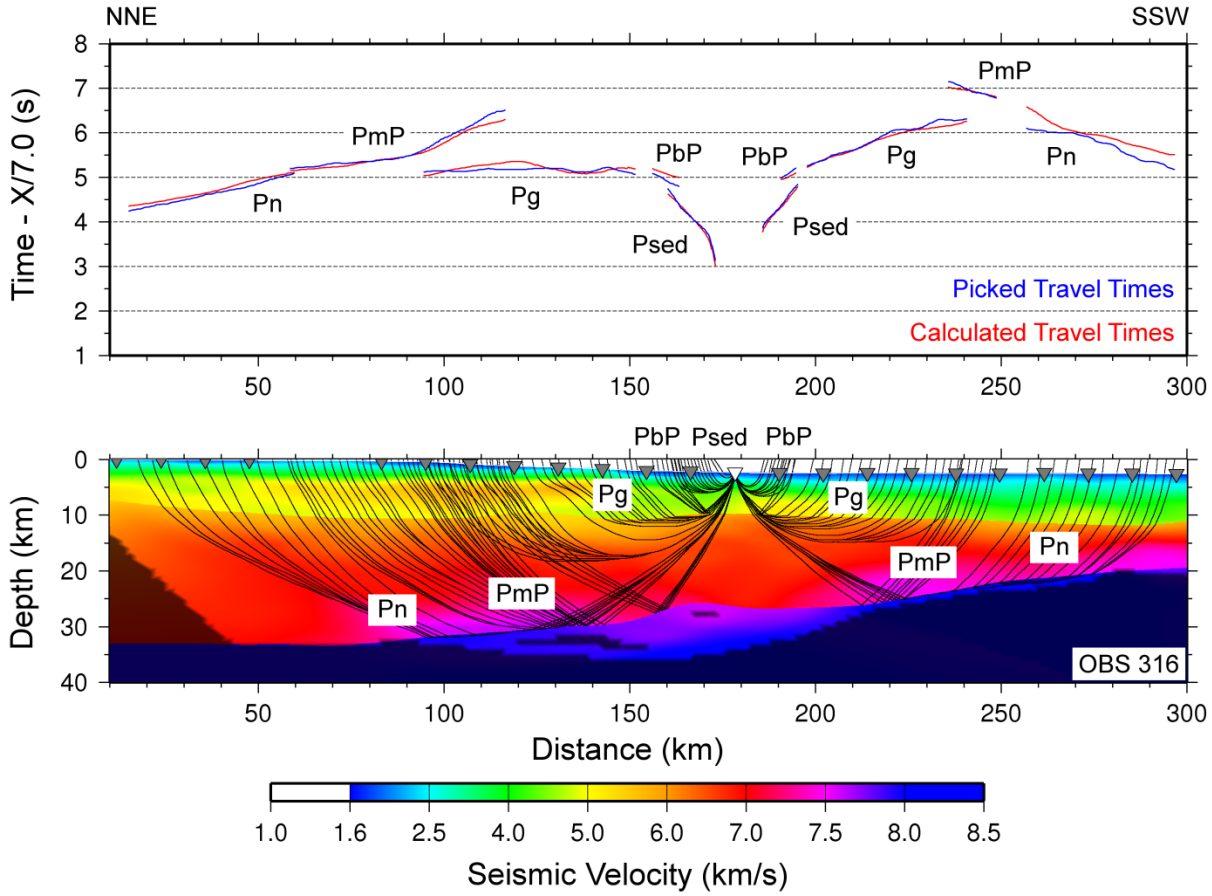

Figure 3.10 - Picked and calculated travel times for OBS 316 (top) and ray paths through final tomographic model (bottom). See Figure 3.9 for further details.

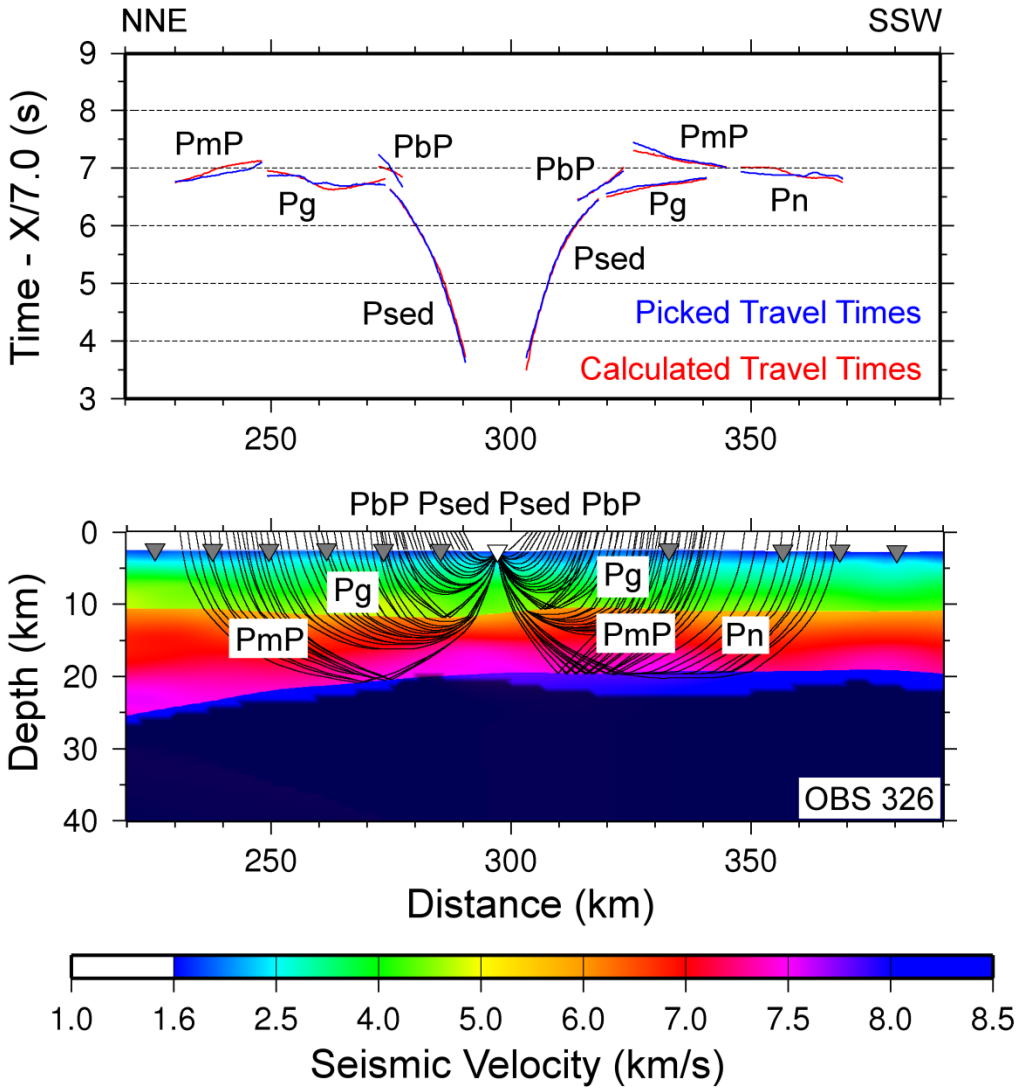

Figure 3.11 - Picked and calculated travel times for OBS 326 (top) and ray paths through final tomographic model (bottom). See Figure 3.9 for further details.

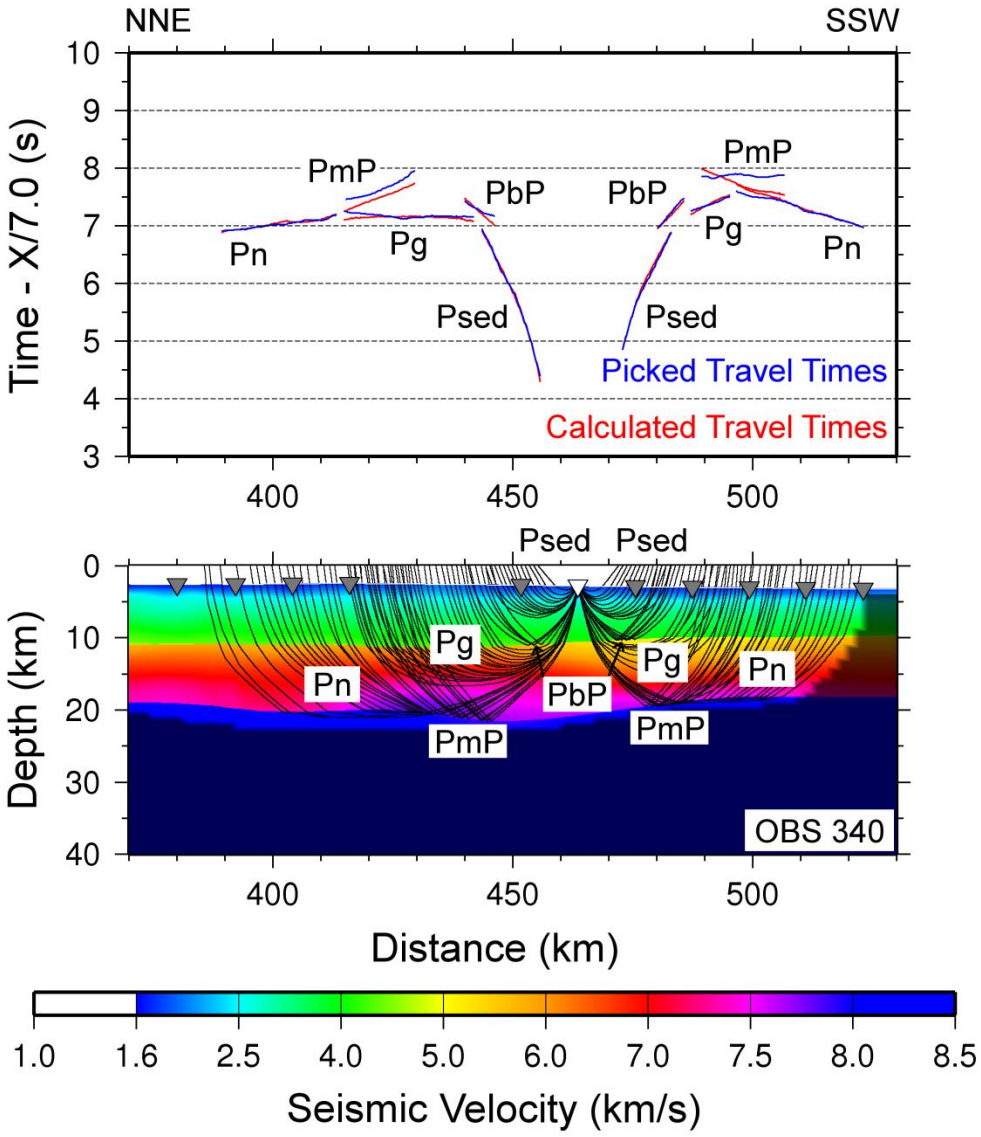

Figure 3.12 - Picked and calculated travel times for OBS 340 (top) and ray paths through final tomographic model (bottom). See Figure 3.9 for further details.

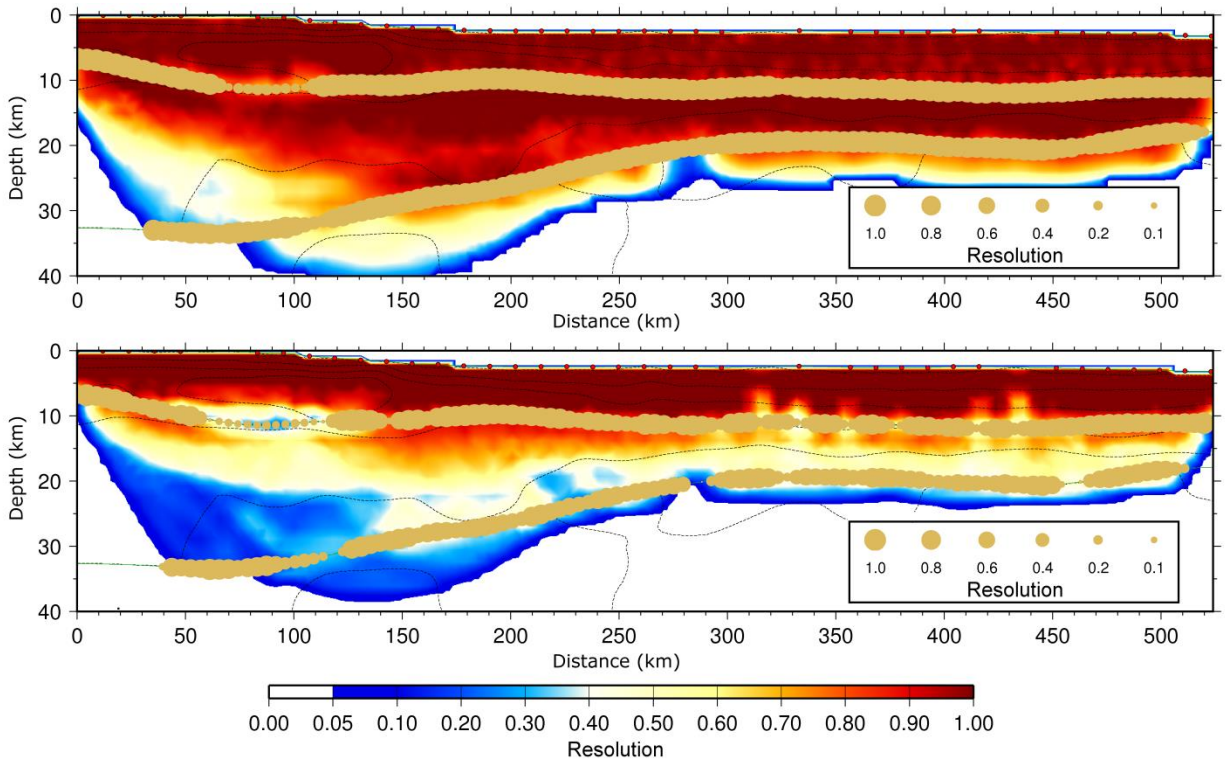

Figure 3.13 - 16 km x 6 km (top) and 8 km x 3 km (bottom) resolution tests for GUMBO Line 3 seismic velocity model in Figure 3.8. Color palate indicates resolution of seismic velocities in the final model. Tan circles indicate resolution of top of basement and Moho model boundaries.

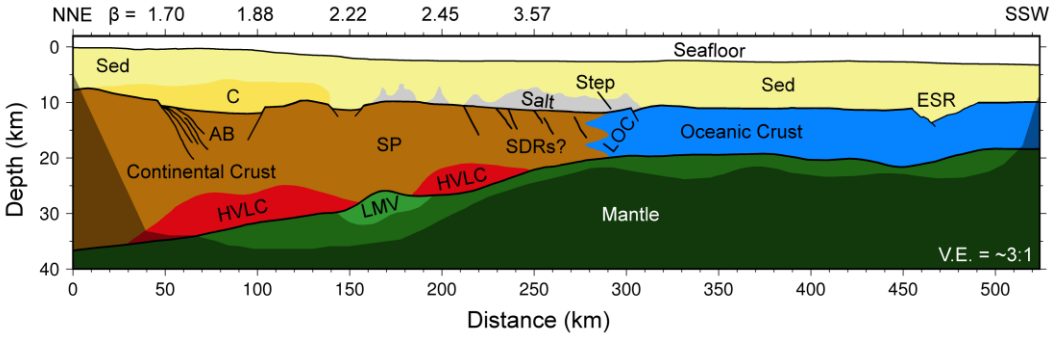

Figure 3.14 - Geologic interpretation of the northeastern Gulf of Mexico rifted margin. Top of basement, faults, and salt bodies are constrained by the depth-migrated FUGRO 533 MCS profile (Figure 3.7). Moho boundary and deeper structural features are constrained by GUMBO Line 3 (Figure 3.8). Shading denotes GUMBO Line 3 model space not constrained by ray paths. Stretching factor for continental crust (β) is plotted at a 50 km interval starting at 50 km model distance. **AB** – Apalachicola Basin; **C** – carbonate platform; **ESR** – extinct spreading ridge; **HVLC** – high velocity lower crust; **LMV** – low mantle velocity zone; **LOC** – limit of oceanic crust; **SDRs** – seaward-dipping reflectors **SP** – Southern Platform.

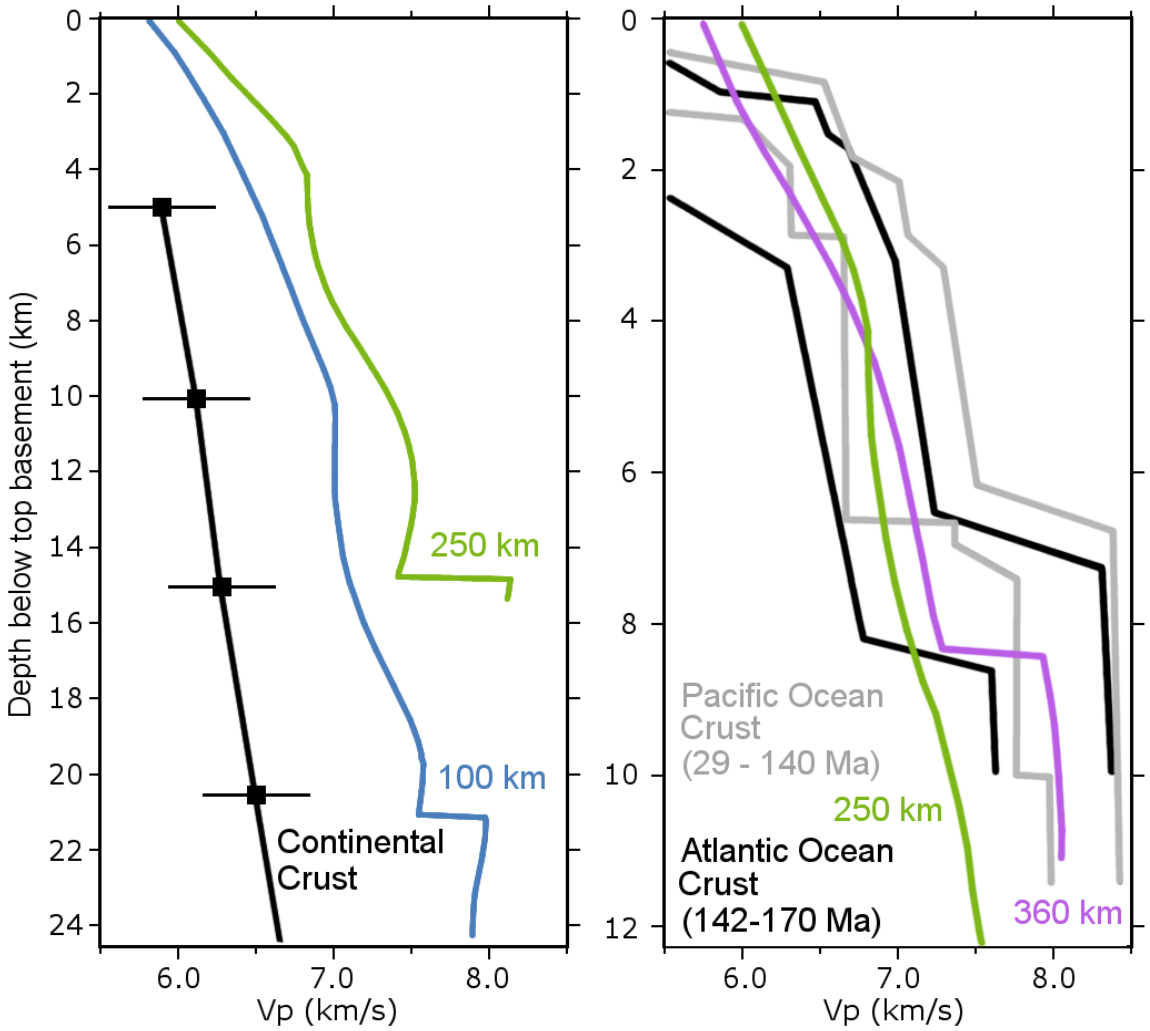

Figure 3.15 - Velocity versus depth below basement profiles for GUMBO Line 3 rifted continental crust (left) and oceanic crust (right). See Figure 3.8 for profile locations. GUMBO Line 3 is compared to profiles for average continental crust (black line with squares) [*Christenson and Mooney*, 1995] and oceanic crust from the Pacific (grey lines) and Atlantic Ocean (black lines) [*White et al.*, 1992].

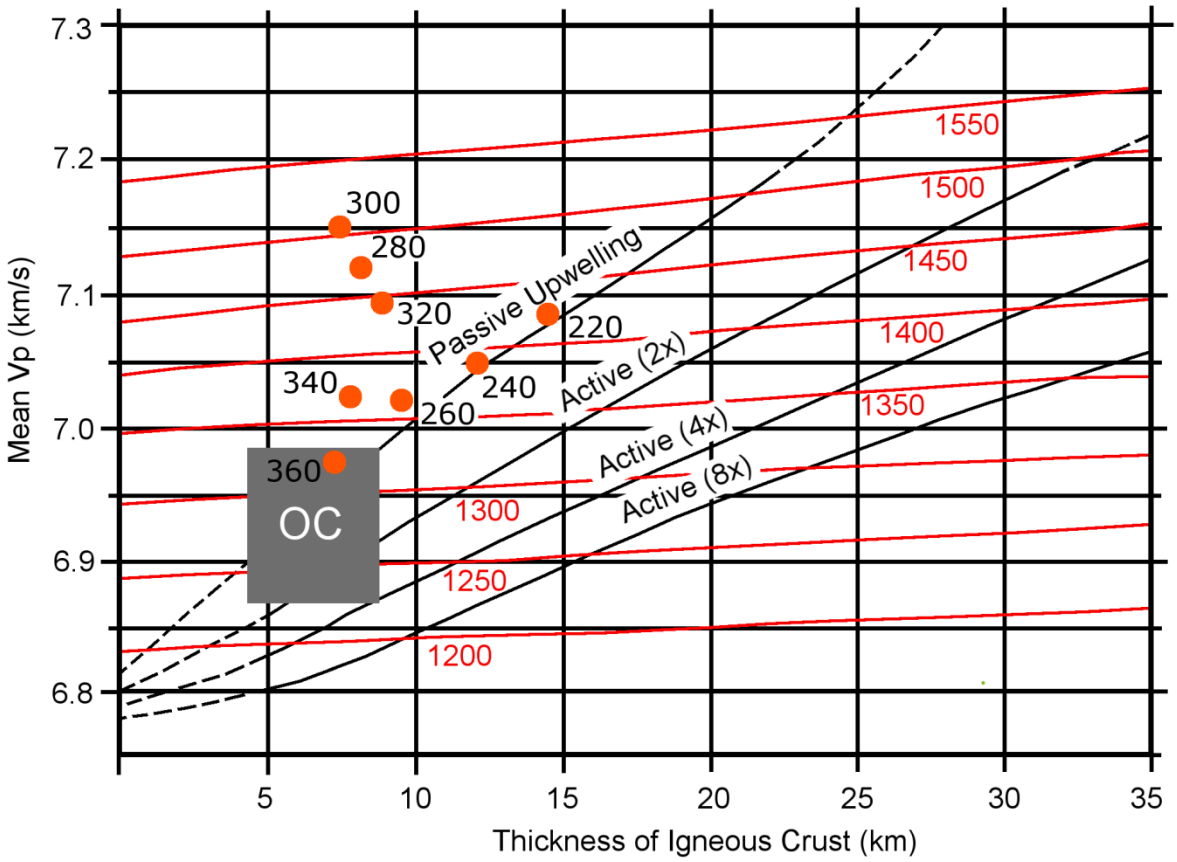

Figure 3.16 - Comparison of average seismic velocity and GUMBO Line 3 crustal thickness near the LOC (220 km – 360 km) with mantle mantling models of *Korenaga et al.* [2000] and *Holbrook et al.* [2001] and plots of normal oceanic crust (OC). Black lines show predicted velocity-thickness curves based on models of passive and active upwelling. Red lines show predicted mantle potential temperatures at a 50 °C interval. Each orange dot represents a 20 km averaging window for GUMBO Line 3. Following the methodology of *Holbrook et al.* [2001], GUMBO Line 3 compressional velocities lower than 6.85 km/s are replaced by 6.85 km/s before averaging to avoid the velocity-lowering effects of basalt porosity. Temperature corrections of -0.0005 km/s/°C are applied assuming a 10°C seafloor temperature increasing linearly to 417 °C at 22 km. Pressure corrections of 0.00022 km/s/MPa are applied using GUMBO Line 3 column heights and densities of water (1000 kg/m^3), sediment (2300 kg/m^3), and igneous crust (2800 kg/m^3).

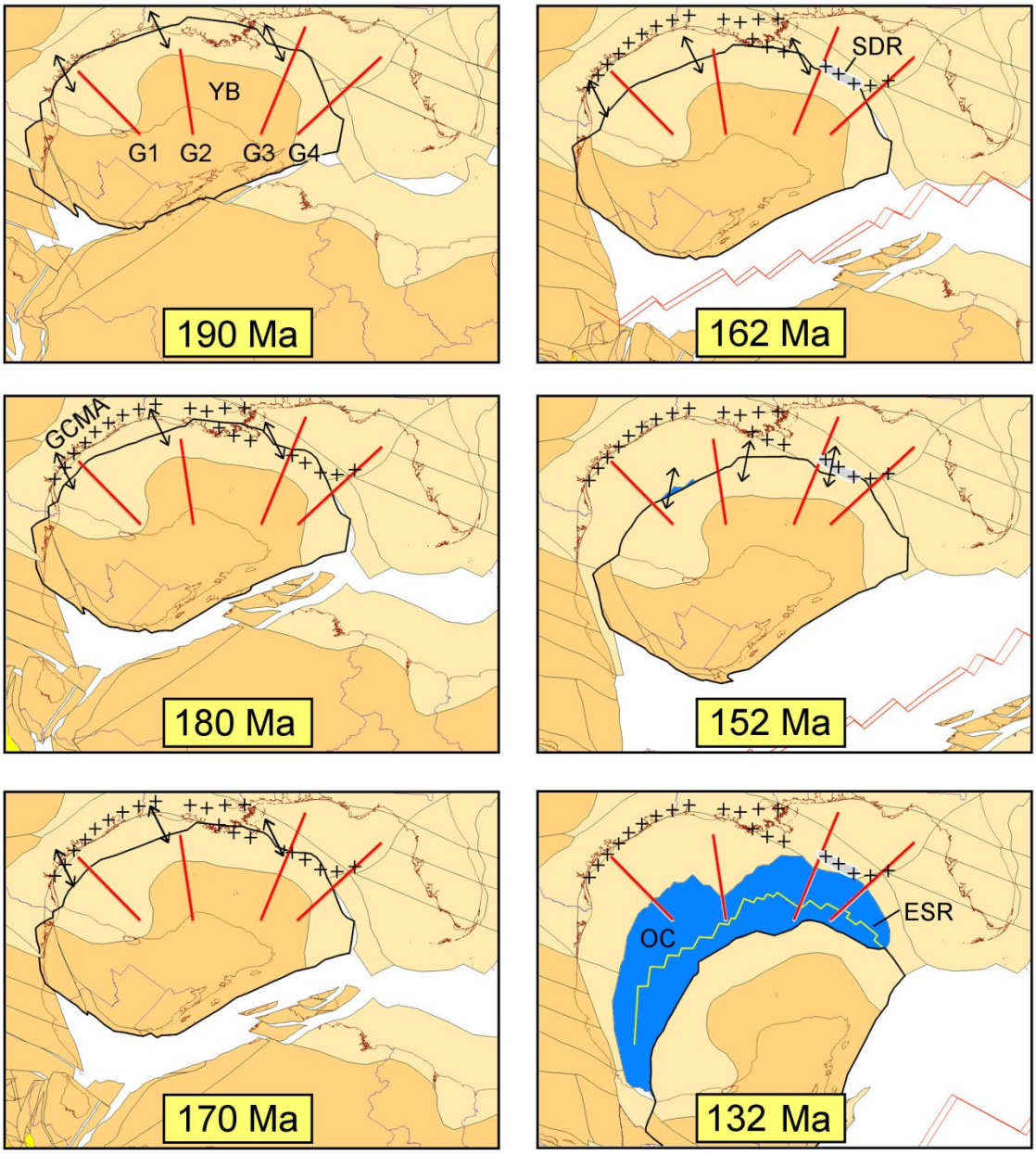

Figure 3.17 -. Kinematic plate reconstruction for the Gulf of Mexico. Arrows indicate relative plate motions between Yucatán block (black outline) and Laurentia. **G1-G4** – GUMBO Lines 1-4 (red lines); **GCMA** – Gulf Coast Magnetic Anomaly (plus symbols); **ESR** – extinct spreading ridge (yellow line); **OC** – oceanic crust (blue); **SDR** – seaward-dipping reflectors (grey).

Chapter 4: Deep crustal structure of the north-central Gulf of Mexico: insights from the GUMBO Line 2 marine seismic transect

Abstract

A linear array of ocean-bottom seismometers from the Gulf of Mexico Basin Opening project (GUMBO Line 2) yields new constraints on deep crustal structure in order to better understand the evolution of rifting and seafloor spreading in the north-central Gulf of Mexico. GUMBO Line 2 extends ~396 km north-south offshore southwestern Louisiana to across the Louisiana shelf and seaward of the Sigsbee escarpment. I resolve the compressional seismic velocity and layer boundaries of sediment, crystalline crust, and upper mantle using travel times from long-offset, wide-angle refractions and reflections, and compare the results with coincident multichannel seismic reflection data. The crust is thin (~10 km) with moderate-high average seismic velocities (~6.2-6.6 km/s) beneath the Louisiana shelf and salt/minibasin province. Velocity-depth profiles and strong Moho reflections suggest exhumed mantle or incipient oceanic crust are unlikely to comprise the crystalline basement here. Crystalline basement in the north-central Gulf of Mexico may instead be either highly thinned continental crust or thickened oceanic crust. Similar to the South China Sea and Vøring rifted margins, velocity-depth profiles and high lower crustal velocities (>7.0 km/s) at GUMBO Line 2 support the emplacement of syn- or post-rift magmatic intrusions (e.g., gabbro, extrusive basalts) within and above the crust from upper mantle melts, which may be related to the emplacement of tholeiitic xenoliths in southern Louisiana. I interpret the limit of oceanic crust (LOC) at the Sigsbee escarpment, as crust thins here to ~7 km, mean seismic

velocities increase to ~6.7 km/s, and a landward-dipping basement ramp is shown in both MCS and refraction data. Salt provinces were formed above thinned continental basement or oceanic crust that was below sea level during evaporite deposition. Shallower basement in the oceanic crustal realm at the seaward end of GUMBO Line 2 limited seaward salt movement, and this height discrepancy may result from low mantle densities beneath the seafloor-spreading ridge.

4.1 Introduction

The shape of the U.S. Gulf of Mexico region is largely determined by the late Paleozoic assembly of Pangaea and subsequent early Mesozoic rifting. Arc-continent collision of Laurentia with Gondwana terranes led to minimal shortening of crust near the Ouachita orogen north of the U.S. Gulf coastal margin, which contrasts with continent-continent collision along the northeastern U.S. Gulf and Atlantic coastal margins that developed a thick lithospheric root that collapsed prior to rifting [*Thomas*, 1976; *Keller et al.*, 1989; *Nelson*, 1992; *Harry and Londono*, 2004]. Geophysical evidence suggests relatively thick continental crust and presumably weaker lithosphere near the Sabine, Monroe, and Wiggins uplifts to the south and east of the orogenic suture, compared to the thin crust and shallow mantle near the Ouachitas that acted as a high-strength barrier to extension during rifting. [*Huerta and Harry*, 2012]. Instead, as the Yucatán block began to separate from the Laurentia during the Triassic, extension trended subparallel to inherited tectonic structures and opened rift basins far inland from the present-day Gulf of Mexico (Figure 4.1) [*Marton and Buffler*, 1994; *Harry and Londono*, 2004]. In the southern U.S., red beds from the Eagle Mills Formation provide direct evidence for

Triassic rifting [*Salvador*, 1987]. On the conjugate Yucatán block the rifted margin is much narrower, suggesting an asymmetry in the distribution of Mesozoic extension [*Marton and Buffler*, 1993].

From the crustal structure in the Gulf of Mexico coastal plain, it may be possible to infer where and by how much the continent stretched and thinned before breakup. However, there are relatively few regional deep-seismic studies that resolve crustal thickness. Early on-land seismic refraction work using explosives [*Hales et al.*, 1970] suggests that 50 km-thick crust lies just 200 km north of the eastern Texas coastline, while surface wave analysis produced a model with 40 km-thick continental crust in central Texas [*Keller and Shurbet*, 1975]. Offshore southeastern Texas, the crust thins to 10-20 km [*Ewing et al.*, 1960; *Hales et al.*, 1970; *Ibrahim and Uchupi*, 1981; *Ibrahim et al.*, 1981; *Buffler and Sawyer*, 1985; *Ebinero et al.*, 1988]. The composition and history of this thinned crust may provide insight into geologic processes that accompanied continental rifting before the onset of seafloor spreading. Prior to rifting, Late Triassic thermal uplift along the southern margin of Laurentia [*Dickinson et al.*, 2010] may signify a phase of active mantle upwelling that culminated in extension and continental breakup. Onshore drill sites, exhumed volcanic xenoliths, and magnetic and gravity potential data suggest a possible decrease in syn-rift magmatism both seaward and east of the Texas coastline [*Salvador*, 1987; *Mickus et al.*, 2009; *Stern et al.*, 2011]. Nevertheless, better constraints are needed on the composition of rifted crust in order to understand the interplay between tectonics and magmatism.

Understanding the nature of the transition from continental rifting to seafloor spreading in the Gulf of Mexico is contingent upon determining the landward limit of oceanic crust (LOC). Present-day distribution of evaporites into northern and southern segments (Figure 4.1) suggests that a previously basin-wide salt province was bisected by Late Jurassic seafloor spreading, which emplaced a wedge of oceanic crust in the center of the basin [*Salvador*, 1987; *Sawyer et al.*, 1991; *Pindell and Kennan*, 2009; *Hudec et al.*, 2013]. However, the signature of seafloor spreading magnetic anomalies in central Gulf basin oceanic crust are ostensibly weak (Figure 4.2), making it difficult to distinguish between the crust of the rifted margin and that of true oceanic crust [*Hall and Najmuddin*, 1994; *Marton and Buffler*, 1994; *Bird et al.*, 2005]. This weak magnetic signal means that the seafloor-spreading rate can only be estimated from plate kinematic reconstructions that are typically derived from the motion of the surrounding continents [*Marton and Buffler*, 1994; *Hudec et al.*, 2013]. Geophysical data suggest the presence of a volcanic rift margin beneath the Texas coastline >200 km from estimates of the LOC in the northwestern Gulf of Mexico [*Bird et al.*, 2005, and references therein; *Mickus et al.*, 2009]. Wide volcanic margins (>200 km) transition to abnormally thick oceanic basement in the Vøring margin offshore Norway (>20 km thick), offering a potential explanation for basement underlying the northwestern Gulf of Mexico [*Mjelde et al.*, 2005; *Mickus et al.*, 2009]. A broader distribution of normal thickness oceanic crust (6-8 km) than that predicted by conventional estimates is also possible, with the LOC near the Texas-Louisiana coastline [e.g., *Schouten and Klitgord*, 1994; *Stern and Dickinson*, 2010]. Conversely, a broad zone of thinned continental crust, exhumed and serpentinized

mantle, and/or proto-oceanic crust may separate the volcanic margin from the LOC [*Pindell and Kennan*, 2009; *Kneller and Johnson*, 2011; *Rowan*, 2014].

I investigate the structure of rifted crust and upper mantle using marine seismic refraction data from the GUMBO project (Gulf of Mexico Basin Opening), the first of this type of study in the Gulf of Mexico in over twenty years. I describe the seismic velocity structure of the N-S transect GUMBO Line 2, which extends over 396 km offshore southwestern Louisiana, from near the coastline to across the Sigsbee escarpment in the central Gulf of Mexico. The GUMBO transects were designed to coincide with existing industry multi-channel seismic (MCS) profiles, which gives insight into the structure of thick deposits of salt and sediment above the basement. I discuss my interpretations for the opening of the north-central Gulf of Mexico, including thinned continental crust, the possibility of substantial post-rift magmatism, and the onset of seafloor spreading in the central Gulf basin.

4.2 Geologic Background

4.2.1 Pre-rift Setting

Two major orogenic events impacted the eastern margin of present-day North America and the Gulf of Mexico from the late Proterozoic to the late Paleozoic [*Thomas*, 1976; 2011]. The earliest documented orogeny created the oldest known lithosphere in the Gulf region during the formation of the supercontinent Rodinia: Precambrian-aged Grenville granites and metamorphic rocks in the Llano uplift of central Texas (Figure 4.1) [*Wilkerson et al.*, 1988; *Bartok*, 1993; *Young and Lee*, 2009]. Cambrian rifting of the Iapetan margin followed the trend of the previous late Proterozoic orogeny and may have

controlled the location of subsequent late Paleozoic orogenic and Mesozoic rifting events [*Thomas*, 2011]. During the assembly of the supercontinent Pangaea and closure of the Rheic ocean in the late Paleozoic, arc-continent collision of Laurentia with Gondwana-derived terranes created the Ouachita orogenic belt, continuous with the Appalachian and Marathon orogenies to the northeast and southwest, respectively [*Poole et al.*, 2005; *Huerta and Harry*, 2012; *Mueller et al.*, 2014]. The Ouachita orogeny was likely diachronous, resulting from an oblique collision that began in the Middle Pennsylvanian in Oklahoma (~310 Ma) and lasted until the Early Permian in Texas (~290 Ma) [*Dickinson et al.*, 2010]. The 'soft' arc-continent collision of the Ouachita orogen may not have led to much crustal shortening and thickening [*Thomas*, 1976; *Huerta and Harry*, 2012]. In comparison, the continent-continent collision in the southern Appalachians formed a deep crustal root that collapsed prior to Mesozoic rifting [*Nelson*, 1992]. Drilled rhyolites and volcanic tuffs in the Sabine uplift support Late Paleozoic arc volcanism [*Marton and Buffler*, 1994], while gravity modeling suggests thicker arc or continental crust beneath the Sabine uplift (>30 km) than adjacent regions [*Mickus and Keller*, 1992]. Therefore, compared to the stronger lithosphere beneath the Ouachita orogeny, thicker crust and weaker lithosphere beneath the Wiggins and Sabine uplifts likely led to localization of Mesozoic rifting seaward of the Ouachitas [*Huerta and Harry*, 2012].

Uplift of the margin before the onset of rifting is inferred for the western Gulf of Mexico on the basis of detrital zircon population analysis of Late Triassic sediments in Texas [*Dickinson et al.*, 2010], and may provide clues that mantle upwelling drove

extension in the northwestern Gulf region [*e.g.*, *Keen*, 1985; *Menzies et al.*, 2002]. Zircon provenance analysis suggests that large-scale recycling of sedimentary assemblages from the Ouachita-Marathon orogeny encountered minor contributions from erosion of the Yucatán block before rifting [*Dickinson et al*., 2010]. The lateral extent of pre-rift thermal uplift is not constrained due to burial of the northern and southern uplift flanks by post-rift subsidence and sedimentation, although sediment volume estimates suggest an average of 4 km of erosion across the Tamaulipas arch to the Sabine uplift (Figure 4.1) [*Dickinson et al*., 2010]. Although there is no direct evidence for pre-rift uplift from Eagle Mills Formation in eastern Texas or Louisiana [*Mickus et al.*, 2009], erosion or non-deposition of Permian to Late Triassic sediments in the north-central Gulf region may indicate an even wider zone of thermal uplift preceding rifting that extends as far as the East Texas salt basin [*Smith et al*., 1981; *Jackson and Seni*, 1983].

4.2.2 Continental Rifting

Continental rifting began in the Gulf of Mexico during the early breakup of Pangaea in the Late Triassic (~220 Ma) as southeastern movement of the Yucatán block from Laurentia led to a protracted rift phase that continued until the Oxfordian (~158 Ma) [*Marton and Buffler*, 1994; *Pindell and Kennan*, 2009]. Rift grabens around the Gulf region filled with Late Triassic – Early Jurassic terrestrial redbeds and associated volcanics of the Eagle Mills and Huizachal (La Boca) formations, which both unconformably overlie late Paleozoic basement and underlie Middle Jurassic to Late Cretaceous sediments [*Salvador*, 1987; *Jackson and Seni*, 1983; *Michalzik*, 1991; *Dawson and Callender*, 1992; *Bartok*, 1993; *Marton and Buffler*, 1994]. The East Texas

basin, Northern Louisiana salt basin, and Mississippi salt basin are extensional features in the north-central Gulf region (Figure 4.1) containing Eagle Mills clastics that constrain the timing of formation of these basins to the earliest phases of Gulf rifting [*Nunn et al.*, 1984]. Furthermore, the NNE-SSW trending East Texas salt basin and the Borderlands rift system of northern Mexico may represent aulacogens north of the rift systems that eventually opened the Gulf basin [*Pindell and Dewey*, 1982; *Jackson and Seni*, 1983; *Stern and Dickinson*, 2010].

Preceding the breakup of Pangea, a brief (~1 Myr), voluminous pulse of extrusive volcanism known as the Central Atlantic Magmatic Province (CAMP) emplaced flood basalts across much of the eastern U.S. and Gulf of Mexico region at the end of the Late Triassic (~200 Ma) [*McHone*, 2000]. Deep wells drilled near the northern limit of Eagle Mills rift basins in Mississippi, Louisiana, Arkansas, and northeast Texas recover almost exclusively diabase volcanic rocks with minor amounts of basalt [*Moody*, 1949; *Smith et al.*, 1981], suggesting that the volcanics originated from a single magma body at the end of the Triassic and erupted quickly with little magmatic differentiation [*Kidwell*, 1951]. Diabase dikes and sills in the eastern Gulf of Mexico show similar timing to CAMP volcanism [*Salvador*, 1987]. Accordingly, *Mickus et al*. [2009] postulate that the Houston magnetic anomaly (Figure 4.2) represents syn-rift volcanism along the Texas coastline, possibly coincident with CAMP.

Early seismic refraction studies in the north-central Gulf of Mexico (Figure 4.2) show >500 km of thinned ‘transitional’ crust between thicker continental crust of the northern Gulf basement highs and oceanic basement in the center of the Gulf basin

[*Hales et al.*, 1970; *Ibrahim and Uchupi*, 1981; *Ibrahim et al.*, 1981; *Ebinero et al.*, 1988]. Onshore refraction data suggest that highly extended continental crust (β = 2.5-4.0) lies beneath eastern Texas and southern Louisiana [*Hales et al.*, 1970; *Worzel and Watkins*, 1973; *Ibrahim and Uchupi*, 1981]. Marine refraction data suggest that this transitional crust likely extends offshore beneath the northwestern Gulf of Mexico shelf [*Ibrahim and Uchupi*, 1981; *Ebeniro et al.*, 1988] and borders a wedge of normal oceanic crust in the central Gulf basin [*Ewing et al.*, 1960; *Ibrahim and Uchupi*, 1981; *Ibrahim et al.*, 1981; *Ebinero et al.*, 1988; *Marton and Buffler*, 1994]. The geographic extent and composition of thinned transitional crust is contentious, leading to poor constraints on the nature of Gulf of Mexico rifting and onset of seafloor spreading. Some workers suggest that the transitional crust is comprised of highly attenuated upper and lower continental crystalline basement [*Buffler and Sawyer*, 1985; *Dunbar and Sawyer*, 1985; 1987; *Ebeniro et al.*, 1988; *Sawyer et al.*, 1991; *Marton and Buffler*, 1994; *Roberts et al*., 2005], while others interpret that the transitional crus is instead thinned continental crust with significant mafic underplating [*Harry and Londono*, 2004], exhumed mantle [*Kneller and Johnson*, 2011; *Rowan*, 2014], and/or incipient oceanic crust [*Keller and Shurbet*, 1975; *Ibrahim and Uchupi*, 1981; *Imbert and Philippe*, 2005; *Mickus et al.*, 2009; *Pindell and Kennan*, 2007, 2009] in the transitional region between continental and oceanic crust.

4.2.4 Seafloor Spreading

Beginning in the Callovian – Oxfordian (~166-158 Ma), counter-clockwise rotation of the Yucatán block away from the U.S. Gulf margin initiated an episode of seafloor spreading in the central Gulf of Mexico [*Bird et al.*, 2005, and references

therein]. Seafloor spreading continued until ~140 Ma when the Yucatán block docked against the Chortis block in the Early Cretaceous [*Pindell and Kennan*, 2009]. Although seafloor spreading magnetic anomalies are poorly defined in the central Gulf basin (Figure 4.2), marine seismic refraction data support the presence of a crescent-shaped zone of 5-6 km-thick ocean crust in the central Gulf of Mexico basin (Figure 4.1) [*Ewing et al*., 1960; *Ibrahim and Uchupi*, 1981; *Ibrahim et al*., 1981; *Buffler and Sawyer*, 1985; *Ebeniro et al*., 1988; *Marton and Buffler*, 1994].

The exact limit of normal oceanic basement (LOC) is debated [*e.g., Bird et al.*, 2005, *Hudec et al.*, 2013]. *Schouten and Klitgord* [1994] interpret a magnetic trend (100 nT contour) near the Louisiana coastline as the LOC; this trend parallels the Gulf Coast magnetic anomaly [*Hall*, 1990] that coincides with the LOC in the northeastern Gulf of Mexico [*Hall and Najmuddin*, 1994; *Schouten and Klitgord*, 1994]. Conversely, *Marton and Buffler* [1994] define an E-W trending LOC ~200 km south of the Louisiana coastline using a separate magnetic trend (0 nT contour) taken into account with gravity and refraction data. *Hudec et al*. [2013] use high quality seismic reflection data to define an irregular LOC ~300 km south of the Louisiana coast. As defined by *Hudec et al.* [2013] and *Pindell and Kennan* [2009], a ~2 km basement ramp separates transitional crust from a higher platform of normal oceanic basement [*Pindell and Kennan*, 2009]. *Pindell and Kennan* [2009] further interpret a positive magnetic anomaly in the central Gulf of Mexico as an extinct spreading axis (Figure 4.2).

4.2.3 Evaporite Deposition

Thick salt was deposited on transitional crust during the Callovian (~161-165 Ma), resulting from evaporation of seawater that may have intermittently flooded a shallow Gulf of Mexico basin [*Saywer et al.*, 1991; *Hudec et al*., 2013; *Rowan*, 2014]. The northern Gulf salt basins (*e.g.*, East Texas, North Louisiana, and Mississippi salt basins) provide insight into the early rift history of the Gulf of Mexico since salt was thickest above preexisting areas of tectonic subsidence and thinner above paleohighs [*Salvador*, 1987; *Galloway*, 2008; *Hudec et al.*, 2013]. The smaller northern Gulf basins and the expansive Louann Salt basins, separated by the Toledo Bend flexure structural high (Figure 4.1), were likely shallow (~1 km) before salt deposition and may have subsequently deepened to 3-4 km with the increasing salt load, maintaining a depositional surface at or near sea level [*Anderson*, 1979; *Hudec et al*., 2013b; *Pindell et al.*, 2014]. In the southern Gulf of Mexico, the smaller size of the Isthmian salt basin indicates an asymmetric distribution of salt, possibly owing to thicker transitional crust with less syn-rift subsidence along the Yucatán margin [*Galloway*, 2008].

Allochthonous salt in the present-day northern Gulf of Mexico has undergone significant mobilization since its initial deposition. By the end of the Cretaceous, most landward autochthonous salt was expelled seaward beneath the paleo-continental slope by thick accumulation of denser terrestrial sediment, leaving behind extensive salt welds and a thin layer of remnant autochthonous salt [*Galloway*, 2008; *Hudec et al.*, 2013b]. With the onset of climate cooling in the Oligocene, pulses of clastic sediment from the interior of North America arrived in the Gulf basin, causing progradation of the continental margin [*Galloway et al.*, 2011] that led to evacuation of allochthonous salt

stocks and remobilization of salt into large canopy complexes [*Galloway*, 2008; *Hudec et al.*, 2013; 2013b]. Continued sedimentation in the Miocene-Pliocene loaded salt canopies with down-dropping sediment minibasins, triggering the development of abundant salt diapirs and causing extrusion of a salt sheet at the toe of the present-day continental slope (*e.g.*, the Sigsbee escarpment) [*Galloway*, 2008].

4.3 Data and Methods

4.3.1 GUMBO Project

I helped collect four wide-angle, long-offset marine seismic refraction profiles in U.S. Gulf of Mexico waters during the 2010 Gulf of Mexico Basin Opening project (Figure 4.1). These wide-angle seismic data aim to image the seismic velocity structure of the crust and complement multi-channel seismic reflection (MCS) data already collected along similar regional transects (Figure 4.2). The goal of the GUMBO project is to ultimately compare different parts of the Gulf of Mexico rifted margin from shelf to deep basin, with profiles in the western (GUMBO Line 1), north-central (GUMBO Line 2; this study), northeastern (GUMBO Line 3; *Eddy et al.*, 2014), and eastern Gulf of Mexico (GUMBO Line 4; *Christeson et al.*, 2014). Additionally, the GUMBO transects are designed to coincide with the location of four high-quality multi-channel seismic (MCS) profiles collected by industry. In the eastern Gulf of Mexico, GUMBO Lines 3 and 4 are interpreted as volcanic rifted margins with magmatically intruded and/or underplated crust across ~150-200 km wide transition zones between stretched continental crust and normal oceanic crust [*Christeson et al.*, 2014; *Eddy et al.*, 2014]. In

the western Gulf of Mexico, GUMBO Line 1 seismic velocities suggest a more magma-poor rift setting with possible regions of exhumed, serpentinized mantle.

The 396-km-long N-S GUMBO Line 2 transect extends from a northern end point at ~50 km offshore the western Louisiana coastline to the deep-water central Gulf of Mexico basin. The seismic line crosses the Louisiana shelf, salt/minibasin provinces of the Garden Banks and Keathley Canon protraction areas, and the Sigsbee escarpment. Towed behind the R/V *Iron Cat* at 9-10 m water depth, three arrays of 12 air-guns provided an average source capacity of 77.4 L. NCS SubSea monitored source navigation and ensured ~150 m shot spacing by initiating a trigger to the R/V *Iron Cat* gun controller. A Novatel GPS receiver determined the exact time of each shot. Thirty-eight short-period ocean bottom seismometers (OBSs) provided by Geopro and the University of Texas Institute for Geophysics (UTIG) were deployed at 10 km instrument spacing along GUMBO Line 2, of which 34 were recovered with useful data. Each OBS recorded data on four channels (i.e., two horizontal, one vertical, and one hydrophone channel). Ten instruments were positioned on the shallow Louisiana shelf (OBS 201-212), 20 in the salt/minibasin province (OBS 213-234), and 4 in the deep basin seaward of the Sigsbee escarpment (OBS 235-238). Hydrophones provided the highest-quality receiver gathers from instruments on the Louisiana shelf, whereas the vertical channel was preferred for interpreting arrivals from instruments in the salt/minibasin province and seaward of the Sigsbee escarpment.

4.3.2 GUMBO Line 2 Seismic Refraction Data

I briefly describe the characteristics of seismic refraction data from receiver gathers of instruments on the shallow Louisiana shelf (<0.25 km deep), salt/minibasin province (0.25-2.4 km deep), and deep water Gulf of Mexico seaward of the Sigsbee escarpment (2.4-3.1 km deep). By comparing the wide-angle OBS records, I recognize three distinct refraction phases (P1, P2, and P3; Figures 4.3-4.6) and two wide-angle seismic reflections (R1 and R2) based on apparent velocities and source-receiver offsets. Since I use all these phases later in the tomographic inversion, I make a total of 15,517 picks with the distribution of phases shown in Table 4.1. All phases are observed in a 5 to 15 Hz frequency range. Compared to seismic refraction data in the eastern Gulf of Mexico, where salt and sediments are relatively thin [*Christeson et al.*, 2014; *Eddy et al.*, 2014] and source-receiver offsets can exceed 150 km, the OBS data along GUMBO Line 2 are generally of lower quality with lower signal-to-noise ratios and much smaller maximum offsets of clear arrivals to 60-100 km, particularly in the salt/minibasin province (Figures 4.3-4.6). Vertical-component geophones and hydrophones equally provide high-quality data from instruments on the Louisiana shelf (Figures 4.3, 4.4), whereas in the salt/minibasin province and seaward of the Sigsbee escarpment, only the vertical-component geophones produce data of good quality (Figures 4.5, 4.6).

I observe the first-arriving seismic refraction phase P1 in both landward and seaward directions on gathers from all 34 instruments (Figure C1). At all water depths, the P1 arrival can be distinguished from the direct wave in water at 5-10 km source-receiver offsets. Instruments on the Louisiana shelf record P1 arrivals up to ~40 km (Figure 4.3), while those in the salt/minibasin province and seaward of the Sigsbee

escarpment record P1 to smaller maximum offsets of 20-30 km (Figures 4.4-4.6). The apparent velocity of most P1 arrivals are remarkably consistent across all water depths and increase gradually with offset from ~2.2 to 3.5 km/s, with apparent velocities approaching 4.0 km/s at maximum offset. However, the presence of shallow salt diapirs with high seismic velocity (Figure 4.7) causes P1 arrivals to often increase abruptly in apparent velocity to >6.0 km/s (Figures 4.4, 4.5). I assign 25-125 ms uncertainties to P1 arrivals with an average of 61 ms, the lowest of any phase in the dataset (Table 4.1).

All but one instrument on GUMBO Line 2 (OBS 218) record the second-arriving phase P2, which is typically observed in x-t space 0.5-1.0 s after the last P1 arrival (Figures 4.3-4.5, A2). Only instruments seaward of the Sigsbee escarpment show a distinct change in apparent velocity from P1 to P2 (Figure 4.6). Instruments on the Louisiana shelf and in the salt/minibasin province record P2 arrivals with relatively consistent apparent velocities of 4.5-6.0 km/s. At these depths, OBSs record P2 arrivals at minimum and maximum offsets of 30 and 60 km, respectively. Instruments seaward of the Sigsbee escarpment show P2 arrivals with faster apparent velocities (5.5-7.0 km/s) at closer offsets (20-40 km; Figure 4.6). I assign an average uncertainty of 133 ms to P2 arrivals, which range from 50-225 ms depending on the quality of the data with offset and the continuity and amplitude of the arrival.

The third-arriving phase P3 is the most difficult refraction arrival to distinguish and, since it is observed at the largest offsets with low signal-to-noise ratios, I am often unable to pick P3 in both landward and seaward directions from the same receiver gather (Figures 4.4, 4.5). Nevertheless, I confidently pick P3 on 25 of the 34 GUMBO Line 2

receiver gathers (Figure C3), although I assign the largest average uncertainties of any phase to P3 (203 ms, Table 4.1). Consistent P3 apparent velocities are found at all water depths and range from 7.6 to 9.0 km/s, with most arrivals having an apparent velocity of ~8.2 km/s. Arrivals of P3 from instruments on the Louisiana shelf have minimum and maximum offsets of 50 km and 90 km, respectively (Figure 4.3). Some OBSs in the salt/minibasin province record a slightly larger maximum offset for P3 arrivals (>100 km), although most display an offset range similar to Louisiana shelf instruments (Figures 4.4, 4.5). Instruments seaward of the Sigsbee escarpment have much closer minimum P3 arrivals (<40 km, Figure 4.6).

I also recognize wide-angle seismic reflections R1 and R2 in the GUMBO Line 2 receiver gathers. These phases appear to have a retrograde travel-time branch in x-t space behind the crossover point of refraction arrivals (Figure 4.6). Only 17 OBSs record the seismic reflection R1, which is visible behind the P1/P2 crossover in x-t space at 15-30 km offsets with apparent velocities of 5.5-6.0 km/s (Figures 4.4, 4.6). Reflection R1 is recorded by most instruments on the Louisiana shelf and seaward of the Sigsbee escarpment, but I only pick this arrival sporadically on OBSs records from the salt/minibasin province, where it must be distinguished from refractions turning in deep salt bodies (Figures 4.5, A4). Reflection R2 is a high-amplitude arrival (Figure 4.6) observed on 30 receiver gathers, often in both landward and seaward directions (Figures 3, 4, A5). I observe R2 behind the P2/P3 crossover with apparent velocities of 6.0-8.5 km/s and at offsets between 35 – 65 km. Reflections R1 and R2 are assigned average uncertainties of 112 ms and 123 ms, respectively (Table 4.1).

Crosschecking reciprocal arrivals adjusted for water depth from nearby receivers is an important step in ensuring the accuracy of travel-time picks (Figure C6), particularly given the relatively low data quality on GUMBO Line 2. Reciprocal checks allow the differentiation of primary refraction arrivals (*e.g.,* P2, P3) from high-amplitude secondary reflections (*e.g.,* R2) for instruments with poorer quality data. Additionally, in the phase interpretations I re-picked reciprocal source-receiver pairs that had travel-times with misfits greater than 250 ms.

4.3.3 Tomographic Inversion

Our observation of several seismic reflections (R1, R2) and refractions (P1, P2, and P3) in the OBS data from GUMBO Line 2 allows us, in principle, to solve for a seismic velocity model that consists of three layers. However, before I attempt to derive a three-layer model, I use all first-arriving phases to construct a preliminary, single-layer model. This inversion of first-arriving phases does not depend on the interpretation of different wide-angle phases; the resulting smooth seismic velocity model therefore does not have a user bias. I construct the single-layer seismic velocity model using 16,554 travel-time picks from all 34 OBSs (Figure C7). To build the preliminary velocity model, I invert the travel times of the first-arriving phase using a stepwise, iterative least-squares inversion using a simple starting model with a smoothly increasing velocity gradient of ~1 km/s per 5 km depth [*Van Avendonk et al.*, 2004, and references therein]. I then calculate ray paths at iterations of the velocity model using shortest path and ray-bending methods [*Moser*, 1991; *Moser et al.*, 1992; *Van Avendonk et al.*, 2001], allowing us to compare the picked and calculated travel times of the first-arriving phase. I apply

smoothness constraints in each linear inversion step to obtain the smoothest seismic velocity model possible while still maintaining a good data fit in comparison to the assigned uncertainties. After 16 iterations the resulting preliminary seismic velocity model reaches a chi-squared value of 3.0 and an RMS misfit of 203 ms, but does not continue to improve substantially after successive iterations. Although this first estimate of seismic velocity structure does not define the top of basement or Moho, if the ray paths of first arrivals sufficiently sample the GUMBO 2 model space, I can use the resulting velocity structure as an appropriate starting point for a layered seismic velocity model, as well as for making basic interpretations of the lithology along GUMBO Line 2 [*Zelt et al.*, 2003; *Van Avendonk et al.*, 2004].

The preliminary, single-layer seismic velocity model serves as a starting point for a layered model that utilizes all wide-angle refraction (P1-P3) and reflection phases (R1-R2). The layered velocity model assigns the first-arriving phase P1 as refractions turning in the sediment (*Psed*), whereas phase P2 and P3 represent crustal (*Pg*) and mantle refractions (*Pn*), respectively. Wide-angle reflections R1 and R2 are modeled as compressional waves that reflect off the top of the basement (*PbP*) and Moho (*PmP*), respectively. I simultaneously constrain both seismic velocities and layer boundaries following the joint inversion method of *Van Avendonk et al.* [2004], in which first-order velocity discontinuities are present at boundary interfaces. After 24 iterations between raytracing and linear inversion, similar to the methods described above for derivation of the preliminary seismic velocity model, I obtain a compressional seismic velocity model with a chi-squared value of 1.5 and an RMS travel-time misfit of 130 ms (Figure 4.8).

Misfits of picked and calculated travel times for the final model are shown for OBSs 204, 213, 226, and 237 (Figures 4.9-4.12), as are the locations of seismic sources and ray paths. Calculated root mean-squared misfits (RMS), the average time in ms between picked and calculated travel time curves, are similar to the uncertainties I assign to the seismic refraction and reflection phases (Table 4.1). Assigned uncertainties are larger than RMS misfits for phases that are the most difficult to pick (*e.g.*, *PmP*, *Pn*). The assigned uncertainties are smaller than the RMS misfit for *Psed* (P1) arrivals, although I am confident in my interpretation of the clear sediment arrivals (Figures 4.3-4.6). This discrepancy may arise from the inability of the inversion method to accurately resolve seismic velocity heterogeneities associated with shallow salt diapirs (Figures 4.7, 4.11). The largest misfits (>100 ms) are associated with wide-angle refraction *Pn* and reflections *PbP* and *PmP*, phases that are also assigned the largest uncertainties.

4.3.4 Resolution Test

The least-squares inversion method allows for examination of the spatial resolution of the seismic velocities and layer boundaries in the GUMBO Line 2 model. In order to test the resolution, a matrix is constructed for the least-squares inversion that produces the final GUMBO Line 2 seismic velocity model [*Menke*, 1984; *Van Avendonk et al.*, 2004] (Figure 4.13). If N is the number of model parameters, the N x N resolution matrix maps the ideal 'true Earth' model onto the GUMBO Line 2 seismic velocity model. Therefore, the resolution matrix approaches the identity matrix if the seismic velocity structure is very well resolved. Off-diagonal elements of the resolution matrix larger than 0 show the blurring that is caused by averaging of the seismic velocity in

areas where the model is not fully constrained by the data. This averaging is most prominent in parts of the model that are not adequately sampled by ray paths, which is especially important to consider for the deepest regions of the GUMBO Line 2 model space (Figures A3, A5). I examine how hypothetical model features of a fixed size are resolved in different parts of the GUMBO Line 2 model. Ellipses are defined that are 8 km tall x 3 km wide and 16 km x 6 km, and pass them through the model space during the tomographic inversion [*Van Avendonk et al.*, 2004]. If the resulting tomographic image generated by the inversion method matches the original ellipse perfectly, the local resolution is 1.0; conversely, if the ellipse does not match the seismic velocity image mapped by the resolution test, resolution is 0.

I find excellent spatial resolution of the GUMBO Line 2 seismic velocity model at the 16x6 km scale and good resolution at the 8x3 km scale (Figure 4.13). Resolution in the sediment layer is high (>0.8) at the 16x6 km scale for the entire length of the transect. Except for the landward edge of model space, basement resolution is also quite high (0.4-1.0) and averages ~0.7. Resolution of the mantle is lower (~0.1-0.7), but still shows an adequate average resolution of ~0.5. Both the top of basement and Moho boundaries are well-resolved at the 16x6 km scale (0.8-1.0), with small zones of lower resolution (0.2-0.4) for the top of basement from 270-320 km, a region of GUMBO Line 2 with an abundance of shallow salt diapirs (Figure 4.7). At the 8x3 km scale, I find an overall lower resolution for the seismic velocity structure at depth (Figure 4.13), suggesting that smaller-scale velocity perturbations along GUMBO Line 2 may not be interpreted in the deeper parts the seismic velocity model with much confidence. Resolution in the

sediment column is still excellent (0.4-1.0), but average basement and mantle resolution values are low (~0.3). The top of basement boundary at the 8x3 km scale shows resolution varying from 0.1 to 1.0. The resolution of the Moho is more consistent with a good average resolution of ~0.6.

4.4. Results

4.4.1 GUMBO Line 2 Seismic Velocity Model

I describe the model of the seismic velocity model of GUMBO Line 2 in detail (Figure 4.8) such that it may be compared to the eastern Gulf of Mexico and other rifted margins. Model distances are measured from a starting point at the first air-gun shot point, ~50 km south of the coast of southwestern Louisiana. For discussion, I divide the 396 km-long seismic velocity model into three sections of GUMBO Line 2, including the Louisiana shelf (0-140 km), the salt/minibasin province (140-340 km), and the deep-water basin near the Sigsbee escarpment (340-396 km).

The shallow Louisiana shelf deepens from 12 m at the landward end of GUMBO Line 2 to 180 m at 140 km model distance. Beneath the shelf, sediment thickness increases slightly from 15.3 km near the landward end of the model to 16.2 km at 140 km. Here, seismic velocities increase from <2.0 km/s at the seafloor to 5.1 km/s at the base of the sediment cover. Seismic velocity anomalies, ~10 km-wide regions where the wave speed is up to 1.5 km/s higher than in the surrounding area, are observed in the uppermost 5 km of sediment at 95 km and 140 km model distance. Crustal thickness beneath the Louisiana shelf is fairly constant (~10 km), but thins by 0.5 km from the landward end of GUMBO Line 2 to 140 km model distance. Seismic velocities in the

crust increase gradually with depth from 5.4 km/s at the top of basement to 7.0 km/s at its base. A zone of steeper seismic velocity gradients is recovered at the seaward end of the Louisiana shelf. Here, seismic velocities increase more rapidly with depth, reaching > 7.0 km/s near the base of the crust. Turning ray paths sample the mantle with seismic velocities of 8.1-8.3 km/s beneath the Louisiana shelf to depths of ~2 km beneath the Moho.

The seafloor in the salt/minibasin province (140-340 km model distance) deepens from ~200 m to 2.0 km (Figure 4.8). Here, massive salt bodies disrupt the clastic strata and create heterogeneities in the seismic velocity structure. Isolated, elliptical regions at 2-10 km depth and 10-15 km in diameter show seismic velocities increasing to 3.5-4.0 km/s, often a full 1.0 km/s faster than the surrounding sediment velocities (Figure 4.8). The vertical seismic velocity gradient in the salt/minibasin province is otherwise similar to the Louisiana shelf in that it increases from ~1.6 km/s at the seafloor to >4.5 km/s above the top of basement. However, lowermost sediments in the salt/minibasin province exhibit heterogeneous seismic velocities that alternate between zones of lower (4.7-4.9 km/s) and higher (5.0-5.3 km/s) seismic velocities. Crustal thickness in the salt/minibasin province fluctuates between 8.9 km at 140 km model distance and 11.5 km at 270 km; from 270 km to 340 km model distance, the basement thins to a minimum thickness of 6.1 km directly landward of the Sigsbee escarpment (Figure 4.8). Crustal seismic velocities increase gradually from 5.3-6.0 km/s at the top of basement to 6.8-7.0 km/s above the Moho. The Moho boundary steps up from a depth of ~26 km at 140 km model distance to ~20 km deep at 340 km model distance near the Sigsbee escarpment. Between

170 km and 220 km model distance the tomographic inversion obtained the lowest mantle velocities (7.6-7.7 km/s) in the GUMBO Line 2 seismic transect. Imaged mantle velocities are higher elsewhere in the salt/minibasin province (8.0-8.6 km/s) and sampled to a depth of ~2 km beneath the Moho.

At the Sigsbee escarpment, a ~1 km drop in the seafloor deepens the Gulf of Mexico basin to ~3 km depth. Seismic refraction data show the sediment cover here is devoid of allochthonous salt bodies (Figure 4.7) and thinner (~11 km) than anywhere else along GUMBO Line 2. Sediment seismic velocities are also slightly lower than elsewhere in the model and increase from ~1.6 km/s at the seafloor to 4.2 km/s near the top of basement (Figure 4.8). Average crustal thickness increases slightly from ~6.4 km at 340 km model space to ~7.5 km at 360 km model distance. Beneath the Sigsbee escarpment, the top of basement displays a pronounced step-up or ramp of ~2 km in height across a distance of ~30 km. In the seaward portion of the GUMBO Line 2 model, crustal seismic velocities increase from between 5.4-6.2 km/s near the top of basement to >7.2 km/s above the Moho. Mantle velocities (8.2-8.5 km/s) are similar to those beneath the Louisiana shelf and parts of the salt/minibasin province.

4.4.2 Seismic Reflection Data

The GUMBO marine seismic refraction project was designed to benefit from the existence of many regional marine seismic reflection lines in the Gulf of Mexico that have been acquired by geophysical companies. The joint interpretation of marine seismic reflection and refraction data has greatly advanced the understanding of rifted margins worldwide, since these data sets complement each other [e.g., *Morgan et al.*, 1989; *Dean*

et al., 2000; *Korenaga et al*., 2000; *Blaich et al.*, 2011; *Lester et al*., 2014]. GUMBO Line 2 lies approximately in the same location as the GXT GulfSPAN Line 2000 (Figure 4.2). The GulfSPAN Line 2000 MCS profile was collected with a 9-km-long streamer and processed in time to 16 seconds, from which a reverse-time migration image was produced (Figure 4.7). Existing interpretations from ION/GXT are plotted in pink [*Radovich et al*., 2011] to show the widespread extent of salt structures in the north-central Gulf of Mexico. The structure of the sediments and mobilized salt deposits can be clearly seen in the MCS image, whereas they are mostly outside the resolution of the wide-angle refraction data. However, the locations of several allochthonous salt diapirs imaged by GXT GulfSPAN Line 2000 (Figure 4.7) closely correspond to seismic velocity anomalies in the sediment layer of the GUMBO Line 2 model (Figure 4.8). The base of the autochthonous Louann Salt, or the 'Louann detachment surface' sensu *Radovich et al.* [2007], is picked as a near-continuous horizon tangential to the lower limit of reflectivity of sedimentary features. This horizon deepens from ~13 km at the Louisiana shelf (0-100 km model distance) to 17 km in the salt/minibasin province (150-250 km), and steps back up to ~13 km depth beneath and seaward of the Sigsbee escarpment (300-396 km).

According to the MCS data and interpretation (Figure 4.7), most of the salt from the northern Gulf of Mexico margin has moved to a more seaward position from an original autochthonous position near the top of basement [*Hudec et al*., 2013]. This remobilization took place during the late Mesozoic and Cenozoic loading of thick sediments [*Galloway*, 2008]. Accordingly, salt is noticeably less abundant offshore

beneath the Louisiana shelf (0-100 km model distance), where sediment progradation has forced the seaward flow of allochthonous salt, leaving behind welds where salt is completely evacuated. In the salt/minibasin province, sediment loading has deformed the originally 2-4 km-thick autochthonous 'mother' salt stock [*Hudec et al.*, 2013] into massive salt sheets and >6-km-tall diapirs. Minibasins drop down into regions of salt evacuation, forming >10-km-thick sediment deposits. South of the Sigsbee escarpment, salt is absent or outside the resolution of MCS imaging.

The thick salt and sediments in the north-central Gulf of Mexico strongly attenuate MCS source energy such that few coherent reflections are found below the base of autochthonous salt (Figure 4.7). However, sporadic reflectivity at 15 km depth is observed beneath sediment minibasins at 180 km, 215 km, and 260 km model distance along GXT GulfSPAN Line 2000. Deep, interspersed reflectivity landward of the Sigsbee escarpment from 310-350 km model distance likely represent multiples of shallower reflections from sediment minibasins [*Radovich et al*., 2011]. Seaward of the Sigsbee escarpment, the basement is observed as a coherent reflection at ~13 km depth. Possible Moho reflections can be seen at 155 km and 195 km model distance at ~23 km depth, but such deep reflectivity is absent elsewhere along GXT GulfSPAN Line 2000.

4.5.Discussion

4.5.1 Kinematic Models

Accurately reconstructing the movement of the Yucatán block during the Jurassic – Early Cretaceous is an important step in understanding the distribution of crustal types in the northern U.S. Gulf region. Competing hypotheses for movement of the Yucatán

block from the southern margin Laurentia during the opening of the Gulf basin have been proposed: (1) a single-stage, southwestern counter-clockwise rotation leading to both continental extension and seafloor spreading [*Pindell*, 1985; *Dunbar and Sawyer*, 1987; *Hall and Najmuddin*, 1994; *Schouten and Klitgord*, 1994; *Bird et al*., 2005; *Stern et al.*, 2010]; and (2) multi-stage models of rotation with an initial southeastern movement of the Yucatán block leading to continental extension, followed by southwestern counterclockwise rotation and seafloor spreading (Figure 4.14) [*Marton and Buffler*, 1994; *Imbert and Philippe*, 2005; *Godínez-Urban et al.*, 2011; *Hudec et al*., 2013]. These kinematic models agree that slow (<20 mm/yr) movement of the Yucatán block took place from the Late Triassic – Middle Jurassic, which thinned the ~40-km-thick continental crust south of the Ouachita orogen near the Sabine uplift and other basement highs [*Huerta and Harry*, 2012]. The boundary between thick and thin crust is interpreted near central Louisiana [*Sawyer et al.*, 1991; *Galloway*, 2008], with a broad zone of transitional crust thinning southward from ~18 km to 10 km beneath the Louisiana shelf and salt/minibasin province in the north-central Gulf of Mexico [*Hales et al.*, 1970; *Ibrahim & Uchupi*, 1981; *Ebeniro et al.*, 1988]. A wide, fan-shaped wedge of ocean crust in the western Gulf of Mexico narrows to the east, its shape the result of Late Jurassic – Early Cretaceous counterclockwise rotation of the Yucatán block (Figure 4.14). However, the landward limit of oceanic crust (LOC) is unclear, with estimates ranging widely from 150 km to 400 km offshore present-day Louisiana (Figure 4.2) [*Sawyer et al.*, 1991; *Marton and Buffler*, 1994; *Bird et al.*, 2005, and references therein]. I interpret the LOC near the Sigsbee escarpment at ~320-350 km GUMBO Line 2 model distance as

crust thins here to ~7 km, mean seismic velocities increase to ~6.7 km/s, and a landward-dipping basement ramp is shown in both MCS and refraction data (Figures 4.7, 4.8).

4.5.2 Crust Beneath Louisiana Shelf and Salt/Minibasin Province

Several workers suggest that thinned crystalline continental crust extends seaward offshore Louisiana to a LOC near the Sigsbee escarpment [*Buffler and Sawyer*, 1985; *Dunbar and Sawyer*, 1985; 1987; *Ebeniro et al.*, 1988; *Sawyer et al.*, 1991; *Marton and Buffler*, 1994; *Roberts et al*., 2005]. Conversely, others have proposed that the thin crust here may be transitional in nature and thus comprise a combination of hyperextended continental crust, exhumed mantle, and incipient oceanic crust [*Imbert and Philippe*, 2005; *Pindell and Kennan*, 2007; 2009; *Mickus et al.*, 2009; *Kneller and Johnson*, 2011; *Rowan*, 2014]. Finally, another possibility is that oceanic crust floors much of the north-central Gulf of Mexico, with the LOC near the Texas-Louisiana coast [*e.g.*, *Schouten and Klitgord*, 1994; *Stern and Dickinson*, 2010].

4.5.2.1. Velocity – Depth Comparisons

In order to determine the nature of crust beneath the Louisiana shelf and salt/minibasin province, I compare GUMBO Line 2 velocity-depth profiles to those from several rifted margins in end-member tectonic settings. Seismic velocities are averaged along three sections of GUMBO Line 2 (35-70 km, brown line; 100-150 km, red line; and 180-270 km, blue line) and plotted against depth below top of basement (Figures 4.8, 4.15). The crust here is clearly thinner and higher in seismic velocity than normal continental crust. However, GUMBO Line 2 crustal velocities are slightly lower than upper crustal seismic velocities of 6.6-6.9 km/s recovered on-shore in eastern Texas

[*Hales et al.,* 1970]. Seismic velocities from this section of GUMBO Line 2 plot within the lower bounds of slow-spreading Atlantic oceanic crust, but are incompatible with faster-spreading Pacific ocean crust with higher velocities (Figure 4.15) [*White et al*., 1992]. Furthermore, the crust beneath the Louisiana shelf and salt/minibasin province at GUMBO Line 2 is 2-4 km thicker than both Atlantic and Pacific Ocean oceanic crust.

Neither a composition of unaltered continental crust nor normal oceanic crust is compatible with the seismic velocity structure of crust in the north-central Gulf of Mexico, which I interpret as transitional in nature. I further constrain the composition of GUMBO Line 2 transitional crust by comparing velocity-depth profiles to a variety of rifted margins. Recently, several authors have put forward the possibility of exhumed mantle in the northern Gulf of Mexico, with estimates of ~40 to 400 km of exhumed mantle and thin, embryonic ocean crust beneath the salt/minibasin province [*Kneller et al.*, 2012; *Hudec et al*., 2013; *Rowan*, 2014]. I test this hypothesis by comparing GUMBO Line 2 to the magma-starved conjugate Newfoundland and Iberian margins (Figure 4.15). At the Newfoundland margin the uppermost 5 km of lithosphere in the transition zone comprises hyperextended lower continental crust, exhumed and partially serpentinized mantle, and small basalt bodies characteristic of embryonic ocean crust [*Van Avendonk et al.*, 2006; *Lau et al.*, 2006a; *Jagoutz et al.*, 2007; *Eddy et al.*, 2013]. Continental crust thins more abruptly at the conjugate Southern Iberian Abyssal Plain, giving way to broad, ~200 km-wide expanses of exhumed, highly serpentinized mantle peridotites in the transition zone [*Dean et al.*, 2001; *Sibuet et al.*, 2007; *Reston*, 2009]. Serpentinization of shallow mantle peridotites could provide an alternate explanation for the high

compressional velocities I observe at GUMBO Line 2 [*Christensen*, 2004], as well as the weak magnetic signal in the north-central Gulf of Mexico (Figure 4.2). However, mantle exhumation at rifted margins is often characterized by a weak or absent Moho [*Van Avendonk et al.*, 2006] and is incompatible with observation of abundant *PmP* reflections (Figures 4.3-4.6, A5). Furthermore seismic velocities in GUMBO Line 2 transitional crust conflict with those of exhumed mantle at the Iberian margin at depths >2 km (Figure 4.15). GUMBO Line 2 transitional crust matches reasonably well with the Newfoundland margin at depths <5 km, although the two margins are incompatible at deeper crustal levels.

High-velocity crust in the north-central Gulf of Mexico is thicker than normal oceanic crust and may be similar to thick igneous/ocean crust at volcanic rifted margins (*e.g.*, Hatton Bank offshore Ireland, southeast Greenland margin, Vøring Plateau offshore Norway) [*Morgan et al*., 1989; *Korenaga et al*., 2000; *Mjelde et al*., 2005]. At volcanic margins, an increased melt supply from active upwelling of the asthenosphere and/or high mantle potential temperatures leads to thicker than normal oceanic crust near the LOC [*Holbrook and Keleman*, 1993; *Korenaga et al*., 2000; *Menzies et al*., 2002]. I compare GUMBO Line 2 transitional crust velocity-depth profiles to the Vøring Plateau offshore Norway, where thick igneous/ocean crust shows high seismic velocities of 6.2 to 7.4 km/s (Figure 4.15) [*Mjelde et al*., 2005]. Volcanic rifted margins show higher crustal seismic velocities and 2-5 km thicker crust than that observed at GUMBO Line 2. At many volcanic margins, the igneous crust thins rapidly seaward from ~25 km to 10 km across a 50-150 km wide zone [*White and McKenzie*, 1989; *Geoffroy*, 2005; *Franke*,

2013], whereas on GUMBO Line 2 I find transitional crust with a near-constant thickness of ~10 km over a width of 300 km (Figure 4.8). Thicker igneous crust could lie landward of GUMBO Line 2 beneath Louisiana, though the weaker magnetic anomalies along the Louisiana coastline may indicate the absence of a volcanic margin there in comparison to potentially volcanic margin beneath Texas coastline [*Mickus et al.*, 2009].

Velocity-depth profiles of altered continental crust at volcanic rifted margins provide an important comparison to transitional crust in the north-central Gulf of Mexico since magmatism is interpreted to affect continental crust in both the eastern and western Gulf regions [*McBride et al.*, 1987; *McBride*, 1991; *Heatherington and Mueller*, 1999; *Imbert*, 2005; *Mickus et al.*, 2009; *Dickinson et al.*, 2010; *Stern et al.*, 2011; *Christeson et al.*, 2014; *Eddy et al.*, 2014]. GUMBO Line 2 crust is shown to be markedly consistent with rifted crust in the northeastern South China Sea, where initially magma-poor, thinned continental basement is interpreted to have experienced post-rift magmatic intrusions and underplating of a high velocity lower crustal layer [*Wang et al.*, 2006; *Franke et al.*, 2011; *Lester et al.*, 2014]. Considerable agreement is also shown between GUMBO Line 2 crust and continental crust at the margin of the Vøring Plateau, where an extensive melt supply throughout rifting and seafloor spreading produced magmatically-intruded continental crust adjacent to abnormally thick (>15 km) oceanic basement [*Mjelde et al.*, 2005].

4.5.2.2 Magmatism

Velocity-depth profile comparisons indicate that the thin transitional crust beneath the Louisiana shelf and salt/minibasin province may be composed of stretched and

thinned continental crust with syn- or post-rift magmatic additions. Magnetic and potential gravity data signify a possible volcanic rift margin near the Texas coast, a decrease in magnetic anomaly strength to the east is interpreted as a reduction in syn-rift magmatism beneath southern Louisiana [*Mickus et al.*, 2009; *Stern and Dickinson*, 2010]. Southeastern movement of the Yucatan block during the Late Triassic – Early Jurassic was likely slow (<20 mm/yr), leading *Kneller et al.* [2012] to suggest serpentinized mantle with pockets of thin oceanic crust in the north-central Gulf [*Kneller et al.*, 2012]. Velocity-depth comparisons of GUMBO Line 2 instead support the presence of thinned and possibly modified continental crust beneath the Louisiana shelf and salt/minibasin province (Figures 4.8, 4.14). Furthermore, the pronounced asymmetry between the conjugate U.S. Gulf coast and Yucatán margins could support the notion that simple-shear detachment faulting led to highly extended continental crust along most of GUMBO Line 2 [*Marton and Buffler*, 1993; *Reston*, 2009].

How and when did magmatism impact crust in the north-central Gulf of Mexico? The onset of seafloor spreading was likely a Gulf-wide event ~158-154 Ma as southeastern movement of the Yucatán block changed to counterclockwise rotation about a pole the southeastern Gulf of Mexico (Figure 4.14) [*Kneller et al.*, 2012; *Hudec et al.*, 2013]. Southern Louisiana xenoliths exhumed by salt diapirs are dated to ~158 Ma and found >300 km from the LOC (Figure 4.2). These alkaline xenoliths show isotopic signatures of low-temperature melting of a depleted mantle [*Stern et al*., 2011], unlike the tholeiitic isotopic signatures of mantle beneath oceanic basement [*Engel et al.*, 1965; *McKenzie and Bickle*, 1988]. I suggest that the Middle Jurassic shift in Yucatán block

movement associated with the ~158 Ma onset of seafloor spreading also resulted in a pulse of decompression mantle melting in the north-central Gulf of Mexico (Figure 4.14). Mantle upwelling during the second phase of drift between Laurentia and the Yucatán block not only spurred the onset of normal seafloor spreading in the central Gulf basin, but may also have led to the off-axis, low-temperature magmatism that has been documented in southern Louisiana [*Stern et al.*, 2011]. I suggest that such post-rift mantle melts were likely also abundant offshore Louisiana, leading to igneous underplating and infiltration of the rifted margin crust beneath the Louisiana shelf and crust in the salt/minibasin province (Figure 4.16).

Alternatively, magmatic underplating and infiltration may have also modified normal ocean crust along GUMBO Line 2 in the north-central Gulf of Mexico (Figure 4.16). In this scenario, all of the basement along GUMBO Line 2 is oceanic in nature. If this hypothesis were upheld, the extinct mid-ocean ridge in the central Gulf produced much more oceanic crust to the north than to the south, so one or more jumps of the mid-ocean ridge system, perhaps in concert with asymmetric ocean ridge accretion [*Hopper et al.*, 2003], must have occurred during the opening of the basin [*e.g.*, *Bird et al.*, 2007, *Kneller et al.*, 2012]. Magmatic additions to normal ocean basement could coincide with the onset of Gulf-wide seafloor spreading ~158 Ma in the central basin as Yucatán block movement shifted from southeastern to counterclockwise rotation. However, it is noted that the tholeiitic isotopic signature of mantle beneath oceanic basement is inconsistent with the alkaline volcanic xenoliths from southern Louisiana [*Stern et al.*, 2011]. Furthermore, the absence of seafloor spreading magnetic anomalies from the Louisiana

shelf and salt/minibasin province (Figure 4.2) could argue against the presence of normal oceanic basement.

4.5.2.3 Salt Deposition

How does the formation of the Gulf of Mexico affect the widespread deposition of Late Jurassic (Callovian) evaporites? If salt deposition were similar to the Messinian salinity crisis in the Mediterranean Sea or the present-day Death Valley basin [e.g., *Anderson and Schmidt*, 1983], in which a large body of water is isolated from the global oceans, one would expect a pre-Callovian, deep ocean basin (>2.5 km) underlain by normal-spreading oceanic crust in the Gulf of Mexico. However, a single episode of desiccation of a basin the size of the Gulf of Mexico would likely not produce enough salt to explain the volume of evaporite deposits on its present-day margins [*Pindell et al.*, 2014]. Conversely, the early Gulf of Mexico basin may have been a wide, shallow sea. This scenario would be more likely if Callovian salt was deposited on thinned continental crust in the north-central Gulf since rifted margin continental crust can occupy depths above or slightly below sea level, whereas mid-ocean ridges are usually >2 km below sea level. Alternating marine incursions and evaporation in the shallow sea could deposit thick salt layers; isostatic subsidence of the continental crust under the increasing salt load would create more accommodation space. Post-rift magmatism ~158-154 Ma would therefore have not only intruded into continental crust, but also into the overlying salt deposits. Accordingly, *Stern et al.* [2011] suggest that the volcanism responsible for the southern Louisiana xenoliths may have been intruded into a salt body above the top of

basement, explaining the later exhumation of the xenolith during the formation of salt diapirs.

4.5.3 Oceanic Crust

The average velocity-depth profile for the seaward end of GUMBO Line 2 (340-396 km) is consistent with normal oceanic crust (Figure 4.15) [*White et al.*, 1992]. I find no evidence for an extinct spreading ridge in the coincident GXT GulfSPAN Line 2000 MCS image (Figure 4.7), unlike in the eastern Gulf of Mexico [*Christeson et al.*, 2014; *Eddy et al.*, 2014]. Accordingly, *Pindell and Kennan* [2009] identify a linear positive magnetic anomaly in the central Gulf basin that may mark the location of an extinct spreading center ~50 km southeast of GUMBO Line 2.

The oceanic crust that formed in the central Gulf of Mexico has thin to normal thickness (5-6 km) [*Ewing et al.*, 1960; *Ibrahim et al.*, 1981; *Ebeniro et al.*, 1988] and at present its basement surface sits ~1-2 km higher than the adjacent crust of the salt/minibasin province. Stepping up to the south, this prominent basement ramp is observed in both refraction and reflection data and coincides with the interpreted LOC (Figures 4.7, 4.8) [*Marton and Buffler*, 1994; *Galloway*, 2008; *Hudec et al.*, 2013; *Rowan et al.*, 2014]. Autochthonous salt does not lie on oceanic basement in the central Gulf basin, and *Hudec et al.* [2013] interpret the basement ramp as a physical barrier that kept salt in place during seafloor spreading (Figure 4.16). However, if one corrects for the difference in sediment loading in the shelf and minibasin province (~15 km sediment) and the central Gulf of Mexico (~8 km sediment), it appears that the basement in the northern Gulf of Mexico was originally relatively flat over several hundred kilometers,

and therefore I suggest the absence of a pronounced, long-wavelength difference in basement depth during the opening of the Gulf of Mexico. Nonetheless, the basement step over 20-30 km observed in MCS data appears to be real. *Hudec et al*. [2013] suggest that deeper basement landward of the basement ramp implies thinner or denser crust in the salt/minibasin province, compared to thicker oceanic crust seaward of the ramp. Instead, GUMBO Line 2 results show crust is >2 km thicker landward of the basement ramp, and the interpretation of thinned continental crust beneath the salt/minibasin province, despite possible additions of post-rift magmatism, would imply lower density crust [*Rudnick and Fountain,* 1995; *Mjelde et al.*, 2005]. To explain the discrepancy in basement height, I use isostatic calculations to suggest anomalously low-density mantle (e.g., ρ = <3200 kg/m^3 to a compensation depth of 5-10 km beneath Moho) beneath normal-spreading ocean crust at the seaward end of GUMBO Line 2 (Figure 4.17). However, such low mantle velocities are difficult to reconcile with normal mantle seismic velocities (8.0-8.2 km/s) at the seaward end of GUMBO Line 2.

4.6 Conclusions

A new seismic velocity model of the crust beneath the Louisiana Shelf and salt/minibasin province, traditionally considered transitional between thick continental crust and oceanic basement, is interpreted as either thinned and magmatically altered continental crust or oceanic basement. Velocity-depth profiles and strong Moho reflections indicate that interpretations of exhumed mantle or incipient oceanic crust are unlikely for the north-central Gulf of Mexico. Louann Salt deposition from ~165-161 Ma either took place in a restricted ocean basin or was deposited near sea level on continental

crystalline basement that subsided with an increasing evaporite load. High lower crustal velocities support a pulse of magmatism contemporaneous with rifting or shortly after the onset of seafloor spreading across the entire Gulf of Mexico basin, likely resulting in mafic underplating and infiltration of crust at GUMBO Line 2. The fact that alkalic xenoliths exhumed by southern Louisiana salt diapirs are dated to ~158 Ma and preserve an isotopic signature of depleted mantle melting may support off-axis melting close to the start of seafloor spreading. Change in direction of the Yucatán block (~158-154 Ma) from southeastern motion to counterclockwise rotation is likely associated with the onset of seafloor spreading across the entirety of the Gulf of Mexico, and potentially led to ocean ridge migration in the north-central Gulf. The seaward end of GUMBO Line 2 near and seaward of the Sigsbee escarpment is likely oceanic crust. Seafloor spreading emplaced shallower ocean basement that bisected an originally Gulf-wide salt province; low mantle densities beneath the central Gulf ocean ridge are suggested as a possible cause for higher-seated oceanic basement surrounded by a landward-dipping basement ramp.

4.7 Tables

Table 4.1. GUMBO Line 2 pick counts, traveltime fits, and uncertainties

Phase	Number of Picks	RMS Misfit (ms)	Average assigned uncertainty (ms)
Psed (P1)	8829	126	61
PbP (R1)	511	125	112
Pg (P2)	2604	136	133
PmP (R2)	1829	88	123
Pn (P3)	1744	160	203
Total	15517	129	98

4.8 Figures

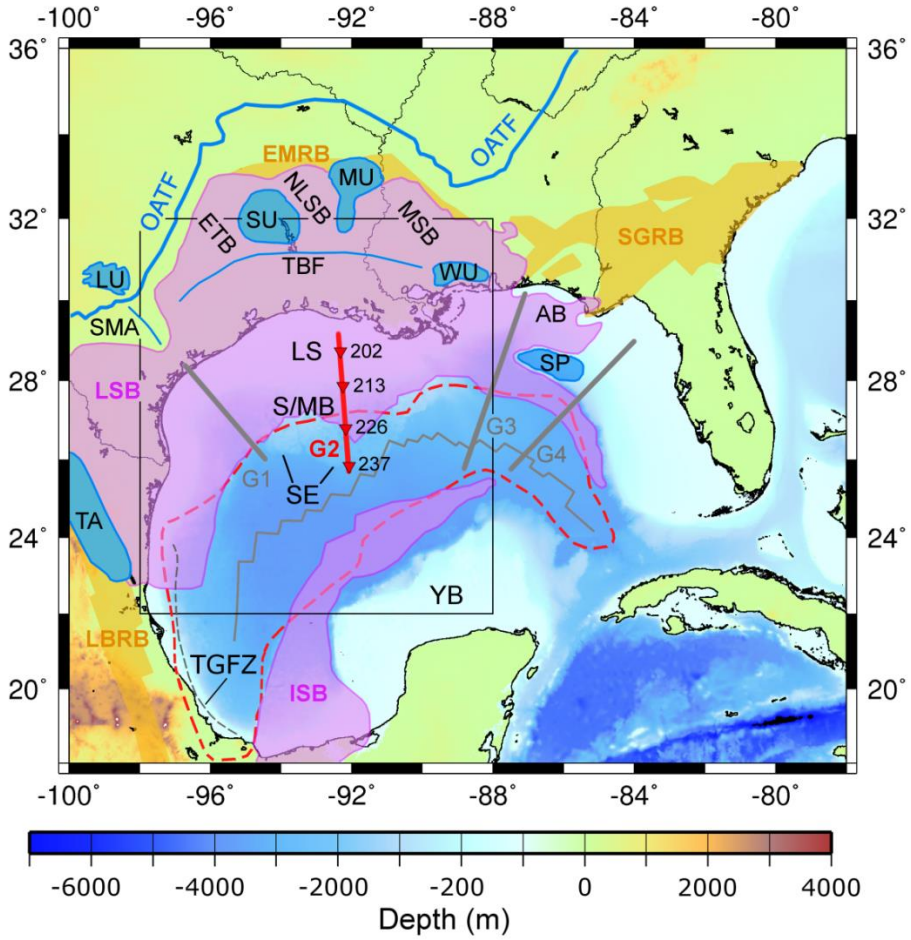

Figure 4.1 – Bathymetric map of the Gulf of Mexico region. Blue shapes denote regions of basement uplift, orange shapes show locations of Mesozoic rifts, and pink shapes are salt provinces. Dashed red line and solid dark grey line indicate ocean-continent transition zone and spreading ridge, respectively, proposed by *Pindell and Kennan* [2009]. Red inverted triangles are locations for GUMBO Line 2 instruments 202, 213, 226, and 237. Box shows Figure 4.2 outline. **AB** – Apalachicola basin; **EMRB** – Eagle Mills rift basins; **ETB** – East Texas salt basin; **G1-G4** – GUMBO transects (grey and red lines); **ISB** – Isthmian salt basin; **LBRB** – La Boca rift basins; **LS** – Louisiana shelf; **LSB** – Louann salt basin; **LU** – Llano uplift; **MSB** – Mississippi salt basin; **MU** – Monroe uplift; **NLSB** – North Louisiana salt basin; **OATF** – Ouachita-Appalachian thrust front (solid blue line) [*Thomas*, 2010]; **SU** – Sabine uplift; **SE** – Sigsbee escarpment; **SGRB** – South Georgia Rift Basin; **SMA** – San Marcos arch; **S/MB** – Salt/minibasin province; **SP** – Southern Platform; **SU** – Suwanee uplift; **TA** – Tamaulipas arch; **TBF** – Toledo Bend flexure; **TGFZ** – Tamaulipas-Golden Lane-Chiapas Fracture Zone [*Bird et al.*, 2005]; **WU** – Wiggins uplift; **YB** – Yucatán block.

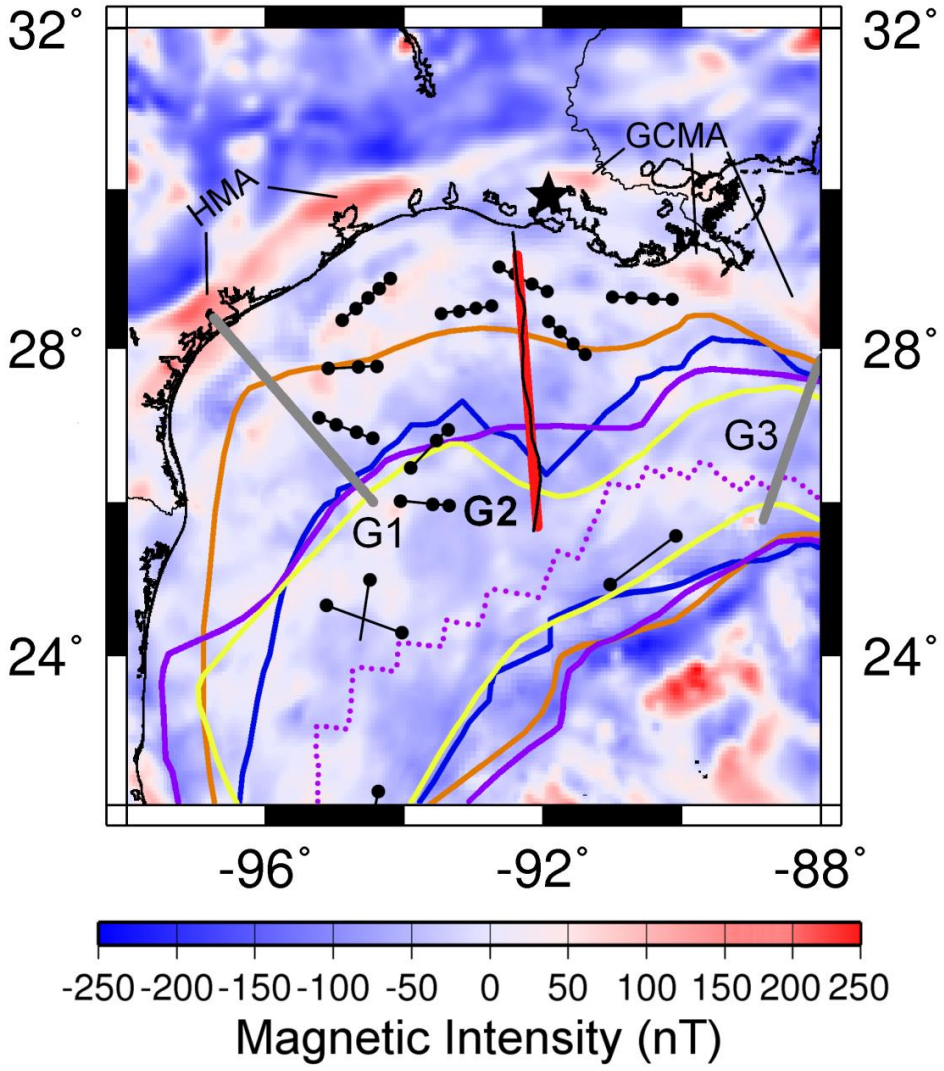

Figure 4.2 – Magnetic anomaly map and limits of oceanic crust (LOC) proposed for the western Gulf of Mexico. Magnetic intensity basemap is from *Maus et al.* [2009]. Colored lines indicate LOC locations from the following studies: *Hudec et al.* [2013a] (blue), *Pindell and Kennan* [2009] (purple), *Sawyer et al.* [1991] (yellow), and *Marton and Buffler* [1994] (orange). Purple dotted line shows spreading ridge proposed by *Pindell and Kennan* [2009]. Star indicates location of exhumed xenoliths described by *Stern et al.* [2010]. Locations shown for GUMBO Lines 1, 2, and 3 (G2 - thick red line; G1, G3 - thick grey lines) and ION/GXT 2000 MCS profile (thin black line). Connected black dots north of 26° latitude show seismic refraction studies of *Ebeniro et al*. [1988] and *Ibrahim and Uchupi* [1981]; black dots south 26° latitude are from *Ibrahim et al.* [1981]; **GCMA** – Gulf Coast magnetic anomaly proposed by *Hall* [1990]; **HMA** – Houston magnetic anomaly proposed by *Hall* [1990] and *Mickus et al.* [2009].

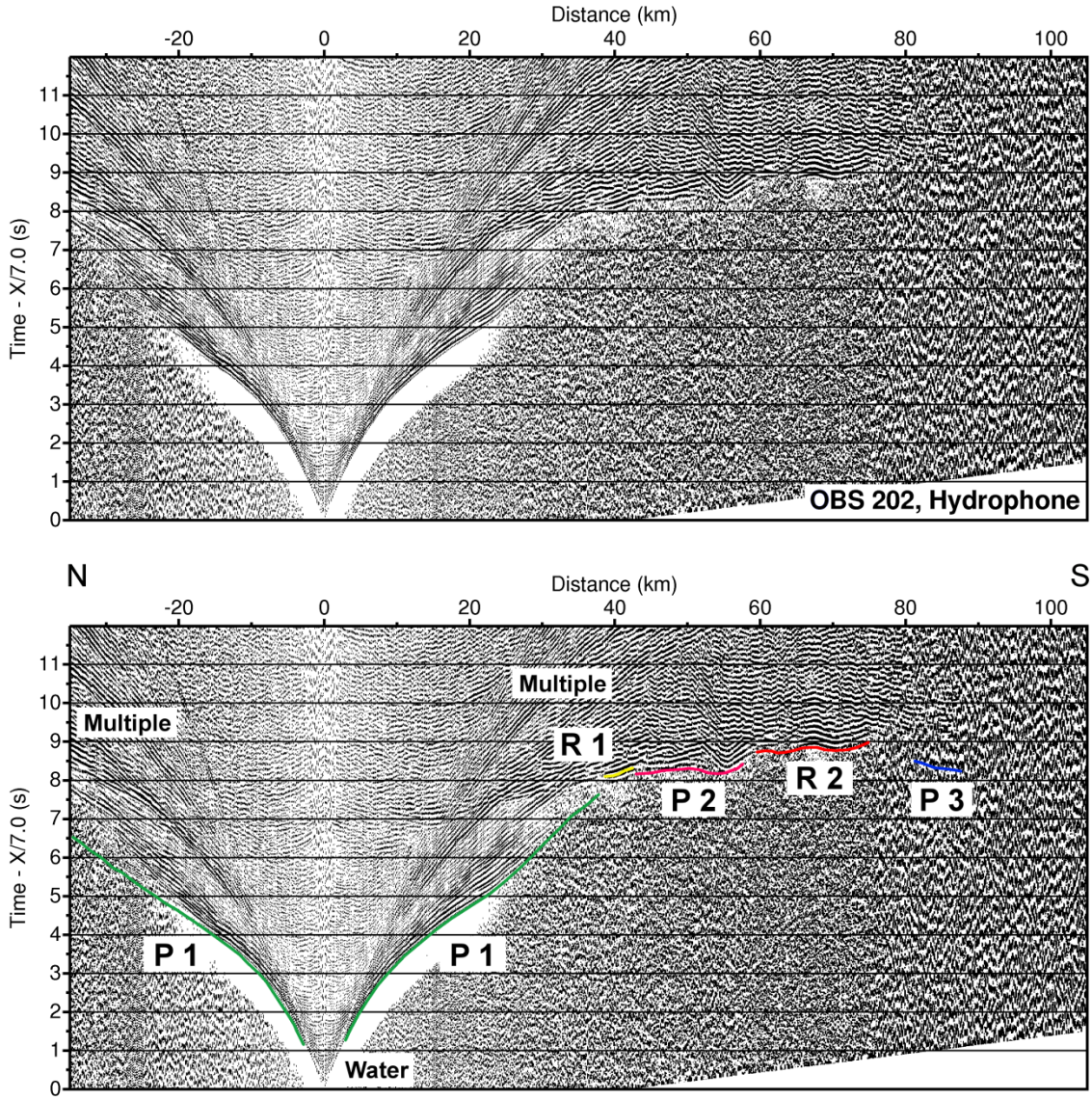

Figure 4.3 – Receiver gather from the hydrophone of OBS 202 (top) with interpreted travel time arrivals (bottom). A reduction velocity of 7.0 km/s is applied. Bandpass filters are used with a frequency range of 6-14 Hz. Gain is set to 1.0 and increases linearly with offset. See text for description of compressional refractions (P1-P3) and reflections (R1-R2). Also labeled are arrivals of the direct wave in water (Water) and multiples (Multiple). OBS location displayed on Figure 4.1.

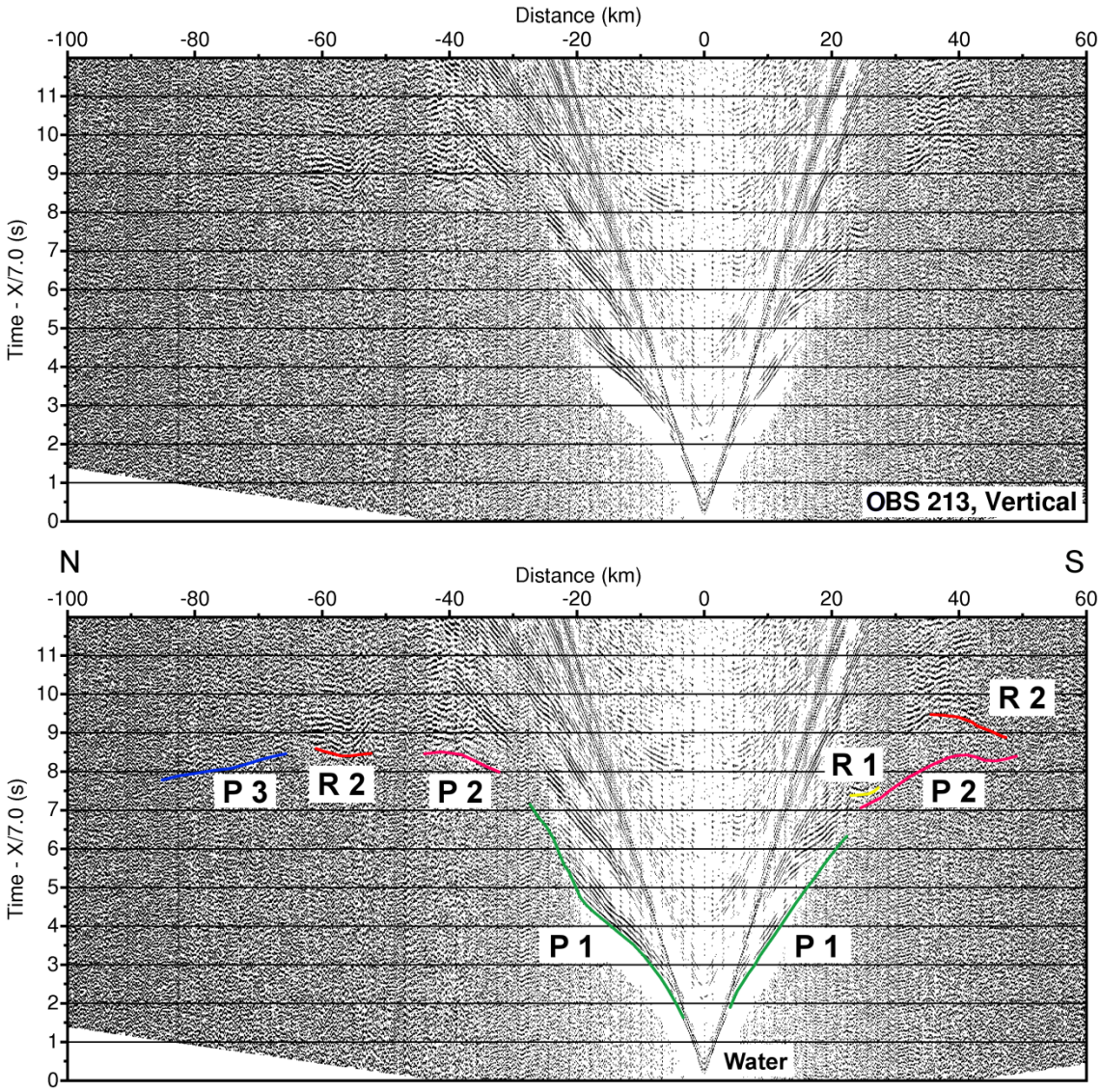

Figure 4.4 – Receiver gather from the vertical component of OBS 213 (top) with interpreted travel time arrivals (bottom). See Figure 4.3 for further details.

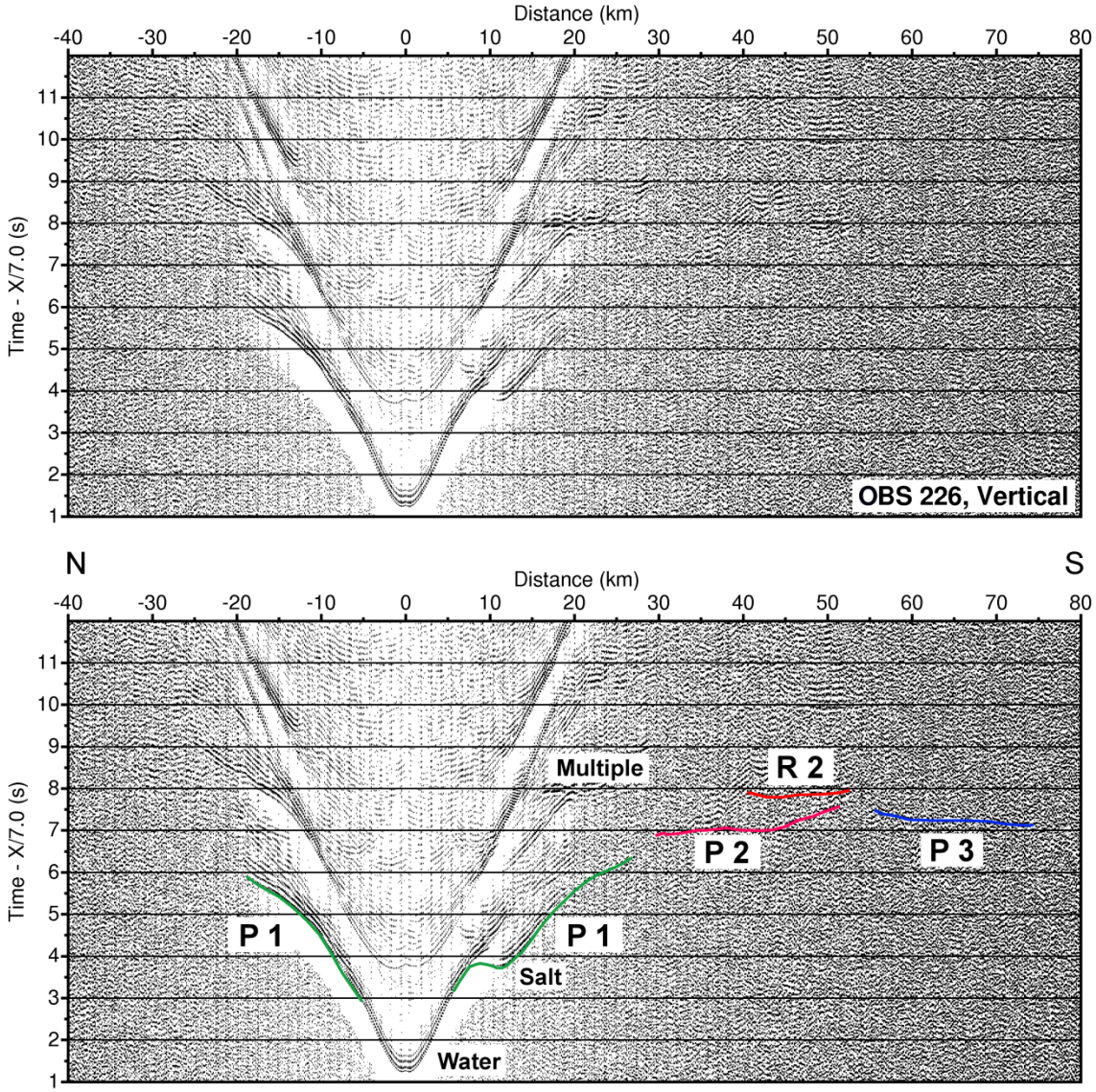

Figure 4.5 – Receiver gather from the vertical component of OBS 226 (top) with interpreted travel time arrivals (bottom). See Figure 4.3 for further details.

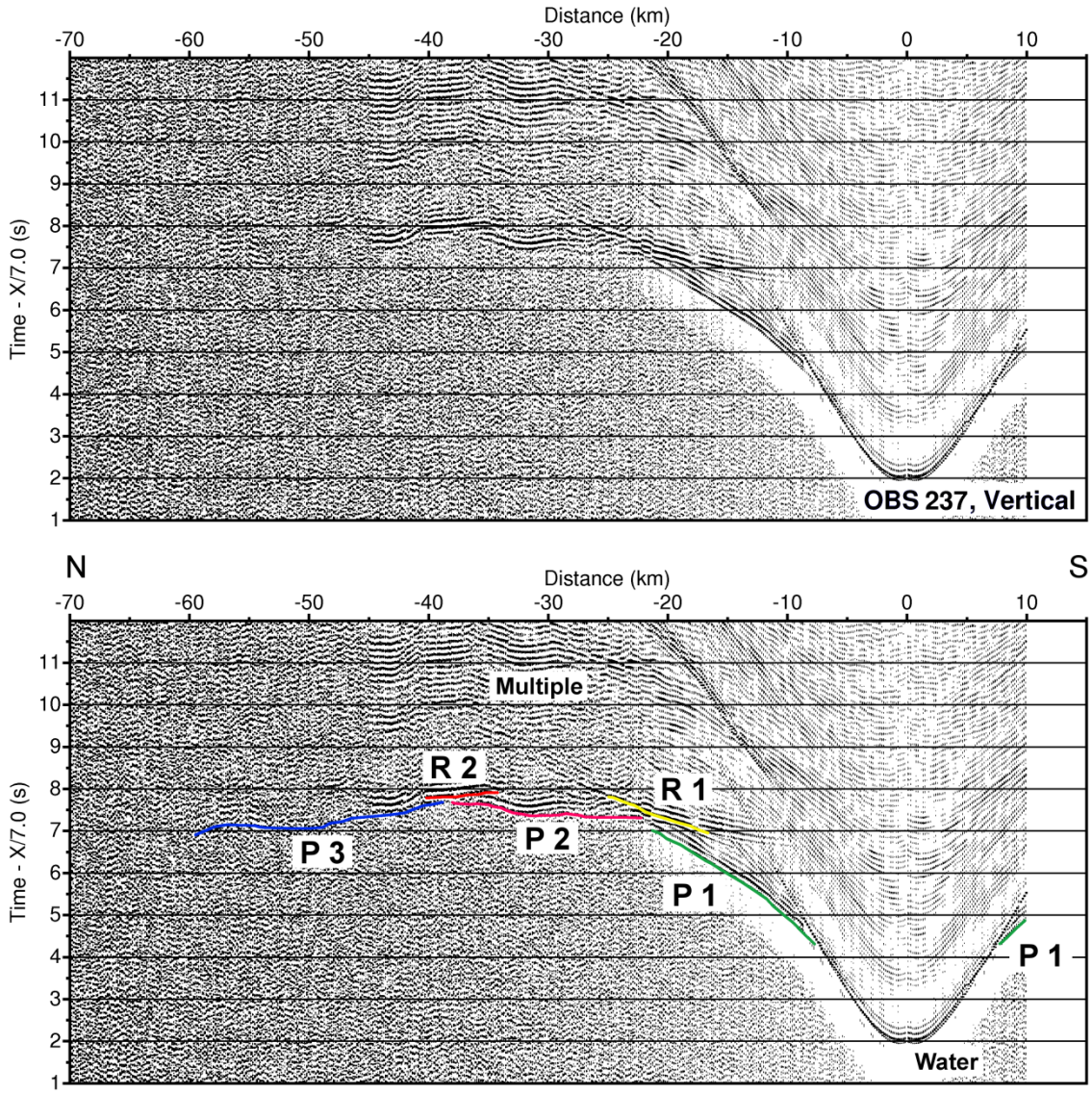

Figure 4.6 – Receiver gather from the vertical component of OBS 237 (top) with interpreted travel time arrivals (bottom). See Figure 4.3 for further details.

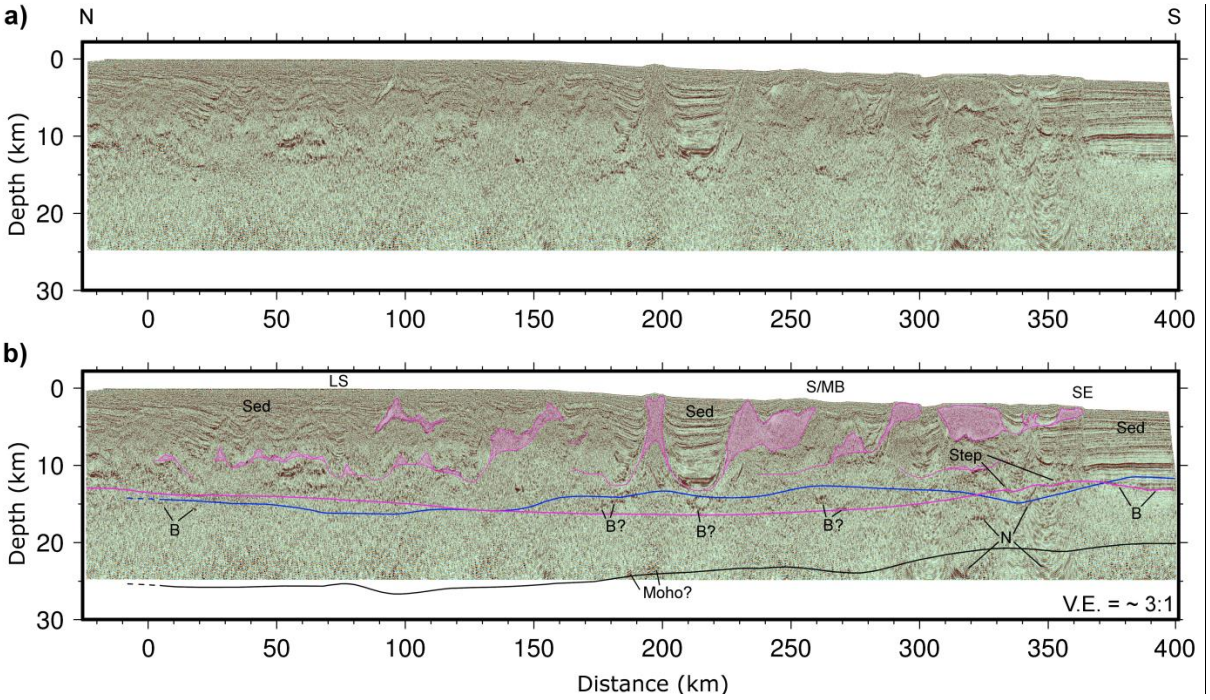

Figure 4.7 – GXT GulfSPAN Line 2000 multi-channel seismic reflection image. a) MCS data without interpretation; b) MCS data with interpretations from *Radovich et al*. [2011]. Top of basement (blue line) and Moho (black line) are boundaries plotted from coincident GUMBO Line 2 seismic velocity model. Pink line and pink shapes represent existing interpretations of Louann salt detachment surface (*e.g.*, base of autochthonous salt) and allochthonous salt structures, respectively. **B** – MCS Basement; **LS** – Louisiana shelf; **N** – Noise; **S/MB** – Salt/minibasin province; **SE** – Sigsbee escarpment.

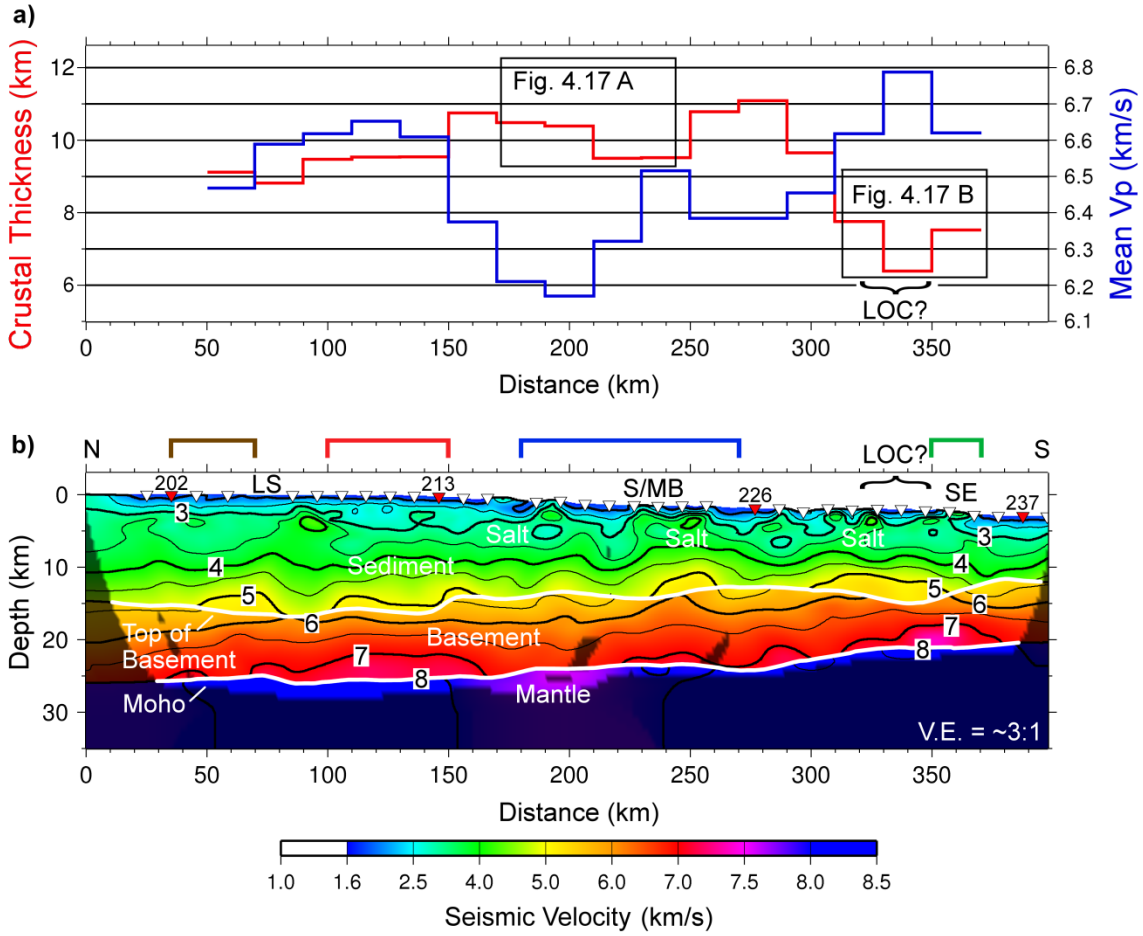

Figure 4.8 – GUMBO Line 2 seismic velocity structure. a) Average crustal thickness and seismic velocity. Mean Vp determined using a 20 km-wide averaging window; b) GUMBO Line 2 seismic velocity model. Shading denotes model space not constrained by ray paths. Inverted triangles denote OBS locations, with red symbols and numbers corresponding to record sections displayed in Figures 4.3-4.6. Colored brackets indicate locations of velocity versus depth profiles for Figure 4.15. **LOC** – Limit of oceanic crust; **LS** – Louisiana shelf; **S/MB** – Salt/minibasin province; **SE** – Sigsbee escarpment.

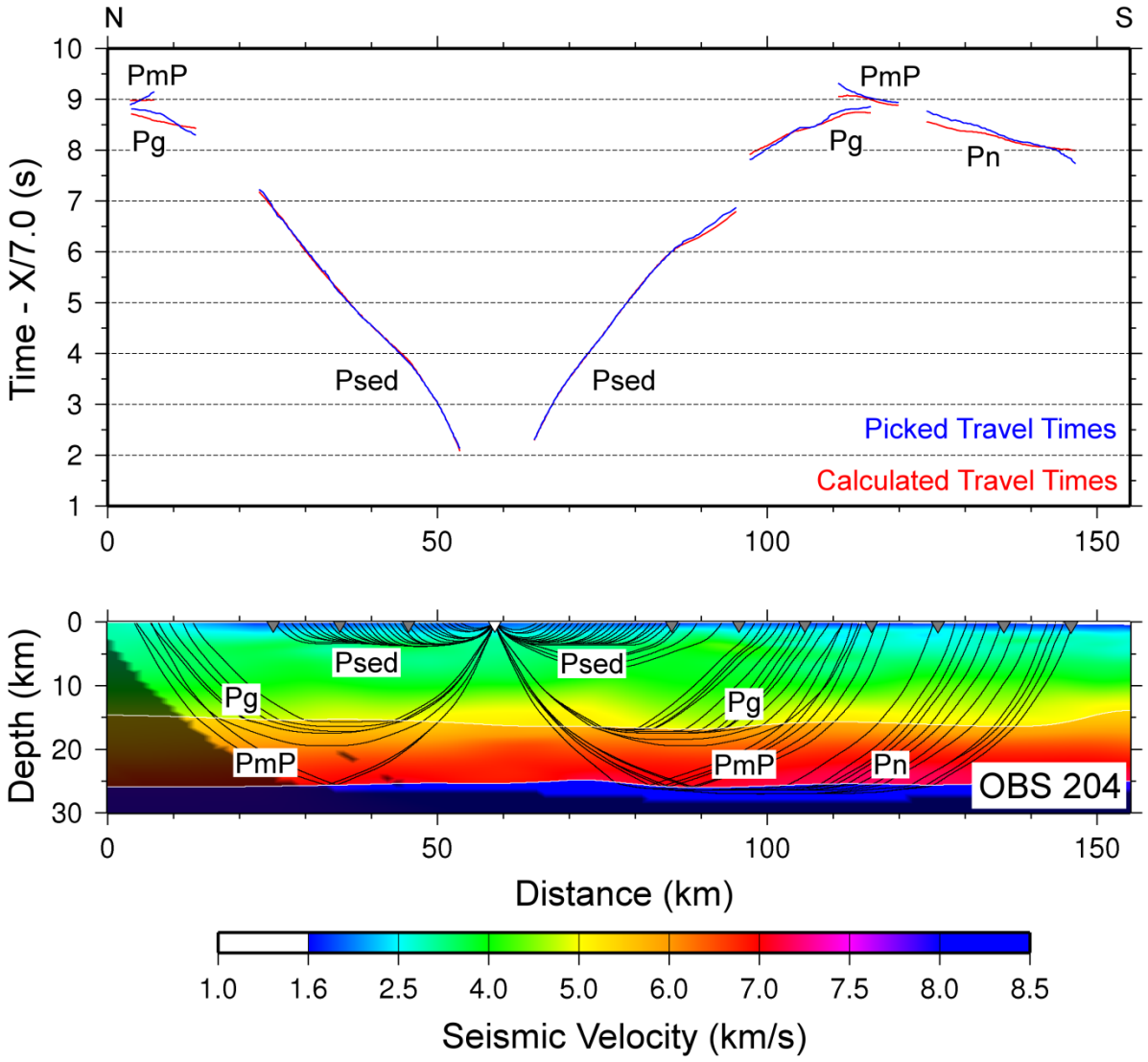

Figure 4.9 – Picked and calculated travel times for OBS 204 (top) and ray paths through final tomographic model (bottom). Shading denotes model space not constrained by ray paths. **PbP** – top of basement reflections; **Pg** – basement layer refractions; **PmP** – Moho reflections; **Pn** – mantle layer refractions; **Psed** – sediment layer refractions.

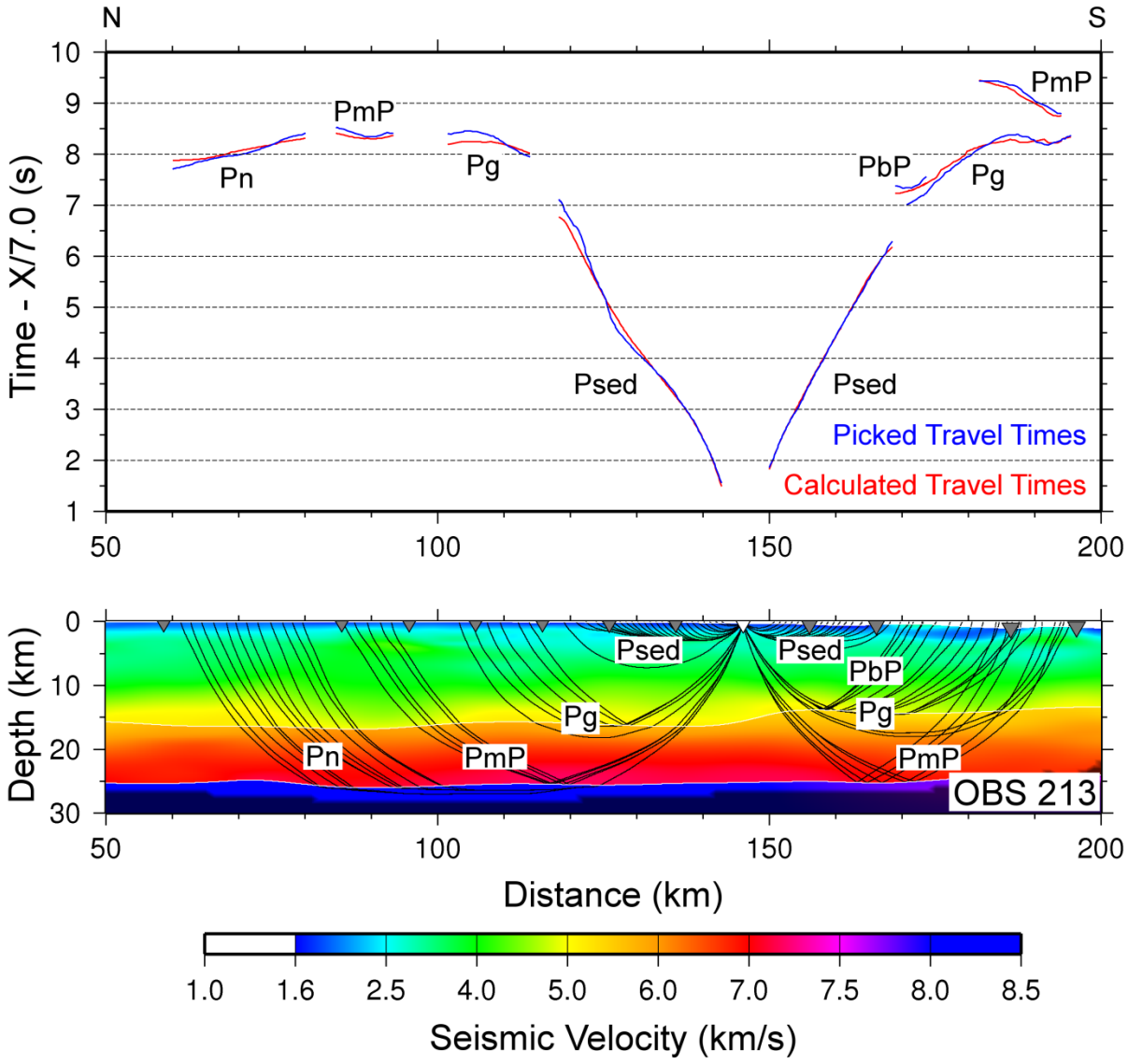

Figure 4.10 – Picked and calculated travel times for OBS 213 (top) and ray paths through final tomographic model (bottom). See Figure 4.9 for further details.

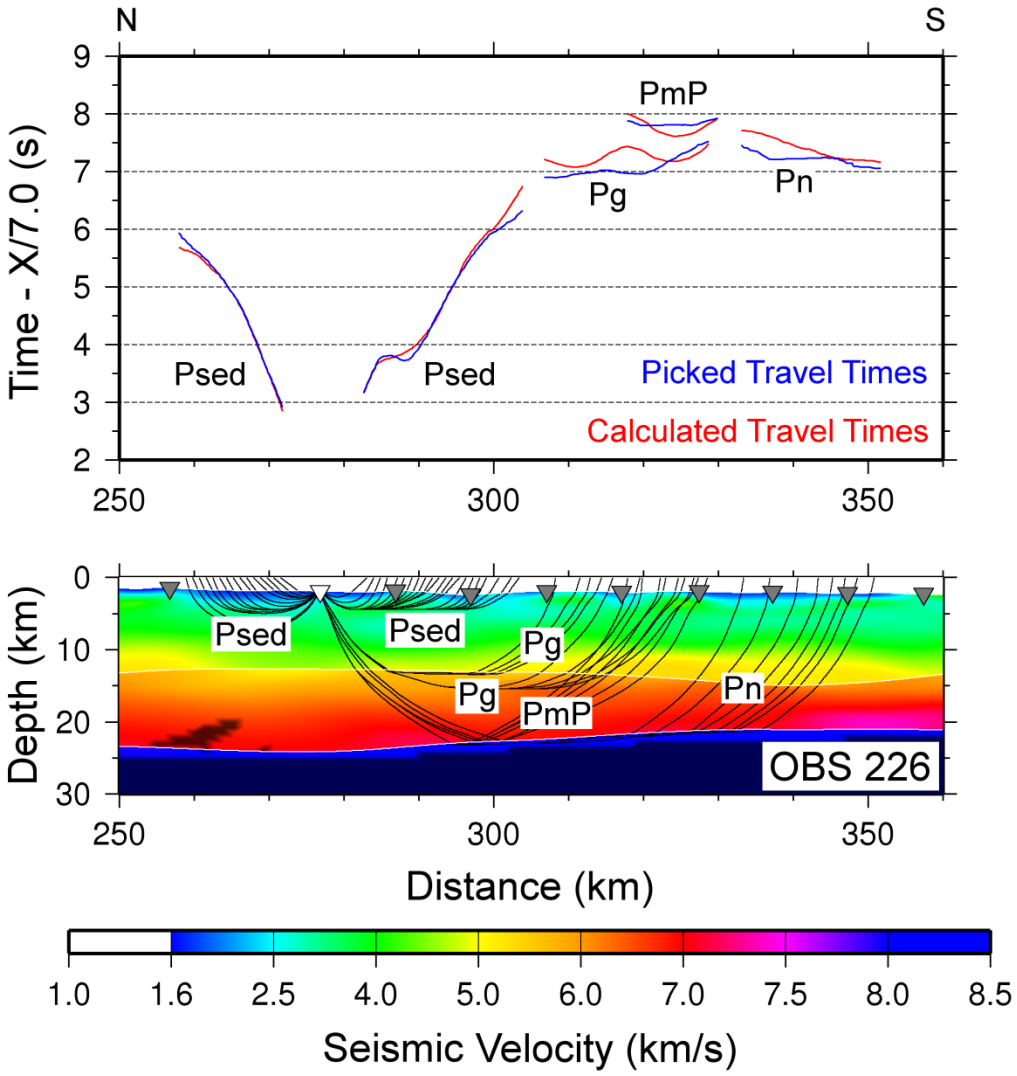

Figure 4.11 – Picked and calculated travel times for OBS 226 (top) and ray paths through final tomographic model (bottom). See Figure 4.9 for further details.

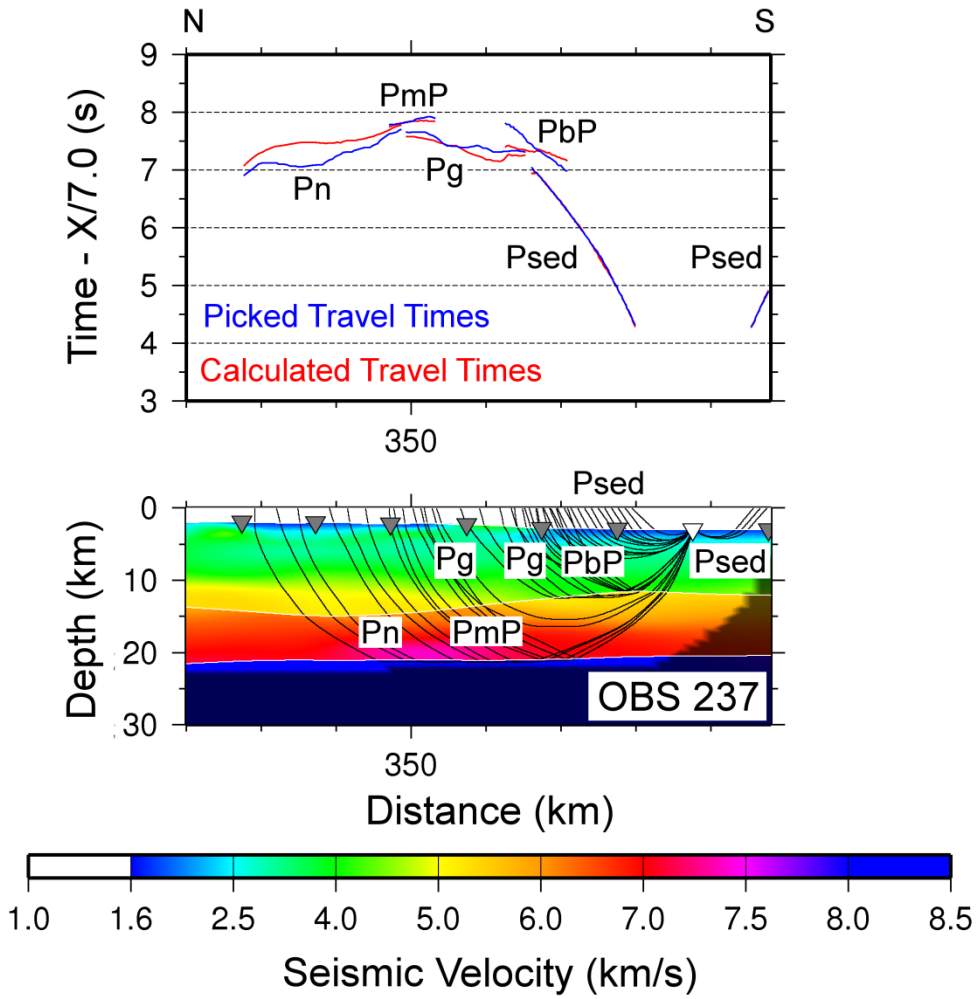

Figure 4.12 – Picked and calculated travel times for OBS 237 (top) and ray paths through final tomographic model (bottom). See Figure 4.9 for further details.

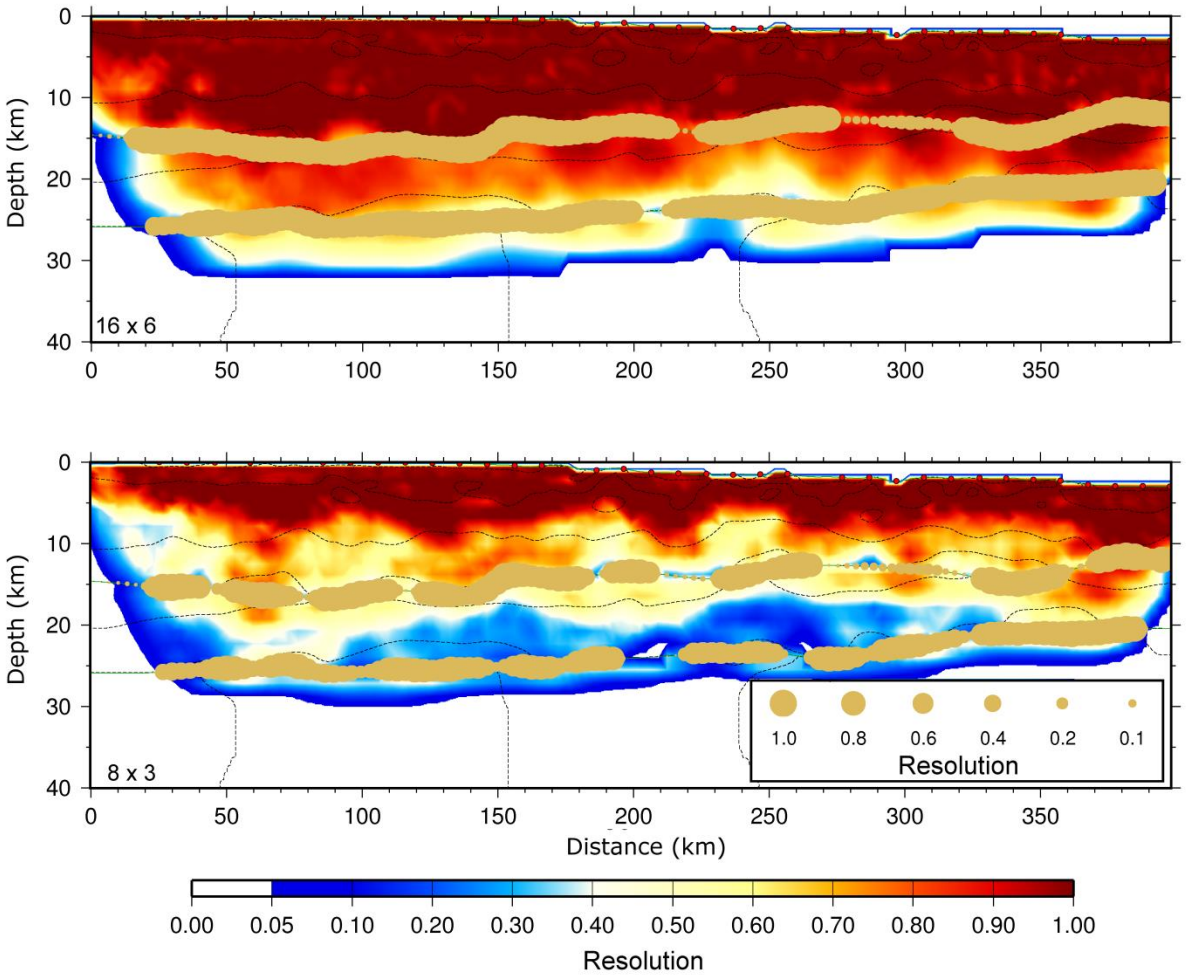

Figure 4.13 - 16 km x 6 km and 8 km x 3 km resolution tests for GUMBO Line 2 seismic velocity model in Figure 4.8. Color palate indicates resolution of seismic velocities in the final model. Tan circles indicate resolution of top of basement and Moho model boundaries.

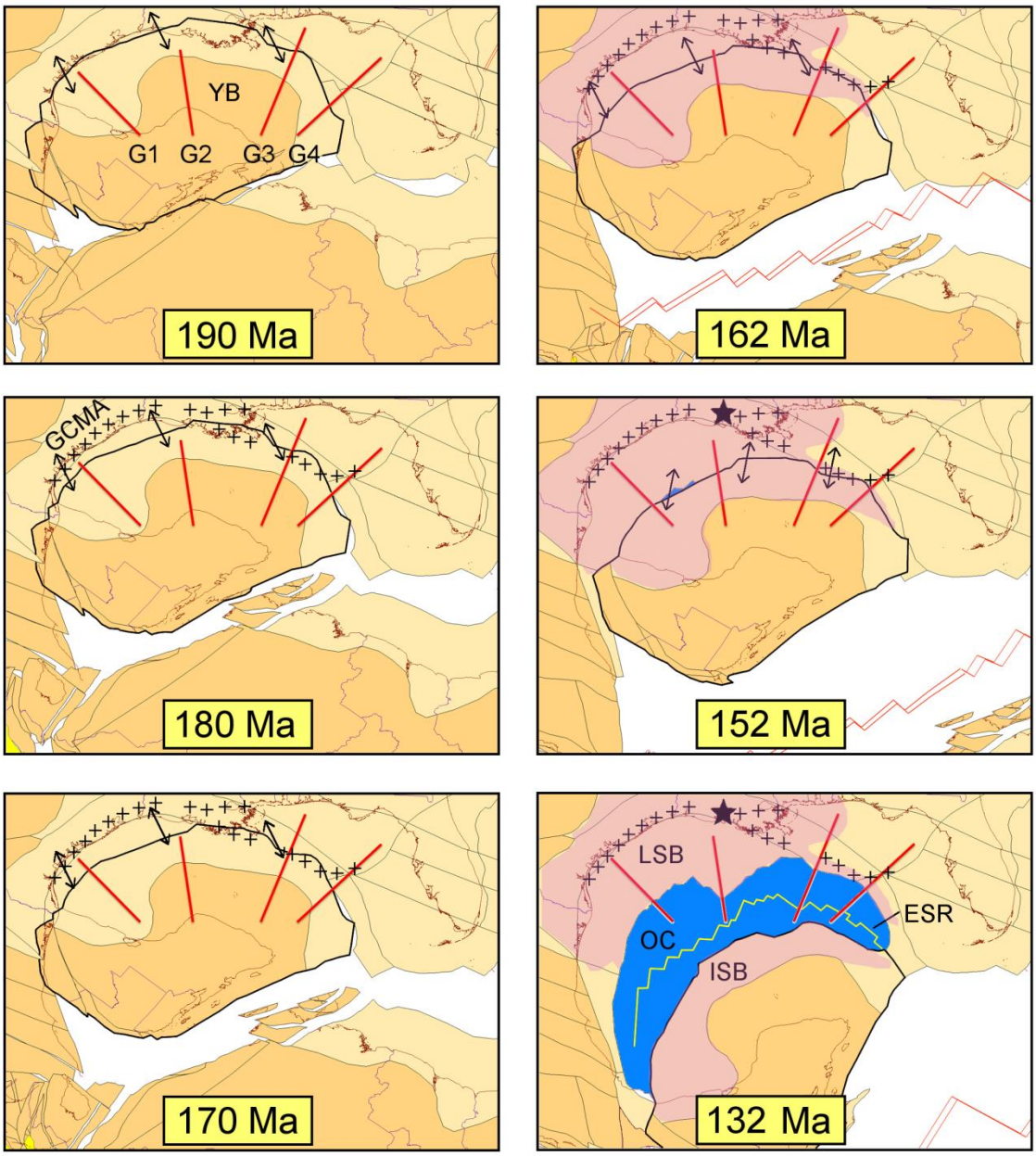

Figure 4.14 – Kinematic model for opening of the Gulf of Mexico. Arrows indicate relative plate motions between Yucatán block (black outline) and Laurentia. Star shows location of southern Louisiana mantle xenoliths. **G1-G4** – GUMBO Lines 1-4 (red lines); **GCMA** – Gulf Coast Magnetic Anomaly (plus symbols); **ESR** – extinct spreading ridge (yellow line); **ISB** – Isthmian salt basin (pink); **LSB** – Louann salt basin (pink); **OC** – oceanic crust (blue).

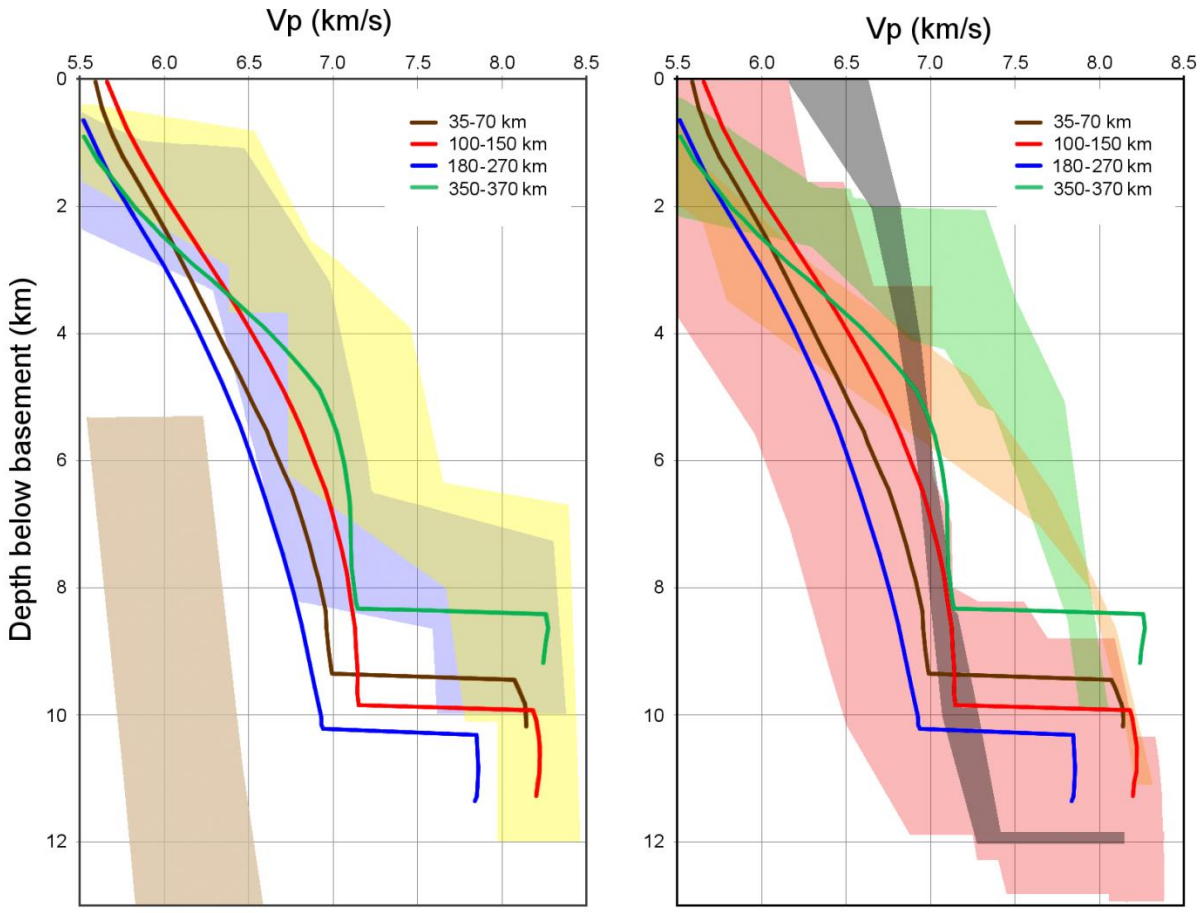

Figure 4.15 – Velocity versus depth profiles for GUMBO Line 2 basement. Depth and seismic velocity measurements are taken from the top of basement and averaged for four regions of GUMBO Line 2 model distance. See Figure 4.8 for profile locations. GUMBO Line 2 is compared to continental crust (brown) [*Christenson and Mooney*, 1995], 29-140 Ma Pacific oceanic crust (yellow), and 142-170 Ma Atlantic ocean crust (blue) [*White et al.*, 1992], as well as rifted margins with thinned lower continental crust and exhumed mantle offshore Newfoundland (orange) [*Eddy et al.*, 2013], highly serpentinized exhumed mantle at the Iberian margin (green) [*Chian et al.*, 1999; *Sibuet et al.*, 2007], magmatically intruded and underplated continental crust in the South China Sea and Vøring Plateau (red) [*Mjelde et al.*, 2005; *Lester et al.*, 2014], and thick oceanic basement at the Vøring Plateau (black) [*Mjelde et al.*, 2005].

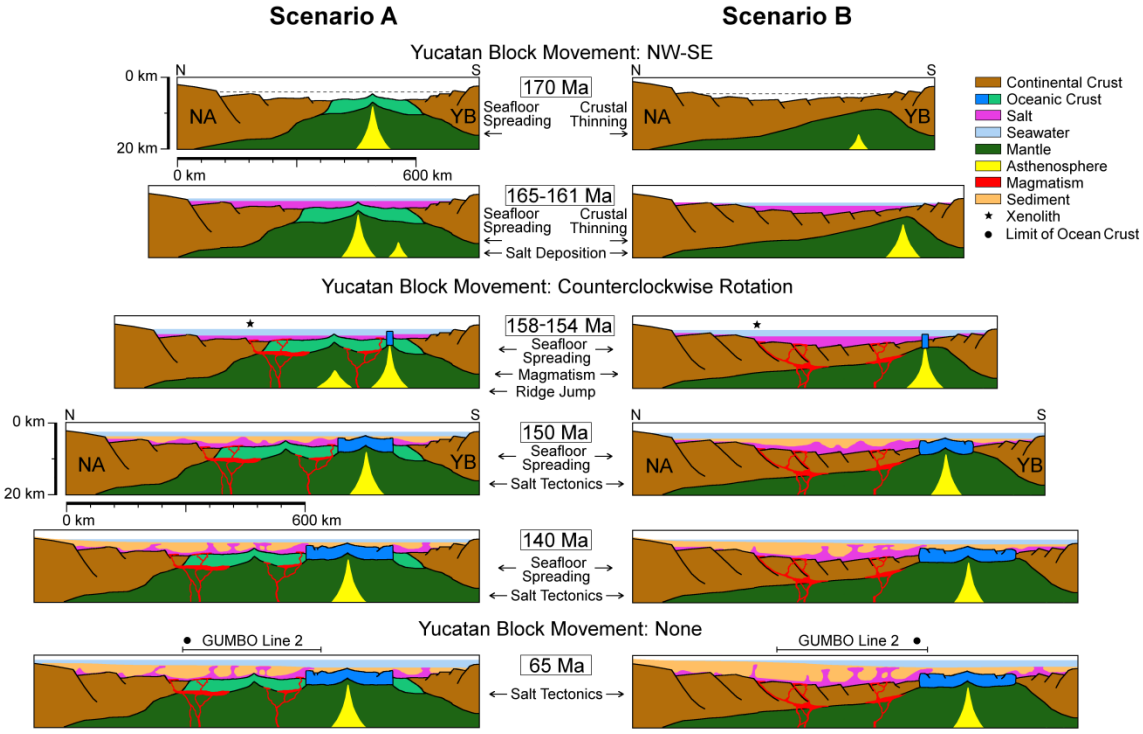

Figure 4.16 – Interpretations of north-central Gulf of Mexico crustal structure. Scenario A shows basin formation by Early Jurassic seafloor spreading, a ridge jump coincident with a pulse of magmatism, and the LOC at the landward end of GUMBO Line 2. Scenario B shows the favored interpretation of basin formation by asymmetric Early Jurassic crustal thinning, post-rift magmatism coincident to the onset of seafloor spreading, and the LOC at the seaward end of GUMBO Line 2.

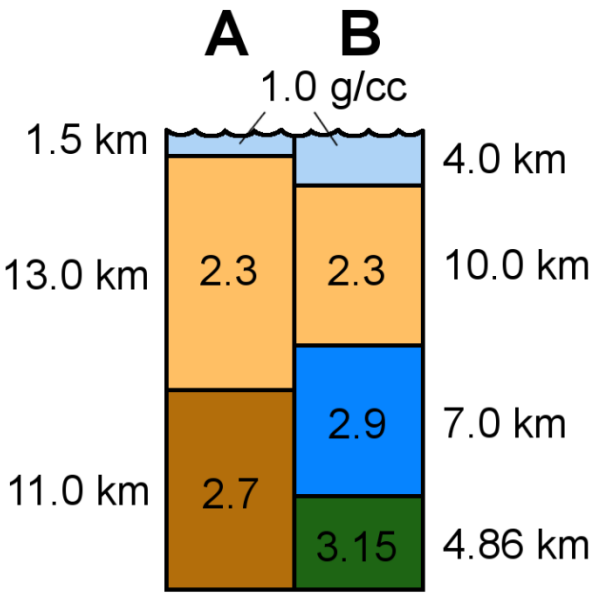

Figure 4.17 – Isostatic compensation of GUMBO Line 2 columns in the salt/minibasin province (A) and near the Sigsbee escarpment (B). Column heights are averaged from GUMBO Line 2 model distances as shown in Figure 4.8. Densities (ρ) are approximated for water (light blue), sediments (tan), intruded continental crust (brown), oceanic crust (blue), and mantle (green).

Conclusions

A better understanding of the interplay among processes of mantle upwelling, magmatism, tectonic inheritance, continental rifting, and seafloor spreading at Mesozoic rifted margins along the eastern seaboard of North America is realized through analysis of marine seismic refraction and reflection data. Deep crustal seismic velocities and MCS reflections provide critical data needed to constrain the present-day structure of rifted margins, from which the effects of continental extension and the volume of syn- and post-rift melts can be inferred.

Serpentinization of the mantle has the ability to weaken the lithosphere, but not to the point of complete lithospheric breakup and onset of seafloor spreading at cold, often magma-poor rifted margins. The mantle potential temperature at the Newfoundland margin was cold during rifting, likely well below the normal ~1280°C isotherm. In the northern Central Atlantic Ocean, slow rates of extension between Newfoundland and Iberia coupled with a lack of syn-rift magmatism and pre-rift thermal uplift suggest passive upwelling of the mantle in response to far-field stresses on the lithosphere. In order for rifting to culminate in seafloor spreading at the magma-poor Newfoundland margin, the strong lithosphere had to be substantially thinned and weakened. Lithosphere-scale detachment faults are interpreted to have exhumed lower continental crust and upper mantle into a broad continent-ocean transition zone (COT). Analysis of *Vp*/*Vs* ratios from SCREECH Line 2 supports this interpretation by constraining the lithology of the COT. Seismic velocities show evidence for felsic crust (*e.g.*, granite and quartzite) at the landward end of the COT and exhumed, hydrated mantle peridotites at

the seaward end (Figures 2.3-2.5). Analysis of *Vp*/*Vs* further supports weakening of the strong upper mantle in the COT by hydrothermal circulation, which led to approximately 25% serpentinization of peridotites. The distal end of the COT also shows *Vp*/*Vs* ratios that suggest the presence of basalts, which likely arrived in the earliest stages of magmatism forming embryonic ocean crust at the Newfoundland margin. I contend that the impact of mantle serpentinization at magma-poor rifted margins is overstated in its contribution to breakup of the lithosphere, especially given the extreme width of continent-ocean transition zones across which mantle serpentinization is interpreted (*e.g.*, SCREECH Line 2). Complete lithospheric separation only occurs if and when heat from an upwelling asthenosphere creates enough melting in the upper mantle to lead to normal seafloor spreading. At this point, far-field stresses are no longer accommodated by detachment faults and mantle exhumation, but rather by magmatic diking associated with the production of oceanic crust.

Structural inheritance plays a key role in determining the location of continental rifting. For example, in the U.S. Gulf coast region the shape of the Ouachita orogen and Suwanee-Wiggins suture zone may control the locus of crustal thinning. Here, seismic transects that approach preexisting structures inherited from older collisional events image a complete rifted margin (*e.g.*, GUMBO Lines 1, 3, and 4; SCREECH Line 2), whereas transects distanced from inherited structural features (*e.g.*, GUMBO Line 2) may instead be located entirely within the realm of oceanic basement. Nevertheless, once a structural feature has thermally re-equilibrated, the only contribution of structural inheritance to the subsequent evolution of the rifted margin is the thickness of the

preexisting crust. I contend that pre- and syn-rift mantle potential temperatures and the type of the mantle upwelling beneath a rifted margin play a more vital role in the rift-to-drift evolution of that margin. Differences in mantle potential temperature exert first-order control on the amount of syn-rift magmatism, which in turn impacts crustal thinning during extension and ultimately the width of the transition from continental to oceanic crust. The fact that the thickness of oceanic crust can vary widely between nearby margins lends further support to the impact of mantle potential temperature anomalies, which may endure at a given margin long after lithospheric breakup.

New seismic refraction data from the GUMBO Project shows the development of a volcanic margin during rifting in the northeastern Gulf of Mexico intricately tied to above average mantle potential temperatures (~1300-1500°C). Tectonic inheritance of warm and potentially weak lithosphere is inferred for the northeastern Gulf of Mexico given its proximity to the Ouachita-Appalachian orogen and the probable origin of Late Triassic volcanics of the Central Atlantic Magmatic Province (CAMP) near the Blake Plateau (Figure 1.3). The seismic velocity structure of GUMBO Line 3 supports thinning of crystalline continental crust from ~20 km to <10 km across a ~100 km-wide necking zone (Figure 3.8). High seismic velocities in the upper crust coincide with dipping reflections from coincident multichannel seismic reflection data (MCS) that suggest syn-rift infilling of the Apalachicola Basin with volcaniclastics (Figure 3.7). Beneath this region, abnormally high seismic velocities in the lowermost crust (>7.2 km/s) are interpreted as magmatic infiltration and/or underplating of mafic rocks at the base of continental crust. Comparison of GUMBO Line 3 to mantle melting models supports

passive upwelling of the mantle during rifting with elevated mantle potential temperatures (Figure 3.16). At the seaward end of the volcanic rifted margin, a stabilization of crustal thickness to ~8 km and an increase in average crustal seismic velocity (~7.0 km/s) is interpreted as the landward limit of oceanic crust (LOC) at 270-290 km GUMBO Line 3 model distance (Figure 3.8). The LOC coincides with both a landward-dipping basement ramp and the seaward termination of evaporites interpreted from MCS data, as well as the edge of the broad Gulf Coast magnetic anomaly (Figures 3.7, 3.8). Oceanic crust at GUMBO Line 3 is thicker than normal oceanic basement and kinematic models predict slow rates of seafloor spreading (~24 mm/yr full spreading rate). The continued presence of elevated mantle potential temperatures during seafloor spreading likely sourced an abundant supply of magma to the spreading ridge (Figure 3.14), leading to thick oceanic crust and an overprinting of seafloor magnetic anomalies in the northeastern Gulf of Mexico.

Rifting in the north-central Gulf of Mexico led to a substantially different type of rifted margin than in the east. The seismic velocity structure at GUMBO Line 2 supports a ~300 km-wide region of ~10 km-thick crust and oceanic crust at the seaward end of the model (Figure 4.8). Velocity-depth comparisons and strong Moho reflections show that the composition of the crust is incompatible with exhumed mantle or incipient oceanic crust that characterizes the magma-poor margins of Newfoundland and Iberia (Figure 4.15). Thinned continental crust or oceanic crust could both explain the seismic velocity structure at GUMBO Line 2, as well as the asymmetry of the north-central Gulf of Mexico with the conjugate Yucatán margin. However, the crust here is devoid of seafloor

spreading magnetic anomalies (Figure 4.2) and too thick to represent normal oceanic basement, instead suggesting thinned continental crust. High seismic velocities in the lower crust (>7.0 km/s) can be explained by magmatic additions that thickened the crust in the north-central Gulf of Mexico during rifting or seafloor spreading, similar to recent interpretations of rifted margins in the South China Sea (Figure 4.16). This interpretation of GUMBO Line 2 agrees with evidence for off-axis, post-rift melting of a depleted mantle from xenoliths in southern Louisiana. The thickest salt provinces are found in the north-central Gulf of Mexico, and may have been deposited above of thinned continental basement that sat slightly below sea level, or in a restricted, deep basin floored by oceanic crust. The onset of Gulf-wide seafloor spreading in the Late Jurassic was likely associated with a change in direction of movement of the Yucatán block ~158 Ma (Figures 3.17; 4.14). Shallower oceanic basement in the central Gulf basin, possibly the result of low mantle densities beneath the spreading ridge, limited the seaward flow of allochthonous salt and split the large salt province into northern and southern sections.

Appendix A: Chapter 2

To investigate how well S-wave arrivals can constrain V_p / V_s in the COT (and thus distinguish between different possible end-member lithologies), we test how models with three specific V_p / V_s ratios affect S-wave travel-time misfits for OBS 15, 17, and 19 in the Newfoundland COT (Figure A7; a, V_p / V_s = 1.65; b, V_p / V_s = 1.77; c, V_p / V_s = 1.87). Blue and red lines represent picked and calculated S-wave travel-time curves, respectively. Reduction velocity is 4.0 km/s. To test for the possible presence of felsic continental upper crust we use a bulk V_p / V_s ratio of 1.65. For more mafic-rich rocks found in oceanic crust or in lower continental crust (either naturally or as exhumed underplated material), we assume V_p / V_s = 1.77 [*Brocher*, 2005]. Alternatively, for mantle peridotites that are 25% serpentinized we assume V_p / V_s = 1.87 [*Christensen*, 2004]. In a few raytracing tests, we keep V_p fixed and locally vary the V_p / V_s ratio to determine how it affects the data fit for shear waves that best sample the flat COT basement. The bulk model with V_p / V_s = 1.77 gives the best fit of S-wave travel times (RMS = 124 ms). The model with V_p / V_s = 1.87 has a higher misfit (RMS = 183 ms), and a V_p / V_s ratio of 1.65 fits very poorly (RMS = 322 ms). Although not shown in Figure A7, additional testing of bulk V_p / V_s models found that landward of the COT, a low V_p / V_s ratio (1.65) fits the S-wave data well, while higher ratios fit poorly. This supports the hypothesis that felsic continental upper crustal rocks characterize the Newfoundland margin here. At the seaward end of SCREECH Line 2, bulk models with V_p / V_s = 1.87 and V_p / V_s = 1.77 produce the lowest misfits (110 ms and 104 ms, respectively), and the nature of the lithosphere is equivocal given our data.

Table A1. Compressional and shear wave velocities of common COT lithologies. Error bars for COT rock types are displayed in Chapter 2, Figure 2.4.

Rock Type	Vp	Vp/Vs	Reference
Quartzite	5.52 ± 0.57	1.55 ± 0.08	*Holbrook et al*., 1992
Granite	6.07 ± 0.23	1.72 ± 0.05	*Holbrook et al*., 1992
Oceanic Basalts	6.12 ± 0.21	1.86 ± 0.05	*Hyndman*, 1979; *Brocher*, 2005
Gabbro	6.95 ± 0.22	1.86 ± 0.04	*Holbrook et al*., 1992
Mafic Granulite	6.86 ± 0.27	1.91 ± 0.05	*Holbrook et al*., 1992
0% Serpentinized Peroditite	8.02 ± 0.25	1.74 ± 0.06	*Holbrook et al*., 1992; *Christensen*, 2004
25% Serpentinized Peridotite	7.20 ± 0.25	1.87 ± 0.05	*Christensen*, 2004
50% Serpentinized Peridotite	6.45 ± 0.20	1.94 ± 0.04	*Christensen*, 2004
75% Serpentinized Peridotite	5.70 ± 0.30	2.04 ± 0.14	*Christensen*, 2004
100% Seprentinized Peridotite	5.00 ± 0.25	2.08 ± 0.07	*Christensen*, 2004

Table A2 – List of 17 instruments used to build SCREECH Line 2 seismic velocity models. Instrument number (OBS #), depth (Z), and model distance (X) are consistent with *Van Avendonk et al.* [2006]. Shear travel time picks for each instrument, N (S-wave), are also shown.

OBS #	Latitude	Longitude	X, km	Z, m	# Picks (P-wave)	# Picks (S-wave)
08	45˚ 53.76′N	45˚ 45.26′W	136.71	2966	337	98
09	45˚ 48.91′N	45˚ 36.74′W	150.87	3154	389	25
10	45˚ 44.98′N	45˚ 27.90′W	164.76	3407	503	56
11	45˚ 40.27′N	45˚ 18.47′W	178.44	3706	565	36
12	45˚ 36.08′N	45˚ 10.51′W	192.63	4077	432	22
13	45˚ 31.61′N	45˚ 1.38′W	206.79	4152	636	0
14	45˚ 27.14′N	44˚ 52.72′W	220.80	4412	418	0
15	45˚ 22.97′N	44˚ 43.96′W	234.60	4552	566	53
16	45˚ 19.62′N	44˚ 37.22′W	245.39	4559	556	43
17	45˚ 16.46′N	44˚ 30.28′W	256.43	4569	545	92
18	45˚ 12.70′N	44˚ 23.70′W	267.22	4630	408	89
19	45˚ 5.46′N	44˚ 10.36′W	289.11	4690	312	149
20	45˚ 2.15′N	43˚ 3.77′W	299.72	4759	352	0
21	44˚ 58.63′N	43˚ 57.22′W	310.66	4935	366	31
22	44˚ 55.46′N	43˚ 50.29′W	321.34	4923	256	0
23	44˚ 51.26′N	43˚ 43.72′W	332.58	4960	443	78
24	44˚ 48.26′N	43˚ 37.52′W	342.76	5010	398	66
Total					7482	838

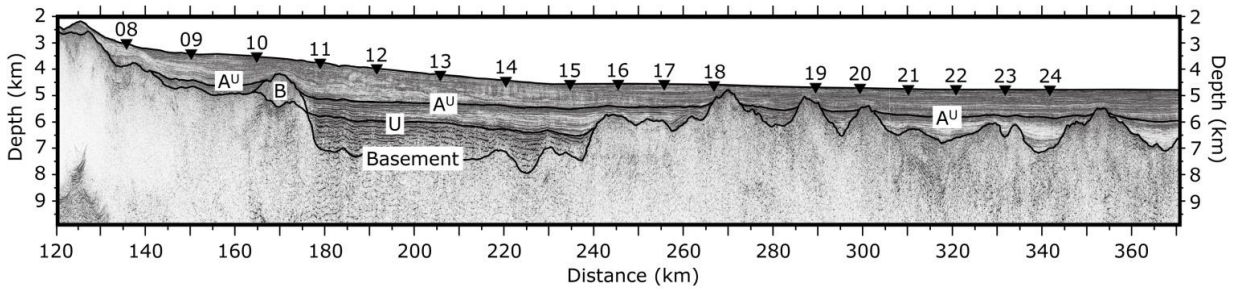

Figure A1 - Multi-channel seismic data (MCS) coincident to SCREECH Line 2. Dark lines correspond to interfaces used to constrain topography and depths to reflections R1 – R3 picked from wide-angle refraction data. Inverted black triangles denote locations of OBS instruments along seafloor. Vertical exaggeration is approximately 6:1. **A^U** – Horizon A^U; **B** – block of pre-rift sediments; **U** – U-reflection; **Basement** – Top of crystalline basement.

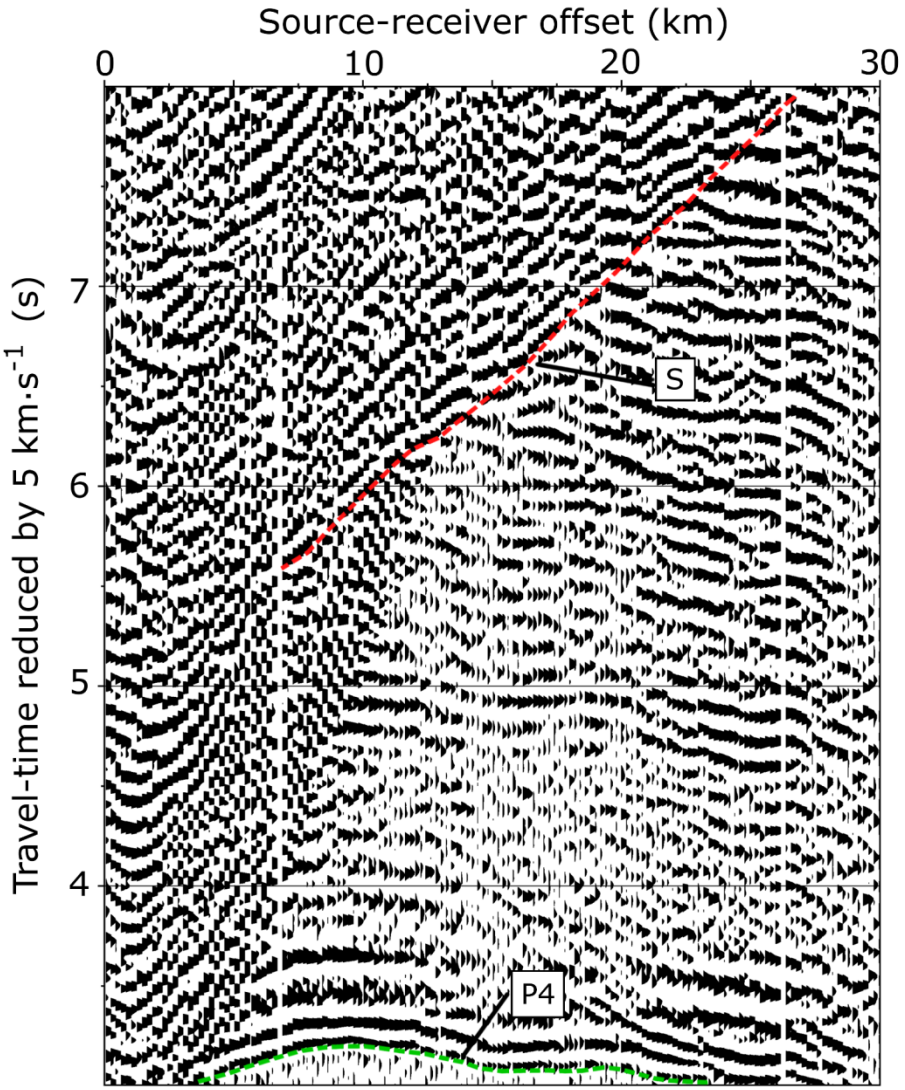

Figure A3 – A portion of the receiver gather for OBS 08 using the vertical component. Labeled are arrivals of a compressional refraction (P4) and a shear wave (S).

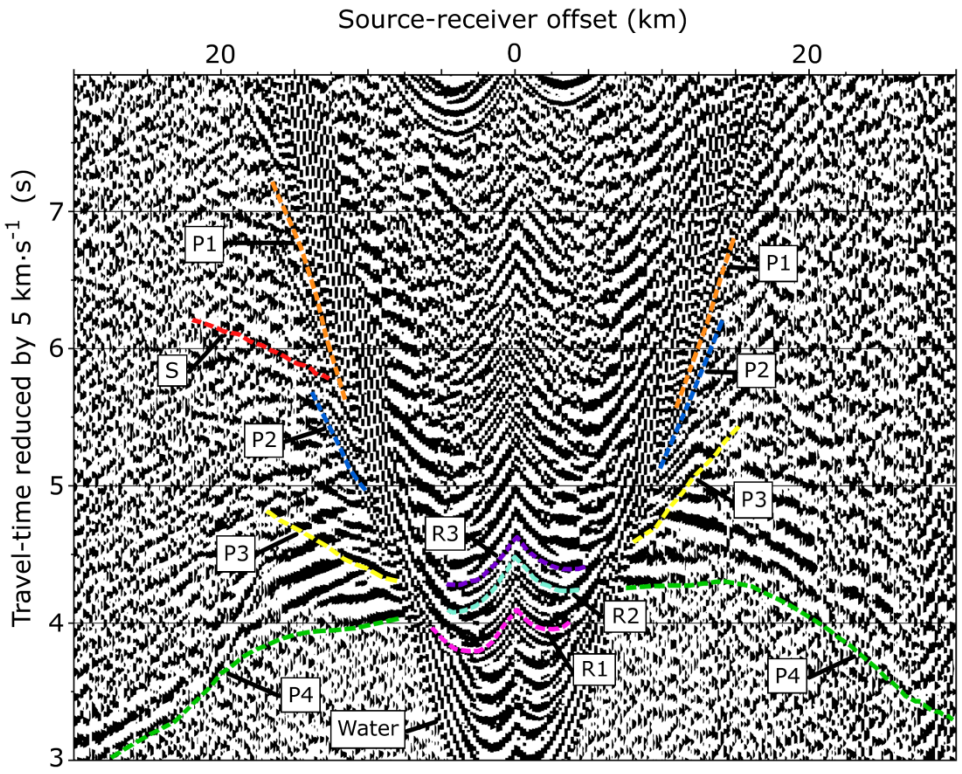

Figure A4 – A portion of the receiver gather for OBS 12 using the vertical component. Labeled are arrivals of compressional refractions and reflections (P1-P4, R1-R3). Also labeled are arrivals of the direct wave in water (Water) and a shear wave (S).

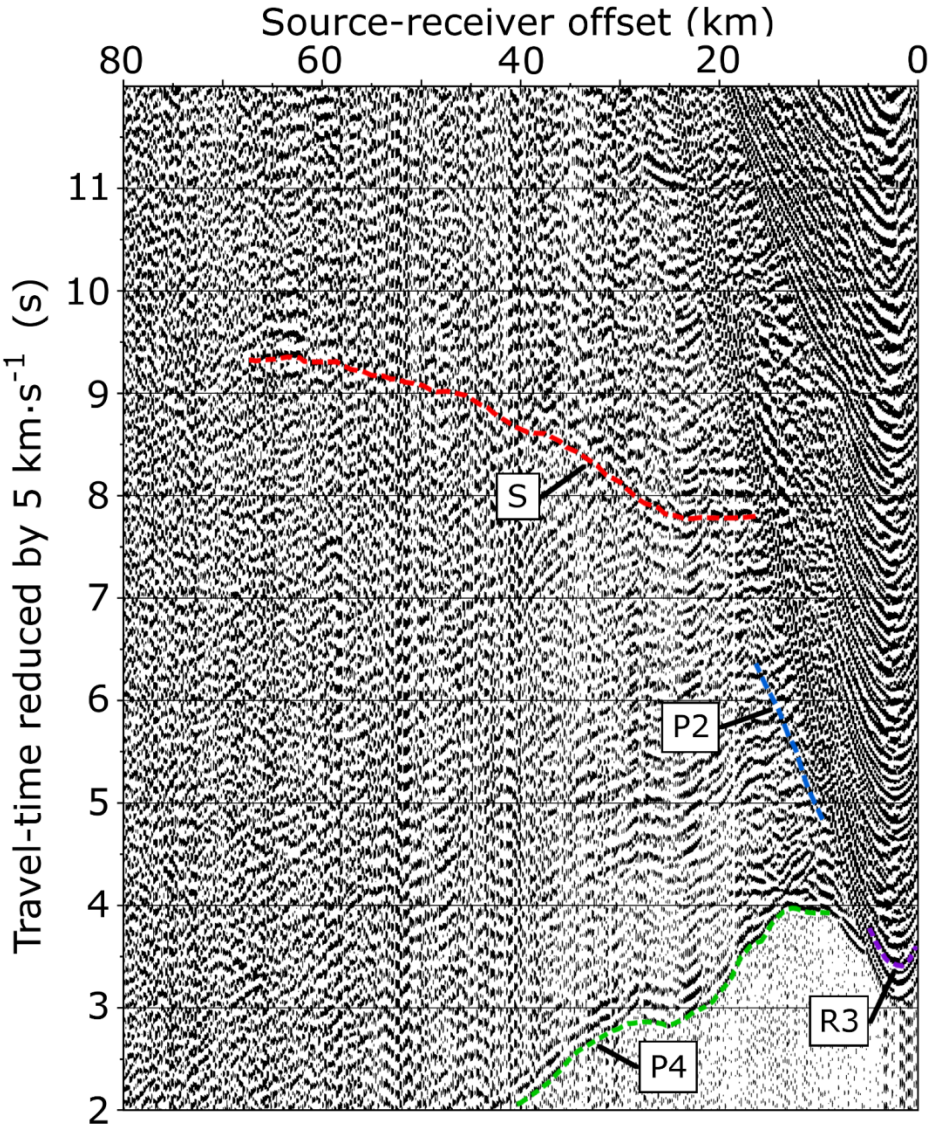

Figure A5 – A portion of the receiver gather for OBS 19 using the vertical component. Labeled are arrivals of compressional refractions (P2, P4), compressional reflections (R3), and a shear wave (S).

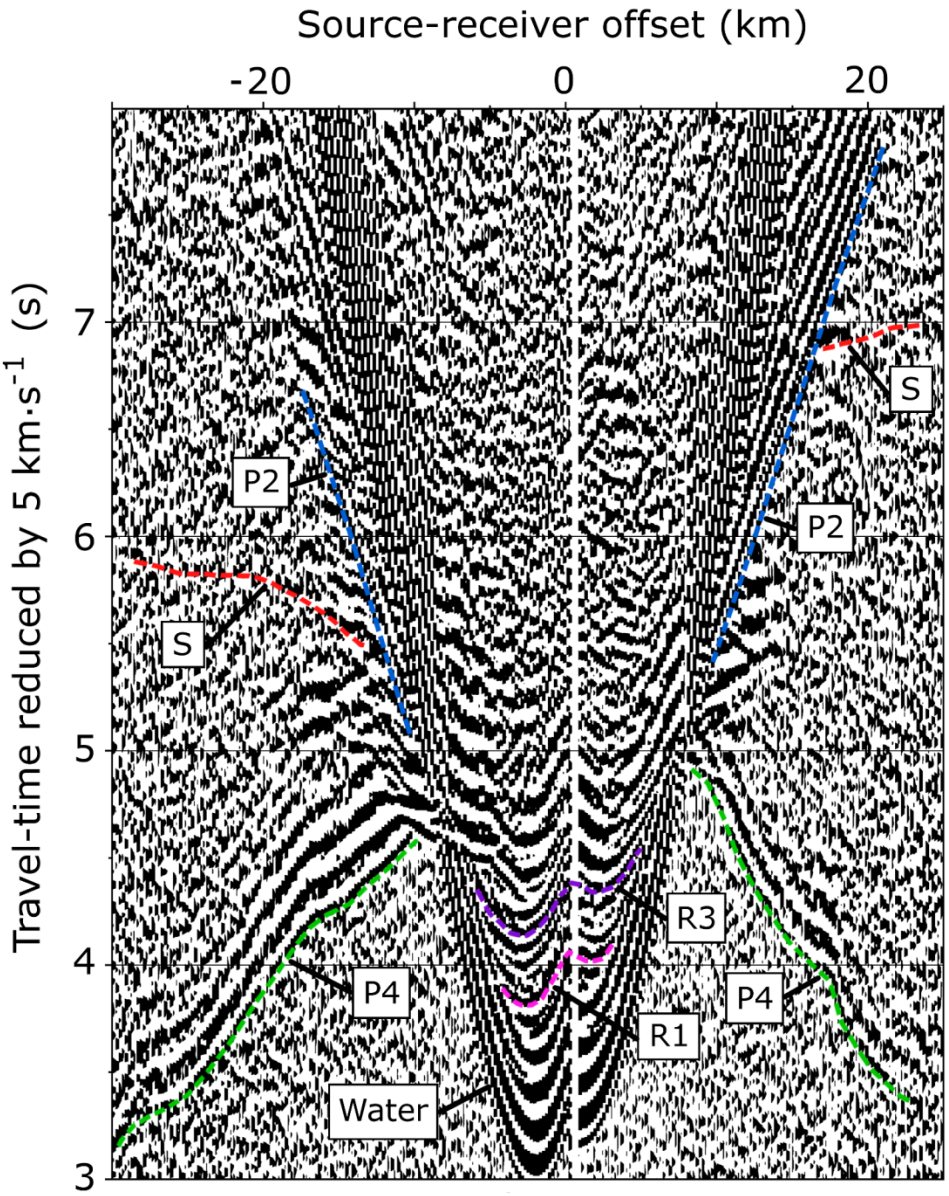

Figure A6 – A portion of the receiver gather for OBS 23 using the vertical component. Labeled are arrivals of compressional refractions and reflections (P1-P4, R1-R3). Also labeled are arrivals of the direct wave in water (Water) and shear waves (S).

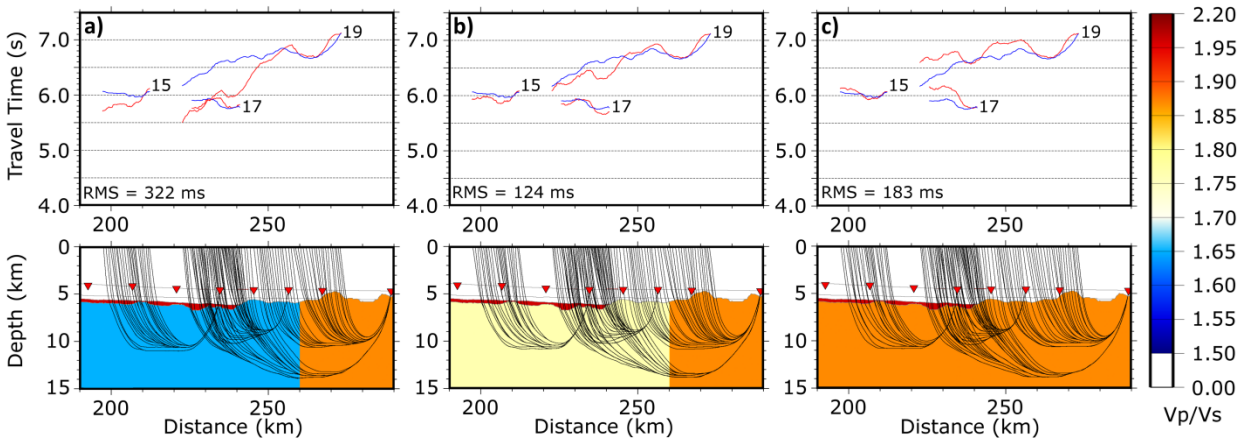

Figure A7 - Three bulk V_p / V_s ratios and their effect on shear-wave travel-time misfits for OBS 15, 17, and 19 in the Newfoundland COT. Blue and red lines are picked and caluclated shear-wave travel-time curves, respectively. Reduction velocity = 4.0 km/s. RMS = root-mean-squared misfit. a) – V_p / V_s = 1.65; b) – V_p / V_s = 1.77; c) – V_p / V_s = 1.87.

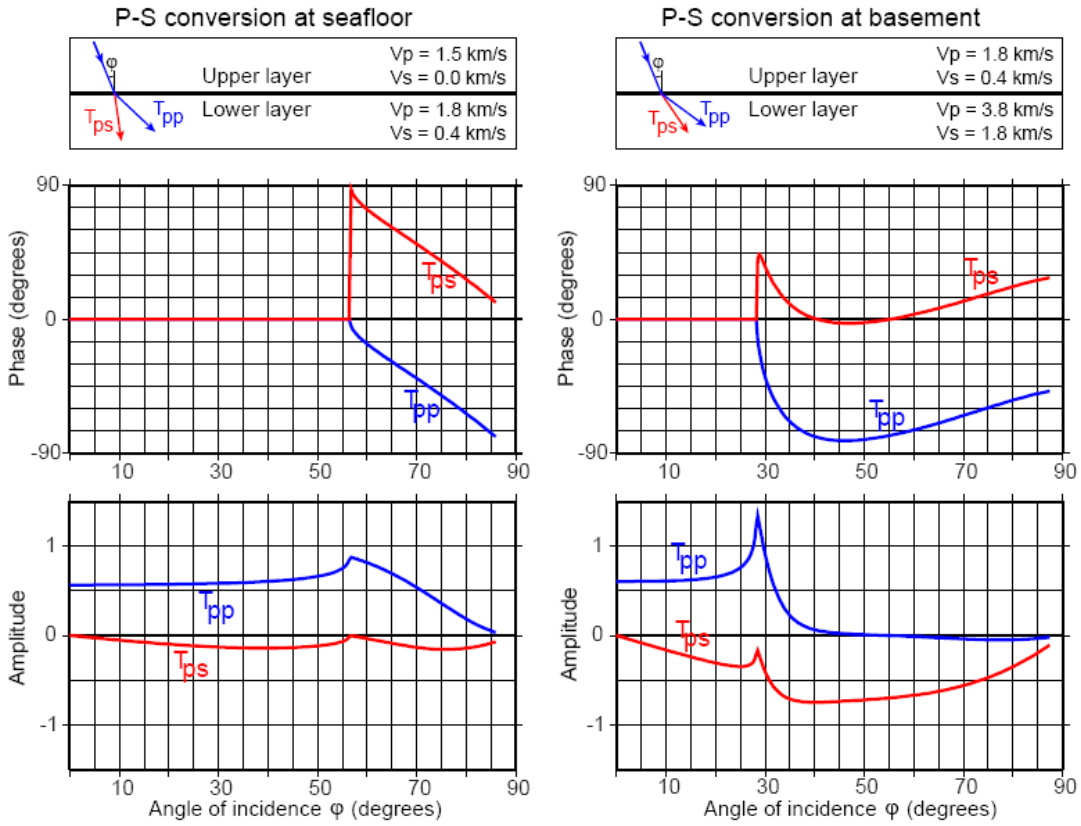

Figure A8 – P-P and P-S transmission coefficients at seafloor (left) and basement (right) as a function of incidence angle, after *Aki and Richards* [2002]. The amplitude of P-S conversions is likely minimal (< 0.20) at the seafloor for all incidence angles, but is quite substantial (0.20 - 0.75) and negative in polarity at the sediment-basement contact for all incidence angles larger than 10°.

Appendix B: Chapter 3

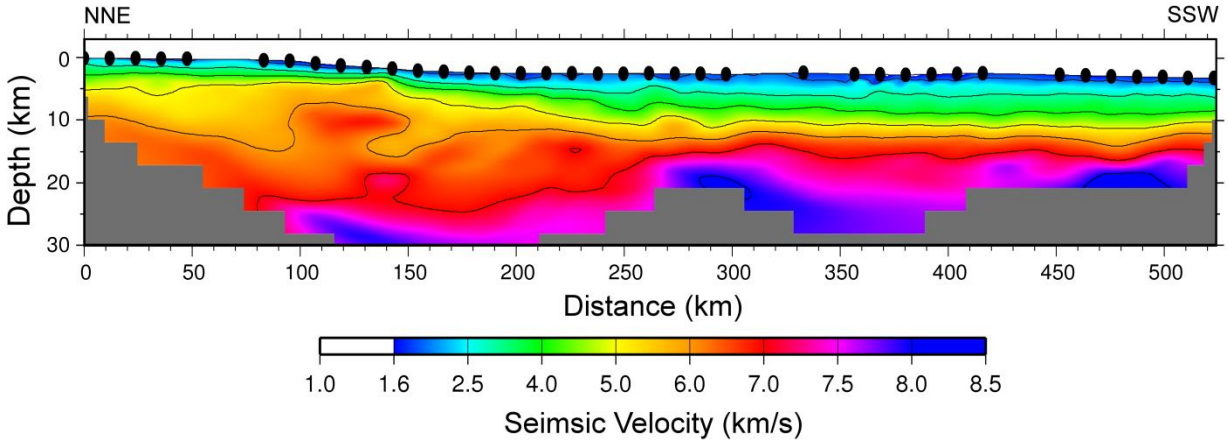

Figure B1 - Single layer seismic velocity model for GUMBO Line 3 built from inversion of only first-arriving travel times. Black dots are OBS locations. Grey material represents model space not constrained by ray paths.

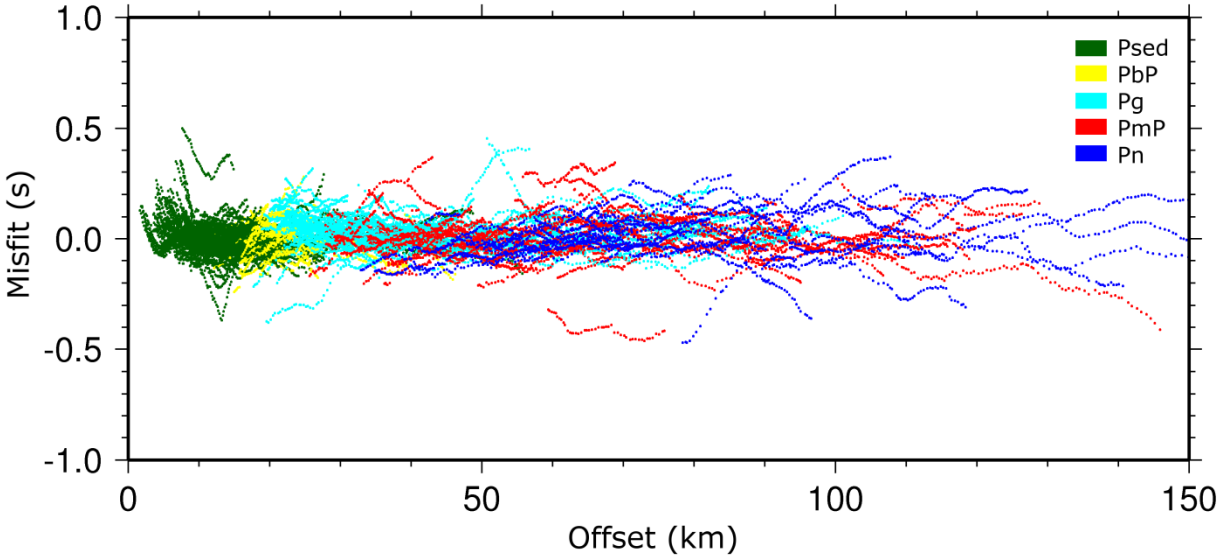

Figure B2 - Travel time misfits compared to pick offset distance for all GUMBO Line 3 OBS receiver gathers. Colors differentiate seismic refraction (*Psed*, *Pg*, *Pn*) and reflection phases (*PbP*, *PmP*).

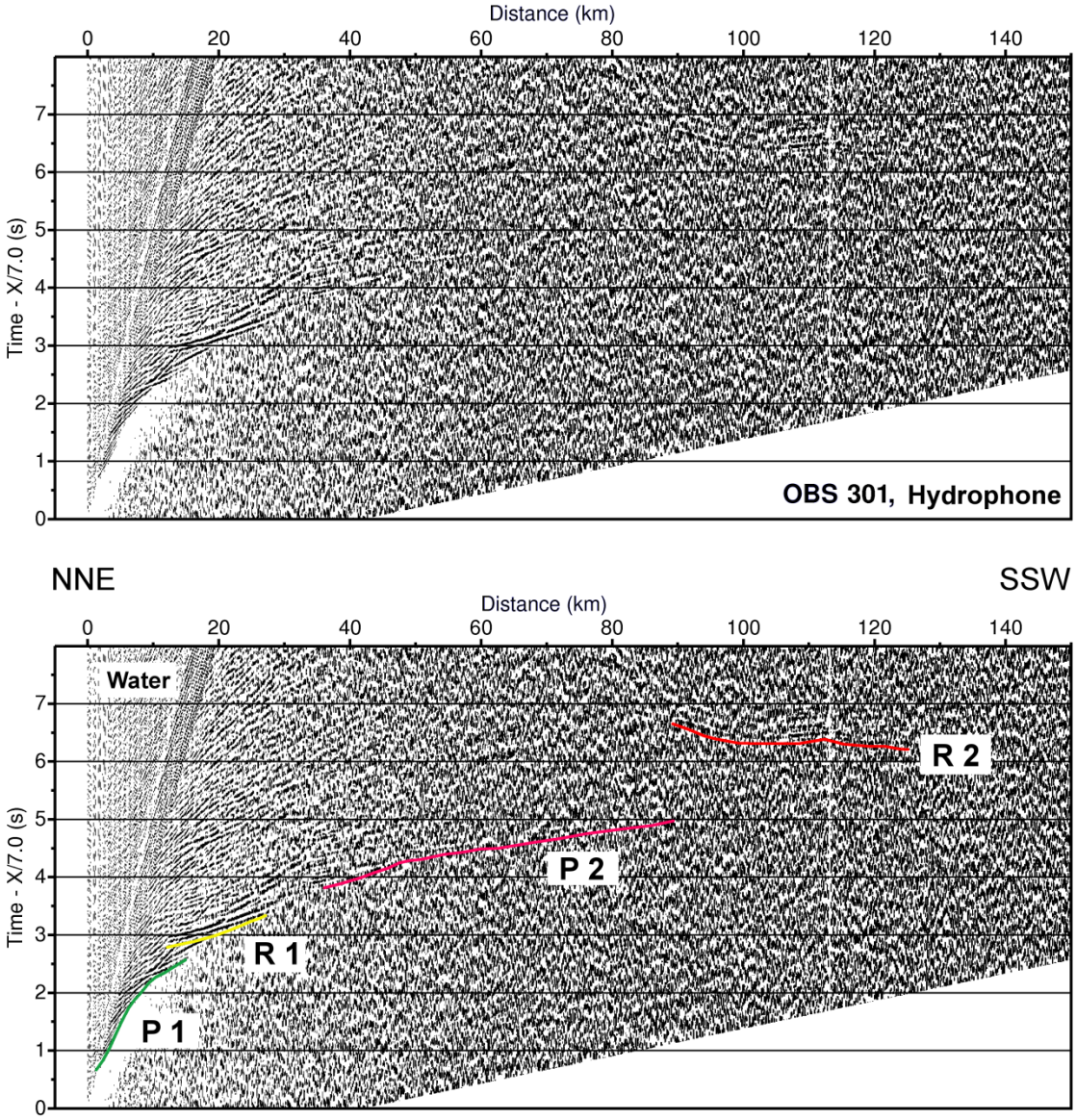

Figure B3 – Receiver gather from the hydrophone of OBS 301 (top) with interpreted travel time arrivals (bottom). A reduction velocity of 7.0 km/s is applied. Bandpass filters are used with a frequency range of 6-14 Hz. Gain is set to 1.0 and increases linearly with offset. See text for descriptions of compressional refractions (P1-P3) and reflections (R1-R2). Also labeled are arrivals of the direct wave in water (Water) and multiples (Multiple).

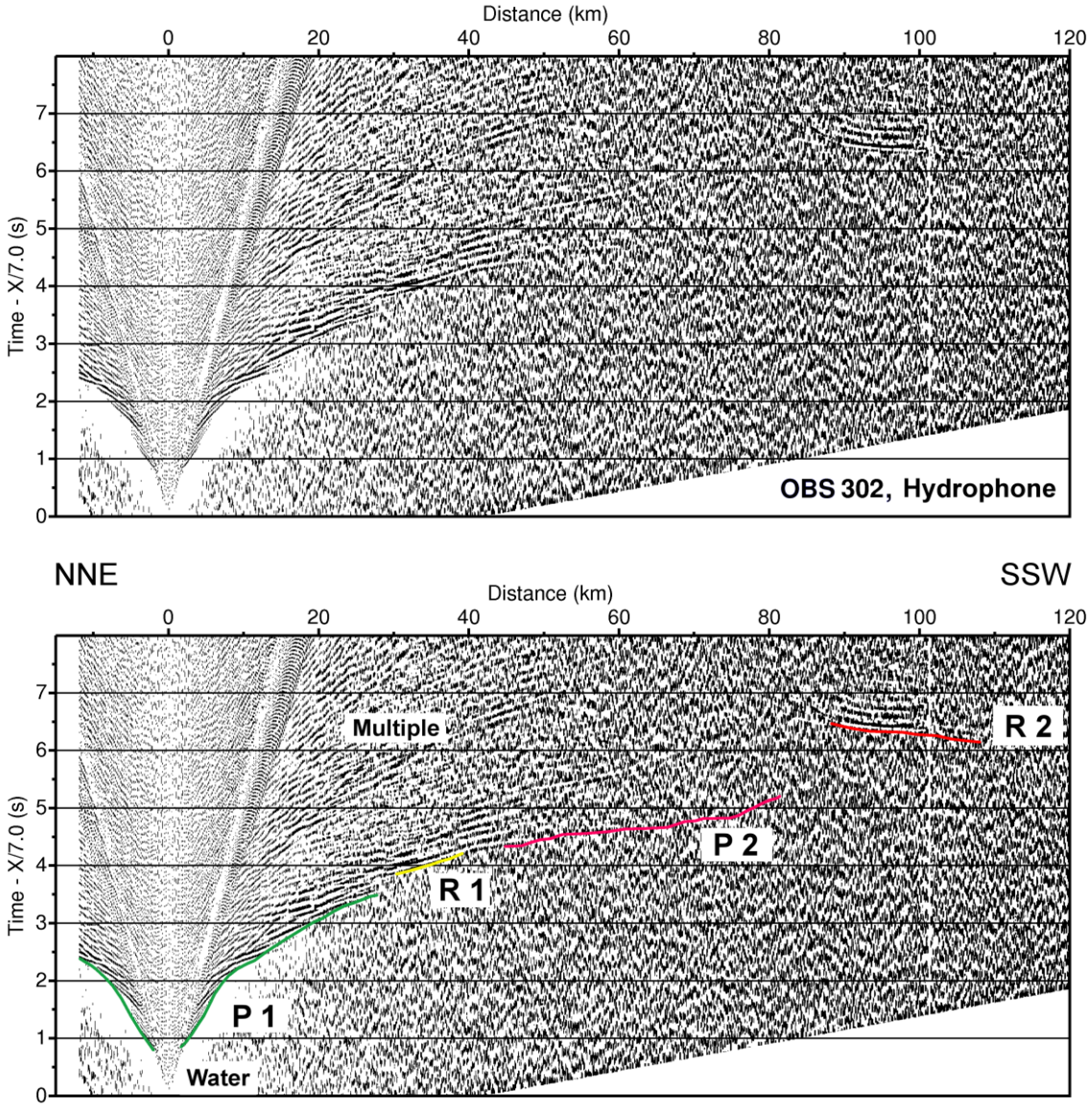

Figure B4 – Receiver gather from the hydrophone of OBS 302 (top) with interpreted travel time arrivals (bottom). See Figure B3 for further information.

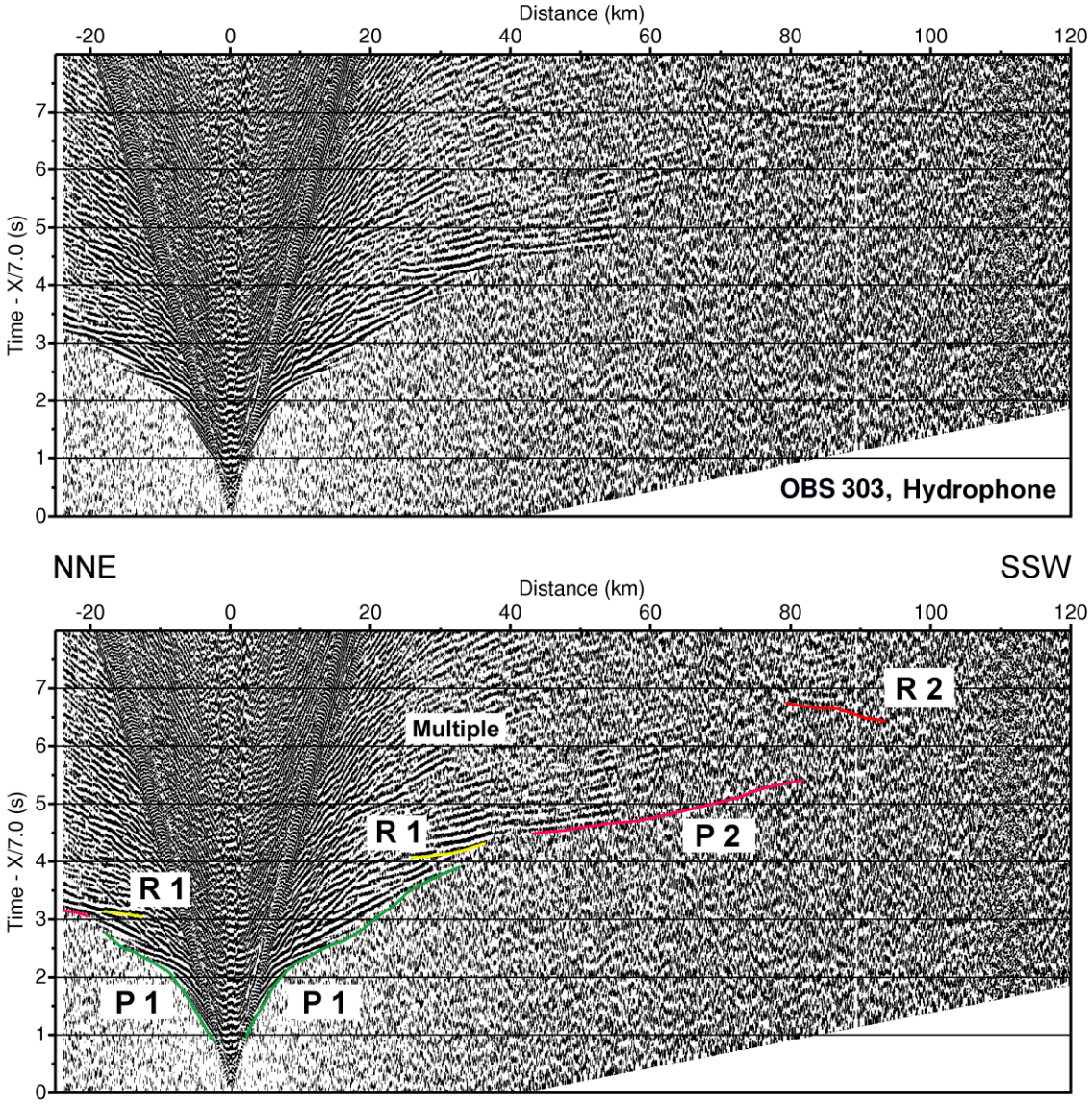

Figure B5 – Receiver gather from the hydrophone of OBS 303 (top) with interpreted travel time arrivals (bottom). See Figure B3 for further information.

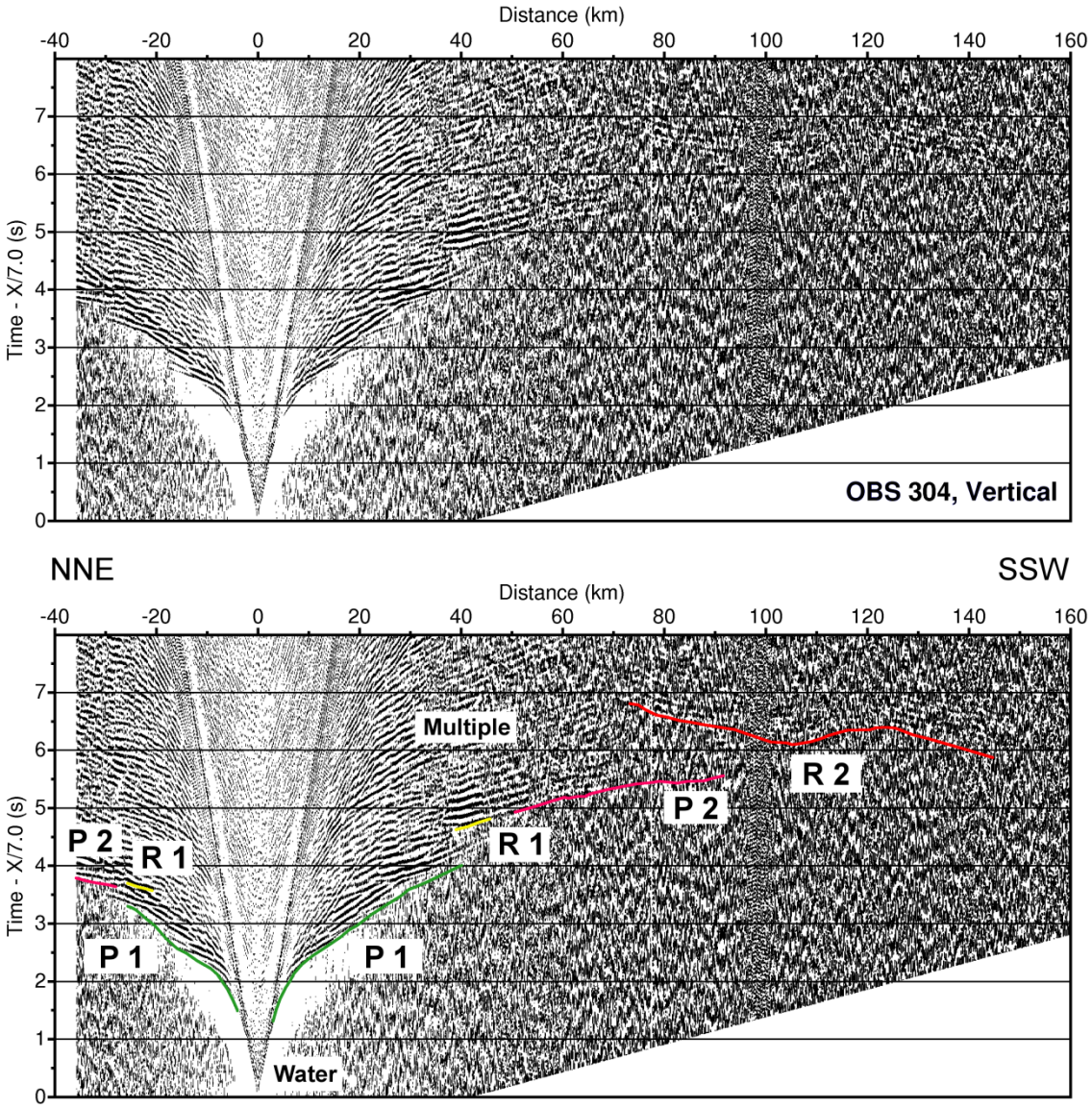

Figure B6 – Receiver gather from the vertical component of OBS 304 (top) with interpreted travel time arrivals (bottom). See Figure B3 for further information.

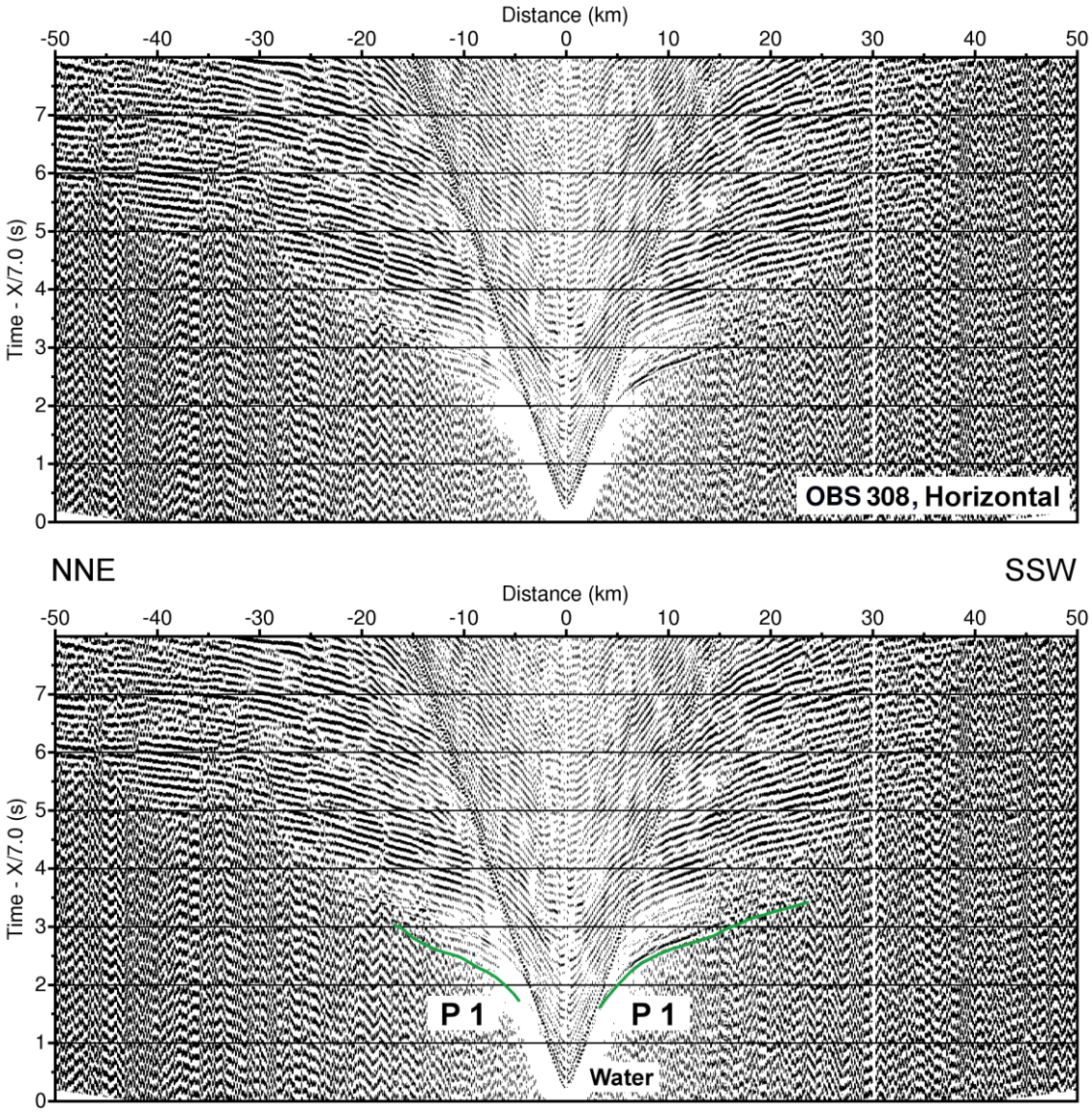

Figure B7 – Receiver gather from the horizontal component of OBS 308 (top) with interpreted travel time arrivals (bottom). See Figure B3 for further information.

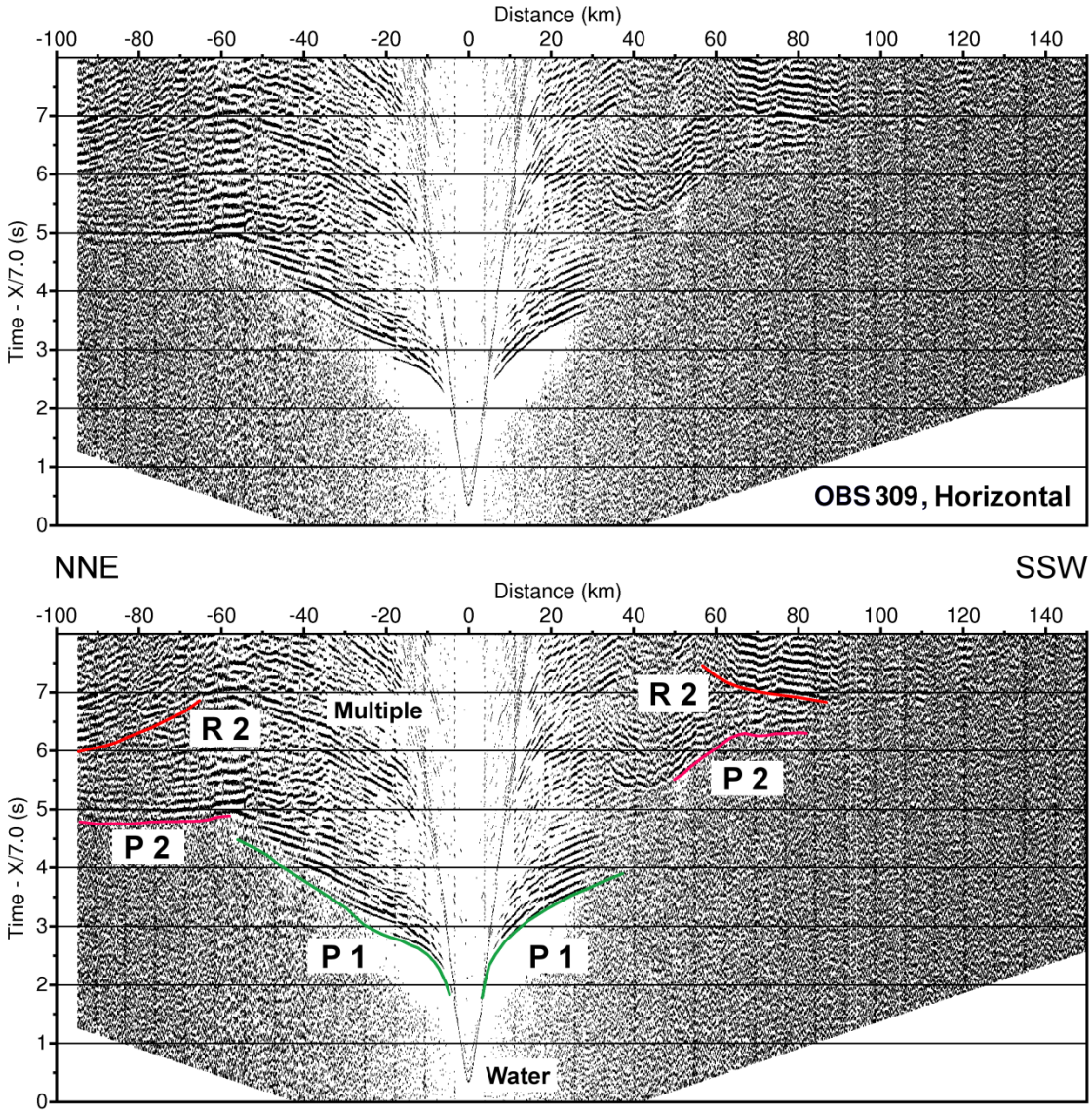

Figure B8 – Receiver gather from the vertical component of OBS 304 (top) with interpreted travel time arrivals (bottom). See Figure B3 for further information.

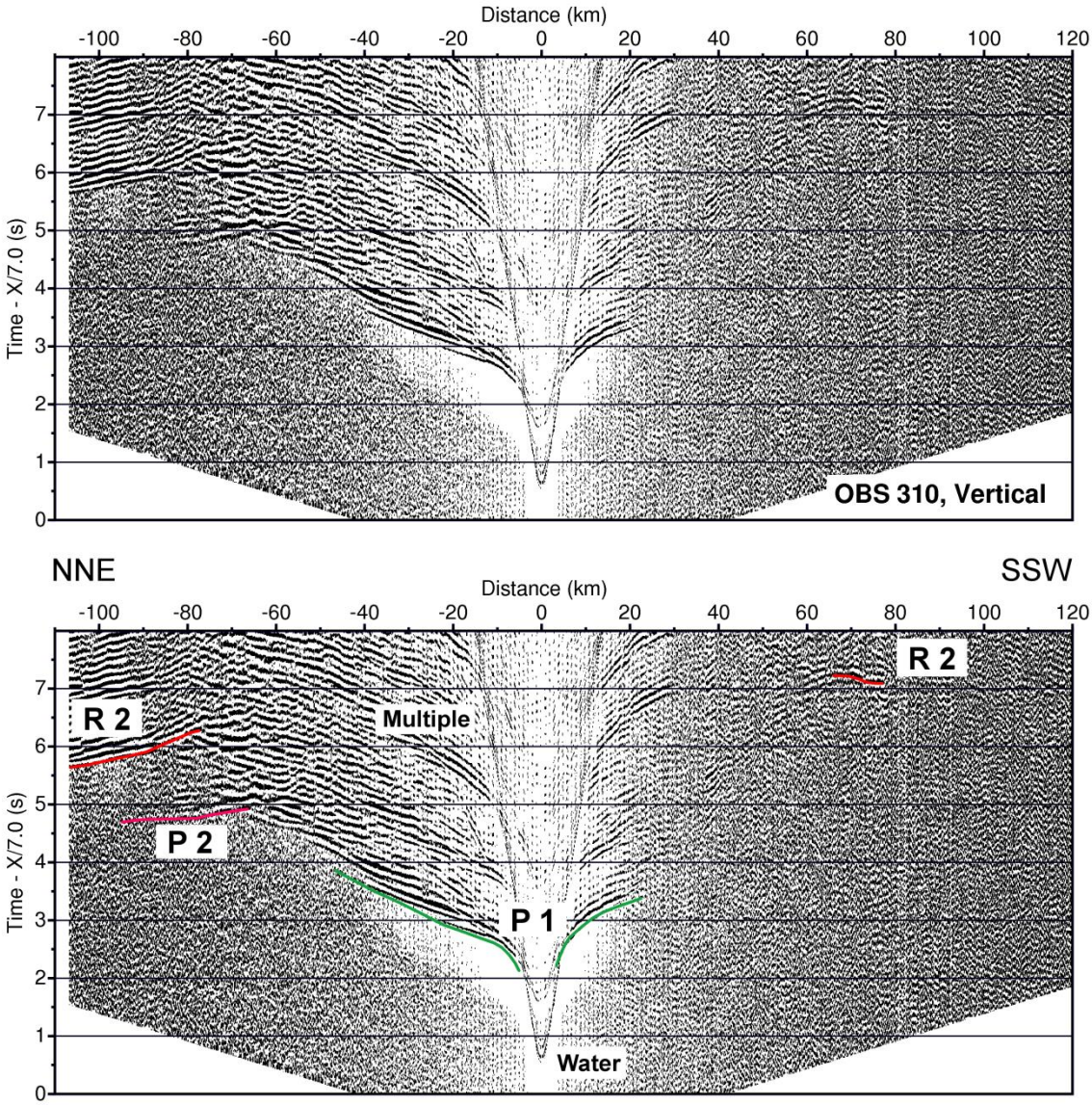

Figure B9 – Receiver gather from the vertical component of OBS 310 (top) with interpreted travel time arrivals (bottom). See Figure B3 for further information.

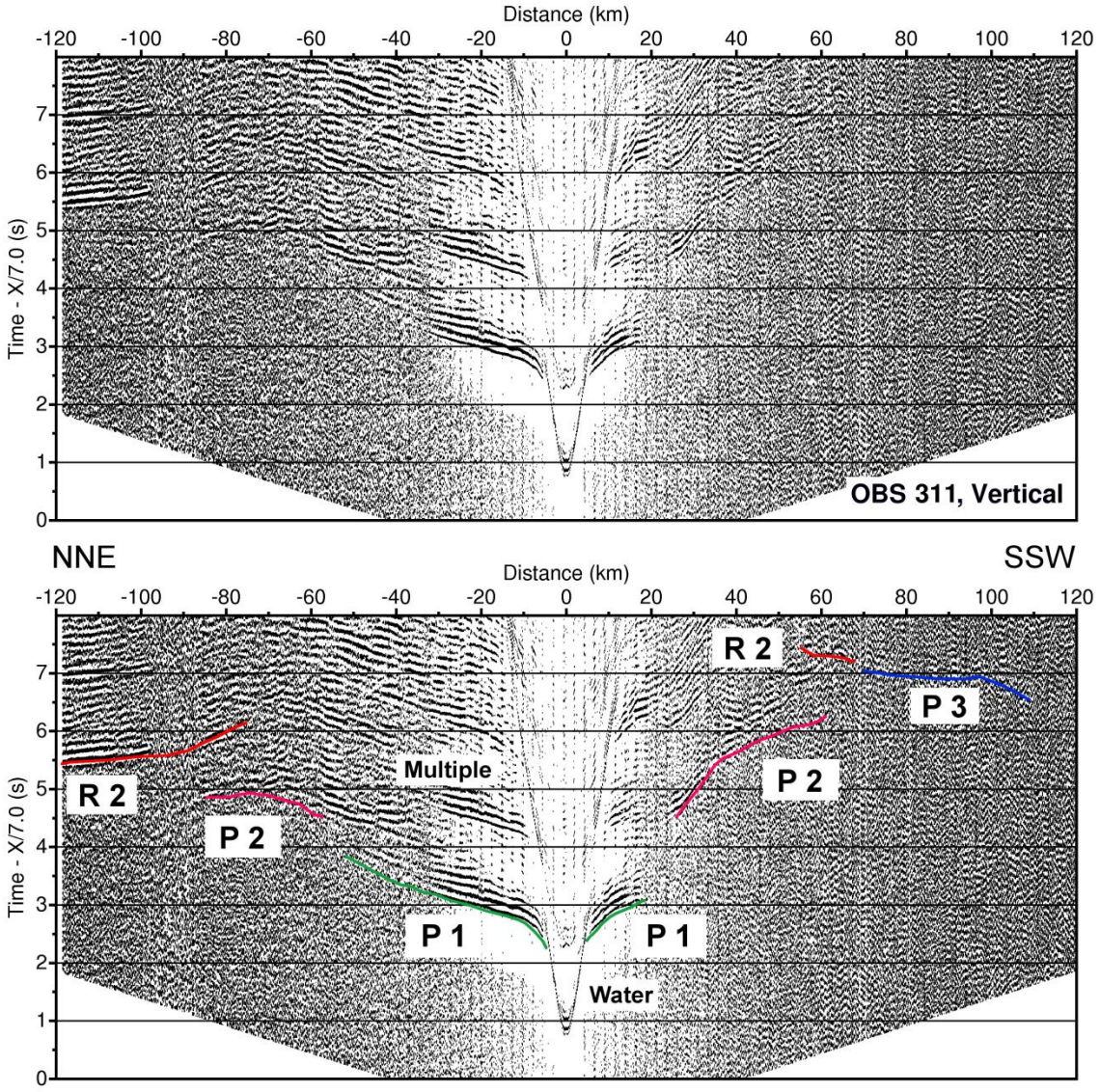

Figure B10 – Receiver gather from the vertical component of OBS 311 (top) with interpreted travel time arrivals (bottom). See Figure B3 for further information.

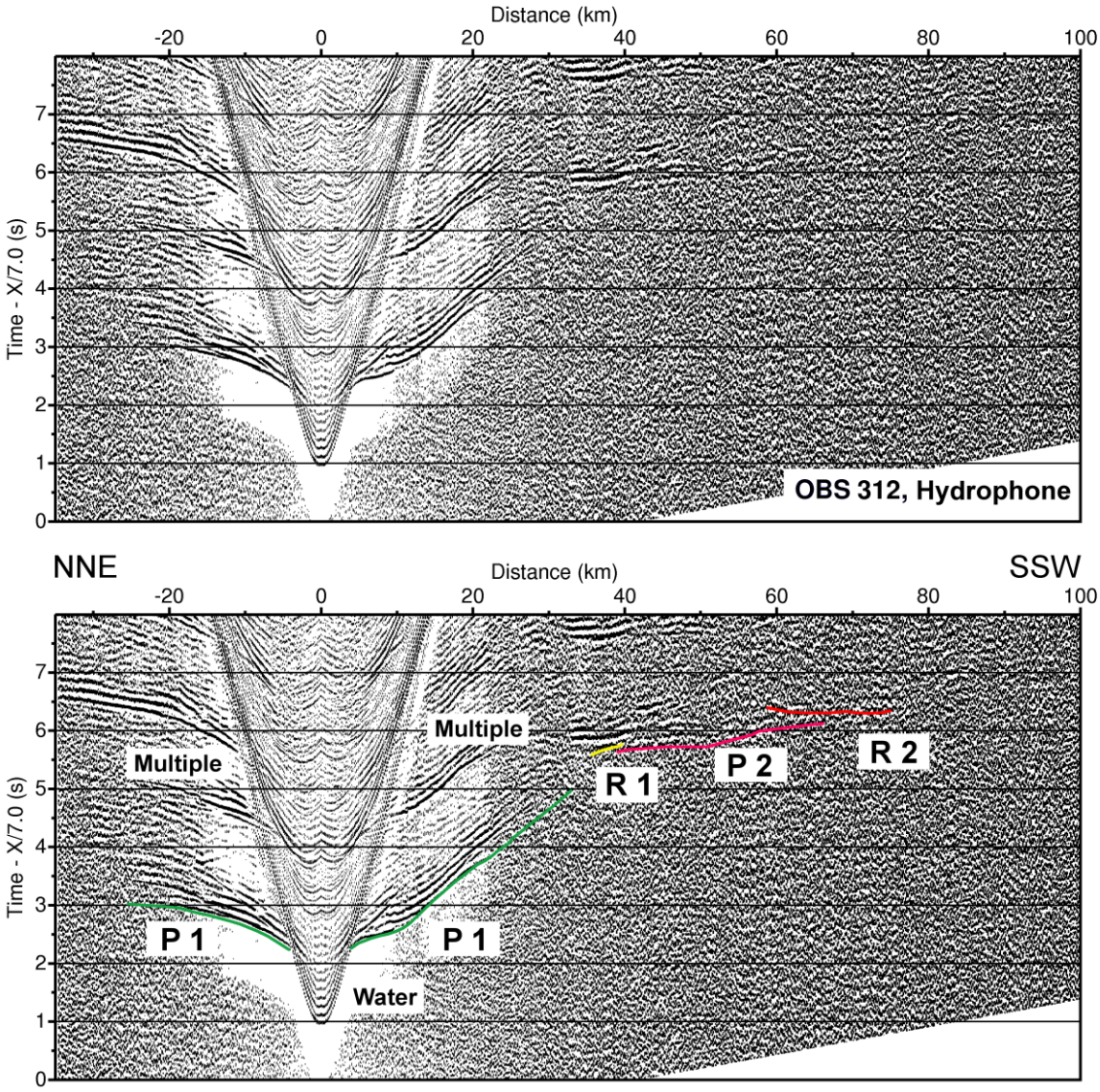

Figure B11 – Receiver gather from the hydrophone of OBS 312 (top) with interpreted travel time arrivals (bottom). See Figure B3 for further information.

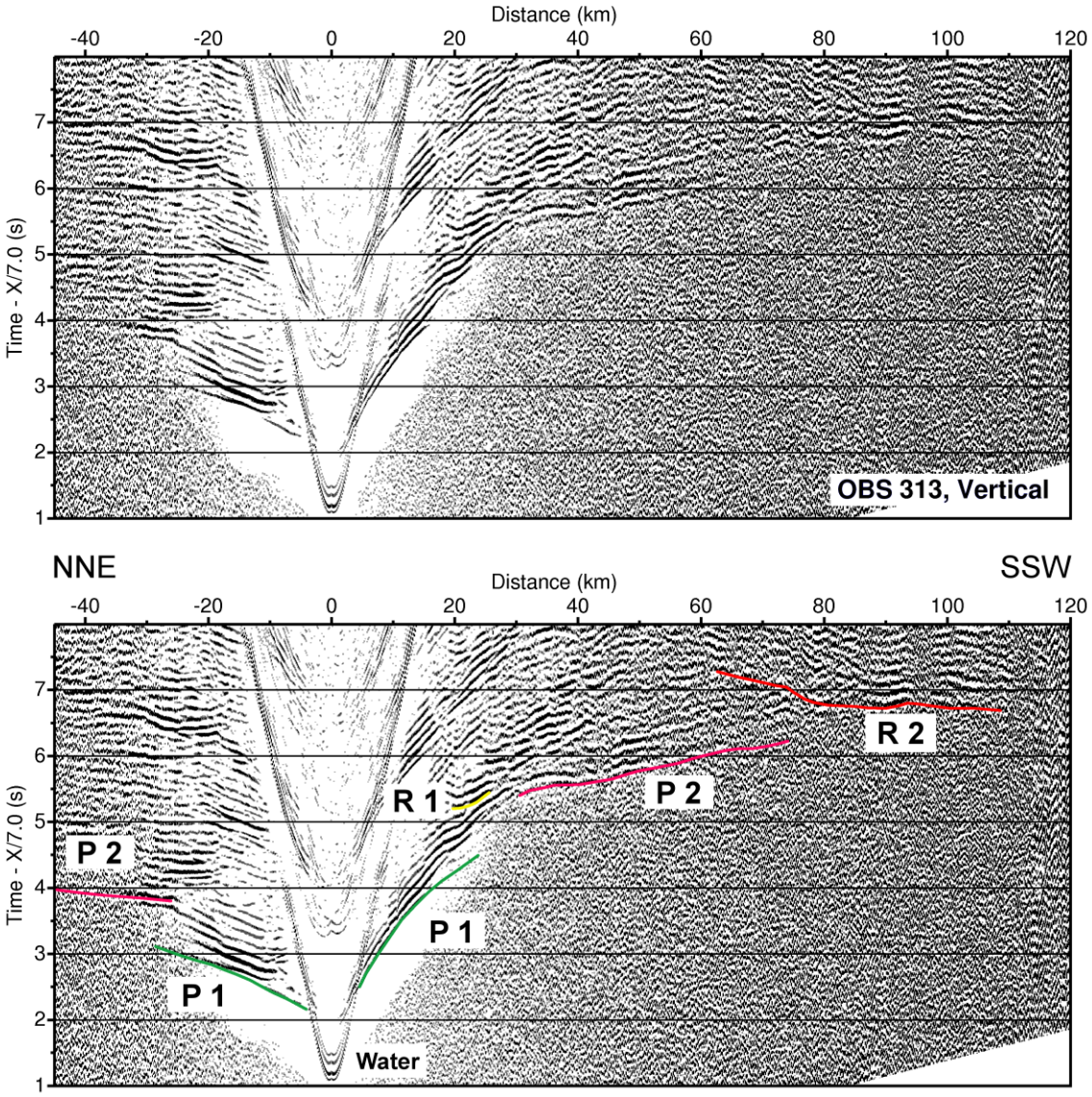

Figure B12 – Receiver gather from the vertical component of OBS 313 (top) with interpreted travel time arrivals (bottom). See Figure B3 for further information.

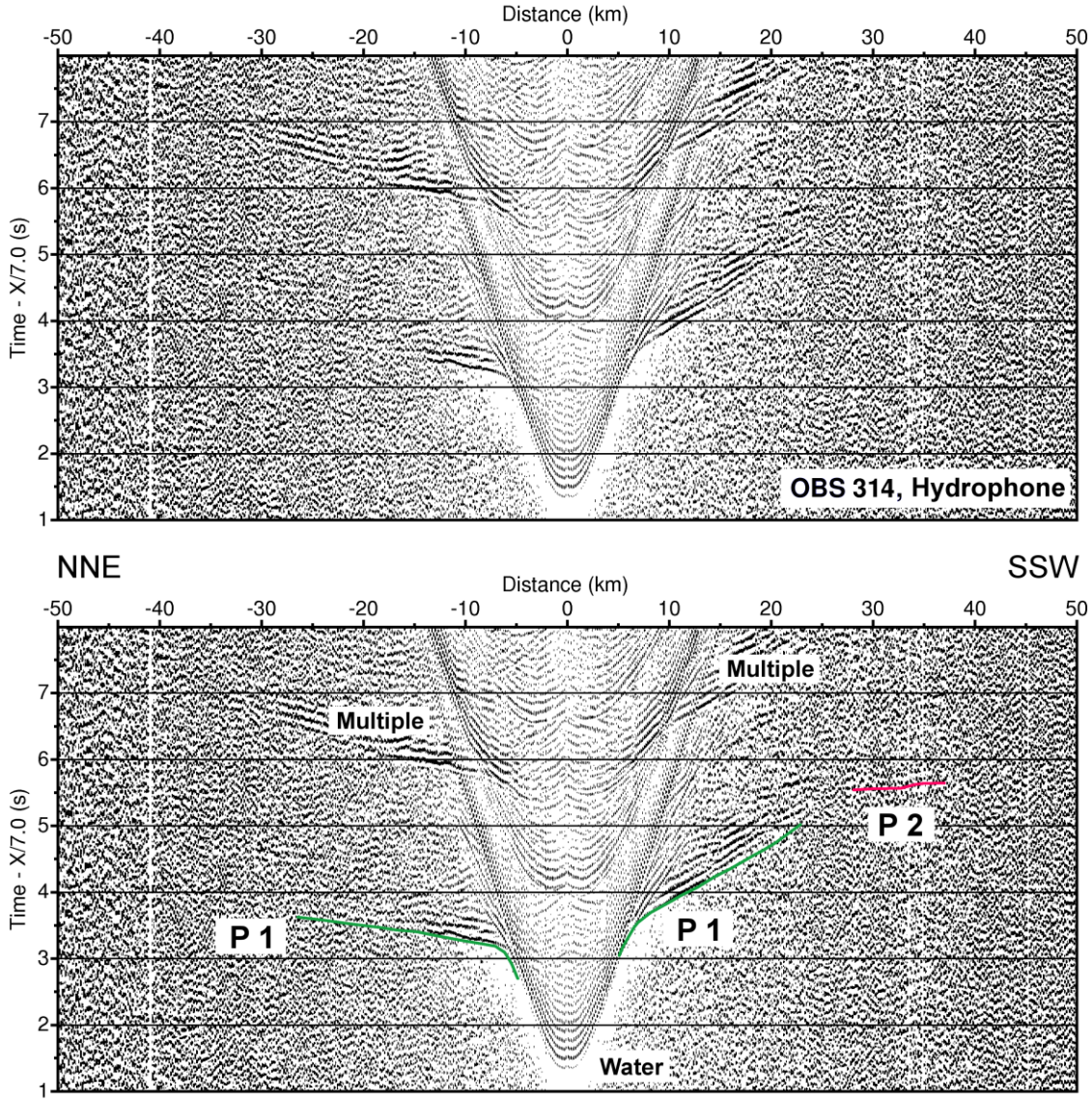

Figure B13 – Receiver gather from the hydrophone of OBS 314 (top) with interpreted travel time arrivals (bottom). See Figure B3 for further information.

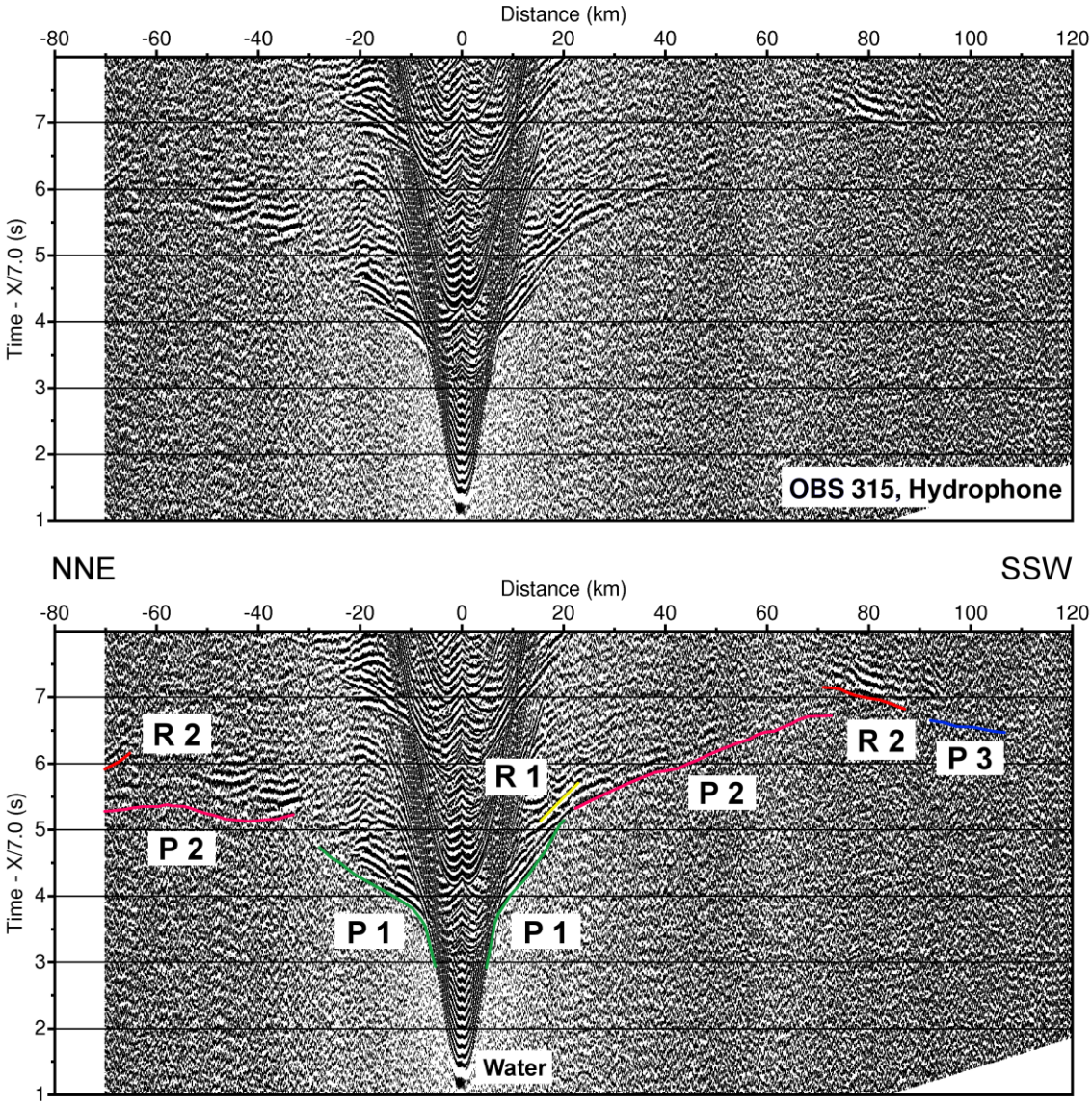

Figure B14 – Receiver gather from the hydrophone of OBS 315 (top) with interpreted travel time arrivals (bottom). See Figure B3 for further information.

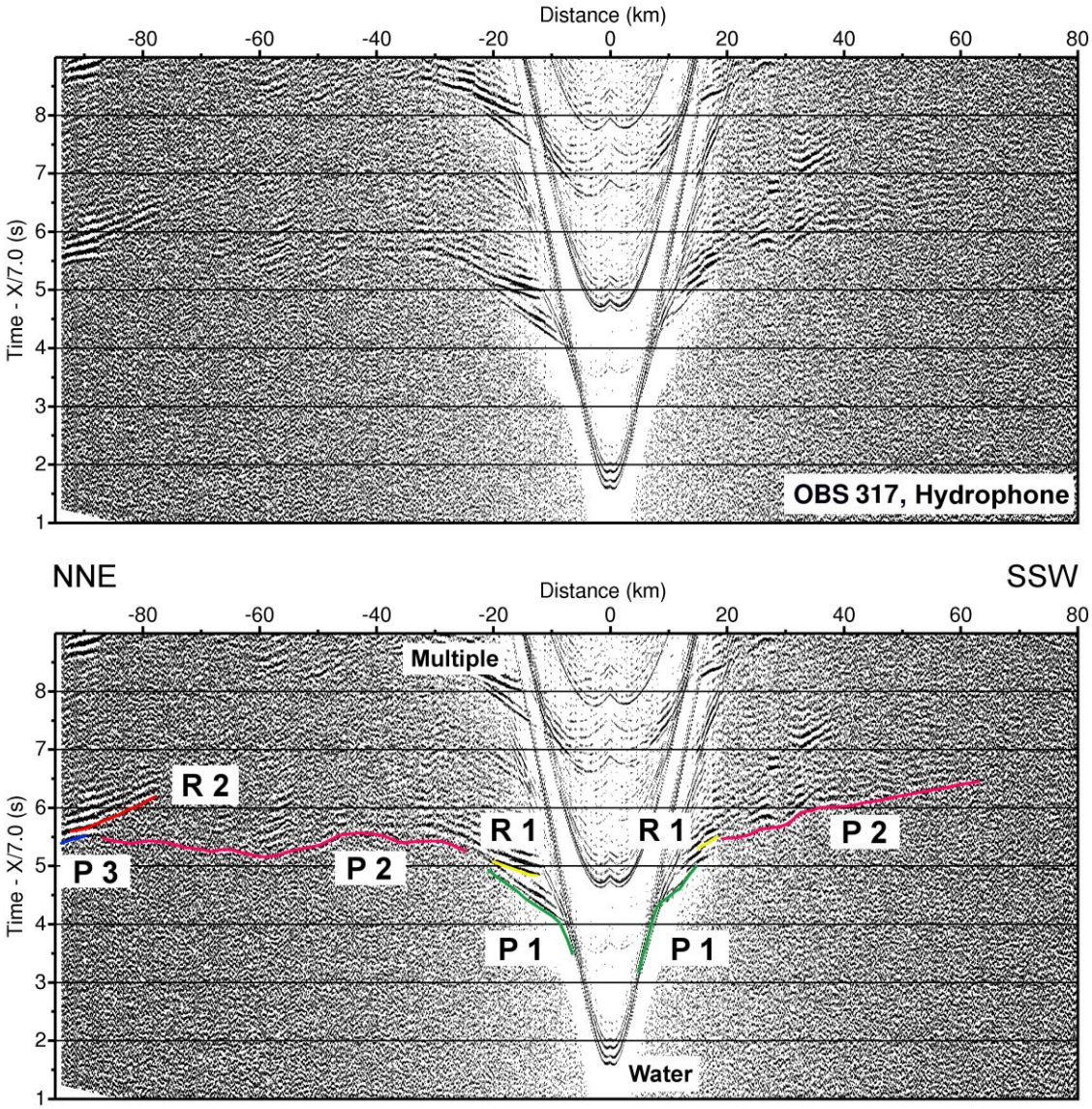

Figure B15 – Receiver gather from the hydrophone of OBS 317 (top) with interpreted travel time arrivals (bottom). See Figure B3 for further information.

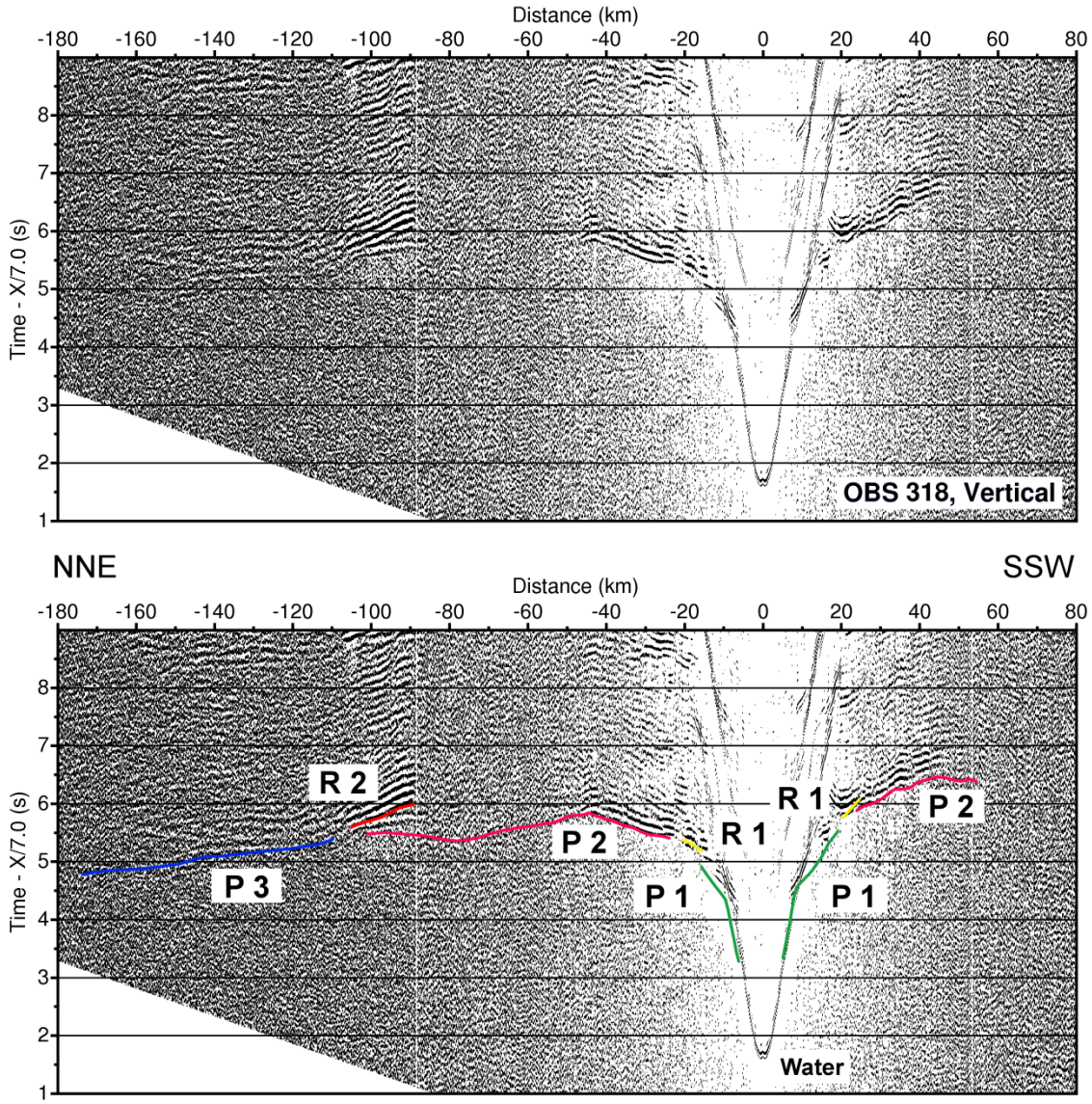

Figure B16 – Receiver gather from the vertical component of OBS 318 (top) with interpreted travel time arrivals (bottom). See Figure B3 for further information.

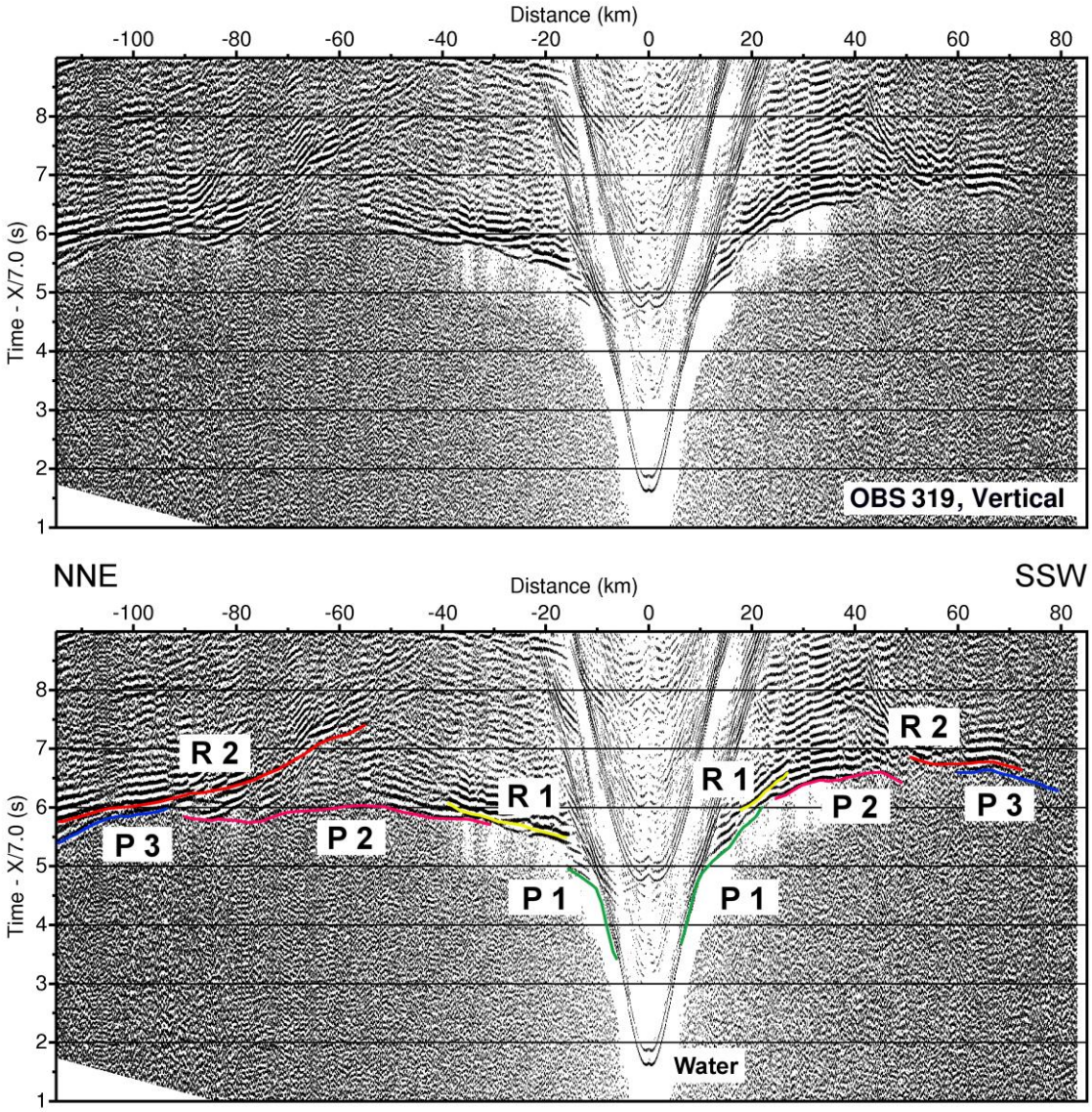

Figure B17 – Receiver gather from the vertical component of OBS 319 (top) with interpreted travel time arrivals (bottom). See Figure B3 for further information.

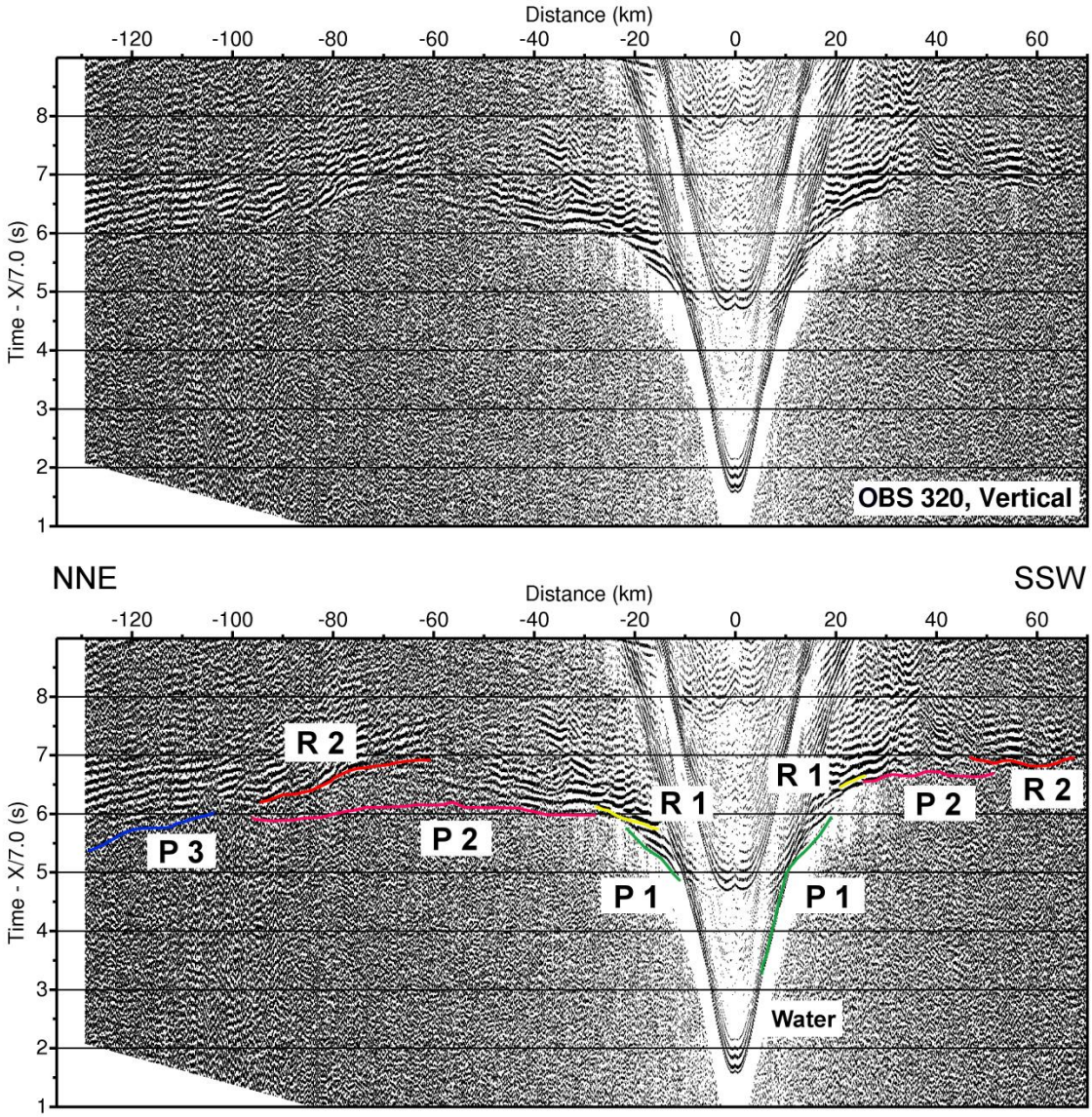

Figure B18 – Receiver gather from the vertical component of OBS 320 (top) with interpreted travel time arrivals (bottom). See Figure B3 for further information.

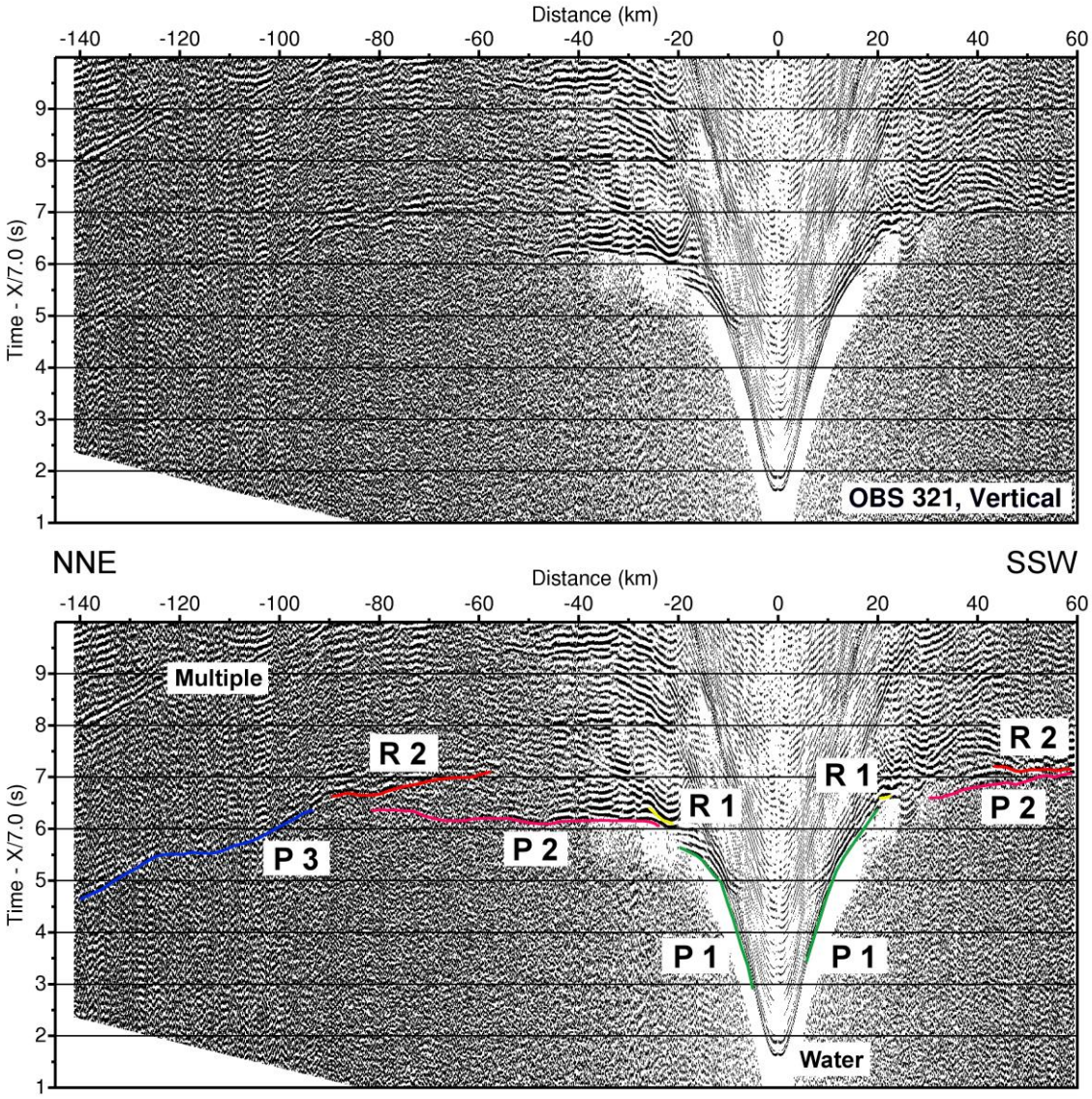

Figure B19 – Receiver gather from the vertical component of OBS 321 (top) with interpreted travel time arrivals (bottom). See Figure B3 for further information.

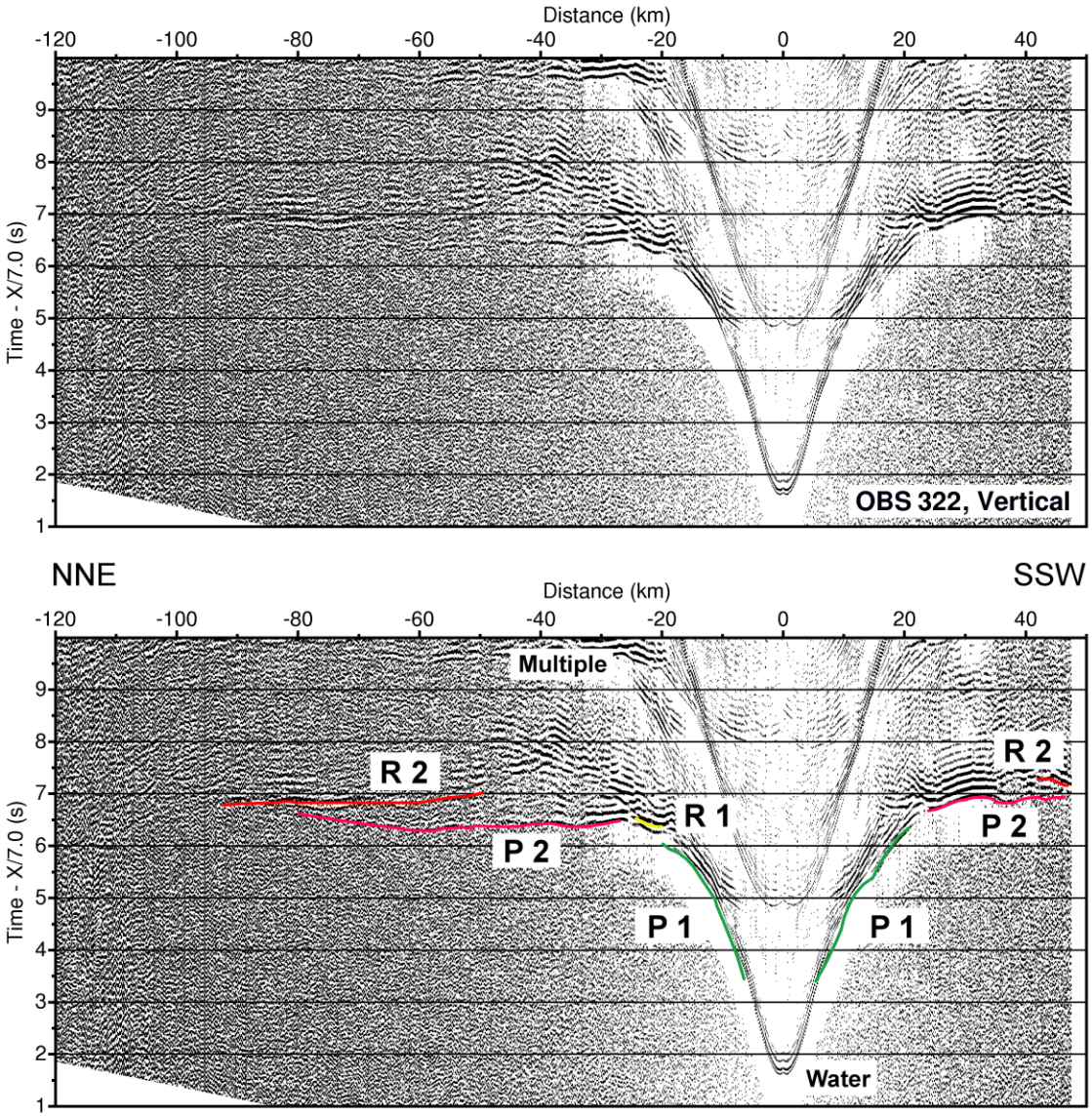

Figure B20 – Receiver gather from the vertical component of OBS 322 (top) with interpreted travel time arrivals (bottom). See Figure B3 for further information.

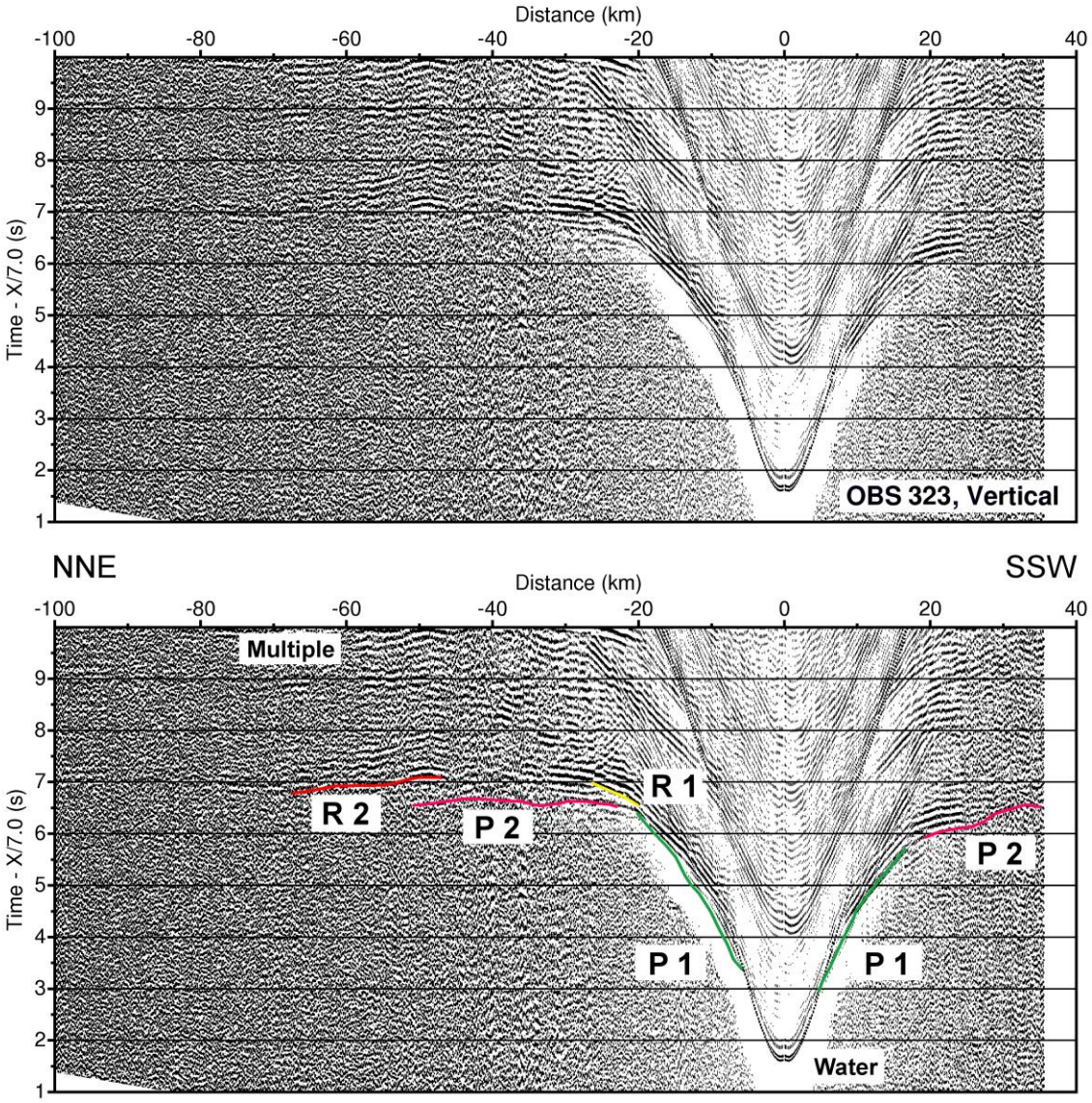

Figure B21 – Receiver gather from the vertical component of OBS 323 (top) with interpreted travel time arrivals (bottom). See Figure B3 for further information.

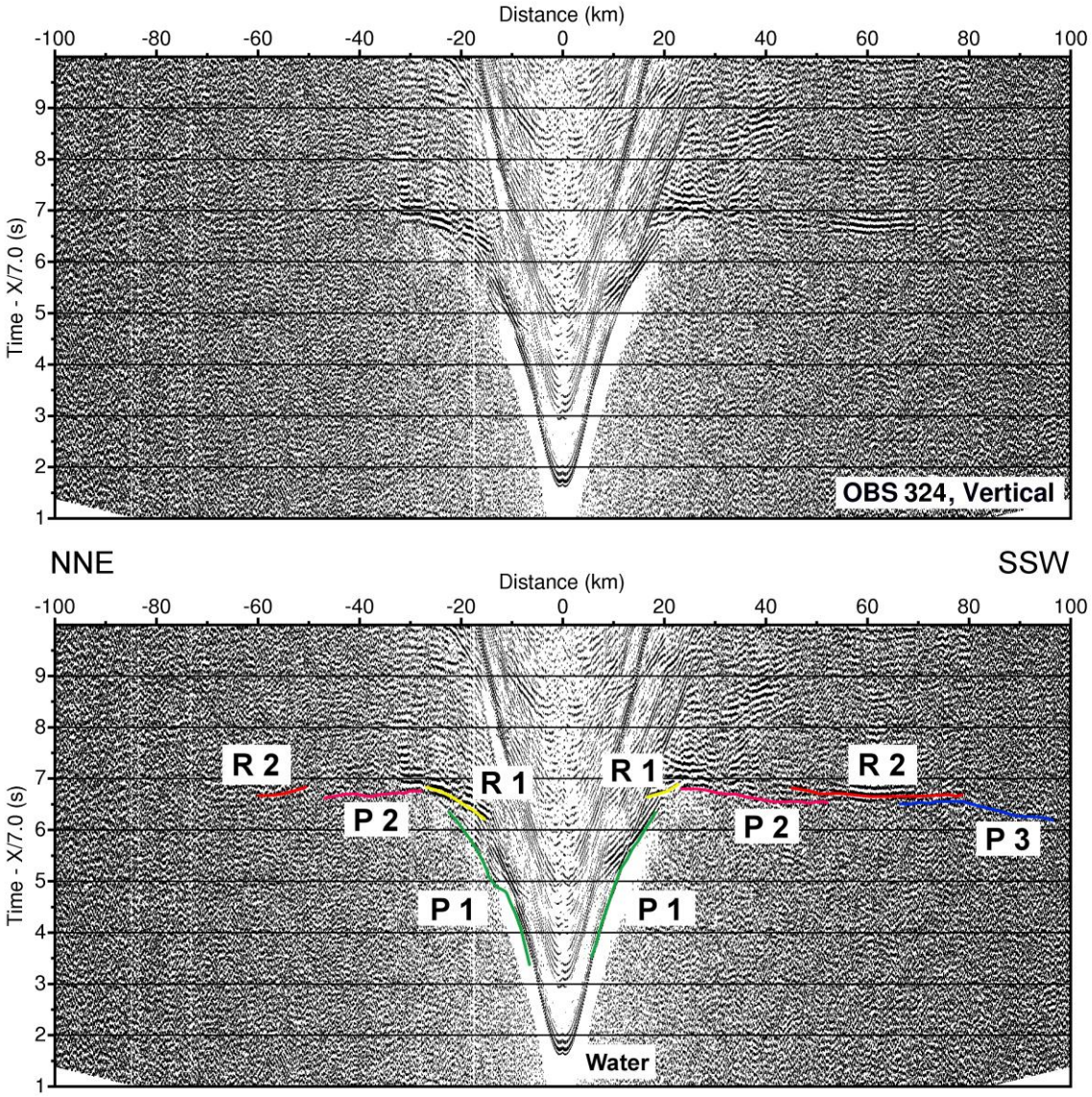

Figure B22 – Receiver gather from the vertical component of OBS 324 (top) with interpreted travel time arrivals (bottom). See Figure B3 for further information.

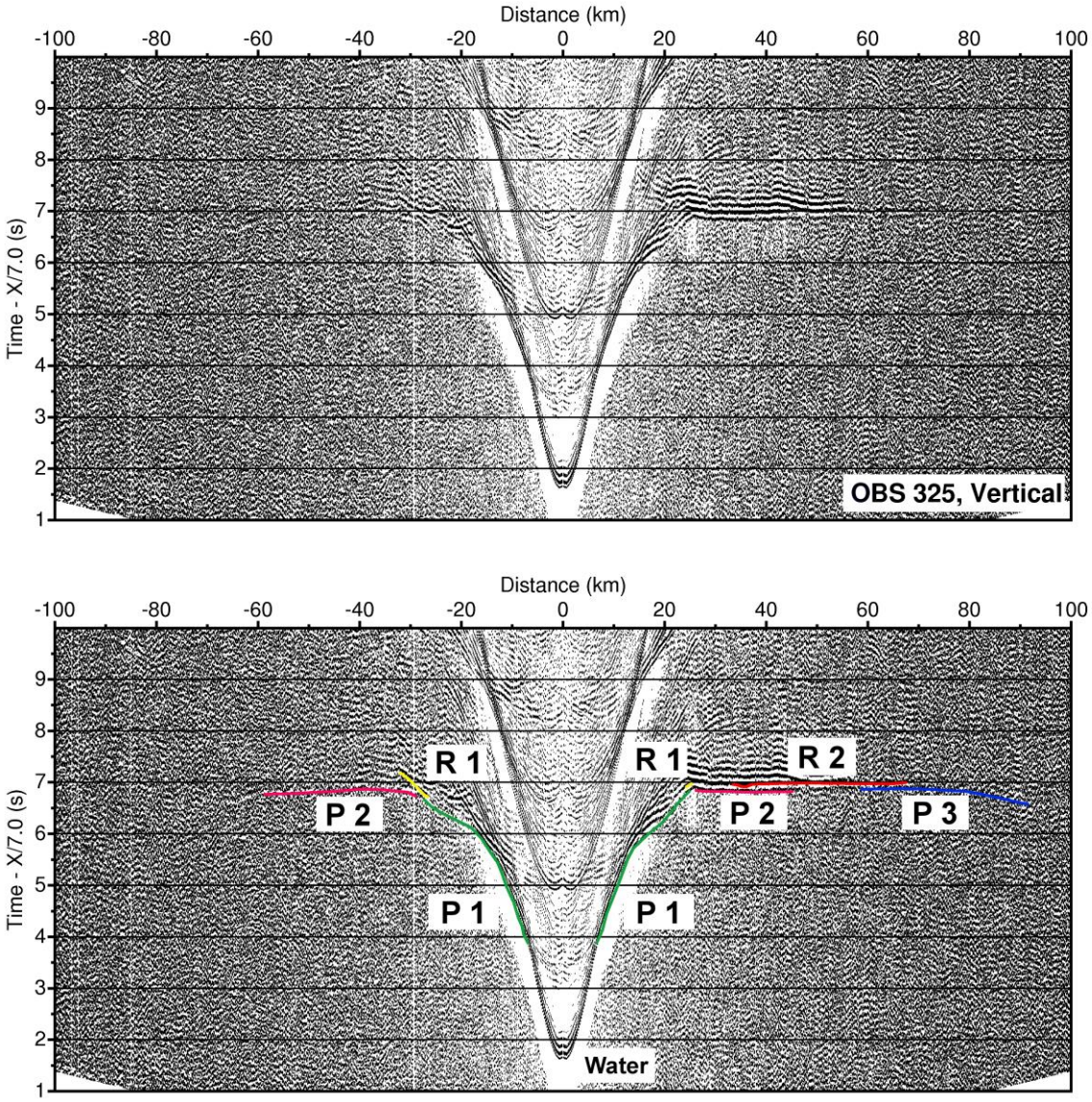

Figure B23 – Receiver gather from the vertical component of OBS 325 (top) with interpreted travel time arrivals (bottom). See Figure B3 for further information.

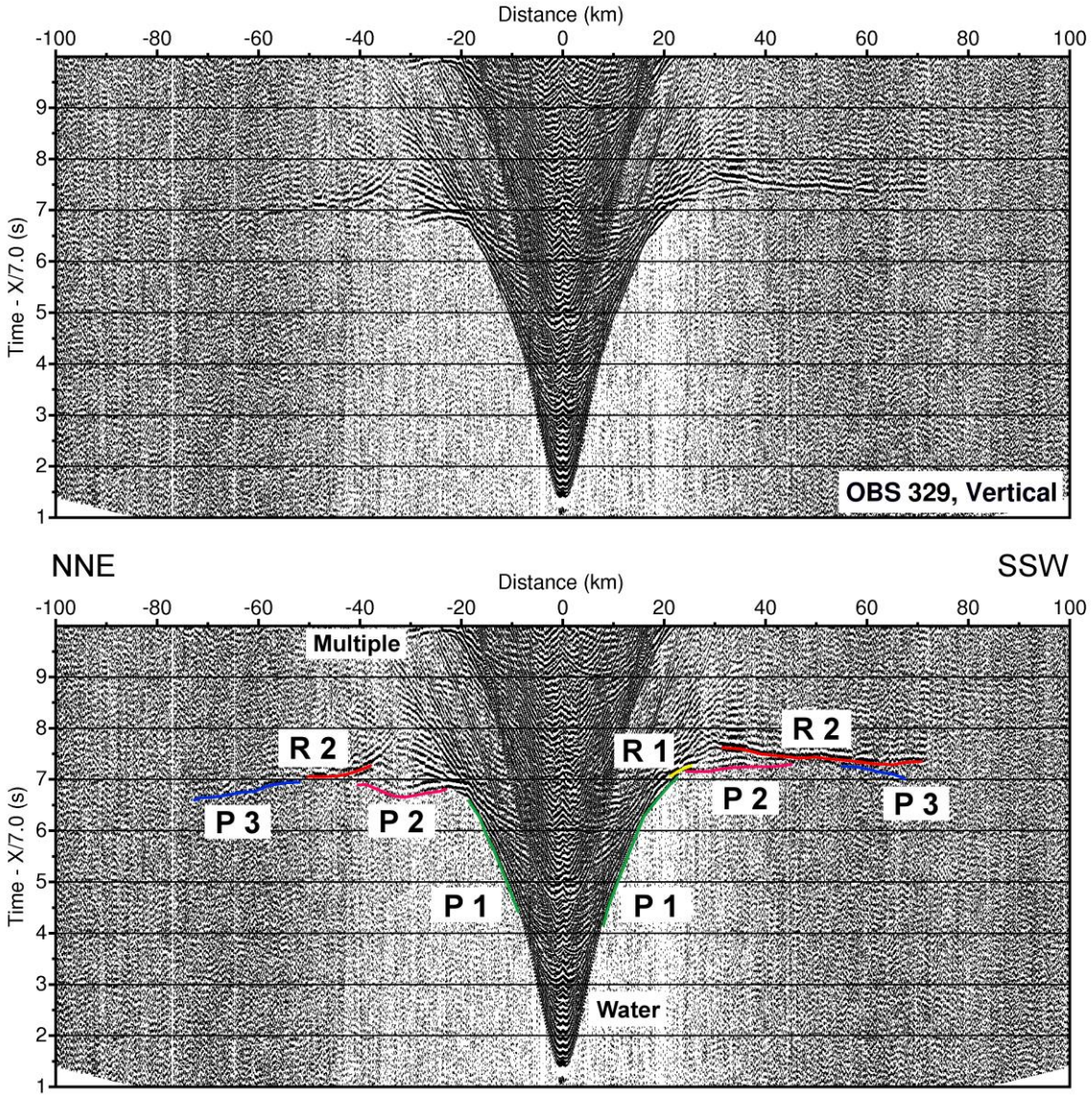

Figure B24 – Receiver gather from the vertical component of OBS 329 (top) with interpreted travel time arrivals (bottom). See Figure B3 for further information.

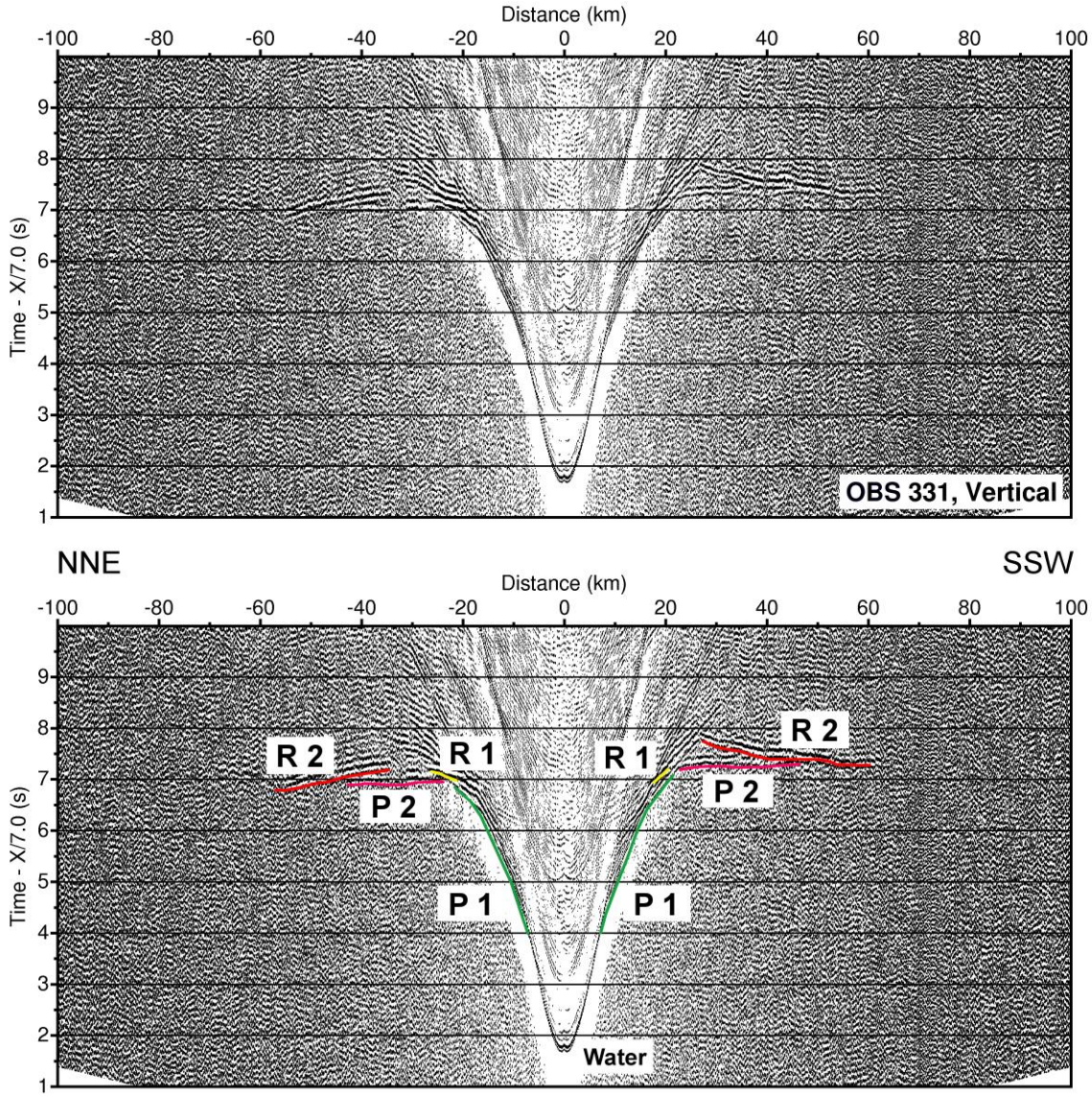

Figure B25 – Receiver gather from the vertical component of OBS 331 (top) with interpreted travel time arrivals (bottom). See Figure B3 for further information.

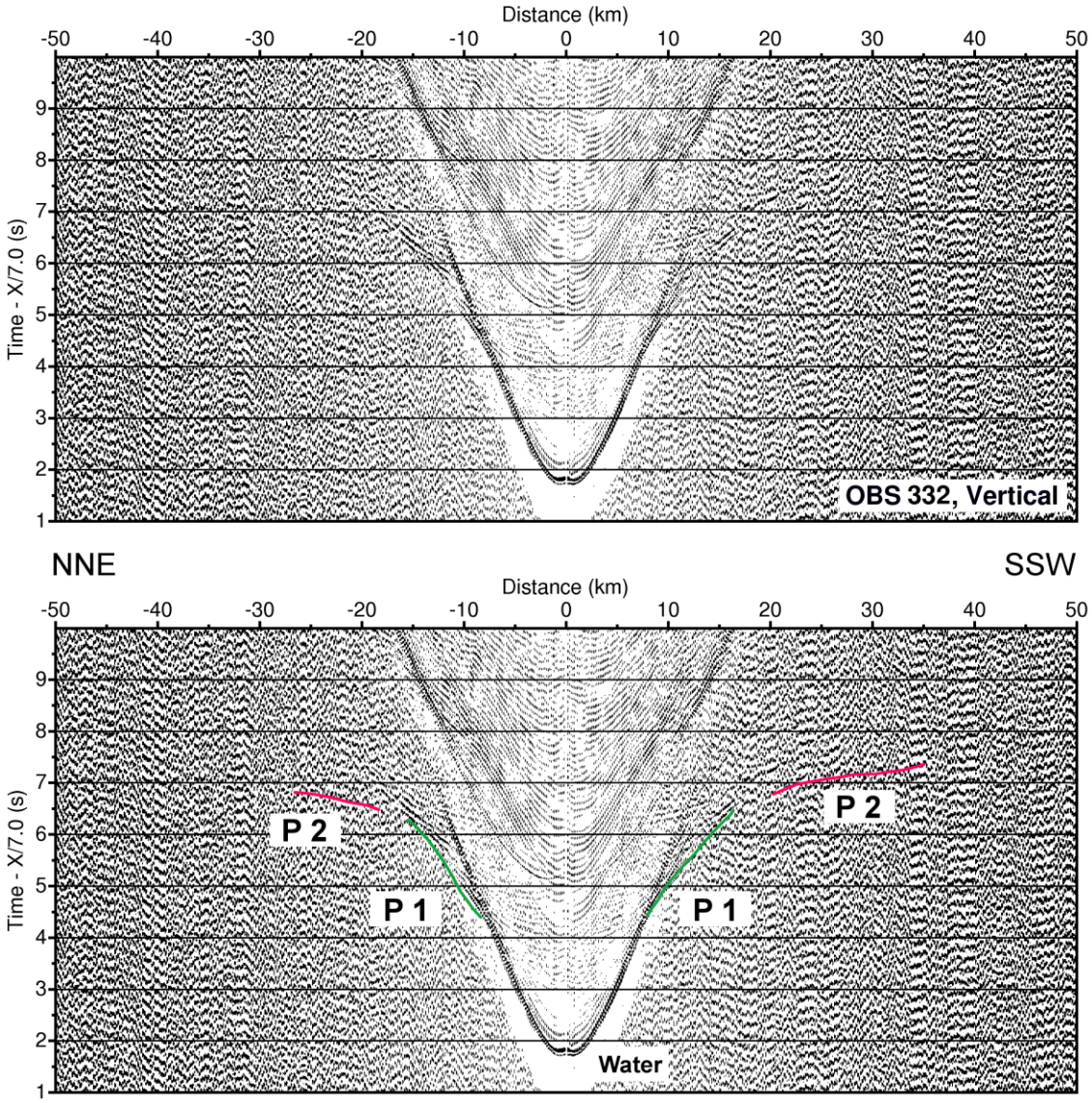

Figure B26 – Receiver gather from the vertical component of OBS 332 (top) with interpreted travel time arrivals (bottom). See Figure B3 for further information.

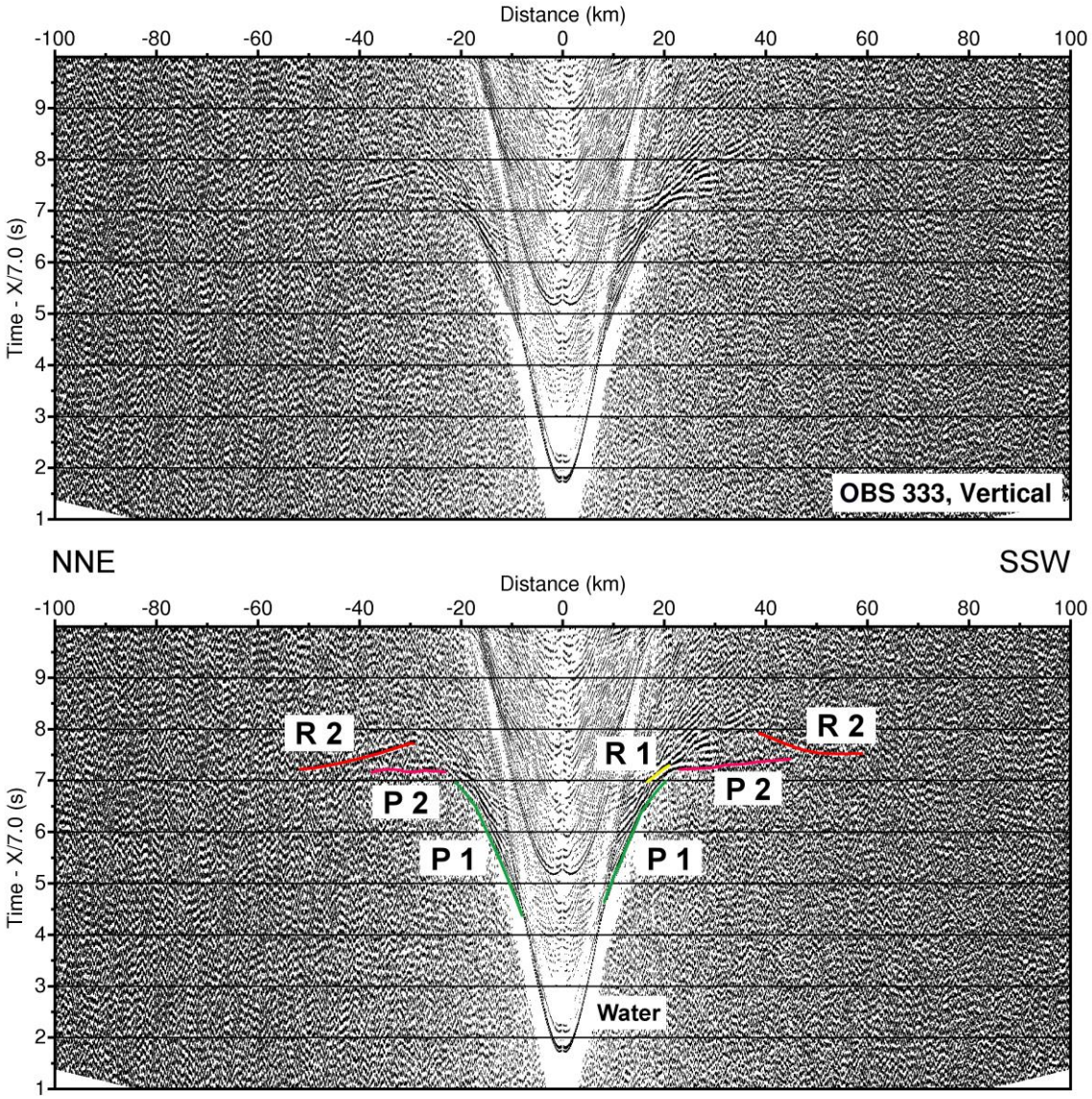

Figure B27 – Receiver gather from the vertical component of OBS 333 (top) with interpreted travel time arrivals (bottom). See Figure B3 for further information.

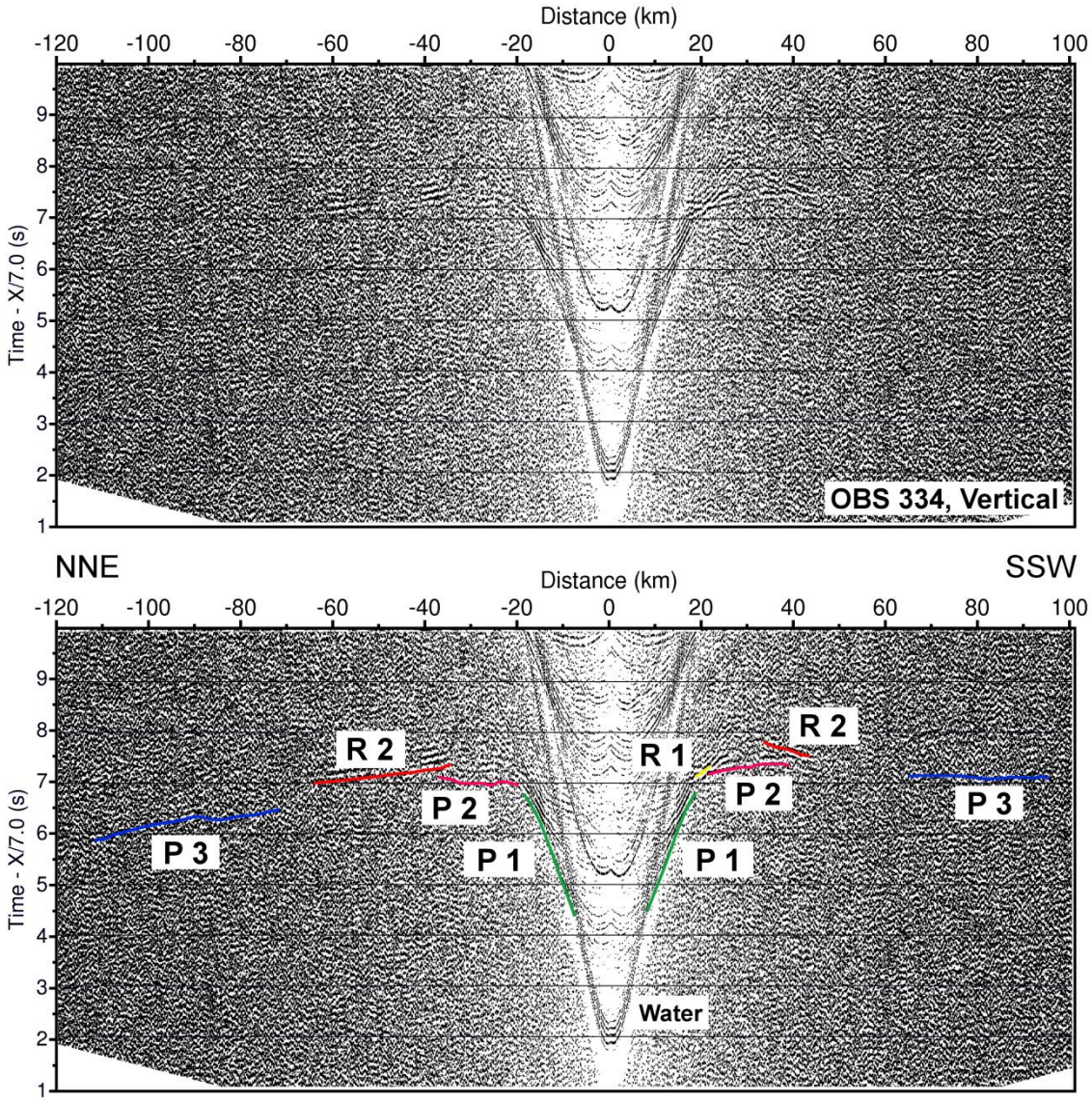

Figure B28 – Receiver gather from the vertical component of OBS 334 (top) with interpreted travel time arrivals (bottom). See Figure B3 for further information.

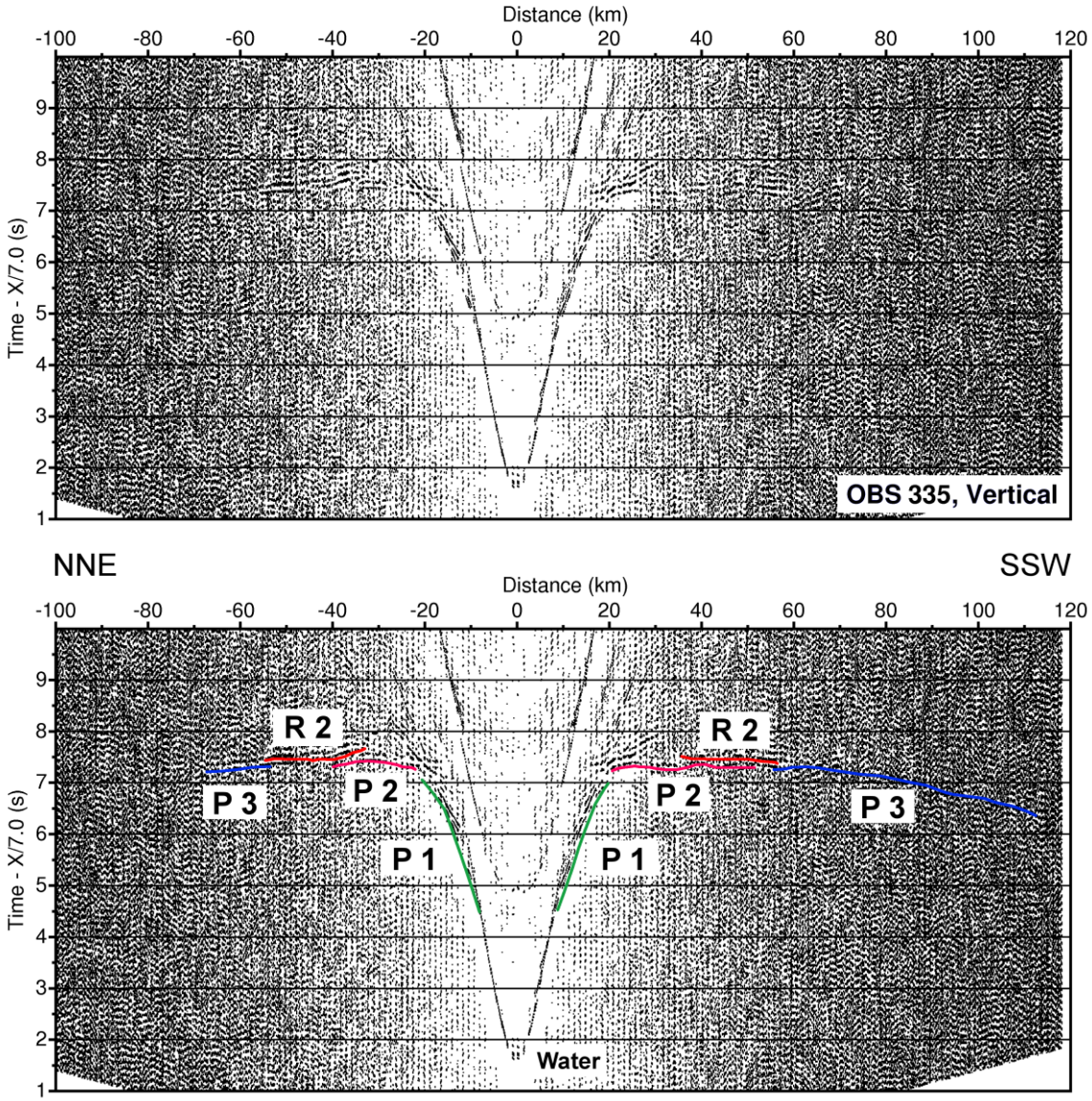

Figure B29 – Receiver gather from the vertical component of OBS 335 (top) with interpreted travel time arrivals (bottom). See Figure B3 for further information.

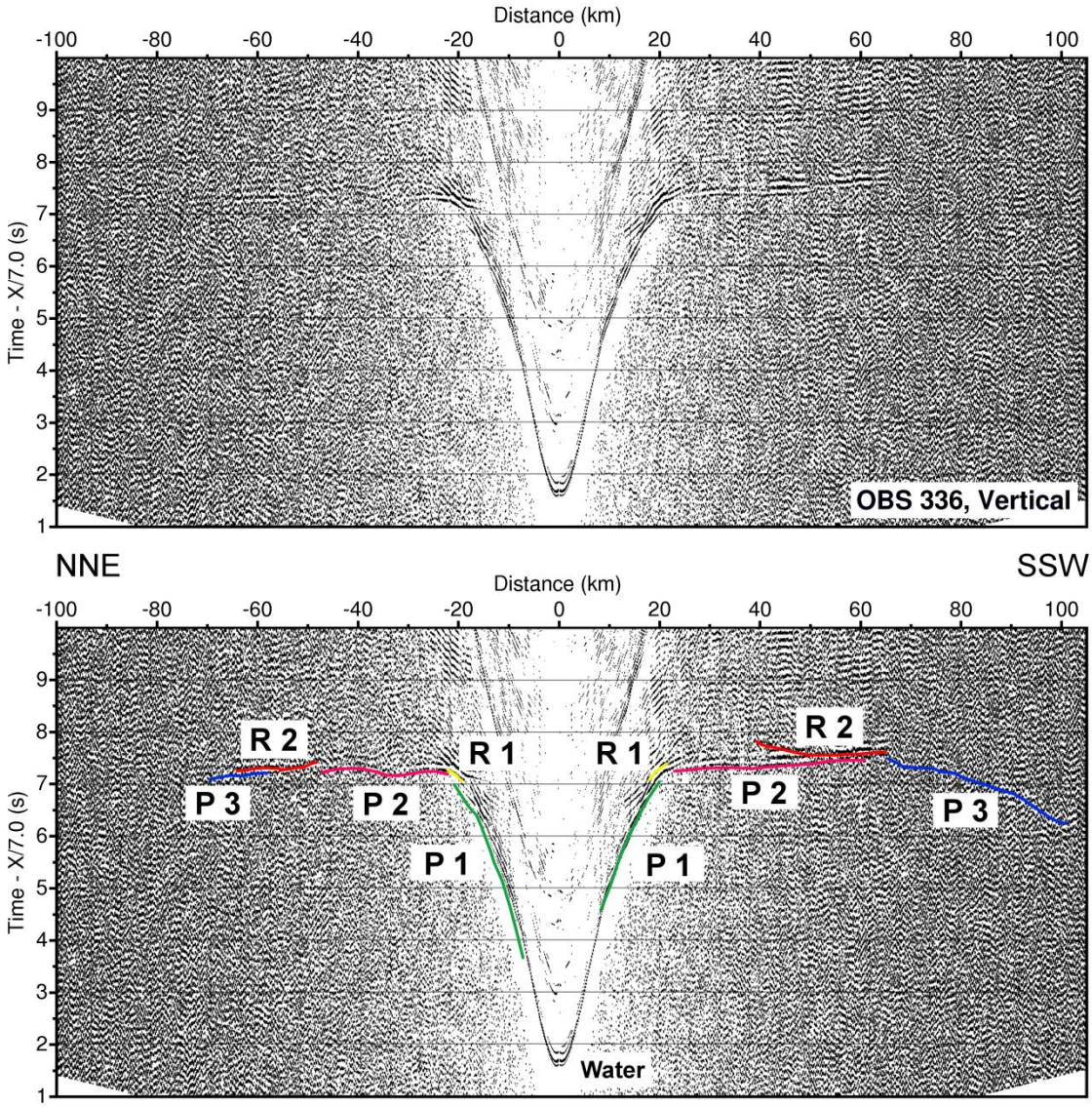

Figure B30 – Receiver gather from the vertical component of OBS 336 (top) with interpreted travel time arrivals (bottom). See Figure B3 for further information.

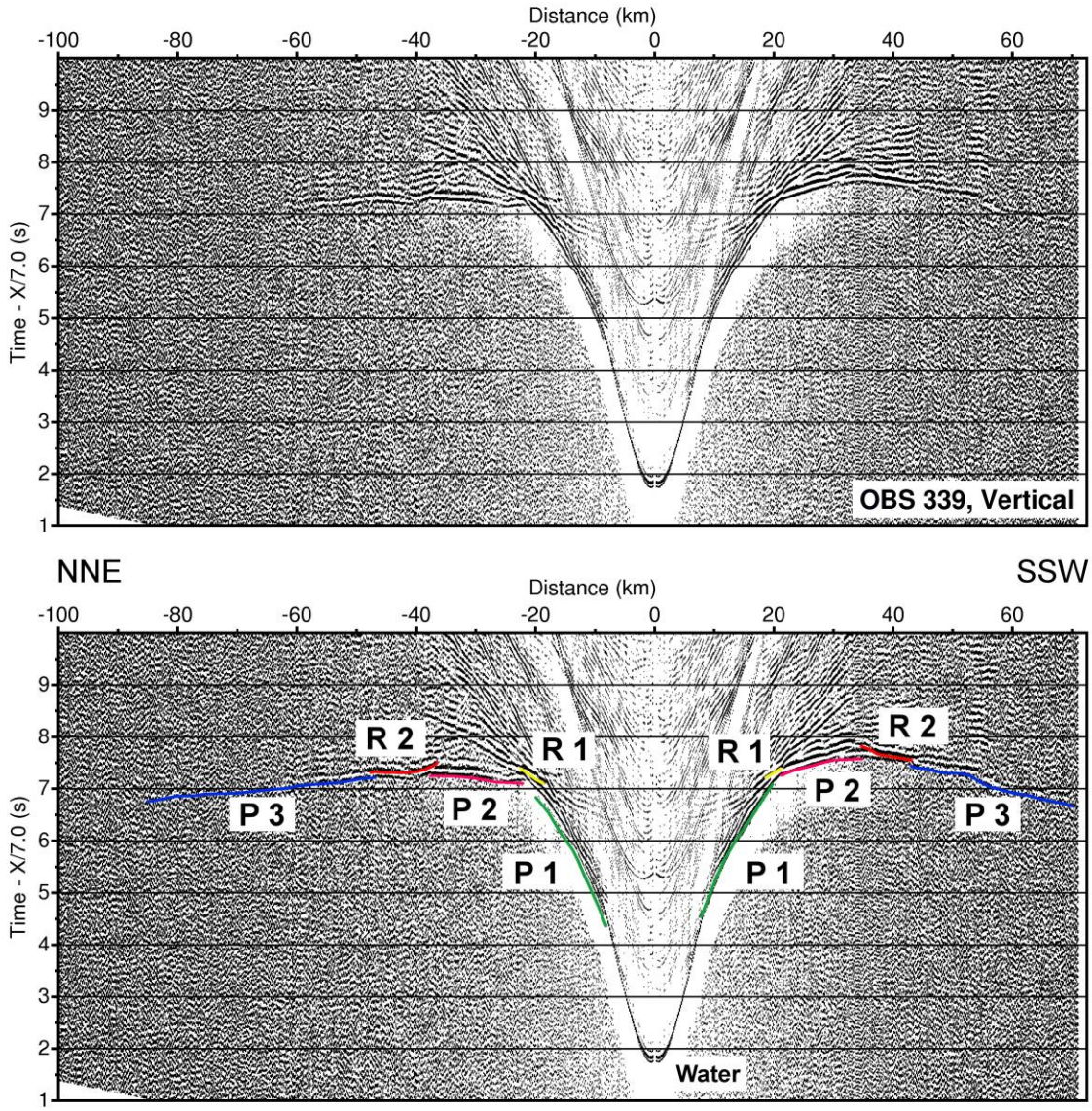

Figure B31 – Receiver gather from the vertical component of OBS 339 (top) with interpreted travel time arrivals (bottom). See Figure B3 for further information.

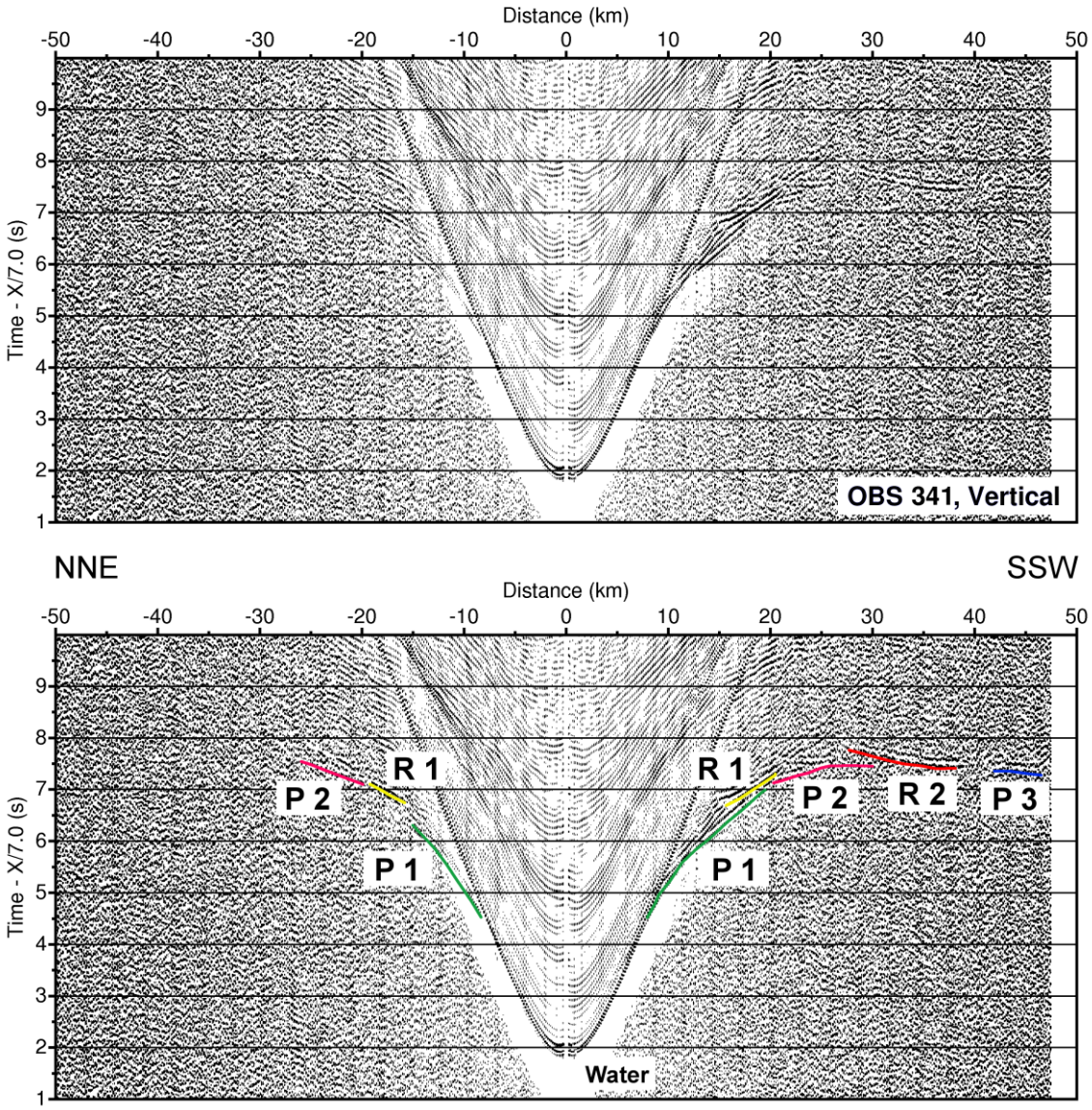

Figure B32 – Receiver gather from the vertical component of OBS 341 (top) with interpreted travel time arrivals (bottom). See Figure B3 for further information.

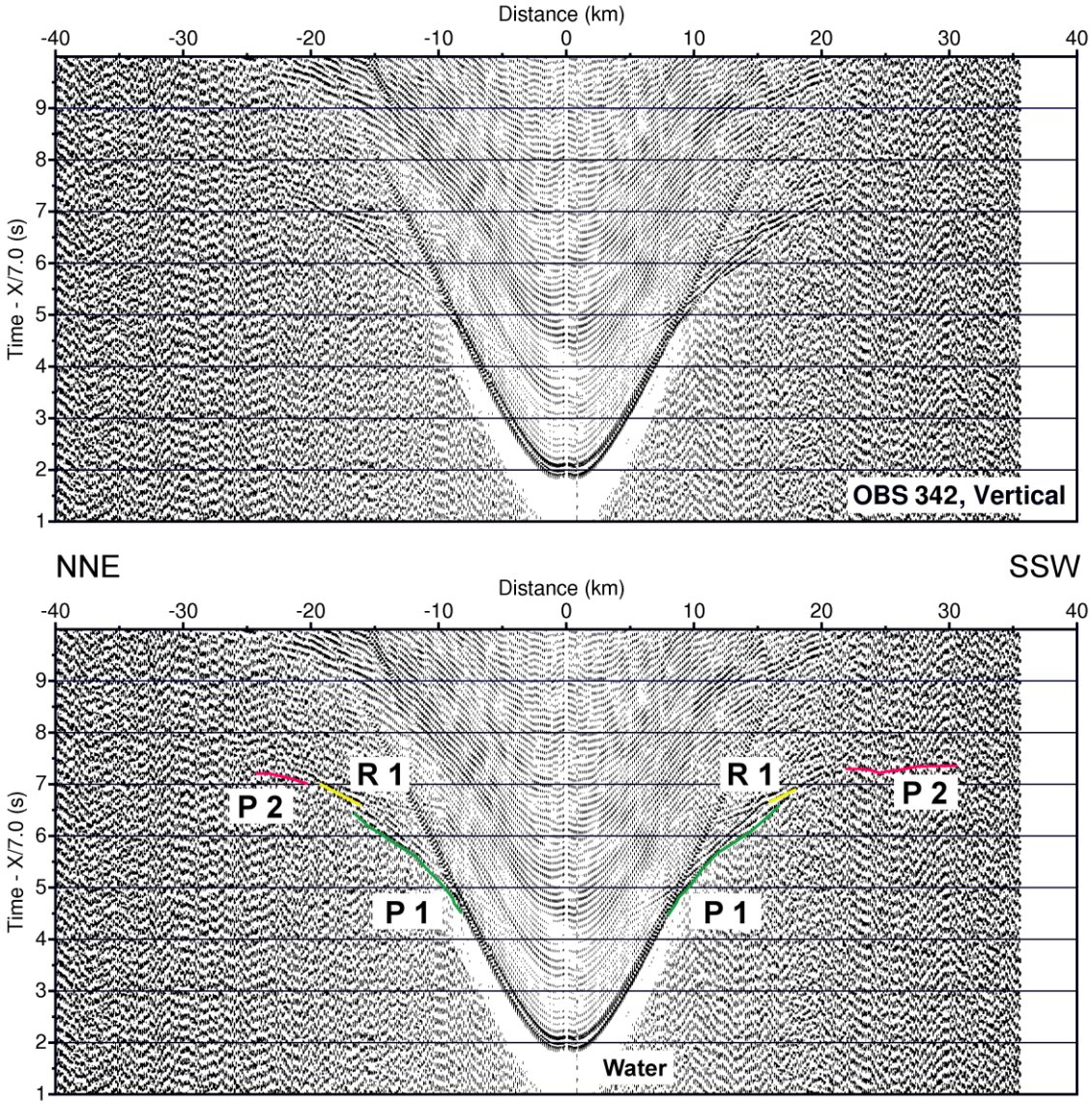

Figure B33 – Receiver gather from the vertical component of OBS 342 (top) with interpreted travel time arrivals (bottom). See Figure B3 for further information.

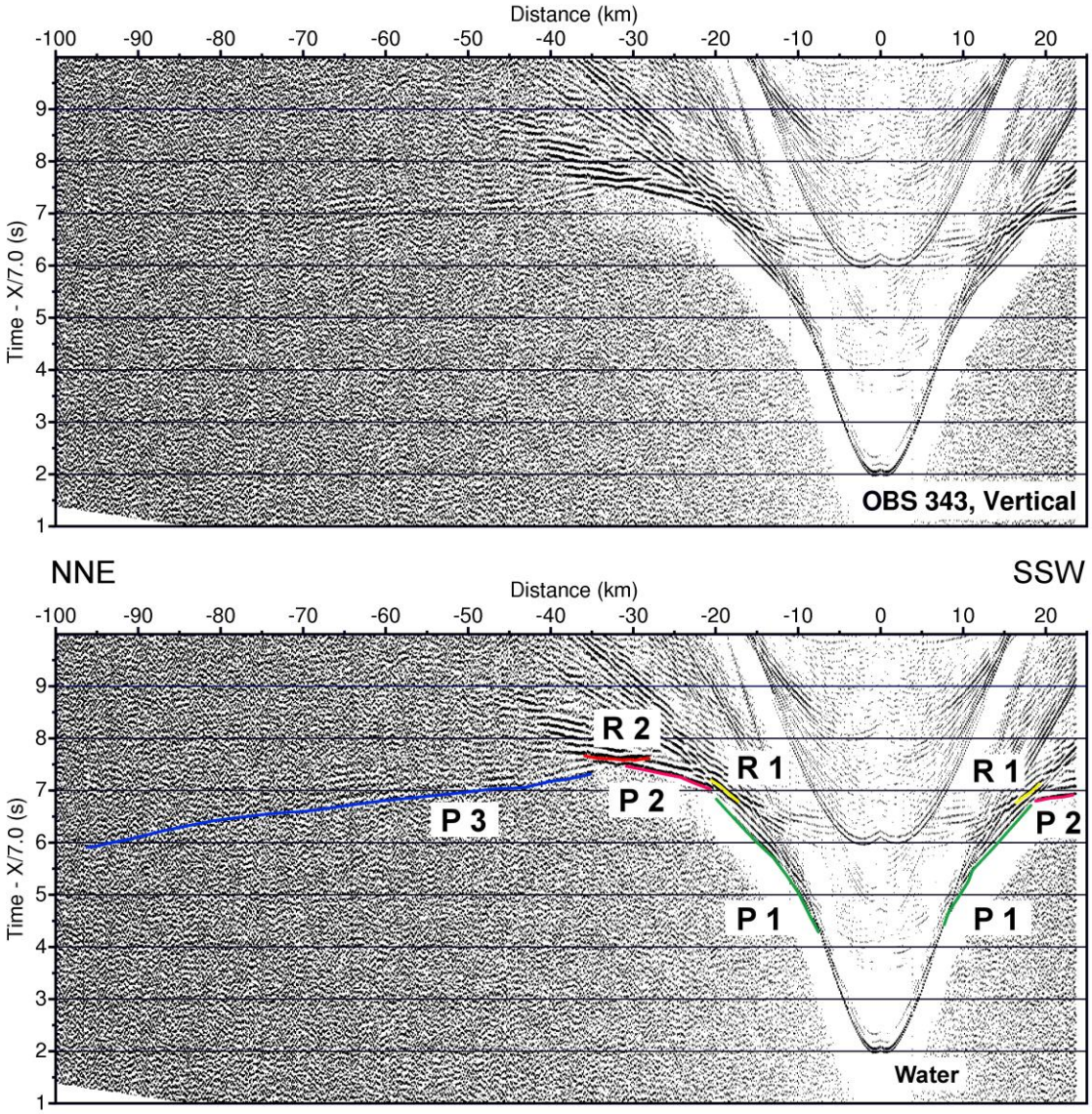

Figure B34 – Receiver gather from the vertical component of OBS 343 (top) with interpreted travel time arrivals (bottom). See Figure B3 for further information.

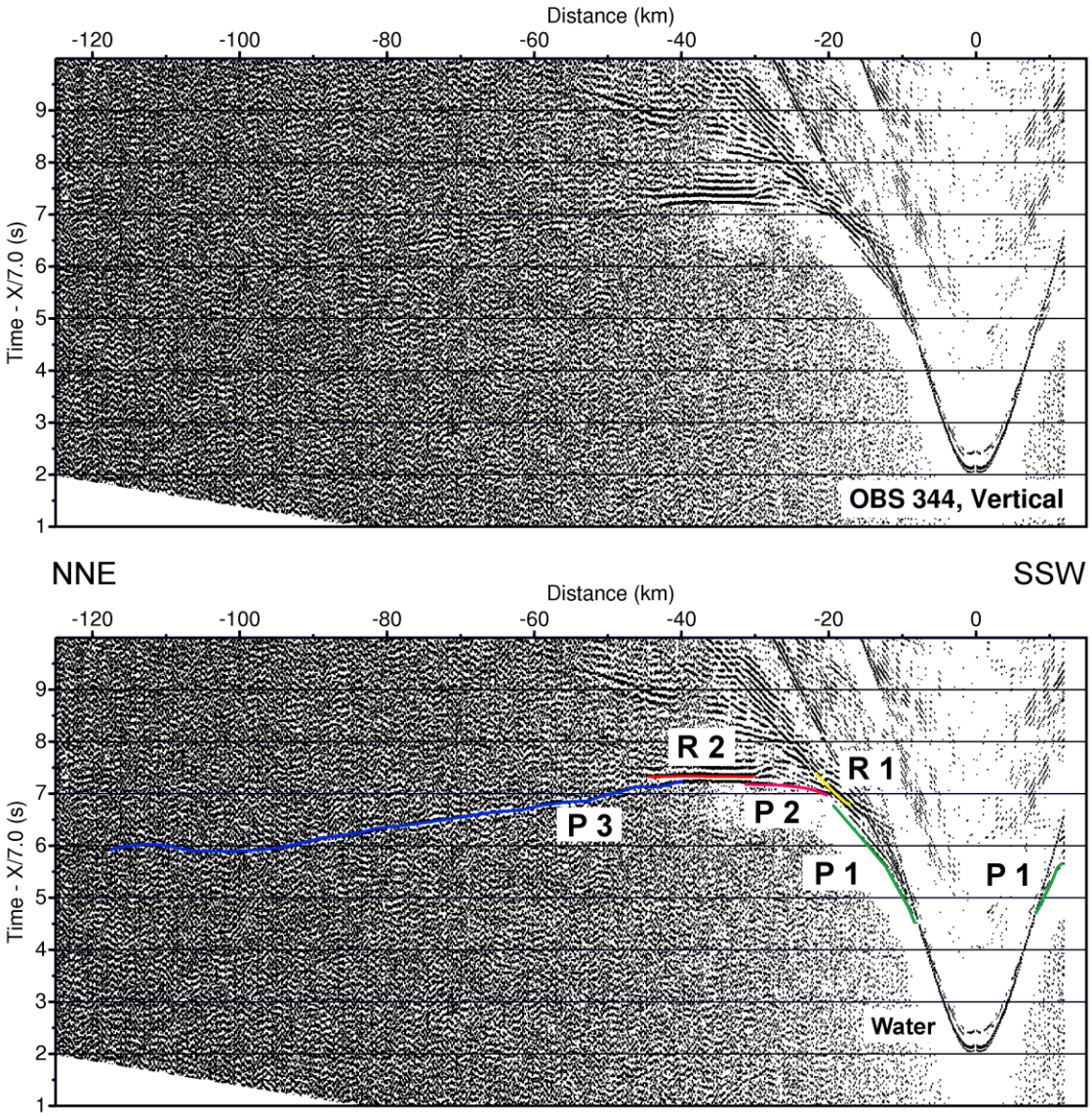

Figure B35 – Receiver gather from the vertical component of OBS 344 (top) with interpreted travel time arrivals (bottom). See Figure B3 for further information.

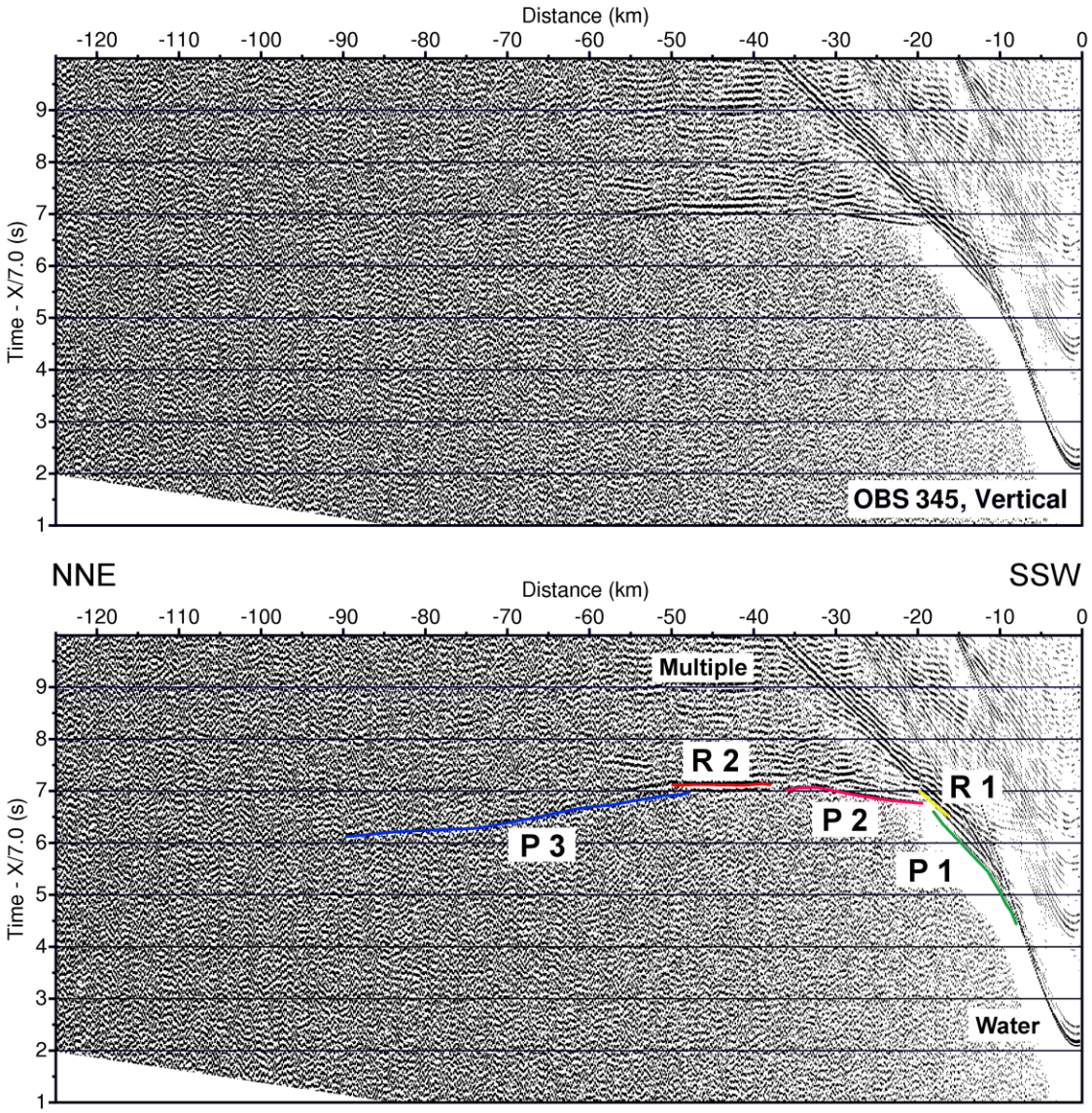

Figure B36 – Receiver gather from the vertical component of OBS 345 (top) with interpreted travel time arrivals (bottom). See Figure B3 for further information.

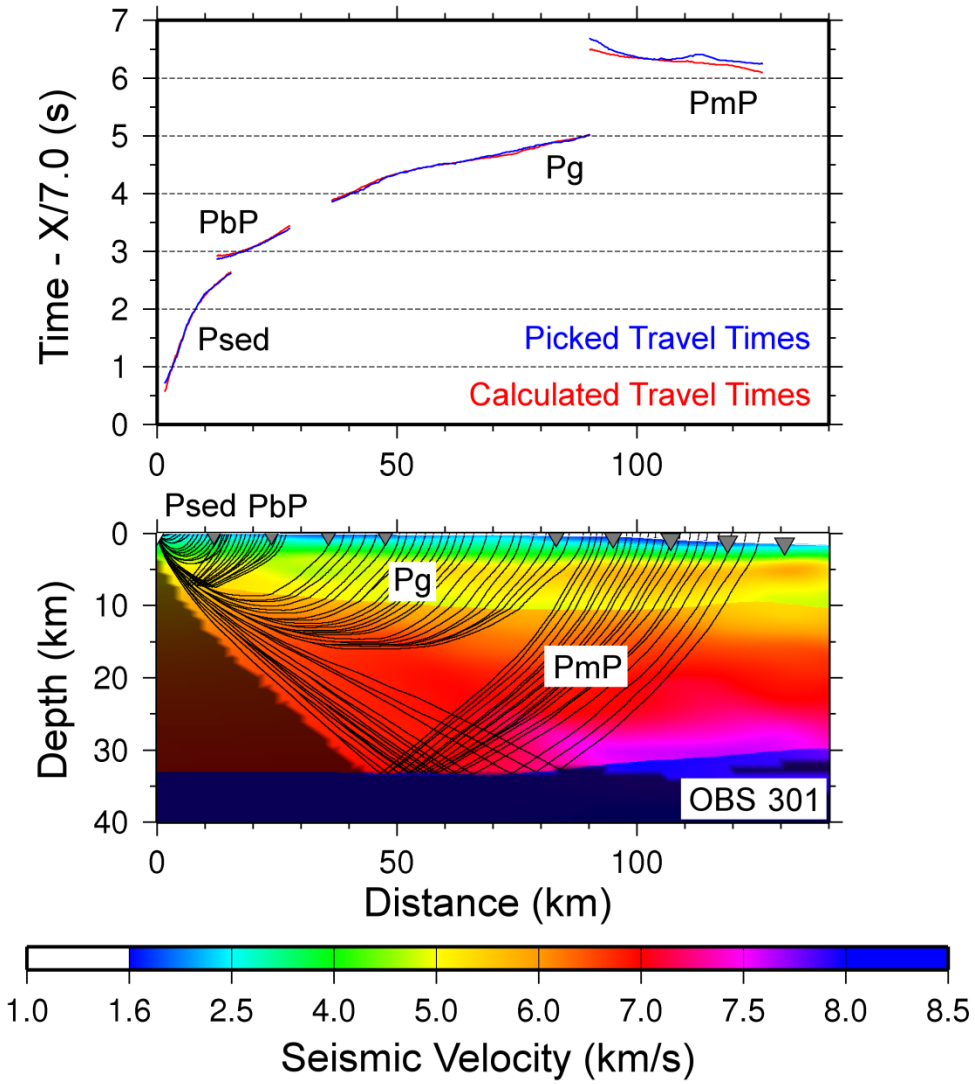

Figure B37 – Picked and calculated travel times for OBS 301 (top) and ray paths through final tomographic model (bottom). Rays plotted for every sixth pick. Shading denotes model space not constrained by ray paths. **PbP** – basement reflections; **Pg** – basement layer refractions; **PmP** – Moho reflections; **Pn** – mantle layer refractions; **Psed** – sediment layer refractions.

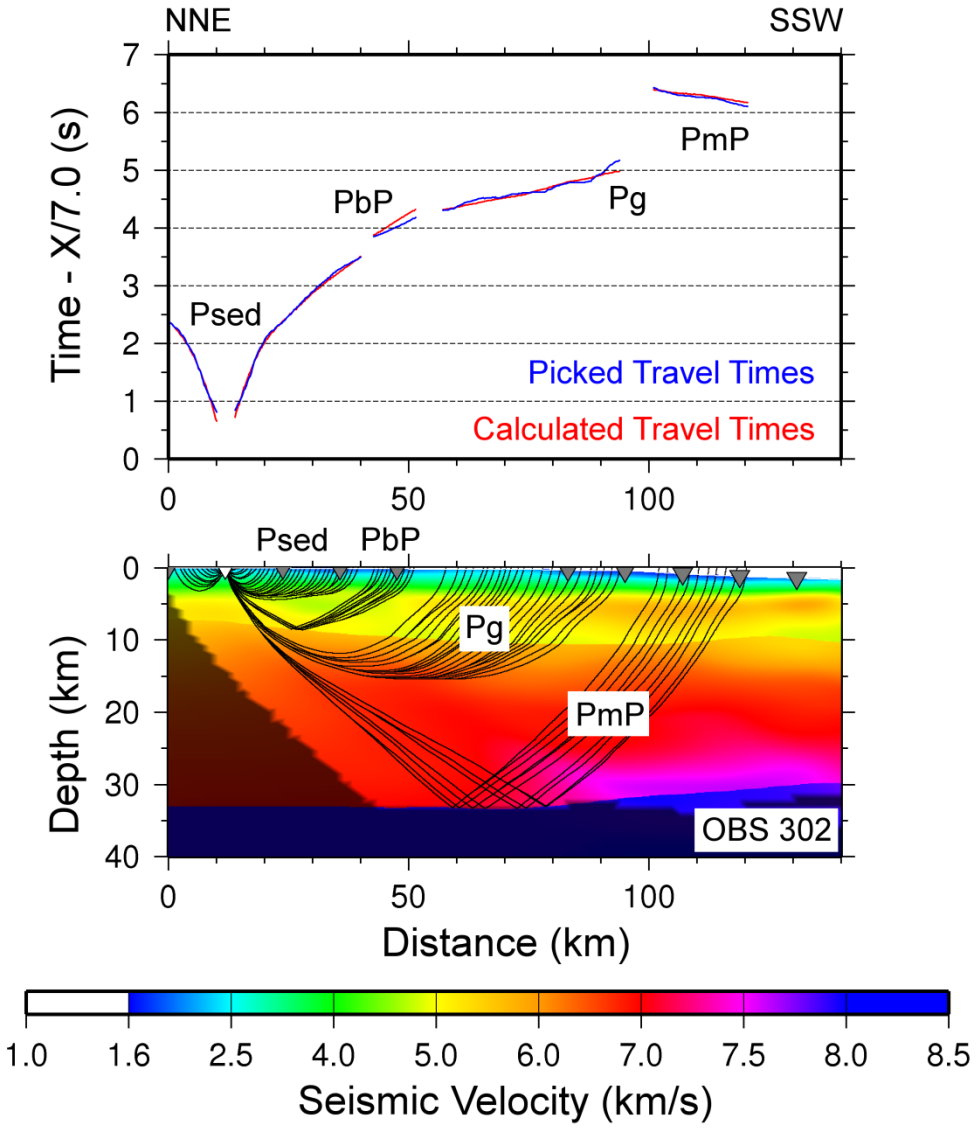

Figure B38 – Picked and calculated travel times for OBS 302 (top) and ray paths through final tomographic model (bottom). See Figure B37 for further information.

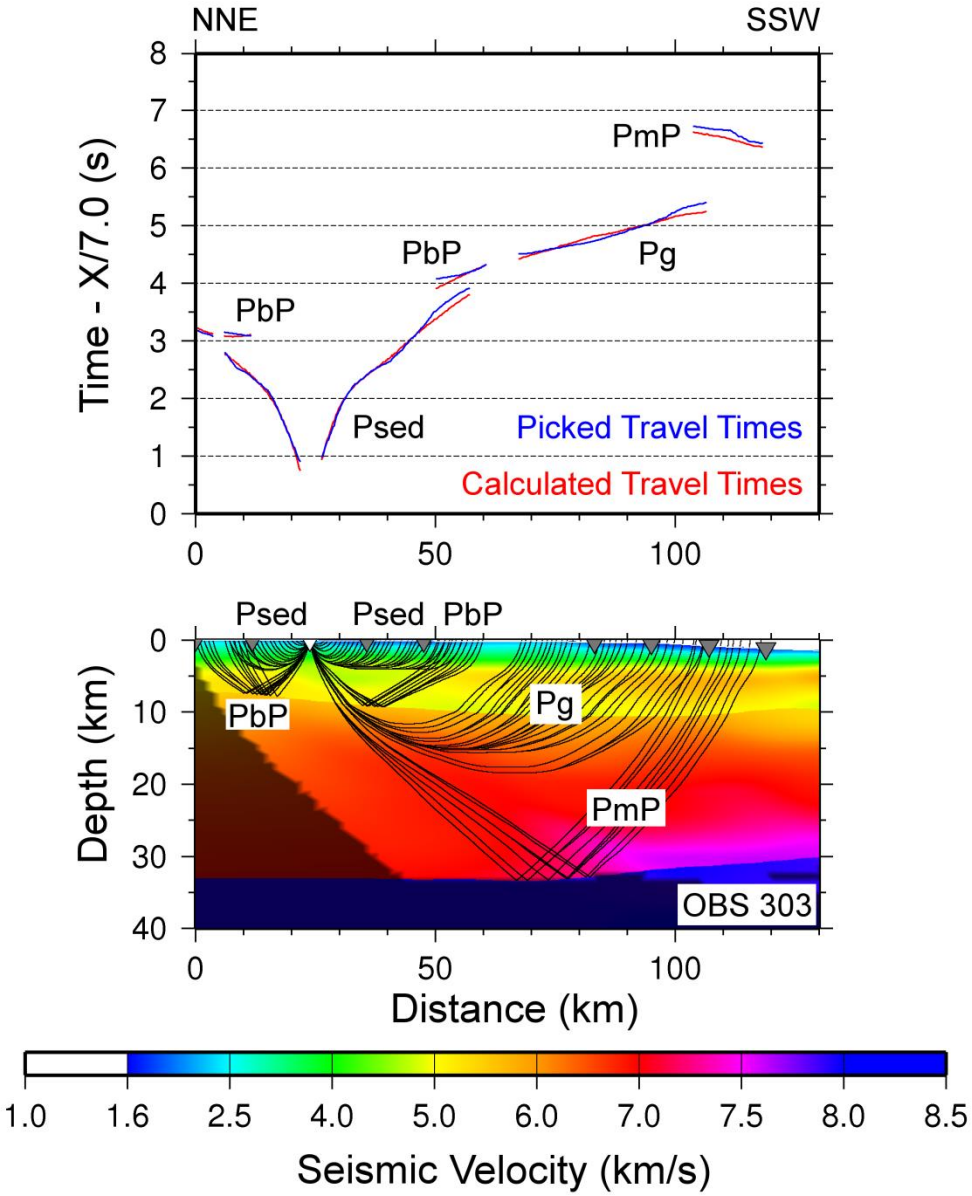

Figure B39 – Picked and calculated travel times for OBS 303 (top) and ray paths through final tomographic model (bottom). See Figure B37 for further information.

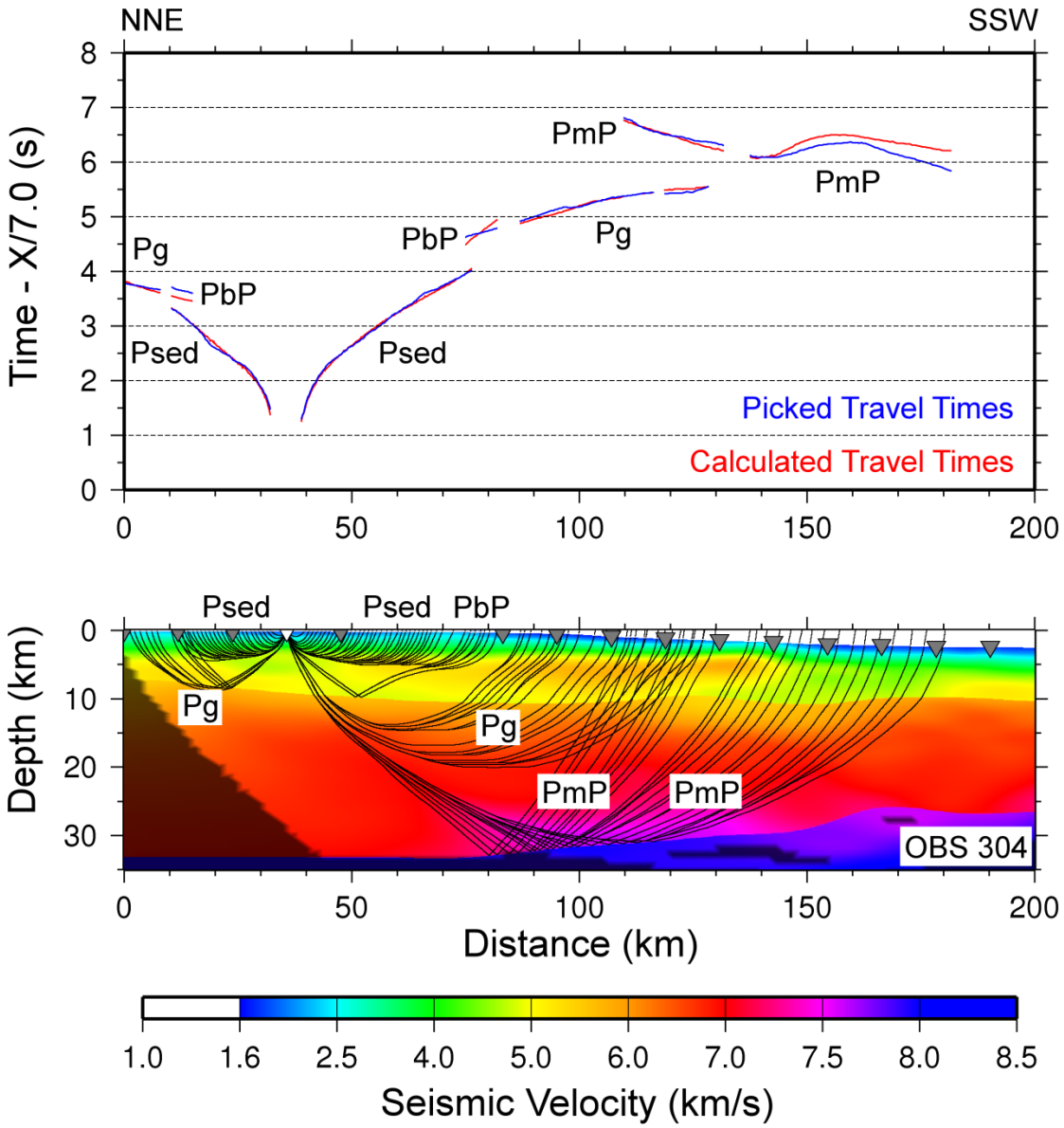

Figure B40 – Picked and calculated travel times for OBS 304 (top) and ray paths through final tomographic model (bottom). See Figure B37 for further information.

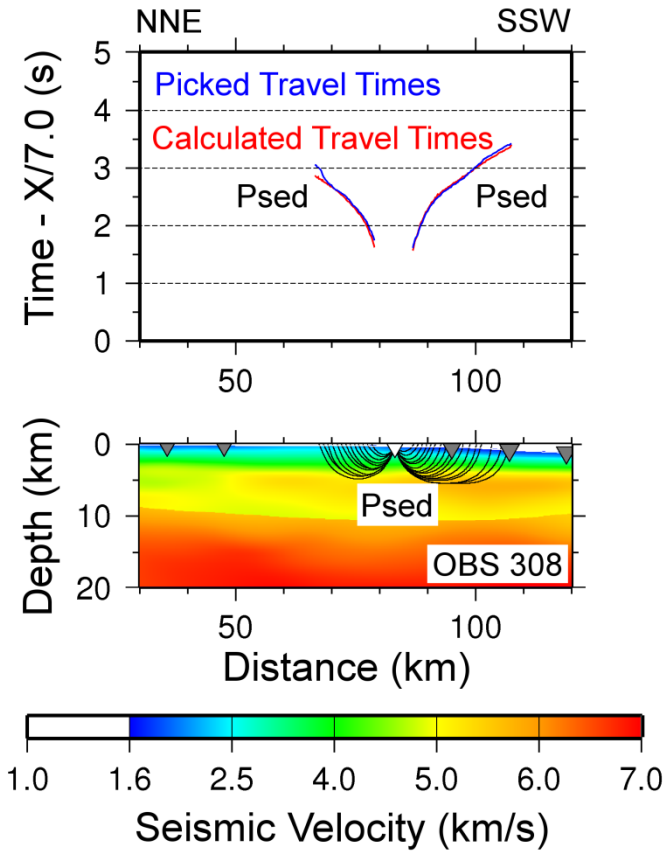

Figure B41 – Picked and calculated travel times for OBS 308 (top) and ray paths through final tomographic model (bottom). See Figure B37 for further information.

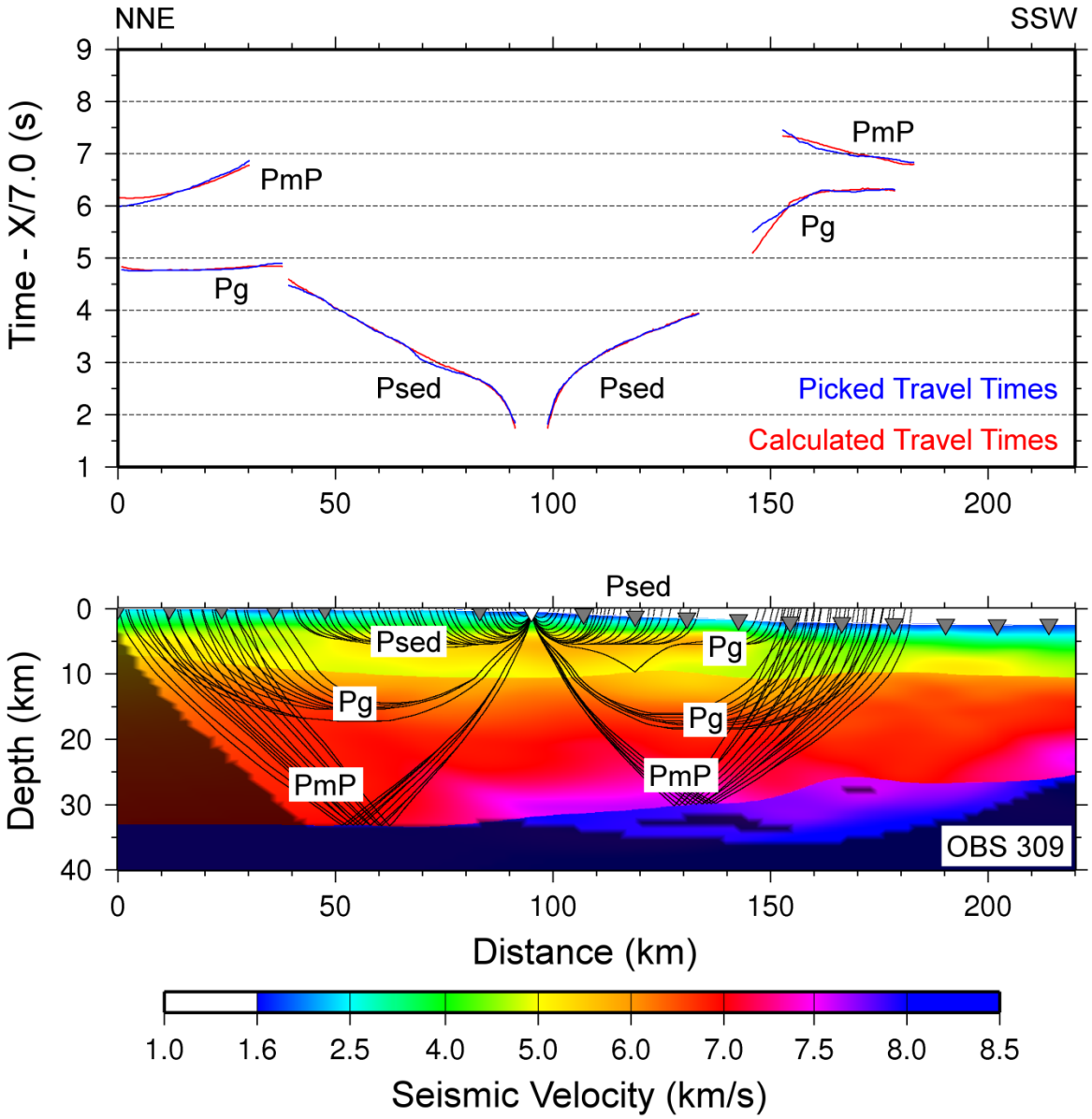

Figure B42 – Picked and calculated travel times for OBS 309 (top) and ray paths through final tomographic model (bottom). See Figure B37 for further information.

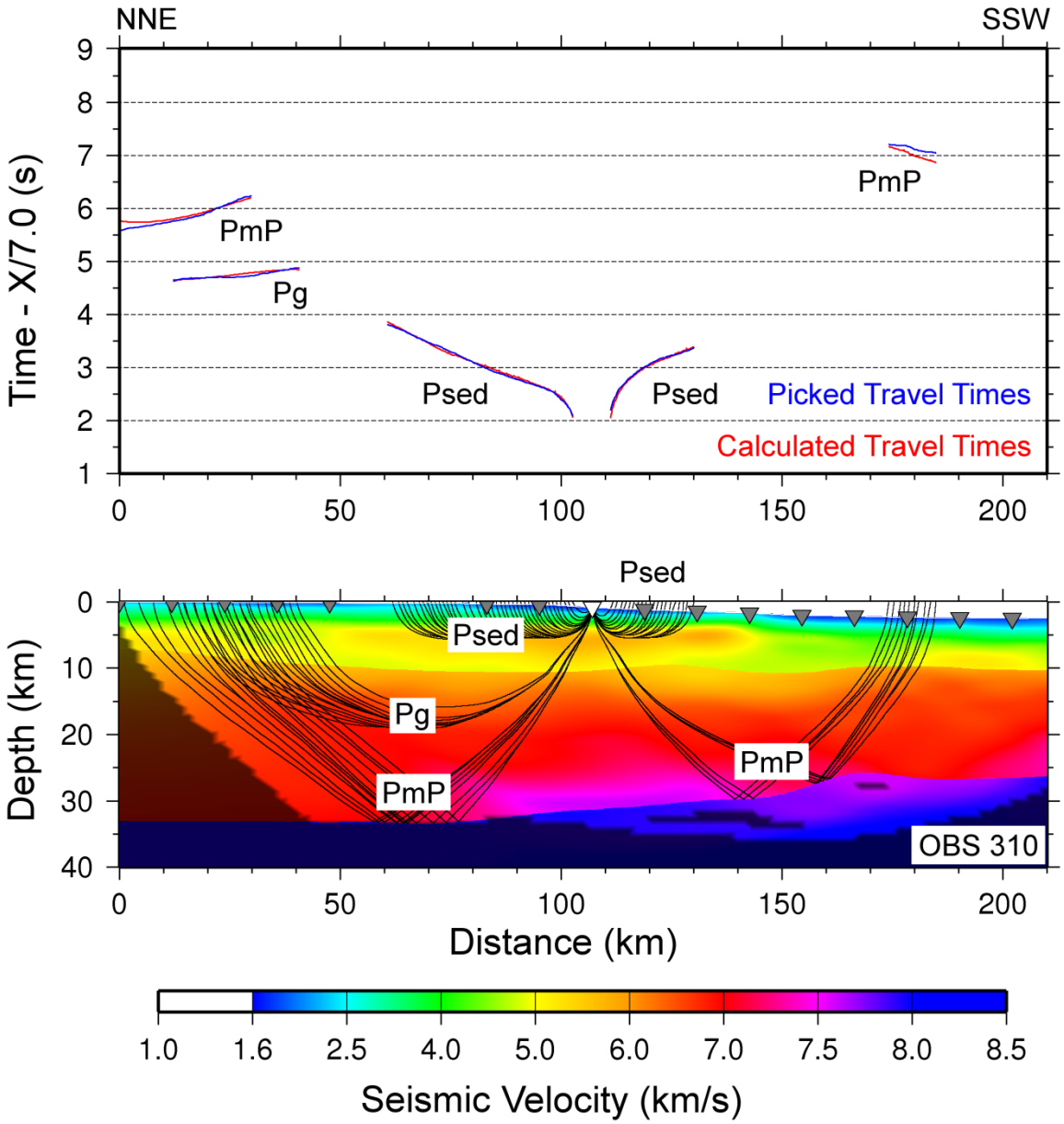

Figure B43 – Picked and calculated travel times for OBS 310 (top) and ray paths through final tomographic model (bottom). See Figure B37 for further information.

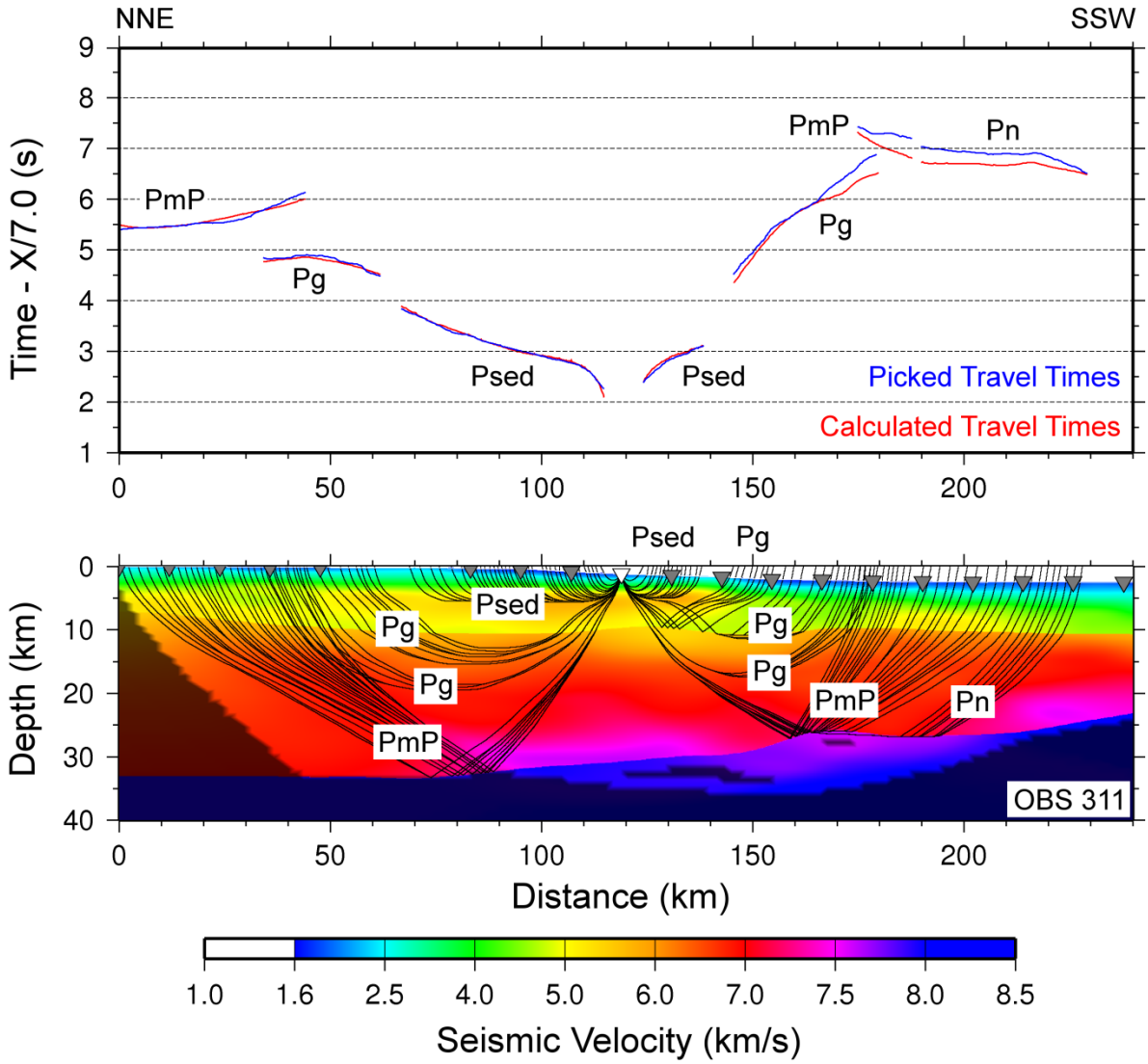

Figure B44 – Picked and calculated travel times for OBS 311 (top) and ray paths through final tomographic model (bottom). See Figure B37 for further information.

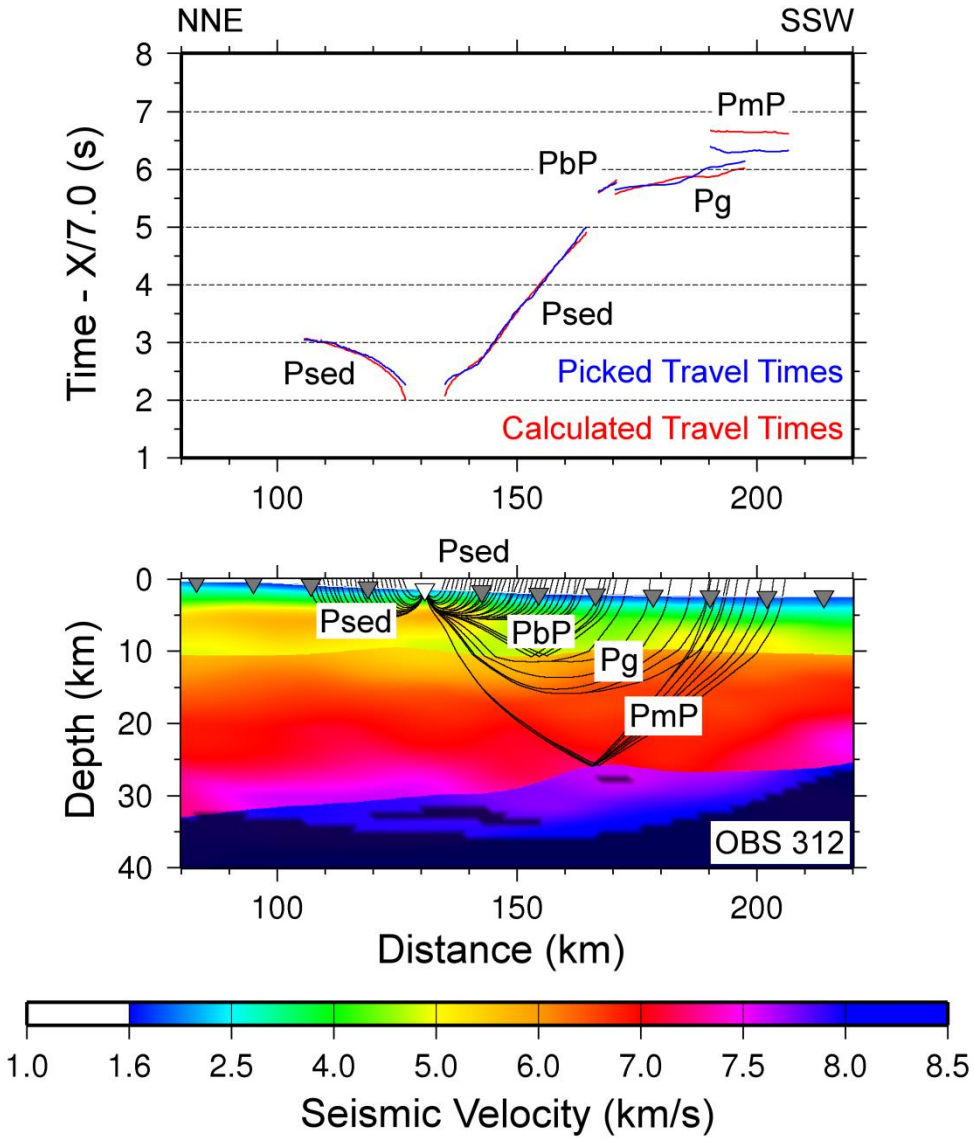

Figure B45 – Picked and calculated travel times for OBS 312 (top) and ray paths through final tomographic model (bottom). See Figure B37 for further information.

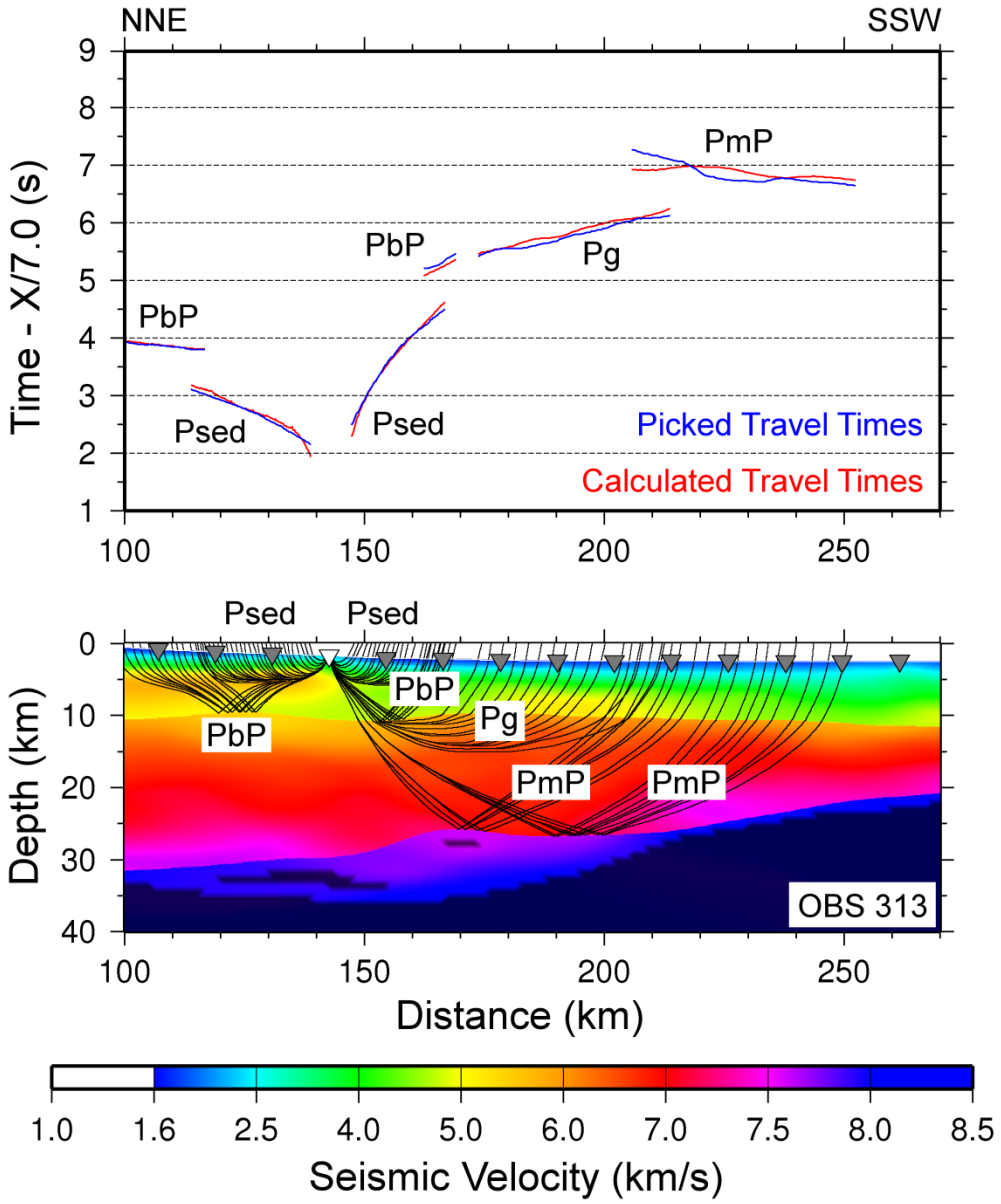

Figure B46 – Picked and calculated travel times for OBS 313 (top) and ray paths through final tomographic model (bottom). See Figure B37 for further information.

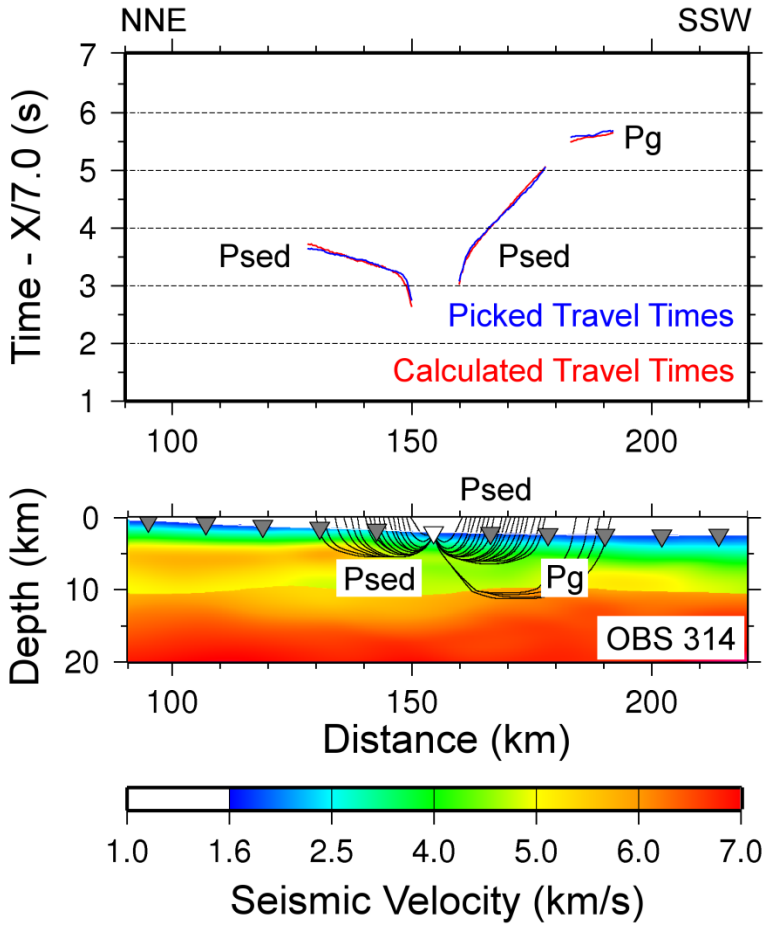

Figure B47 – Picked and calculated travel times for OBS 314 (top) and ray paths through final tomographic model (bottom). See Figure B37 for further information.

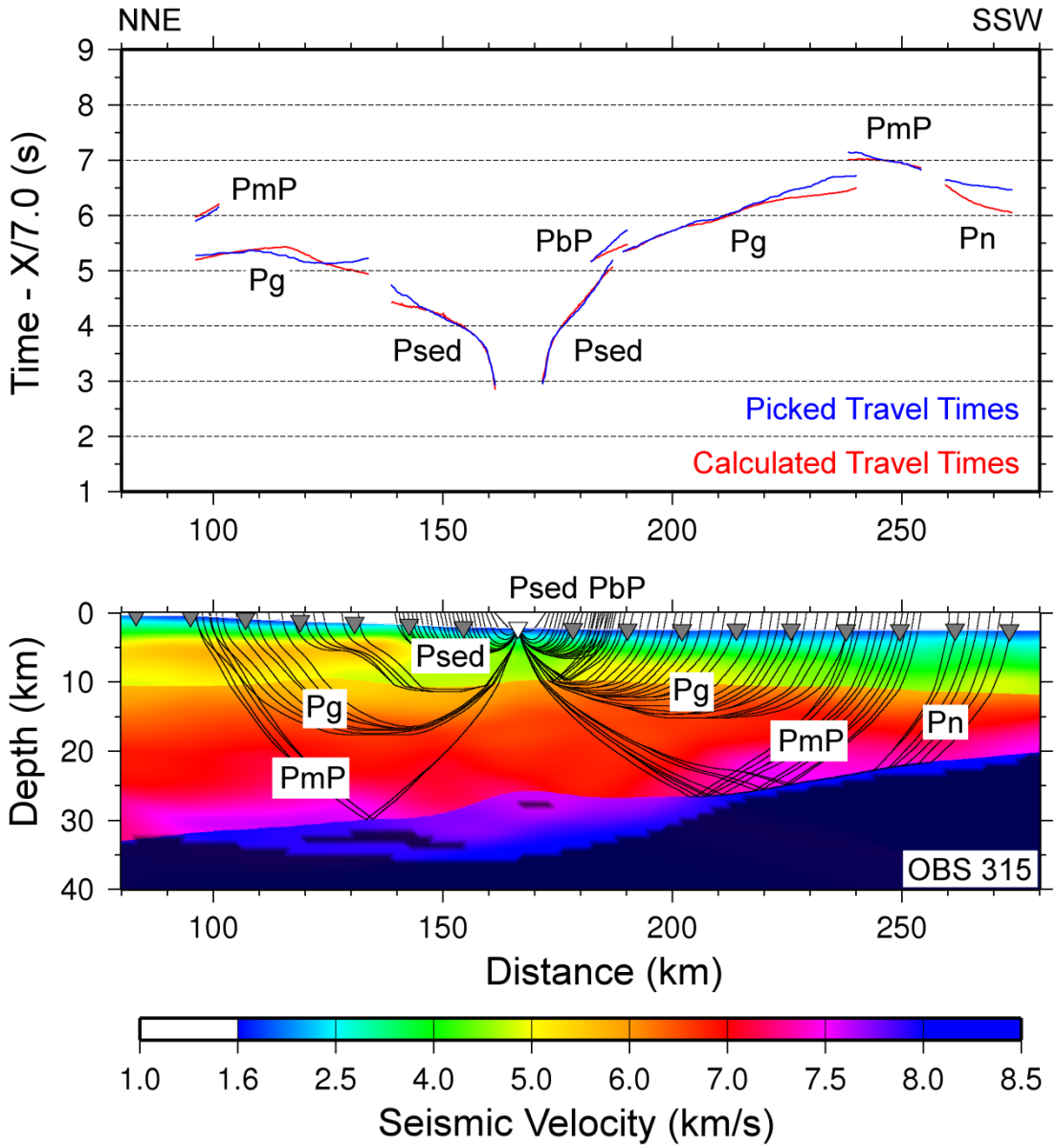

Figure B48 – Picked and calculated travel times for OBS 315 (top) and ray paths through final tomographic model (bottom). See Figure B37 for further information.

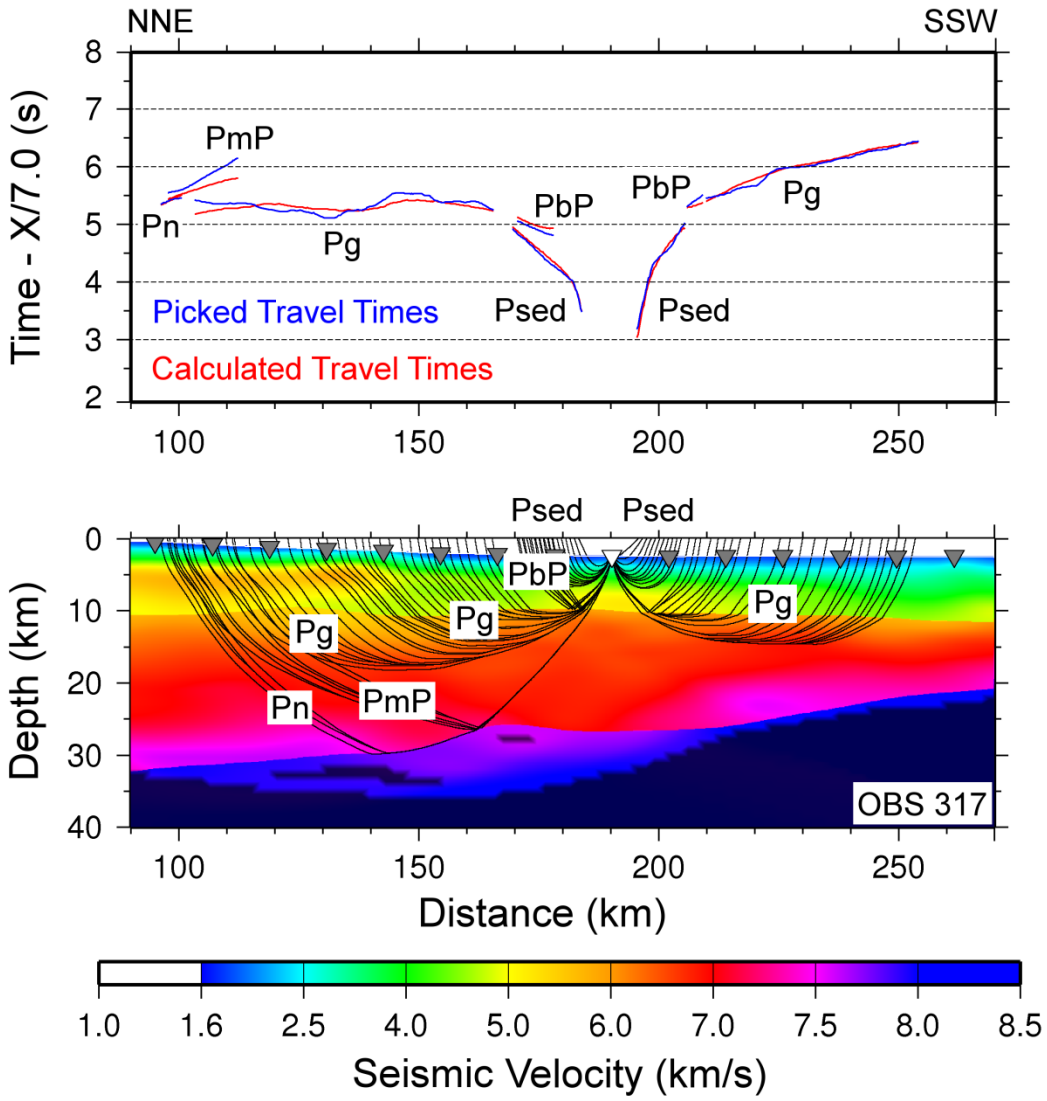

Figure B49 – Picked and calculated travel times for OBS 317 (top) and ray paths through final tomographic model (bottom). See Figure B37 for further information.

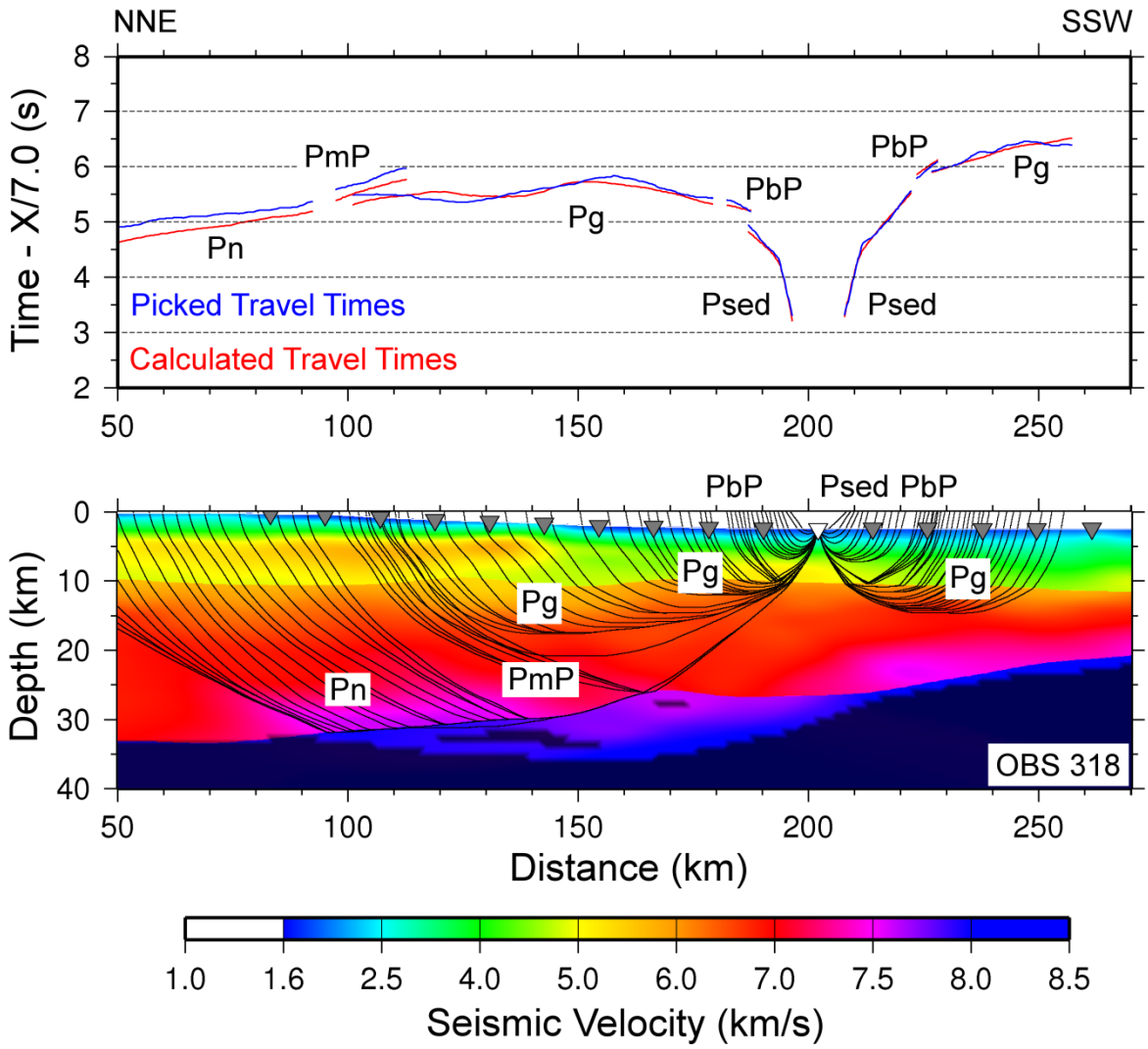

Figure B50 – Picked and calculated travel times for OBS 318 (top) and ray paths through final tomographic model (bottom). See Figure B37 for further information.

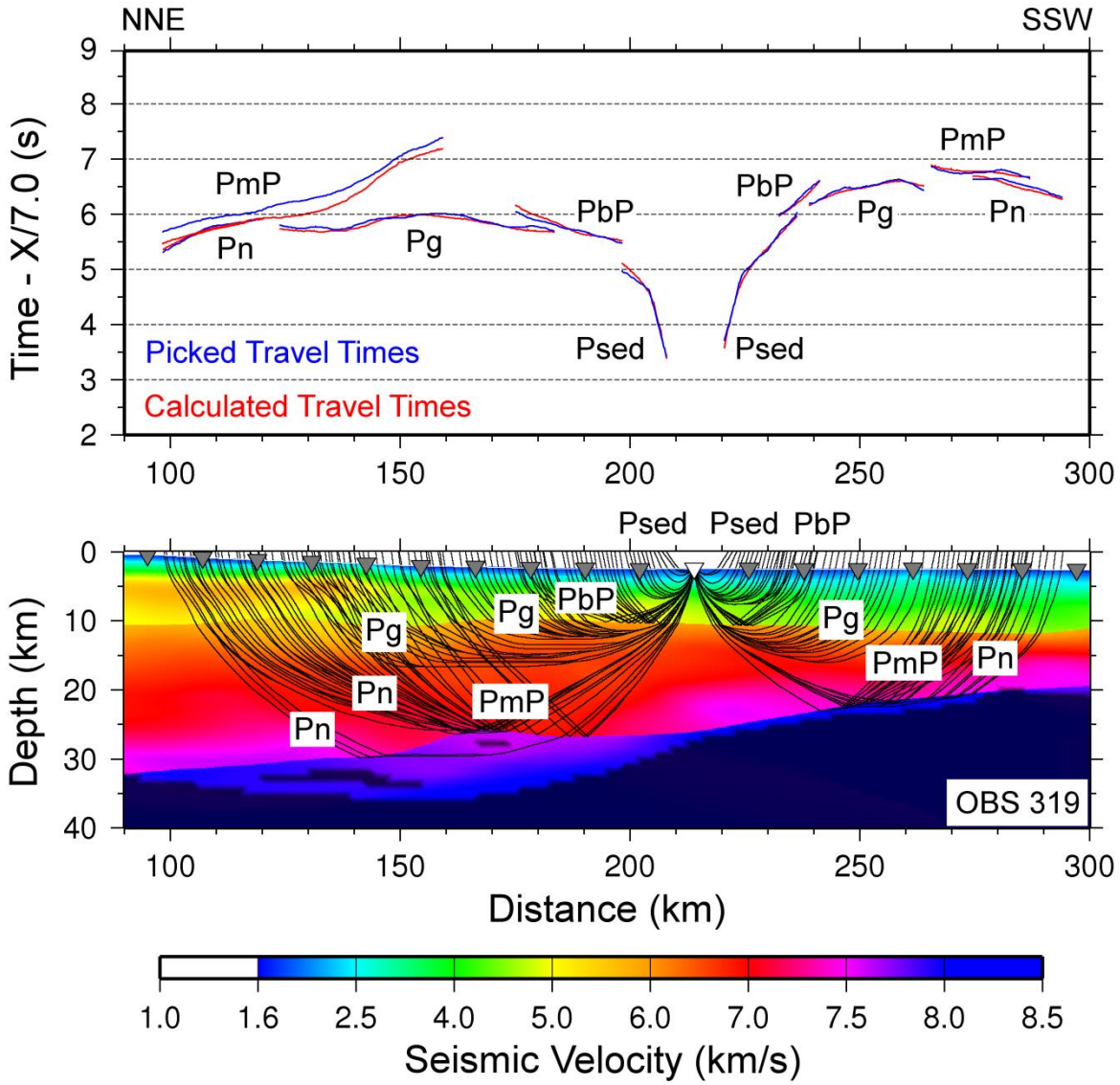

Figure B51 – Picked and calculated travel times for OBS 319 (top) and ray paths through final tomographic model (bottom). See Figure B37 for further information.

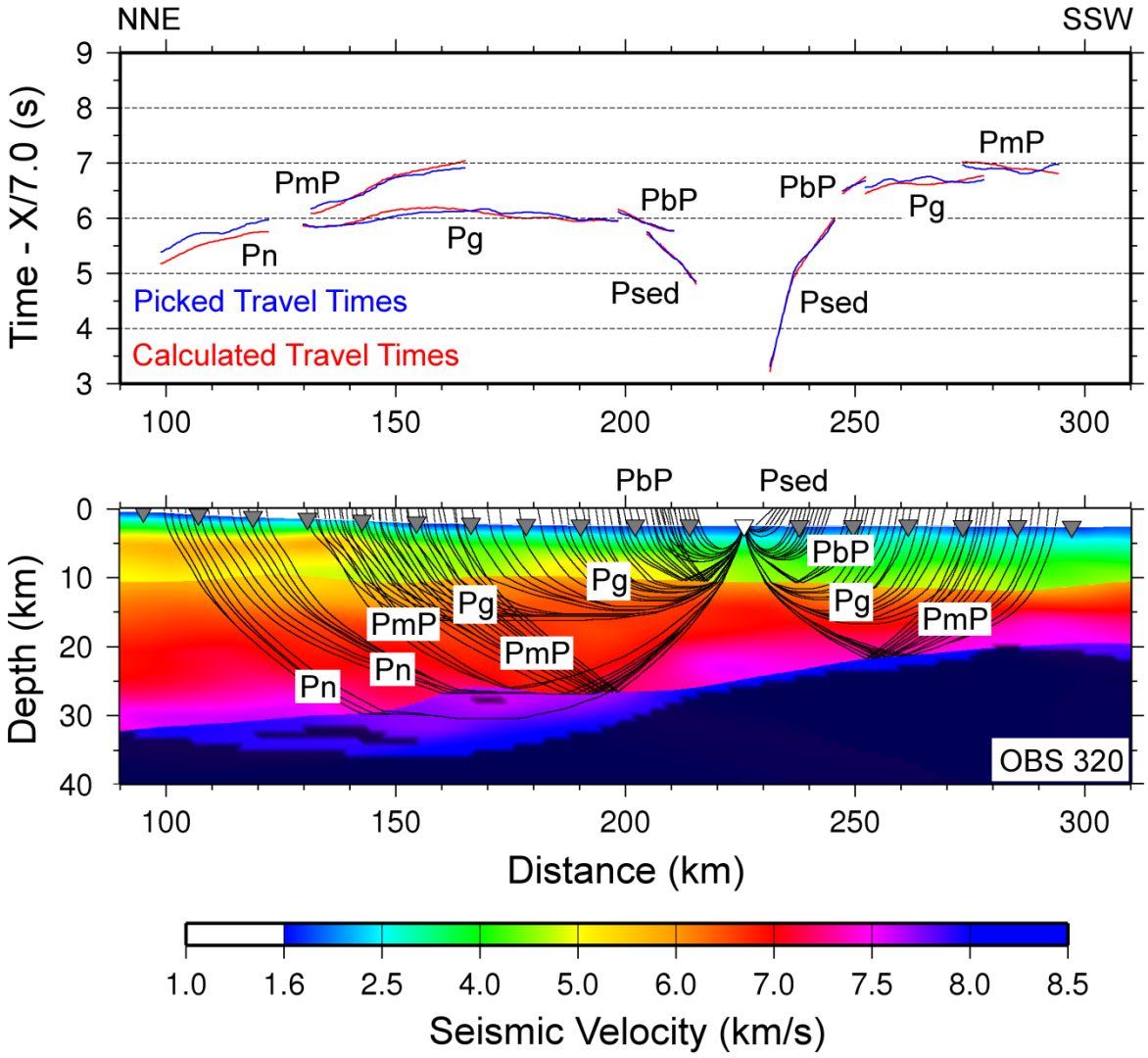

Figure B52 – Picked and calculated travel times for OBS 320 (top) and ray paths through final tomographic model (bottom). See Figure B37 for further information.

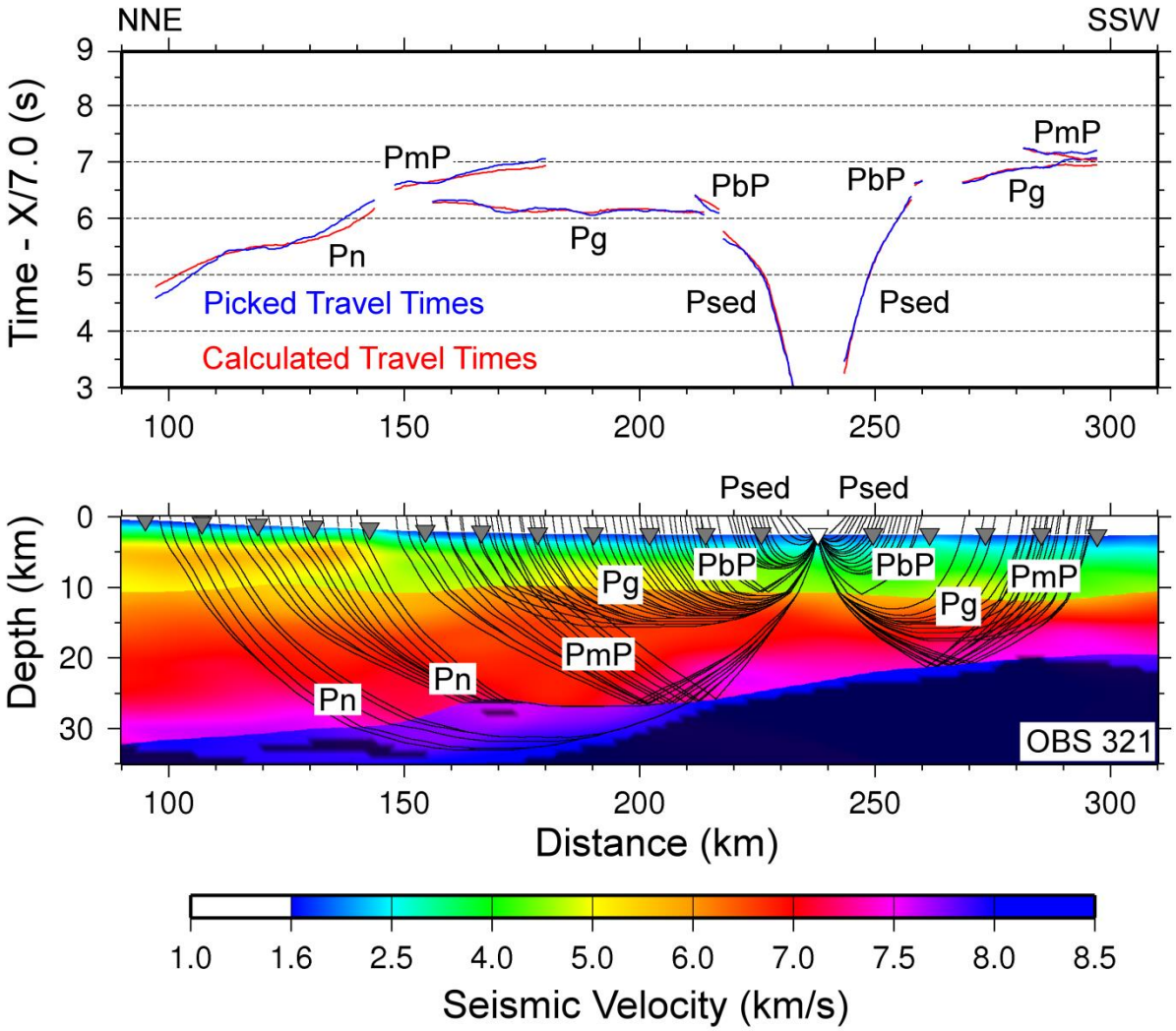

Figure B53 – Picked and calculated travel times for OBS 321 (top) and ray paths through final tomographic model (bottom). See Figure B37 for further information.

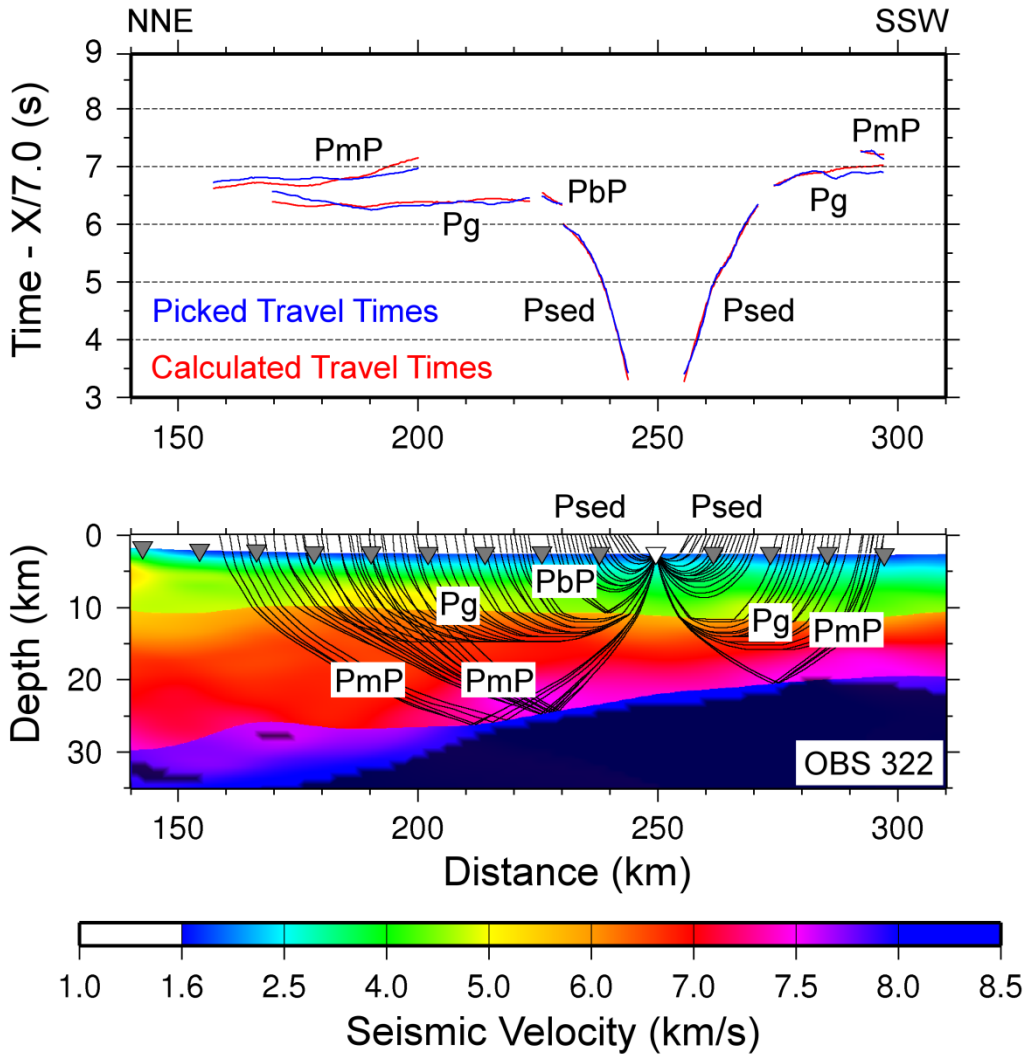

Figure B54 – Picked and calculated travel times for OBS 322 (top) and ray paths through final tomographic model (bottom). See Figure B37 for further information.

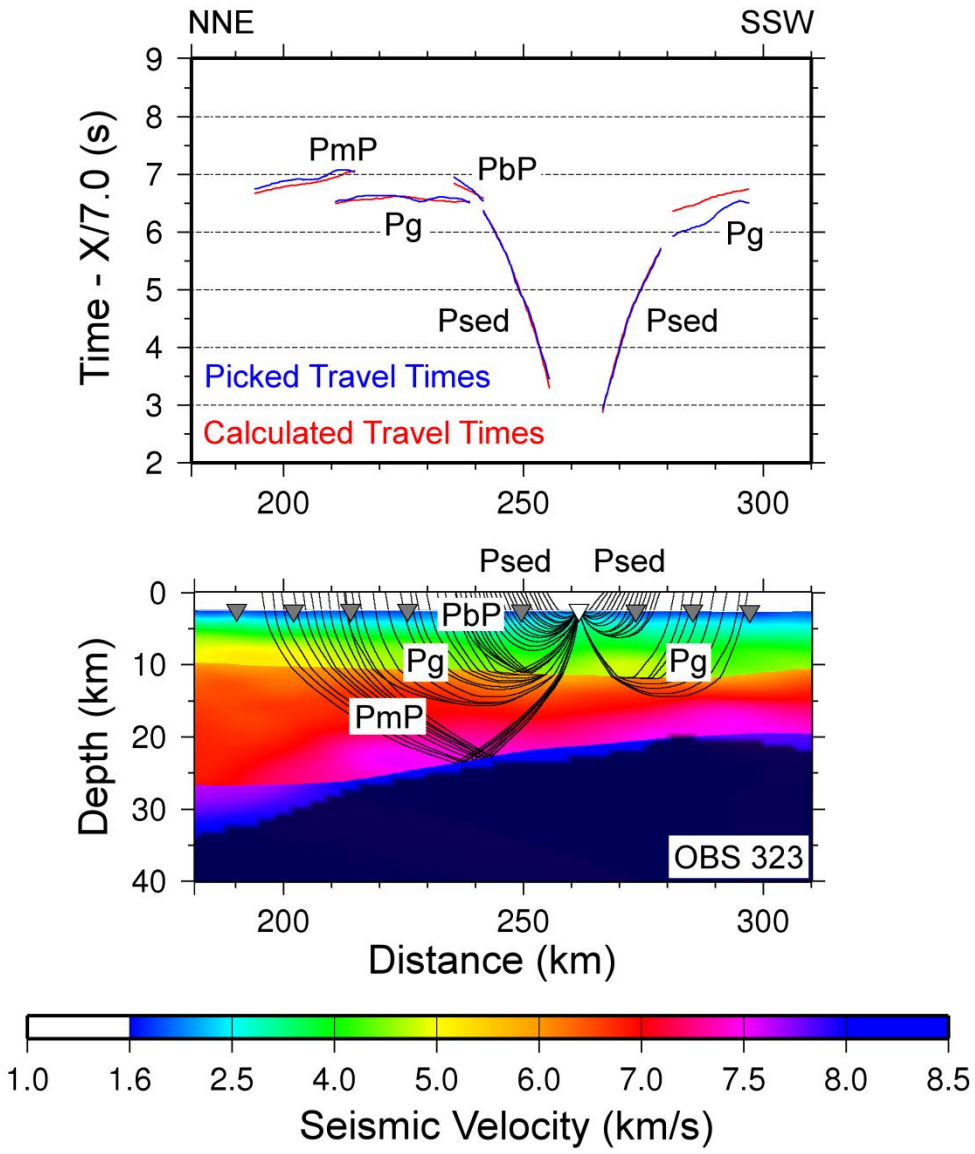

Figure B55 – Picked and calculated travel times for OBS 323 (top) and ray paths through final tomographic model (bottom). See Figure B37 for further information.

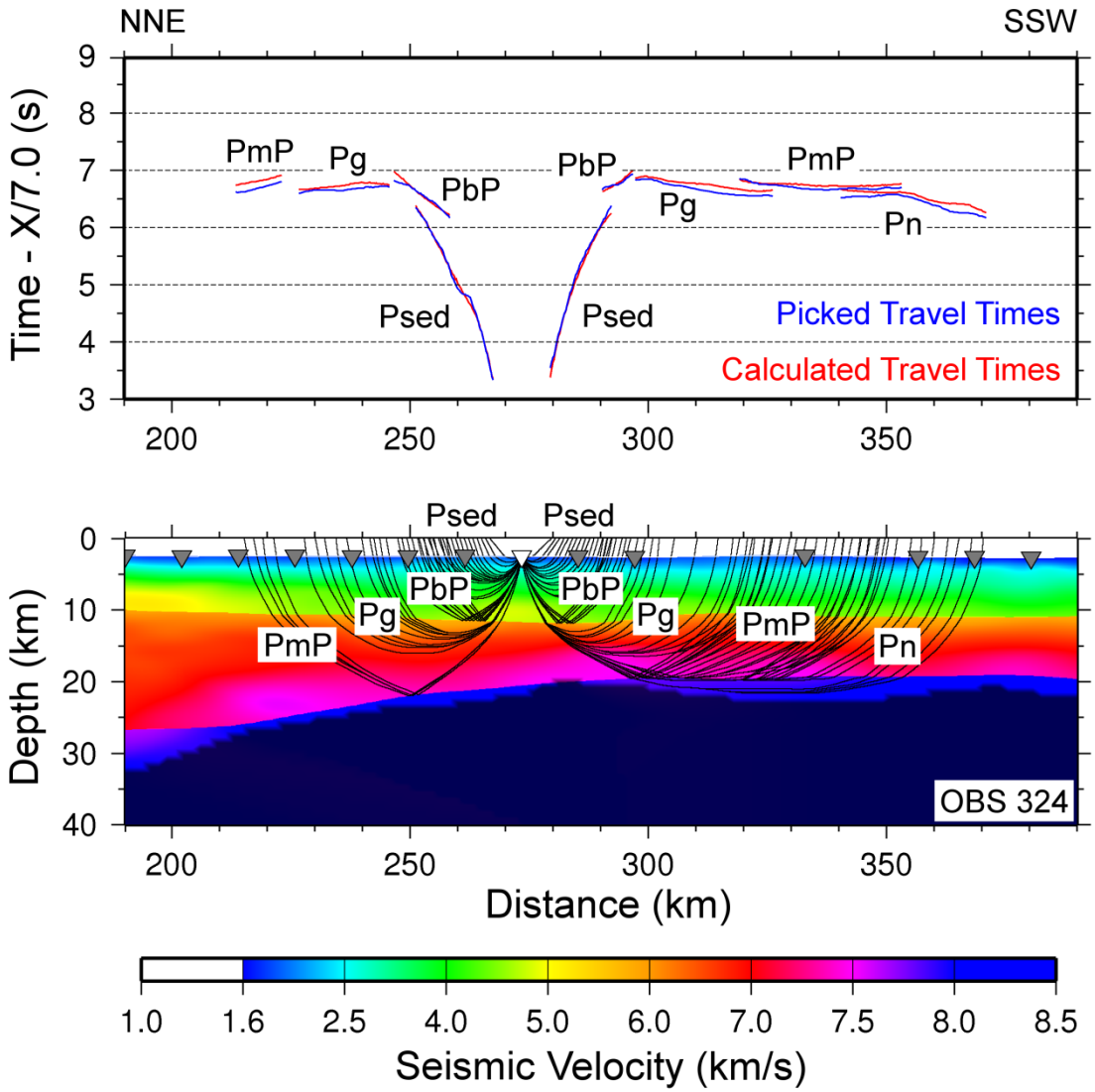

Figure B56 – Picked and calculated travel times for OBS 324 (top) and ray paths through final tomographic model (bottom). See Figure B37 for further information.

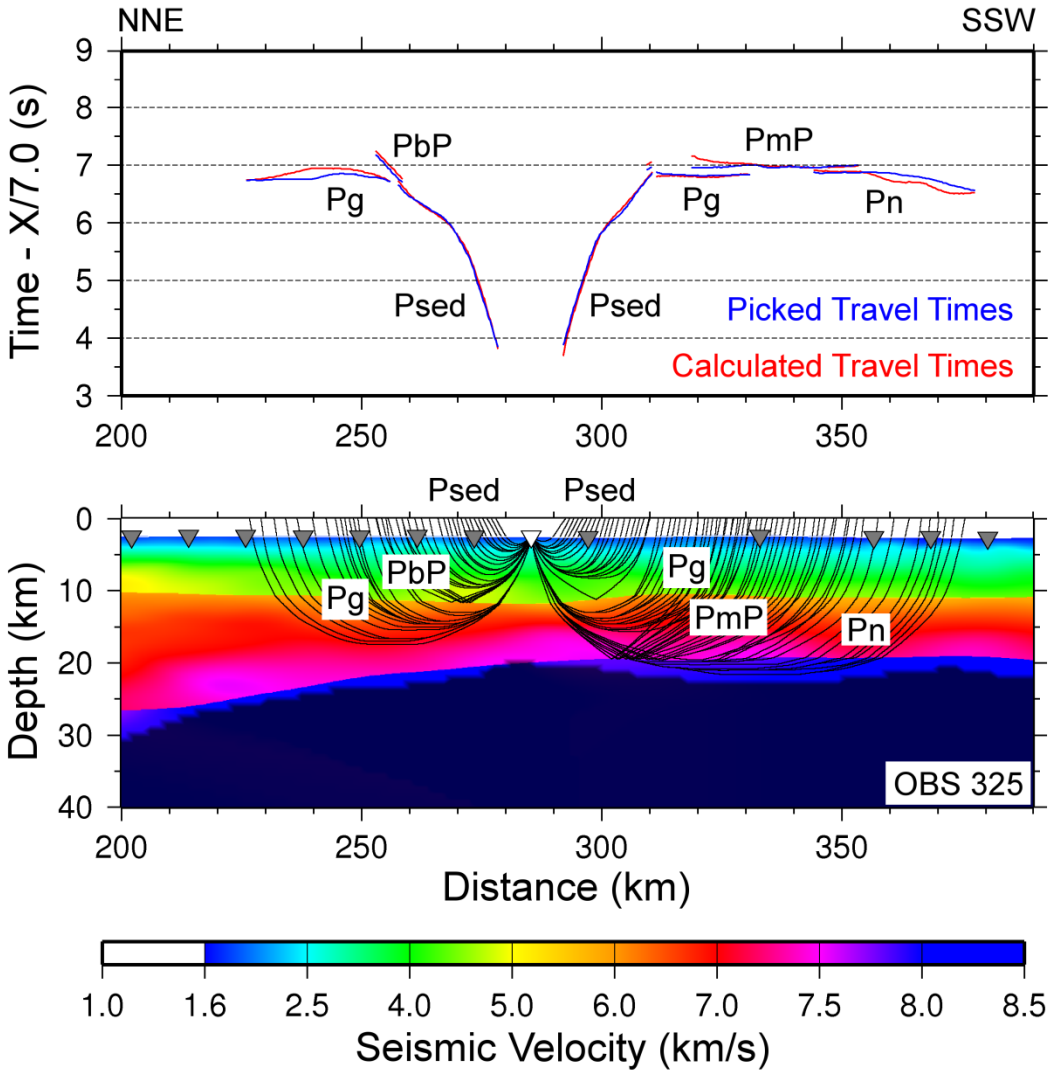

Figure B57 – Picked and calculated travel times for OBS 325 (top) and ray paths through final tomographic model (bottom). See Figure B37 for further information.

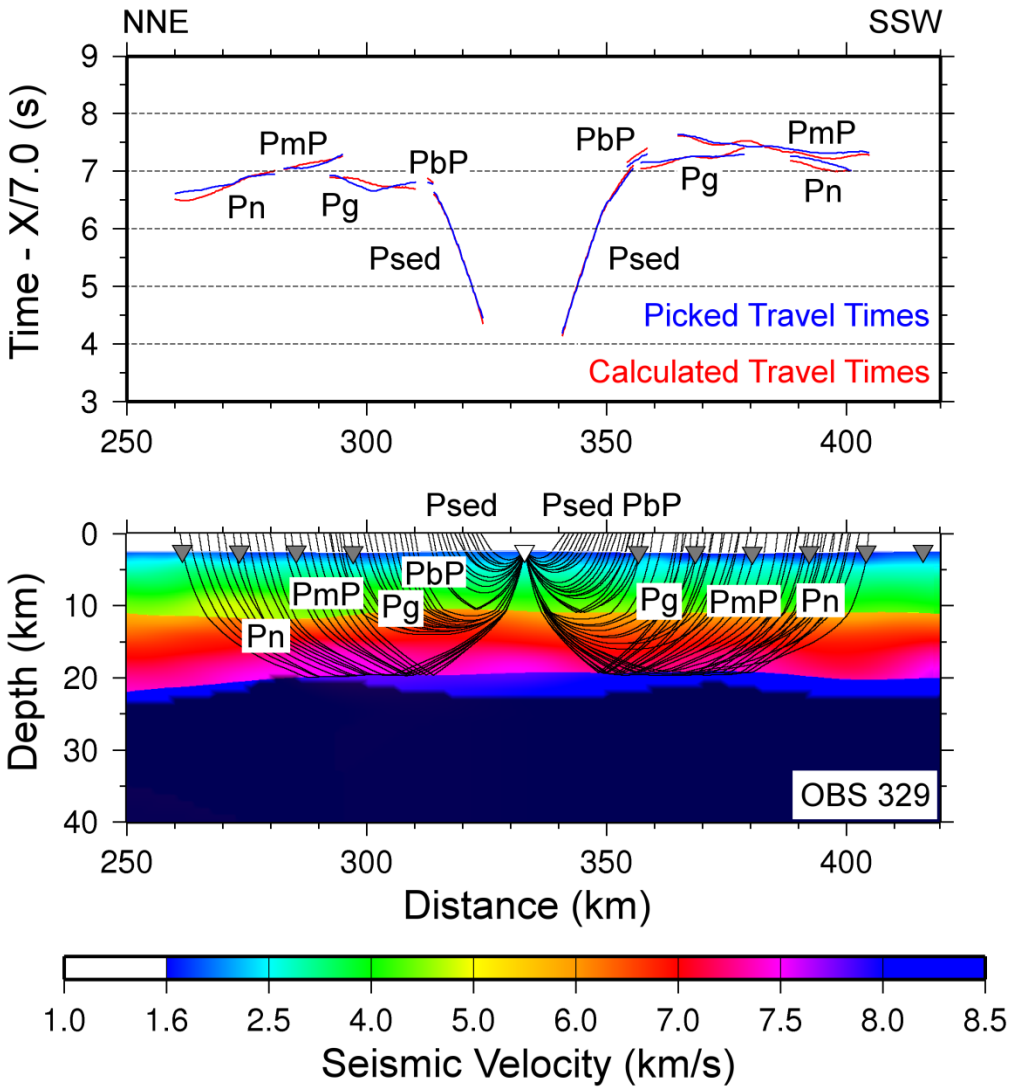

Figure B58 – Picked and calculated travel times for OBS 329 (top) and ray paths through final tomographic model (bottom). See Figure B37 for further information.

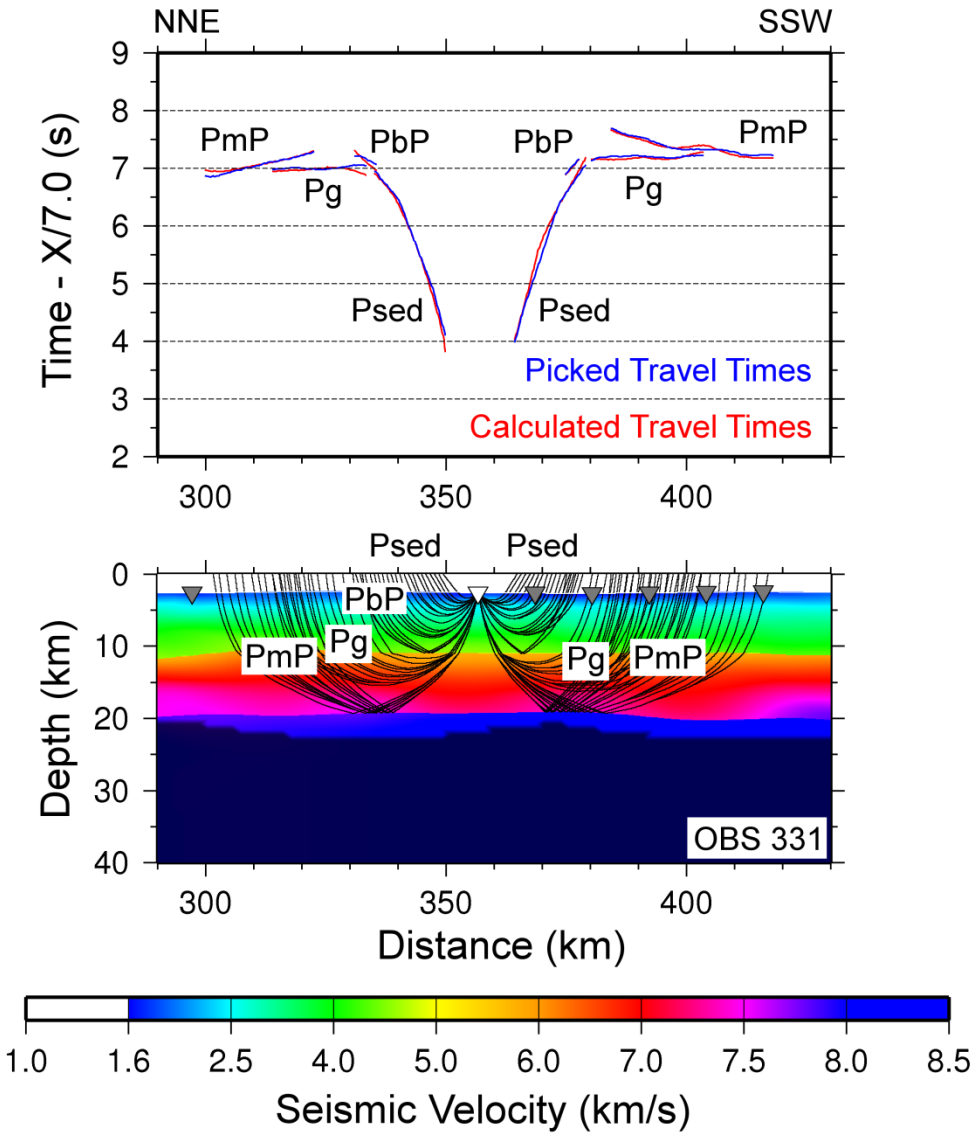

Figure B59 – Picked and calculated travel times for OBS 331 (top) and ray paths through final tomographic model (bottom). See Figure B37 for further information.

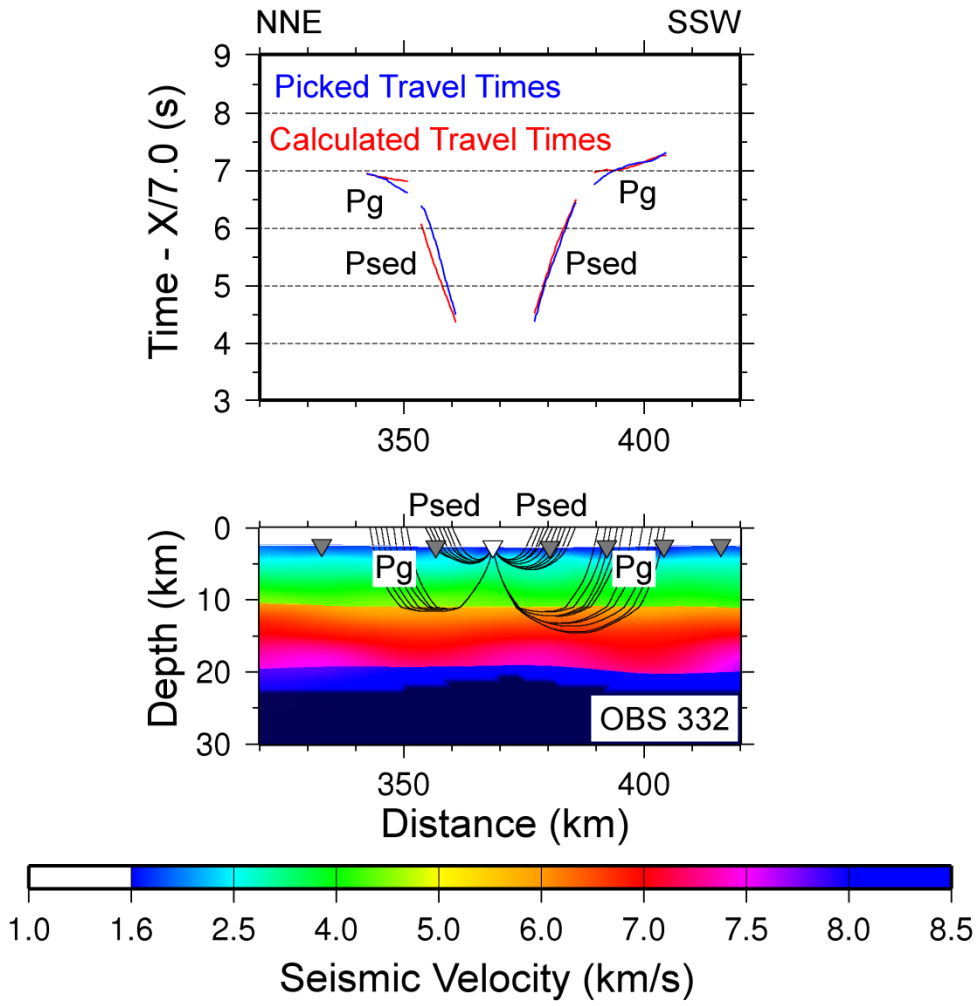

Figure B60 – Picked and calculated travel times for OBS 332 (top) and ray paths through final tomographic model (bottom). See Figure B37 for further information.

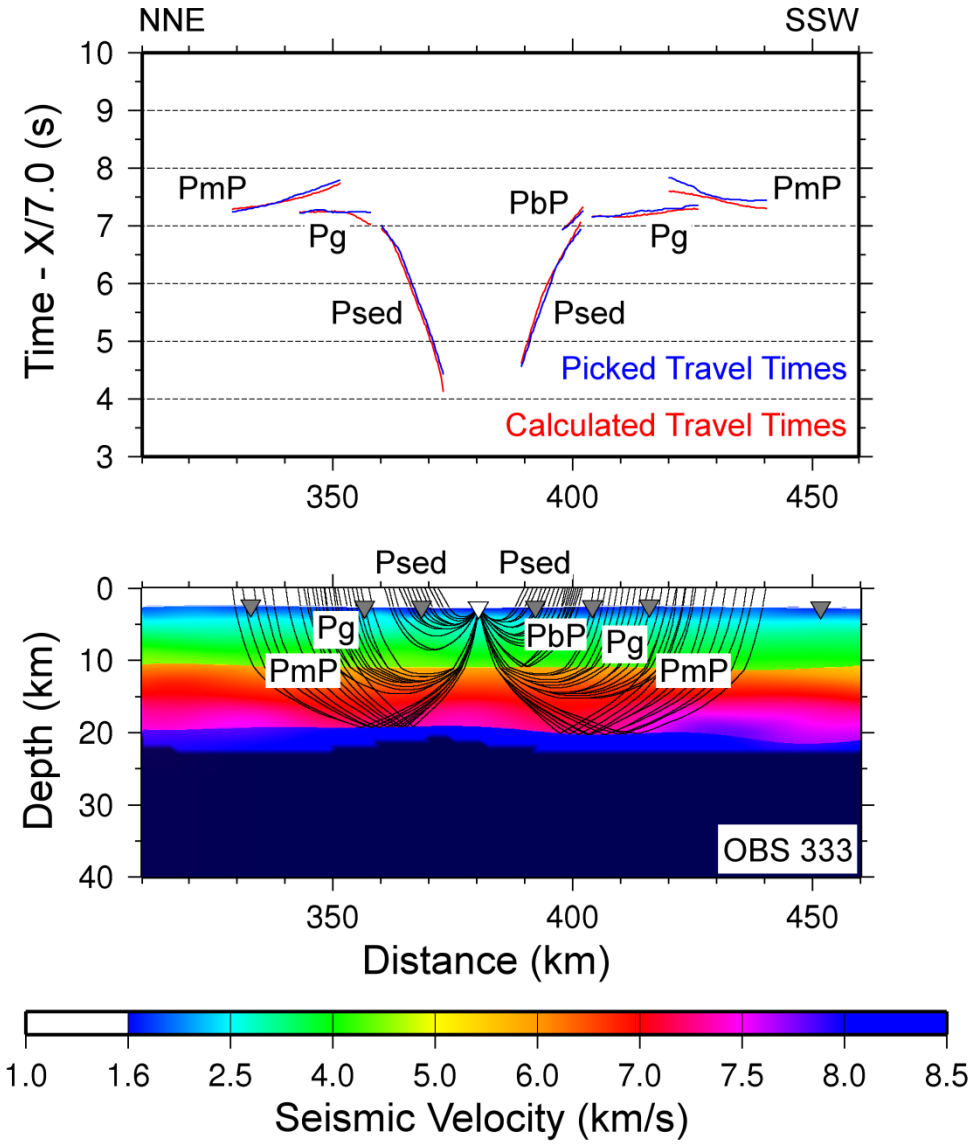

Figure B61 – Picked and calculated travel times for OBS 333 (top) and ray paths through final tomographic model (bottom). See Figure B37 for further information.

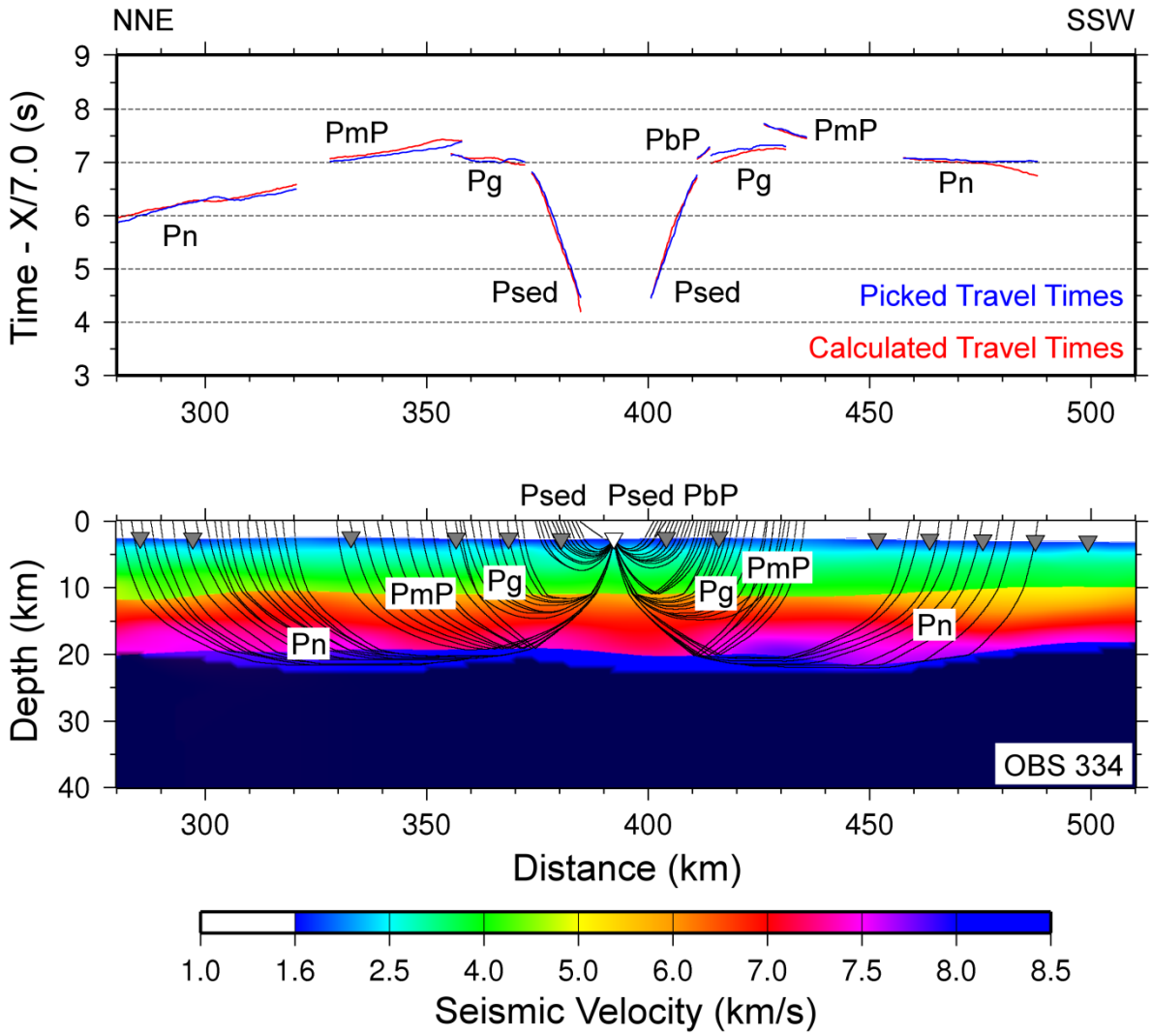

Figure B62 – Picked and calculated travel times for OBS 334 (top) and ray paths through final tomographic model (bottom). See Figure B37 for further information.

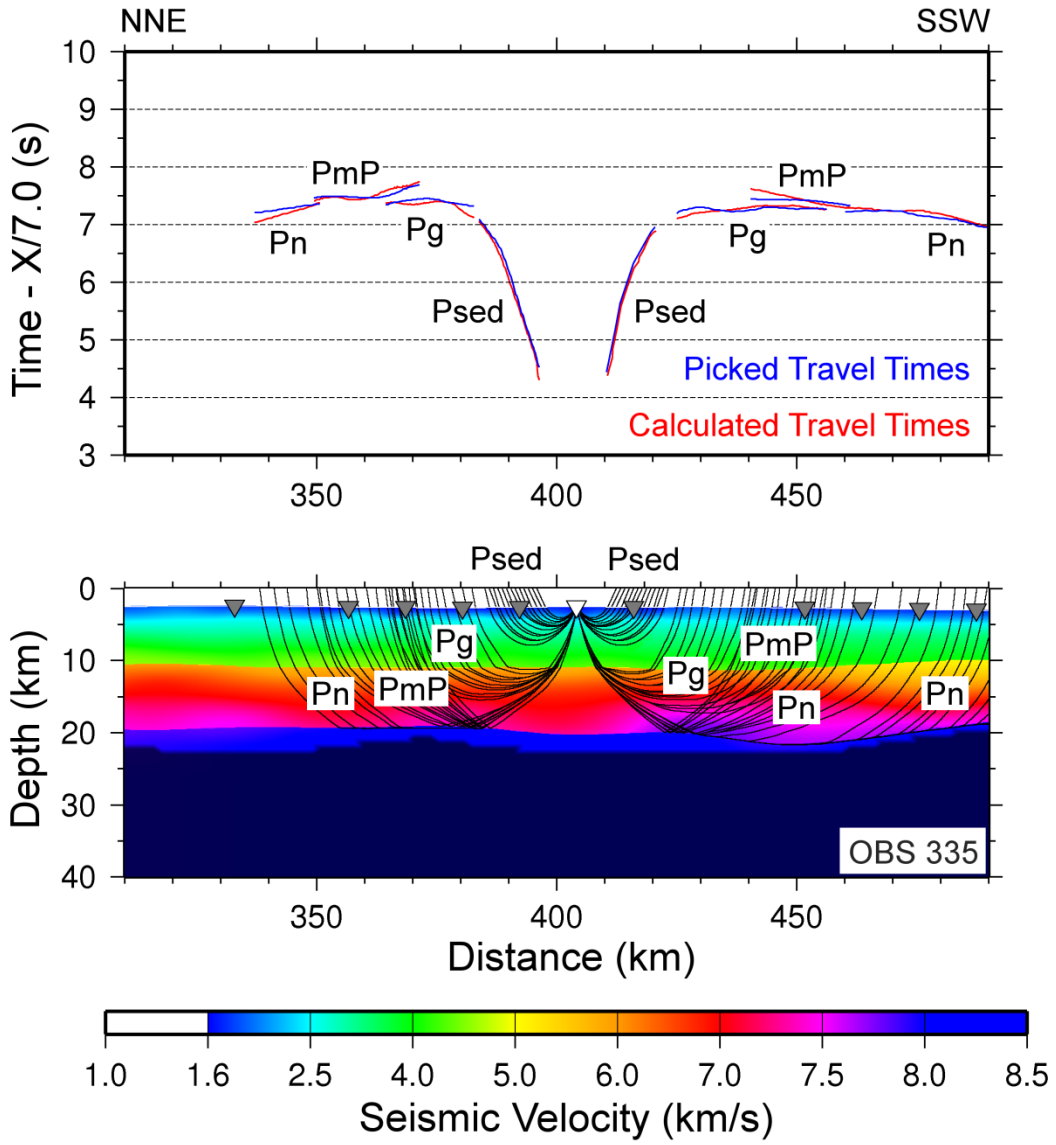

Figure B63 – Picked and calculated travel times for OBS 335 (top) and ray paths through final tomographic model (bottom). See Figure B37 for further information.

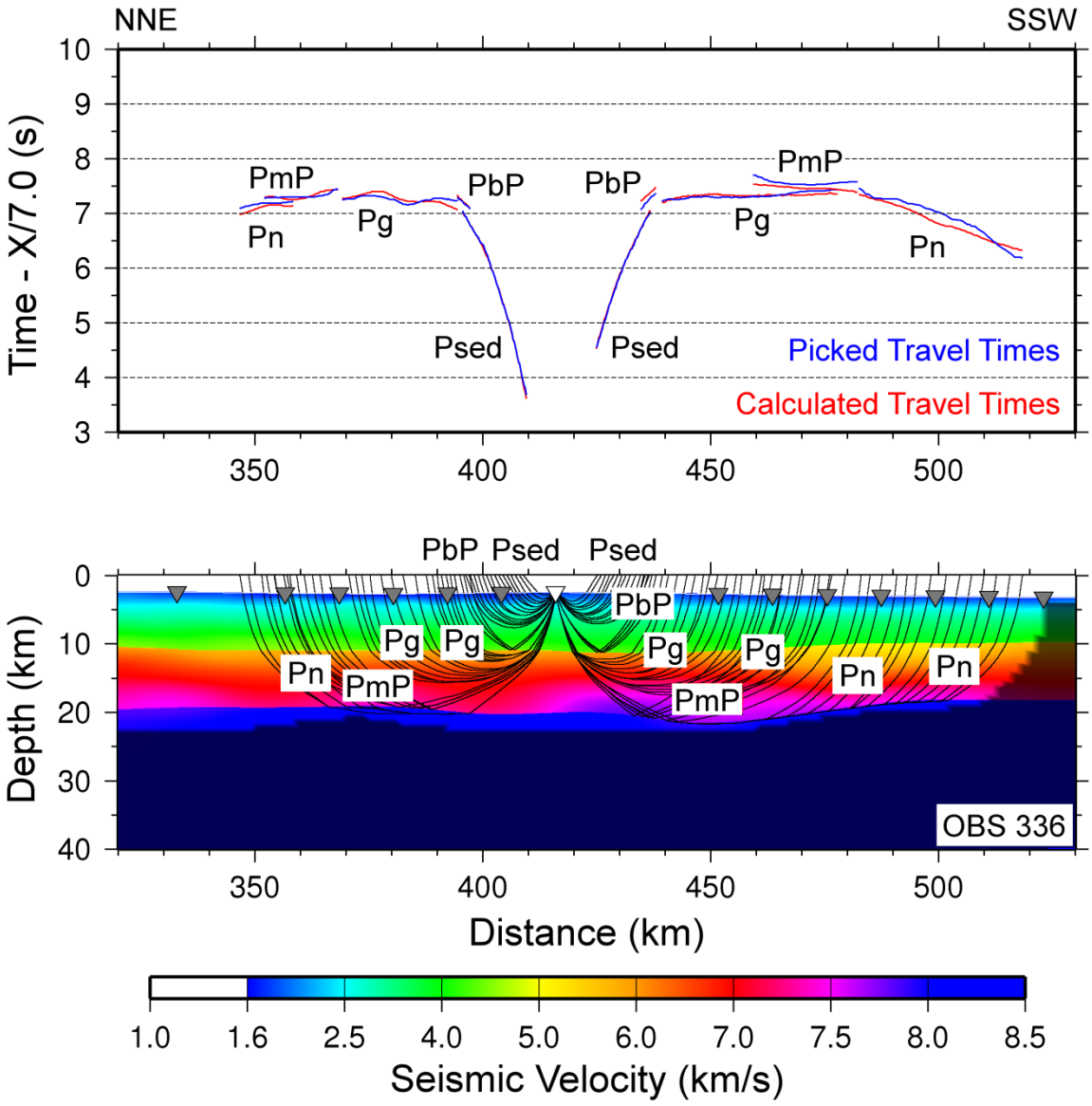

Figure B64 – Picked and calculated travel times for OBS 336 (top) and ray paths through final tomographic model (bottom). See Figure B37 for further information.

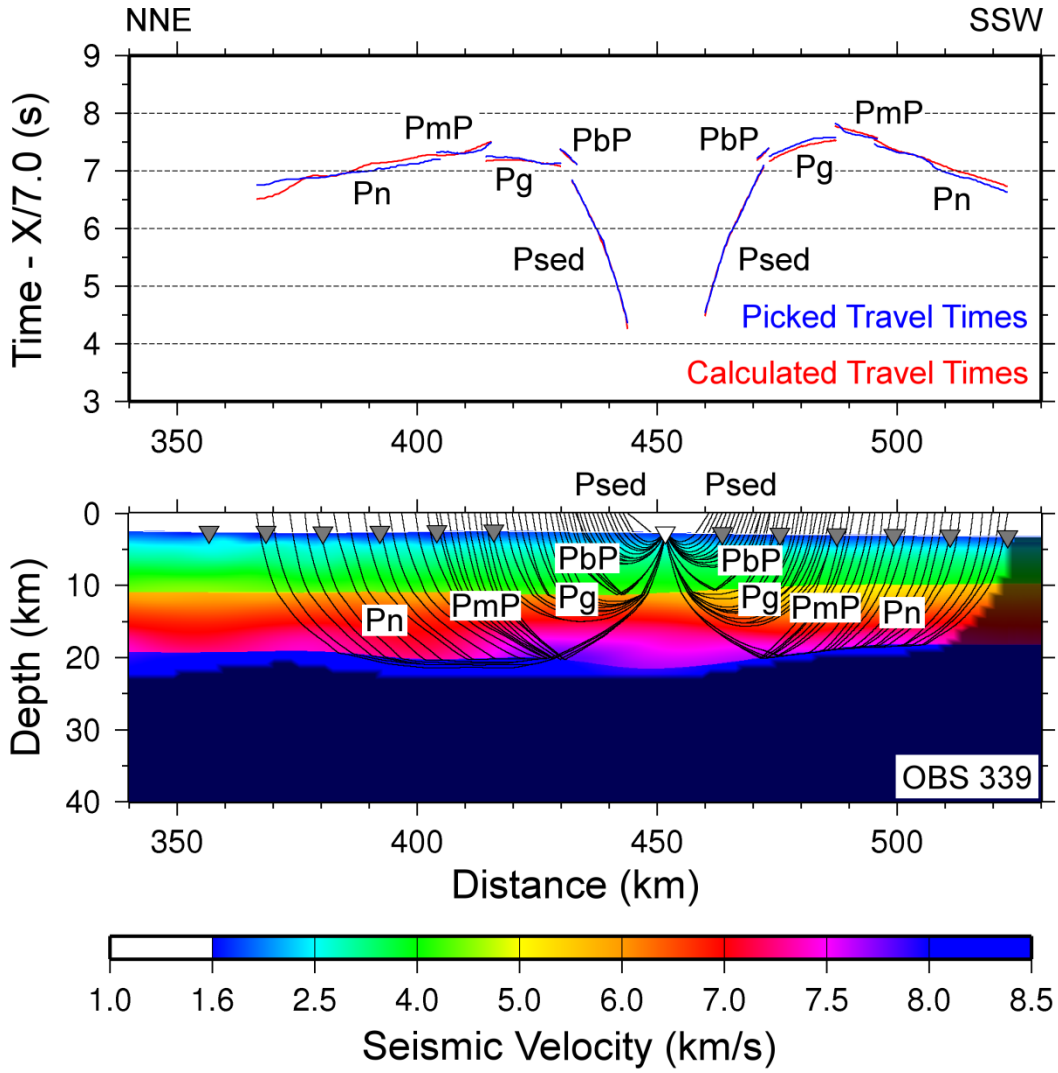

Figure B65 – Picked and calculated travel times for OBS 339 (top) and ray paths through final tomographic model (bottom). See Figure B37 for further information.

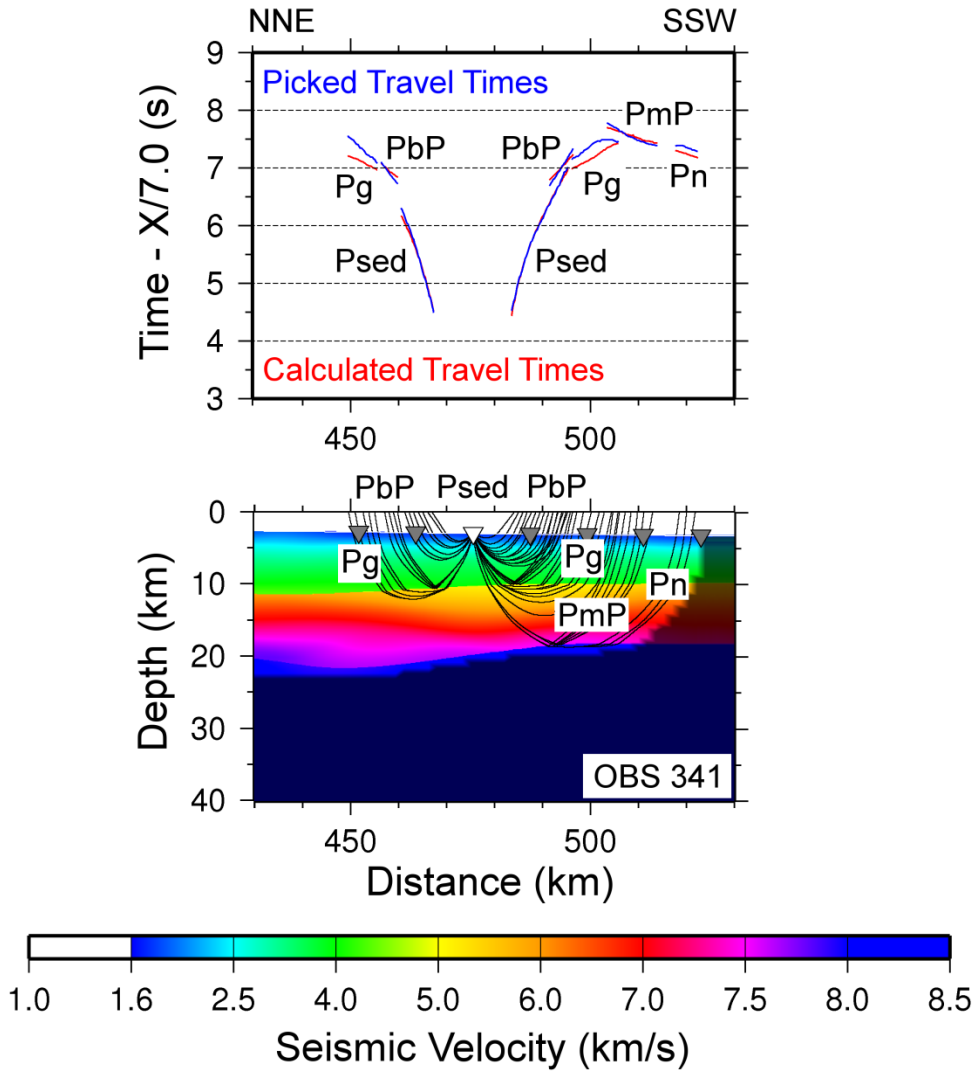

Figure B66 – Picked and calculated travel times for OBS 341 (top) and ray paths through final tomographic model (bottom). See Figure B37 for further information.

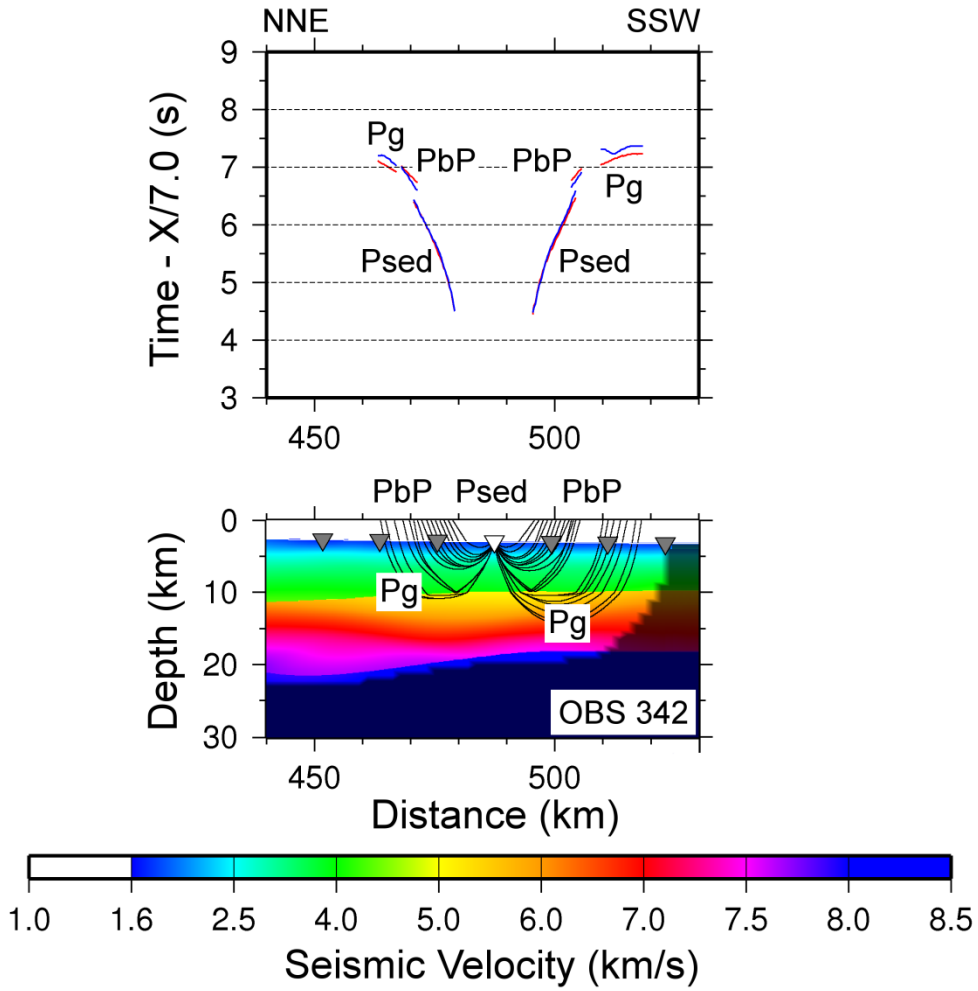

Figure B67 – Picked and calculated travel times for OBS 342 (top) and ray paths through final tomographic model (bottom). See Figure B37 for further information.

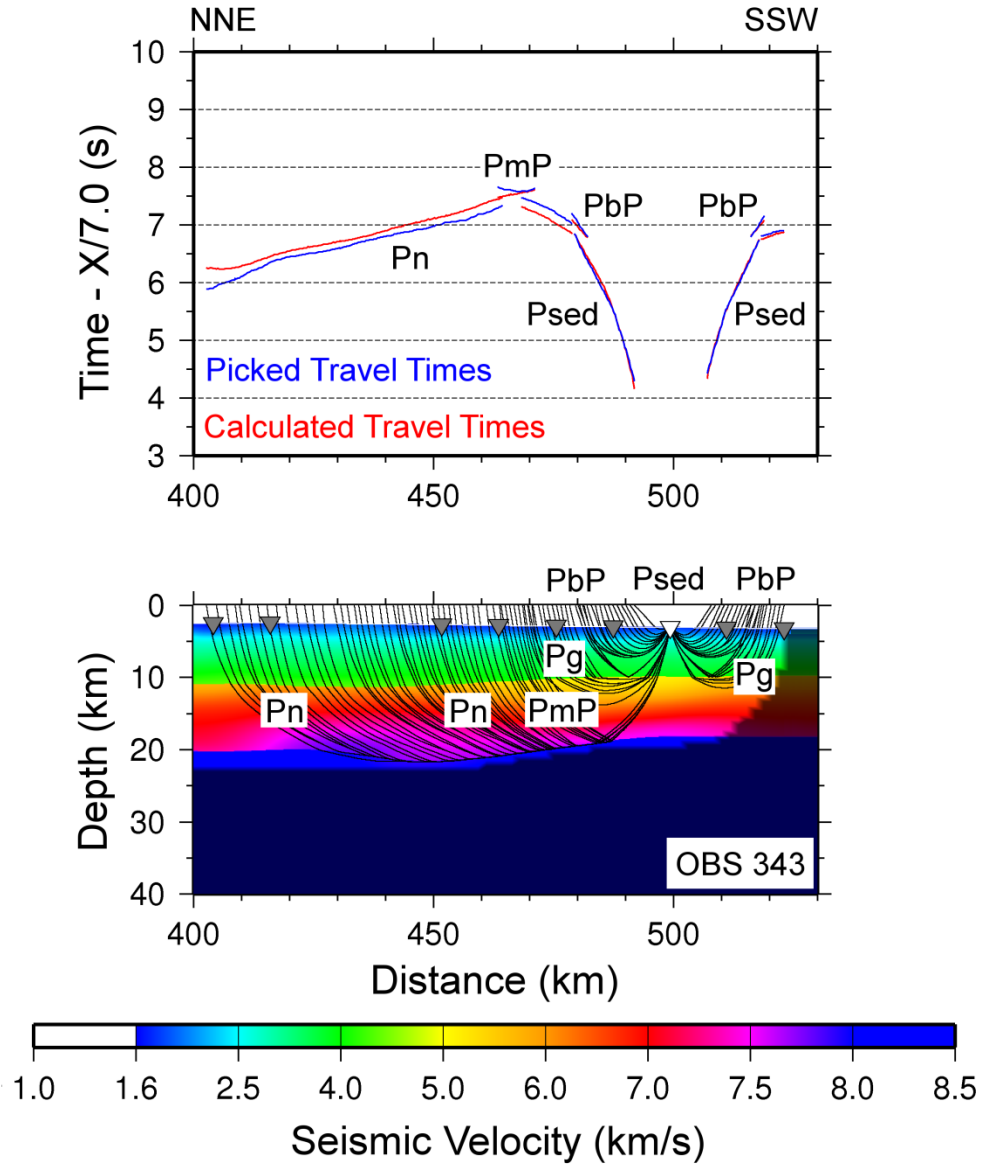

Figure B68 – Picked and calculated travel times for OBS 343 (top) and ray paths through final tomographic model (bottom). See Figure B37 for further information.

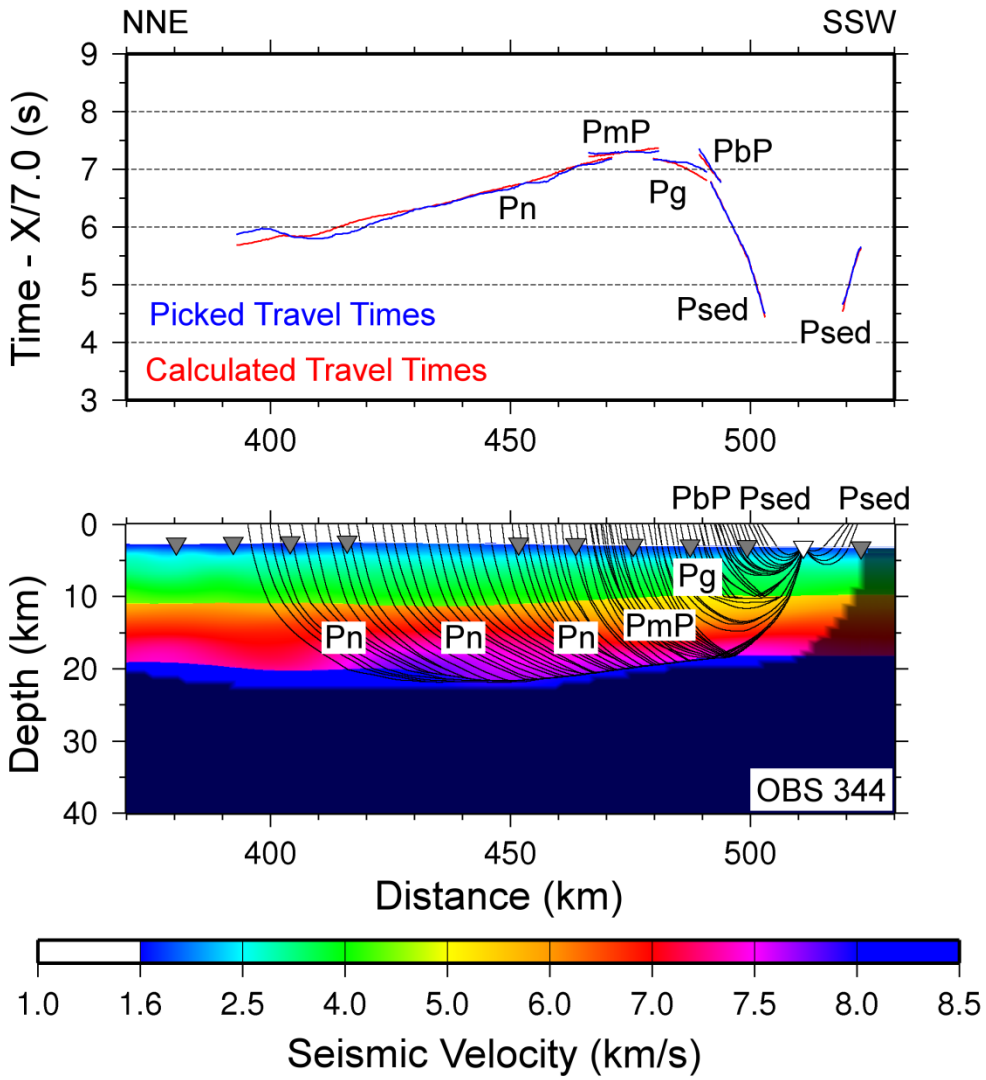

Figure B69 – Picked and calculated travel times for OBS 344 (top) and ray paths through final tomographic model (bottom). See Figure B37 for further information.

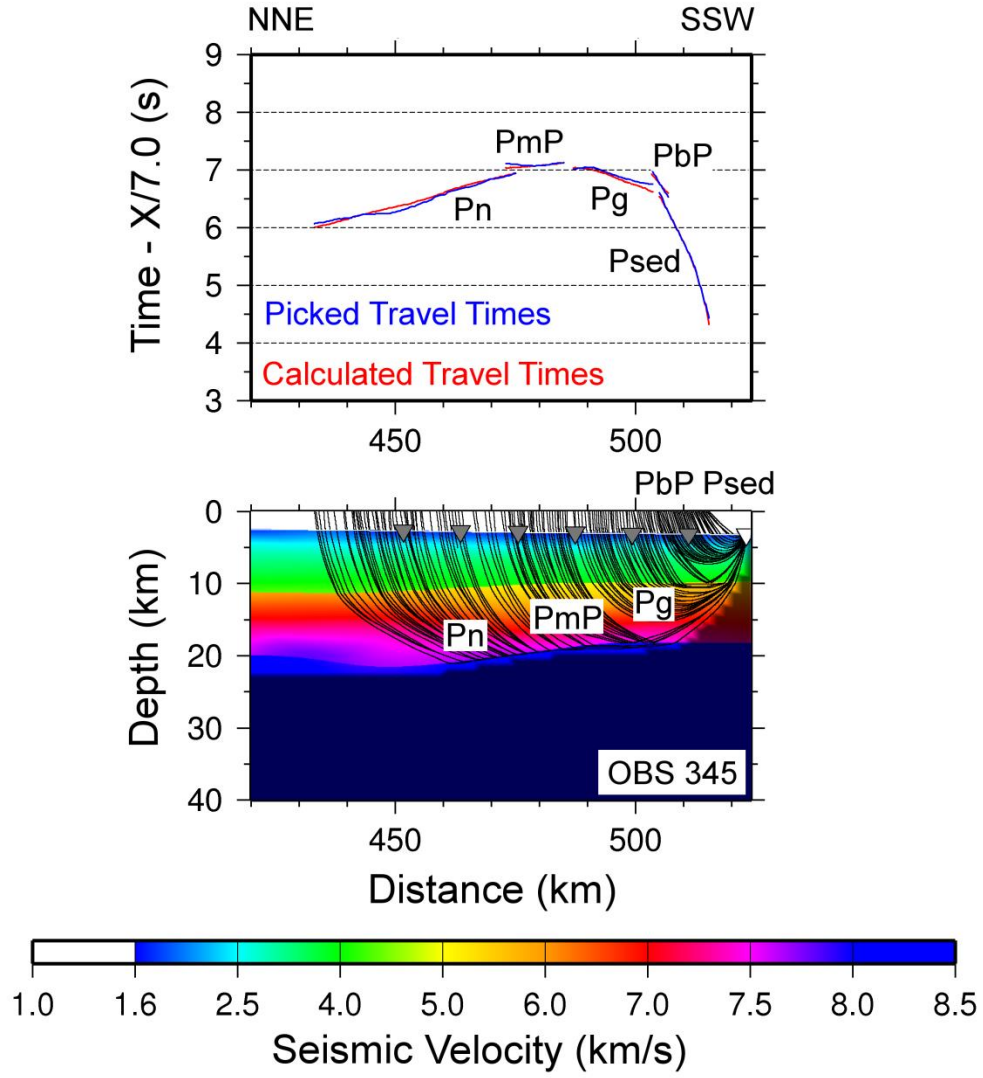

Figure B70 – Picked and calculated travel times for OBS 345 (top) and ray paths through final tomographic model (bottom). See Figure B37 for further information.

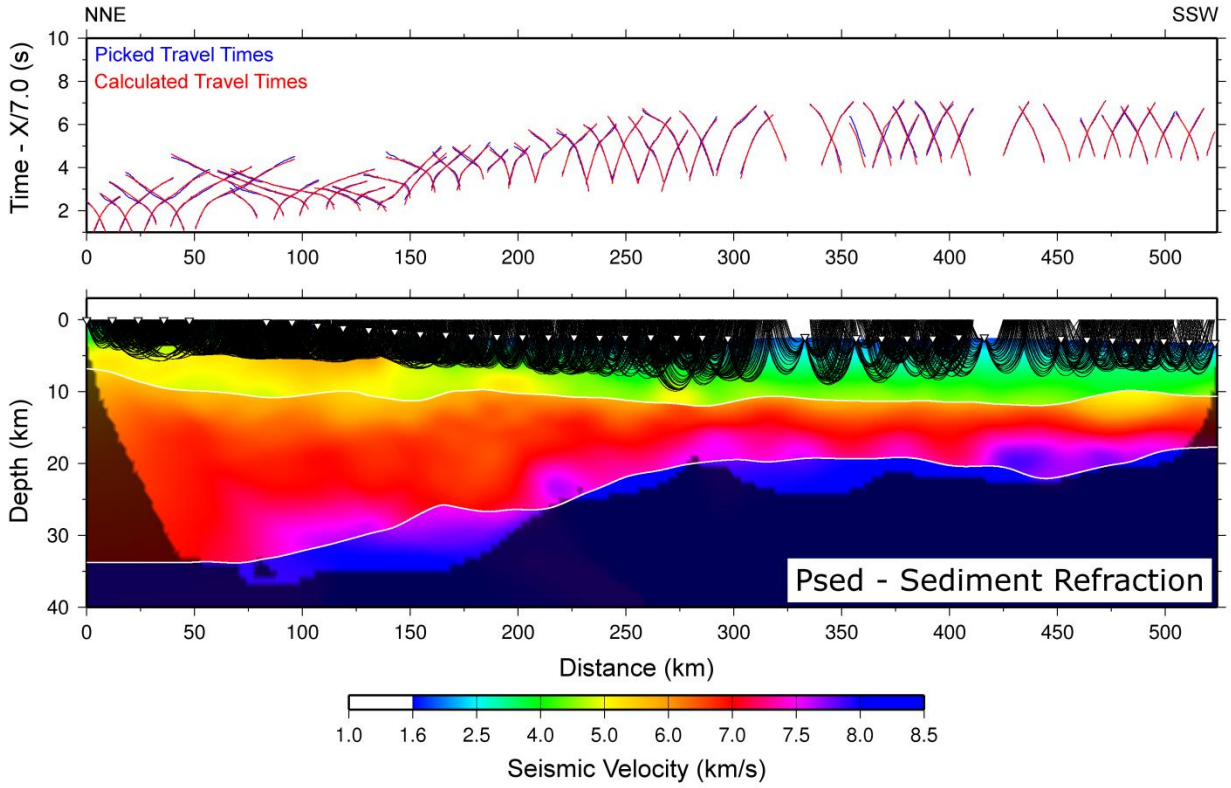

Figure B71 – Picked and calculated travel times (top) and ray paths through final tomographic model (bottom) for the *Psed* refraction phase across all GUMBO Line 3 OBSs.

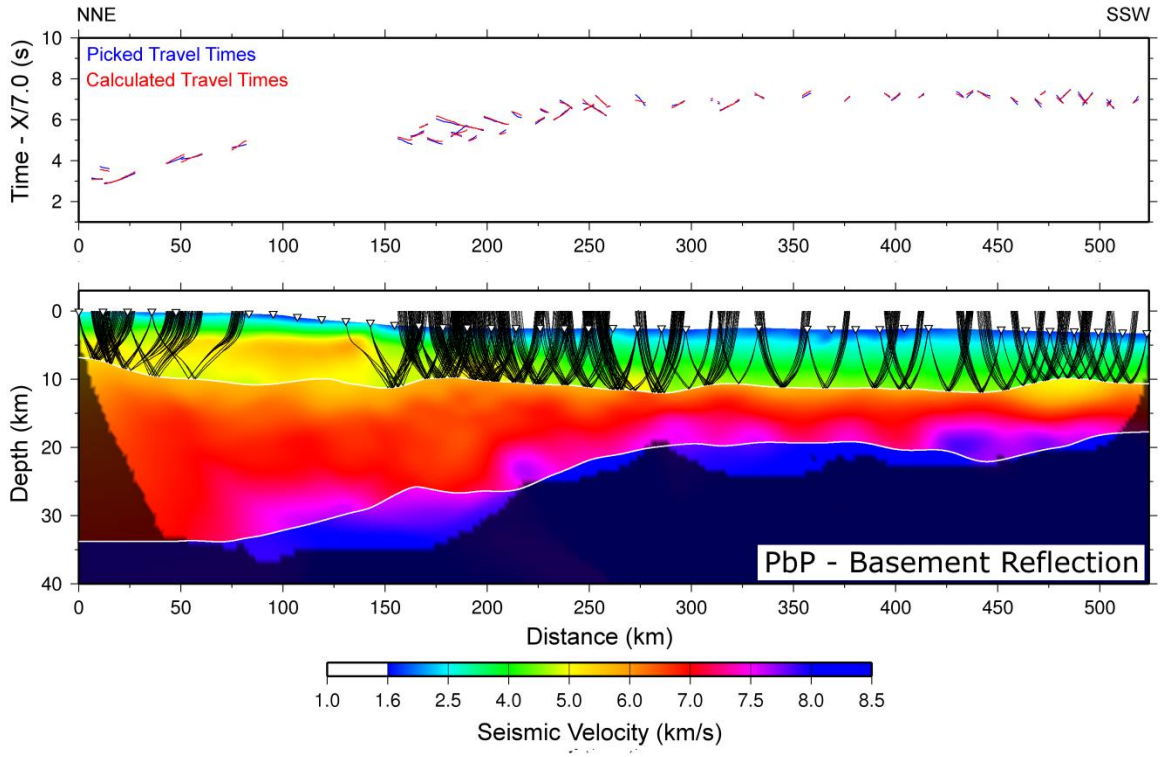

Figure B72 - Picked and calculated travel times (top) and ray paths through final tomographic model (bottom) for the *Pbp* reflection phase across all GUMBO Line 3 OBSs.

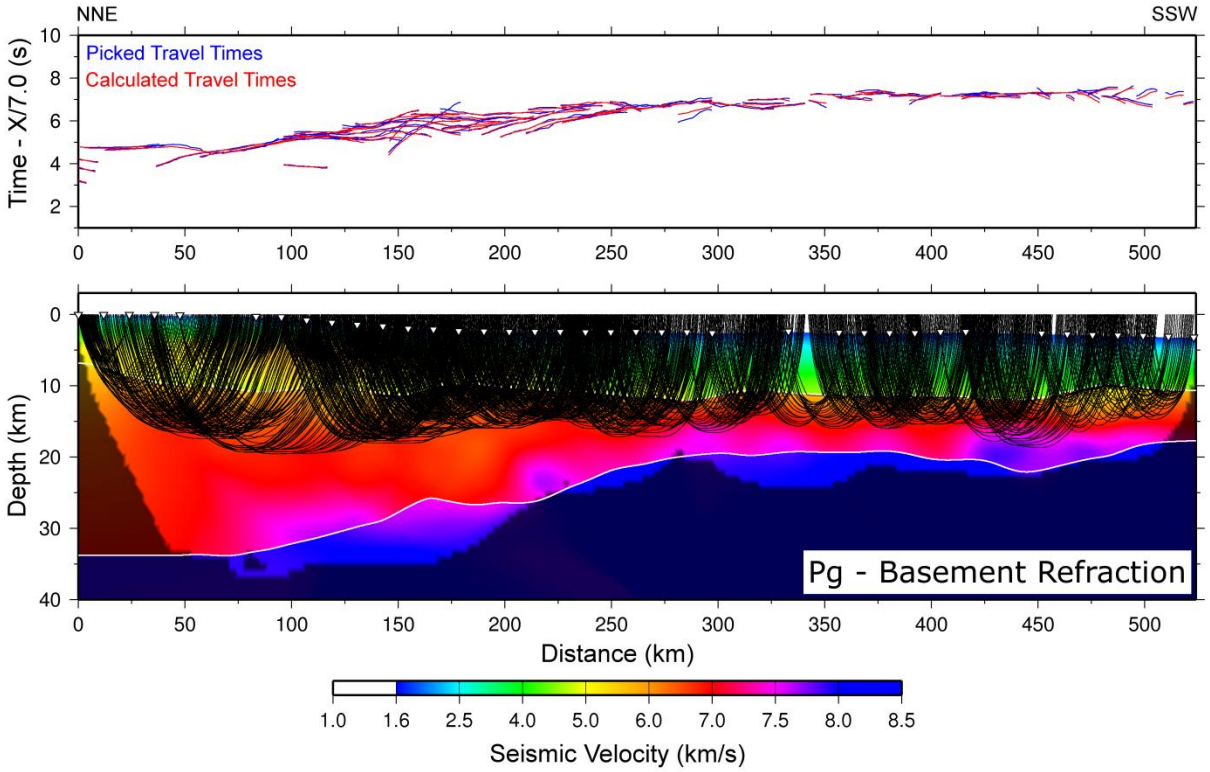

Figure B73 - Picked and calculated travel times (top) and ray paths through final tomographic model (bottom) for the *Pg* refraction phase across all GUMBO Line 3 OBSs.

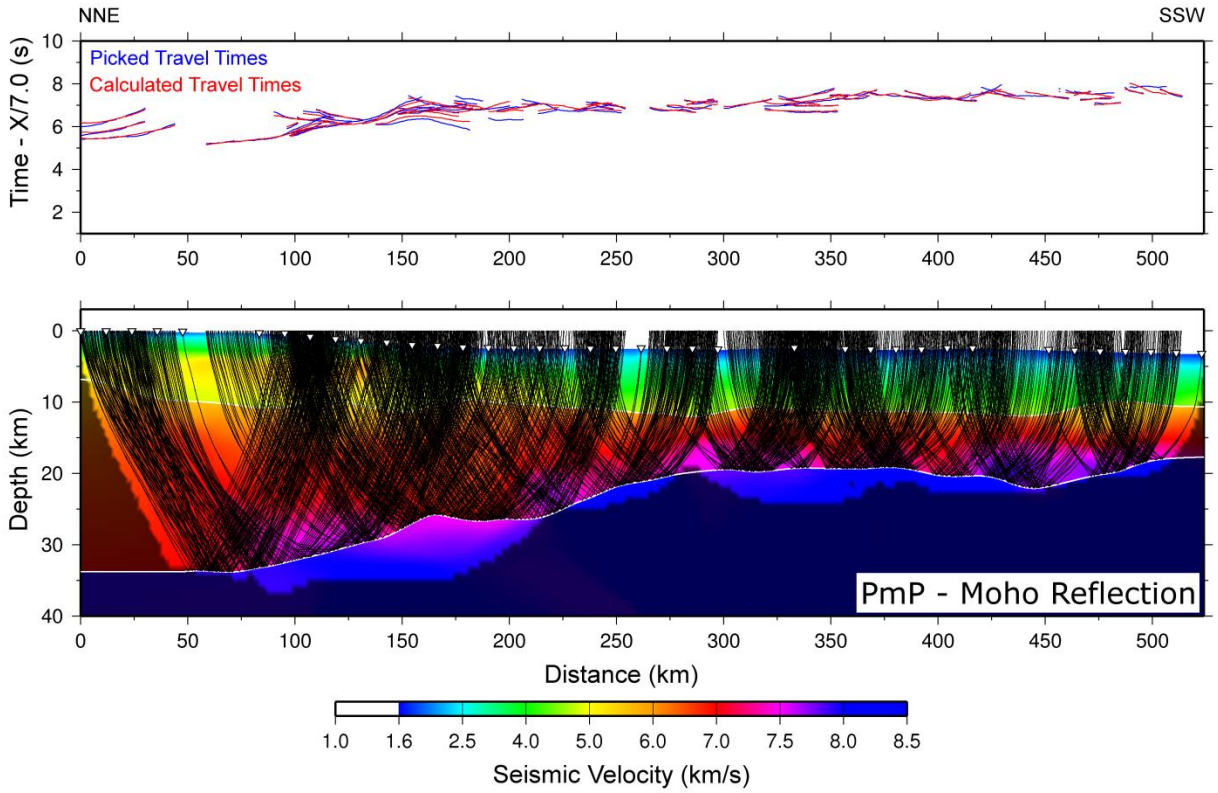

Figure B74 - Picked and calculated travel times (top) and ray paths through final tomographic model (bottom) for the *PmP* reflection phase across all GUMBO Line 3 OBSs.

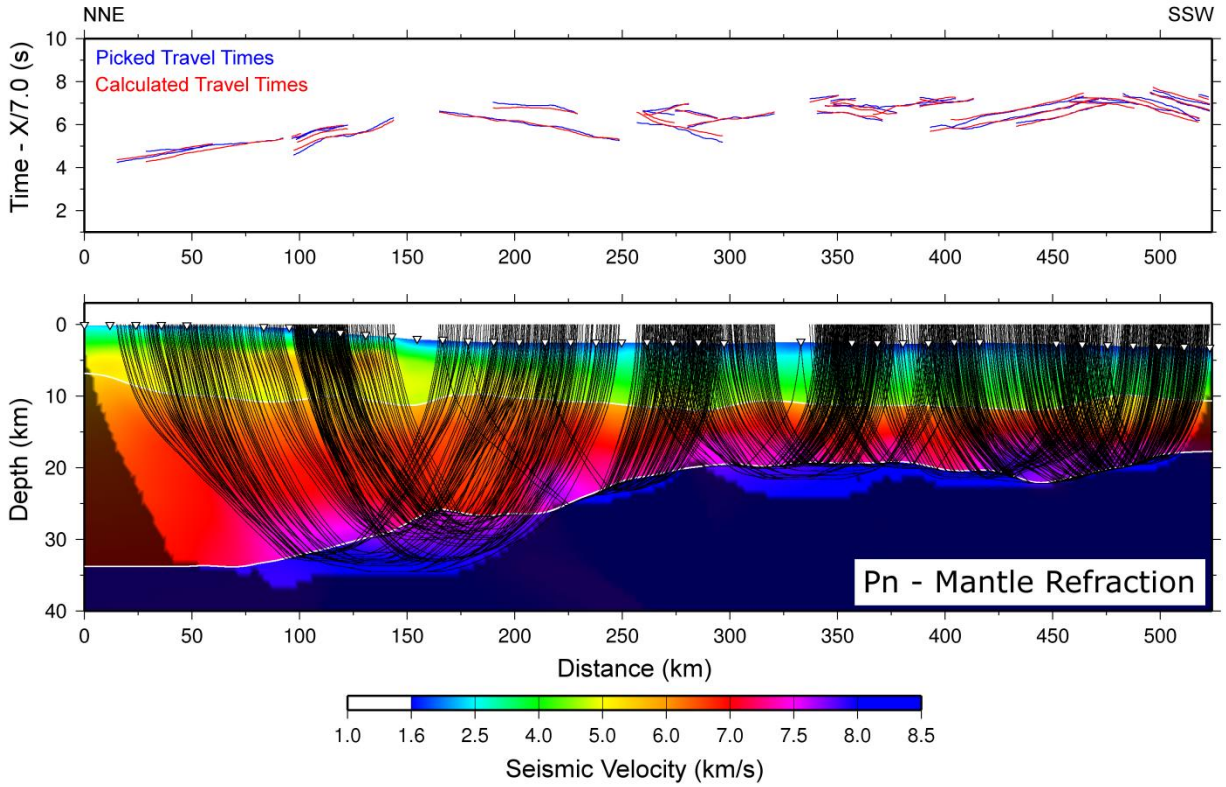

Figure B75 - Picked and calculated travel times (top) and ray paths through final tomographic model (bottom) for the *Pn* refraction phase across all GUMBO Line 3 OBSs.

Appendix C: Chapter 4

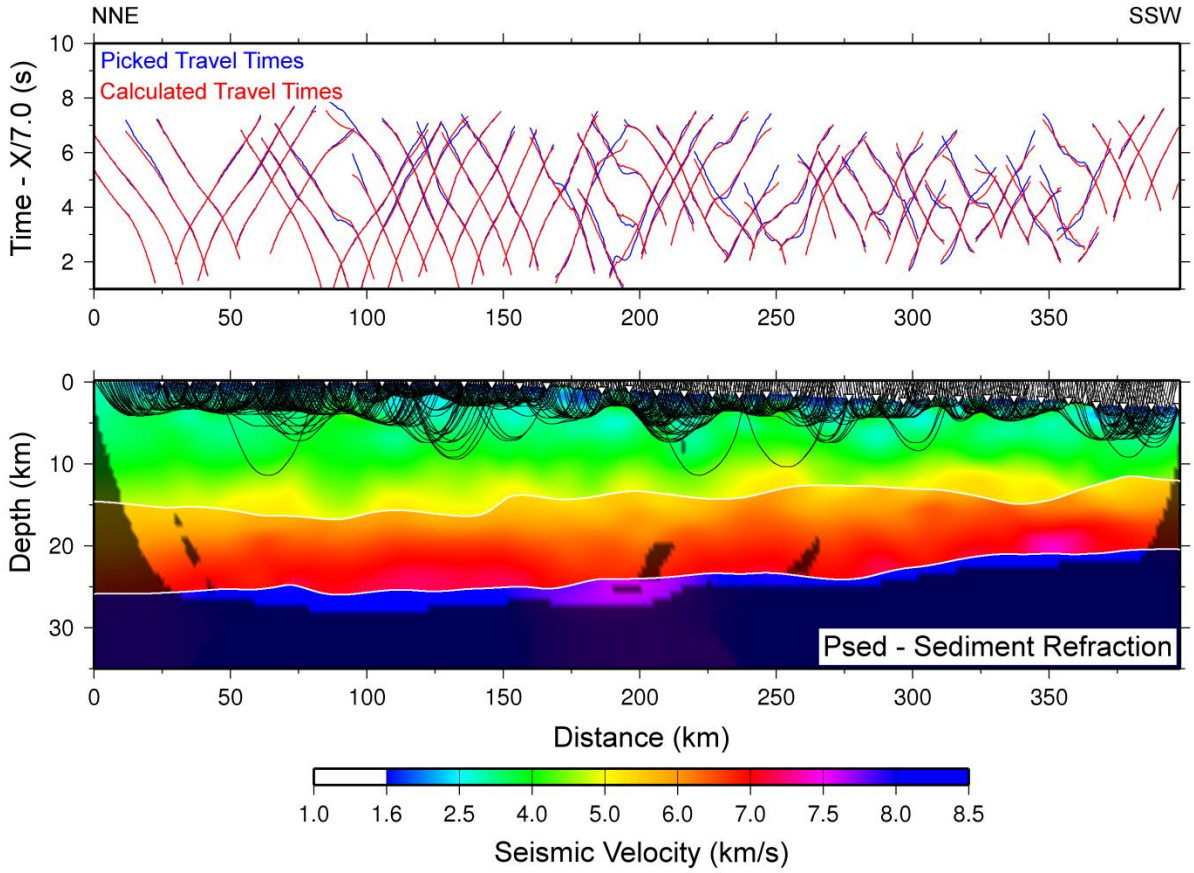

Figure C1 - Picked and calculated travel times for sediment refractions (P1, *Psed*) from all GUMBO Line 2 OBSs (top) and corresponding ray paths through final tomographic model (bottom).

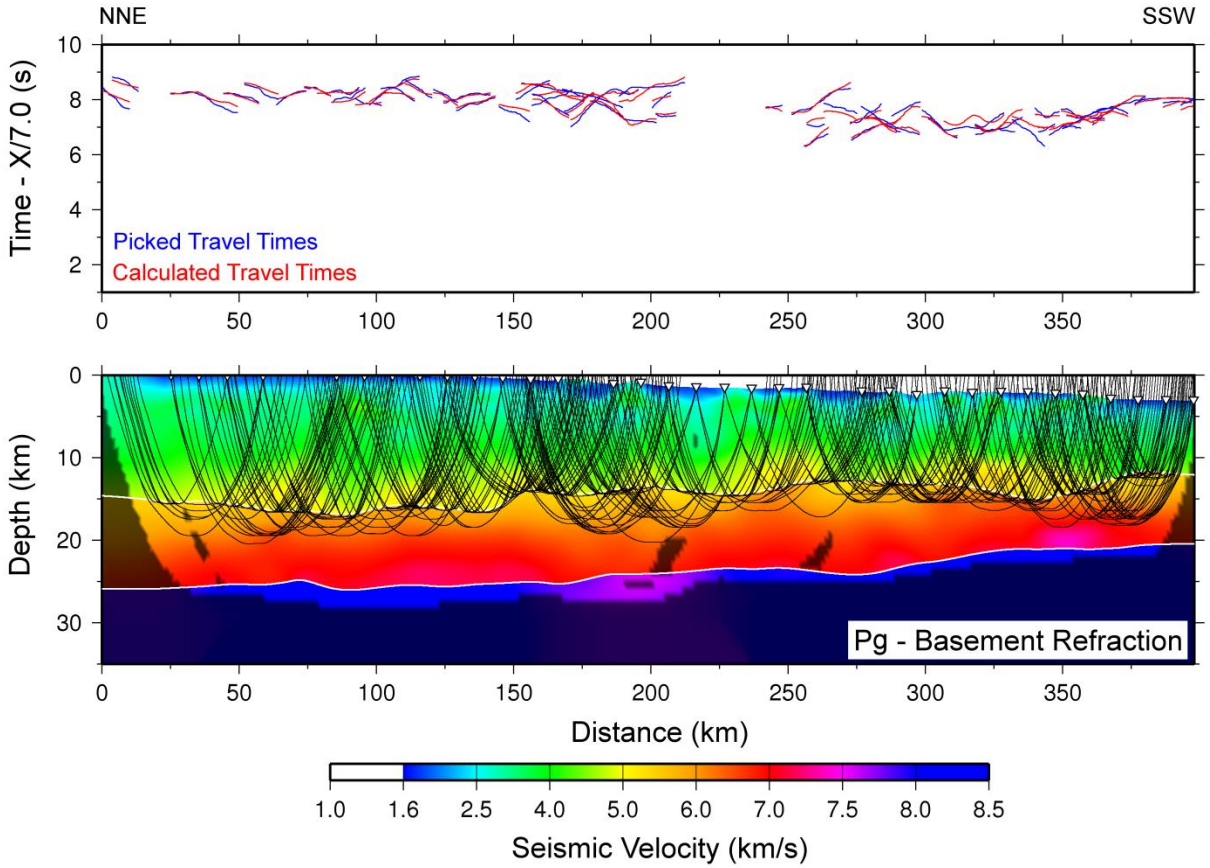

Figure C2 - Picked and calculated travel times for basement refractions (P2, *Pg*) from all GUMBO Line 2 OBSs (top) and corresponding ray paths through final tomographic model (bottom).

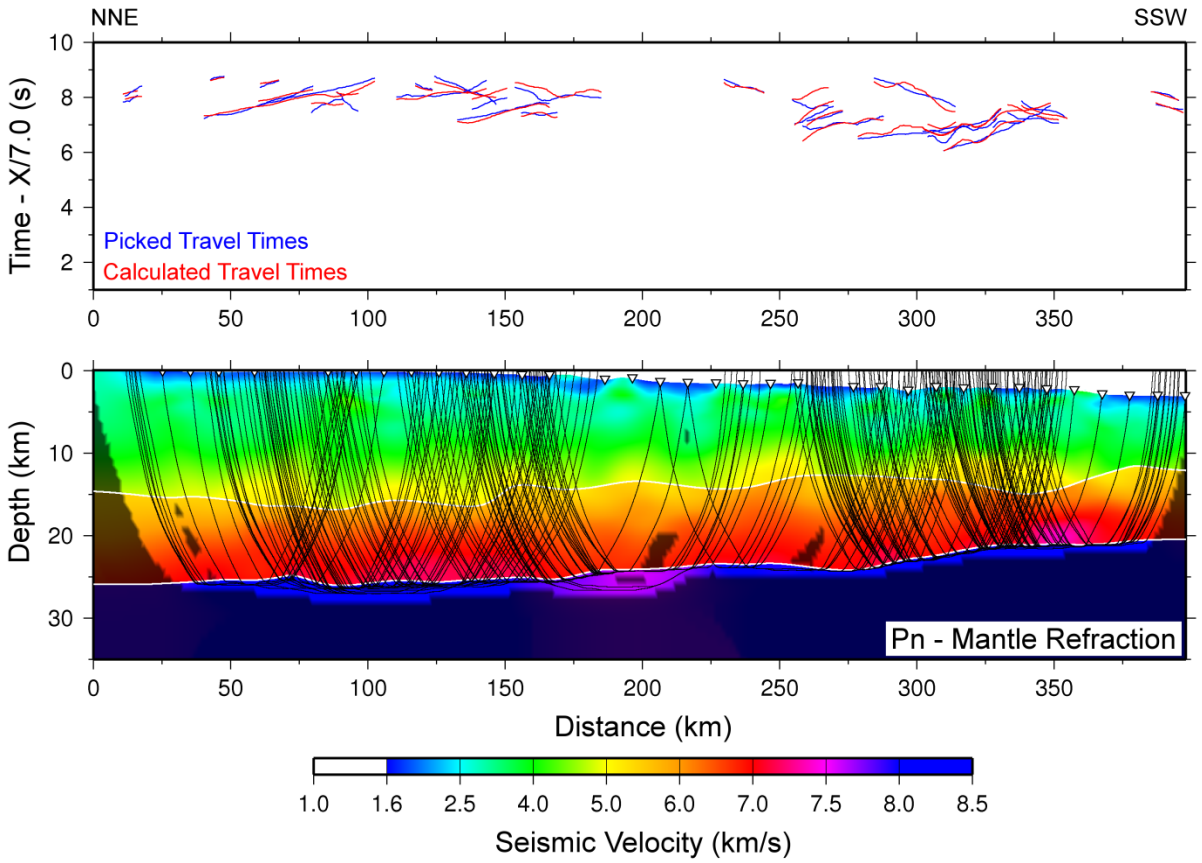

Figure C3 - Picked and calculated travel times for mantle refractions (P3, *Pn*) from all GUMBO Line 2 OBSs (top) and corresponding ray paths through final tomographic model (bottom).

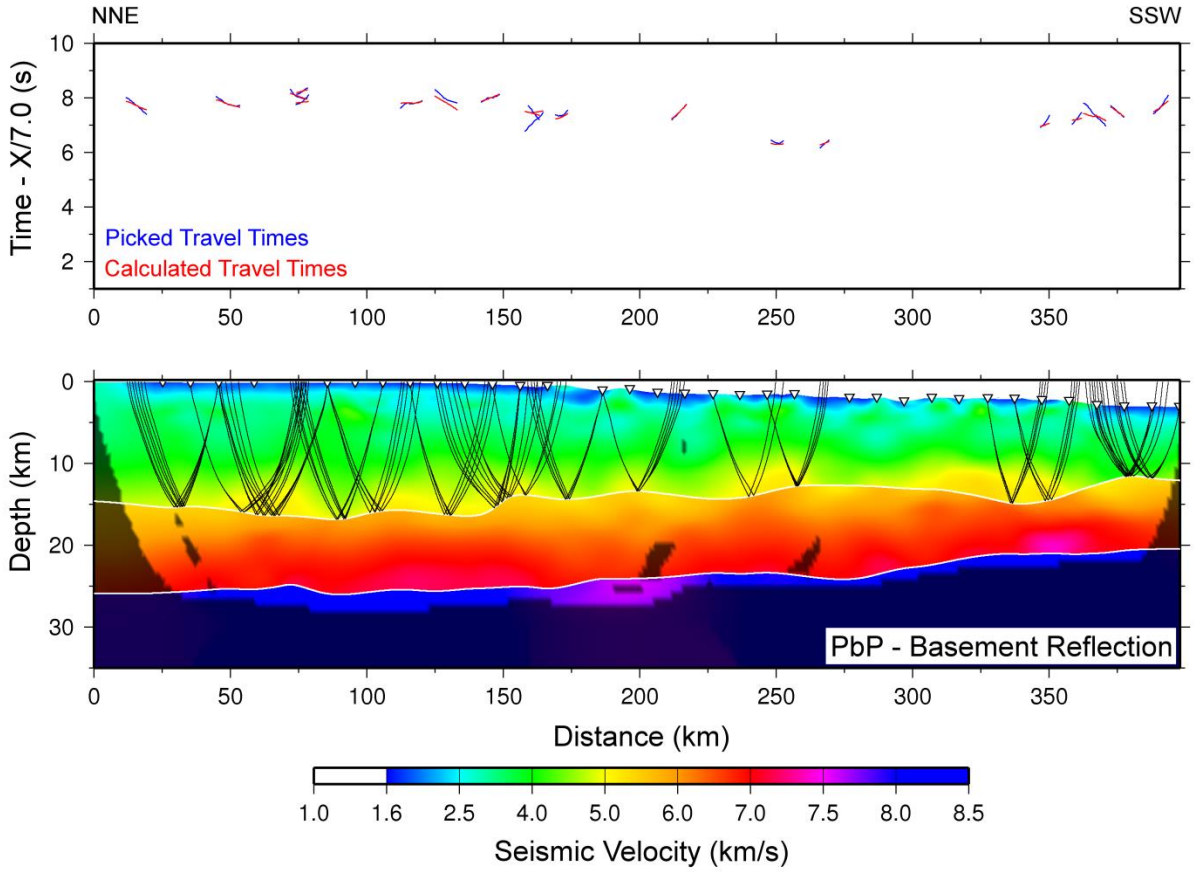

Figure C4 - Picked and calculated travel times for basement reflections (R1, *PbP*) from all GUMBO Line 2 OBSs (top) and corresponding ray paths through final tomographic model (bottom).

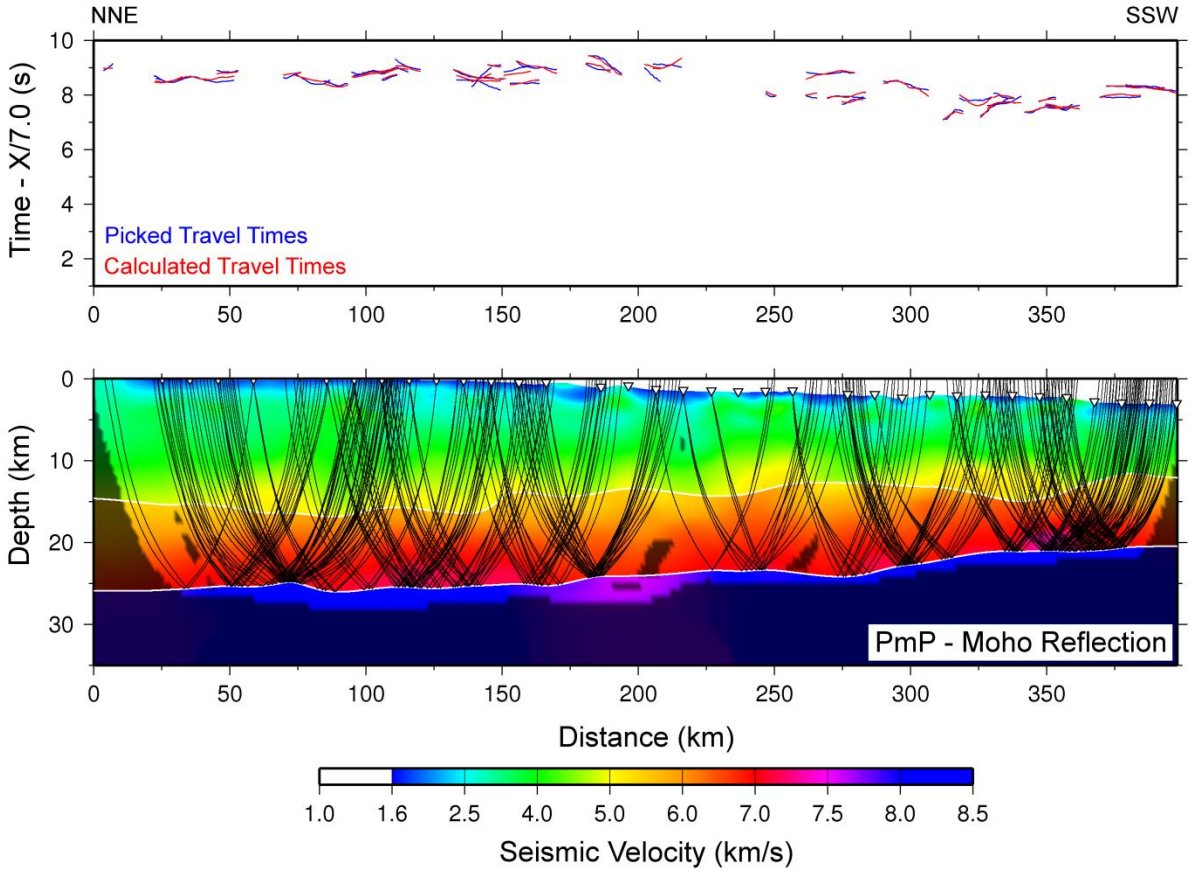

Figure C5 - Picked and calculated travel times for Moho reflections (R2, *PmP*) from all GUMBO Line 2 OBSs (top) and corresponding ray paths through final tomographic model (bottom).

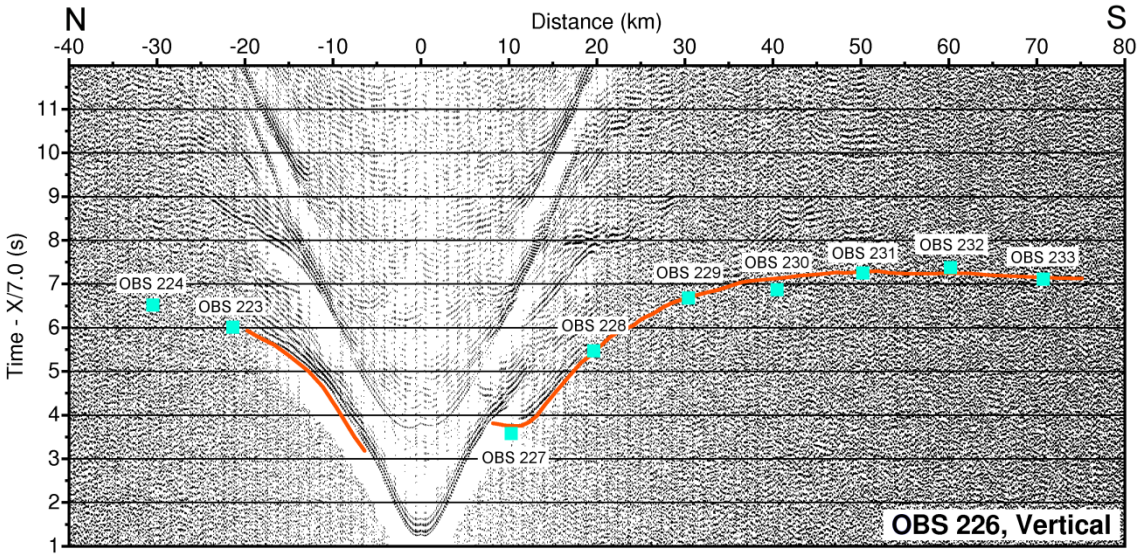

Figure C6 – Receiver gather from the vertical component of OBS 226 plotted with interpreted first-arriving travel times (orange line) and reciprocities from nearby instruments (blue squares). A reduction velocity of 7.0 km/s is applied.

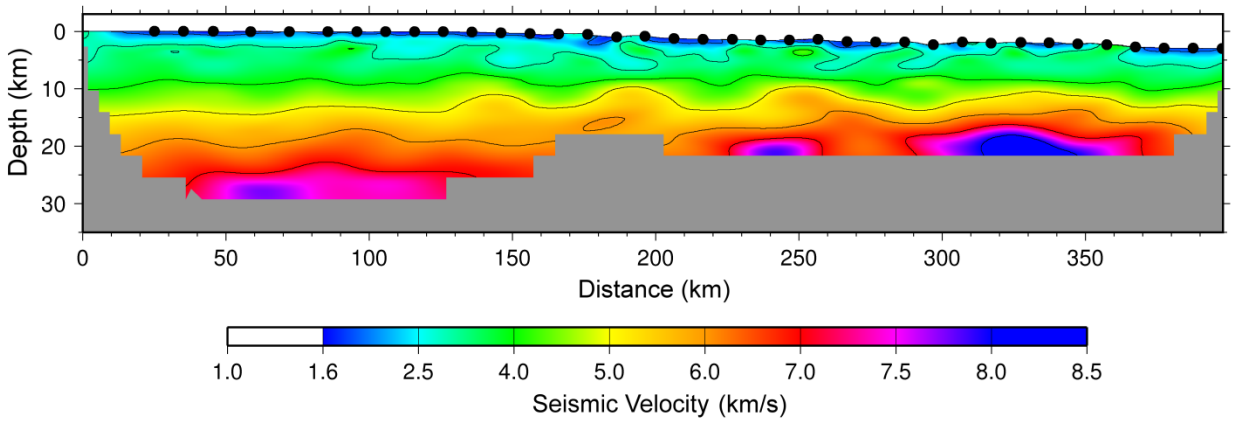

Figure C7 – First estimate of GUMBO 2 seismic velocity model built using only travel times from an undifferentiated first-arrival phase. Black dots are OBS locations. Gray regions are not constrained by ray paths.

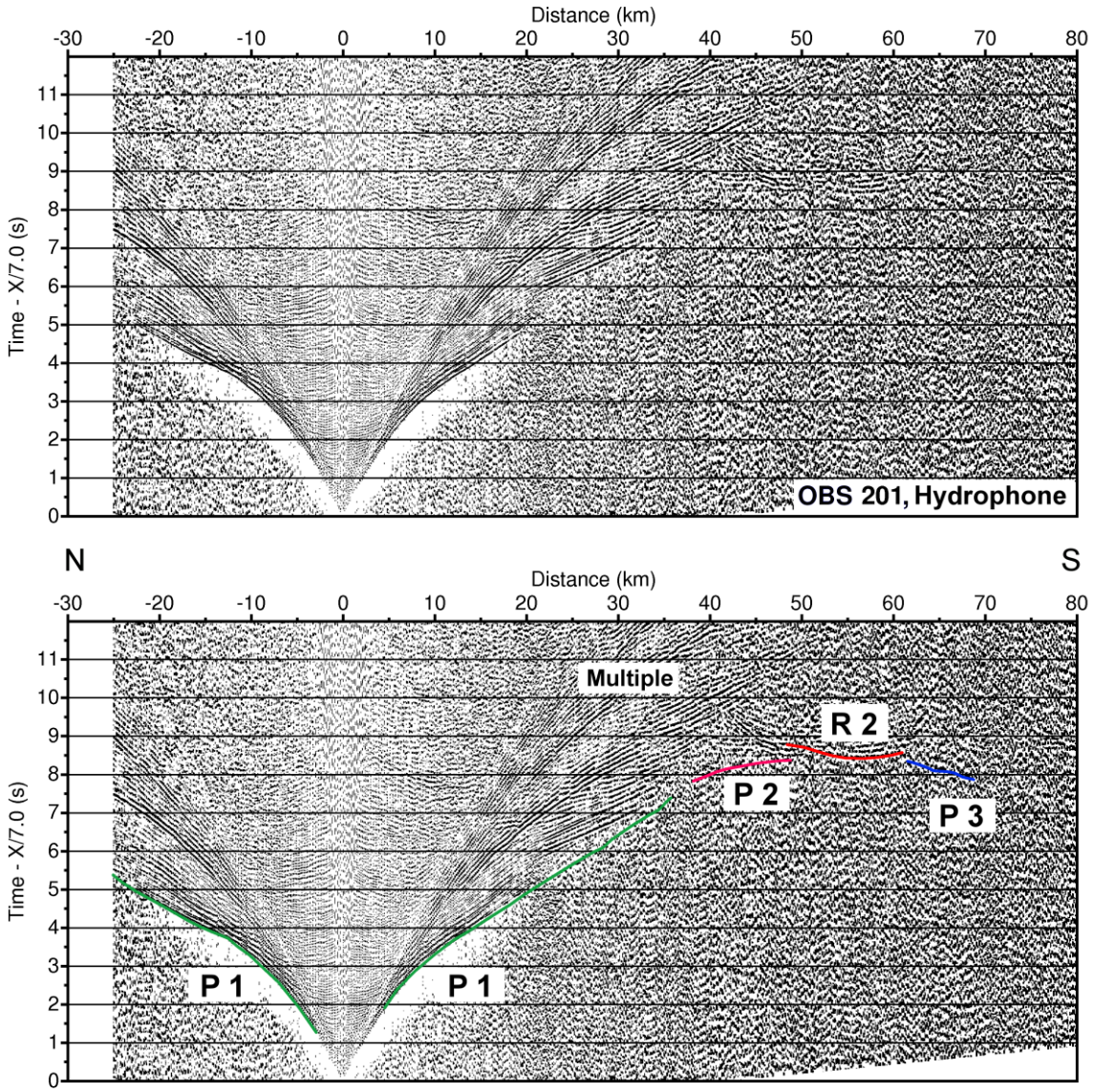

Figure C8 – Receiver gather from the hydrophone of OBS 201 (top) with interpreted travel time arrivals (bottom). A reduction velocity of 7.0 km/s is applied. Bandpass filters are used with a frequency range of 6-14 Hz. Gain is set to 1.0 and increases linearly with offset. See text for description of compressional refractions (P1-P3) and reflections (R1-R2). Also labeled are arrivals of direct wave in water (Water) and multiples (Multiple).

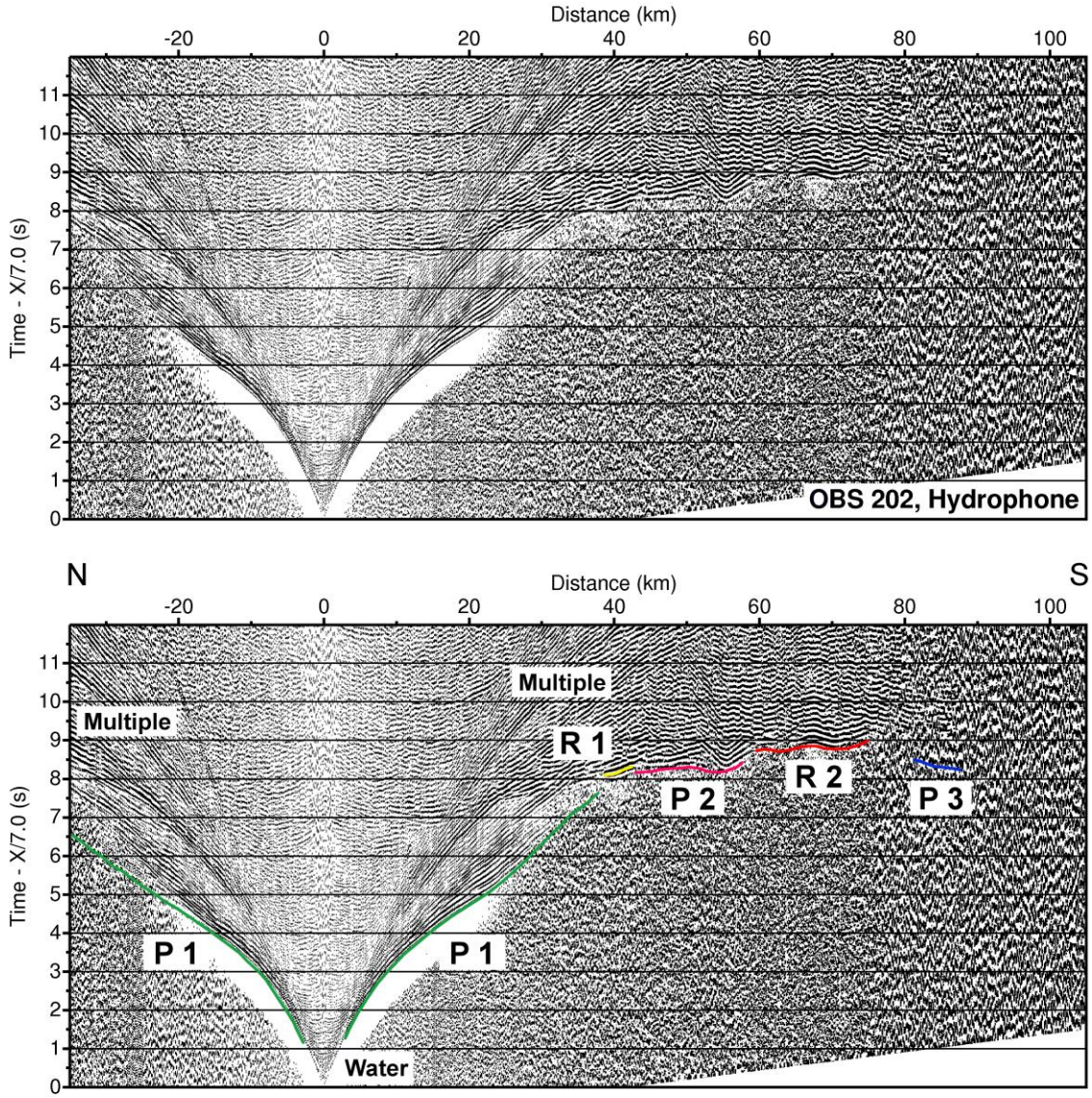

Figure C9 – Receiver gather from the hydrophone of OBS 202 (top) with interpreted travel time arrivals (bottom). See Figure C8 for further information.

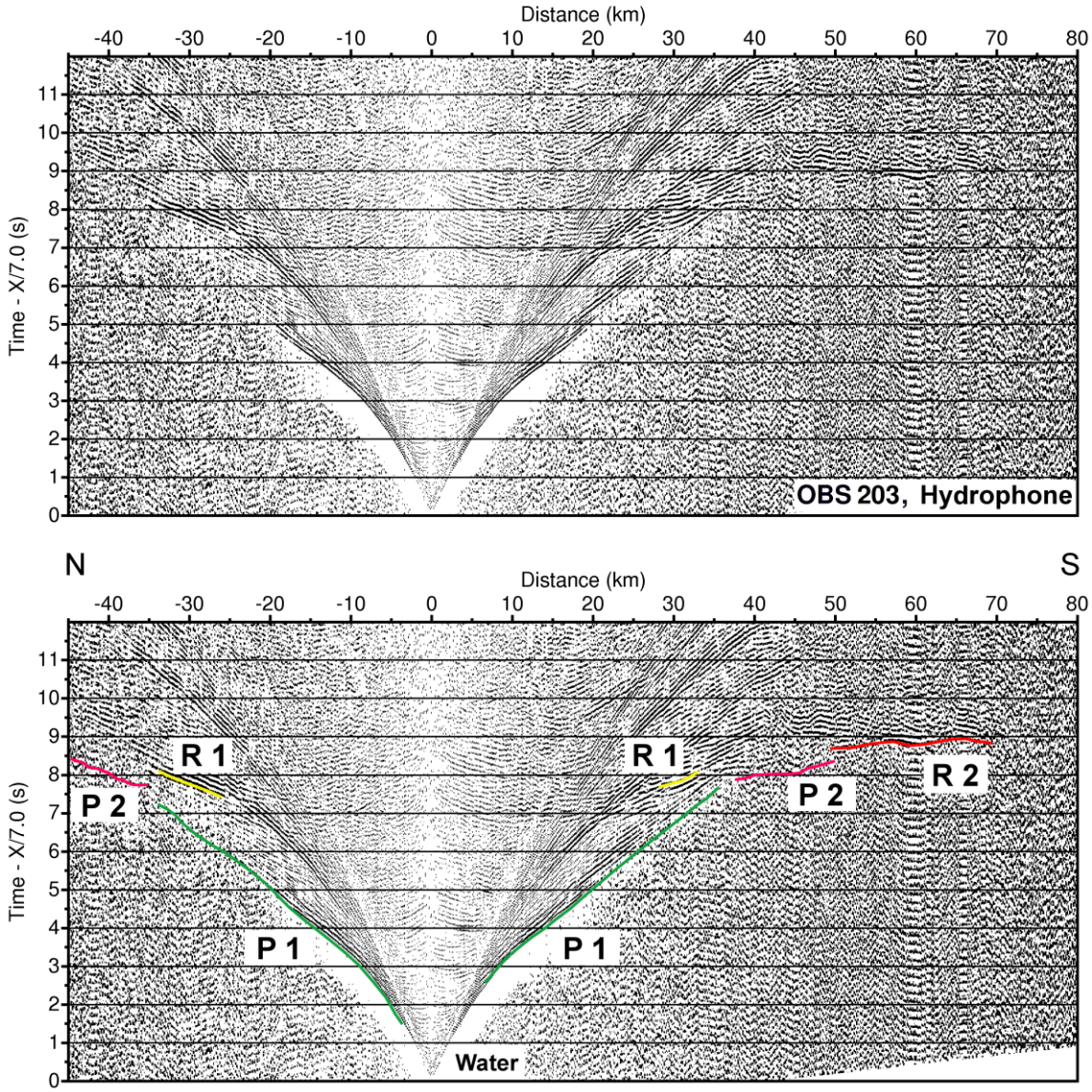

Figure C9 – Receiver gather from the hydrophone of OBS 203 (top) with interpreted travel time arrivals (bottom). See Figure C8 for further information.

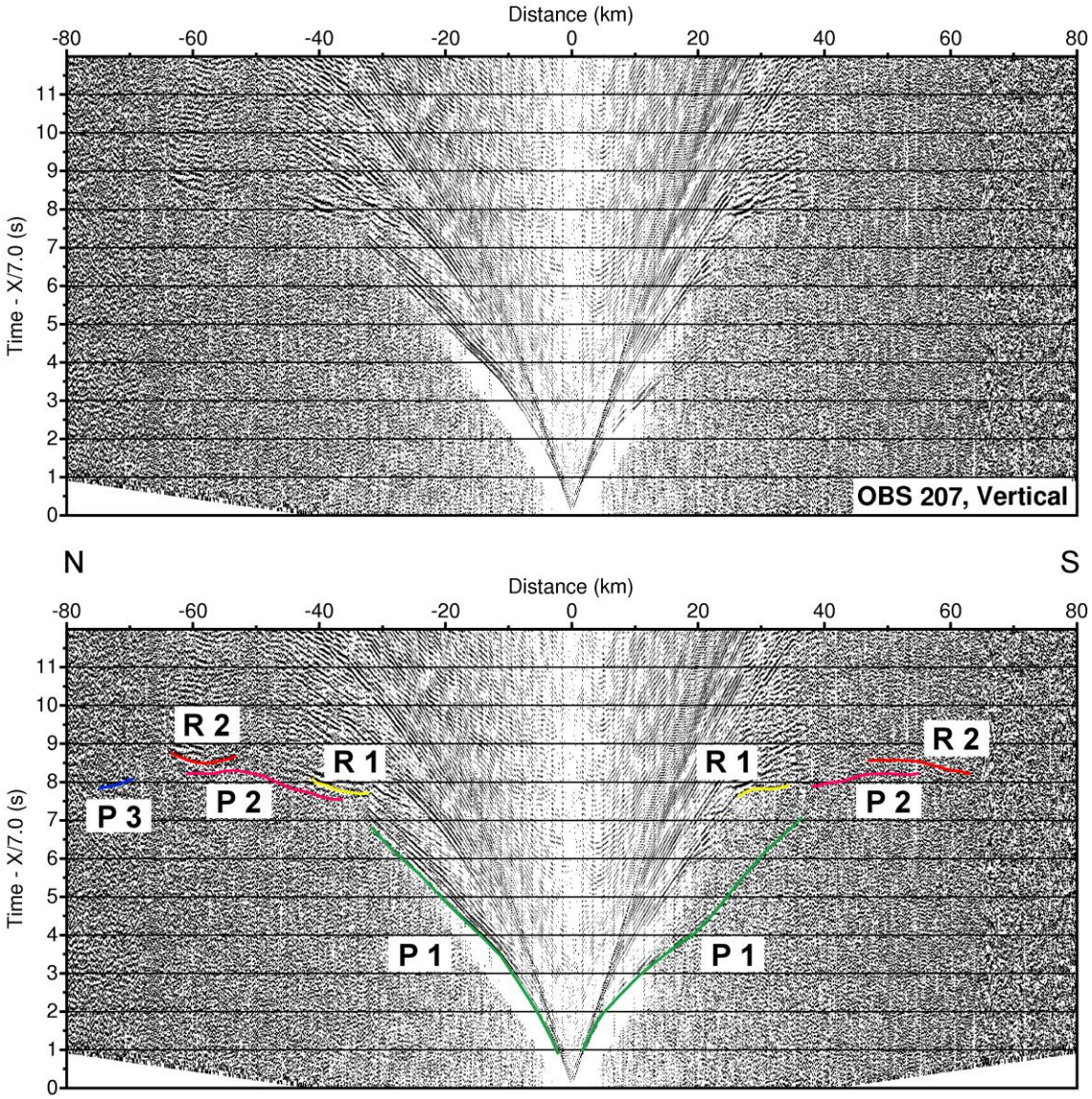

Figure C10 – Receiver gather from the vertical component of OBS 207 (top) with interpreted travel time arrivals (bottom). See Figure C8 for further information.

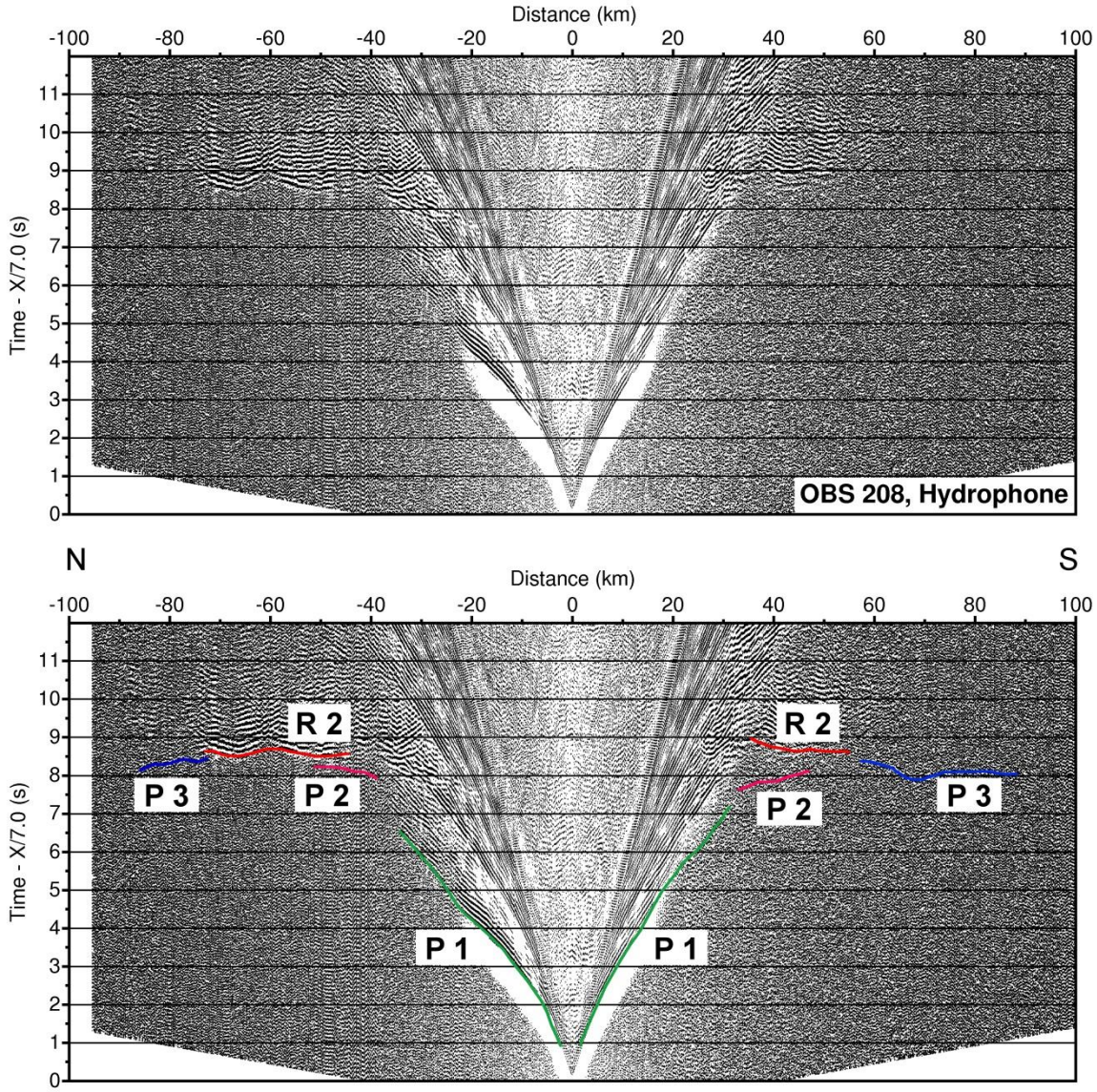

Figure C11 – Receiver gather from the hydrophone of OBS 208 (top) with interpreted travel time arrivals (bottom). See Figure C8 for further information.

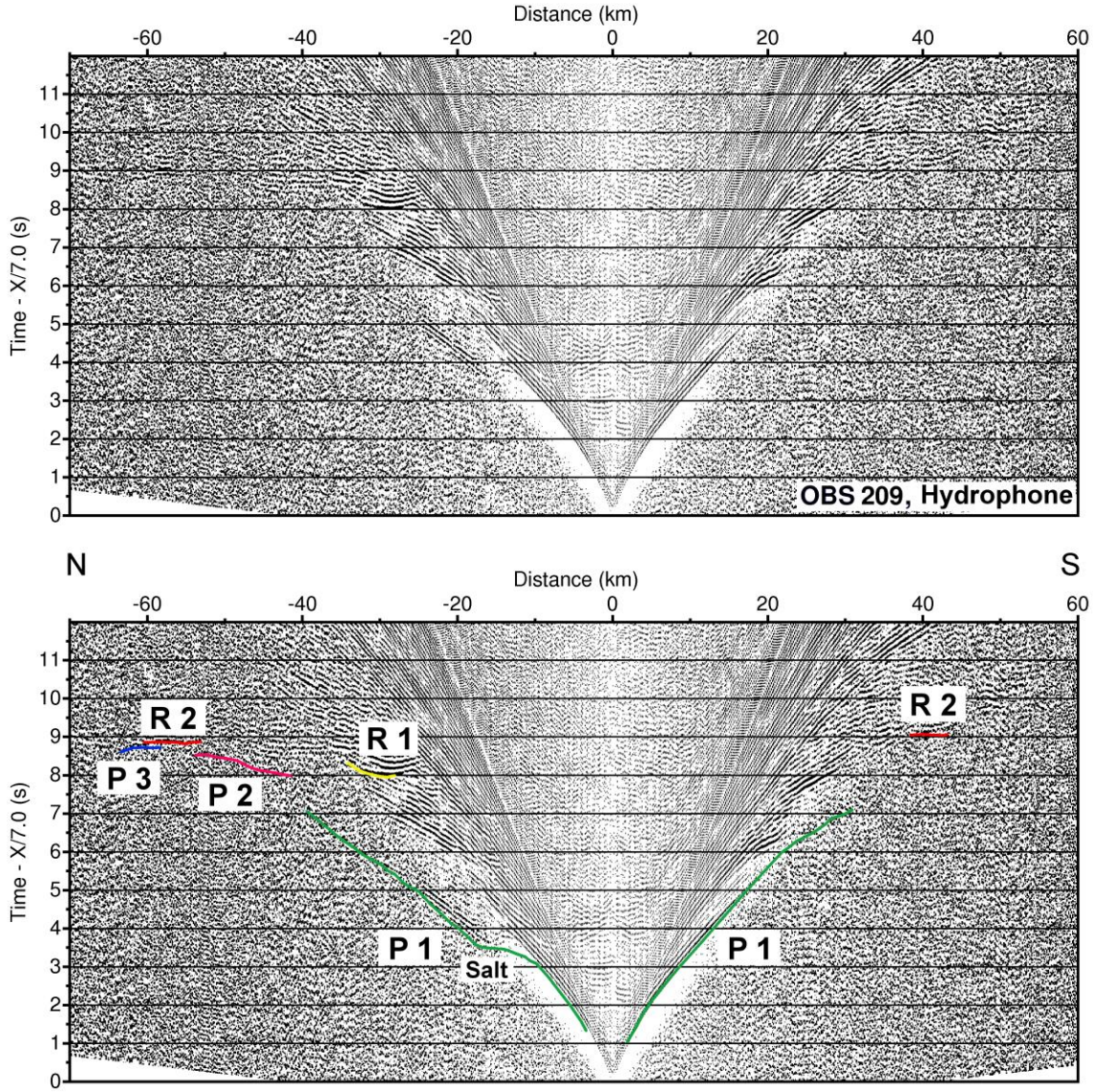

Figure C12 – Receiver gather from the hydrophone of OBS 209 (top) with interpreted travel time arrivals (bottom). See Figure C8 for further information.

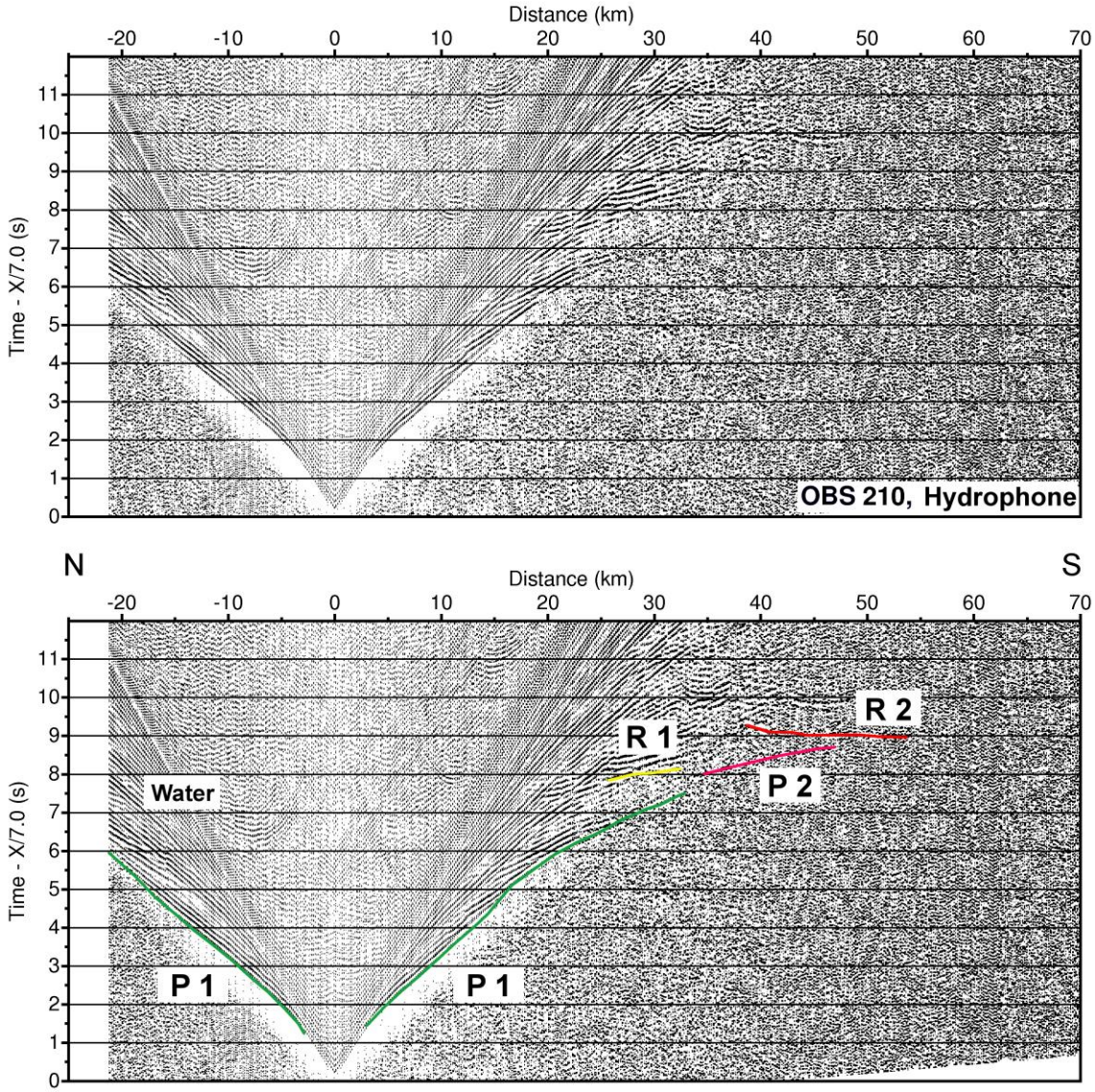

Figure C13 – Receiver gather from the hydrophone of OBS 210 (top) with interpreted travel time arrivals (bottom). See Figure C8 for further information.

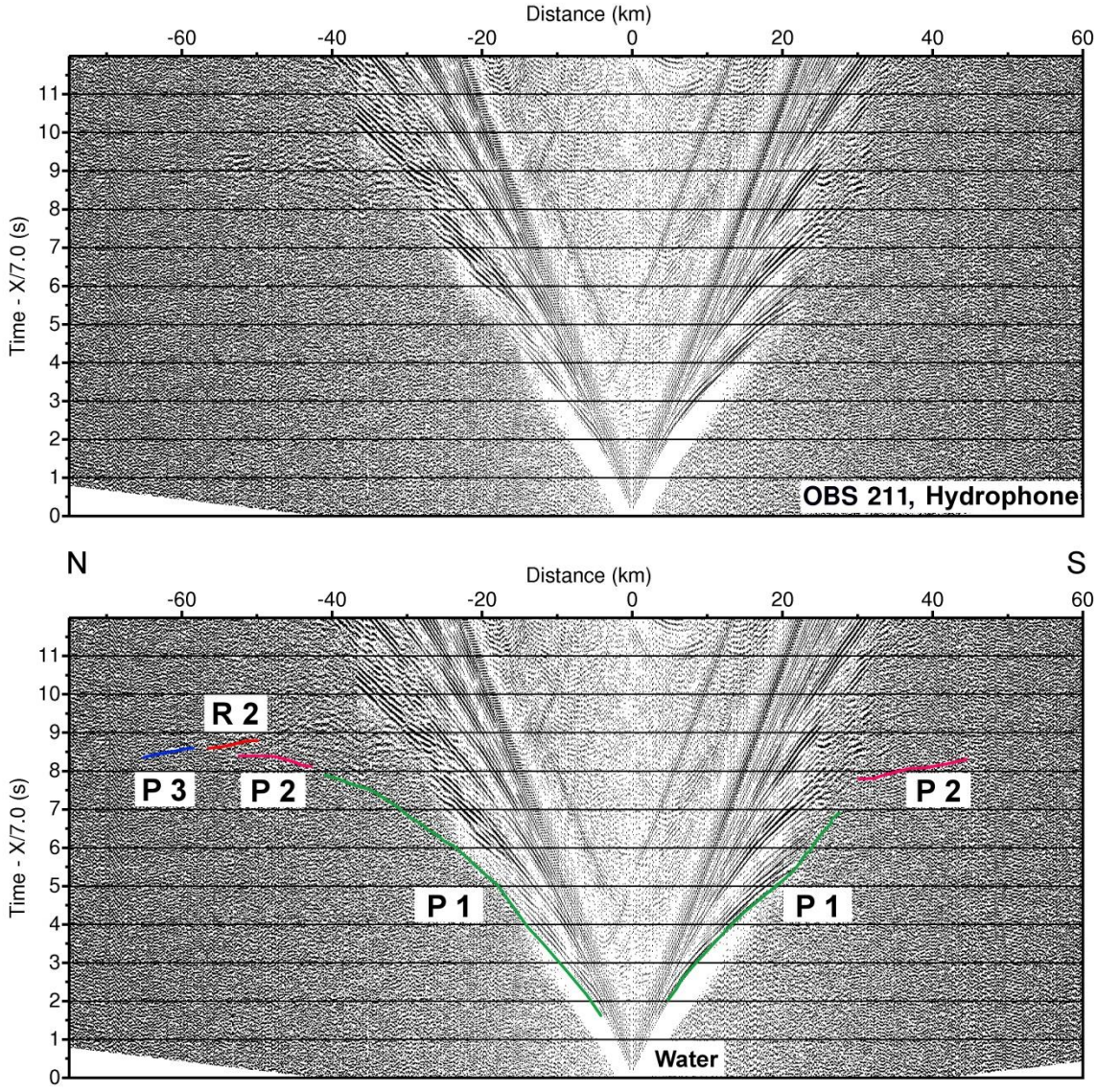

Figure C14 – Receiver gather from the hydrophone of OBS 211 (top) with interpreted travel time arrivals (bottom). See Figure C8 for further information.

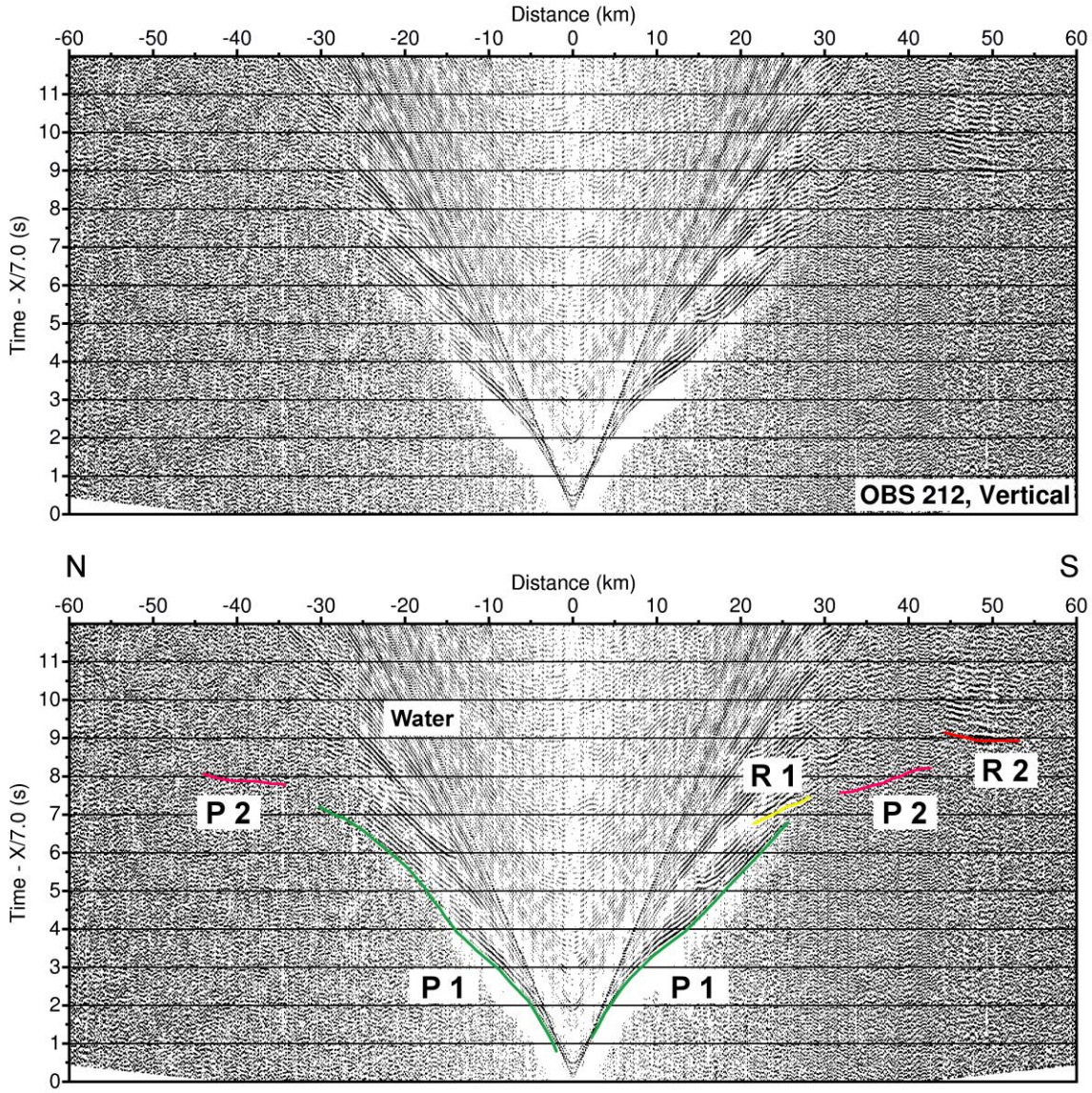

Figure C15 – Receiver gather from the vertical component of OBS 212 (top) with interpreted travel time arrivals (bottom). See Figure C8 for further information.

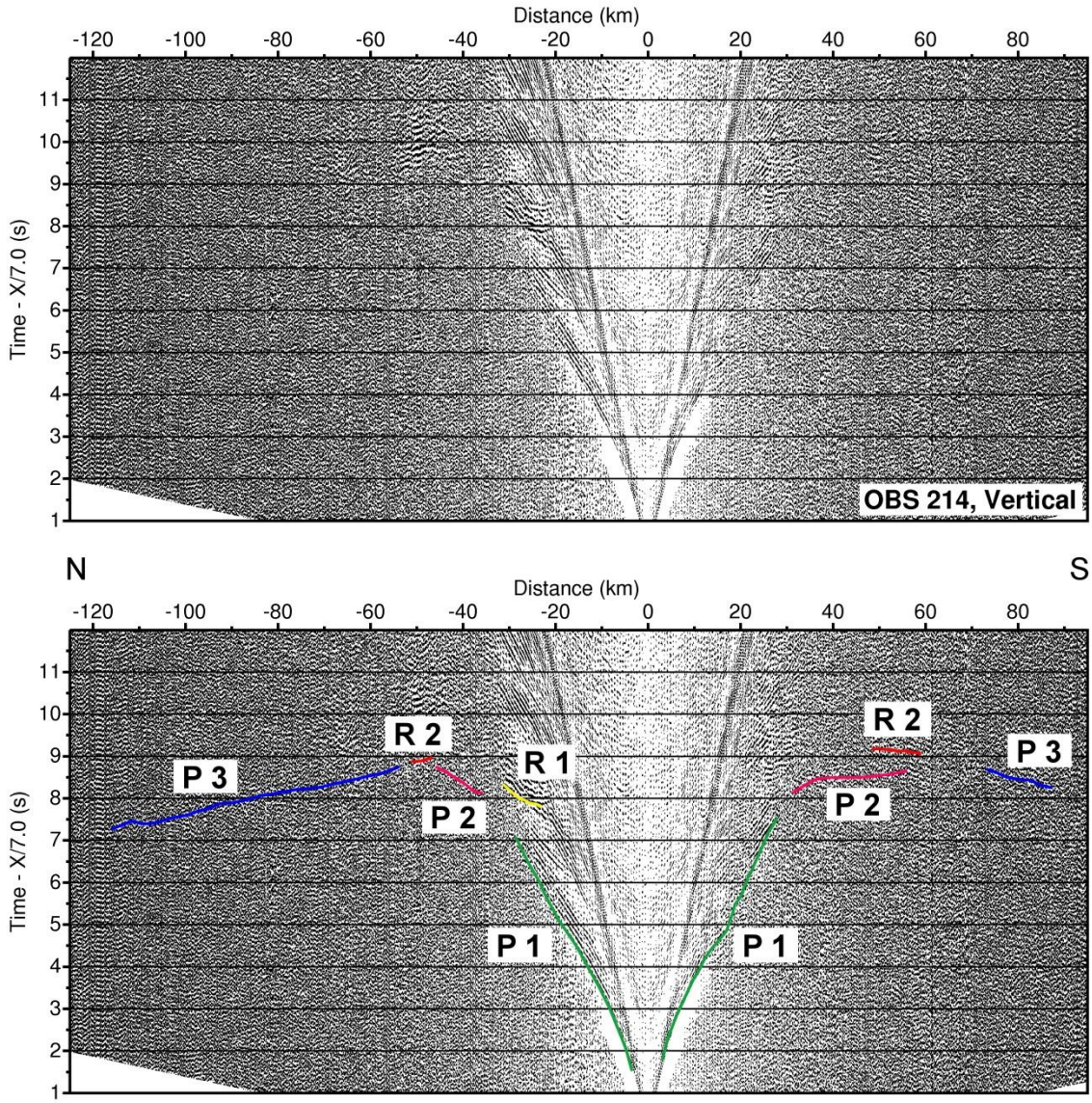

Figure C16 – Receiver gather from the vertical component of OBS 214 (top) with interpreted travel time arrivals (bottom). See Figure C8 for further information.

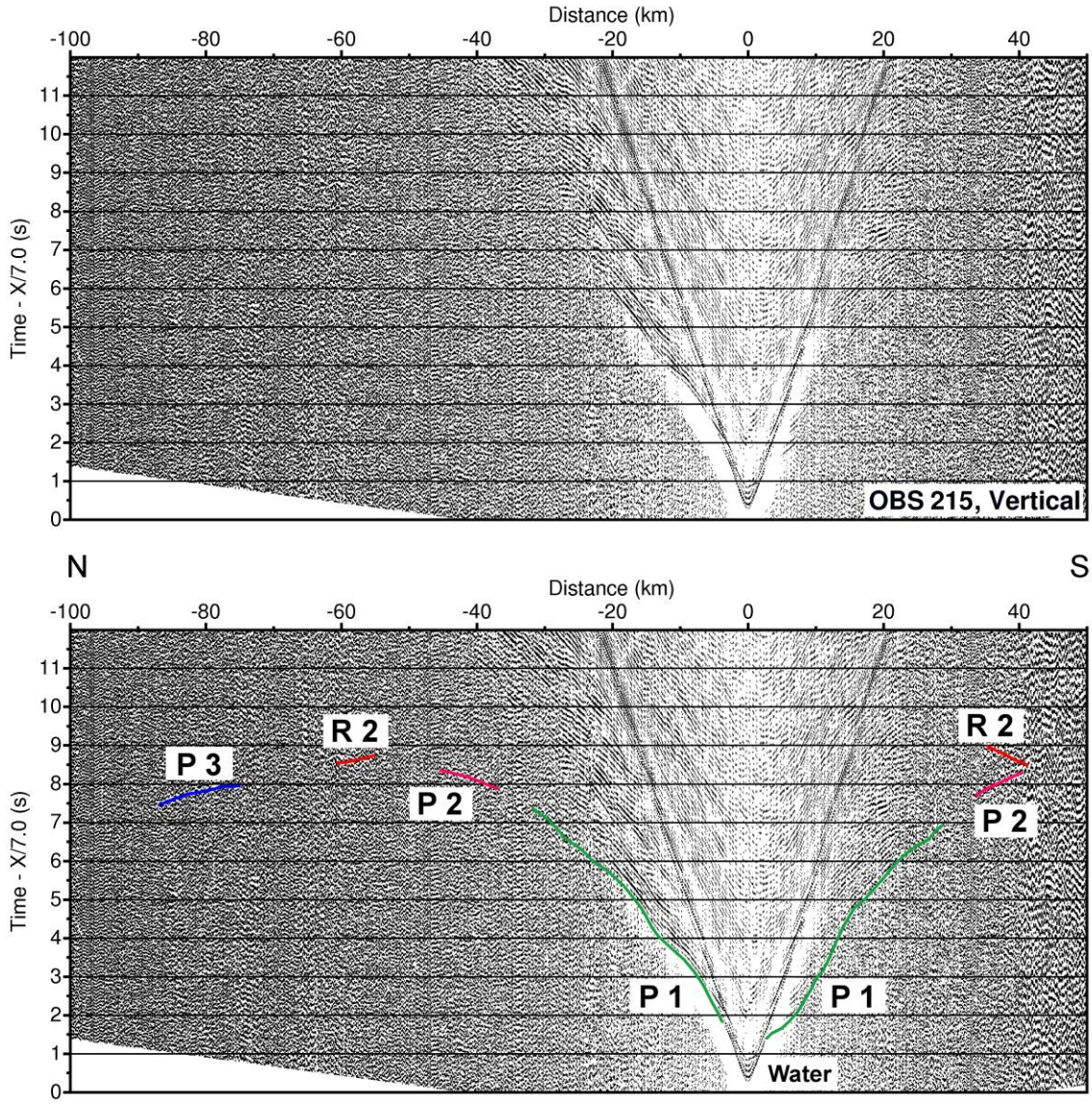

Figure C17 – Receiver gather from the vertical component of OBS 215 (top) with interpreted travel time arrivals (bottom). See Figure C8 for further information.

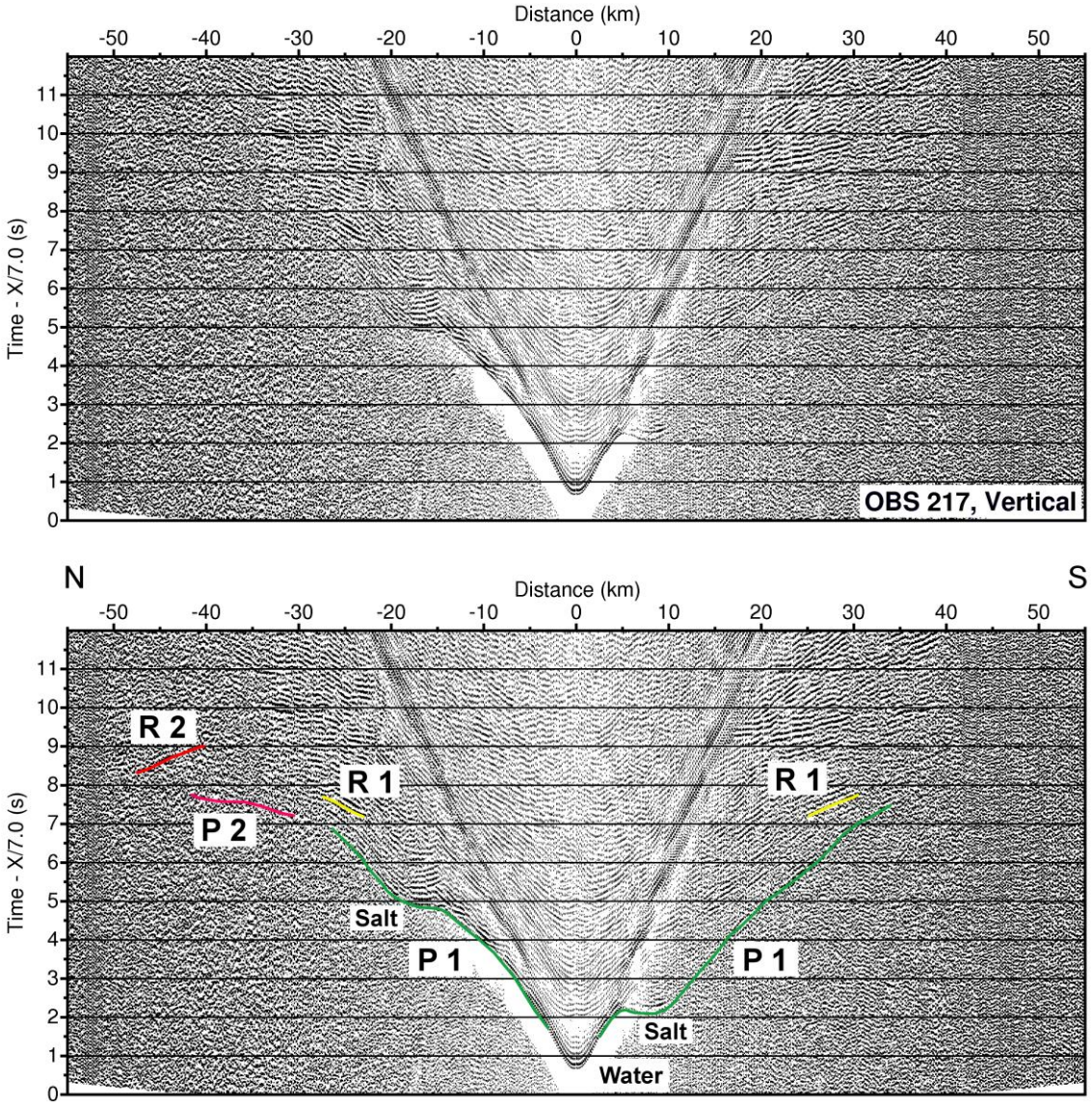

Figure C18 – Receiver gather from the vertical component of OBS 217 (top) with interpreted travel time arrivals (bottom). See Figure C8 for further information.

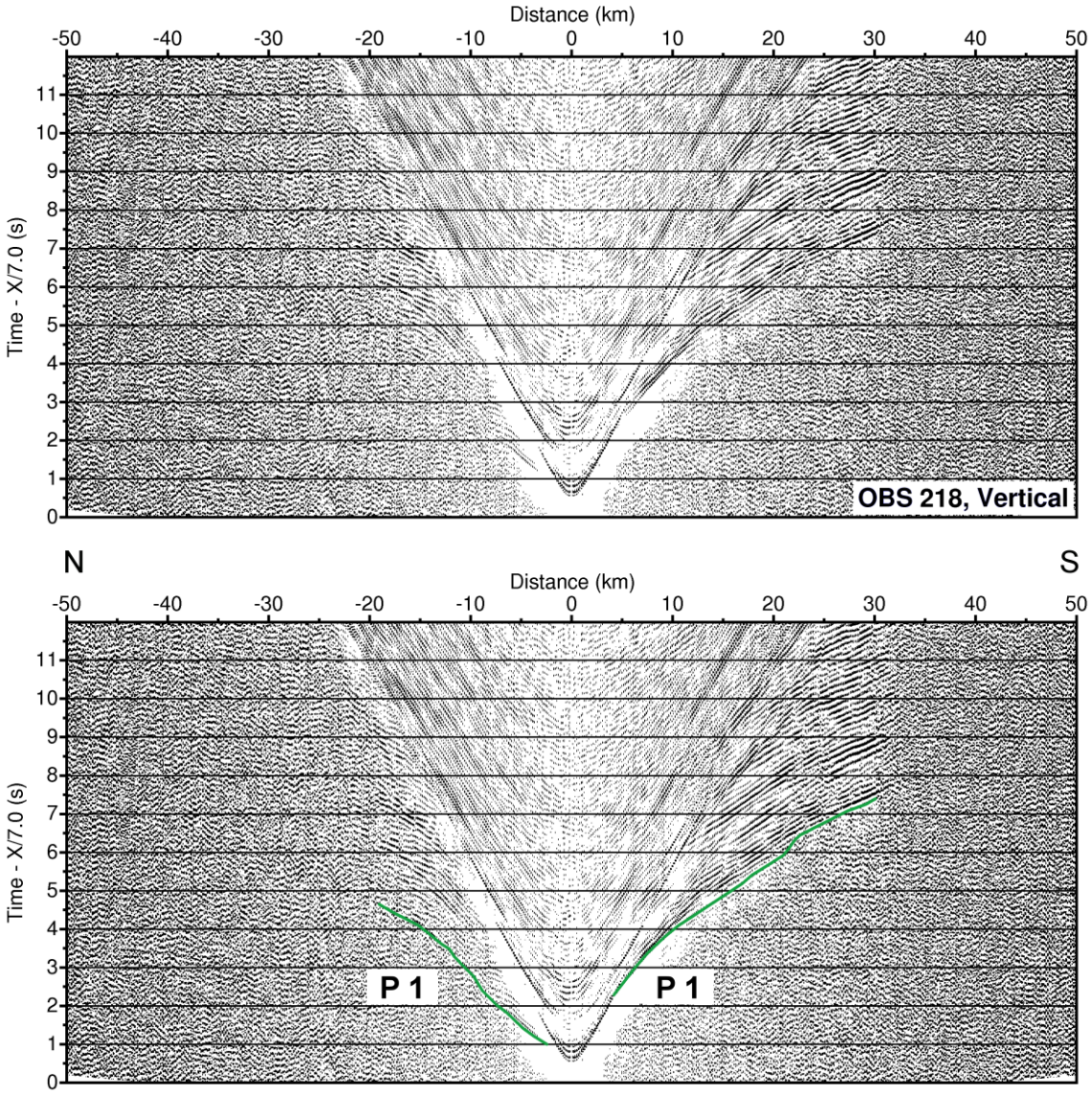

Figure C19 – Receiver gather from the vertical component of OBS 218 (top) with interpreted travel time arrivals (bottom). See Figure C8 for further information.

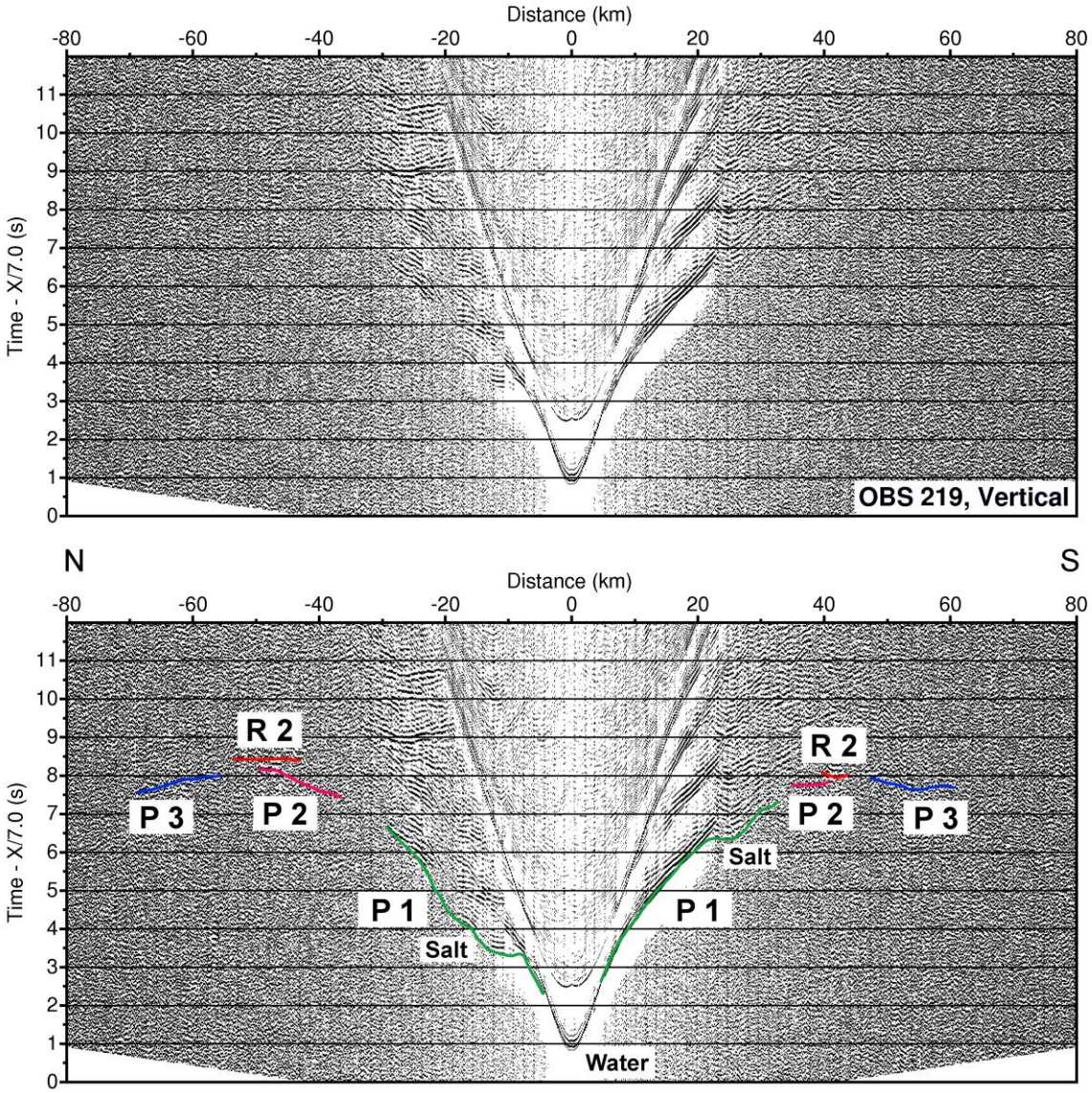

Figure C20 – Receiver gather from the vertical component of OBS 219 (top) with interpreted travel time arrivals (bottom). See Figure C8 for further information.

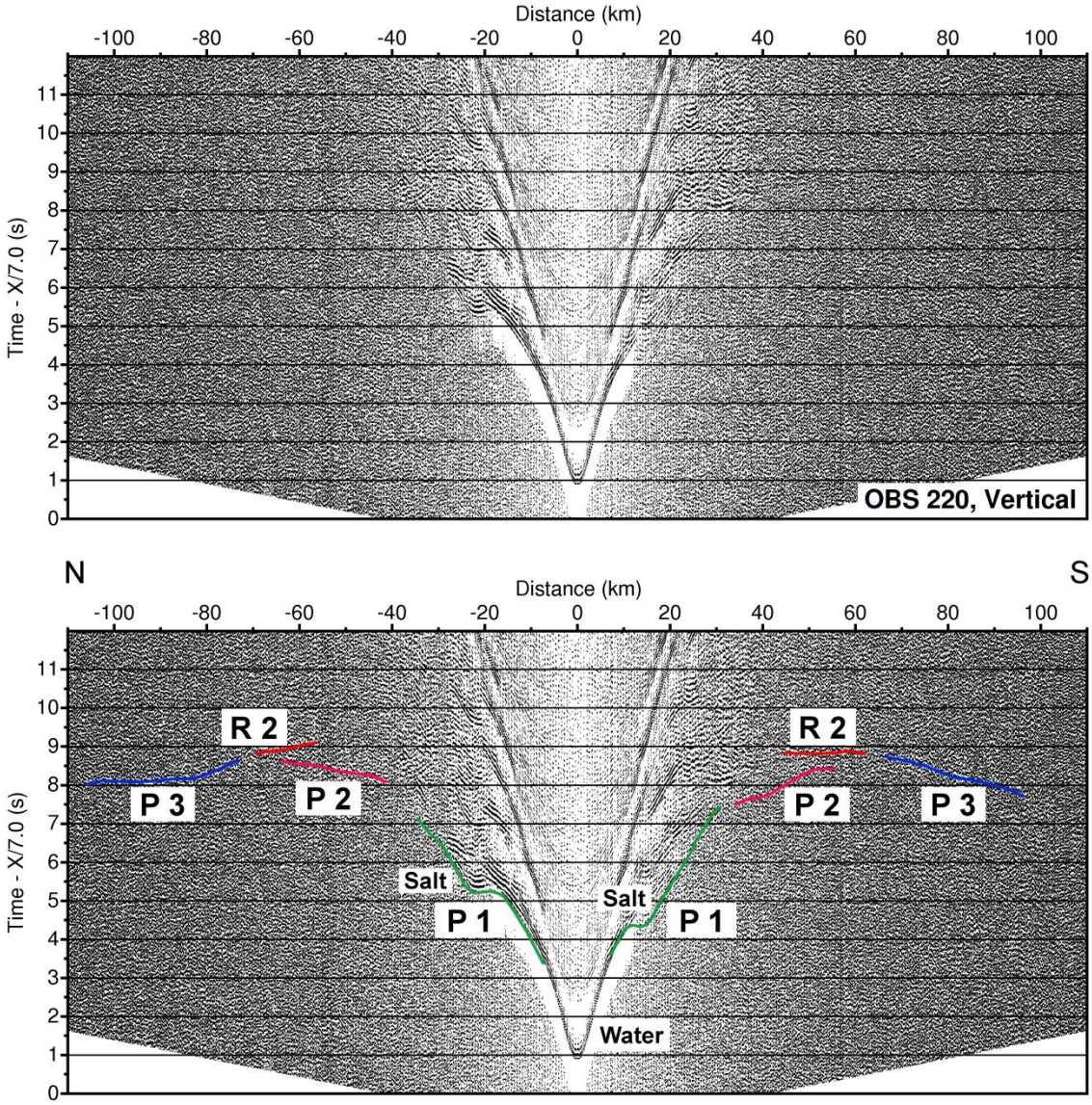

Figure C21 – Receiver gather from the vertical component of OBS 220 (top) with interpreted travel time arrivals (bottom). See Figure C8 for further information.

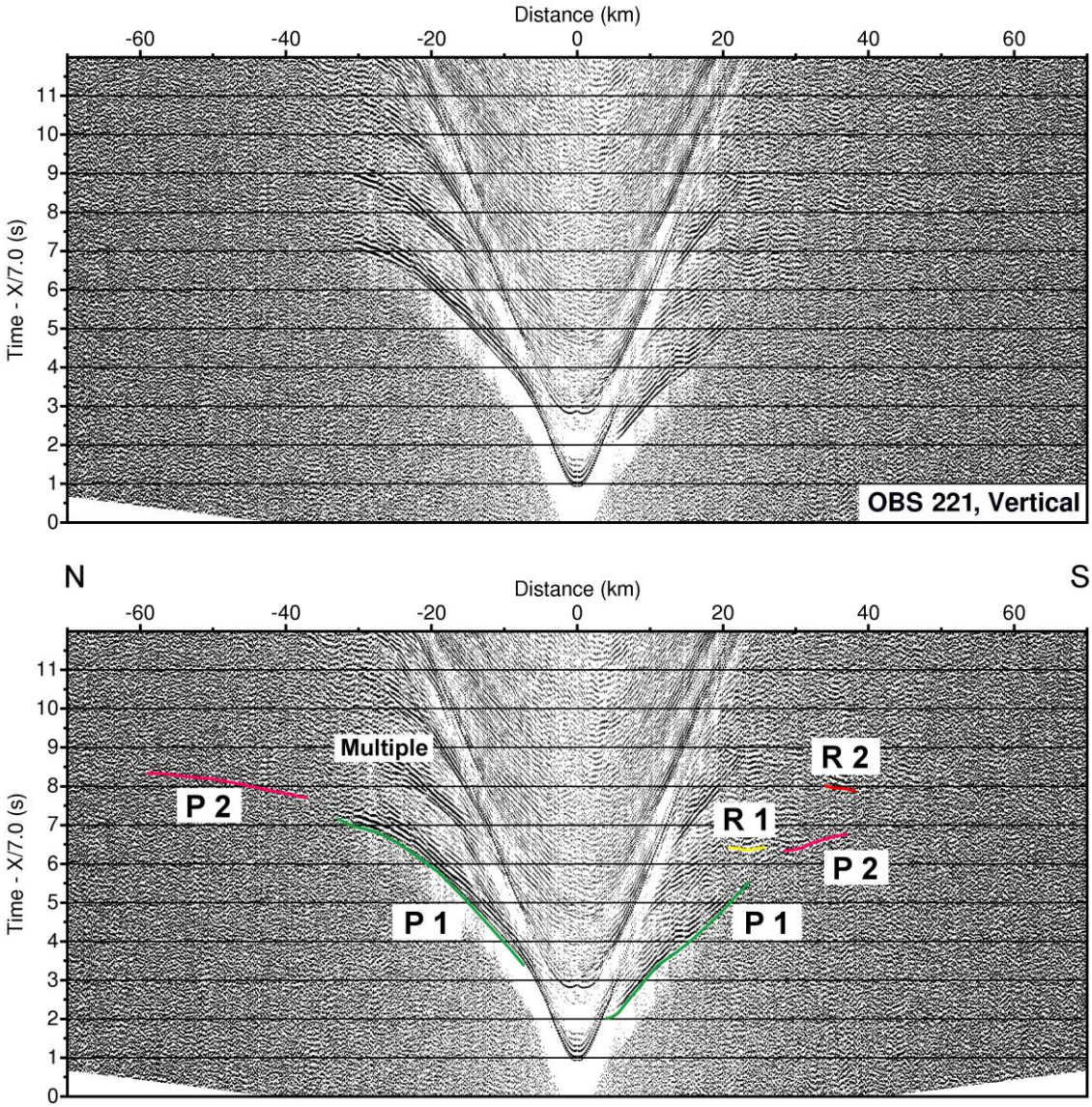

Figure C22 – Receiver gather from the vertical component of OBS 221 (top) with interpreted travel time arrivals (bottom). See Figure C8 for further information.

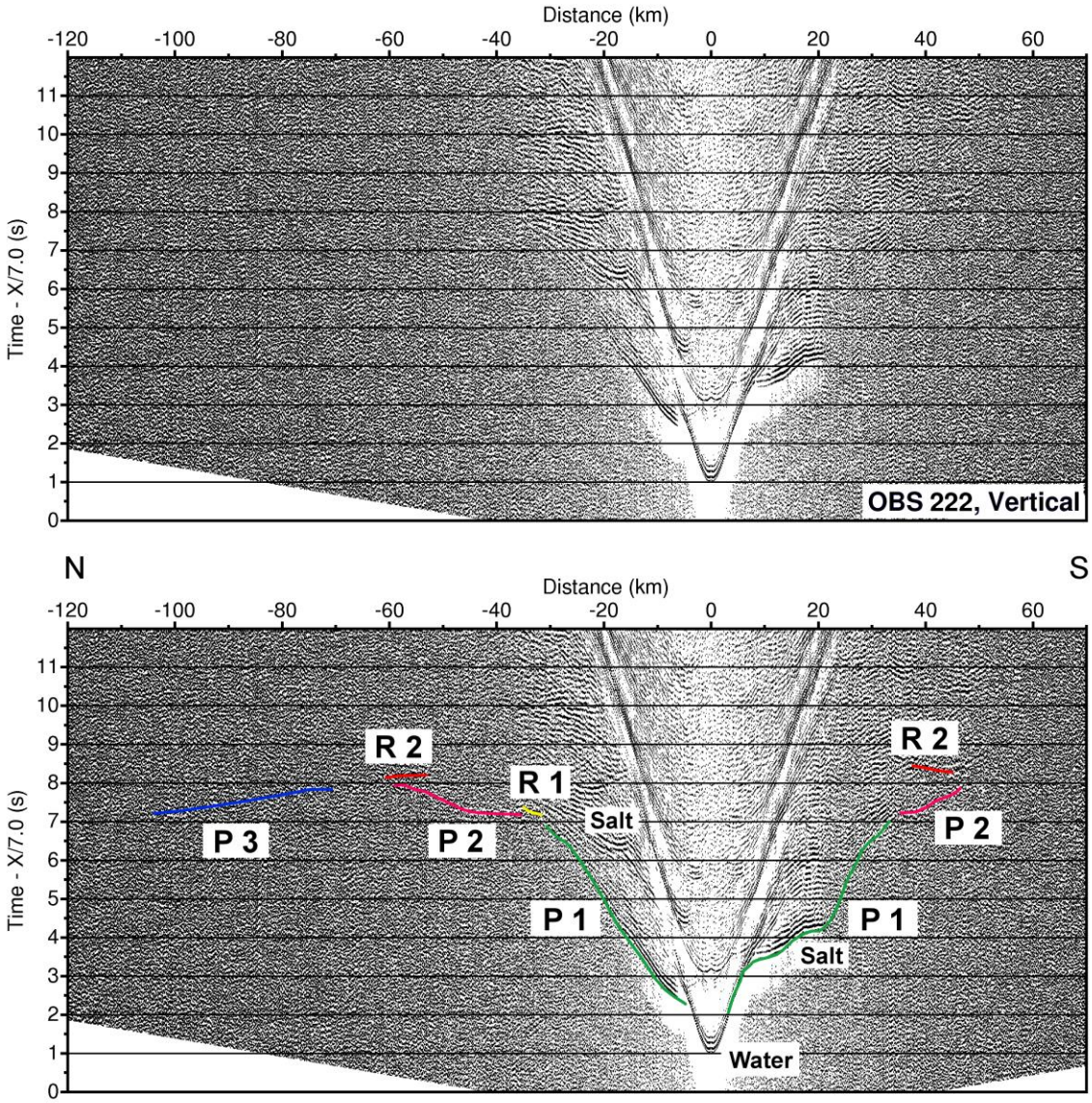

Figure C23 – Receiver gather from the vertical component of OBS 222 (top) with interpreted travel time arrivals (bottom). See Figure C8 for further information.

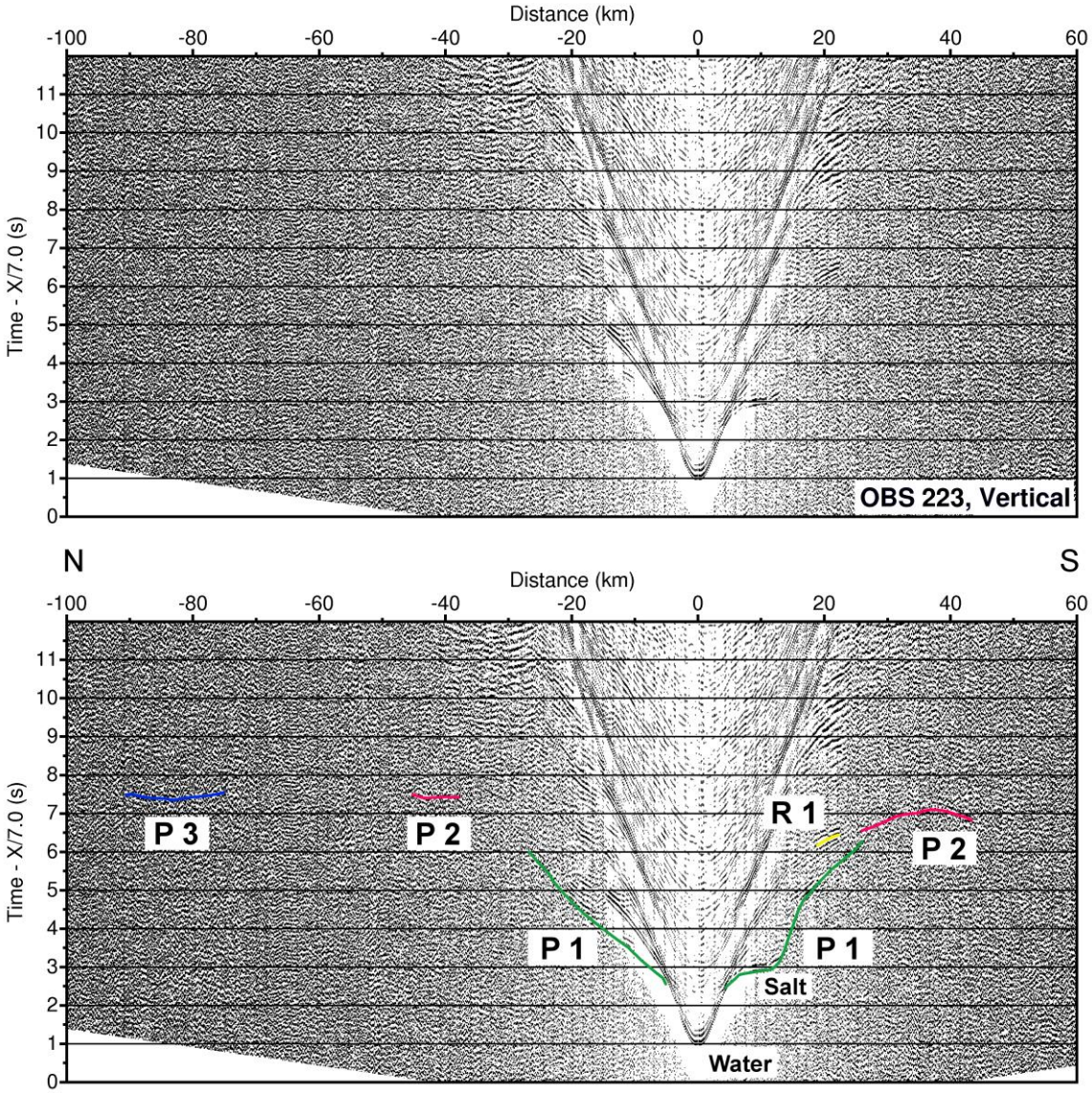

Figure C24 – Receiver gather from the vertical component of OBS 223 (top) with interpreted travel time arrivals (bottom). See Figure C8 for further information.

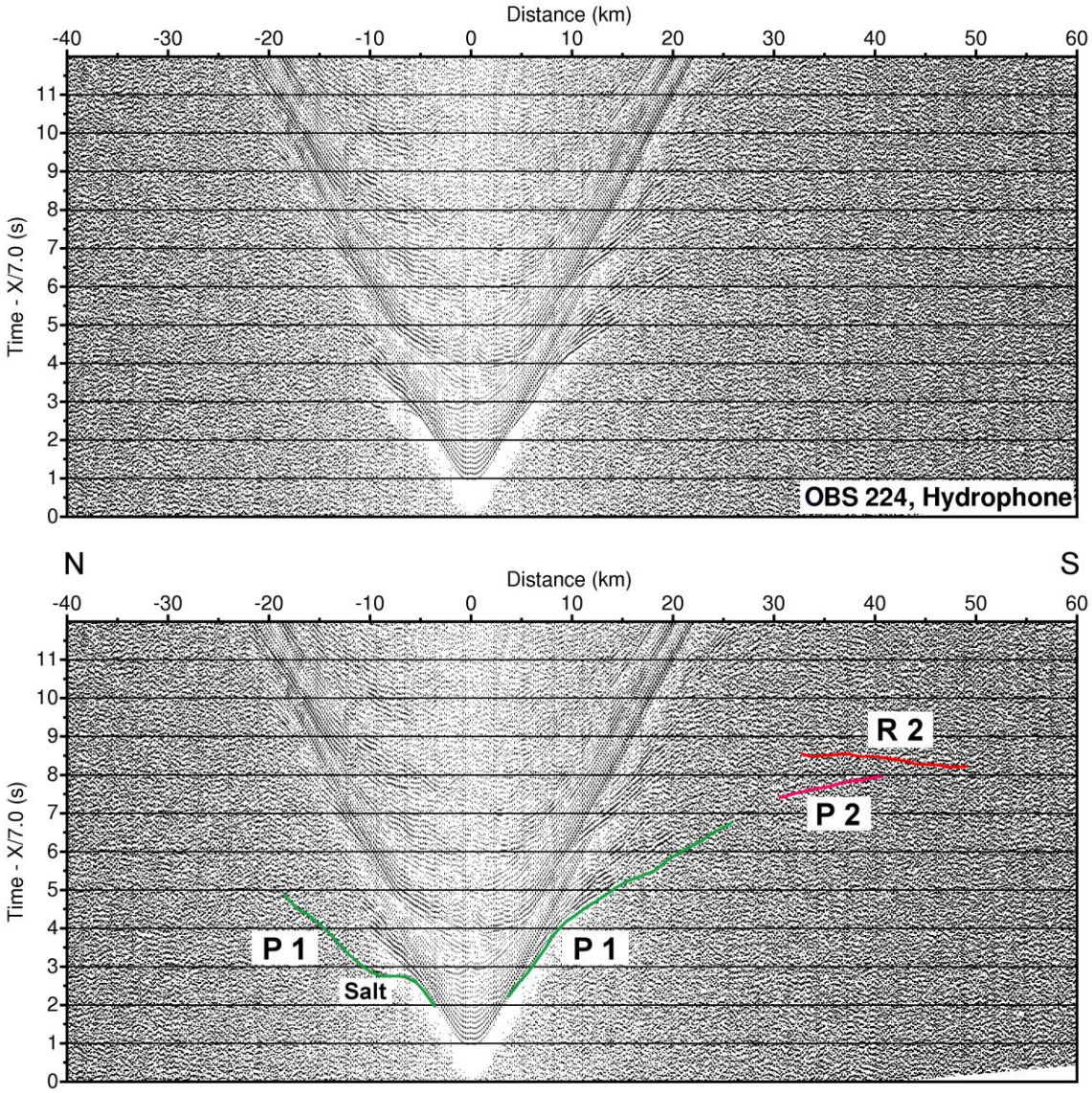

Figure C25 – Receiver gather from the hydrophone of OBS 224 (top) with interpreted travel time arrivals (bottom). See Figure C8 for further information.

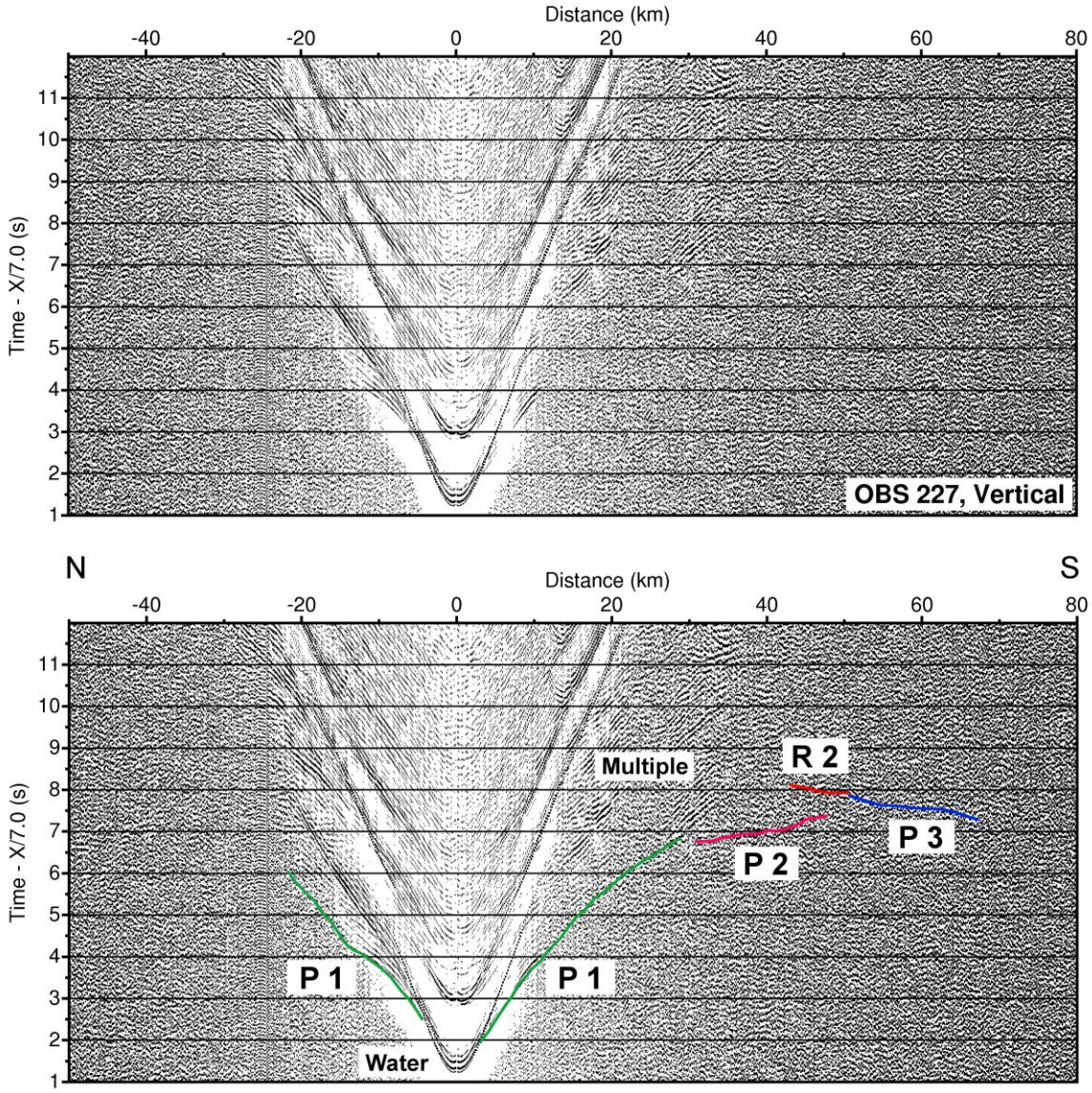

Figure C26 – Receiver gather from the vertical component of OBS 227 (top) with interpreted travel time arrivals (bottom). See Figure C8 for further information.

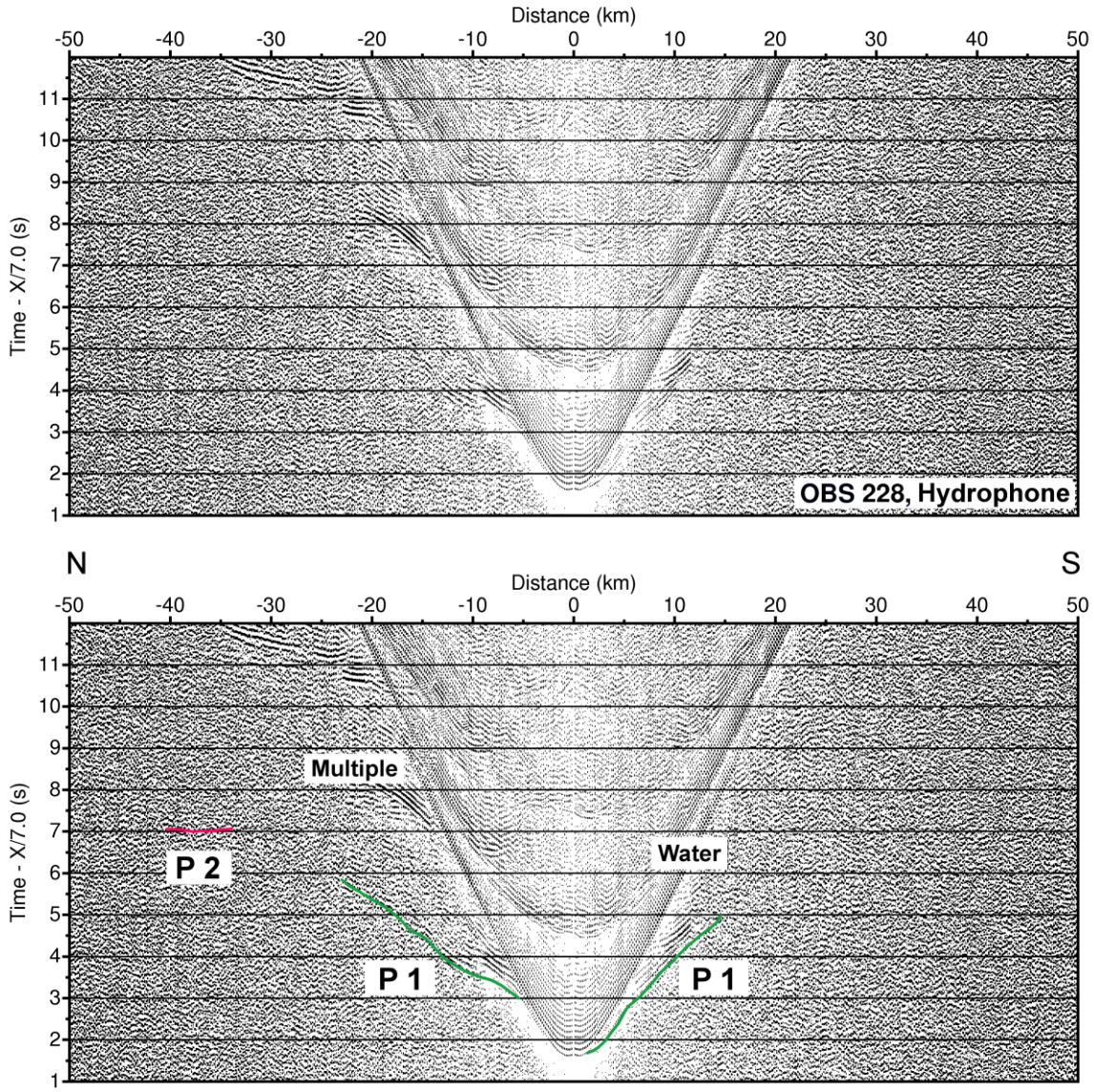

Figure C27 – Receiver gather from the hydrophone of OBS 228 (top) with interpreted travel time arrivals (bottom). See Figure C8 for further information.

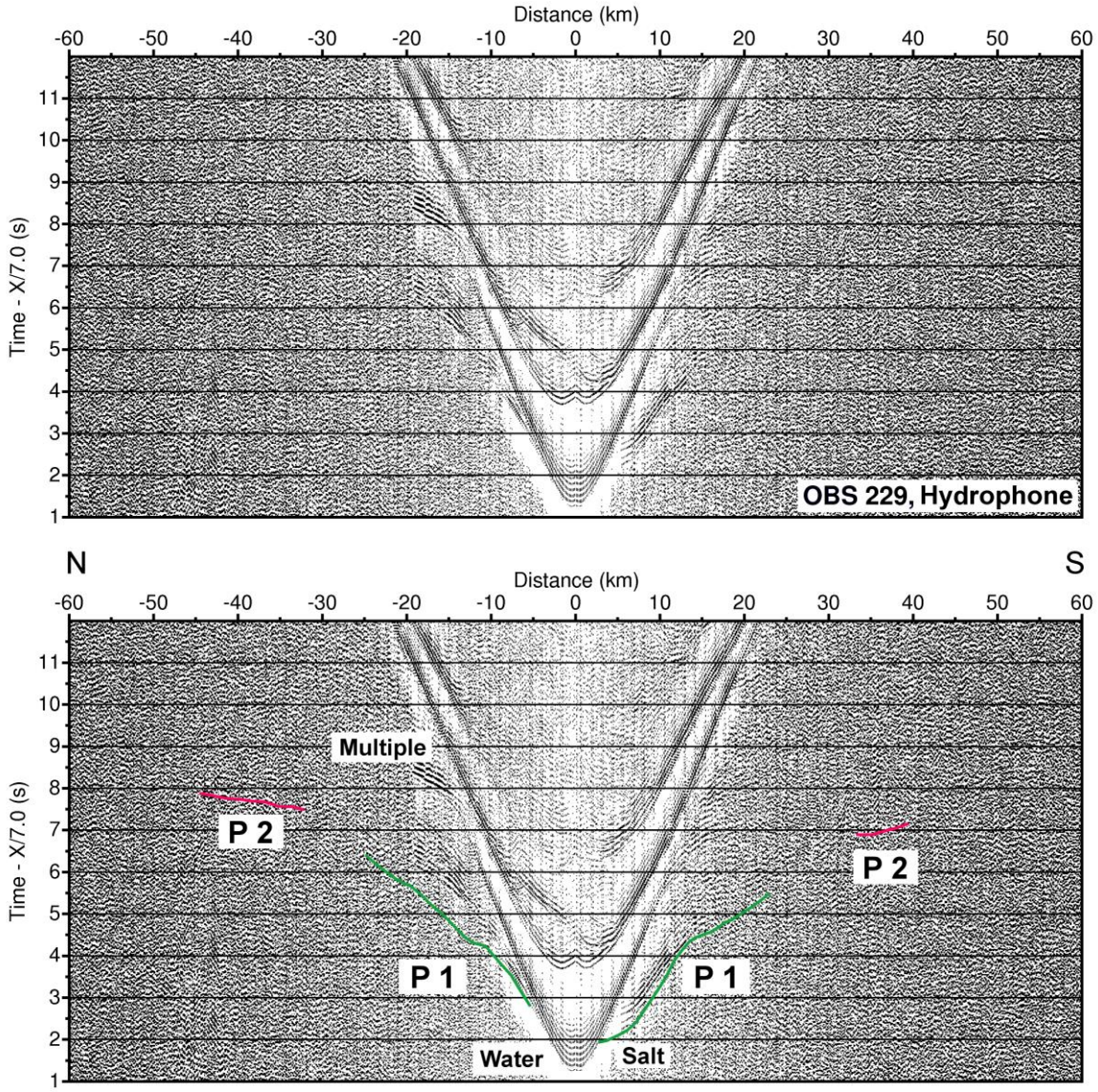

Figure C28 – Receiver gather from the hydrophone of OBS 229 (top) with interpreted travel time arrivals (bottom). See Figure C8 for further information.

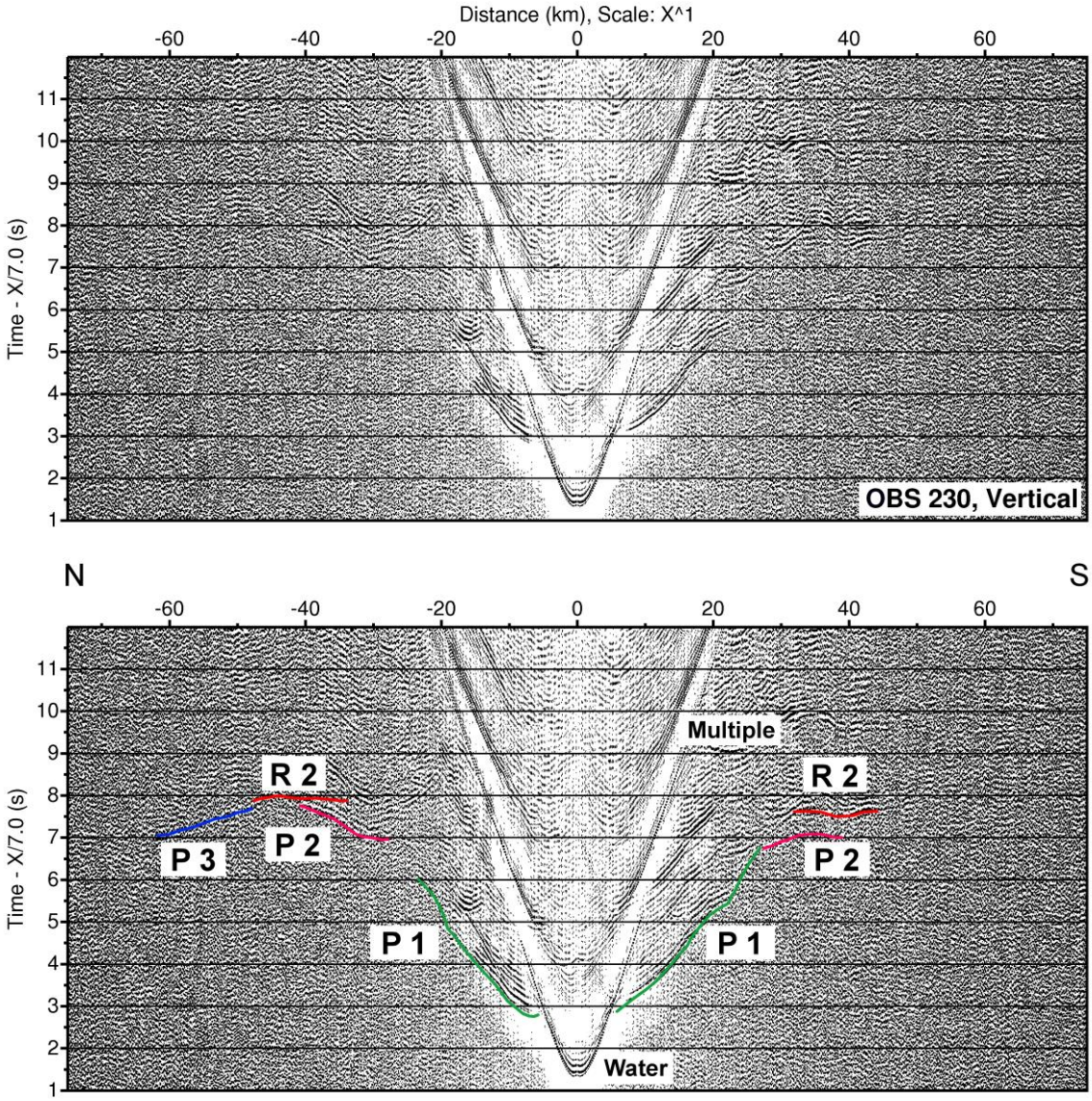

Figure C29 – Receiver gather from the vertical component of OBS 230 (top) with interpreted travel time arrivals (bottom). See Figure C8 for further information.

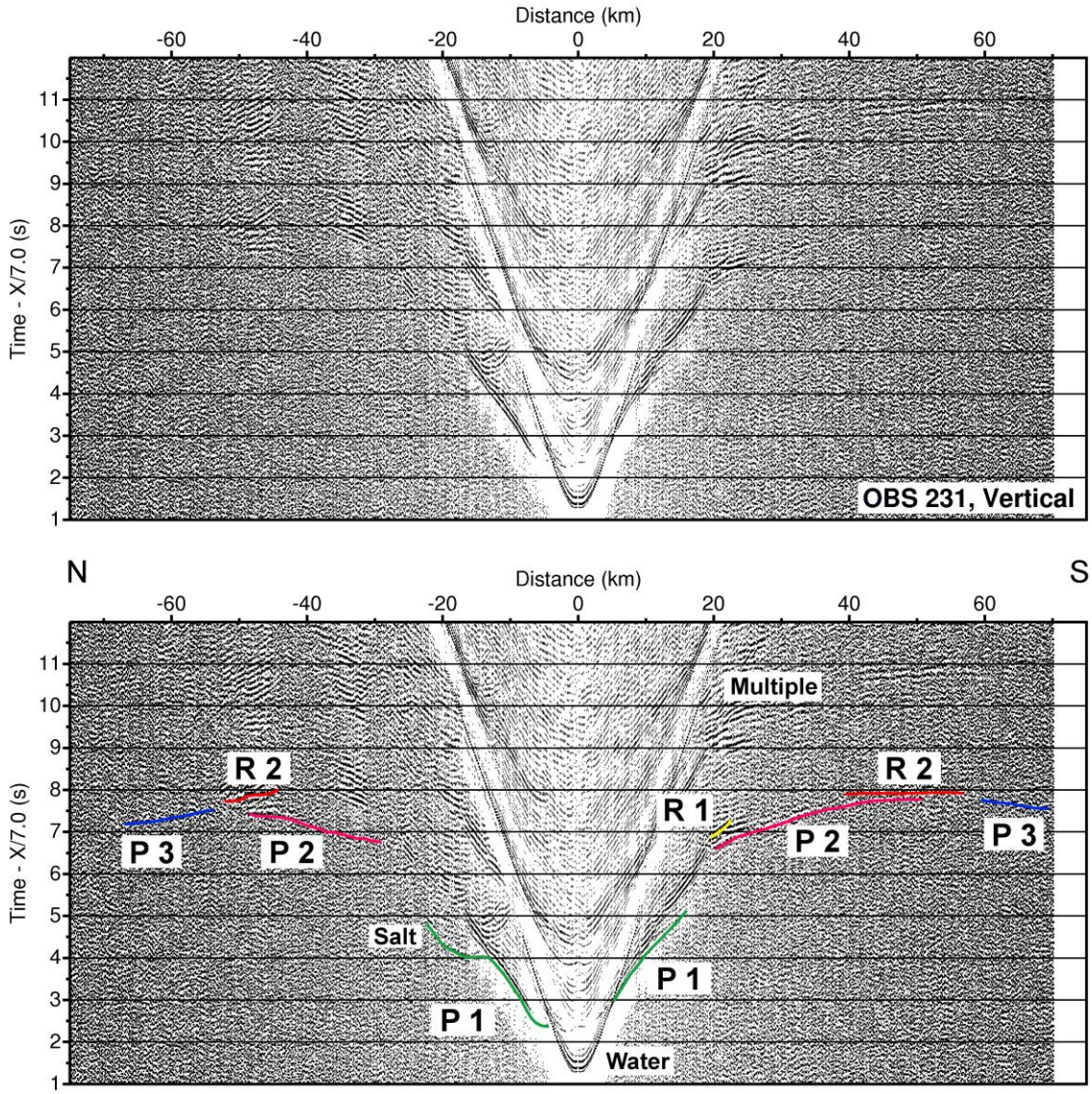

Figure C30 – Receiver gather from the vertical component of OBS 231 (top) with interpreted travel time arrivals (bottom). See Figure C8 for further information.

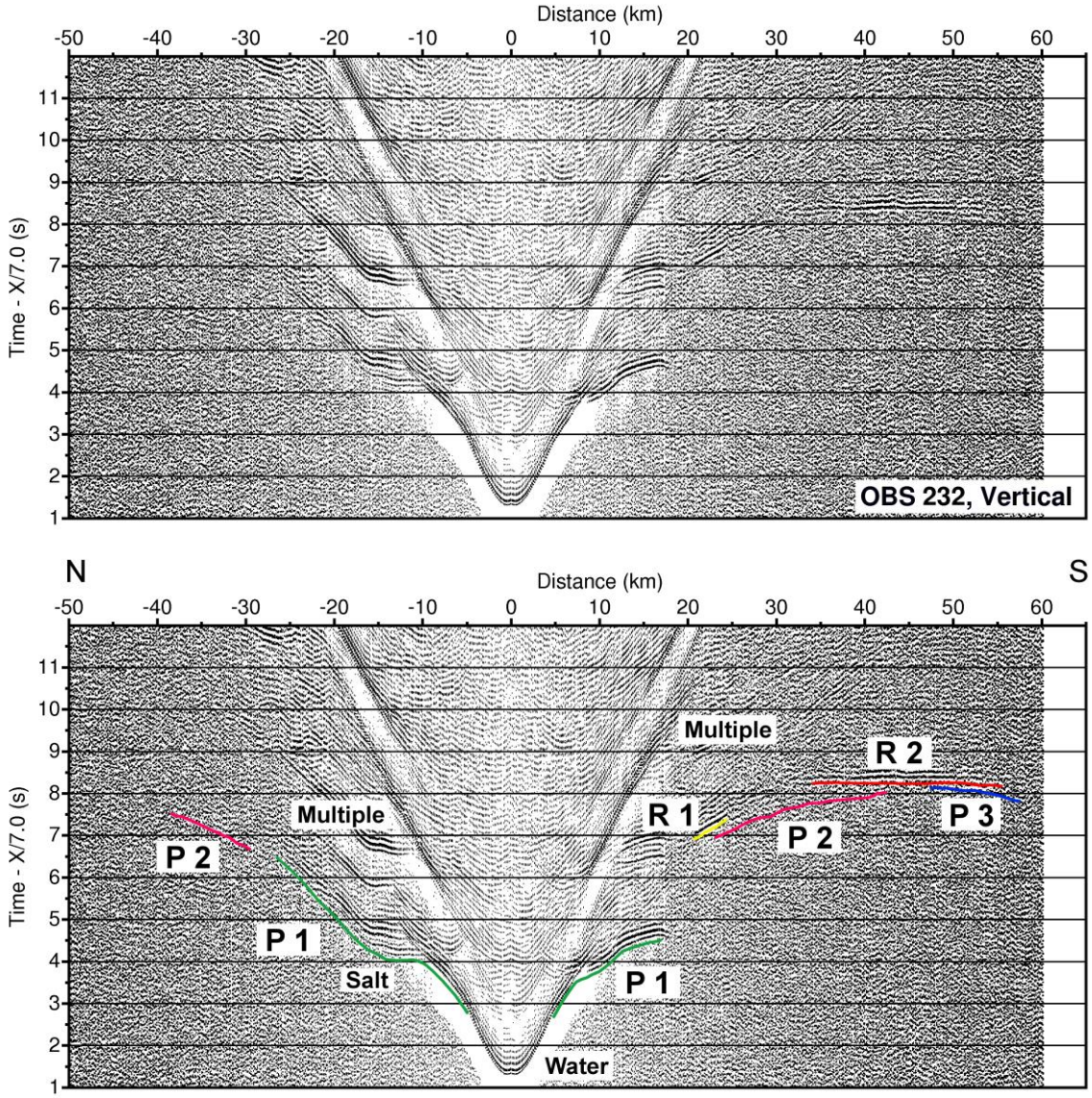

Figure C31 – Receiver gather from the vertical component of OBS 232 (top) with interpreted travel time arrivals (bottom). See Figure C8 for further information.

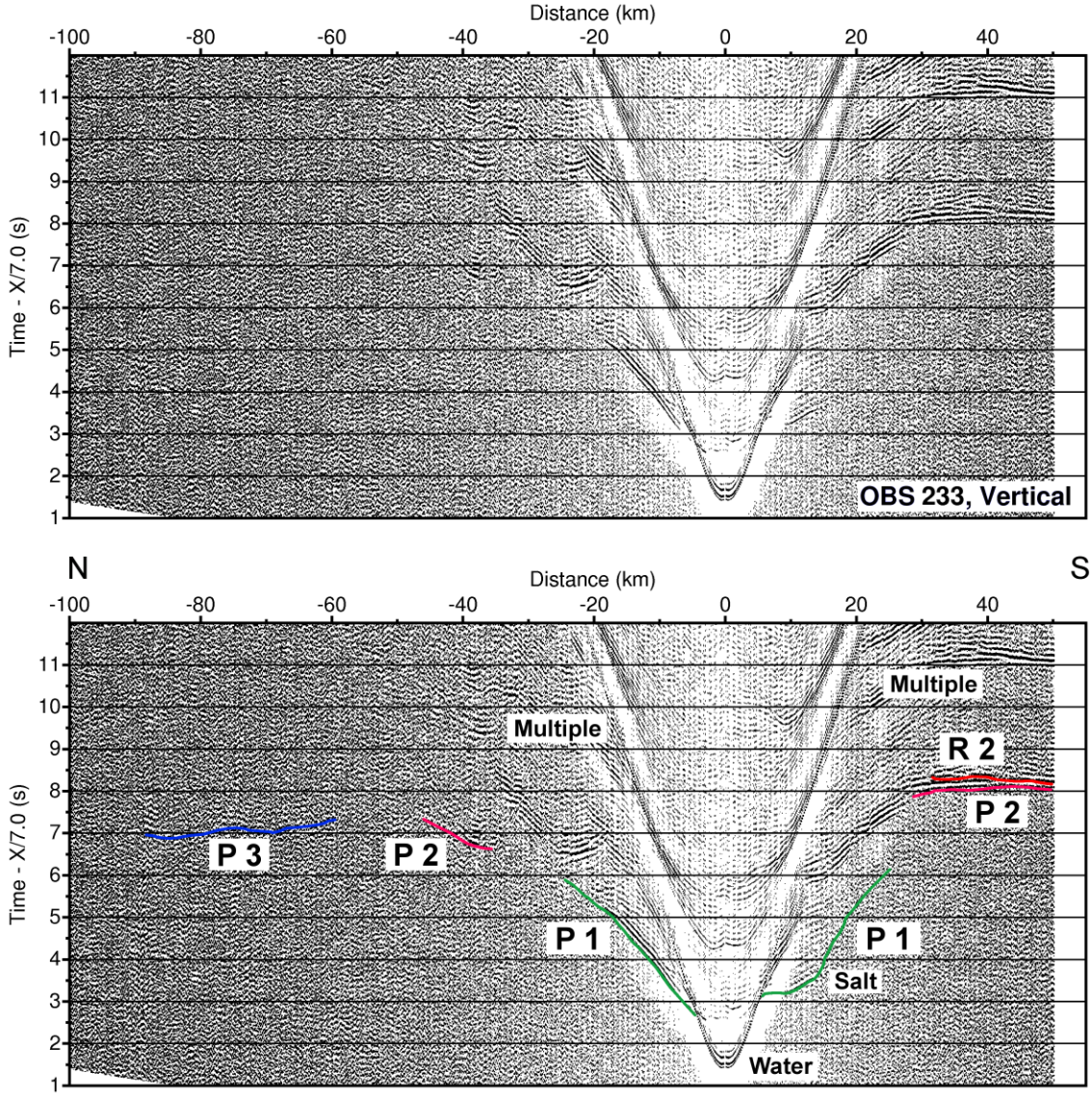

Figure C32 – Receiver gather from the vertical component of OBS 233 (top) with interpreted travel time arrivals (bottom). See Figure C8 for further information.

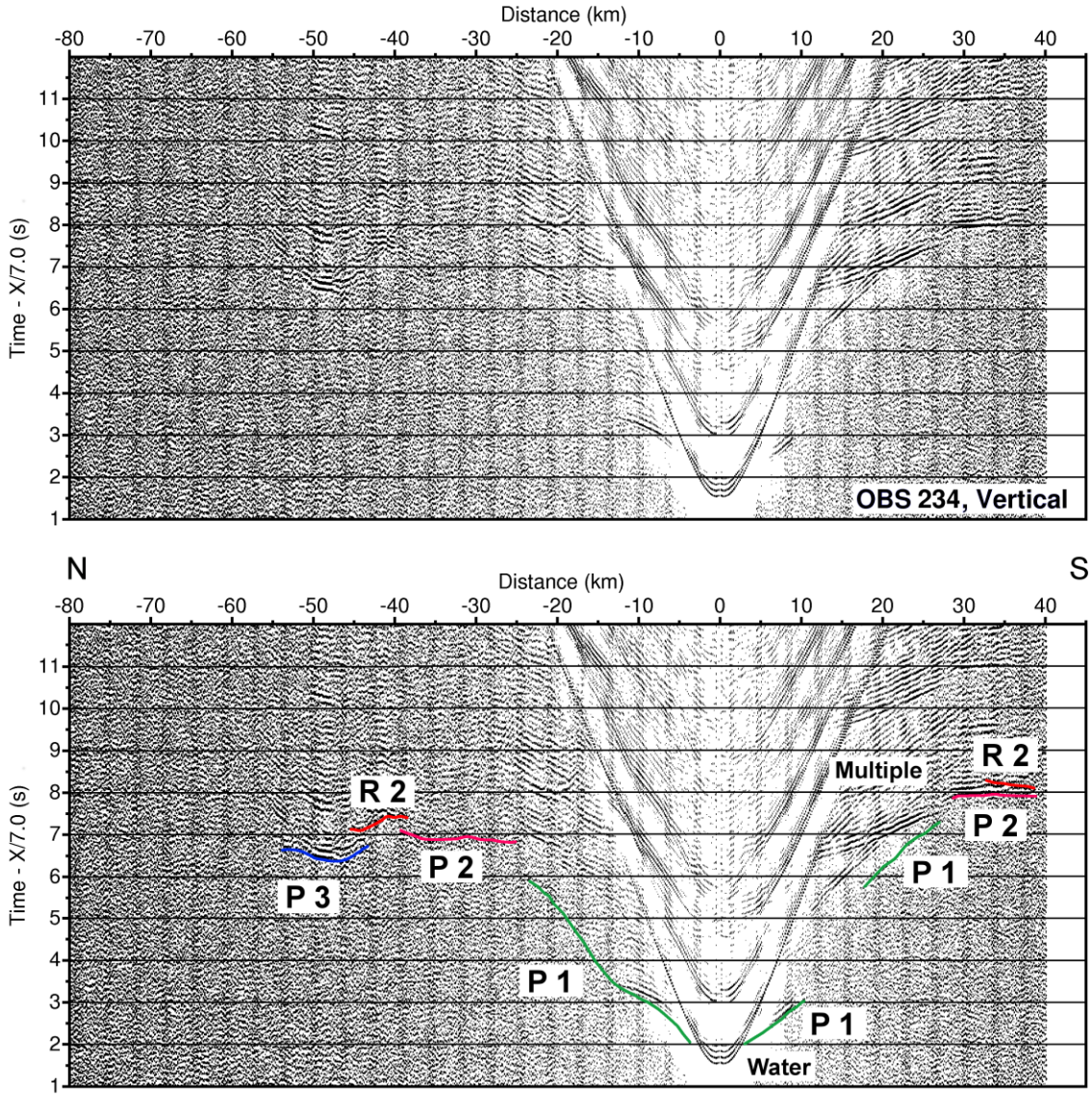

Figure C33 – Receiver gather from the vertical component of OBS 234 (top) with interpreted travel time arrivals (bottom). See Figure C8 for further information.

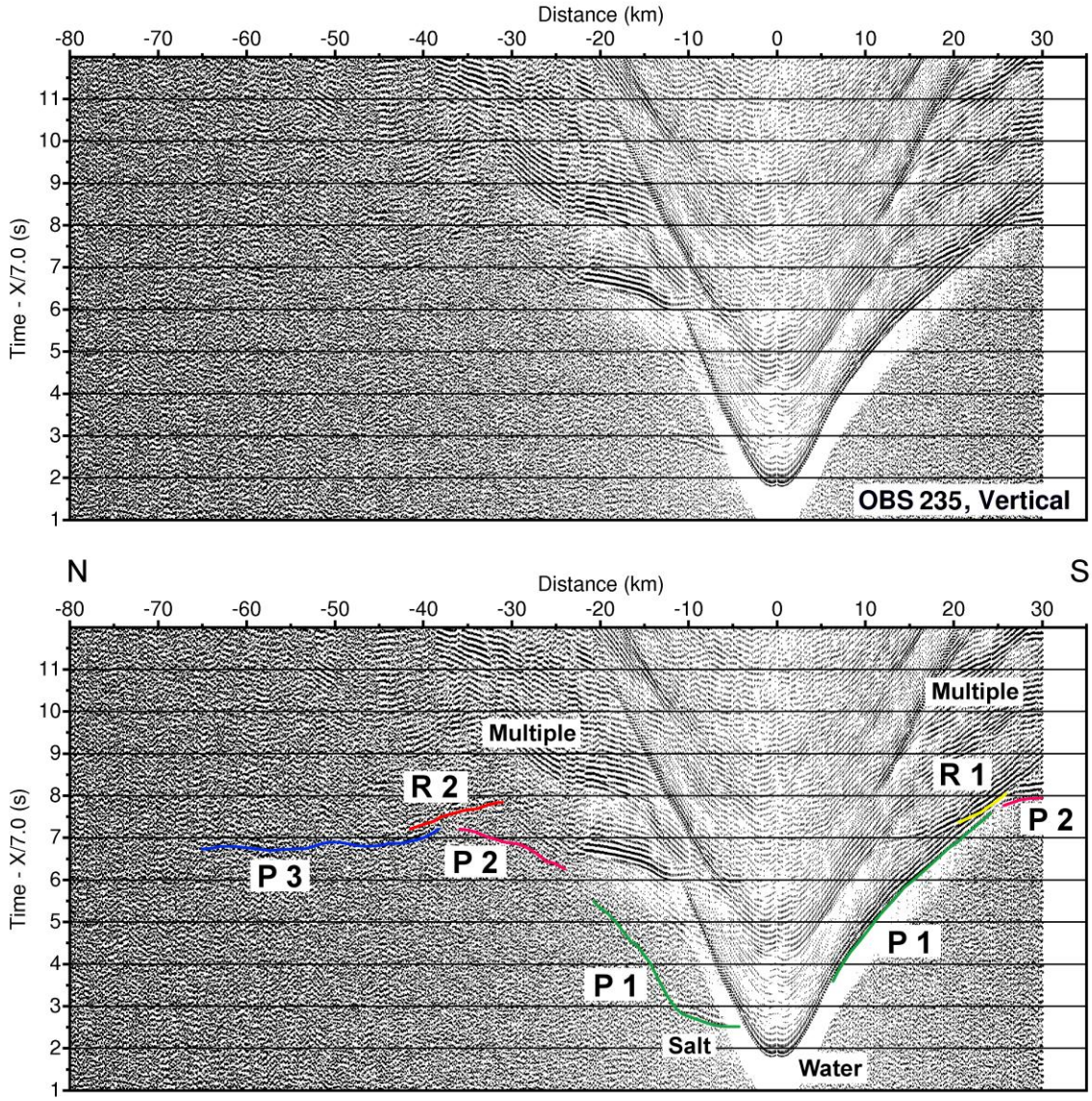

Figure C34 – Receiver gather from the vertical component of OBS 235 (top) with interpreted travel time arrivals (bottom). See Figure C8 for further information.

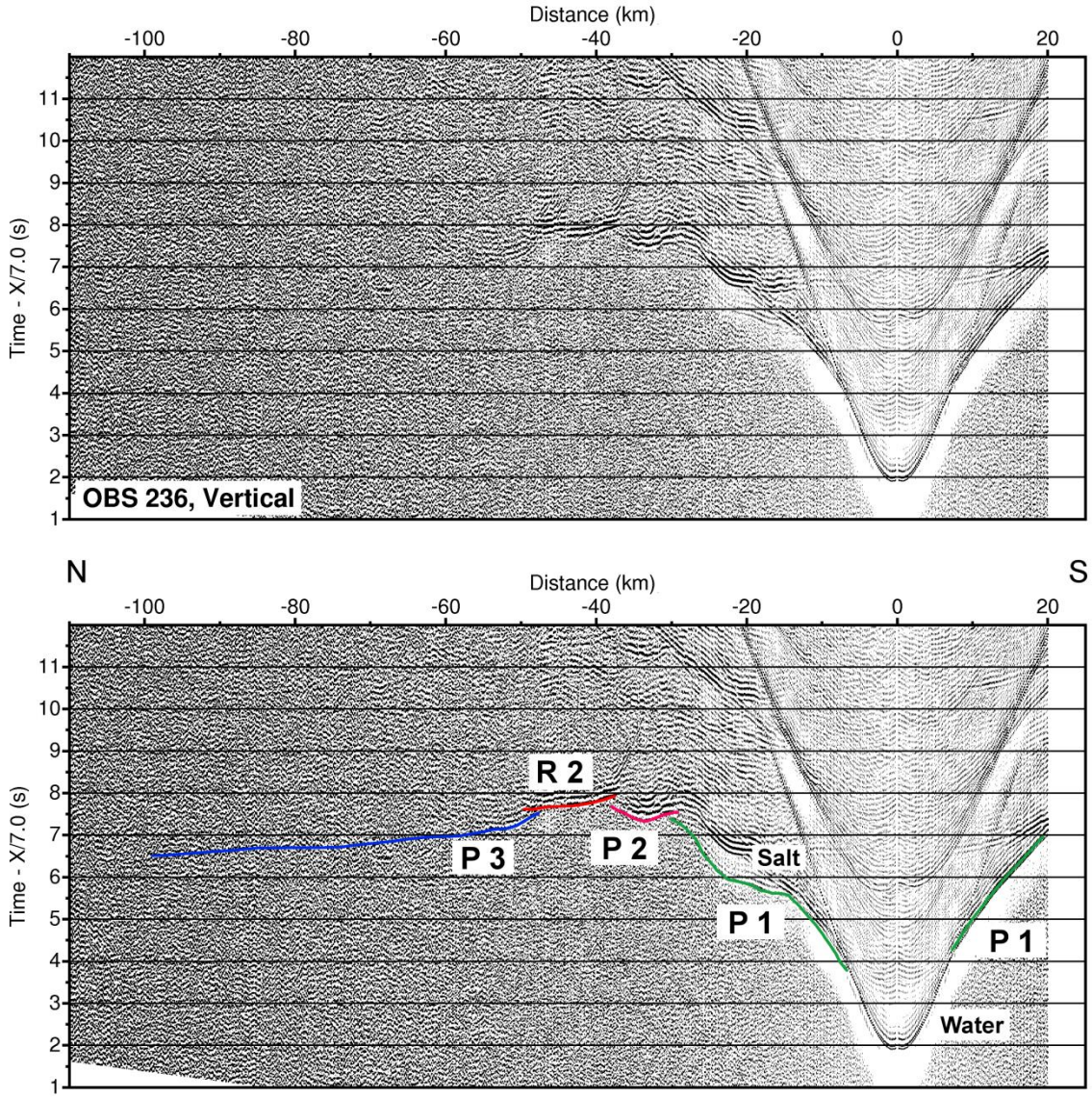

Figure C35 – Receiver gather from the vertical component of OBS 236 (top) with interpreted travel time arrivals (bottom). See Figure C8 for further information.

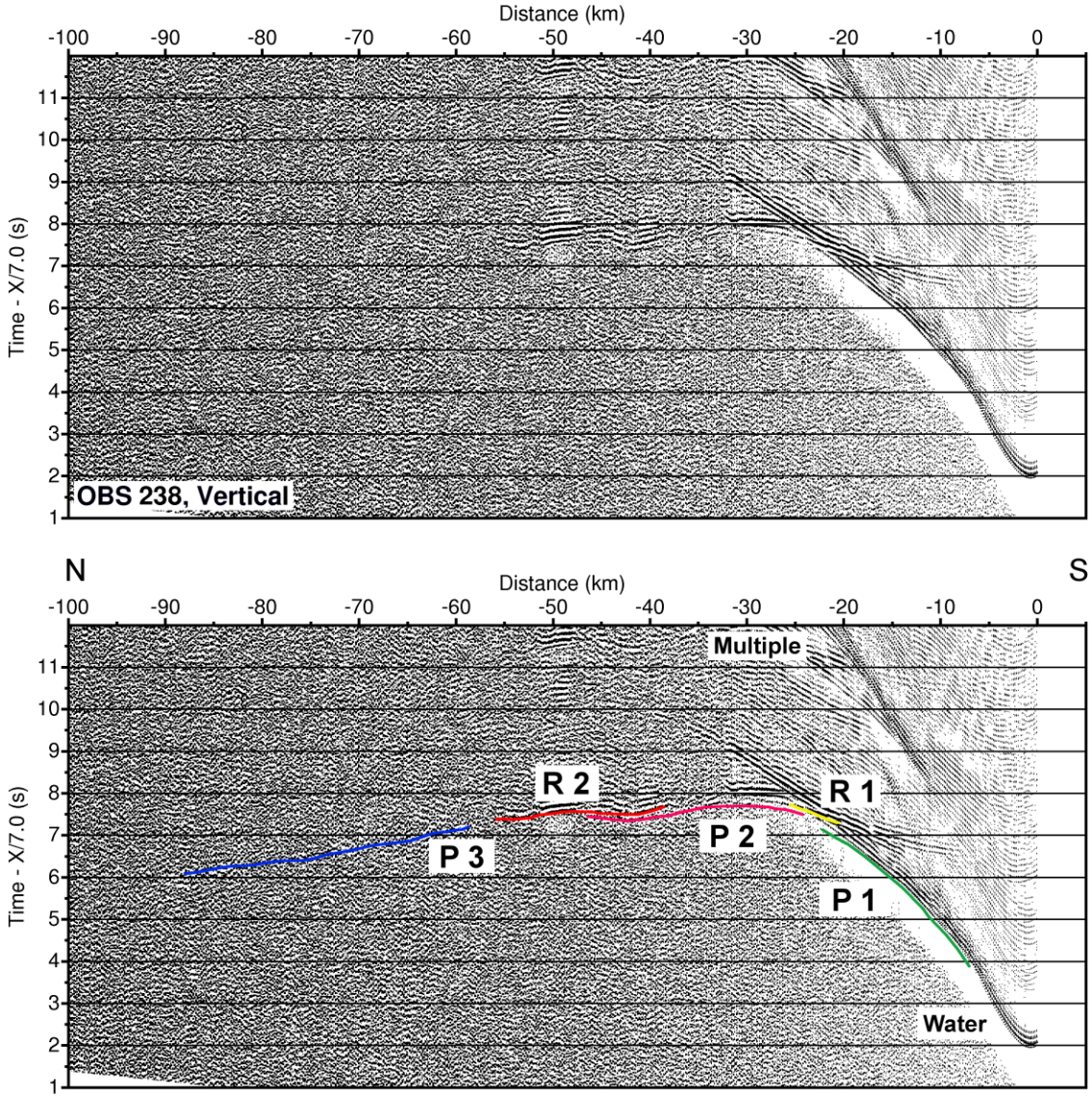

Figure C36 – Receiver gather from the vertical component of OBS 238 (top) with interpreted travel time arrivals (bottom). See Figure C8 for further information.

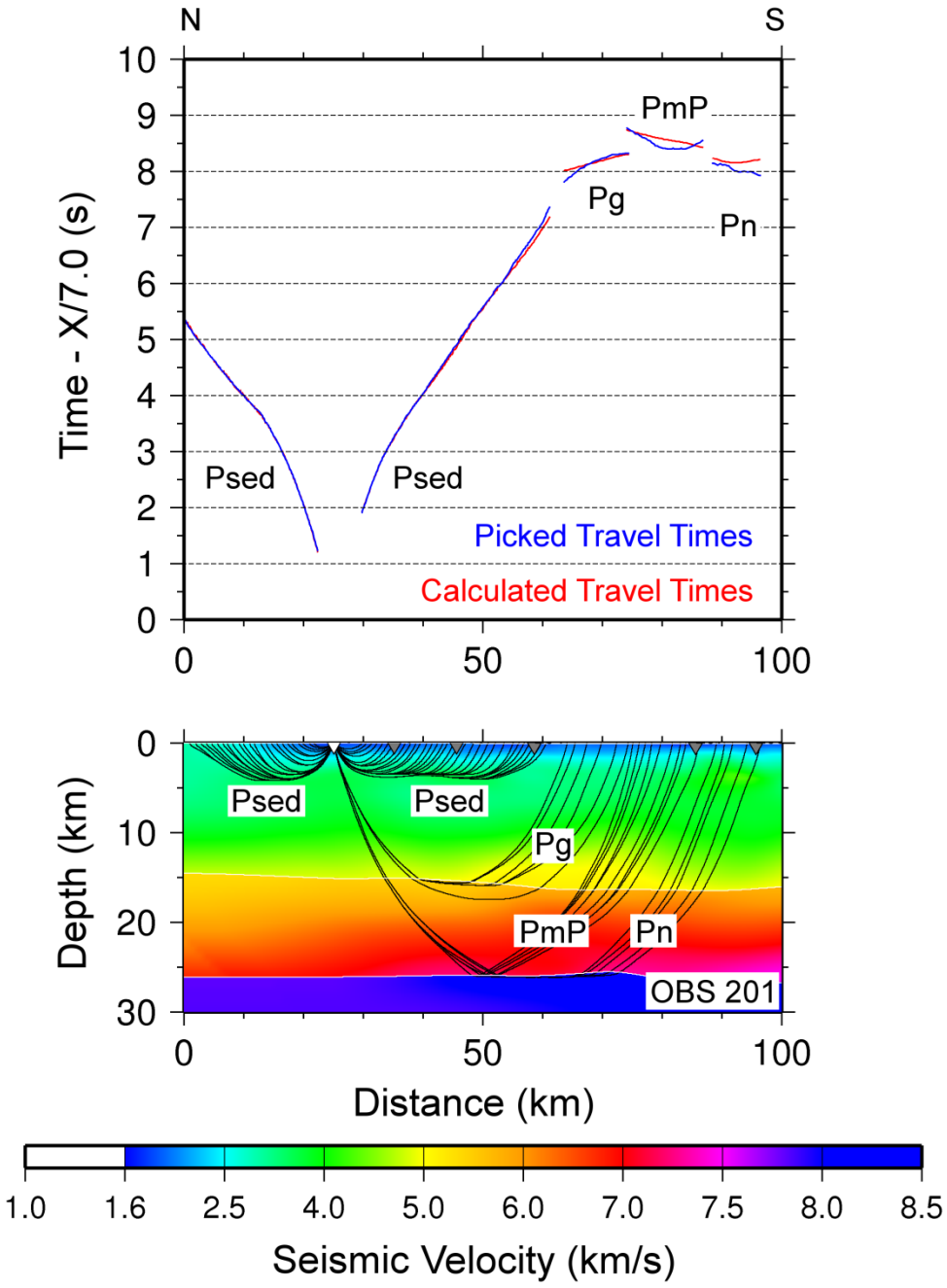

Figure C37 – Picked and calculated travel times for OBS 201 (top) and ray paths through final tomographic model (bottom). Rays plotted for every sixth pick. Shading denotes model space not constrained by ray paths. **PbP** –basement reflections; **Pg** – basement layer refractions; **PmP** – Moho reflections; **Pn** – mantle layer refractions; **Psed** – sediment layer refractions.

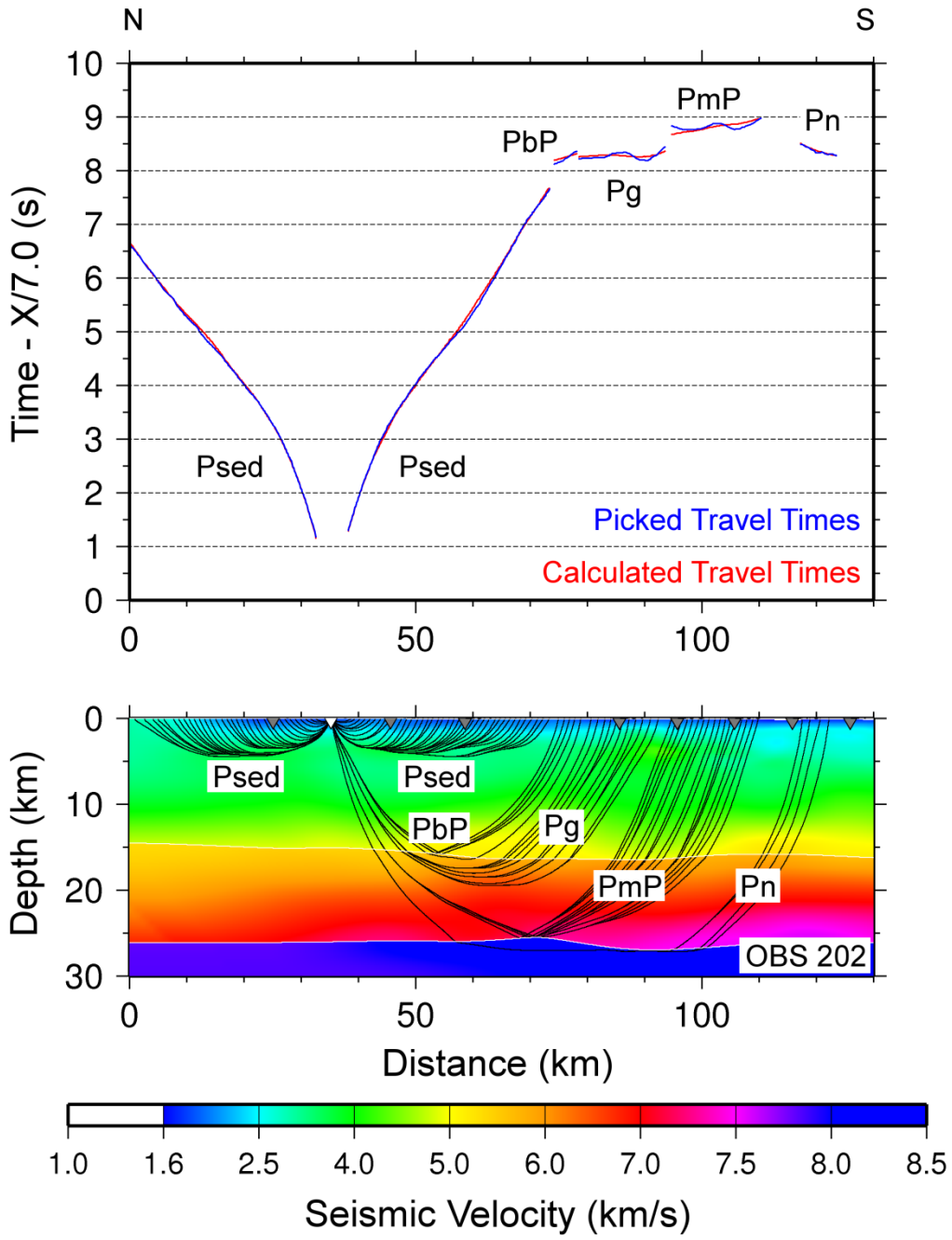

Figure C38 – Picked and calculated travel times for OBS 202 (top) and ray paths through final tomographic model (bottom). See Figure C37 for further information.

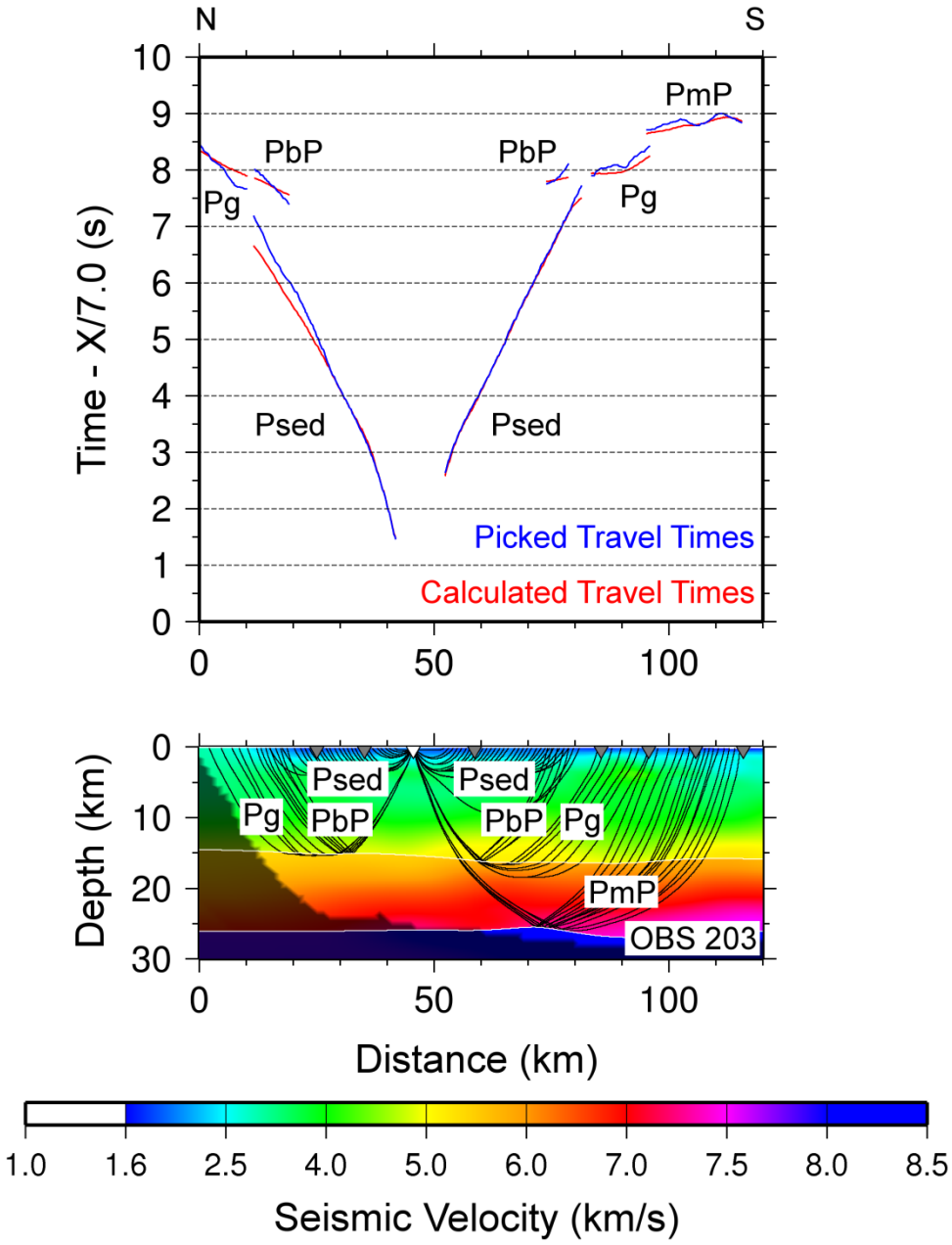

Figure C39 – Picked and calculated travel times for OBS 203 (top) and ray paths through final tomographic model (bottom). See Figure C37 for further information.

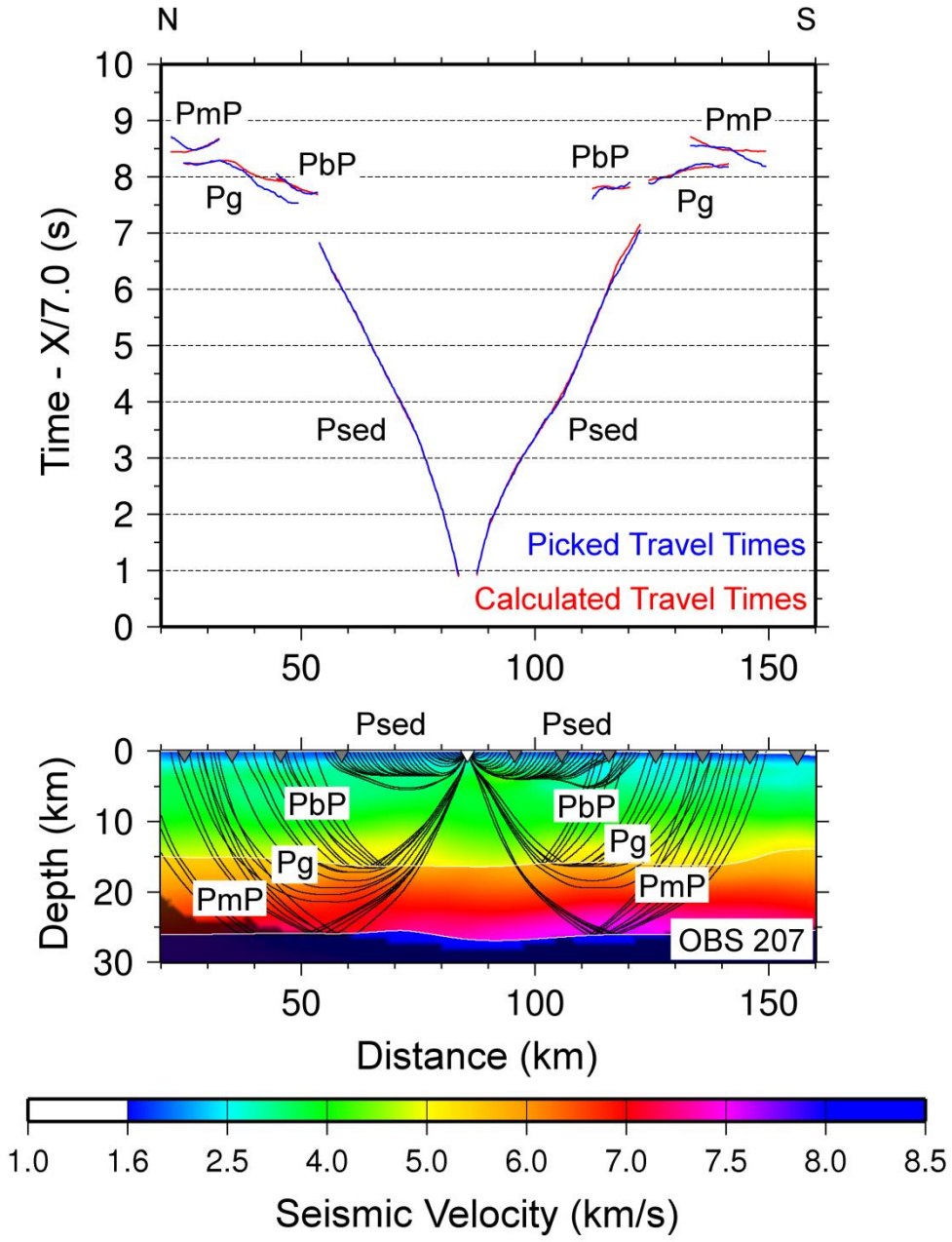

Figure C40 – Picked and calculated travel times for OBS 207 (top) and ray paths through final tomographic model (bottom). See Figure C37 for further information.

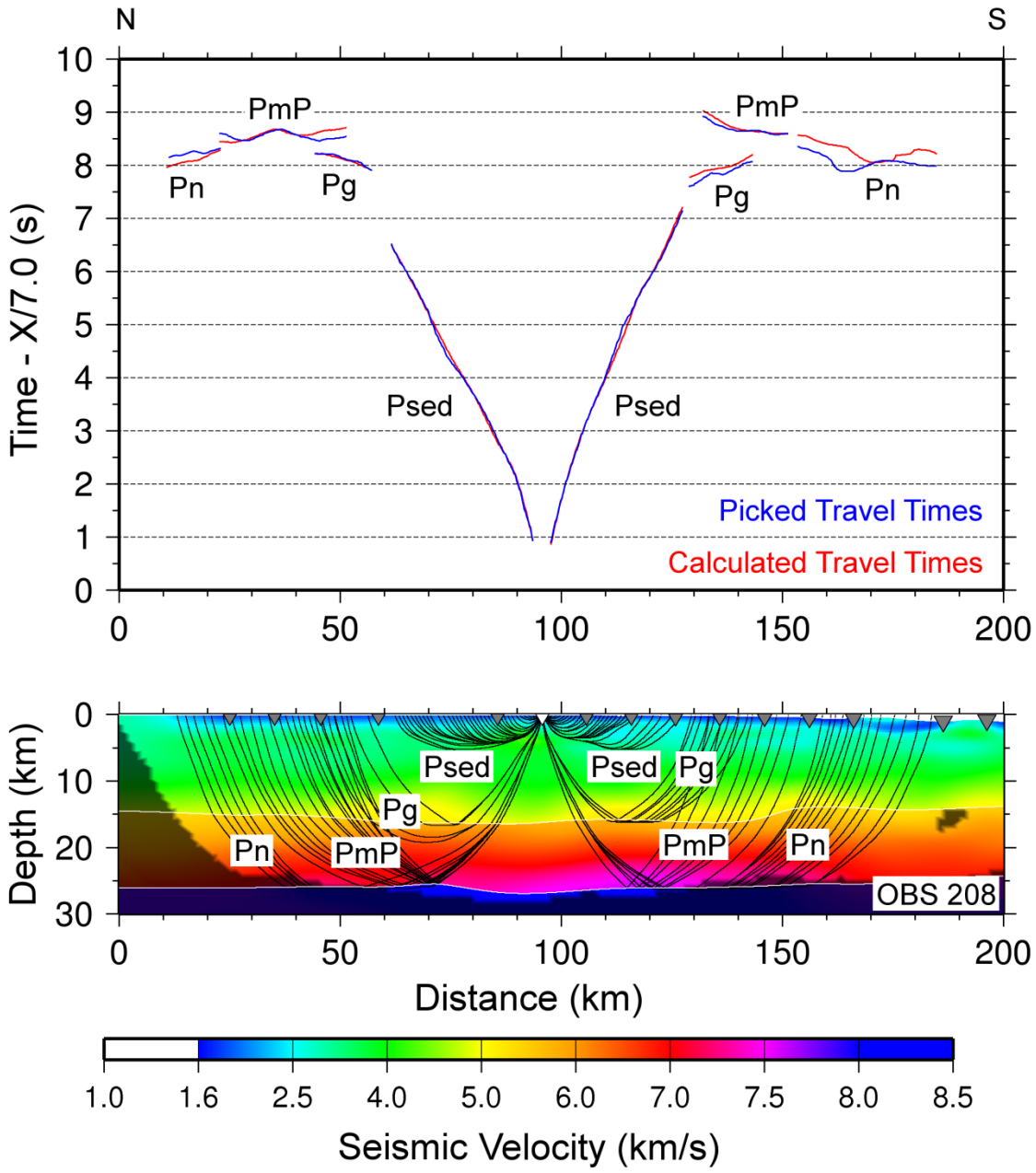

Figure C41 – Picked and calculated travel times for OBS 208 (top) and ray paths through final tomographic model (bottom). See Figure C37 for further information.

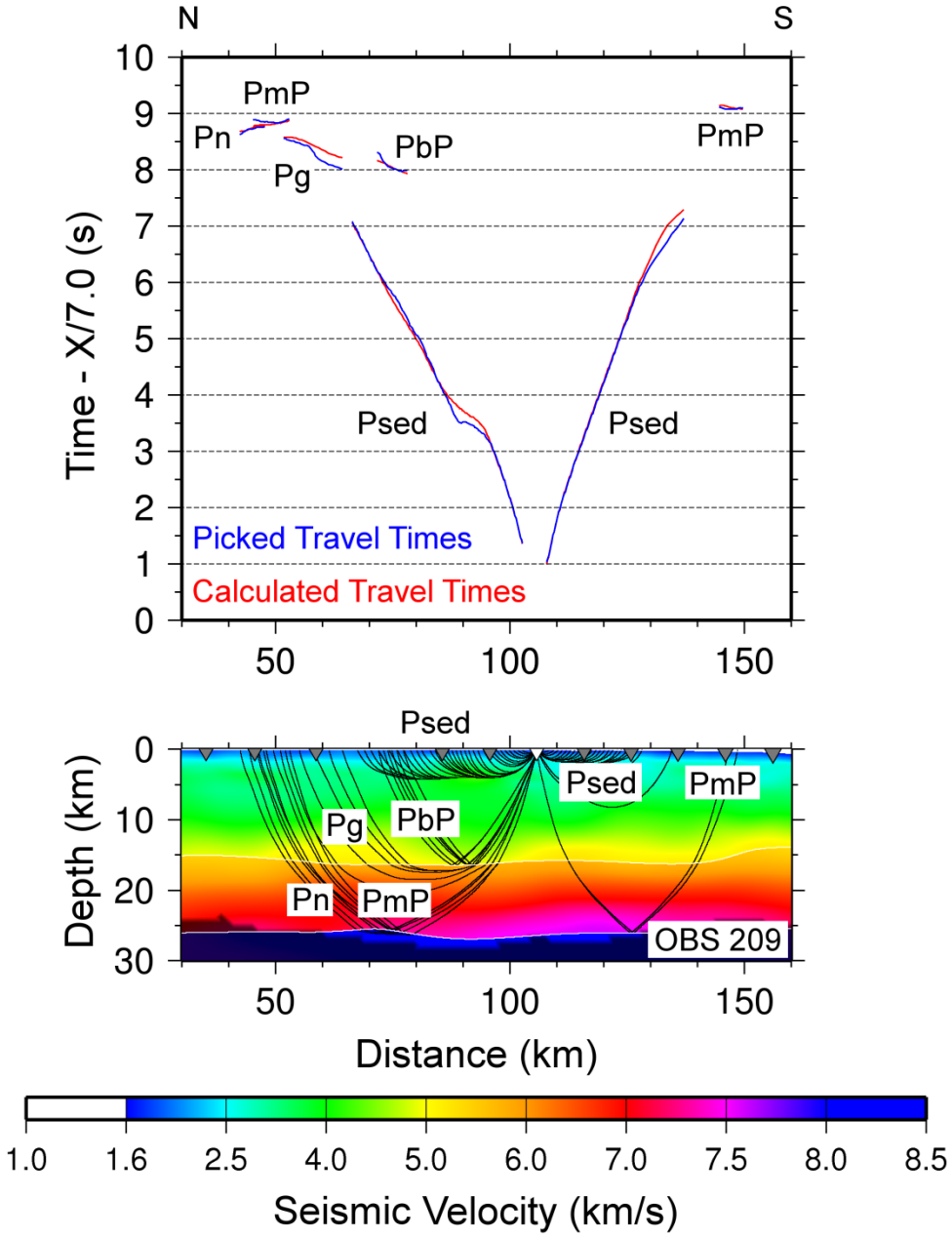

Figure C42 – Picked and calculated travel times for OBS 209 (top) and ray paths through final tomographic model (bottom). See Figure C37 for further information.

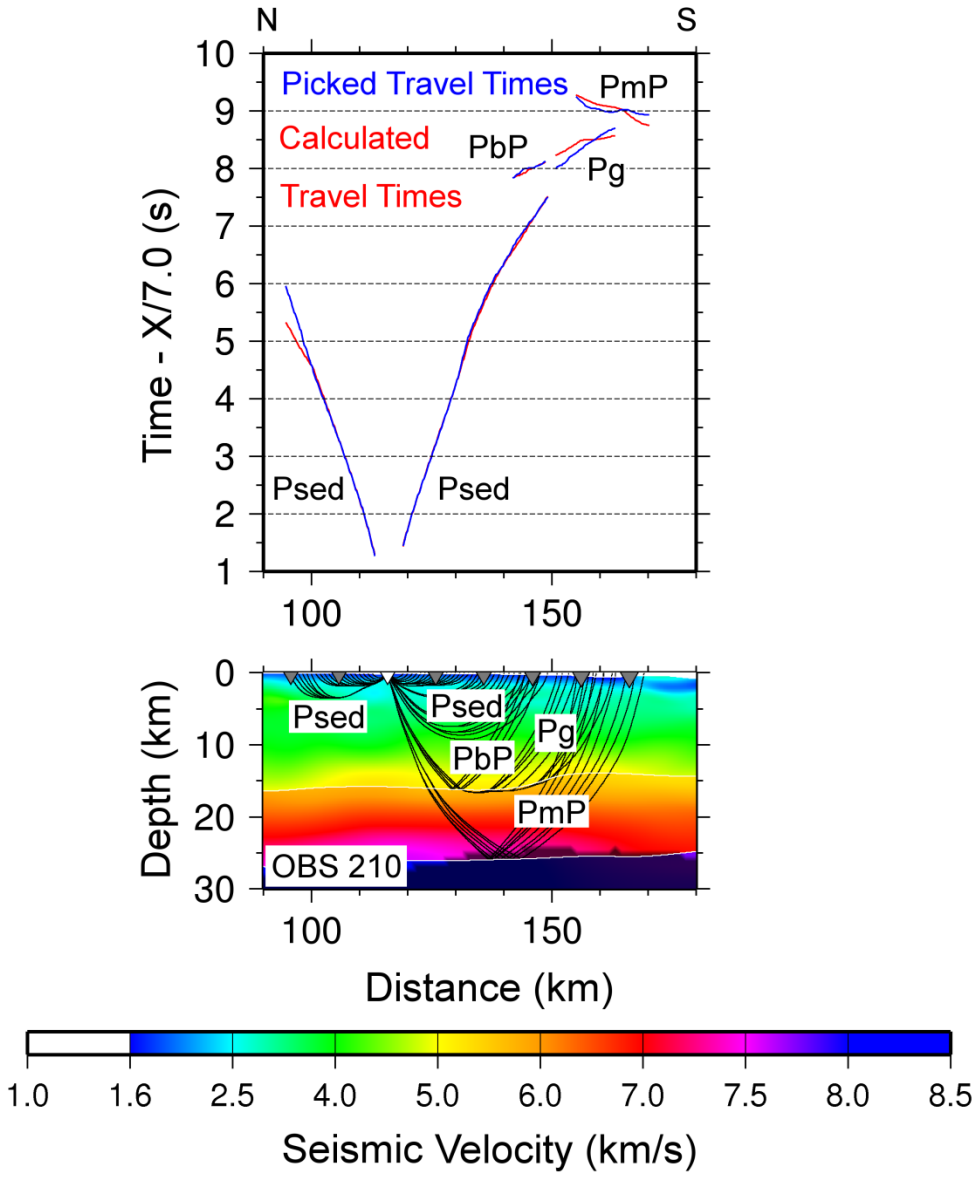

Figure C43 – Picked and calculated travel times for OBS 210 (top) and ray paths through final tomographic model (bottom). See Figure C37 for further information.

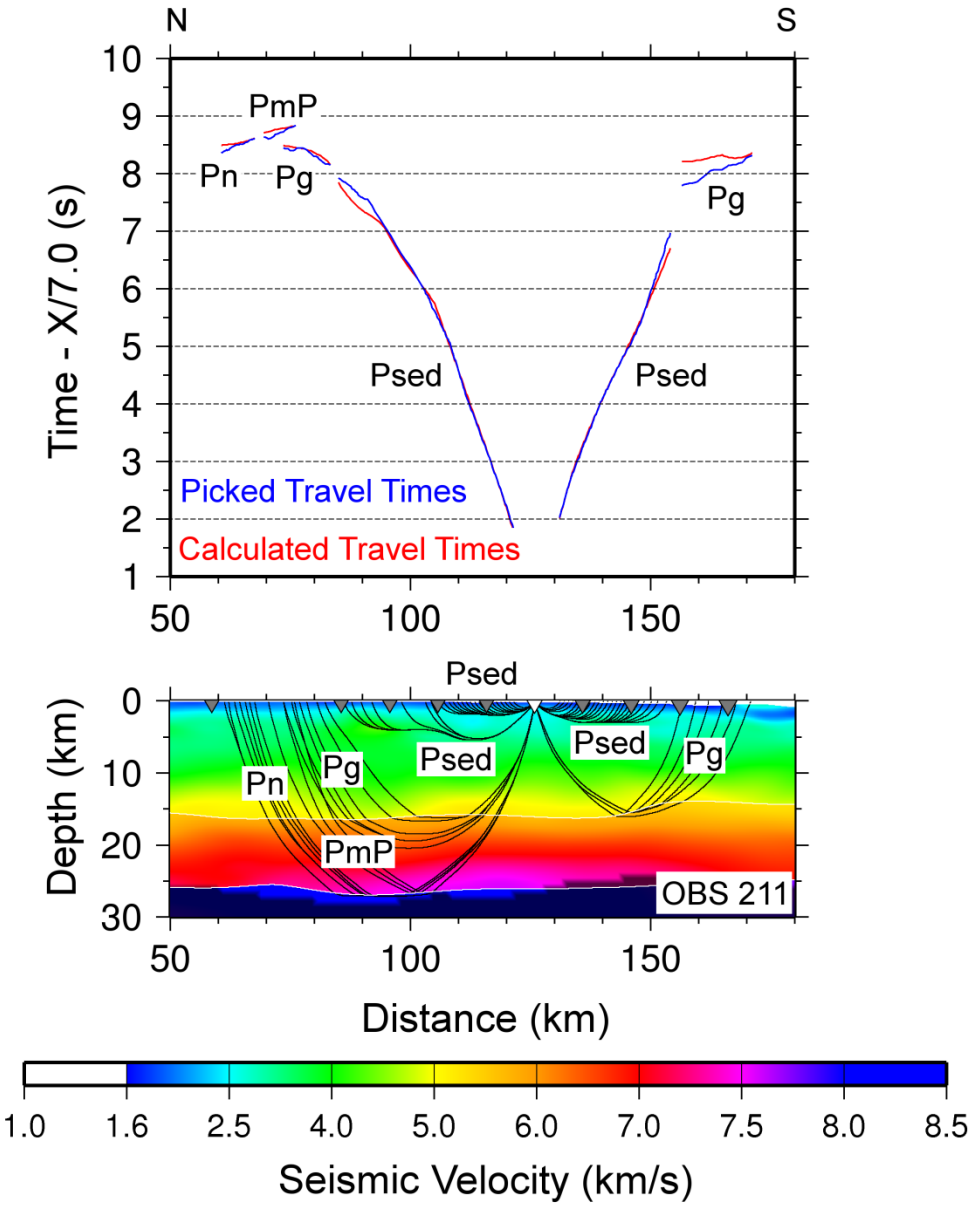

Figure C44 – Picked and calculated travel times for OBS 211 (top) and ray paths through final tomographic model (bottom). See Figure C37 for further information.

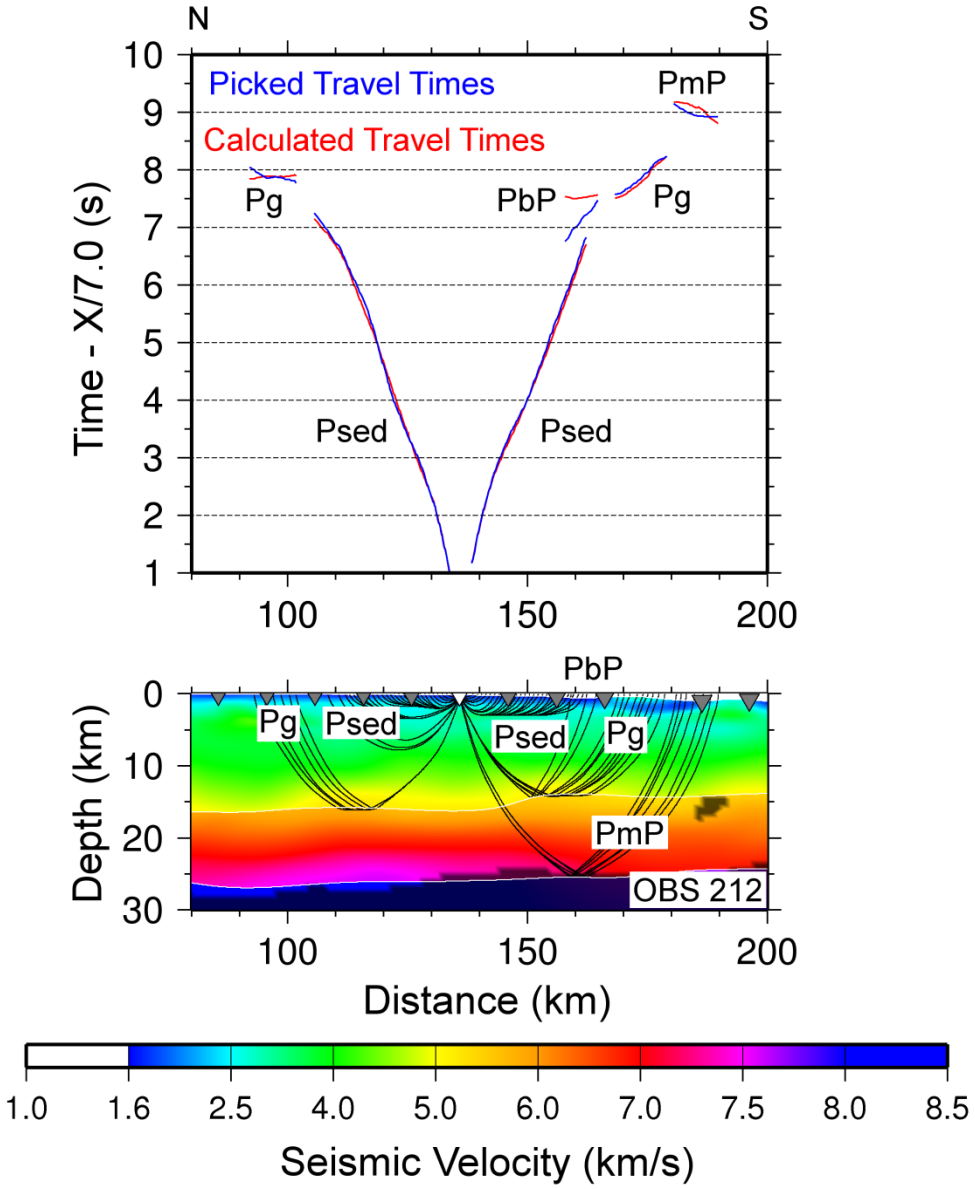

Figure C45 – Picked and calculated travel times for OBS 212 (top) and ray paths through final tomographic model (bottom). See Figure C37 for further information.

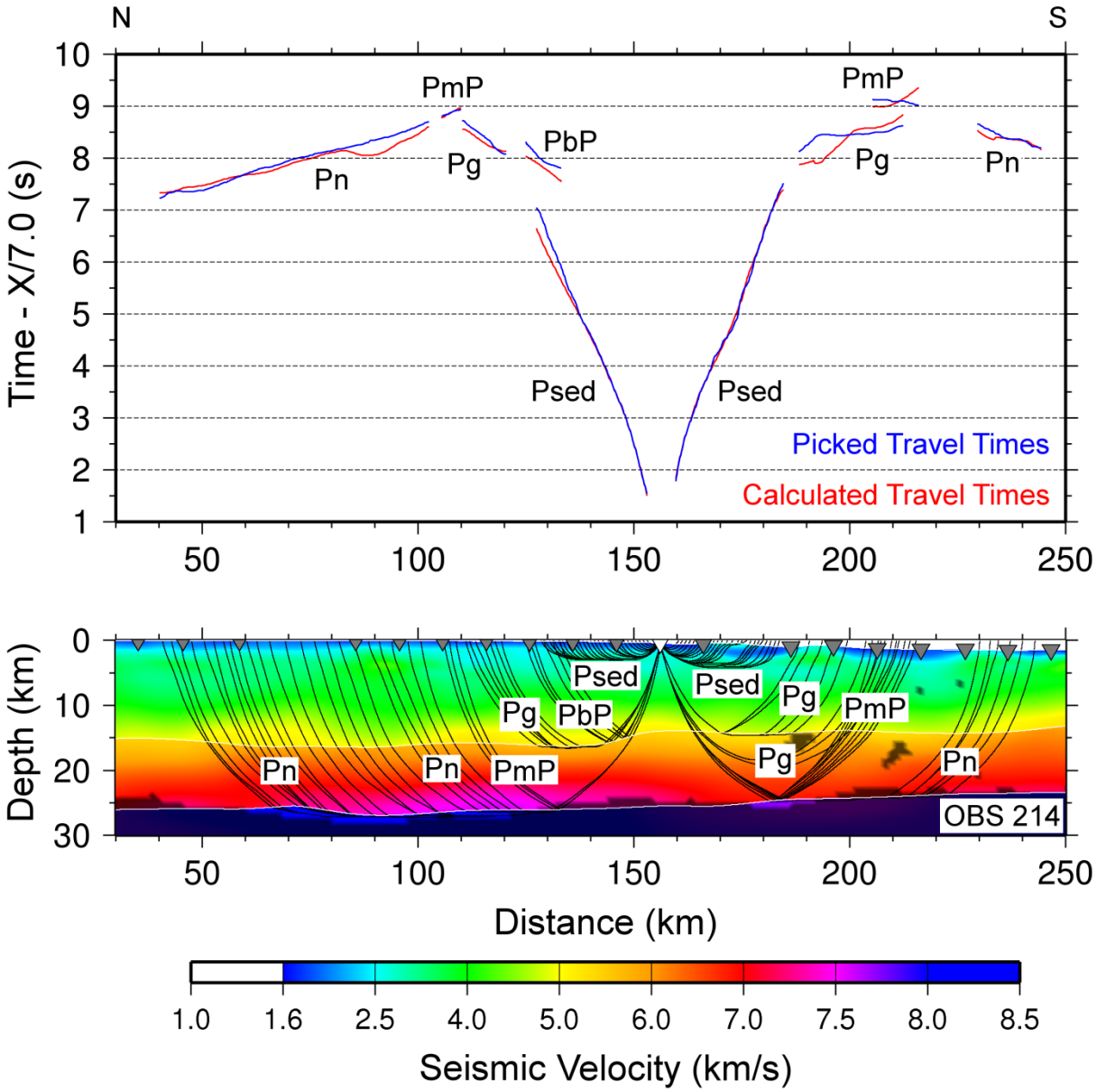

Figure C46 – Picked and calculated travel times for OBS 214 (top) and ray paths through final tomographic model (bottom). See Figure C37 for further information.

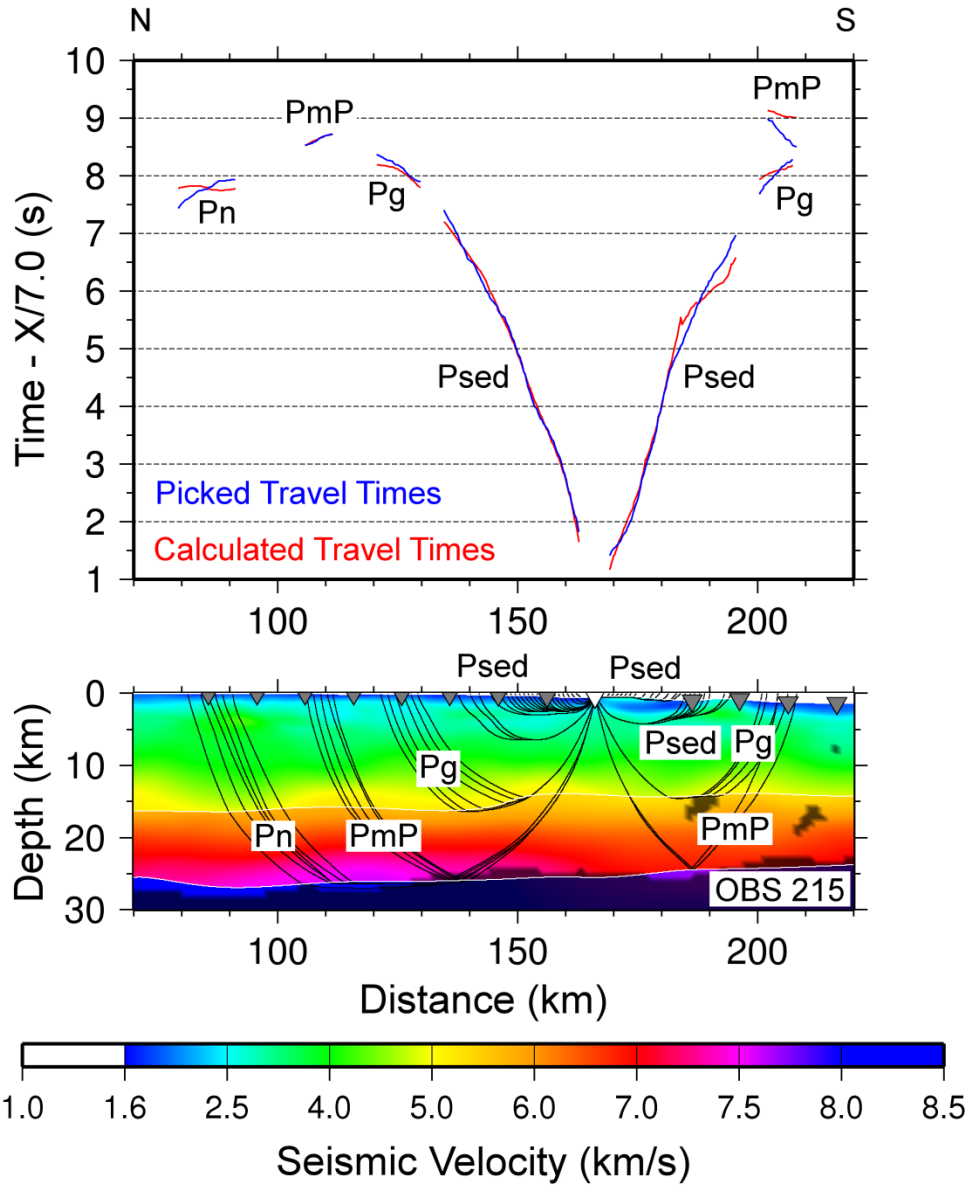

Figure C47 – Picked and calculated travel times for OBS 215 (top) and ray paths through final tomographic model (bottom). See Figure C37 for further information.

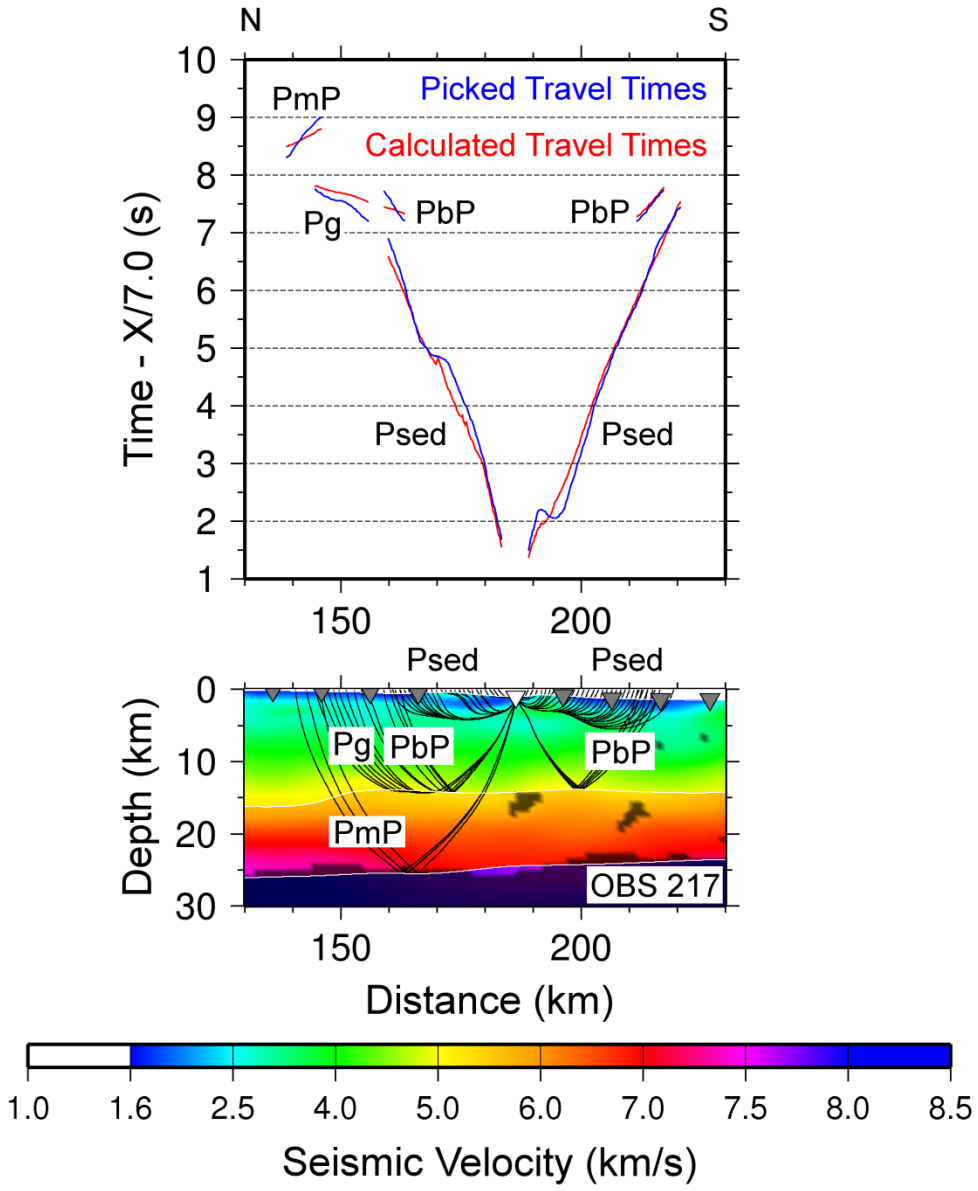

Figure C48 – Picked and calculated travel times for OBS 217 (top) and ray paths through final tomographic model (bottom). See Figure C37 for further information.

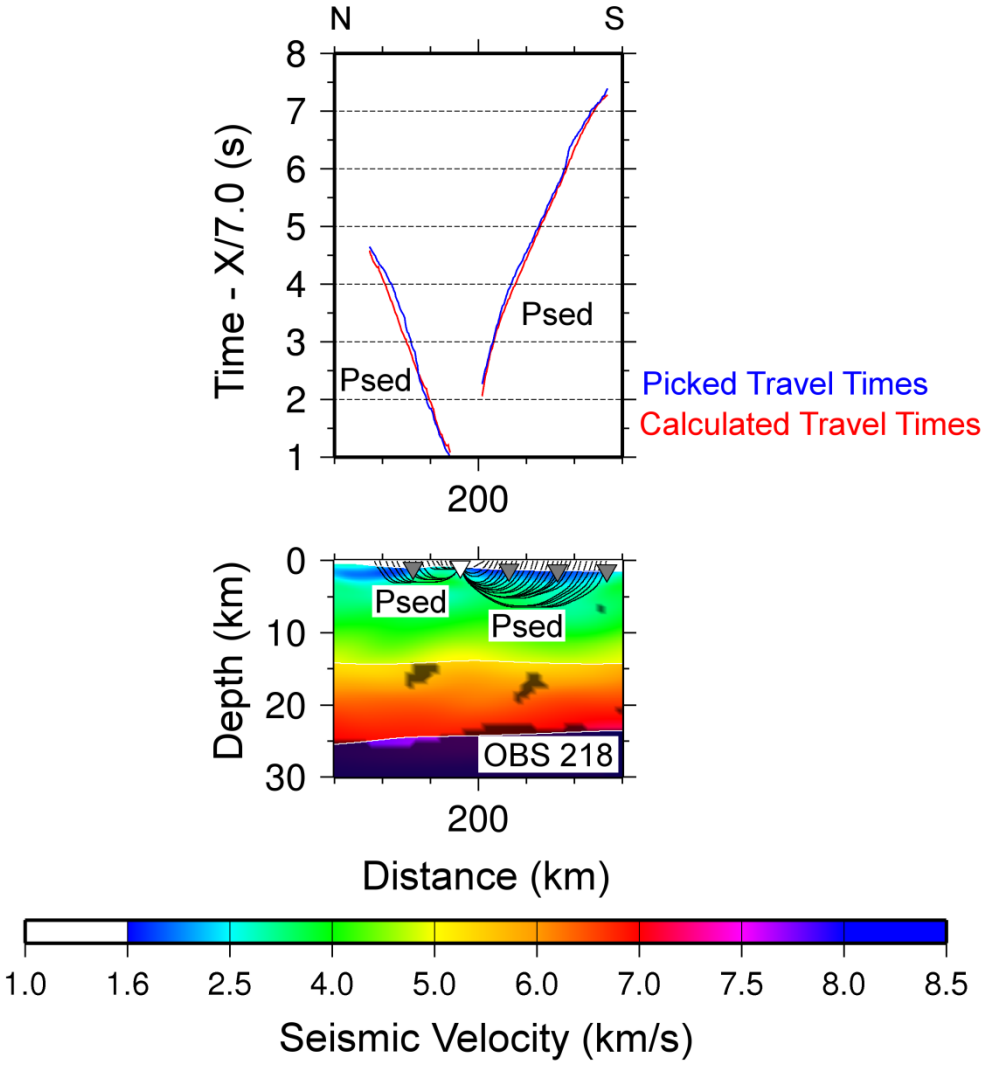

Figure C49 – Picked and calculated travel times for OBS 218 (top) and ray paths through final tomographic model (bottom). See Figure C37 for further information.

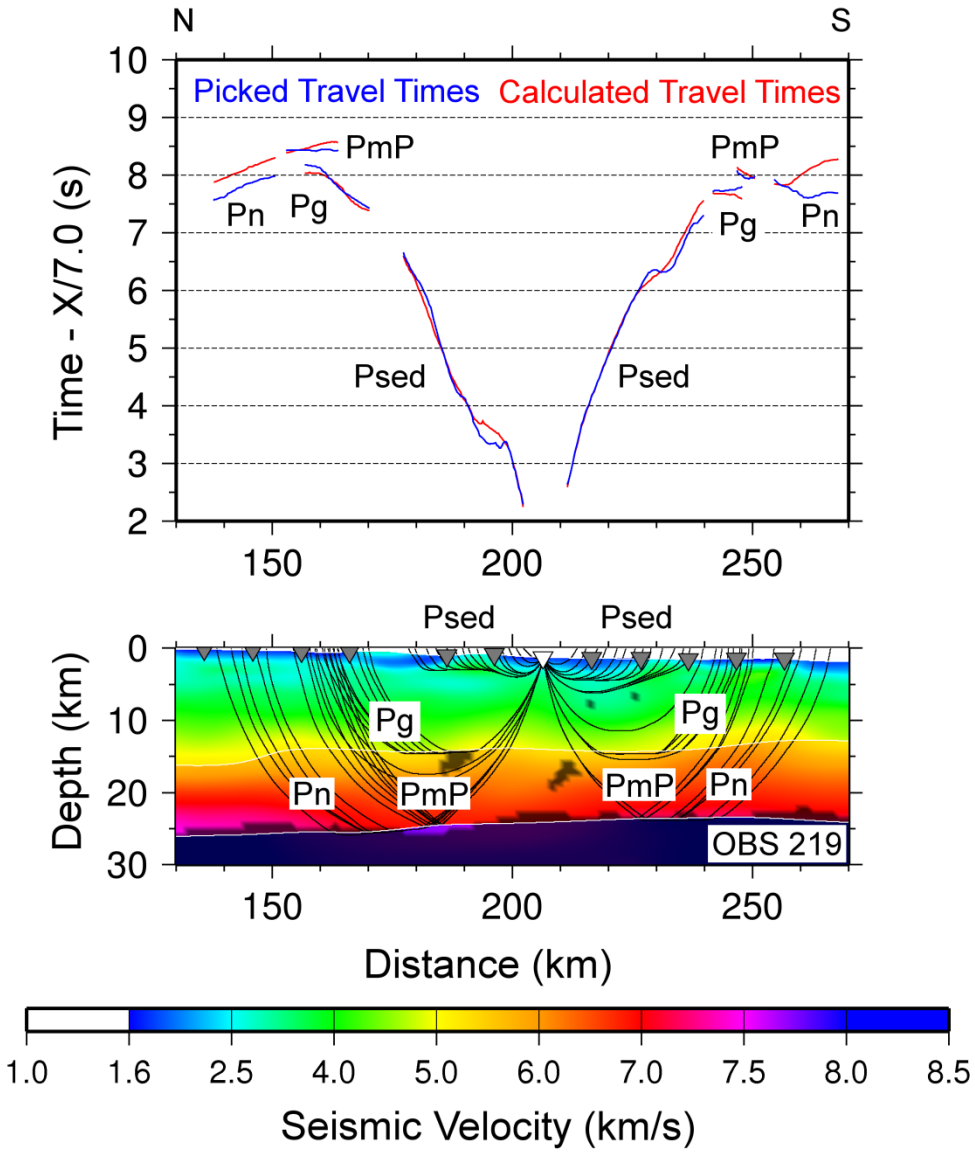

Figure C50 – Picked and calculated travel times for OBS 219 (top) and ray paths through final tomographic model (bottom). See Figure C37 for further information.

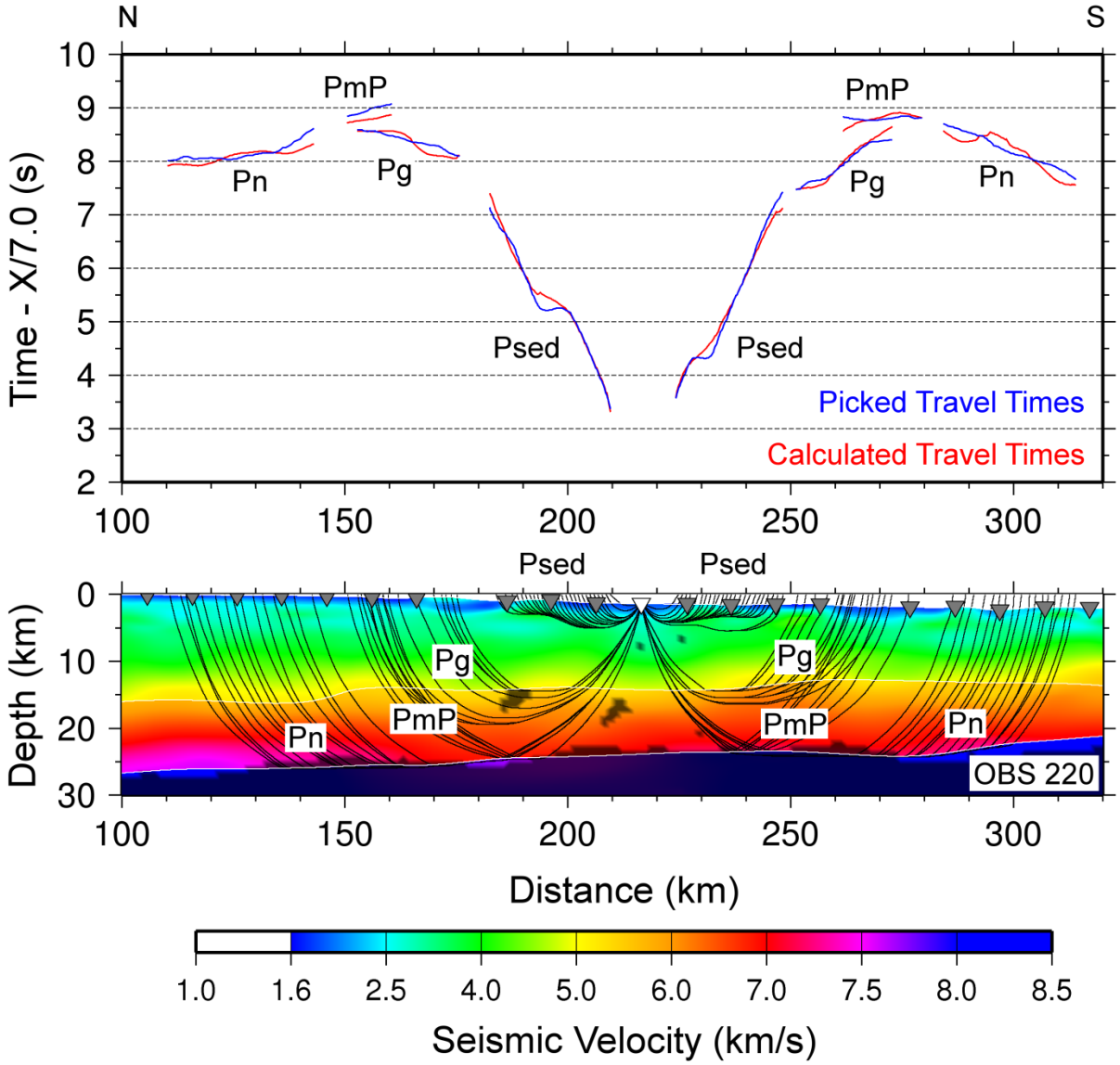

Figure C51 – Picked and calculated travel times for OBS 220 (top) and ray paths through final tomographic model (bottom). See Figure C37 for further information.

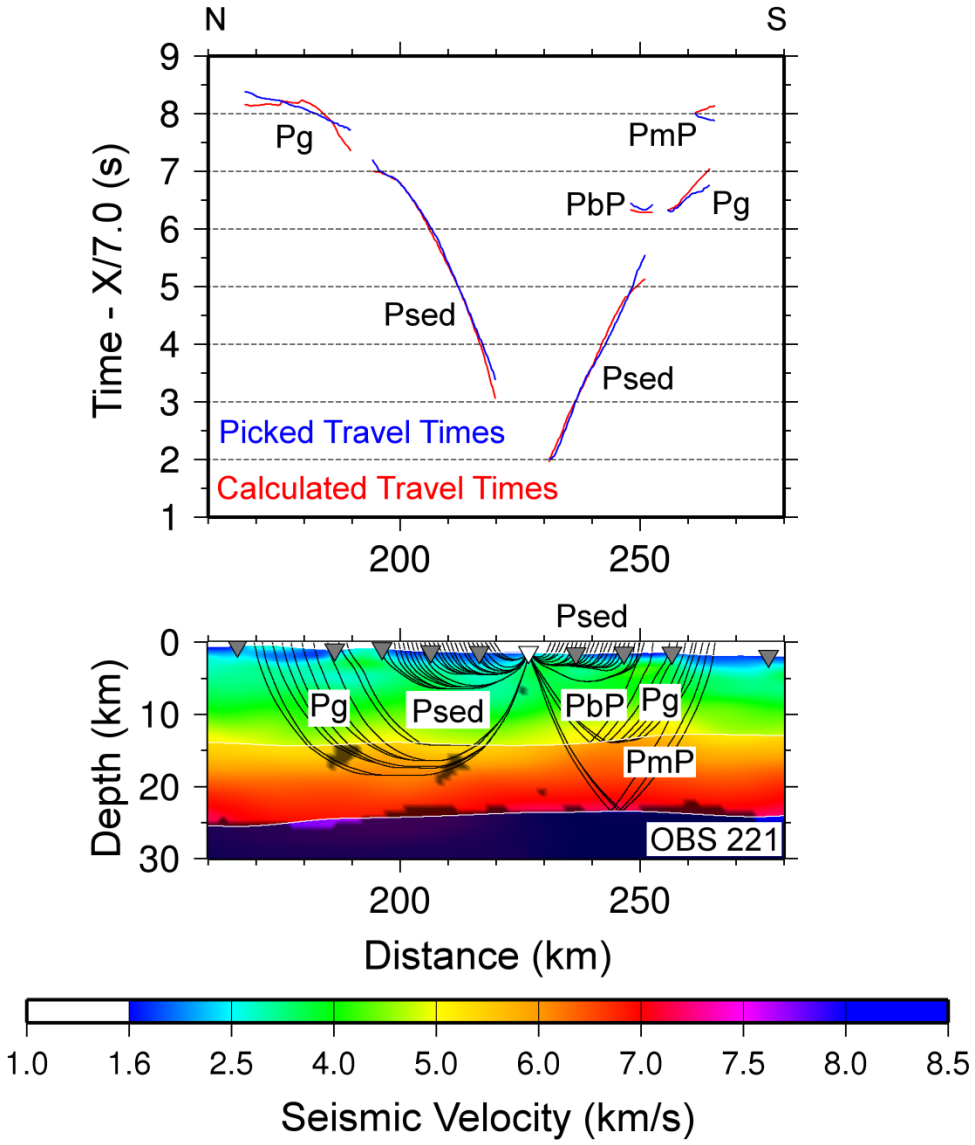

Figure C52 – Picked and calculated travel times for OBS 221 (top) and ray paths through final tomographic model (bottom). See Figure C37 for further information.

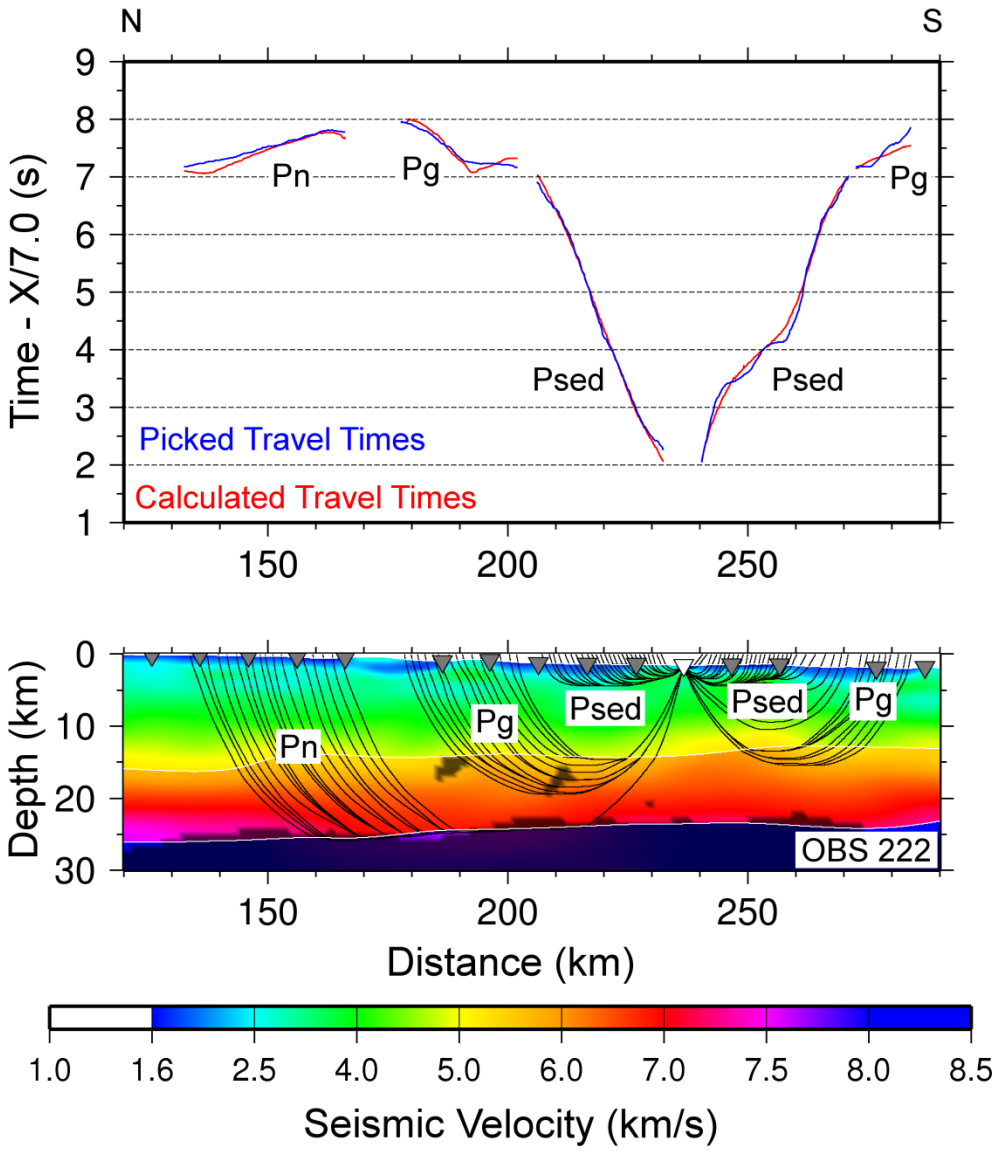

Figure C53 – Picked and calculated travel times for OBS 222 (top) and ray paths through final tomographic model (bottom). See Figure C37 for further information.

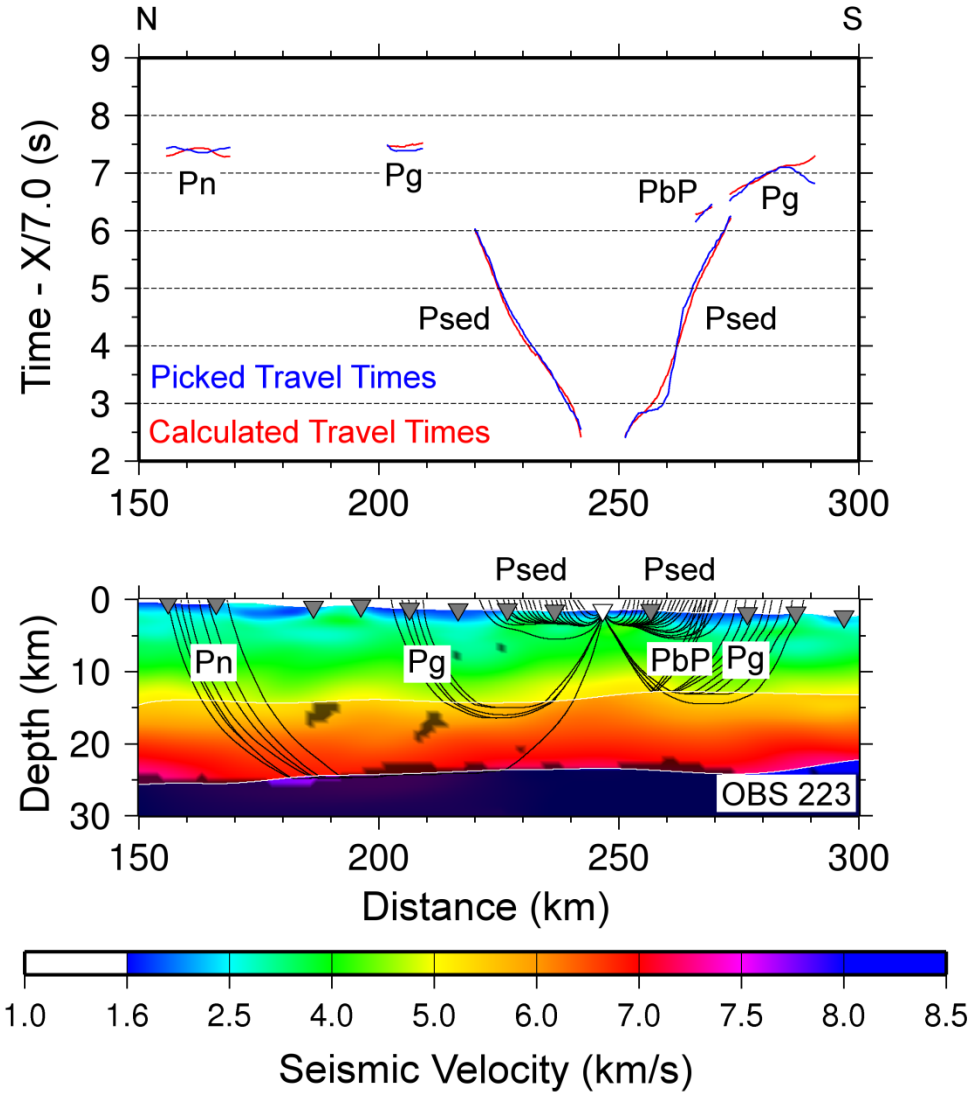

Figure C54 – Picked and calculated travel times for OBS 223 (top) and ray paths through final tomographic model (bottom). See Figure C37 for further information.

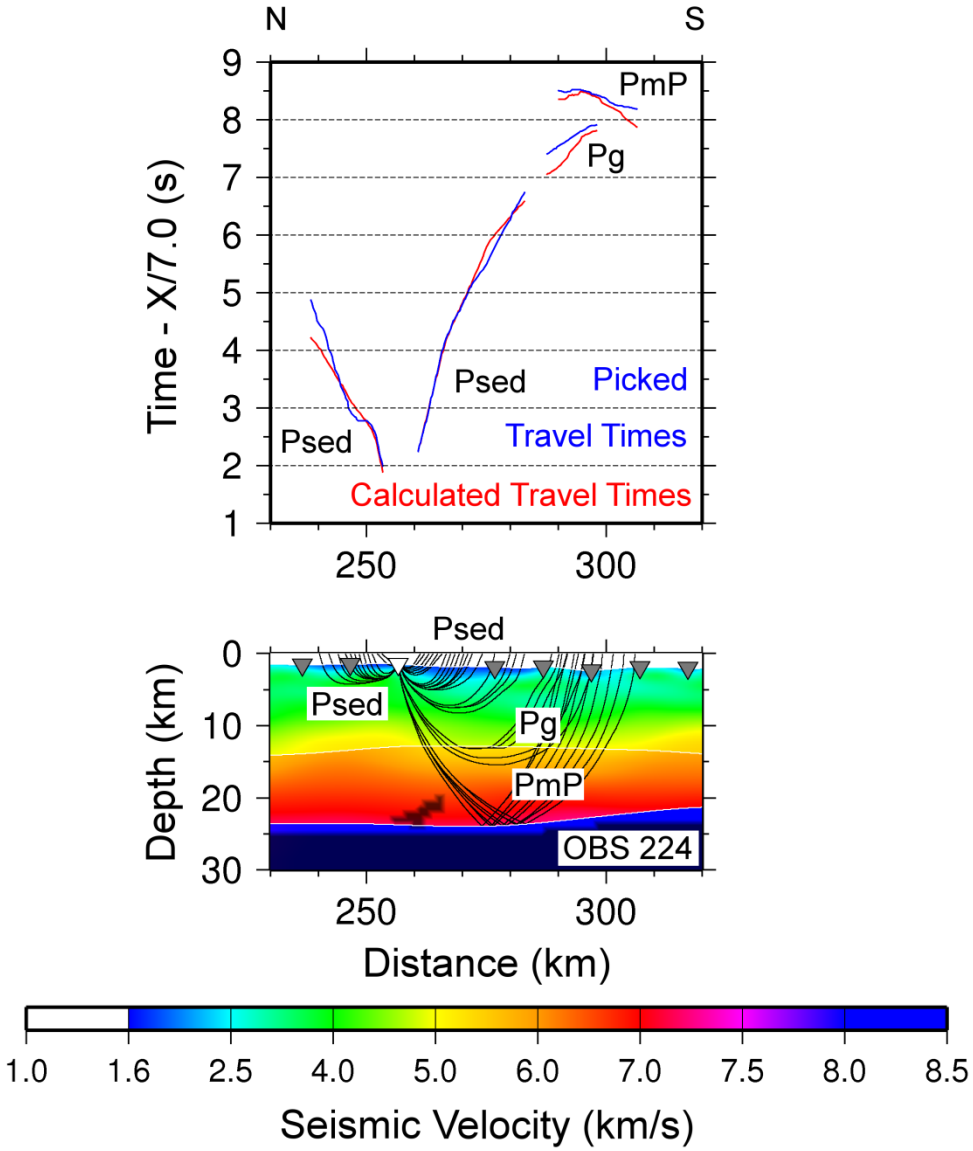

Figure C55 – Picked and calculated travel times for OBS 224 (top) and ray paths through final tomographic model (bottom). See Figure C37 for further information.

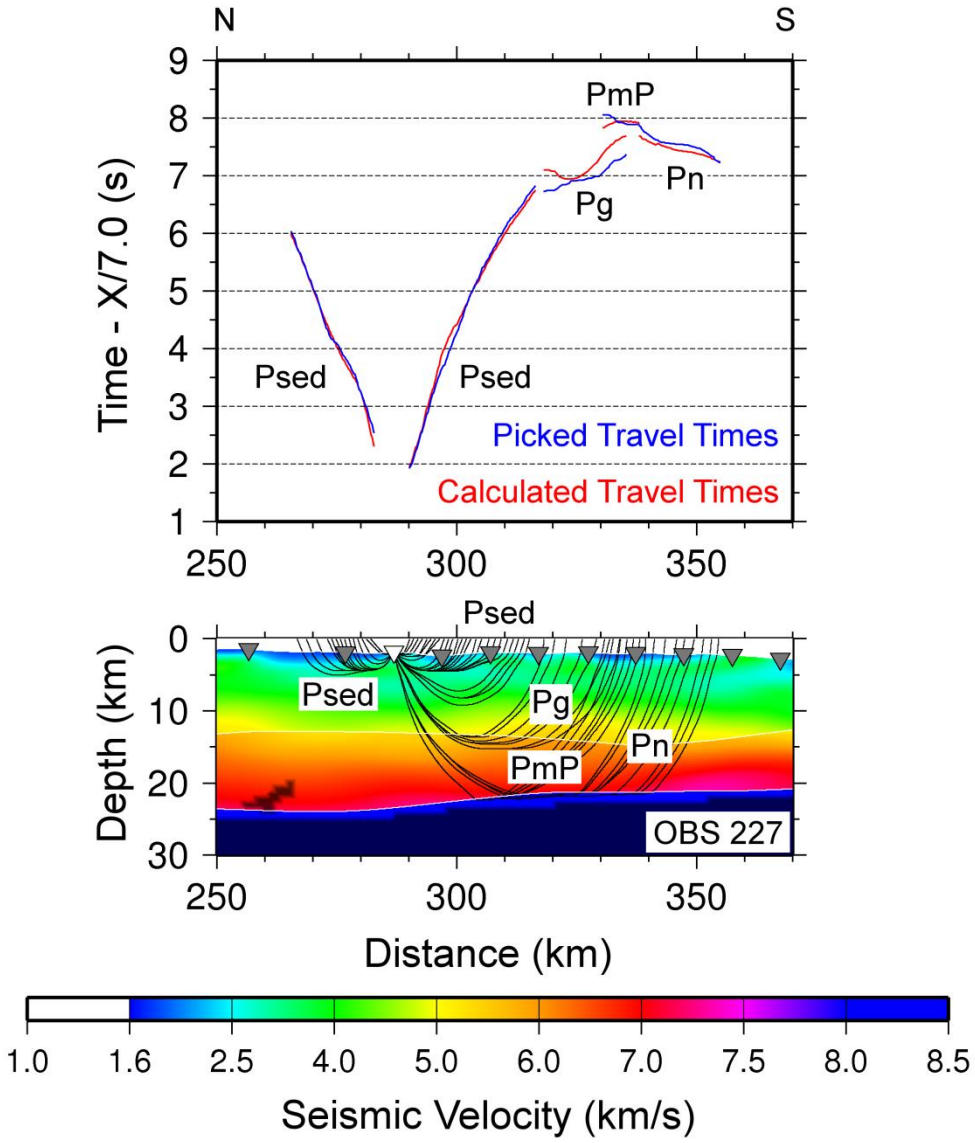

Figure C56 – Picked and calculated travel times for OBS 227 (top) and ray paths through final tomographic model (bottom). See Figure C37 for further information.

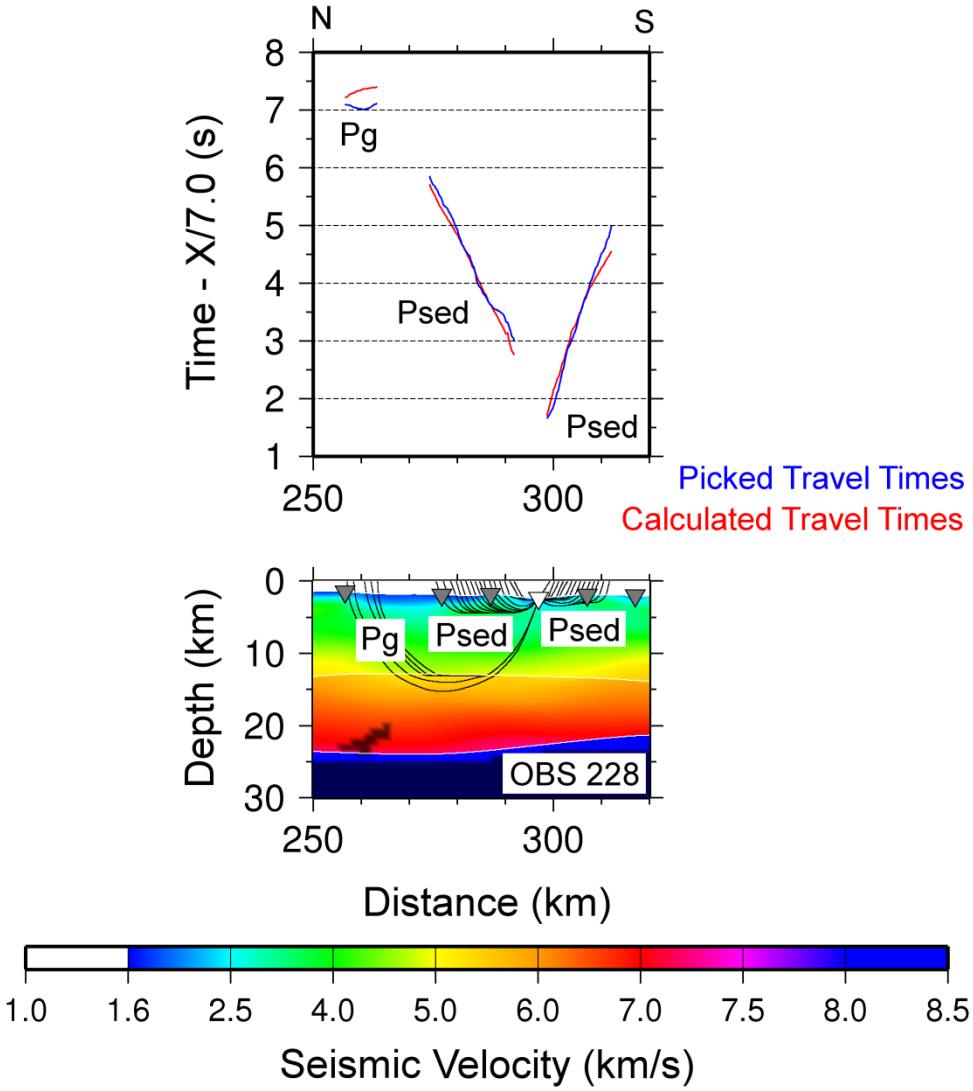

Figure C57 – Picked and calculated travel times for OBS 228 (top) and ray paths through final tomographic model (bottom). See Figure C37 for further information.

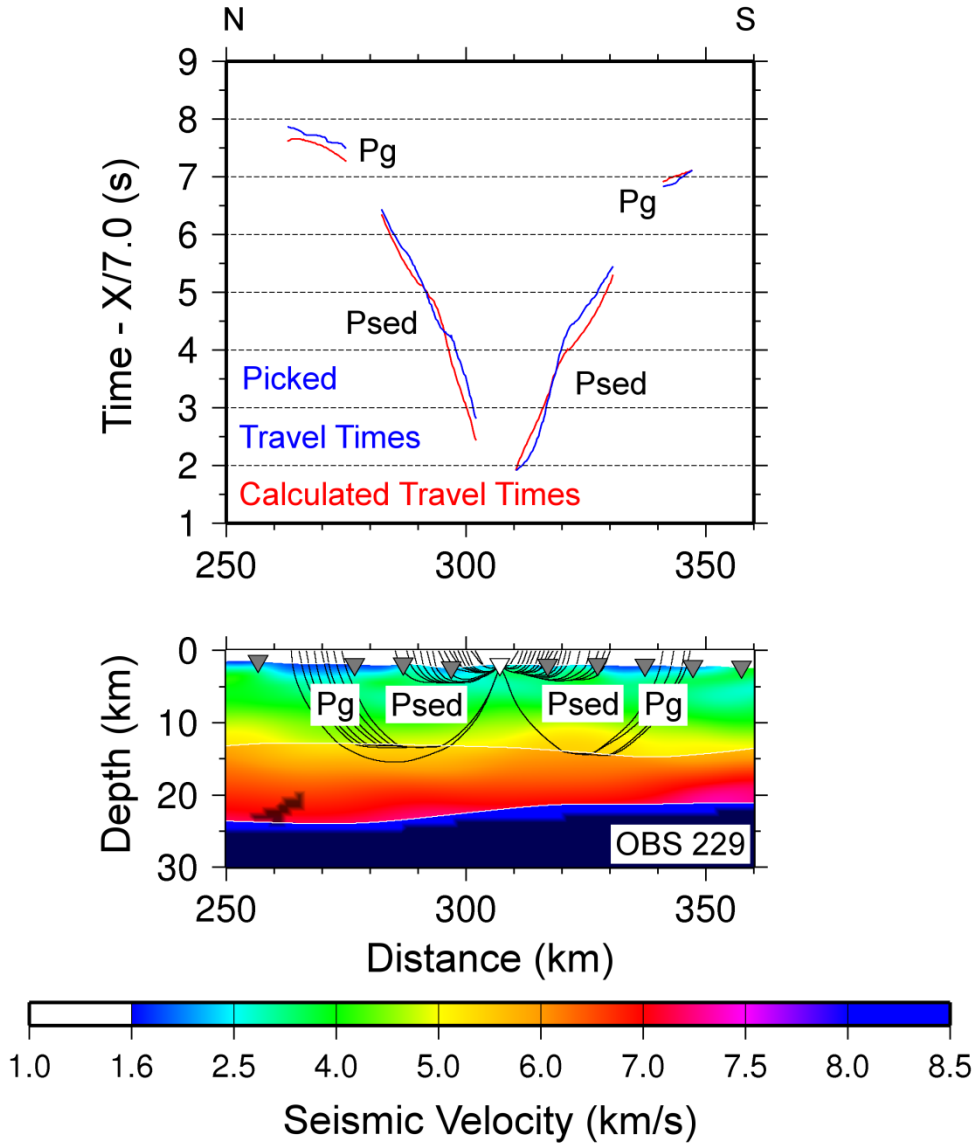

Figure C58 – Picked and calculated travel times for OBS 229 (top) and ray paths through final tomographic model (bottom). See Figure C37 for further information.

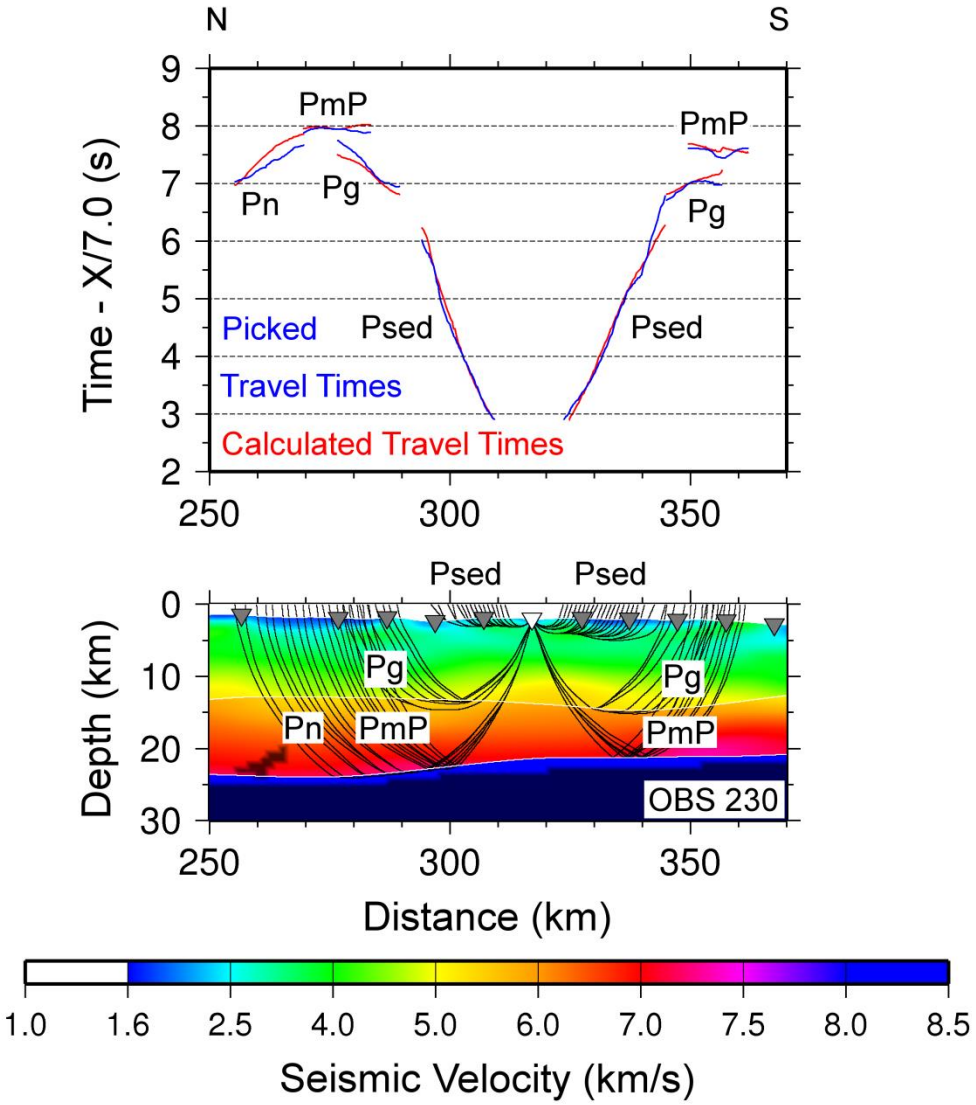

Figure C59 – Picked and calculated travel times for OBS 230 (top) and ray paths through final tomographic model (bottom). See Figure C37 for further information.

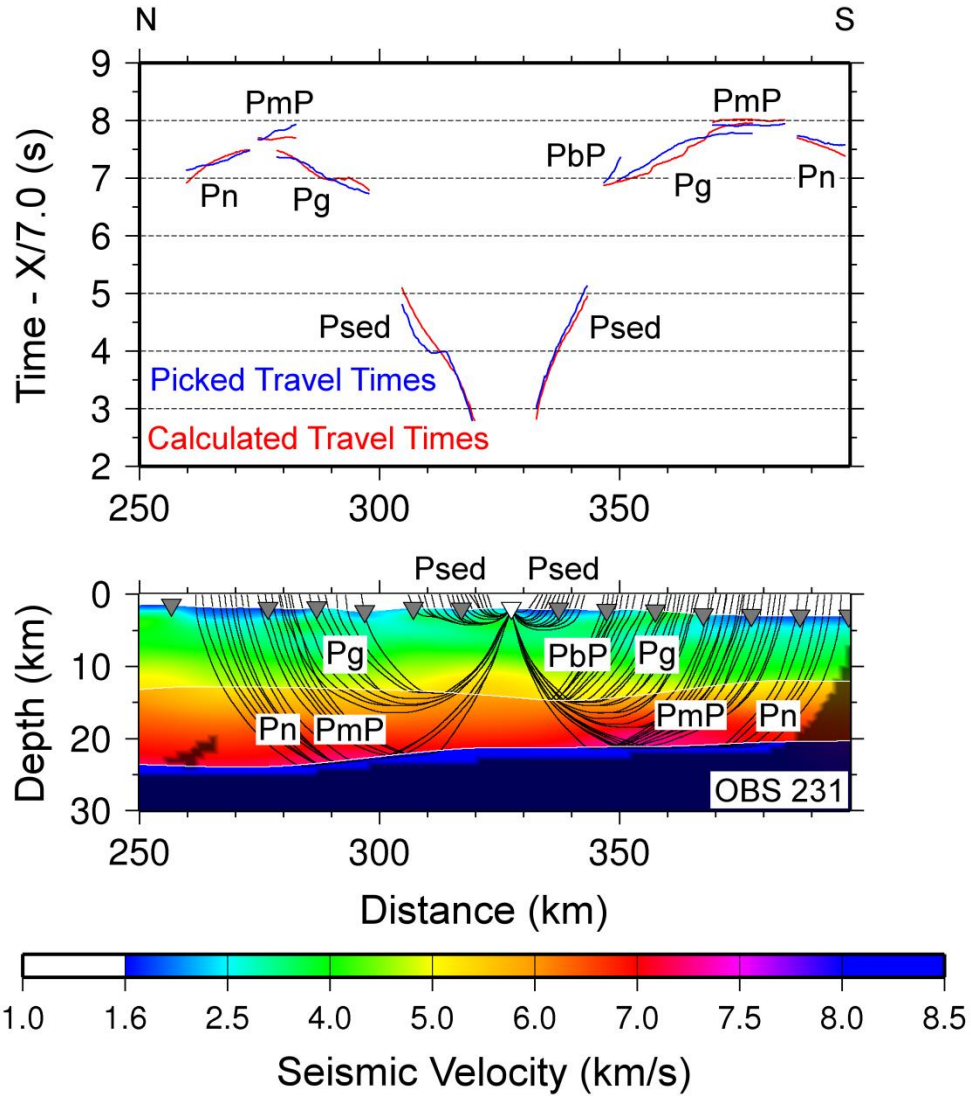

Figure C60 – Picked and calculated travel times for OBS 231 (top) and ray paths through final tomographic model (bottom). See Figure C37 for further information.

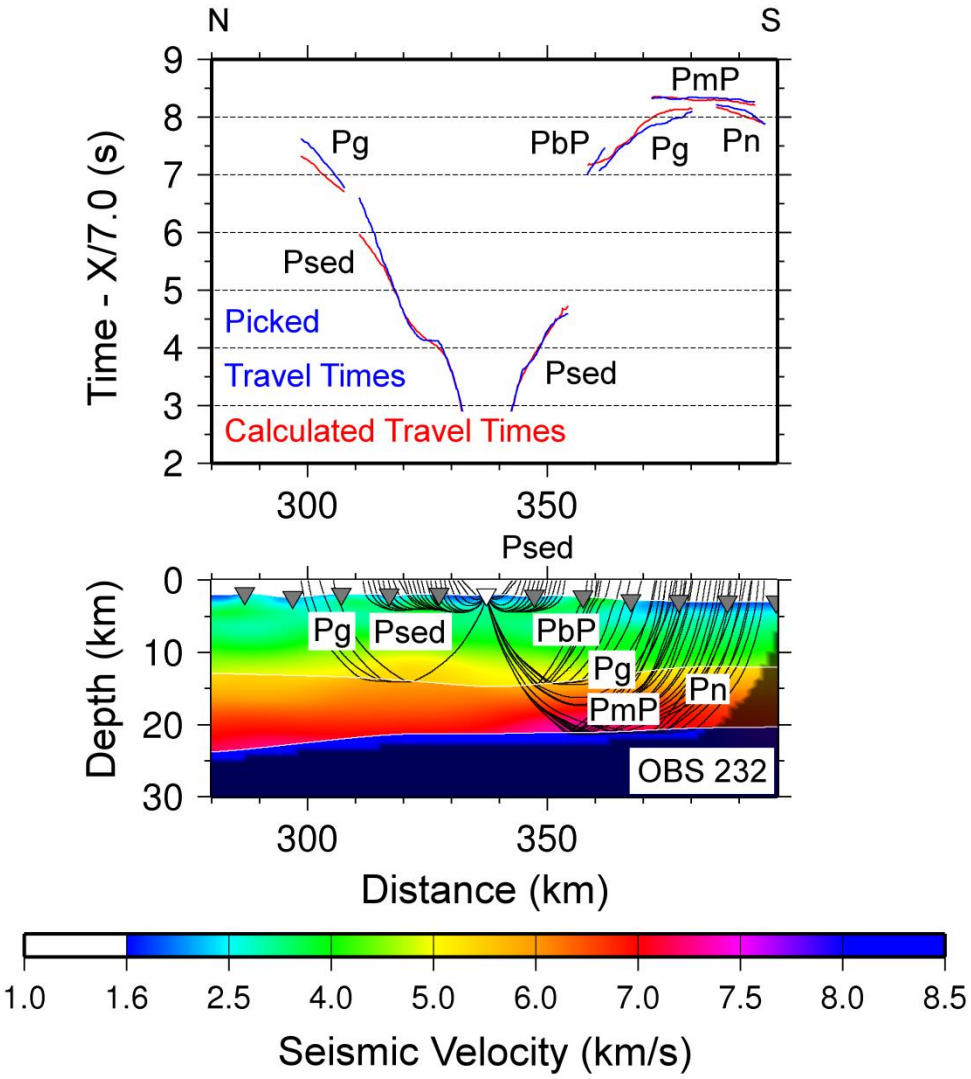

Figure C61 – Picked and calculated travel times for OBS 232 (top) and ray paths through final tomographic model (bottom). See Figure C37 for further information.

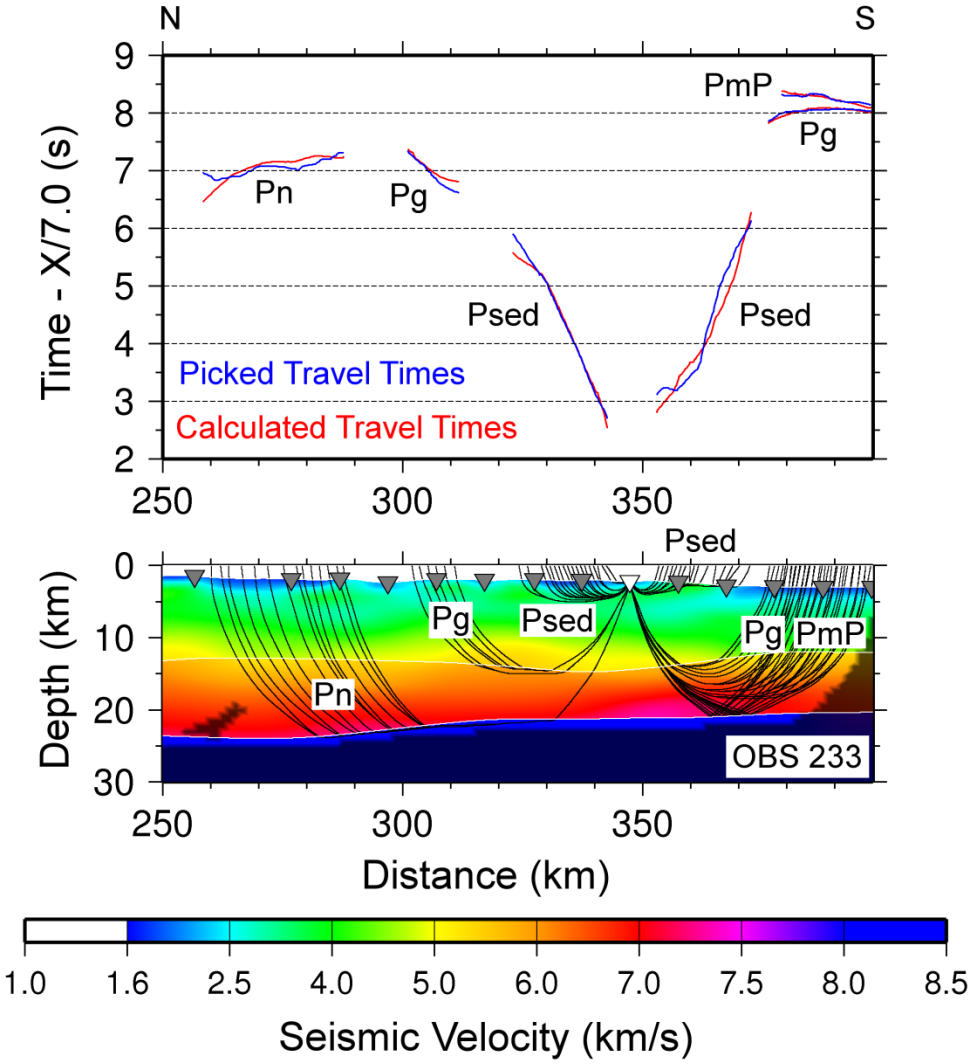

Figure C62 – Picked and calculated travel times for OBS 233 (top) and ray paths through final tomographic model (bottom). See Figure C37 for further information.

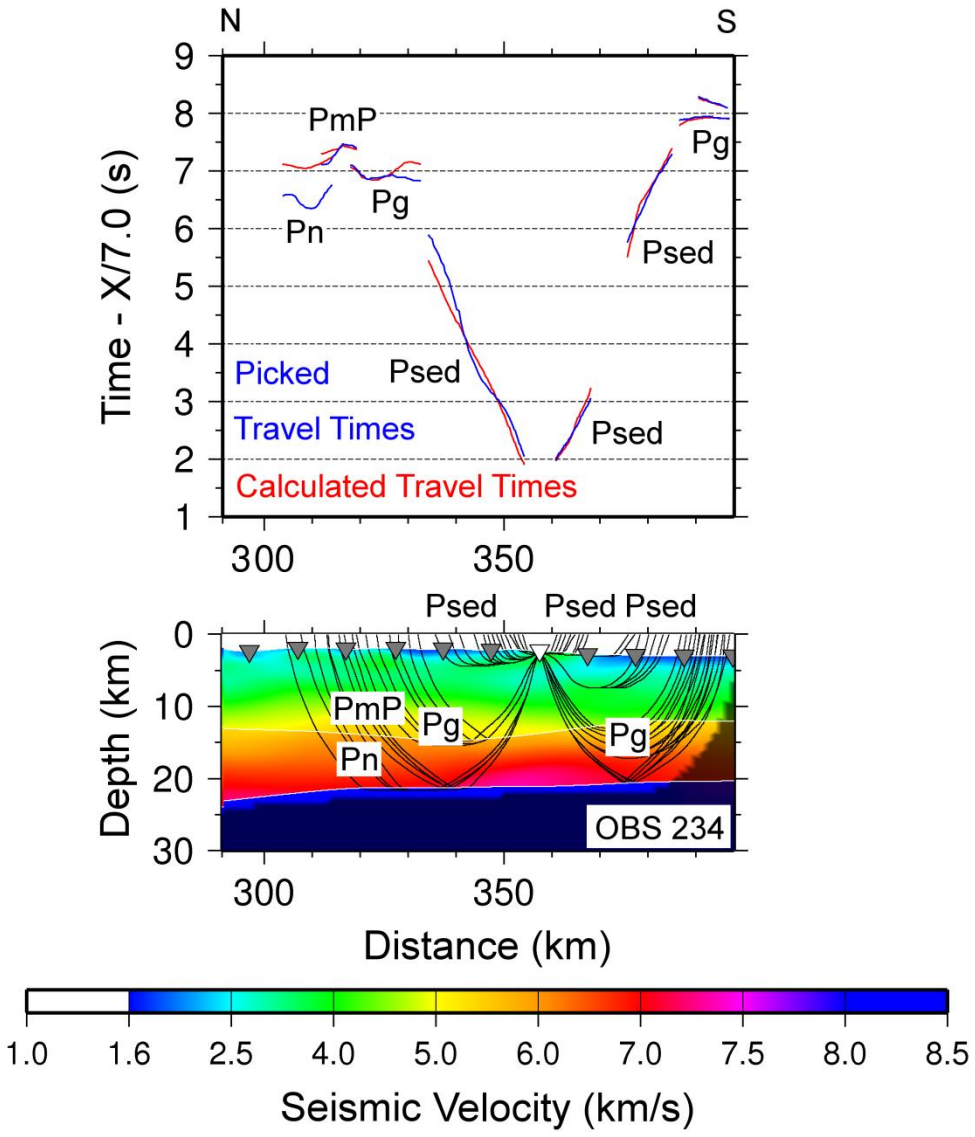

Figure C63 – Picked and calculated travel times for OBS 234 (top) and ray paths through final tomographic model (bottom). See Figure C37 for further information.

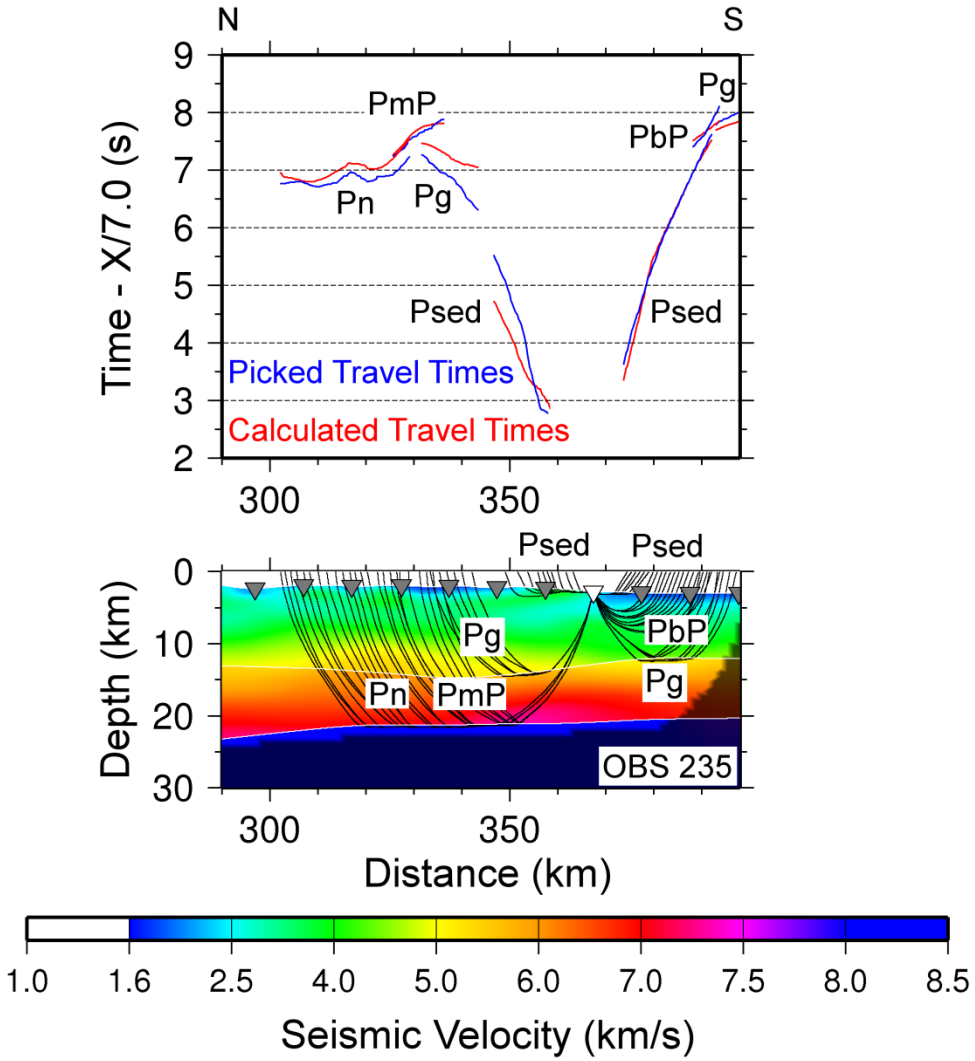

Figure C64 – Picked and calculated travel times for OBS 235 (top) and ray paths through final tomographic model (bottom). See Figure C37 for further information.

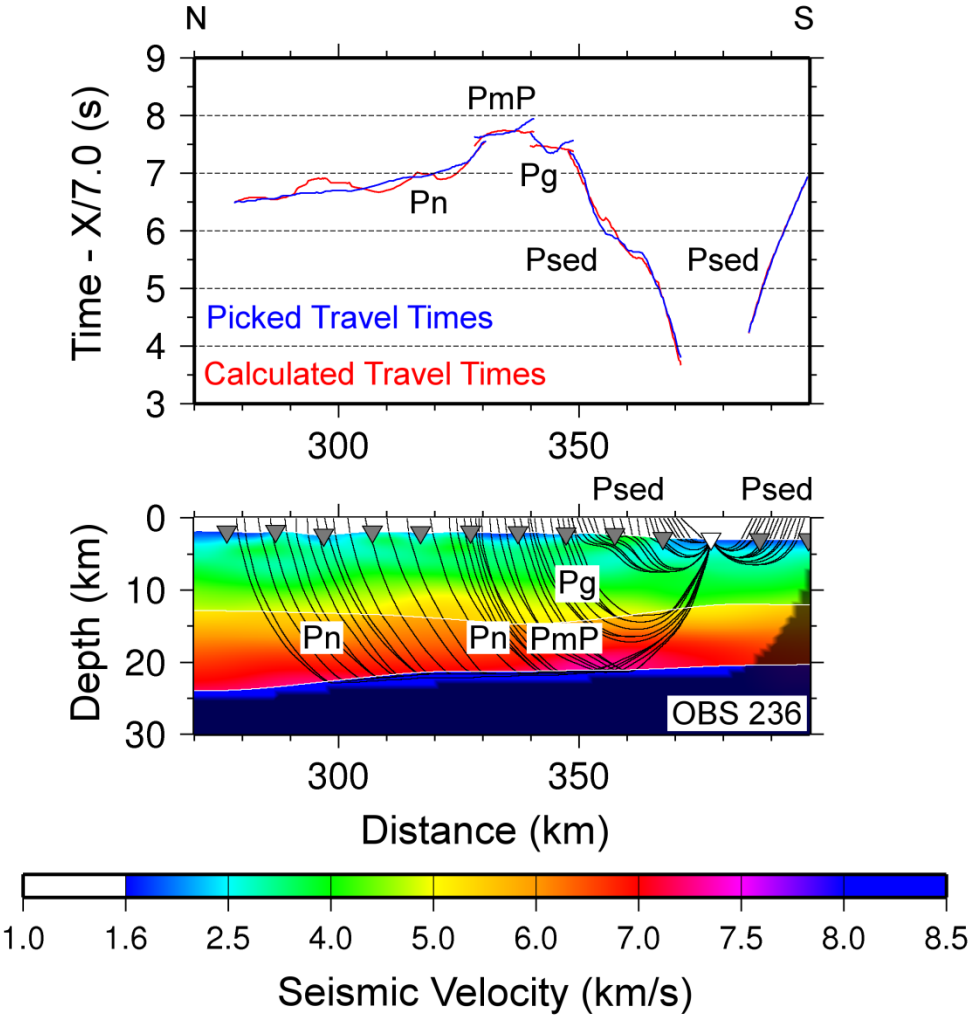

Figure C65 – Picked and calculated travel times for OBS 236 (top) and ray paths through final tomographic model (bottom). See Figure C37 for further information.

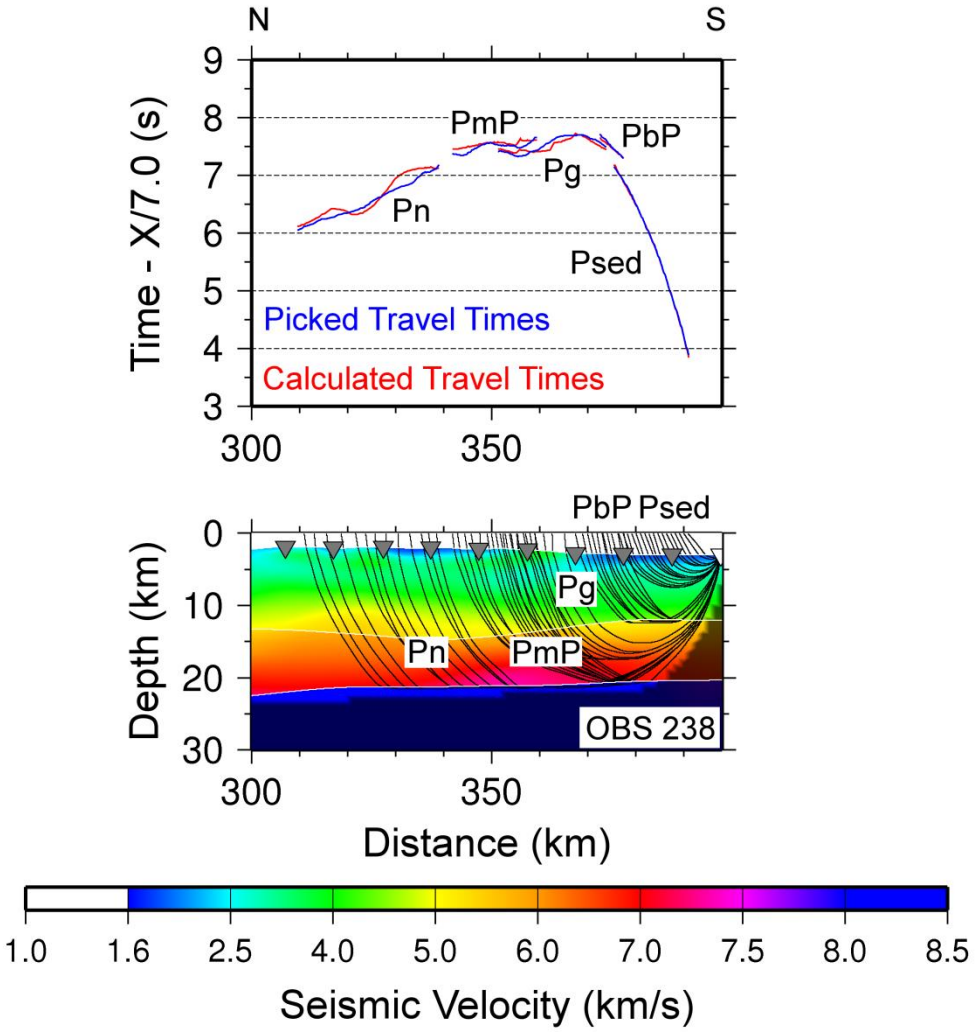

Figure C66 – Picked and calculated travel times for OBS 238 (top) and ray paths through final tomographic model (bottom). See Figure C37 for further information.

References

Aki, K. and P. G. Richards (2002), Quantitative Seismology, 2nd Edition, University Science Books

Anderson, T. H., and V. A. Schmidt (1983), The evolution of Middle America and the Gulf of Mexico − Caribbean Sea region during Mesozoic time, *Geol. Soc. Am. Bull.*, *94*, 941-966.

Armitage, J. J., T. J. Henstock, T. A. Minshull, and J. R. Hopper (2009), Lithospheric controls on melt production during continental breakup at slow rates of extension: application to the North Atlantic, *Geochem. Geophys. Geosyst.*, *10*(6), Q06018, doi: 10.1029/2009/GC002404.

Bartok, P. (1993), Prebreakup geology of the Gulf of Mexico-Caribbean: its relation to Triassic and Jurassic rift systems of the region, *Tectonics*, *12*(2), 441-459.

Bird, D. E., K. Burke, S. A. Hall, and J. F. Casey (2005), Gulf of Mexico tectonic history: hotspot tracks, crustal boundaries, and early salt distribution, *Am. Assoc. Petr. Geol. B.*, *89*(3), 311-328, doi: 10.1306/10280404026.

Bird, D. E., S. A. Hall, K. Burke, J. F. Casey, and D. S. Sawyer (2007), Early central Atlantic Ocean seafloor spreading history, *Geosphere*, *3*(5), 282-298, doi: 10.1130/GES00047.1.

Bown, J. W., and R. S. White (1994), Variation with spreading rate of oceanic crustal thickness and geochemistry, *Earth Planet. Sc. Lett.*, *121*, 435-449, doi: 10.1016/0012-821X(94)90082-5.

Brocher, T. M. (2005), Empirical relations between elastic wavespeeds and density in the Earth's crust, *B. Seismol. Soc. Am.*, *95*(6), 2081-2092, doi: 10.1785/0120050077.

Bronner, A., D. Sauter, G. Manatschal, G. Péron-Pinvidic, and M. Munschy (2011), Magmatic breakup as an explanation for magnetic anomalies at magma-poor rifted margins, *Nat. Geosci.*, *4*, 549-553, doi: 10.1038/ngeo1201.

Buck, W. R., F. Martinez, M. S. Steckler, and J. R. Cochran (1988), Thermal consequences of lithospheric extension: pure and simple, *Tectonics*, 7, 213-234.

Buck, W. R. (2004), Consequences of asthenospheric variability on continental rifting, in *Rheology and deformation of the lithosphere at continental margins*, edited by G. D. Karner, B. Taylor, N. W. Driscoll, and D. L. Kohlstedt, pp. 1-30, Columbia University Press, New York.

Buffler, R. T. and D. S. Sawyer (1985), Distribution of crust and early history, Gulf of Mexico basin, *Trans. – Gulf Coast Assoc. Geol. Soc.*, *35*, 333-344.

Chen, Y. J. (1992), Oceanic crustal thickness versus spreading rate, *Geophys. Res. Lett.*, *19*, 753-756, doi: 10.1029/92GL00161.

Chian, D., C. Keen, I. Reid, and K.E. Louden (1995), Evolution of nonvolcanic rifted margins: new results from the conjugate margins of the Labrador Sea, *Geology*, *23*, 589-592.

Christensen, N. I. (2004), Serpentinites, peridotites, and seismology, *Int. Geol. Rev.*, *46*(9), 795-816, doi: 10.2747/0020-6814.46.9.795.

Christensen, N. I., and W. D. Mooney (1995), Seismic velocity structure and composition of the continental crust: a global view, *J. Geophys. Res.*, *100*(B7), 9761-9788.

Christeson, G. L., H. J. A. Van Avendonk, I. O. Norton, J. W. Snedden, D. R. Eddy, G. D. Karner, and C. A. Johnson, Deep crustal structure in the eastern Gulf of Mexico, *J. Geophys. Res.*, *119*, doi: 10/1002/2014JB011045.

Clendenin, C. W., Jr., (2013), Insights into the mode of the South Georgia rift extension in eastern Georgia, USA, *Tectonophysics*, *608*, 613-621, doi: 10.1016/j.tecto.2013.08.019.

Dawson, W. C., and C. A. Callender (1992), Diagenetic and sedimentologic aspects of Eagle Mills-Werner conglomerate sandstones (Triassic-Jurassic), northeast Texas, *Trans. – Gulf Coast Assoc. Geol. Soc.*, *24*, 449-457.

Dean, S. M., T. A. Minshull, R. B. Whitmarsh, and K. E. Louden (2000), Deep structure of the ocean-continent transition in the southern Iberia Abyssal Plain from seismic refraction profiles: The IAM-9 transect at 40°20′N, *J. Geophys. Res.*, *105*(B3), 5859-5885, doi: 10.1029/1999JB900301.

Dickinson, W. R., and T. F. Lawton (2001), Carboniferous to Cretaceous assembly and fragmentation of Mexico, *Geol. Soc. Am. Bull.*, *113*, 1142–1160, doi: 10.1130/0016-7606(2001)113<1133:UIEFGC>2.0.CO;2.

Dickinson, W. R., G. E. Gehrels, and R. J. Stern (2010), Late Triassic Texas uplift preceding Jurassic opening of the Gulf of Mexico: evidence from U-Pb ages of detrital zircons, *Geosphere*, *6*(5), 641-662, doi: 10.1130/GES00532.1.

Dobson, L. M., and R. T. Buffler (1991), Basement rocks and structure, northeast Gulf of Mexico, *Trans. Gulf Coast Assoc. Geol. Soc.*, *41*, 191-206.

Dobson, L. M., and R. T. Buffler (1997), Seismic stratigraphy and geologic history of Jurassic rocks, northeastern Gulf of Mexico, *Am. Assoc. Petr. Geol. Bull.*, *81*(1), 100-120.

Driskill, B. W., J. A. Nunn, R. Sassen, and R. H. Pilger (1988), Tectonic subsidence, crustal thinning and petroleum generation in the Jurassic trend of Mississippi, Alabama and Florida, *Trans. Gulf Coast Assoc. Geol. Soc.*, *38*, 257-266.

Dunbar, J. A., and D. S. Sawyer (1987), Implications of continental crust extension for plate reconstruction: an example from the Gulf of Mexico, *Tectonics*, *6*(6), 739-755.

Dunbar, J.A., and D. S. Sawyer (1989), Patterns of continental extension along the conjugate margins of the central and north Atlantic Oceans and Labrador Sea, *Tectonics*, *8*(5), 1059-1077.

Ebeniro, J. O., W. P. O'Brien, Jr., and F. J. Shaub (1986), Crustal structure of the South Florida Platform, eastern Gulf of Mexico: an ocean-bottom seismograph refraction study, *Mar. Geophys. Res.*, *8*, 363-382.

Ebeniro, J. O., Y. Nakamura, D. S. Sawyer, and W. P. O'Brien, Jr., (1988), Sedimentary and crustal structure of the northwestern Gulf of Mexico, *J. Geophys. Res.*, *93*, 9075-9092.

Eccles, J. D., R. S. White, and P. A. F. Christie (2009), Identification and inversion of converted shear waves: case studies from the European North Atlantic continental margins, *Geophys. J. Int.*, *179*(1), 381-400, doi: 10.1111/j.1365-246X.2009.04290.x.

Eddy, D. R., H. J. A. Van Avendonk, and D. J. Shillington (2013), Compressional and shear-wave velocity structure of the continent-ocean transition zone at the eastern Grand Banks, Newfoundland, *Geophys. Res. Lett.*, *40*, 3014-3020, doi: 10/1002/grl.50511.

Eddy, D. R., H. J. A. Van Avendonk, G. L. Christeson, I. O. Norton, G. D. Karner, C. A. Johnson, and J. W. Snedden (2014), Deep crustal structure of the northeastern Gulf of Mexico: Implications for rift evolution and seafloor spreading, *J. Geophys. Res.*, *119*, doi: 10/1002/2014JB011311.

Engel, A. E. J., C. G. Engel, and R. G. Havens (1965), Chemical characteristics of oceanic basalts and the upper mantle, *Geol. Soc. Am. Bull.*, *76*, 719-734.

Ewing, J., J. Antoine, and M. Ewing (1960), Geophysical measurements in the western Caribbean Sea and in the Gulf of Mexico, *J. Geophys. Res.*, *65*(12), 4087-4126, doi: 10.1029/JZ065i012p04087.

Franke, D. (2013), Rifting, lithosphere breakup and volcanism: comparison of magma-poor and volcanic rifted margins, *Mar. Petrol. Geol.*, *43*, 63-87, doi: 10.1016/j.marpetgeo.2012.11.003.

Funck, T., H. R. Jackson, K. E. Louden, S. A. Dehler, and Y. Wu (2004), Crustal structure of the northern Nova Scotia rifted continental margin (eastern Canada). *J. Geophys. Res.*, *109*, B09102, doi: 10.1029/2004JB003008.

Galloway, W. E. (2008), Depositional evolution of the Gulf of Mexico sedimentary basin, in *Sedimentary basins of the world*, edited by A. Miall, pp. 505-549, Elsevier, Amsterdam.

Galloway, W. E., T. L. Whiteaker, and P. Ganey-Curry (2011), History of Cenozoic North American drainage basin evolution, sediment yield, and accumulation in the Gulf of Mexico basin, *Geosphere*, *7*, 938-973, doi: 10.1130/GES00647.1.

Geoffroy, L. (2005), Volcanic passive margins, *Comptes Rendus Geosci*., *337*, 1395-1408.

Gerlings, J., K. E. Louden, and H. R. Jackson (2011), Crustal structure of the Flemish Cap Continental Margin (eastern Canada): an analysis of a seismic refraction profile, *Geophys. J. Int.*, *185*(1), 30-48, doi: 10.1111/j/1365-246X.2011.04931.x.

Godínez-Urban, A., R. S. Molina-Garza, J. W. Geissman, and T. Wawrzyniec (2011), Paleomagnetism of the Todos Santos and La Silla Formations, Chiapas: implications for the opening of the Gulf of Mexico, *Geosphere*, *7*, 145-158, doi: 10.1130/GES00604.1.

Guerrero, J. C., E. Herrero-Bervera, and C. E. Helsley (1990), Paleomagnetic evidence for post-Jurassic stability of southeastern Mexico: Maya terrane, *J. Geophys. Res.*, *95*(B5), 7091-7100, doi: 10.1029/JB095iB05p07091.

Hales, A.L., C. E. Helsley, and J. B. Nation (1970), Crustal structure study on Gulf Coast of Texas, *Am. Assoc. Petr. Geol. Bull.*, *54*(11), 2040-2057.

Hall, D. J. (1990), Gulf Coast-East Coast magnetic anomaly I: root of the main crustal decollement for the Appalachian-Ouachita orogeny, *Geology*, *18*, 862-865.

Hall, S. A., and I. J. Najmuddin (1994), Constraints on the tectonic development of the eastern Gulf of Mexico provided by magnetic anomaly data, *J. Geophys. Res.*, *99*(B4), 7161-7165, doi: 10.1029/93JB02570.

Harry, D. L., and J. Londono (2004), Structure and evolution of the central Gulf of Mexico continental margin and coastal plain, southeast United States, *Geol. Soc Am. Bull.*, *116*(1-2), 188-199, doi: 10.1130/B25237.1.

Heatherington, A. L., and P. A. Mueller (1991), Geochemical evidence for Triassic rifting in southwestern Florida, *Tectonophysics*, *188*, 291-302.

Heatherington, A. L., and P. A. Mueller (2003), Mesozoic igneous activity in the Suwannee terrane, southeastern USA: petrogenesis and Gondwanan affinities, *Gondwana Res.*, *6*(2), 296-311, doi: 10/1016/S1342-937X(05)70979-5.

Heffner, D. M., J. H. Knapp, O. M. Akintunde, and C. C. Knapp (2012), Preserved extent of Jurassic flood basalt in the South Georgia Rift: a new interpretation of the J Horizon, *Geology*, *40*(2), 167-170, doi: 10.1130/G32638.1.

Hess, H. H. (1964), Seismic anisotropy of the uppermost mantle under the ocean, *Nature*, *203*, 629-631.

Holbrook, W. S., and P. B. Kelemen (1993), Large igneous province on the US Atlantic margin and implications for magmatism during continental breakup, *Nature*, *364*, 433-436.

Holbrook, W. S., W. D. Mooney, and N. I. Christensen (1992), The seismic velocity structure of the deep continental crust, in *The Lower Continental Crust*, edited by D. M. Fountain, R. Arculus, and R. W. Kay, pp. 1-43, Elsevier, Amsterdam.

Holbrook, W. S., H. C. Larsen, J. Korenaga, T. Dahl-Jensen, I. D. Reid, P. B. Kelemen, J. R. Hopper, G. M. Kent, D. Lizarralde, S. Bernstein, and R. S. Detrick (2001), Mantle thermal structure and active upwelling during continental breakup in the North Atlantic, *Earth Planet. Sci. Lett.*, 190, 251-266, doi:10.1016/S0012-821X(01)00392-2.

Hopper, J. R., T. Dahl-Jensen, W. S. Holbrook, H. C. Larsen, D. Lizarralde, J. Korenaga, G. M. Kent, and P. B. Kelemen (2003), Structure of the SE Greenland margin from seismic reflection and refraction data: Implications for nascent spreading center subsidence and asymmetric crustal accretion during North Atlantic opening, *J. Geophys. Res.*, 108(B5), doi: 10/1029JB001996.

Hudec, M. R., I. O. Norton, M. P. A. Jackson and F. J. Peel (2013), Jurassic evolution of the Gulf of Mexico salt basin, *Am. Assoc. Petr. Geol. Bull.*, *97*(10), 1683-1710, doi: 10.1306/04011312073.

Huerta, A. D., and D. L. Harry (2012), Wilson cycles, tectonic inheritance, and rifting in the North American Gulf of Mexico continental margin, *Geosphere*, *8*(2), 374-385, doi: 10.1130/GES00725.1.

Hudec, M. R., I. O. Norton, M. P. A. Jackson and F. J. Peel (2013a), Jurassic evolution of the Gulf of Mexico salt basin, *AAPG Bull.*, *97*(10), 1683-1710, doi: 10.1306/04011312073.

Hudec, M. R., M. P. A. Jackson, and F. J. Peel (2013b), Influence of deep Louann structure on the evolution of the northern Gulf of Mexico, *AAPG Bull.*, *97*(10), 1711-1735, doi: 10.1306/04011312074.

Hyndman, R. D. (1979), Poisson's ratio in the oceanic crust – a review, *Tectonophysics*, *59*, 321-333.

Ibrahim, A. K., and E. Uchupi (1981), Continental oceanic crustal transition in the Gulf coast geosyncline, in Studies in Continental Margin Geology, Mem. 34, edited by J. S. Watkins and C. L. Drake, pp. 155-166, American Association of Petroleum Geologists, Tulsa.

Ibrahim, A. K., J. Carye, G. Latham, and R. T. Buffler (1981), Crustal structure in the Gulf of Mexico from OBS refraction and multichannel reflection data, *Am. Assoc. Petr. Geol. Bull.*, *65*(7), 1207-1229.

Imbert, P. (2005), The Mesozoic opening of the Gulf of Mexico: part 1, evidence for oceanic accretion during and after salt deposition, in *Transactions of the 25th Annual GCSSEPM Research Conference: Petroleum Systems of Divergent Continental Margins*, edited by P. J. Post, N. C. Rosen, D. L. Olson, S. L. Palmes, K. T. Lyons, and G. B. Newton, pp. 1119-1150, SEPM, Tulsa.

Imbert, P. and Y. Philippe (2005), The Mesozoic opening of the Gulf of Mexico: part 2, integrating seismic and magnetic data into a general opening model, in *Transactions of the 25th Annual GCSSEPM Research Conference: Petroleum Systems of Divergent Continental Margins*, edited by P. J. Post, N. C. Rosen, D. L. Olson, S. L. Palmes, K. T. Lyons, and G. B. Newton, pp. 1151-1189, SEPM, Tulsa.

Jackson, M. P. A., and S. J. Seni (1983), Geometry and evolution of salt structures in a marginal rift basin of the Gulf of Mexico, east Texas, *Geology*, *11*, 131-135.

Jagoutz, O., O. Müntener, G. Manatschal, D. Rubatto, G. Péron-Pinvidic, B.D. Turrin, and I.M. Villa (2007), The rift-to-drift transition in the North Atlantic: A stuttering start of the MORB Machine?, *Geology*, *35*, 1087-1090.

Jourdan, F., A. Marzoli, H. Bertrand, S. Cirilli, L. H. Tanner, D. J. Kontak, G. McHone, P. R. Renne, and G. Bellieni (2009), $^{40}Ar/^{39}Ar$ ages of CAMP in North America: implications for the Triassic–Jurassic boundary and the ^{40}K decay constant bias. *Lithos*, *110*(1), 167-180, doi: 10.1016/j.lithos.2008.12.011.

Karlstrom, K. E., K. I. Ahäii, S. S. Harlan, M. L. Williams, J. McLelland, and J. W. Geissman (2001), Long-lived (1.8-1.0 Ga) convergent orogen in southern Laurentia, its extensions to Australia and Baltica, and implications for refining Rodinia, *Precambrian Res.*, *111*, 5-30, doi: 10.1016/S0301-9268(01)00154-1.

Karner, G. D., and D. J. Shillington (2005), Basalt sills of the U reflector, Newfoundland Basin: a serendipitous dating technique, *Geology*, *33*(12), 985-988, doi: 10.1130/G2197.1.

Kaczmarek, M. A., and O. Müntener (2010), Juxtaposition of melt impregnation and high-temperature shear zones in the upper mantle; field and petrological constraints from the Lanzo Peridotite (Northern Italy), *J. Petrol.*, *49*, 2187-2220, doi: 10.1093/petrology/egn065.

Keen, C. E. (1985), The dynamics of rifting: deformation of the lithosphere by active and passive driving forces, *Geophys J. Int.*, *80*, 95-120, doi: 10.1111/j.1365-246X.1985.tb05080.x.

Kelemen, P. B. and W. S. Holbrook (1995), Origin of thick, high-velocity crust along the US east coast margin, *J. Geophys. Res.*, *100*, 10077-10094.

Keller, G. D., and D. H. Shurbet (1975), Crustal structure of the Texas Gulf coastal plain, *Geol. Soc. Am. Bull.*, *86*, 807-810.

Keller, G. D., L. W. Braile, G. A. McMechan, W. A. Thomas, S. H. Harder, W.-F. Chang, and W. G. Jardine (1989), Paleozoic continent-ocean transition in the Ouachita Mountains imaged from PASSCAL wide-angle seismic reflection-refraction data, *Geology*, *17*, 119-122.

Kidwell, A. L. (1951), Mesozoic igneous activity in the northern Gulf Coastal Plain, *Trans. – Gulf Coast Assoc. Geol. Soc.*, *1*, 182-199.

Klingelhöefer, F., R. A. Edwards, and R. W. Hobbs (2005), Crustal structure of the NE Rockall Trough from wide-angle seismic data modeling, *J. Geophys. Res.*, *110*(B11105), 1-25, doi: 10.1029/2005JB003763.

Klingelhöefer, F., C. Labails, E. Cosquer, S. Rouzo, L. Geli, D. Aslanian, J.-L. Olivet, M. Sahabi, H. Nouze, and P. Unternehr (2009), Crustal structure of the SW-Moroccan margin from wide-angle and reflection seismic data (the DAKHLA experiment) Part A: wide-angle seismic models, *Tectonophysics, 1-4*, 63-82, doi: 10/1016/j.tecto.2008.07.022.

Klitgord, K. D., P. Popenoe, and H. Schouten (1984), Florida: a Jurassic transform boundary, *J. Geophys. Res.*, *89*(B9), 7753-7772, doi: 10.1029/JB089iB09p07753.

Klitgord, K. D., and H. Schouten (1986), Plate kinematics of the central Atlantic, in *The Geology of North America Volume M: The Western North Atlantic Region*, edited by P. R. Vogt and B. E. Tucholke, pp. 351-378, GSA, Boulder.

Kneller, E. A., and C. A. Johnson (2011), Plate kinematics of the Gulf of Mexico based on integrated observations from the Central and South Atlantic, *Trans. Gulf Coast Assoc. Geol. Soc.*, *35*, 283-299.

Kneller, E. A., C. A. Johnson, G. D. Karner, J. Einhorn, and T. A. Queffelec (2012), Inverse methods for modeling non-rigid plate kinematics: application to Mesozoic plate reconstructions of the Central Atlantic, *Comput. Geosci.*, *49*, 217-230, doi: 10/1016/j.cageo.2012.06.019.

Korenaga, J., W. S. Holbrook, G. M. Kent, P. B. Kelemen, R. S. Detrick, H.-C. Larsen, J. R. Hopper, and T. Dahl-Jensen (2000), Crustal structure of the southeast Greenland margin from joint refraction and reflection seismic tomography, *J. Geophys. Res.*, *105*(B9), 21591-21614, doi: 10.1029/2000JB900188.

Krawczyk, C. M., T. J. Reston, M.-O. Beslier, and G. Boillot (1996), Evidence for detachment tectonics on the Iberia Abyssal Plain rifted margin, in *Proc. ODP Sci. Results, 147*, edited by R. B. Whitmarsh, et al., pp. 603-615, Ocean Drilling Program, College Station, Texas.

Labails, C., J.-L. Olivet, D. Aslanian, and W. R. Roest (2010), An alternative early opening scenario for the Central Atlantic Ocean, *Earth Planet. Sci. Lett.*, *297*, 355-368, doi:10.1016/j.epsl.2010.06.024.

Lavier, L. L. and G. Manatschal (2006), A mechanism to thin the continental lithosphere at magma-poor margins, *Nature*, *440*, 324-328, doi: 10.1038/nature04608.

Lavier, L. L., W. R. Buck, and A. N. B. Poliakov (1999), Self-consistent rolling-hinge model for the evolution of large-offset low-angle normal faults. *Geology*, 27, 1127-1130.

Lester, R., H. J. A. Van Avendonk, K. McIntosh, L. Lavier, C.-S. Liu, T. K. Wang, and F. Wu (2014), Rifting and magmatism in the northeastern South China Sea from wide-angle tomography and seismic reflection imaging, *J. Geophys. Res.*, *119*, 2305-2323, doi:10.1002/2013JB010639.

Lau, K. W. H., K. E. Louden, T. Funck, B. E. Tucholke, W. S. Holbrook, J. R. Hopper, and H. C. Larsen (2006), Crustal structure across the Grand Banks - Newfoundland Basin continental margin – I. Results from a seismic refraction profile, *Geophys. J. Int.*, *167*(2), 127-156, doi: 10.1111/j.1365-246x.2006.02988.x.

Lizarralde, D., J. B. Gaherty, J. A. Collins, G. Hirth, and S. D. Kim (2004), Spreading-rate dependence of melt extraction at mid-ocean ridges from mantle seismic refraction data, *Nature*, *432*, 744-747, doi: 10.1038/nature03140.

Malinverno, A., J. Hildebrandt, T. Masako, and J. E. T. Channell (2012), M-sequence geomagnetic polarity time scale (MHTC12) that steadies global spreading rates and incorporates astrochronology constraints, *J. Geophys. Res.*, *117*(B6), B06104, doi: 10.1029/2012JB009260.

Manatschal, G. (2004), New models for evolution of magma-poor rifted margins based on a review of data and concepts from West Iberia and the Alps, *Int. J. Earth Sci.*, *93*(3), 432-466, doi: 10.1007/s00531-004-0394-7.

Manatschal, G., O. Muntener, L. L. Lavier, T. A. Minshull, and G. Peron-Pinvidic (2007), Observations from the Alpine Tethys and Iberia Newfoundland margins pertinent to the interpretation of continental breakup. *Geol. Soc. Lond.-Sp. Pub.*, 282, 291-324.

Mancini, E. A., J. C. Llinás, W. C. Parcell, M. Aurell, B. Bádenas, R. R. Leinfelder, and D. J. Benson (2004), Upper Jurassic thrombolite reservoir play, northeastern Gulf of Mexico, *Am. Assoc. Petr. Geol. Bull.*, *88*(11), 1573-1602.

Marton, G., and R. T. Buffler (1994), Jurassic reconstruction of the Gulf of Mexico Basin, *Int. Geol. Rev.*, *36*, 545-586.

Marton, G. L., and R. T. Buffler (1993), Application of a simple-shear model to the evolution of passive continental margins of the Gulf of Mexico basin, *Geology*, *21*, 495-498.

Marton, G. L., and R. T. Buffler (1994), Jurassic reconstruction of the Gulf of Mexico Basin, *Int. Geol. Rev.*, *36*, 545-586.

Marton, G. L. and R. T. Buffler (1999), Jurassic–Cretaceous tectono-paleogeographic evolution of the southeastern Gulf of Mexico basin, in *Sedimentary basins of the world*, Vol. 4, *Caribbean basins*, edited by P. Mann, pp. 63-91, Elsevier, Amsterdam.

Maus, S., U. Barckhausen, H. Berkenbosch, N. Bournas, J. Brozena, V. Childers, F. Dostaler, J. D. Fairhead, C. Finn, R. R. B. von Frese, C. Gaina, S. Golynsky, R. Kucks, H. Lühr, P. Milligan, S. Mogren, R. D. Müller, O. Olesen, M. Pilkington, R. Saltus, B. Schreckenberger, E. Thébault, and F. Caratori Tontini (2009), EMAG2: a 2–arc min resolution Earth Magnetic Anomaly Grid compiled from satellite, airborne, and marine magnetic measurements, *Geochem. Geophys. Geosyst.*, *10*(8), Q08005, doi: 10.1029/2009GC002471.

May, P. R (1971), Pattern of Triassic-Jurassic diabase dikes around the north Atlantic in the context of predrift position of the continents. *Geol. Soc. Am. Bull.*, *82*, 1285-1292.

McBride, J. H. (1991), Constraints on the structure and tectonic development of the early Mesozoic South Georgia Rift, southeastern United States; seismic reflection data processing and interpretation, *Tectonics*, *10*(5), 1065-1083.

McBride, J.H., and K.D. Nelson (1988), Integration of COCORP deep reflection and magnetic anomaly analysis in the southeastern United States: Implications for origin of the Brunswick and East Coast magnetic anomalies, *Geol. Soc. Am. Bull.*, *100*(3), 436-445.

McBride, J. H., K. D. Nelson, and L. D. Brown (1987), Early Mesozoic basin structure and tectonics of the southeastern United States as revealed from COCORP reflection data and the relation to Atlantic rifting, in *Sedimentary Basins and Basin-forming Mechanisms*, edited by C. Beaumont and A. J. Tankard, *Can. Soc. Pet. Geol.*, *12*, 173-184.

McHone, J. G (1996), Broad-terrane Jurassic flood basalts across northeastern North America, *Geology*, *24*, 319-322.

McHone, J. G. (2000), Non-plume magmatism and rifting during the opening of the central Atlantic Ocean, *Tectonophysics*, *316*, 287-296.

McKenzie, D., and M. J. Bickle (1988), The volume and composition of melt generated by extension of the lithosphere, *J. Petrol.*, *29*(3), 625-629.

Menke, W. (1984), *Geophysical data analysis: discrete inverse theory*, Academic, San Diego.

Menzies, M. A., S. L. Klemperer, C. J. Ebinger, and J. Baker (2002), Characteristics of volcanic rifted margins, in *Volcanic rift margins*, edited by M. A. Menzies, S. L. Klemperer, C. J. Ebinger, and J. Baker, *Spec. Pap. Geol. Soc. Am., 362*, 1-14.

Michalzik, D. (1991), Facies sequence of Triassic-Jurassic red beds in the Sierra Madre Oriental (NE Mexico) and its relation to the early opening of the Gulf of Mexico, *Sediment. Geol., 71*, 243-259.

Mickus, K. L., and G. R. Keller (1992), Lithospheric structure of the south-central United States, *Geology*, *20*, 335-338.

Mickus, K. L., R. J. Stern, G. R. Keller, and E. Y. Anthony (2009), Potential field evidence for a volcanic rifted margin along the Texas Gulf Coast, *Geology*, *37*(5), 387-390, doi: 10.1130/G25465A.1.

Mjelde, R., H. Shimamura, T. Kanazawa, S. Kodaira, T. Raum, and H. Shiobara (2003), Crustal lineaments, distribution of lower crustal intrusives and structural evolution of the Vøring Margin, NE Atlantic; new insight from wide-angle seismic models, *Tectonophysics*, *369*, 199-218.

Mjelde, R., T. Raum, B. Myhren, H. Shimamura, Y. Murai, T. Takanami, R. Karpuz, and U. Næss (2005), Continent-ocean transition on the Vøring Plateau, NE Atlantic, derived from densely sampled ocean bottom seismometer data, *J. Geophys. Res.*, *110*(B05101), 1-19, doi: 10.1029/2004JB003026.

Molina-Garza, R. S., R. van der Voo, and J. Urrutia-Fucugauchi (1992), Paleomagnetism of the Chiapas Massif, southern Mexico: evidence for rotation of the Maya Block and implications for the opening of the Gulf of Mexico, *Geol. Soc. Am. Bull., 104*, 1156-1168.

Moody, C. L. (1949), Mesozoic igneous rocks of northern Gulf Coastal Plain, *AAPG Bull., 33*(8), 1410-1428.

Morgan, J. V., P. J. Barton, and R. S. White (1989), The Hatton Bank continental margin—III. Structure from OBS and multichannel seismic refraction profiles, *Geophys. J. Int., 98*, 367-384.

Moser, T. J. (1991), Shortest path calculation of seismic rays, *Geophysics*, *56*, 59-67.

Moser, T. J., G. Nolet, and R. Sneider (1992), Ray bending revisited, *Bull. Seismol. Soc. Am.*, *82*, 259-288.

Mueller, P. A., A. L. Heatherington, D. A. Foster, W. A. Thomas, and J. L. Wooden (2014), The Suwannee suture: significance for Gondwana-Laurentia terrane transfer and formation of Pangaea, *Gondwana Res.*, doi: 10.1016/j.gr.2013.06.018.

Müller, R. D., M. Sdrolias, G. Gaina, and W. R. Roest (2008), Age, spreading rates, and spreading asymmetry of the world's ocean crust, *Geochem. Geophys. Geosyst.*, *9*(4), 1-19, doi: 10.1029/2007GC001743.

Müntener, O., and G. Manatschal (2006), High degrees of melt extraction recoded by spinel harzburgite of the Newfoundland margin: the role of inheritance and consequences for the evolution of the southern North Atlantic, *Earth Planet. Sc. Lett.*, *252*, 437-452, doi: 10.1016/j.epsl.2006.10.009.

Mutter, J. C. (1985), Seaward dipping reflectors and the continent-ocean boundary at passive continental margins, Tectonophysics, 114, 117-131.

Nelson, K. D. (1992), Are crustal thickness variations in old mountain belts like the Appalachians a consequence of lithospheric delamination?, *Geology*, *20*(6), 498-502.

Nelson, K. D., J. H. McBride, J. A. Arnow, J. E. Oliver, L. D. Brown, and S. Kaufman (1985), New COCORP profiling in the southeastern United States. Part II: Brunswick and east coast magnetic anomalies, opening of the north-central Atlantic Ocean, Geology, 13(10), 718-721.

Nunn, J. A., A. D. Scardina, and R. H. Pilger, Jr. (1984), Thermal evolution of the north-central Gulf coast, *Tectonics*, *3*(7), 723-740.

Olsen, P. E., D. V. Kent, M. Et-Touhami, and J. Puffer (2003), Cyclo-, magneto-, and bio-stratigraphic constraints on the duration of the CAMP event and its relationship to the Triassic-Jurassic boundary, in *The Central Atlantic Magmatic Province, Insights from Fragments of Pangaea*, edited by W. E Hanes, J. G. McHone, P. R. Renne, and C. Ruppel, pp. 7-32, American Geophysical Union, Washington, D. C.

Osmundsen, P. T., and J. Ebbing (2008), Styles of extension offshore mid-Norway and implications for mechanisms of crustal thinning at passive margins, *Tectonics*, 27, 1-25.

Oyarzun, R., M. Doblas, J. Lopez-Ruiz, and J. M. Cebria (1997), Opening of the central Atlantic and asymmetric mantle upwelling phenomena: implications for long-lived magmatism in western North Africa and Europe, *Geology*, *25*, 727-730.

Perfit, M. R., and W. W. Chadwick, Jr., (1998), Magmatism at mid-ocean ridges: constraints from volcanological and geochemical investigations, in *Faulting and Magmatism at Mid-Ocean Ridges*, edited by W. R. Buck, P. T. Delaney, J. A. Karson, and Y. Lagabrielle, pp. 59-115, AGU, Washington, D.C.

Péron-Pinvidic, G., D. J. Shillington, and B. Tucholke (2010), Characterization of sills associated with the U reflection on the Newfoundland margin: evidence for widespread early post-rift magmatism on a magma-poor rifted margin, *Geophys. J. Int.*, *182*(1), 113-136, doi: 10.1111/j.1365-246X.2010.04635.x.

Phipps Morgan, J., E. M. Parmentier, and J. Lin (1987), Mechanisms for the origin of mid-ocean ridge axial topography: implications for the thermal and mechanical structure of accreting plate boundaries, *J. Geophys. Res.-Sol. Ea.*, *92*(B12), 12823-12836, doi: 10.1029/JB092iB12p12823.

Pilger, R. H., Jr., (1981), The opening of the Gulf of Mexico: implications for the tectonic evolution of the northern Gulf coast, *Trans. – Gulf Coast Assoc. Geol. Soc.*, *31*, 377-381.

Pindell, J. L. (1985), Alleghenian reconstruction and subsequent evolution of the Gulf of Mexico, Bahamas, and Proto-Caribbean, *Tectonics*, *4*(1), 1-39, doi: 10.1029/TC004i001p00001.

Pindell, J. L., and J. F. Dewey (1982), Permo-Triassic reconstruction of western Pangea and the evolution of the Gulf of Mexico/Caribbean region, *Tectonics*, *1*(2), 179-211, doi: 10.1029/TC001i002p00179.

Pindell, J. L., and L. Kennan (2007), Rift models and the salt-cored marginal wedge in the northern Gulf of Mexico: implications for deep water Paleogene Wilcox deposition and basinwide maturation, in *Transactions of the 27th Annual GCSSEPM Research Conference: The Paleogene of the Gulf of Mexico and Caribbean Basins: Processes, Events and Petroleum Systems*, edited by L. Kennan, J. L. Pindell, and N. C. Rosen, pp. 146-186, SEPM, Tulsa.

Pindell, J. L., and L. Kennan (2009), Tectonic evolution of the Gulf of Mexico, Caribbean and northern South America in the mantle reference frame: an update, in *The origin and evolution of the Caribbean plate*, edited by K. H. James, M. A. Lorente, and J. L. Pindell, *Geol. Soc. Spec. Publ.*, *328*, 1-55, doi: 10.1144/SP328.1.

Pindell, J., R. Graham, and B. Horn (2014), Rapid outer marginal collapse at the rift to drift transition of passive margin evolution, with a Gulf of Mexico case study, *Basin Res.*, *26*, 1-25, doi: 10.1111/bre.12059.

Planke, S., and O. Eldholm (1994), Seismic response and construction of seaward dipping wedges of flood basalts: Vøring volcanic margin, *J. Geophys. Res.*, *99*(B5), 9263-9278, doi: 10.1029/94JB00468.

Planke, S., P. A. Symonds, E. Alvestad, and J. Skogseid (2000), Seismic volcanostratigraphy of large-volume basaltic extrusive complexes on rifted margins, *J. Geophys. Res.*, *105*(B8), 19335-19351, doi: 10.1029/1999JB900005.

Poole, F. G., W. J. Perry, R. J. Madrid, and R. Amaya-Martínez (2005), Tectonic synthesis of the Ouachita-Marathon-Sonora orogenic margin of southern Laurentia: stratigraphic and structural implications for timing of deformational events and plate-tectonic model, in *The Mojave-Sonora Megashear Hypothesis: Development, Assessment, and Alternatives*, edited by T. H. Anderson, J. A. Nourse, J. W. McKee, and M. B. Steiner, *Geol. Soc. Am. Special Pap.*, *393*, 543-596, doi: 10.1130/0-8137-2393-0.543.

Radovich, B. J., J. Moon, C. D. Connors, and D. Bird (2007), Insights into the structure and stratigraphy of the northern Gulf of Mexico from 2D pre-stack depth migration imaging of mega-regional onshore to deep water, long-offset seismic data, *Trans. – Gulf Coast Assoc. Geol. Soc.*, *57*, 633-637.

Radovich, B. J., E. Haire, C. Connors, and D. Howard (2011), *GulfSPAN Report: Interpretation framework of the northern Gulf of Mexico – basin margins to deep water, gravity sliding, and salt*, ION/GX Technology, Houston, pp. 1-223.

Rafavich, F., C. H. St. C. Kendall, and T. P. Todd (1984), The relationship between acoustic properties and the petrographic character of carbonate rocks, *Geophysics*, *49*(10), 1622-1636.

Reid, I. D. (1994), Crustal structure of a nonvolcanic rifted margin east of Newfoundland, *J. Geophys. Res.*, *99*(B8), 15161-15180.

Reid, I., and H. R. Jackson (1981), Oceanic spreading rate and crustal thickness, *Marine Geophys. Res.*, *5*(2), 165-172, doi: 10.1007/BF00163477.

Reston, T. J. (2009), The structure, evolution and symmetry of the magma-poor rifted margins of the North and Central Atlantic: a synthesis, *Tectonophysics*, *468*, 6-27, doi: 10.1016/j.tecto.2008.09.002.

Reston, T. J., and K. G. McDermott (2011), Successive detachment faults and mantle unroofing at magma-poor rifted margins, *Geology*, *39*(11), 1071-1074, doi: 10.1130/G32428.1.

Robertson, A. H. F. (2007), Evidence of continental breakup from the Newfoundland rifted margin (Ocean Drilling Program Leg 210): Lower Cretaceous seafloor formed by exhumation of subcontinental mantle lithosphere, in *Proc. ODP Sci. Results,210*, edited by B.E. Tucholke, et al., pp. 1-69, Ocean Drilling Program, College Station, Texas.

Ross, M. I., and C. R. Scotese (1988), A hierarchical tectonic model of the Gulf of Mexico and Caribbean region, *Tectonophysics*, *155*, 139-168.

Rowan, M. G. (2014), Passive-margin salt basins: hyperextension, evaporite deposition, and salt tectonics, *Basin Res.*, *26*, 154-182, doi: 10.1111/bre.12043.

Rudnick, R. L. and D. M. Fountain (1995), Nature and composition of the continental crust: a lower crustal perspective, *Rev. Geophys.*, *33*, 267-309.

Ruppel, C. (1995), Extensional processes in continental lithosphere, *J. Geophys. Res.*, *100*, 24187-24215.

Russell, S. M., and R. B. Whitmarsh (2003), Magmatism at the west Iberia non-volcanic rifted continental margin: evidence from analyses of magnetic anomalies. *Geophys. J. Int.*, *182*, 113-136.

Sahabi, M., D. Aslanian, and J. -L. Olivet, (2004), Un nouveau point de départ pour l'histoire de l'Atlantique central (A new starting point for the history of the central Atlantic), *Comptes Rendus Geosci.*, *336*(12), 1041-1052, doi:10.1016/j.crte.2004.03.017.

Salvador, A. (1987), Late Triassic-Jurassic paleogeography and origin of the Gulf of Mexico basin, *Am. Assoc. Petr. Geol. Bull.*, *71*(4), 419-451.

Salvador, A. (1991), Triassic – Jurassic, in *The geology of North America*, Vol. J, *The Gulf of Mexico Basin*, edited by A. Salvador, pp. 131-181, GSA, Boulder.

Sawyer, D. S., R. T. Buffler, and R. H. Pilger, Jr., (1991), in *The geology of North America*, Vol. J, *The Gulf of Mexico Basin*, edited by A. Salvador, pp. 53-72, GSA, Boulder.

Schouten, H., and K. D. Klitgord (1994), Mechanistic solutions to the opening of the Gulf of Mexico: Geology, in *Tectonostratigraphic terranes and tectonic evolution of*

Mexico, edited by R. L. Sedlock, F. Ortega-Gutiérrez, and R. C. Speed, *Geol. Soc. Am. Special Pap., 22*, 507–510.

Sempéré, J-C., J. Lin, H. S. Brown, H. Schouten, and G. M. Purdy (1993), Segmentation and morphotectonic variations along a slow-spreading center: the Mid-Atlantic ridge (24°00´ N – 30°40´ N), *Mar. Geophys. Res.*, *15*, 153-200.

Shillington, D. J., W. S. Holbrook, H. J. A. Van Avendonk, B. E. Tucholke, J. R. Hopper, K. E. Louden, H. C. Larsen, and G. T. Nunes (2006), Evidence for asymmetric nonvolcanic rifting and slow incipient oceanic accretion from seismic reflection data on the Newfoundland margin, *J. Geophys. Res.*, *111*, B09402, doi: 10.1029/2005JB003981.

Shillington, D. J., J. R. Hopper, and W. S. Holbrook (2008), Seismic signal penetration beneath postrift sills on the Newfoundland rifted margin, *Geophysics*, *73*(5), B99-107, doi: 10.1190/1.29 72131.

Sibuet, J. -C., S. P. Srivastava, and G. Manatschal (2007), Exhumed mantle-forming transitional crust in the Newfoundland-Iberia rift and associated magnetic anomalies, *J. Geophys. Res.*, *112*, B06105, doi: 10.1029/2005JB003856.

Smallwood, J. R., and R. S. White (1998), Crustal accretion at the Reykjanes Ridge, 61°-62°N, *J. Geophys. Res.*, *103*(B3), 5185-5201, doi: 10.1029/97JB03387.

Smith, D. L. (1983), Basement model for the panhandle of Florida, *Trans. Gulf Coast Assoc. Geol. Soc.*, *33*, 203-208.

Smith, D. L., W. T. Dees, and D. W. Harrelson (1981), Geothermal conditions and their implications for basement tectonics in the Gulf coast margin, *Trans. Gulf Coast Assoc. Geol. Soc.*, *31*, 181-190.

Snedden, J. W., D. R. Eddy, G. L. Christeson, H. V. A. Van Avendonk, H. Olson, P. Ganey-Curry, and I. O. Norton (2013), A new temporal model for eastern Gulf of Mexico Mesozoic deposition, *Trans. Gulf Coast Assoc. Geol. Soc.*, *63*, 609-612.

Srivastava, S. P., J. -C. Sibuet, S. Cande, W. R. Roest, and I. D. Reid (2000), Magnetic evidence for slow seafloor spreading during the formation of the Newfoundland and Iberian margins, *Earth Planet. Sc. Lett.*, *182*, 61-76.

Steiner, M. B. (2005), Pangean reconstruction of the Yucatan block: its Permian, Triassic, and Jurassic geologic and tectonic history, in *The Mojave-Sonora Megashear Hypothesis: Development, Assessment, and Alternative*, edited by T. H. Anderson,

J. A. Nourse, J. W. McKee and M. B. Steiner, *Geol. Soc. Am. Spec. Pap.*, *393*, 457-480, doi: 10.1130/0-8137-2393-0.457.

Stern, R. J., and W. R. Dickinson (2010), The Gulf of Mexico is a Jurassic backarc basin, *Geosphere*, *6*(6), 739-754, doi: 10.1130/GES00585.1.

Stern, R. J., W. R. Dickinson, and T. Lawton (2010), Introduction: making the southern margin of Laurentia, *Geosphere*, *6*(6), 737-738, doi: 10.1130/GES00642.1.

Stern, R. J., E. Y. Anthony, M. Ren, B. E. Lock, I. Norton, J.-I. Kimura, T. Miyazaki, T. Hanyu, Q. Chang, and Y. Hirahara (2011), Southern Louisiana salt dome xenoliths: first glimpse of Jurassic (ca. 160 Ma) Gulf of Mexico crust, *Geology*, *39*(4), 315-318, doi: 10.1130/G31635.1.

Stork, C., and R. W. Clayton (1991), Linear aspects of tomographic velocity analysis, *Geophysics*, *56*(4), 483-495.

Thomas, W. A. (1976), Evolution of the Ouachita-Appalachian continental margin, *J. Geol*., 84, 323-342.

Thomas, W. A. (2010), Interactions between the southern Appalachian-Ouachita orogenic belt and basement faults in the orogenic footwall and foreland, in *From Rodinia to Pangea: the lithotectonic record of the Appalachian region*, edited by R. Tollo, M. Bartholomew, J. Hibbard, and P. Karabinos, *Geol. Soc. Am. Mem.*, *206*, 897–916, doi: 10.1130/2010.1206(34).

Thomas, W. A. (2011), The Iapetan rifted margin of southern Laurentia, *Geosphere*, *7*, 97-120, doi: 10.1130/GES00574.1.

Thurber, C. H. (1985), Nonlinear earthquake location: theory and examples, *B. Seismol. Soc Am.*, *75*(3), 779-790.

Tommasi, A., and A. Vauchez (2001), Continental rifting parallel to ancient collisional belts: an effect of the mechanical anisotropy of the lithospheric mantle, *Earth Planet. Sc. Lett.*, *185*, 199-210, doi: 10.1016/S0012-821X(00)00350-2.

Tucholke, B. E., D. S. Sawyer, and J. -C. Sibuet (2007), Breakup of the Newfoundland Iberia rift, *Geol. S., Lond., S. P.*, *282*, 9-46, doi: 10.1144/SP282.2.

Van Avendonk, H. J. A., A. J. Harding, J. A. Orcutt, and W. S. Holbrook (2001), Hybrid shortest path and ray bending method for traveltime and raypath calculations, *Geophysics*, *66*(2), 648-653.

Van Avendonk, H. J. A., D. J. Shillington, W. S. Holbrook, and M. J. Hornbach (2004), Inferring crustal structure in the Aleutian arc from a sparse wide-angle seismic data set, *Geochem. Geophys. Geosyst.*, *5*(8), Q08008, doi:10.1029/2003GC000664.

Van Avendonk, H. J. A., W. S. Holbrook, G. T. Nunes, D. J. Shillington, B. E. Tucholke, K. E. Louden, H. C. Larsen, and J. R. Hopper (2006), Seismic velocity structure of the rifted margin of the eastern Grand Banks of Newfoundland, Canada, *J. Geophys. Res.*, *111*, B11404, doi: 10.1029/2005JB004156.

Van Avendonk, H. J. A., L. L. Lavier, D. J. Shillington, and G. Manatschal (2009), Extension of continental crust at the margin of the eastern Grand Banks, Newfoundland, *Tectonophysics*, *468*, 131-148, doi: 10.1016/j.tecto.2008.05.030.

Van Wijk, J.W. (2005), Role of weak zone orientation in continental lithosphere extension, *Geophys. Res. Lett.*, *32*, L02303, doi: 10.1029/2004GL022192.

Voss, M., and W. Jokat (2007), Continent-ocean transition and voluminous magmatic underplating derived from P-wave velocity modelling of the East Greenland continental margin, *Geophys. J. Int.*, *170*, 580-604, doi: 10.1111/j.1365-246X.2007.03438.x.

Wang, Z. (1997), Seismic properties of carbonate rocks, in *Carbonate Seismology*, *Geophys. Dev. Ser.*, Vol. 6, edited by I. Palaz, and K. J. Marfurt, pp. 29–52, SEG, doi:10.1190/1.9781560802099.ch3.

White, R. S., and D. McKenzie (1989), Magmatism at rift zones: the generation of volcanic continental margins and flood basalts, *J. Geophys. Res.*, *94*(B6), 7685-7729, doi: 10.1029/JB094iB06p07685.

White, R. S., D. McKenzie, and K. O'Nions (1992), Oceanic crustal thickness from seismic measurements and rare earth element inversions, *J. Geophys. Res.*, *97*, 19683-19715, doi: 10.1029/92JB01749.

White, R. S., T. A. Minshull, M. J. Bickle, and C. J. Robinson (2001), Melt generation at very slow-spreading oceanic ridges: constraints from geochemical and geophysical data, *J. Petrol.*, *42*(6), 1171-1196, doi: 10.1093/petrology/42.6.1171.

Whitmarsh, R. B., G. Manatschal, and T. A. Minshull (2001), Evolution of magma-poor continental margins from rifting to seafloor spreading, *Nature*, *413*, 150-153, doi: 10.1038/35093085.

Wilkerson, A., W. D. Carlson, D. Smith (1988), High-pressure metamorphism during the Llano orogeny inferred from Proterozoic eclogite remnants, *Geology*, *16*, 391-394.

Wilson, M. (1997), Thermal evolution of the Central Atlantic passive margins: continental break-up above a Mesozoic super-plume, *J. Geol. Soc.-Lond., 154*, 491-495.

Winker, C. D., and R. T. Buffler (1988), Paleogeographic evolution of early deep-water Gulf of Mexico and margins, Jurassic to middle Cretaceous (Comanchean), *Am. Assoc. Petr. Geol. Bull., 72*(3), 318–346.

Withjack, M. O., R. W. Schlische, and P. E. Olsen (1998), Diachronous rifting, drifting, and inversion on the passive margin of central eastern North America: an analog for other passive margins, *Am. Assoc. Petr. Geol. Bull., 82*(5), 817-835.

Withjack, M. O., R. W. Schlische, and P. E. Olsen (2012), Development of the passive margin of eastern North America: Mesozoic rifting, igneous activity, and breakup, in *Regional geology and tectonics: Phanerozoic rift systems and sedimentary basins*, edited by D. G. Roberts and A.W. Bally, pp. 301-335, Elsevier Science, Burlington.

Young, H. P., and C.-T. A. Lee (2009), Fluid-metasomatized mantle beneath the Ouachita belt of southern Laurentia: Fate of lithospheric mantle in a continental orogenic belt, *Lithosphere, 1*, 370-383, doi:10.1130/L72.1.

Zandt, G., and C. J. Ammon (1995), Continental crust composition constrained by measurements of crustal Poisson's ratio, *Nature*, 374, 152-154.

Zelt, C. A., K. Sain, J. V. Naumenko, and D. S. Sawyer (2003), Assessment of crustal velocity models using seismic refraction and reflection tomography, *Geophys. J. Int., 153*(3), 609-626, doi: 10.1046/j.1365-246X.2003.01919.x.

Ziegler, P. A. and S. Cloetingh (2004), Dynamic processes controlling evolution of rifted basins, *Earth-Sci. Rev., 64*(1-2), 1-50, doi: 10.1016/S0012-8252(03)00041-2.